



Issue 52



***International Journal
of Energy and
Environmental
Engineering***



Influence of architectural space layout and building perimeter on the energy performance of buildings: A systematic literature review

Harsha Latha¹ · Shantharam Patil¹ · Pradeep G. Kini¹

Received: 6 June 2022 / Accepted: 13 August 2022 / Published online: 8 September 2022
© The Author(s) 2022

Abstract

The space layout is very essential in building design development and can significantly influence the energy performance of the built environment. Space layout design, which occurs during the early stages of scheme conception and design development, is one of the most important tasks in architectural design. This systematic literature review focused on the investigation of space layout and perimeter design variables on the energy performance of the buildings and the study of major energy performance indicators, such as lighting, ventilation, heating, and cooling load considering climatic factors. The Scopus database was used for a thorough investigation of the publications using space layout relevant keywords to study building energy performance. About 55 primary articles were assessed based on the impact of different variables concerned with space layout design mainly building perimeter variables on the energy performance of the building. From the review, we can conclude that by enhancing the perimeter design variables and spatial configuration substantial amount of energy can be saved. The orientation of the building, climate occupancy, and building form have a major role in the energy consumption investigation. According to the study, hospitals consumes more energy due to specific functional requirement than other buildings, and studies on the spatial configuration of the hospital is comparatively less where further studies can consider this issue along with the combination of multiple performance indicators. Well-configured space layout design may prevent unreasonable energy consumption and enhance the overall sustainability of the building and contribute to climate change mitigation.

Keywords Sustainable built environment · Energy efficiency · Building envelope · Cooling load · Lighting · Ventilation

Abbreviations

ASHRAE	American Society of Heating, Refrigerating and Air-Conditioning Engineers
CO ₂	Carbon dioxide
DHW	Domestic hot water
ECBC	Energy conservation building code
EPB	Energy performance of the building
EPI	Energy performance indicator
HVAC	Heating ventilation and air conditioning
kWh/m ²	Kilo watt-hour/square meter
SLR	Systematic literature review
WWR	Window to wall ratio

Introduction

Globally buildings consume 30–40% of total energy and emit 30% of CO₂ [1, 2]. Worldwide energy consumption increased by approximately 2–3%, twice the average rate of growth since 2010, owing to a strong global economy as well as increased cooling and heating energy requirements [3]. The building sector is responsible for about 55% of the global electricity use [4]. The buildings like schools, restaurants, hotels, hospitals, museums, and others with a wide variability of uses and energy requirements, i.e., lighting, heating, ventilation, air-conditioning (HVAC), domestic hot water (DHW), refrigeration, food preparation, etc. Economic and population growth raises the demand for services in the field of healthcare, education, culture, hospitality, etc. along with its energy consumption [5]. Buildings have a lot of potential for energy efficiency, but there are some special regulations and acts that must be followed to achieve this. To achieve energy efficiency, appropriate design solutions should be established related to the causes that influence

✉ Shantharam Patil
patil.s@manipal.edu

¹ Manipal School of Architecture and Planning, Manipal Academy of Higher Education, Manipal, Karnataka 576104, India



the energy performance of the building (EPB). Climate, architectural form, construction materials, and enclosure are some of the elements that need to be considered, as well as overall equipment efficacy, building occupancy, and occupant behavior patterns. Modern energy efficiency technologies are largely focused on improving building envelope performance, efficient lighting systems, water conservation, renewable resource adaptation, intelligent control systems, HVAC, and so on. A combination of excellent architectural and energy system design, as well as efficient operations and maintenance post occupancy, determines the amount of energy utilized. Many countries have implemented energy-saving policies and standards, and energy conservation in architectural design is a significant factor [6]. According to the 2015 report by US Department of Energy, it is indeed important to remember that different climates will almost certainly require different designs and equipment and that the performance and value of any component technology are dependent on the system for which it is used. The rate of energy needs and the physical comfort of the users are all commonly linked. The building and its design, in combination with the surrounding environment, have a substantial effect on the energy system adopted and its related efficiency.

Influence of architectural space layout on the energy performance of the building

Architecture involves the design, construction, and conception of built space. Architects design and develop structures that are complex systems with a variety of architectural elements. From the user's perspective, many factors of environmental ability, legibility, and imageability, such as structured space and building typology, as well as the intimate interaction between inside and outside space, are required to interpret building layouts. The building design is a complicated process in which crucial decisions about the building's various systems are made at an early stage [7]. Any building's usage with a combination of architectural design, including geometry and materials, can have a significant impact on its environmental behavior [8]. Due to shifting interior and external walls, the layout boundary can also be one of the design variables of the space layout design with a non-fixed boundary. Changing space layout variables proved a reduction in the annual final energy consumption [9]. It has also been demonstrated that most of the existing unneeded space in buildings results from oversized public access and waiting rooms, as well as incorrect hallway design, unnecessary passages, oversized spaces, and increased service areas such as washrooms, offices, service areas, and others. Unacceptable height, place, and shape values for a building can lead to ineffective space use, resulting in wastage of space and added energy and material consumption [10]. The

energy-efficient spatial configurations include effective volumetric variation in spaces along with strategic positioning of windows, and the use of elements such as window shades, and shaded courtyards to reduce direct solar radiation as well as reduce mechanical energy consumption. Well-thought-out layout design may avoid unnecessary energy consumption to enhance the overall sustainability of the building and contribute to climate change mitigation [11]. Gracia et al. [12] concluded appropriate infrastructure planning turns out to be a key element in meeting energy efficiency requirements where they investigated that an optimal building layout or efficient building design reduces energy consumption due to heating and air conditioning systems. Zhang et al. [13] tested by modifying many passive design characteristics of the buildings to maximize the daylight, energy, and thermal performance of three classic types of classrooms in the north of China. There are a less number of research conducted that focuses on space planning and the ways space layout influences energy performance. Musau et al. [14, 15] found the possible influences of typical mixed, closed, and open layouts and their space utilization on the energy performance of the laboratories and office buildings. The study was conducted at all occupancy levels to conclude the best combination of different layout configurations that helps to achieve a reduction in the floor area as well as its energy consumption. Bano et al. [16] investigated the placement of service rooms with minimal openings as thermal buffering on the west side and decreasing the surface-area-to-volume ratio as a design strategy to regulate the heat gain and, as a result, reduce the cooling load in six office buildings located in India's composite climate. They also determined that locating the service core all along the exterior provides for natural ventilation and sunlight. Du et al. [17] experimented with the effect of spatial layout on energy performance by creating 11 office layout variants and evaluating them for three different climatic zones to determine the day illumination effect through the design and execution of shading devices. The study used dynamic simulation and suggested future investigation of the influence of neighboring structures on natural ventilation systems related to air pressure, air velocity, and air direction. Effective space arrangement designs also resulted in a 65% reduction in lighting and a 10% reduction in heating and cooling demand. Shahzad et al. [18] analyzed energy use by comparing standard cellular plans to open office plans and discovered that the cellular plans had higher energy consumption. Gärtner et al. [19] by using three distinct HVAC systems with four different control zoning schemes, investigated the influence of a flexible workspace layout design on thermal comfort and energy demand in a contemporary open-plan office space using dynamic thermal simulation. Zhang et al. [20] investigated the different spatial configurations such as a single-sided covered corridor type, a single-sided open corridor type,



and a double-sided corridor type school. The study found that the double-sided enclosed corridor type was the best option due to its high energy performance and that the one-side covered corridor type concluding was the least suitable due to its relatively decreased visual comfort quality for the cold climate. Short et al. [21] recommended a feasible overall design approach as well as more detailed configurations for specific space types to empower clients and architects to execute low-energy ventilation and cooling strategies. Aldawoud [22] studied that atrium shape is a significant component to consider from a design and energy efficiency standpoint, primarily affecting the building's heating and cooling loads. The overall space layout is always associated with space characteristics such as measurements, space form, internal partitions and openings, function allocation, boundary characteristics such as building form and orientation, enclosure design space properties such as functional requirements such as heating, cooling, ventilation, and lighting, and these are all integrated based on EPB. It is necessary to use integrated design approaches that go beyond functional requirements to enhance the passive potential of different areas for a variety of environmental requirements across varied activities [14]. We can observe the multiple variables related to the space layout effect from the research of Delgarm et al. [23] where they evaluated with the help of simulation-based multi-objective optimization, the influences of specific architectural elements of a standard room on the energy consumption of buildings in four different climatic regions in Iran and it was discovered that using optimized spatial configuration for each climatic condition can save a significant amount of energy. The study looked at the impact of various building spatial design aspects such as building orientation, details of overhang, shading, window size, glazing, and wall material qualities on building energy usage in four different Iranian climates. Lavy et al. [24] found an incremental examination of simplified core building forms, daylighting controls, and 9 layout variants based on the shape (length and breadth ratio), the number of floors, window to wall ratio (WWR) of 40% along with external overhangs and their impact on the building exterior, as well as building orientation using simulation method of US military hospitals.

The research on the influence of architectural space layout on EPB is very less compared to the research on energy-efficient design considering various approaches with related variables or parameters of architectural space layout like geometry/form, envelope, façade, windows, and shading devices. Along with these variables, geographic locations and climate for different building typologies also investigated energy performance through various methodologies and for different occupancy rates. From past analysis, much research has been conducted exclusively on other design objectives like safety, wayfinding, logistics, connectivity,

functional performance, etc. than energy performance. Because of the solar gain and solar exposure of the areas, the spatial arrangement determines the thermal and daylighting properties of a building. As a result, tools aimed at early design should consider the spatial configuration of the building as a component of energy-related aspects [7]. The novelty of this systematic literature review (SLR) highlights the influence of building design variables on the energy performance of various building typologies. The various energy indicators of buildings mainly cooling, and heating load, lighting, and ventilation are comprehensively investigated.

The main objective of this SLR is to identify the most significant space layout-related variables on the EPB along with effective methodology as well as gap identification in this field to direct further research. Because an SLR is a synthesis of previous research to answer specific questions, it aids researchers in synthesizing a large amount of evidence by explaining differences between studies and providing direction for future research or directing researchers to use a scientific approach in their studies. The questions that are subjected to framework and scientific investigation in SLRs can pave the way for more research by looking into the consistency and generalizations of data in building EPB in connection to space layout, particularly in hospitals. It is indeed useful for generating hypotheses that may be empirically tested [25].

The research questions are as below

1. What are the main aspects that are considered in the study on the EPB in association with architectural space layout and building perimeter parameters?
2. What are the different space layouts and perimeter variables influencing the EPB?
3. What are the different methodologies that are used to investigate the energy performance in association with architectural space layout along with building perimeter aspect?

Methodology

This SLR aims to identify crucial areas where more scientific research is needed, with an emphasis on the EPB. The concerns investigated in SLR through meticulous and scientific analysis may open the path for additional research by examining the consistency and generality of data in the field of EPB, particularly in hospitals. It is also useful for generating hypotheses that may be tested empirically. A literature review was undertaken to determine the impact of variables of spatial configurations on EPB, as well as different approaches and performance metrics, along with interconnection between the various objectives. We used the terms influence of “Space



layout on EPB”, “Simulation-based EPB”, and “influence of space layout variable on EPB” in our search. A literature review was undertaken to determine the impact of space layout variables on EPB, as well as different approaches and performance metrics, as well as the inter-connection between the various objectives. The Scopus database was used to find papers published during the period 2006–2021 and approximately 4300 records were retrieved in the beginning using the defined keywords and the number of publications kept increasing year wise as shown in Fig. 1.

The number of works of literature was decreased to 579 articles after excluding grey literature, extended abstracts, presentations, book chapters, keynotes, non-English language papers, and inaccessible publications. Only 186 articles remained for the main body reading from the selected abstracts. 140 of them were evaluated for EPB concerning space layout and its perimeter variables, and these articles were downloaded for additional screening. There are 128 articles considered for quality assessment. In the end, 55 papers met all the inclusion criteria considered in this SLR from selected journals that are having a greater number of articles in the context of the subject area (Fig. 2).

The review papers concentrated on typologies other than residential buildings in the final exclusion step in the interest of improving global comparisons [27]. The structure of the paper includes the beginning introduction, where the description of the space layout and EPBs are elaborated. The next four parts of the paper discussed determining factors for space layout on the EPB, space layout and its related variables on EPB, performance indicators, methodologies involved in the investigation of space layout variables, and sample design details during the investigation of the EPB. Then, the entire study analysis and conclusion with potential areas for future investigation are formulated in this review paper.

Inclusion criteria for articles

Articles on investigating the EPB of buildings of various typologies in connection to various space layout variables and energy performance indicators, as well as the various approaches used in the research, were included. For this systematic literature evaluation, only research publications with an impact factor of greater than 2.0 from the Scopus database were chosen. Impact factor calculation of journal as shown in the equation below.

$$ISx = \frac{\text{Citations} - x + \text{Citations} - y}{\text{Publications} - x + \text{Publications} - y}$$

IS = On average, the articles of the Journal. x = Year of calculation, y = Previous year.

Exclusion criteria for articles

The articles concentrating exclusively on thermal comfort, construction related, the impact of environmental factors, and Net-zero building theory, and older than 2006 articles are excluded in this review article. The conference papers, book chapters, thesis reports along with review articles are excluded. The articles from the journal had an impact factor of less than 2.0 and articles from other than Scopus databases are not considered for this paper.

Quality assessment

The selection of reliable and quality papers related to the identification of topics is a very big challenge in the SLR. Even though there is no standard methodology or process to select high-quality papers, journals with clear context and methodologies and value addition to the body of knowledge on the energy performance of buildings are considered for the review along with an impact factor of more than 2.0 (Fig. 3).

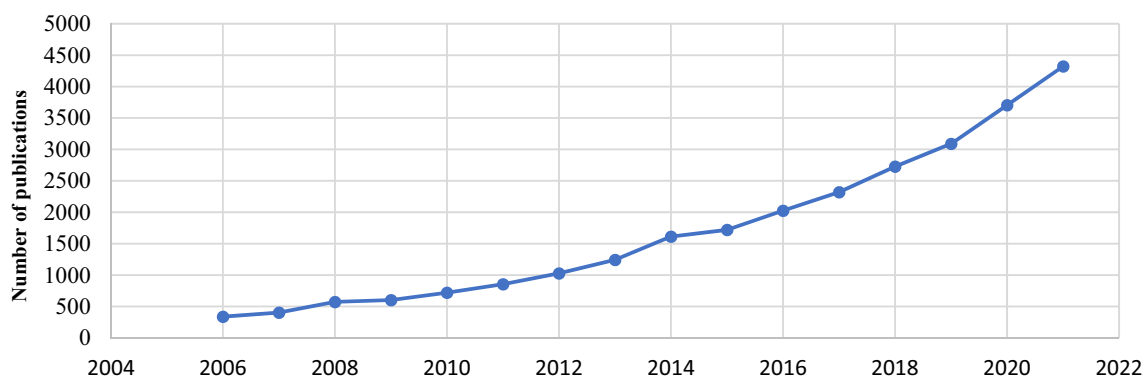


Fig. 1 Publication trend from 2006 to 2021 on EPB based on search criteria. Source: Scopus database



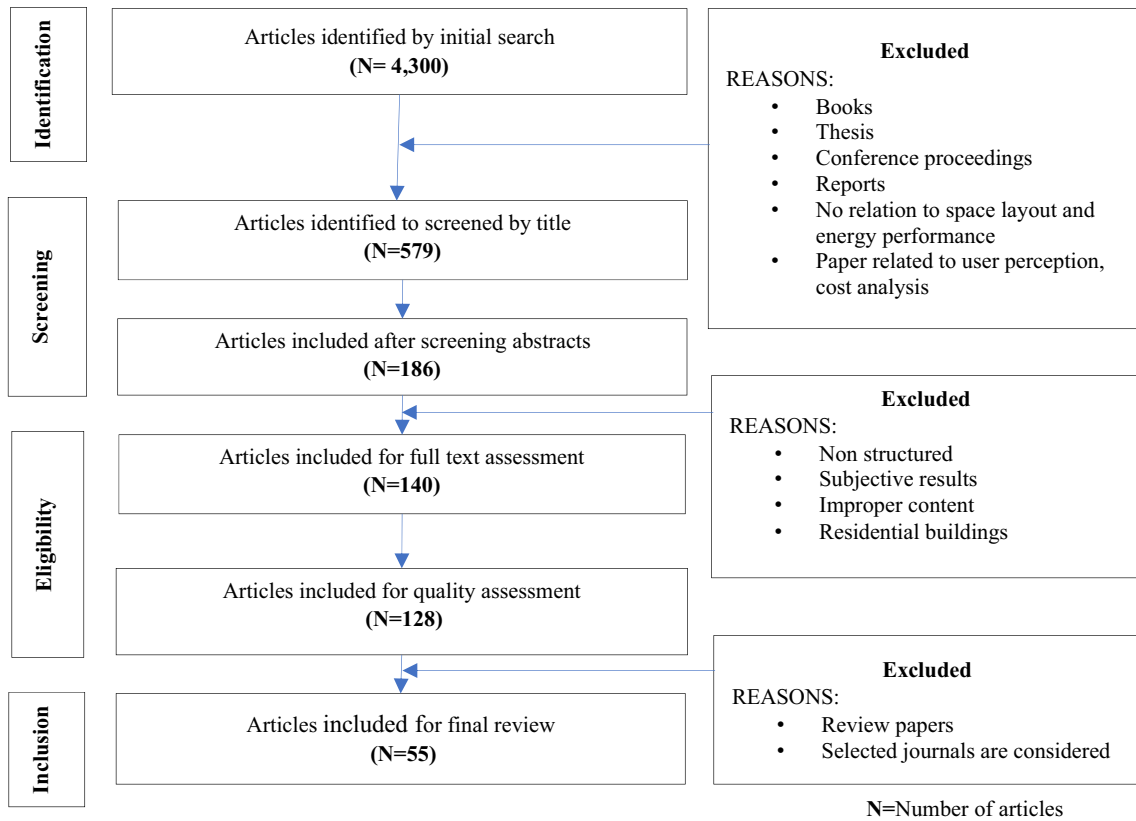
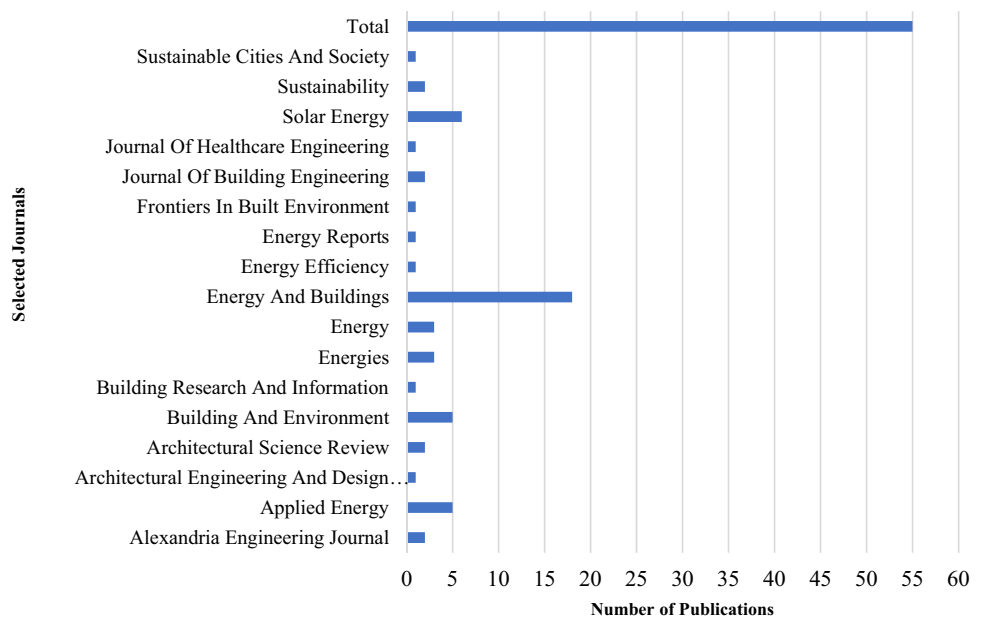


Fig. 2 Flow diagram of the systematic review process [26]

Fig. 3 The selected journal list and publication numbers of review articles. Source: Scopus database



Data extraction

- Determining factors for space layout influencing EPB.
- Space layout and perimeter-related variables on energy performance.
- EPB indicators like total building energy performance, natural ventilation, heating, and cooling load, etc.
- Methodologies on an investigation of energy performance along with simulation software.

The typical format for reviewing each article included the following parts: Authors, year of publication, journal with impact factor, geographic location, and climate zone of the study, building typology, keywords, focus area, methodology, variables, software used, performance indicator, sample design, a summary of the study as mentioned in Tables 1 and 2.

General characteristics of reviewed literatures

- A. The keywords, “space layout”, “Energy”, “Buildings”, “Simulation”, and “Efficiency” are repeated in most of the reviewed papers. Thermal comfort, optimization, office, cooling, ventilation, and daylight also occurred repeatedly by many authors along with performance, consumption, etc.
- B. Building typology- The search result shows many researchers focused on office buildings that had very basic functional parameters, and researchers discovered an ideal model to experiment and analyze the impact of space layout configurations and space boundary parameters and then the emphasis on hospital buildings (Fig. 4).
- C. From the identified review papers, we can analyze that a major part of publications from Europe followed by Asia. The major Number of publications country-wise are from China.

Determining factors for space layout to influence the energy performance of the building

Before moving on to the full review, it's critical to understand how the space layout parameters of the building can influence the EPB. There are several determining factors to decide the influence of space layout variables on the performance of energy. Orientation of the building and windows, layout configurations, shading details, window-to-wall ratio, glazing details along with climate and occupancy are the

more prominent variables from the reviewed works of literature which significantly affect the total energy demand including heating, cooling, lighting, and ventilation along with thermal comfort and visual comfort.

Occupancy

Many studies ignored the effects of user activity on EPB by employing constant or inevitable occupancy inputs, which frequently result in differences between simulated and actual building performance, as well as the simulated setting becomes less realistic to real-world conditions. Because inhabitants, not buildings, are the principal users of energy, correct integration of technology and human elements may influence the design and functioning of low-energy structures [73]. Space layout, usage patterns, and system control approach defined during the design stage will differ once the buildings start functioning and result in energy ineffectiveness [15]. Space layouts also influence occupant behavior, such as whether they attend an activity or change the environment where the activity takes place. Varied occupancy levels have variable internal gains as well as different comfort requirements, such as the overall quantity of ventilation. Furthermore, diverse functions have varying levels of comfort requirements. Different comfort requirements among functions have an impact on overall energy usage [7]. The annual energy utilization of the building are all can be predicted by occupancy. Interior space design and control for diverse occupancy patterns must be carefully studied, as their effects on energy consumption may have a considerable impact on the use of office ventilation in a building. Buildings often have multiple zones, including heat transfer and balancing between them. Loads in one zone may escalate due to the varying thermal conditions of neighboring zones induced by occupant diversity [50]. These buildings may house a variety of activities with different operating hours, functional requirements, and occupancy patterns, all of which might affect their efficiency [73]. García Sanz-Calcedo et al. [35] predicted the direct proportionate correlation between the number of users in a Medical Clinic, its floor space, and the yearly energy usage of the building. Musau et al. [15] proposed an integrated planning strategy that goes beyond functional requirements to maximize the passive potential of varied spaces and activities for a variety of environmental needs. The strategy also showed users, systems organization, and activities are the determinant factors of energy performance by demonstrating the wide differences in per capita loads with space utilization intensity across activity spaces as well as layout options. Rajagopalan and Elkadi [44] studied the energy performance of three medium-sized hospitals in Victoria, Australia that is only operational during the day to find variances in energy use between different functional sections within the



Table 1 General details of the reviewed articles

Sl. No	Author	Year	Journal	Impact factor	Publisher	Place	Climate	Building type
1	Aksoy et al. [28]	2006	Building and Environment	7.176	Elsevier BV	Europe/Turkey	Cold	NS
2	Musau et al. [14]	2007	Architectural Science Review	3	Taylor and Francis Ltd	Europe/UK	NS	Laboratory Buildings
3	Tzempelikos et al. [29]	2007	Solar Energy	5.742	Elsevier Ltd	Europe/Sweeden	NS	Office
4	Yang et al. [30]	2008	Applied Energy	10.81	Elsevier BV	China–Harbin, Beijing, Shanghai, Kunming, and Hong Kong	Warm temperate	Office
5	Musau and Steemers [15]	2008	Architectural Science Review	3	Taylor and Francis Ltd		NS	Office
6	Aldawoud et al. [31]	2008	Energy and Buildings	6.675	Elsevier BV	USA/Arizona, Florida, Chicago, Minneapolis	Hot/dry, hot/humid, temperate, cold	Office
7	Pourazis et al. [32]	2008	Energy and Buildings	6.675	Elsevier BV	Europe/Sweeden	NS	Office
8	Short et al. [21]	2009	Building Research and Information	6.11	Taylor and Francis Ltd	Europe/UK	NS	Hospital/Healthcare Facilities
9	Sozer [33]	2010	Building and Environment	7.176	Elsevier BV	Europe/Izmir, Turkey	hot Mediterranean climate	Hotels
10	Nielsen et al. [34]	2011	Solar Energy	5.742	Elsevier Ltd	Europe/Denmark	cold north-European climate,	Office
11	Justo García Sanz-Calcedo et al. [35]	2011	Energy and Buildings	6.675	Elsevier BV	Europe–Spain/Extremadura	NS	Hospital/Healthcare Facilities
12	Pisello et al. [36]	2012	Energies	3.454	MDPI	USA/New York	NS	Institute Building
13	Adamu et al. [37]	2012	Building and Environment	7.176	Elsevier BV	Europe/UK	NS	Hospital/Healthcare Facilities
14	Ascione et al. [38]	2013	Energy and Buildings	6.675	Elsevier BV	Europe/Italy, Naples	Mediterranean climates	Hospital/Healthcare Facilities
15	Schulze and Eicker [39]	2013	Energy and Buildings	6.675	Elsevier BV	Europe/Germany, Italy and Turkey	Moderate	Office
16	Zhou and Zhao [40]	2013	Energy and Buildings	6.675	Elsevier BV	Asia/China (Shanghai, Beijing, Shenyang, Harbin)	Hot summer with hot and warm winter, cold, severe cold, temperate	Office
17	Tulsyan et al. [41]	2013	Energy and Buildings	6.675	Elsevier BV	Asia/India, Jaipur	Hot and dry	Hotels, Hospitals, Institutes, Retail, Government Offices, Private Offices
18	Aldawoud [22]	2013	Energy and Buildings	6.675	Elsevier BV	USA/Phoenix, Arizona, Miami, Florida, Chicago, Illinois, Minneapolis, Minnesota	Hot-dry, hot-humid, temperate, cold	Office
19	Susorova et al. [42]	2013	Energy and Buildings	6.675	Elsevier BV	USA	Hot, warm, mixed cool cold, very cold	Office



Table 1 (continued)

Sl. No	Author	Year	Journal	Impact factor	Publisher	Place	Climate	Building type
20	García-Sanz-Calcedo [43]	2014	Energy and Buildings	6.675	Elsevier BV	Europe/Extremadura (Spain)	NS	Hospital/Healthcare Facilities
21	Rajagopalan and Elkadi [44]	2014	Journal of Healthcare Engineering	3.06	Hindawi Limited	Australia/Victoria	Temperate	Hospital/Healthcare Facilities
22	Lavy et al. [24]	2015	Architectural Engineering and Design Management	2.19	Taylor and Francis Ltd	USA/Fairbanks, Alaska, San Antonio, Texas	NS	Hospital/Healthcare Facilities
23	Wang and Greenberg [45]	2015	Energy and Buildings	6.675	Elsevier BV	USA—Chicago, Houston and San Francisco	Humid, Mediterranean mild climate	Commercial
24	Chedwal [46]	2015	Energy and Buildings	6.675	Elsevier BV	Asia/India, Jaipur	Hot and dry	Hotel
25	Echenaguacia et al. [47]	2015	Applied Energy	10.81	Elsevier BV	USA/Palermo, Torino, Frankfurt, and Oslo	Climates of Palermo, Torino, Frankfurt, and Oslo	Office
26	Zahiri and Altan [48]	2016	Frontiers in Built Environment	2.11	Frontiers Media S.A	Asia/Iran, Tehran	Hot and Dry Climate	School Building
27	Taleb [49]	2016	Journal of Building Engineering	5.318	Elsevier BV	Asia/UAE Abu Dhabi	Warm humid	Hospital/Healthcare Facilities
28	Yang et al. [50]	2016	Energy	7.477	Elsevier Ltd	USA/Los Angeles, California	NS	Office
29	Amaral et al. [51]	2016	Sustainable Cities and Society	8.53	Elsevier BV	Europe/Coimbra, Portugal	Summer Mediterranean climate	NS
30	Delgarm et al. [23]	2016	Applied Energy	10.81	Elsevier BV	Asia/Iran	NS	NS
31	Goia et al. [52]	2016	Solar Energy	5.742	Elsevier Ltd	Europe/Oslo, Frankfurt, Rome and Athens	Cold, temperate	Office
32	Harmathy et al. [53]	2016	Energy	7.477	Elsevier BV	Europe/Serbia	Temperate climate	Office
33	Morgenstern et al. [54]	2016	Energy and Buildings	6.675	Elsevier BV	Europe/England	NS	Hospital/Healthcare Facilities
34	Lu et al. [55]	2016	Energy and Buildings	6.675	Elsevier BV	Asia/China (West of Inner Mongolia Autonomous Region)	Severe cold area	Office
35	Zhang et al. [20]	2017	Energy and Buildings	6.675	Elsevier BV	Asia/China	Cold	School Buildings
36	Shahzad et al. [56]	2017	Applied Energy	10.81	Elsevier BV	Europe/Norway/British	NS	Office
37	Ma et al. [57]	2017	Energy and Buildings	6.675	Elsevier BV	Asia/Northern China	NS	Public Building
38	Alhuwayil et al. [58]	2019	Energy	7.447	Elsevier BV	Dhahran/Saudi Arabia	Warm humid	Hotel
39	Wagdy et al. [59]	2017	Solar Energy	5.742	Elsevier Ltd	Africa/Egypt, Cairo	Desert	Hospital/Healthcare Facilities
40	Bayoumi [60]	2017	Building and Environment	7.176	Elsevier BV	Asia/Jeddah and Riyadh	Hot humid and hot arid	Office



Table 1 (continued)

Sl. No	Author	Year	Journal	Impact factor	Publisher	Place	Climate	Building type
41	Bano and Sehgal [16]	2018	Solar Energy	5.742	Elsevier Ltd	Asia/India (Delhi, Gurgaon, and Hyderabad)	Composite climate	Office
42	Prieto et al. [61]	2018	Energy and Buildings	6.675	Elsevier BV	Asia/Hongkong	Warm climate	Commercial
43	González et al. [62]	2018	Sustainable Cities and Society	8.53	Elsevier BV	Europe/Spain	NS	Hospital/Healthcare Facilities
44	Omar et al. [63]	2018	Alexandria Engineering Journal	3.732	Alexandria University	Asia/Beirut	Mediterranean climate	Educational Building
45	Bawaneh et al. [64]	2019	Energies	3.454	MDPI Multidisciplinary Digital Publishing Institute	USA	NS	Hospital/Healthcare Facilities
46	Guo and Bart [65]	2020	Sustainability	3.25	MDPI AG	Asia/China (Changchun, Beijing, Shanghai, Haikou, Kunning)	Cold, hot summer and cold winter, hot summer, and warm winter	Office
47	William et al. [66]	2020	Alexandria Engineering Journal	3.732	Alexandria University	Africa/Egypt, Alexandria	Hot-humid	Hospital/Healthcare Facilities
48	Cesari et al. [67]	2020	Energies	3.454	MDPI Multidisciplinary Digital Publishing Institute	Europe–Italy (Milan, Bologna, Rome, and Naples)	NS	Hospital/Healthcare Facilities
49	Fang et al. [68]	2019	Solar Energy	5.74	Elsevier BV	Miami, Atlanta, and Chicago	Hot, mixed, and cold climates	Office
50	Kyritsi et al. [69]	2020	Building and Environment	4.971	Elsevier BV	Europe/Urban Center of Nicosia, Cyprus	Mediterranean	Office
51	Gärtner et al. [19]	2020	Energy and Buildings	6.675	Elsevier BV	Europe/Stuttgart, Germany	Performance of different HVAC systems	Commercial Building
52	Pilechiha et al. [70]	2020	Applied Energy	10.81	Elsevier BV	Asia/Iran, Tehran	Hot, semi-arid climate	Office
53	Aumón-Villa et al. [71]	2021	Energy Efficiency	2.57	Springer Nature B.V	Europe/Madrid (Spain)	NS	Hospital/Healthcare Facilities
54	Du et al. [17]	2021	Journal of Building Engineering	5.318	Elsevier BV	Europe/Amsterdam, Netherlands, Harbin, Asia–China, Singapore	Temperate, cold, tropical	Office
55	Zou et al. [72]	2021	Energy Reports	6.87	Elsevier BV	Asia/China	Hot and humid area	School Building

NS = Not specified



Table 2 Study focus and findings along with the methodology and sample design from reviewed articles

Author	Study focus	Method of research	Software	Independent variables	Dependent variables	Sample details	Key findings
Aksoy et al. [28]	The impact of passive design parameters along with building shape and orientation position-on heating demand in Turkey has been studied theoretically	Mathematical analysis	NA	Orientation, shape, insulation material	Heating load	The intermediate floor of a multi-story building-3 shape having the length to breadth ratio- 1:1, 1:2, 2:1	Buildings with a square shape have greater advantages in heating design. The best orientation angles are 0° and 80° for buildings with a length-to-depth ratio of 2/1 and 1/2, respectively
Musau et al. [14]	In the United Kingdom, the TAS, Lightscape, and Excel software programs were used to investigate the possible implications of conventional open, mixed, and closed design and their space utilization densities/intensities of energy use in laboratory buildings	Building energy simulation	Thermal analysis software (TAS), Lightscape and excel software	Open, closed, and mixed layouts, orientation	Energy performance	3 Types of layouts -open, closed, and mixed layouts	The various ways in which users, activities, and systems can be structured in response to space-to-space environmental diversity are important factors of laboratory energy performance
Tzempelikos et al. [29]	A linked lighting and thermal simulation in Sweden was used to calculate the simultaneous influence of glass area, shading device attributes, and shading control on building cooling and lighting demand of an office	Building energy simulation	Energy Plus/TRN-SYS	WWR	Lighting load	A typical private perimeter office space of 4 m × 4 m × 3 m size in Montreal	An integrated approach for automatic control of motorized shading in conjunction with programmable electric lighting systems could result in a large reduction in energy consumption for cooling and lighting in peripheral spaces, depending on climatic conditions and orientation



Table 2 (continued)

Author	Study focus	Method of research	Software	Independent variables	Dependent variables	Sample details	Key findings
Yang et al. [30]	The energy performance of office building envelope designs in the five key climate zones of china was evaluated	Mixed method-case study/statistical analysis	NA	Ratio and shading parameters, orientation, wall, window, roof, skylights, WWR	Energy performance, cooling demand	113 offices -Harbin-9 + Beijing-55 + shanghai-18 + Kunming-12 + Hong kong-19	Wall, roofs, windows, and skylights have higher heat gain/loss than those specified by local design/energy rules, prompting recommendations to increase the energy efficiency of existing buildings in china in the different climatic zone
Musau et al. [15]	In the United Kingdom, the TAS, Lightscape, and Excel software packages were used to examine the impact of space planning and usage on the energy performance of office spaces	Building energy simulation	Thermal analysis software (TAS), Lightscape, and excel software	5-space layout variants, occupancy, space area	Energy performance	5 Different types of office layout-hive, den, club, cell, and combi	Space planning and utilization have a significant impact on energy consumption and are crucial in assessing energy performance. Differences in combined thermal and lighting loads are 19% and 51% throughout the UK peak winter and summer seasons, respectively, with an average occupancy of 50%, whereas variations in per capita load are 80% and 16% during the inquiry

Table 2 (continued)

Author	Study focus	Method of research	Software	Independent variables	Dependent variables	Sample details	Key findings
Aldawoud et al. [31]	The energy performance of a central atrium is evaluated and compared to that of a courtyard with the same Geometric proportions	Building energy simulation	DOE2.1E	Glazing types and glazing area ratios, climate, number of floors	Energy performance	An open central courtyard surrounded by four adjacent spaces, a space in each direction	The open courtyard structure performs better in terms of energy efficiency than the shorter buildings. However, as the building height grows, the enclosed atrium demonstrates higher energy performance
Poirazis et al. [32]	To investigate the effect of glass on energy consumption during the occupation stage of building options with 30%, 60% and 100% window to exterior wall area in Sweden	Building energy simulation/Sensitivity analysis	IDA ICE 3.0	Orientation, open and cell type plan, the control set points, type and size of windows, type and position of shading devices	Thermal comfort, energy consumption	Six-story high building having a total height of 21 m and the floor area of 6177 m ² with two long and facades are identical. The room height was 2.7 m and the distance between floors was 3.5 m	Highly glazed single-skin structures consume more energy during the occupation stage, which can be reduced by lowering the thermal transmittance and the total solar transmittance of glass
Short et al. [21]	Evaluation of ventilation and energy performance of 200 bed hospitals at UK	Building energy simulation	NS	Floor area	Ventilation, energy performance, cost	More than 1000 room types including clinical and non-clinical spaces of 200-bed, medium sized acute hospitals under NHS Public Sector Comparator (PSC) level of United Kingdom	70% of the net floor space of small-to-medium-sized acute hospitals might be naturally ventilated whereas a hybrid ventilation technique could serve an additional 10% of the net floor area
Sozer [33]	An investigation into the building envelop design on heating and cooling loads, as well as the scope of energy efficiency in a hotel building in Turkey	Building energy simulation	e-QUEST	Walls and roof insulation, Window sizes, window glazing	Heating and cooling loads	A hypothetical model of 21 story light weight structured hotel building which was based on an existing hotel which was constructed in 1992 in Izmir	Precise building envelope design te glazing, insulations and shading reduced 86% of heating load, 60% decrease in cooling and 40% of total site energy load reduction



Table 2 (continued)

Author	Study focus	Method of research	Software	Independent variables	Dependent variables	Sample details	Key findings
Nielsen et al. [34]	Investigation on the façade treatment without solar shading, with fixed and dynamic solar shading for the evaluation of the building's overall energy demand, heating, cooling, and lighting energy demand, as well as its daylight factors in Denmark	Building energy simulation	iDbuild	Solar shading, window heights and orientations	Total energy demand, energy for heating, cooling and lighting, daylight factors	Facades without solar shading, with fixed solar shading, and with dynamic solar shading	Compared to fixed solar shading, the use of dynamic solar shading significantly increased the quantity of daylight available
Justo García Sanz-Calcedo et al. [35]	Assess the impact of the number of users on the energy and environmental characteristics of a health center in Extremadura, Spain	Sensitivity/Statistical analysis based on simple/Multiple correlations	NS	Floor area, Number of users	Energy consumption	69 Health Centers of Extremadura, Spain	Annual energy usage was shown to be lower in facilities with a high associated management factor. It should also be mentioned that energy management can be implemented more effectively in smaller facilities
Pisello et al. [36]	Post-Occupancy Evaluation through In-Situ Analysis on Energy Savings in a New York Institutional Building Using a Dynamic Simulation Model	Numerical analysis, In-field monitoring, Occupants' survey, Dynamic building energy simulation	EnergyPlus	Indoor environmental parameters, Occupancy, thermal zoning	Thermal and Indoor Air Quality	A multipurpose building of having 14 floors + three basements with the total area of 73,019 m ² and 72 m height located in the campus of The Baruch College, Manhattan, New York	Post-occupancy evaluation is an useful method for reducing energy waste in buildings, particularly in complicated and high-efficiency structures that are not operating as well as expected during the concept-design-commissioning stage



Table 2 (continued)

Author	Study focus	Method of research	Software	Independent variables	Dependent variables	Sample details	Key findings
Shahzad et al. [56]	In both summer and winter in Norway, the traditional cellular plan workplace consumed significantly more energy than the open plan office	Statistical analysis (Empirical regression analysis/ANOVA)	NA	Layout, environmental factors, window positioning	Thermal comfort, visual comfort, ventilation-energy consumption, CO ₂ and light level	Two office buildings -Norwegian office built in 2000 and British office built in 2011	Thermal control is secondary in the British approach and the primary system in the Norwegian approach. The energy consumption in Norwegian case studies is significantly higher than in British case studies
Ma et al. [57]	The investigation revealed that the traditional cellular layout workplace consumed much more energy than the open plan office in both summer and winter in Norway	Statistical analysis	eQUEST	Building envelope, heat transfer coefficient/WWR, shading coefficient of external window, lighting/equipment power density		119 public buildings- 99 office buildings + 11 hospital buildings+9 school buildings	According to the orthogonal test, the key elements impacting energy consumption are the air conditioning system, lighting density, and building envelop. The average total energy consumption per unit area of China's public, school, office, and commercial buildings is 147.20 kWh/(m ²), while the average power consumption is 47.96 kWh/(m ² a)
Alhuwayil et al. [58]	the study explored the energy saving potential and economics of incorporating external shading devices with self-shading envelope for a multi-story hotel building in hot-humid climate of Saudi Arabia	Building energy simulation	EnergyPlus/design builder	Shading devices	Energy consumption, heating and cooling load, cost analysis	10-story hotel building	By providing additional space and balcony for hotel rooms along with shading devices, 20.5% of annual energy consumption reduced with reference to baseline hotel building



Table 2 (continued)

Author	Study focus	Method of research	Software	Independent variables	Dependent variables	Sample details	Key findings
Wagdy et al. [59]	Determine the range of sun-breaker cut-off angles and their related tilt angles that resulted in sufficient daylighting performance for the two patient room types at varying WWR and with the wall for Cairo hospitals	Building energy simulation	EnergyPlus/ Grasshopper, Rhinoceros	Sun-breaker cut off-angle, WWR, tilt angles	Energy demand, indoor thermal quality	Two patient room designs -the outboard bathroom patient room design and the inboard bathroom patient room design	When determining the success of a sun breaker, the cut-off angle is more crucial than the tilt angle in delivering acceptable daylighting performance
Bayoumi [60]	Investigation on the relationship between the grade of a window opening and energy savings in a one-sided window opening in two hot settings of an office building in Asia with one humid and one desert climate	Building energy simulation	IDA-ICE	Window opening grade, facade integrated photovoltaics	Cooling load, air changes per hour (ACH)	A typical north-south-oriented office building	The Window opening grade (WOG) and window fraction (WF) in the façade wall is crucial in defining the cooling load of the space and thus its energy demand and these parameters also considered in the daylight optimization
Bano and Sehgal [16]	The efficiency of various design solutions for reducing the HVAC and lighting loads of six office buildings in India was investigated	Case study	NA	Building form, envelope configuration, service core position, WWR percentage of air conditioned space	HVAC load, lighting load, equipment load	Six energy-efficient office buildings in Delhi, Gurgaon, and Hyderabad of India have composite climates	Determined the most cost-effective building envelope design options. Building plan arrangement, mixed-mode ventilation system, and WWR in decreasing HVAC and lighting energy consumption in composite climatic energy-efficient mid- and high-rise office buildings



Table 2 (continued)

Author	Study focus	Method of research	Software	Independent variables	Dependent variables	Sample details	Key findings
Prieto et al. [61]	Investigates the efficiency of selected passive cooling solutions in commercial buildings in Hong Kong's warm environment	Statistical analysis	Energy Plus/Design-Builder	Orientation, climate, shading, glazing size, and type, ventilation	Cooling energy load		The use of passive methods alone will not result in significant savings. Their effectiveness was influenced by the hardness of a certain climate as well as varied building factors
Adamu et al. [37]	The performance of buoyancy-driven airflows was studied in four different natural ventilation approaches suitable for single-bed hospital wards in the United Kingdom	Building energy simulation	PHOENICS, IES	Window opening, inlet/stack/ceiling based natural ventilation (CBNV)	Airflow capacity, thermal comfort, summer overheating, and heating energy consumption in winter	A single occupant of 3.78 m × 6.23 m × 3.5 m with a floor area of 23.55 m ² and a volume of 82.42m ³ of the Great Ormond Street Hospital (GOSH)	A 25 percent trickling ventilation opening fraction is necessary to produce required airflow rates and adequate thermal comfort in winter, and other solutions, except for window-based design, minimize summer overheating to varying degrees
Ascione et al. [38]	Explores a significant application in the realm of energy demand for air-conditioning and thermal-physical properties of the building envelope with reference to a medium-sized hospital in a Mediterranean climate	Case study	Energy Plus/Design-Builder	External wall, basement, and flat roof, building envelope, windows	heating, ventilating, and air conditioning systems, indoor comfort conditions	The National Institute for the Cancer Treatment "G. Pascale" is located on the hill area of Naples having basement + ground + 5 floors	The refurbishment of the building envelope implies an improvement in internal thermal conditions for all HVAC systems under consideration



Table 2 (continued)

Author	Study focus	Method of research	Software	Independent variables	Dependent variables	Sample details	Key findings
Zhou and Zhao [40]	Building envelopes energy-saving technology (BEEST) optimization to improve the energy performance of office buildings in Shanghai, Beijing, Shenyang, and Harbin, China	Mixed method-Building energy simulation/Optimization	TRNSYS	Exterior walls, roof, and exterior windows		11-story typical office building with an area of 26,400 m ² having a story height of 4 m and its aspect ratio is 2.67–5 climatic regions	In cold climates, the building envelopes energy-saving technology with Expanded Polystyrene (EPS) insulation system that has significant energy-saving potential
Schulze and Eicker [39]	Coupled airflow network and dynamic building simulations were carried out to determine the annual thermal comfort and energy savings of office buildings located in Germany, Italy, and Turkey	Building energy simulation	EnergyPlus	Window openings	Thermal comfort, energy consumption	3-story small administration building with a floor area of 1146 m ² and a surface-to-volume ratio (A/V) of 0.48 m ⁻¹ with a flat roof, no basement, and the offices east or west orientated	Natural ventilation systems that are well-designed save between 13 and 44 kWh/m ² of cooling net energy per year for the three locations Stuttgart, Turin, and Istanbul. The electrical energy savings from fan ventilation are around 4 kWh/m ² per year
Tulsyan et al. [41]	Investigation of the energy-saving potential with ECBC for different typologies of the buildings in India	Mixed method -Case study, Building energy simulation	eQUEST software	Envelope parameters, building typology, HVAC, building occupancy/activity	Energy consumption, HVAC load	6 case study buildings -hotels, hospital, institute, retail, government office, and private office	The specific energy usage ranges from 137 kWh/m ² /y for a government facility to 386 kWh/m ² /y for a private office. The percentage of energy saved with ECBC compliance ranges from 17% for institutions to 42% for hospitals

Table 2 (continued)

Author	Study focus	Method of research	Software	Independent variables	Dependent variables	Sample details	Key findings
Aldawoud [22]	The purpose of the study is to determine the impact of the atrium form on the total energy consumption of the building and to find the best energy-efficient atrium design in USA/Phoenix, Arizona, Florida Miami, Chicago, Illinois Minneapolis, Minnesota, and office buildings	Building energy simulation	DOE-2.1E	Geometry, glazing type, glazing ratio, climate	Thermal and energy performance	Hypothetical model—four variants	The energy performance of the courtyard building type showed more energy efficiency compared to the atrium building for low-rise structures while the atrium building performed better with high-rise structures
Susorova et al. [42]	Evaluated the impact of geometry parameters on building energy performance in a commercial office building in the United States, such as window orientation, window to wall ratio, and room width to depth ratio	Building energy simulation	Energy Plus/Design-Builder	6 climate zones, 8 window orientations, 7 windows to wall ratios, and 4 widths to depth ratios	Lighting, heating, cooling, auxiliary hot water, and total energy consumption/year/square meter	An office room located on a middle floor and midway along a building's width—6 climate zones + 8 window orientations + 7 window to wall ratios + 4 widths to depth ratios	Geometry influences energy usage greatly in hot and cold climates, but very marginally in temperate regions. Energy savings ranged from 3 to 6% on average, with a maximum of 10–14% in hot climates and 1% in temperate and cold climates
García-Sanz-Calcedo [43]	An investigation of the direct relationship between the number of health center users, floor space, annual energy usage, and architectural design element of an Extremadura hospital (Spain)	Statistical analysis (single and multiple correlations)	NA	Building size, three different climates	Final annual energy consumption per unit floor area	70 Health centers in Extremadura (Spain)	The energy consumption of the health center might increase up to 15% if the building size is not optimized



Table 2 (continued)

Author	Study focus	Method of research	Software	Independent variables	Dependent variables	Sample details	Key findings
Rajagopalan and Elkadi [44]	Investigates the energy performance of three medium-sized healthcare buildings in Victoria, Australia	Case study	NA	Building fabric, type of functional spaces, climatic conditions, HVAC systems	Electricity, gas, and water consumption	Three medium-sized health-care facilities in the public healthcare sector in Victoria, Australia	Energy transmission across the building envelope, such as walls, windows, and roofs, as well as heat generation from users and equipment, are the primary sources of HVAC load. The case study of small hospitals found that 45% of the heating load is from the envelope, with 20% and 13.5% from the windows and walls, respectively, while 16 percent is from the envelope and 37% is from the equipment
Lavy et al. [24]	Investigate the influence that elements such as EBD-supported design interventions, ASHRAE recommendations, and energy code compliance on the hospital building envelope in cities across the United States	Mixed method-Case study/Building energy simulation	eQUEST	Orientation, day-lighting controls, window/wall percentage, and exterior shading devices	Energy performance	2 Hospitals—base model + 10 variants	HVAC systems are a significant part of the overall energy efficiency of a building

Table 2 (continued)

Author	Study focus	Method of research	Software	Independent variables	Dependent variables	Sample details	Key findings
Wang and Greenberg [45]	The impacts of window operation on building performance for different types of ventilation systems-natural, mixed-mode, and standard variable air volume systems, were evaluated in a medium-sized reference office. In the United States	Building energy simulation	Energy plus	Open windows, natural ventilation, HVAC equipment, and system sizing	Temperature, energy demand profiles, heating, and cooling electric demand	5 Zone floor of 3 stories of commercial building	Identified HVAC energy savings of 17–47% with mixed-mode ventilation during summer for various climates
Chedwal [46]	Potential application of the ECBC code to existing hotel structures in India in order to improve energy efficiency and reduce energy consumption in Indian hotels	Building energy simulation	eQUEST software	Wall, roof, glass, HVAC system properties, lighting, and other types of equipment	Energy consumption, HVAC load, lighting load	3 Hotels out of 79 hotels	Implementation of ECBC to hotels Category-1, Category-2 and Category-3 demonstrates energy savings of 37.2%, 18.42% and 25.82%, respectively with a payback period of 2.39–6.41 years whereas application of advance
Echenagucia et al. [47]	Changing the number, position, shape, and kind of windows, as well as the thickness of the masonry walls, to reduce the energy used for heating, cooling, and lighting in an office building at USA	Multi-objective optimization	EnergyPlus	Number, position, shape, and type of windows and the thickness of the masonry walls, WWR	Heating, cooling, and lighting load	An open space office located on the first floor of a five-story masonry building with internal dimensions of 20 m × 14 m × 4 m	The Pareto front solutions were defined by extremely low WWR values, particularly on the east, west, and north-facing façades of the study building, while the area of the south-facing windows was larger, with a greater spread, than the other orientations



Table 2 (continued)

Author	Study focus	Method of research	Software	Independent variables	Dependent variables	Sample details	Key findings
Zahiri and Altan [48]	Investigation of optimal design options for secondary school buildings using passive design principles to improve the indoor thermal conditions in Tehran	Building energy simulation	Energy Plus/Design-Builder	Orientation, solar shading devices, thermal mass, natural ventilation, external wall, and roof insulation	Indoor air temperatures	A female secondary school building in the city of Tehran	The passive design solutions had a significant impact on the indoor air temperature and can keep it within an acceptable range based on the thermal requirements of the female students
Taleb [49]	An examination of the renovation of a hospital building in Abu Dhabi, United Arab Emirates, with a focus on building envelope renovation	Mixed method-case study/Building energy simulation	IES	Sunshade, exterior wall, a cool roof, glazing, and green roofs	External conduction gain	Five wards are located on various floors with a capacity of 300 beds and the ground floor with public services and casualty area of Al Cornich Hospital—a maternity and neonatal hospital	The green roof performed the best in terms of heat gain reduction among the five skin characteristics tested—a sunshade, exterior wall design, cool roof, green roof, and glazing. It also gave useful analysis on how to meet the recommended comfort standards for hospital structures
Yang et al. [50]	Quantitative evaluation of the energy implications of occupancy diversity at the building level for an office in California	Building energy simulation	NS	Space layout and form	Heating/cooling load	A 3-story north-facing office building having an area of 3735 m ² with 89 mechanically ventilated rooms of varying sizes and functions on the USC (University of Southern California) campus in Los Angeles, California	Introduces a framework for quantitatively evaluating the energy implications of occupancy diversity at the building level, using building information modelling to provide building geometries, HVAC system layouts, and spatial information as inputs for computing potential energy implications if occupancy diversity is eliminated



Table 2 (continued)

Author	Study focus	Method of research	Software	Independent variables	Dependent variables	Sample details	Key findings
Amaral et al. [51]	Proposal of a methodology for the parametric evaluation of a window ideal dimension based on the thermal performance of a reference room in the climate region of Coimbra, Portugal	Building energy simulation	EnergyPlus	Opening type, orientation, and size, overhangs, glazing	Thermal performance and energy efficiency	A reference room - the opening orientation in a two-degree step around the 360°, starting at 0° (north) and then turning east	For the specific research region, triple glazing outperforms single and double glazing, particularly in the north direction. The worst opening orientations, regardless of window type, are northeast and northwest
Delgarm et al. [23]	A mono- and multi-objective particle swarm optimization (MOPSO) algorithm is combined with Energy Plus building energy simulation engine to find a set of non-dominated solutions to improve building energy performance, demonstrating a powerful and useful tool that can save time when searching for optimal solutions with competing objective functions. efficiency	Building energy simulation	EnergyPlus	Building orientation, shading details, window size, glazing, and wall properties	Annual cooling, heating, and lighting load, electricity consumption	Single room model	By contrast to the baseline model, the annual cooling electricity drops by approximately 19.8–33.3%, while the annual heating and lighting electricity increases by 1.7–4.8% and 0.5–2.6%, respectively, for four varied climatic zones of Iran. Furthermore, the optimal design reduces total yearly building electricity demand by 1.6–11.3%



Table 2 (continued)

Author	Study focus	Method of research	Software	Independent variables	Dependent variables	Sample details	Key findings
Goia et al. [52]	Investigation of the optimal WWR for each of the main orientations in four different locations, covering the mid-latitude region, from temperate to continental climates for the specific type of office building with a single corridor layout with cell office rooms equipped with cutting-edge building envelope components and installations	Mixed method-Building energy simulations, Sensitivity analysis	EnergyPlus	WWR (0.20; 0.35; 0.50; 0.65; 0.80), transparency range 20–80% of façade	Energy performance	7-story office building (45.9 m × 14.4 m × 28.9 m)- Typical plan located above the entrance floor with a central corridor and 12 office cells (3.6 m × 5.4 m × 2.7 m) on both sides of the corridor. Services, staircases, and lifts are placed at the two ends of the corridor	The most ideal WWR values are in the 0.30–0.45 range—but not for south-facing façades. Furthermore, with the best façade technology, WWR has a minimal impact on energy performance
Harmathy et al. [53]	Formulation of an optimal building envelope model utilizing multi-criterion optimization methods to calculate efficient WWR and window geometry (WG) to interior illumination quality, followed by an assessment of glazing parameters' influence on annual energy demand for a Serbian office	Building energy simulation	BIM (Autodesk Revit software)/Energy Plus (Open Studio)/Radiance	WWR, window geometry, glazing, time, sky conditions, and zone orientation	Advanced spatial daylight dispersion, average indoor daylight factor	Existing reference office building	The integral methodology for improving overall energy performance through the use of multi-criterion optimization methods, highly detailed Building Information Modeling (BIM) programs, and a dynamic energy simulation engine is both flexible and adaptable for use in a variety of climatic conditions and construction types

Table 2 (continued)

Author	Study focus	Method of research	Software	Independent variables	Dependent variables	Sample details	Key findings
Morgenstern et al. [54]	To investigate how relevant energy benchmarks—reflecting effective energy management and design—can be built for hospital buildings in England, a category that includes complex structures with various set-ups and wide variation between them	Case study	NA	Different departments	Electricity consumption	28 departments of 8 medium to large General Acute hospitals of England	The different hospital departments have hugely varied electricity consumption characteristics. Wards, day clinics, and some other departments have lower average consumption intensities which are reasonably well reflected by current hospital electricity benchmarks
Lu et al. [55]	Establishment of standardized linear regression models between these selected parameters and total and subentry energy consumption intensity of an office building	Statistical analysis (regression analysis), Univariate analysis of variance—(ANOVA)	NA	Climatic parameters, the air conditioning form, building envelope, heat transfer coefficient, U-value-external wall, integral window, the roof, window/window glass type	Energy consumption	27 Office buildings in China-12 buildings from Bayan Nur + 12 buildings from Ordos + 3 buildings from Wuhan city	The percentage of total equivalent power consumption consumed by electricity was a significant element influencing the total energy consumption intensity of an office building in the west of Inner Mongolia Autonomous Region
Zhang et al. [20]	Describes the use of simulation optimization methods to discover the best trade-off between lowering energy use for heating and lighting, minimizing summer discomfort time, and boosting comfort. Daylight illumination is useful in Chinese school buildings	Multi-objective optimization	Energy Plus/Rhinoseros, Grasshopper, Ladybug and Honeybee, Radiance, Octopus	Orientation, room depth and corridor depth, window-to-wall ratio, glazing materials, and shading types	Heating load, daylight illuminance, thermal comfort	Chinese schools of 2–3 story buildings	The double-sided corridor design performs best in China's cold environment, while the one-sided enclosed corridor style performs the worst



Table 2 (continued)

Author	Study focus	Method of research	Software	Independent variables	Dependent variables	Sample details	Key findings
González et al. [62]	The correlation analysis of hospitals in Spain reveals the links between average energy usage in hospitals and the number of personnel, available beds, and building surface area	Statistical analysis (ANOVA)	NA	Location, built area, number of workers	Annual energy consumption	80 Eco-management and audit schemes from 20 hospitals were analyzed in the period 2005–2014	The average yearly energy consumption in a Spanish hospital for regular operating conditions was 0.27 MWh/m ² , 9.99 MWh/worker, and 34.61 MWh/bed, with standard deviations of 0.07 MWh/m ² , 3.96 MWh/worker, and 12.49 MWh/bed
Omar et al. [63]	In Beirut, investigate the conditions of indoor daylight and the energy performance of the library using various architectural features such as space depth, window size, external obstruction angle, and glazing apparent transmittance	Mixed-method-experimental/ Building energy simulation	Ecotect, Hobo loggers, Dial DIALux	Space depth, window size, external obstruction angle, and glazing visible transmittance	Daylighting, artificial lighting, user behavior	Library of Faculty of Architectural Engineering in Beirut Arab University, Debbiah, Campus and Beirut, Le5n	The daylight designs based on hollow prismatic light function as luminaires, boosting the overall efficiency and uniformity of natural light distribution into library spaces

Table 2 (continued)

Author	Study focus	Method of research	Software	Independent variables	Dependent variables	Sample details	Key findings
Bawaneh et al. [64]	Analytical review of end-use energy data in US healthcare systems and hospitals that can be used as a standard to analyze the energy-related performance of US hospitals	Statistical analysis	NA	Floor space	Energy consumption	71 Healthcare centers in the USA	In the United States, the energy intensity of hospitals ranges from 640.7 to 738.5 kWh/m ² . This is over 2.6 times the average for commercial constructions. HVAC and lighting (non-process energy) account for around 61% of a typical hospital's energy consumption in the United States, confirming the need for technology advancements and design upgrades, particularly for HVAC systems and non-process energy consumption
Guo and Bart [65]	To accomplish the unity of energy usage and indoor thermal comfort level of an office located in different cities in China, various design criteria that meet the principle of climate adaptation are recommended	Mixed mathematical analysis/Building energy simulation	EnergyPlus/Open Studio	Orientation, a layer of insulation board, U-value of exterior fenestration, SHGC, WWR, infiltration rate	Heating, cooling, and total energy consumption, thermal comfort	5 Typical benchmark geometric models were established as per local energy conservation codes	The severe cold zone and hot summer & cold winter zone appeared to have the greatest energy-saving potential, with 18–24% and 16–19%, respectively, while the cold zone and mild zone approximately equaled 15% and 12–15%, and the hot summer and warm winter zone appeared to have a relatively low (5–7%)



Table 2 (continued)

Author	Study focus	Method of research	Software	Independent variables	Dependent variables	Sample details	Key findings
William et al. [66]	High temperatures and high humidity levels in hot and humid climate zones like Alexandria, Egypt, induce human discomfort, resulting in high HVAC energy consumption in healthcare facilities	Building energy simulation	Energy Plus/Design-Builder	Envelop-glazing, insulation, lighting	HVAC LOAD	An Alexandrian medical facility in Egypt consisting of five stories with an approximate area of 10,000 m ²	Energy savings and operational costs can be reduced by 67% through smart retrofitting and system sizing
Cesari et al. [67]	The influence of various window sizes and glazing types on heating, cooling and lighting energy demand in a hospital patient room healthcare facility in Europe cities—Italy (Milan, Bologna, Rome, and Naples)	Building energy simulation	EnergyPlus/TRN-SYS	Glazing types, Window sizes, Room orientations, Climatic conditions, and Lighting control strategies	Heating/cooling load an artificial lighting energy demand	A typical representative hospital building of healthcare building stock—experimented with 4 Italian cities, Milan, Bologna, Rome, and Naples having different climate conditions. Simulations model—two patient rooms on the third floor facing no external obstruction	Wider windows with adequate glazing and a daylight-linked dimming lighting control approach can reduce primary energy demand by up to 17%

Table 2 (continued)

Author	Study focus	Method of research	Software	Independent variables	Dependent variables	Sample details	Key findings
Fang et al. [68]	Simultaneous evaluation of the daylighting and energy performance of building with design options and also to generate the optimized design	Building simulation	EnergyPlus/Radiance	Building depth, the roof ridge location, the dimensions, and orientation of the skylights, the Width of the windows on the north and south, and the length of the Louver	Daylighting and energy performance	A small single-story office building	Proposed a multi-objective method to automatically explore building design alternatives, evaluate daylighting and energy performance, and find design options with optimal performance, where the daylighting performance metric UDI is increased by 38.7%, 31.6 percent, and 28.8%, and the energy performance metric EUI is decreased by 20.2 percent, 18.5%, and 17.9% compared to average performance values
Kyritsi et al. [69]	Examining the impact of natural airflow on the passive cooling of an office unit in the Mediterranean region of Europe using quantitative field research	Case study	NA	Windows details	Thermal comfort, energy consumption	An open layout office space on the Fourth Floor of a five-story building in the urban center of Nicosia	The findings revealed that night ventilation is the most effective passive cooling approach



Table 2 (continued)

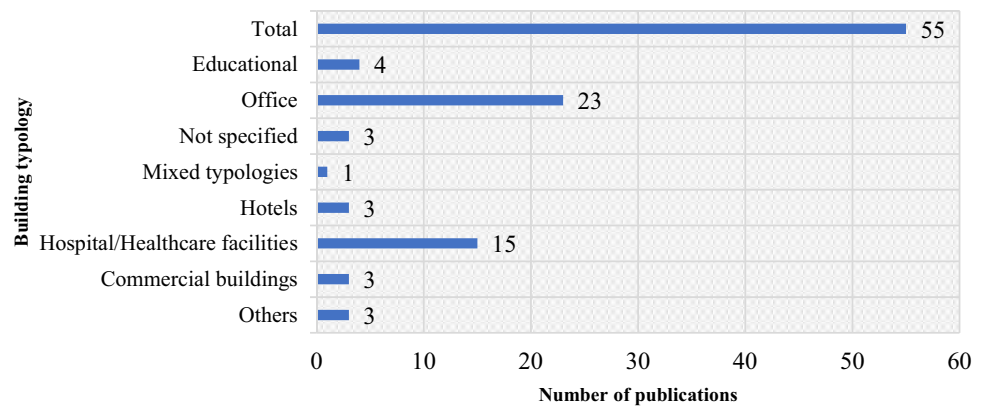
Author	Study focus	Method of research	Software	Independent variables	Dependent variables	Sample details	Key findings
Gärtner et al. [19]	Exploring the influence of a flexible space layout design on thermal comfort and energy demand in a modern open-plan office space in Stuttgart, Germany	Building energy simulation	Energy plus/TRN-SYS 18, Grasshopper	Space layout, 3 types of HVAC system configurations, four different control zoning strategies	Thermal comfort	In a single-floor plan of an office building located in Stuttgart, Germany-12 different spaces layout designs	Radiant ceilings and thermally active building systems are attractive options for flexible office spaces in Stuttgart, whereas mechanical ventilation systems necessitate a more complicated control technique to provide thermal comfort
Pilechiha et al. [70]	Presents a new multi-objective strategy for analyzing and optimizing the energy processes connected with window system design in Tehran, Iran	Multi-objective optimization	EnergyPlus/Open Studio, Grasshopper-Ladybug, and Honeybee	Windows, room dimensions, orientation	Quality view, daylighting, energy consumption	The office room is located on the middle floor of a multi-story building, with an approximate area of 2300 m ² , having dimensions of 3.9 m×8.5 m×2.8 m with single-zone space	Consideration of window system configuration in the early stage of the design process is very important to reduce the lighting energy
Aunión-Villa et al. [71]	Investigating the energy intensity of a hospital by area and developing energy performance indicators in Madrid (Spain)	Case study	NA	Open, closed, and mixed layouts	Energy consumption	182-bed hospital—an experiment area of 25,177 m ² (electromedicine, radiology, radiotherapy, and nuclear medicine), 3 layout variants—open, closed, and mixed layout	Operating rooms and intensive care units used more than 1000 kWh/m ² per year, whereas catering and nuclear medicine used 500–1000 kWh/m ² per year, radiology used 350–500 kWh/m ² , and most other units used less than 250 kWh/m ²

Table 2 (continued)

Author	Study focus	Method of research	Software	Independent variables	Dependent variables	Sample details	Key findings
Du et al. [17]	The energy performance assessment combines daylighting simulation with energy simulation for an office building in Europe and Asia	Mixed method-building energy simulation/Sensitivity analysis	Energy Plus/Radiance, Daysim, Grasshopper-Ladybug and Honeybee	Layout variants, climate, WWR, shading systems	Daylighting	An existing office building in Madrid, Spain-11 variants of space layout and 3 different climates	The plan variation has the greatest impact on lighting consumption, with the highest difference occurring in Harbin, where it is 46% without shade and 35% with shading. In Amsterdam, the highest difference in the sum of the final energy for heating, cooling, and lighting using a heat pump system is 8% for the layouts both without and with the shading system
Zou et al. [72]	Creating a complete method for optimizing the design of a standard architectural space to increase building performance in China	Mixed method-Mathematical analysis/Multistage optimization	Energy Plus/Grasshopper, Diva-for-Rhino, and SpeedSim-for-DIVA	Orientation, geometry, shading devices, wall, windows	Thermal comfort, visual comfort, total energy consumption	A typical type of classroom in Guangzhou, China	On average, the 3-step optimization process improved energy performance by 24.6%, 18.7% and 14.2%, suggesting that this strategy is practicable and useful for improving building design in actual assignments



Fig. 4 Building typologies investigated in reviewed articles (Source: Scopus database)



studied hospitals in comparison to available benchmarks. Paula Morgenstern et al. [54] concluded that as per defined benchmarks, various departments of hospitals consume different amounts of electrical energy, with inpatient wards, day care clinics along with other departments having lower average usage intensities than high electricity usage areas of hospitals such as operating rooms, laboratories, and imaging and radiotherapy departments. Yang et al. [30] introduced a framework for quantifying the energy implications of building-level occupancy diversity, using building information modeling to stipulate building shapes, HVAC system configurations, and spatial data as inputs for computing.

Daylighting

Daylighting is a passive approach for improving energy performance and visual comfort without incurring high installation and operating costs [74]. Daylighting is seen as a key component of space identity and space quality [75]. Also, an efficient sustainable strategy to improve the EPB [76]. Lighting constitutes a significant portion of building energy consumption [77]. Insufficient natural daylight in the space and reliance on artificial lighting systems during the daytime waste more energy [63]. Building shape or geometry, along with primary design factors such as window design, shading design, roof design, façade design, building shape design, and so on, is one of the most impactful design decisions on daylighting to be considered in the early design stage [68]. An atrium, windows, and openings are potentially a major source of daylight for buildings and offer other environmental benefits in terms of solar gain, reduced energy losses, and natural ventilation [63]. According to Du et al. [17], the effect of daylighting can be explained by the different layouts including courtyards, atrium, the form of the buildings that impart different levels, and an appropriate space layout combined with the glazing design/orientation, window design and the positioning of interior partitions. Optimizing space layout design may greatly reduce energy demand, particularly lighting requirements. Furthermore, the impact of space layouts on EPB varies depending

on the environment. The maximum daylight is set around the windows on the edge of the space, while it becomes minimal as we move deeper into the interior and far from the windows. As a result, approaches to enhance the depths of space with the use of daylight are required [63]. The width-to-depth ratio is a vital room geometry factor that affects the interface of isothermal interior walls and outer walls, but also the dispersion of sunshine throughout the interior space of a room. The extent of the perimeter wall of the room determines the surface exposed to heat transmission through the façade and the amount of daylight. The depth of a room defines the amount of daylight penetration inside the building. Due to the large area of its exterior wall, a wide and shallow space with proper sunlight and light dispersion has a lot of heat reception and dissipation. A narrower and deeper chamber receives less sunlight, but it also receives less heat due to the small area of its exterior wall [42]. Norbert Harmathy et al. [53] studied to enhance the indoor illumination quality, an improved building envelope model emphasizing the perimeter of the building was created utilizing a multi-criterion optimization process and identified the most efficient window-to-wall ratio (WWR), window geometry, and glazing parameters. The design and control of a shade system are heavily influenced by climatic conditions and daylight availability. The shading device's location, characteristics, and control have a big impact on the natural lighting and thermal performances of peripheral office areas. The shading features and control have a direct impact on lighting electricity usage [29]. Omar et al. [63] investigated the circumstances of interior daylight and the energy performance of the library at Beirut Arab University using various architectural factors such as space depth, window size, exterior angle of obstruction as well as glazing visible transmittance. Also proposed the daylighting designs based on hollow prismatic light guides in space design. Pilechiha et al. [70] present a method for assessing the effectiveness of view in office spaces while keeping energy efficiency and daylighting in mind, allowing for a window design optimization framework. Zhang et al. [13] investigated different spatial configurations to enhance daylight illuminance and reduce visual discomfort through an

optimization process for a school building in China to prove that double-sided corridors are best compared to single-sided corridors for the study area located in the cold region.

Natural ventilation

By integrating openings with an appropriate space arrangement, fresh air is provided to the rooms as needed. A function that needs more ventilation, such as a facility room, can be located near the windward external wall, whereas a function that demands less ventilation, such as a storage or equipment room, can be located near the leeward external wall. Slight changes in cloud cover, wind speed, and direction would have an impact on the availability of daylight and natural ventilation, which appear to be the most important aspects influenced by internal space arrangement [14, 15]. The following factors influence natural ventilation efficiency: climates, window opening schedule, building material, built area, and the number of building occupants in a building plan. Optimized window designs help to improve energy efficiency and thermal comfort in naturally ventilated structures [78]. According to Du et al. [7] changing the placement and size of buffer spaces, such as a courtyard, solar chimney, atrium, and light-well, has a significant impact on natural ventilation within buildings. The building with better space connection and integration has a higher natural ventilation velocity. The potential for natural ventilation is extreme in hot-dry and warm humid climates during all periods of the year [60]. Schulze and Eicker [39] determined that there is a need for regulating opening methods to avoid overcooling of rooms as well as provide sufficient fresh air during the heating season. Regulated natural ventilation was compared to mechanical ventilation and cooling for the assessment of cooling energy conservation. According to the simulation results, properly created natural ventilation systems save between 13 and 44 kWh/m² of cooling net energy per year for the 3 places Stuttgart, Turin, and Istanbul. Short et al. [21] created, cataloged, and aggregated environmental design propositions for clinical as well as non-clinical space types into a typical plan module, their energy performance along with the ventilation modeled to conclude that 70% of the gross floor area of small to medium-sized healthcare buildings could have passive ventilation and hybrid ventilation approach might serve an additional 10% of net floor area.

Control of the heating, cooling, ventilation, and lighting system

Different space layouts are suitable for different types of control for space heating, space cooling, ventilation, and lighting systems [7]. HVAC systems are required under various climatic circumstances to create a suitable indoor

thermal environment for occupants, equipment, and devices [79, 80]. Room geometry, window type, and positioning may significantly affect the air-flow rate and the cooling effect [81]. Previous research has shown that proper shade design and control, combined with simultaneous control of electric lighting and HVAC mechanisms, can substantially decrease peak cooling capacity and energy usage for lighting and cooling whilst still maintaining good thermal and illuminance for interior conditions [29]. The size, number of rooms /floors, building type, and intended usage of the facility all influence the type of HVAC system employed in a structure [46]. Buildings consume energy for hot water, cooling, heating, lighting, services, and equipment, and a significant portion of this consumption can be minimized by using passive design principles [33]. According to statistical regression research by Shilei Lu et al. [55], the proportion of the air condition area that accounts for the ground floor area is significantly associated with the standardized energy utilization intensity of the HVAC system.

Influencing variables related to space layout on the energy performance of the building

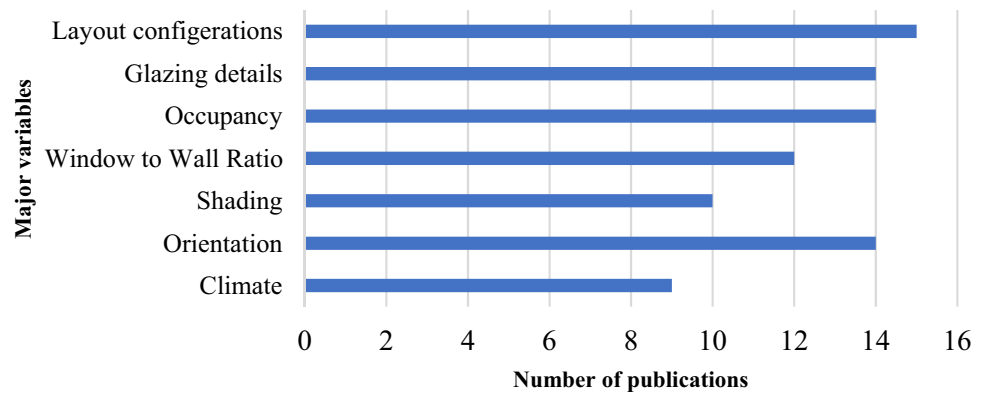
We can see from a prior study that it is very difficult to isolate the influence of space layout on EPB without considering the geographic location, climate, space occupancy data, and functional/environmental requirements [7]. Most of the studies merged other design aspects with the layout of the room (Fig. 5). Other design variables that influence EPB are discovered through their interactions with space layouts, allowing the impact of space layouts to be examined. Aspect ratio, direction, usage, climate, material, and other architectural factors, for example, have varying influences on energy performance [78].

Geographic location and climate

The amount of solar radiation and mean outdoor temperature that a building is exposed to influence the climate. The climate also influences the quantity of energy required for heating and cooling, as well as the amount of energy used for lighting [82]. The unique characteristics of the natural environment, such as the amount of sun, wind, and local vegetation can have a significant impact on building design and energy efficiency. Energy fluctuation due to space planning and usage considerations is site-specific, hence its importance varies depending on the building environment. This means that, in addition to standard building design criteria, space planning solutions along with perimeter details are targeted at enhancing energy performance by responding to their contexts [14]. One of the key aspects of spatial layout design concepts to reduce building energy use is the



Fig. 5 The major variables considered for the investigation of EPB in reviewed articles



correlation of a local climate with both the shape and thermal efficiency of the building [48]. The environment has a significant impact on the selection of appropriate building technology, such as cooling systems and high-efficiency appliances. Also where natural ventilation is used, thermal comfort should be accomplished with low building energy usage [82]. For different kinds of buildings in different regions, there is a clear disparity in power consumption per unit at the proposed site because temperature conditions in different places fluctuate greatly [57]. Bawaneh et al. [64] found that the geographic context has a significant impact on heating energy, with varied energy usage in hospitals in different parts of the United States. Hospitals in the United States have an average annual energy concentration of 738.5 kWh/m², which is greater than similar reported statistics in European countries. In California, the energy consumption of healthcare complexes along with universities, schools, and accommodations through the study of monthly electric and natural gas usage invoices, as well as the total cost of energy usage data, were collected to examine the energy intensity. Guo et al. [65] proposed different design criteria that match the climate adaptation concept to attain unity in energy usage and indoor thermal comfort level. González et al. [62] concluded that the kind of management, the available bed number, the Gross Domestic Product (GDP), or the climatic circumstances, had a more direct impact on annual energy consumption than the geographic location. Several studies have also revealed that selecting an adequate WWR value is especially important in hot climates because a WWR value outside of the optimal range results in the biggest rise in energy consumption [52].

Form and orientation

The shape of a building has an impact on its energy use. Low-energy architecture necessitates careful articulation of a building's shape and forms to reduce energy use. Traditionally as a thumb rule, in passive solar building design, the form and orientation are important factors for overall energy

efficiency in a building [83]. For most geometric factors, the subtropical climate has the largest difference between the ideal and worst solution, whereas the tropical climate has the least difference. Building orientation, shape, plan depth, and window-to-wall ratio have the greatest impact on EPB. The influence of plan shape on building energy consumption is largest in sub-tropical climates and lowest in temperate climates and tropical climates [84]. The ecological impact of courtyard buildings is directly influenced by their orientation. A courtyard's spatial structure can help regulate solar heat. Furthermore, a courtyard's natural ventilation system regulates convective heat transfer [85]. The ellipse was discovered to be the optimal plan form in all climates. It is the most efficient form in temperate and subtropical climates and the second most efficient shape in tropical temperatures after the octagon. Furthermore, the “Y” form is the least efficient in all climates [30]. In typical architectural practices, geometry factors are specified by a building's form, type, structural, and HVAC systems [42]. Building and fenestration geometry characteristics, when combined with other fenestration elements such as shading, room geometry, energy-efficient glazing, and adaptable building systems, will dramatically cut overall energy consumption to improve building energy performance. Aksoy [28] The influence of building form and orientation on heating demand has been thoroughly researched, and the results show that structures with a square shape have more advantages, and the ideal orientation angles for buildings with shape factors of 2/1 and 1/2, respectively, are 0° and 80°. When different geometries are employed, there will surely be differences in the form coefficient and energy utilization. Susorova et al. [42] observed through energy simulations using Energy Plus, that the impact of geometry parameters comprising room width to depth ratio, window orientation, and WWR on BEP in a commercial office structure in various temperature zones. The study found that geometrical considerations had a considerable impact on energy usage in hot and cold climate zones, but only a little impact in moderate climates in the United States. Pilechiha et al. [70] presented

a novel multi-objective method to change the room shape to meet the lighting and view criteria specified according to the optimization model and building performance standards. By using virtual reference buildings. Zheng Yang et al. [50] proposed a framework that was consistent across different building geometries, different building layouts, and different diversities, and discovered that the increased complexity of building geometries, the greater the influence of diversity on HVAC system energy efficiency. Building orientation is a significant design consideration, mainly regarding solar radiation and wind. In predominantly cold regions, buildings should be oriented to maximize solar gain whereas in hot climates the orientation should encourage to reduce the heat gain inside the building.

Building envelope

Building envelopes, which distinguish the indoor and exterior environments, and especially building façades play an important role in energy conservation in buildings. The thermal barrier that separates the internal and exterior environments is largely made up of façades [86]. The external and interior walls, windows, and roofs of a structure, as well as its function and location, are referred to as “building envelope” [87]. Building envelopes have been utilized for a variety of purposes over time. Control of physical environment variables (temperature, light, noise, rain, moisture, air infiltration, etc.), structural support for the structure, fire safety, security, energy conservation, and aesthetics are among these roles [88]. The design of building envelope parameters has a significant influence on building energy-saving design and hospital spatial layout [89]. The building envelope is critical in reducing heat gains and controlling the amount of energy required for space cooling. Several studies have been undertaken to assess and make recommendations on the impact of various building envelope factors on energy performance. Window details, insulation properties of the wall and roof, color, the finish of exterior surfaces, and shading details of surfaces and windows are the main building envelope features that influence cooling demand and thermal comfort along with lighting and ventilation in hospitals. The type of fenestration employed in a structure has a big impact on energy efficiency and occupant comfort in healthcare buildings and influences determining overall energy and cooling usage in the building [7]. Several studies investigated the design of an energy-efficient façade while considering the environment, building type, and physical properties of glass and framing material such as visible transmissions, solar heat gain coefficients, and thermal conductivity. In conventional architectural methods, geometry factors are often established by a building's form, type, structural, and HVAC systems. Because the form, orientation, and enclosure of a building can influence its energy consumption, it is critical

to make objective energy-saving and daylighting decisions when determining its form, orientation, and enclosure [42]. Ascione et al. [38] by examining medium-sized healthcare amenities in Mediterranean climates, suggested that refurbishing the building envelope improved indoor thermal conditions in all relevant HVAC systems. Because the maximum external insulation enhances the shell's thermal capacity, the improved envelope would undoubtedly result in better internal conditions in terms of a more stable microclimate. Hanan M. Taleb [49] did a detailed examination of annual EPB for the case study and used a computer simulation to explore EPB shortfalls that define as a 'base case,' and then compared to modified building envelopes that included unshaded, exterior wall retrofitting, cool roof, new glazing, and green roofs. Hatice Sozer [33] demonstrated that proper thermal insulation, glazing type, and shading components can help to limit heat transfer through the building envelope. This research reveals that precise building envelope design can considerably aid in achieving heating and cooling targets and improving the building's energy performance. Reduced cooling thermal energy consumption improved thermal comfort, and appropriate daylighting should all be goals of an efficient hospital building envelope design [90]. The building envelope determines the energy exchange between the outdoor environment and indoor spaces and hence governs the overall EPB [33]. William et al. [66] using building simulations, looked at the impact of building envelopes on HVAC and overall energy usage in commercial buildings of Egypt. Ma et al. [57] stated that the air conditioning system, lighting density, and building envelope are the main factors influencing energy consumption according to the orthogonal test. After researching the effects of shadings, window types, and so on, Poirazis et al. [32] determined that during the occupancy stage, highly glazed single-skin buildings are likely to consume more energy, and the increase was reduced to 15% while maintaining an acceptable level of thermal comfort when compared to a typical reference building with a percentage window to external wall area. Zahiri and Altan [48] implemented to have a significant improvement in indoor air temperatures, passive design strategies such as south and south-east orientation, thermal mass, thermal insulation in walls and roofs, as well as side fins and overhangs as solar shading devices, as well as all-day ventilation for a school building. Passive envelope design solutions also increase indoor environmental quality, allowing users to function better and reducing the need for mechanical systems. Wang et al. [45] investigated in a moderate-size reference office structure, the effects of window opening systems on building functioning for many types of ventilation systems, including natural ventilation, mixed-mode ventilation, and classic Variable air volume systems. The results of using the Energy Plus building performance simulation tool revealed the benefits of window opening systems on energy use and comfort,



as well as HVAC, resulting in energy savings of 17–47% in varied regions throughout the summer. A computerized simulation was employed in the case study to investigate power outages. Meanwhile, the energy consumption of a new building skin was compared to that of a new building skin using ASHRAE (American Society of Heating, Refrigerating and Air-Conditioning Engineers) based parameters to limit heat gain, such as sunshade, retrofitting outside walls, cool surrounding roofs, and new windows, and green towers. Bayoumi et al. [60] investigated the relationship between the amount of window opening and energy use in two hot climate office environments particularly on certain days of the year. Rajagopalan et al. [44] assessed by dividing the envelope area by volume, and the compactness ratio to compare the energy loss against HVAC system operation. The degree of compactness determined how much heat is gained and lost via the envelope. Zahiri et al. [48] developed an optimal design solution for secondary school buildings to improve the indoor thermal conditions, which included all-day natural ventilation, the installation of side fins and overhangs, and the use of thermal mass and thermal insulation in the external walls, and roof, as well as the orientation through dynamic building thermal simulation.

Windows are one of the most important aspects of a building's design. Windows are frequently a significant component of the exterior appearance of the building, whether there are little perforated openings in the facades or a total glass curtain wall. Windows are inseparable parts of the building's envelope. They represent the source of daily light, provide visual contact with the environment and provide ventilation and natural cooling [91]. The amount of energy consumed through heating, cooling, or lighting in a building is mainly influenced by its window systems [92]. Windows can be thought of as thermal holes for a building in terms of energy use. As a result, window design and selection must include both aesthetics and serviceability [93]. Windows influence the energy needs of a building in four ways: heat conduction, solar radiation conduction, air conduction, and daily light transmission. That influence also depends on the characteristics and orientation of windows, climate conditions of the building's location, solar radiation, and the building's heating and cooling systems. Energy losses through the window can be minimized by careful and adequate design, both of a window as a whole and its elements [94]. Appropriate window orientation and careful design of a window as a whole along with its different elements also help to restrict solar radiation gains and losses, reduce the frequency with which mechanical ventilation is used, and so lower energy expenses [95]. Windows and other glazed spaces are the most vulnerable to heat gain or loss of all the elements in the building envelope. Windows in general, are the weakest parts of the building elements which act as a bridge to allow the outdoor condition to be transferred into

the indoor space [96]. The room's air velocity and flow are moderated by the size, shape, and orientation of the openings; a tiny input and big outlet improve the room's airflow velocity and distribution. Glazed openings also allow natural light to enter a structure. The important components of a window that govern requirements of heat gain and loss, ventilation, and daylighting are the glazing systems and shading devices [29]. Most of the reviewed articles investigated the energy performance of the hospitals by considering window details as one of their important variables which includes window size [23, 67], WWR [17, 44], window opening grade [53], window orientation, and geometry [24, 42, 52], etc. Norbert Harmathy et al. [53], optimized the building envelope model using a multi-criterion optimization methodology to determine efficient WWR, window geometry, and glazing parameters to enhance the indoor illumination quality. Mohannad Bayoumi et al. [60] explored the relationship between the window opening grade and energy savings in a one-sided window opening in two hot environments, one humid and one arid. Cesari et al. [67] by examining four distinct orientations in four Italian cities, the energy performance of nine different glazing systems was examined concerning a typical size opening with a 25% WWR and a floor-to-ceiling window with a 77% WWR. The optimized WWR for each of the major orientations was observed in four locations, covering the mid-latitude area from temperate to continental climates by integrated thermal lighting simulations, coupled with a sensitivity analysis for an office building with a single corridor that the total energy use may increase in the range of 5–25% when the worst WWR configuration is adopted by using integrated thermal and lighting simulations. Wang et al. [45] in a medium-sized reference office building evaluated the effects of window operation on building performance for several types of ventilation systems, including natural ventilation, mixed-mode ventilation, and conventional variable air volume (VAV) systems.

The shading device's location, characteristics, and control have a big impact on the natural lighting and thermal efficiency of peripheral space. To combine daylighting requirements with the need to limit solar gains, shading must be considered an integral aspect of facade system design for every building [29]. The major goal of utilizing shading devices is to keep direct sunlight from reaching the exterior walls and windows. Overhangs, fins, blinds, and shading of neighboring buildings and far obstructions are all examples of shading [48]. Several factors must be addressed when designing glazed facades with shading devices in any building, including the building type, natural light perspective, and latitude. Shade device types are influenced by building form and orientation in particular. The type of shading device utilized influences the level of ideal daylight, thermal comfort, and visual comfort [97]. Tzempelikos et al. [29] used a connected lighting and thermal simulation module to



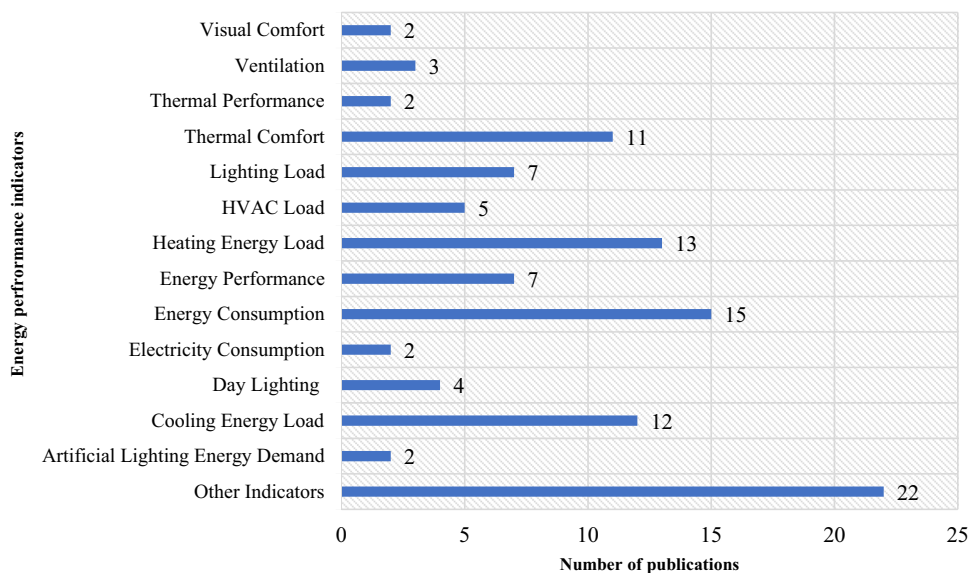
calculate the simultaneous impact of glazing area, shading device attributes, and shading control on building cooling and lighting requirements in peripheral spaces including examination of window-to-wall ratio and shading characteristics. The simulation results show that, depending on climate patterns and orientation, when an integrated approach for the control system of mechanized shading is used in connection with easily controlled electric lighting systems, substantial reductions in energy consumption for cooling and lighting could be accomplished in perimeter spaces. Du et al. [17] simulated office building variants in three different climates with two situations, without a shading system and with an exterior screen to evaluate the final energy consumption concerning lighting, heating, and cooling load. The simulation findings demonstrated that the geographical arrangement of produced variants and the huge difference in energy needs in different climates had the largest impact on lighting demand when the shading device was used as an independent variable. Nielsen et al. [34] investigated the three types of facades i.e., without solar shading, with fixed and dynamic solar shading along with various window orientations and heights. To evaluate the total energy demand for heating, cooling, lighting, and daylight factors of the building. Compared to fixed solar shading, dynamic solar shading significantly increased the quantity of daylight available, emphasizing the importance of using dynamic as well as integrated simulations early design stage to make educated decisions about the façade. Alejandro Prieto et al. [61] explored the effectiveness of passive cooling strategies considering envelope parameters like windows and shading devices in commercial buildings from warm climates through the statistical analysis and simulation process. Waleed Khalid Alhuwayil et al. [58] researched the energy usage of a multi-story hotel structure in a hot and humid

environment using various external shading schemes. When compared to the base scenario, the findings showed that the proposed retrofit plan with external shading and self-shading effectively eliminated a large amount of the energy demand, and the investment was cost-effective due to the short pay-back period.

Building energy performance indicators

Several studies focused on single and multi-performance indicators or energy efficiency with thermal comfort, lighting, ventilation, along with HVAC load in healthcare structures. There are some research focused solely on energy performance or thermal performance or daylighting or natural ventilation and many others are focused on multiple parameters including energy demand, thermal comfort, and indoor environmental quality (Fig. 6). Thermal performance and energy consumption together got investigated mainly by considering window details along with orientation, and shading devices as variables [69, 72, 80]. There are many other indicators along with main performance indicators like energy consumption, heating, and cooling, lighting load like airflow, average indoor daylight factor, daylight factor, equipment load, external conduction gain, gas consumption, indoor air quality, indoor air temperatures, and indoor environmental quality. According to the international standard ISO 50006-2014 [98], “an EPI (Energy Performance Indicator) is a value or measure that quantifies energy efficiency, energy use, and energy use performance in facilities, systems, processes, and equipment” [99]. The energy performance indicator is noted as EPI, which is stated in kWh/ m²/year. The EPI is calculated by dividing the yearly energy expended by a building in kilowatt-hours by the gross floor area in square

Fig. 6 Energy performance indicators investigated in review articles



meters of the building. Numerous energy performance indicators are used to describe building performance, and they differ in terms of the boundary at which they are monitored, and the contributions used for their calculation [16]. Regarding the calculation period, most studies calculated the energy use for the whole year, for only some seasons and peak days for different building typologies located in the various climatic zone [7]. Single rooms, zone-wise, or entire buildings were investigated through case studies or through developing a simulation model to calculate the EPB. Nielsen et al. [34] calculated the total energy demand, heating load, cooling load and lighting load, and daylight factors of office buildings by investigating shading details as a variable through simulation. Also, we can find from works of literature that opening details, orientation, and climatic factors play a major role in heating, cooling, lighting, and ventilation load which directly influence thermal comfort and total energy consumption of the buildings [49, 52, 67]. The thermal performance of the building was investigated by considering window detailing in terms of size, geometry, orientation, and glazing parameters in different climatic parameters to achieve a significant result [14, 51].

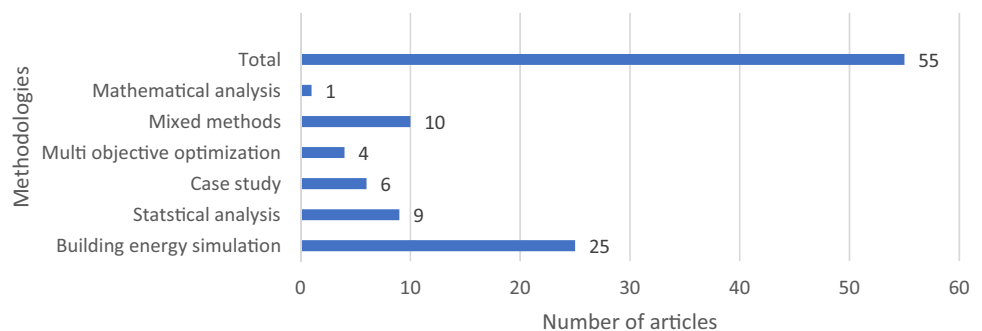
Methodologies considered for investigating the EPB

There are several different methodologies are considered to study the EPB concerning different space layout variables and performance indicators of different building typologies as well as the climatic zone (Fig. 7).

Most of the research in this area was conducted using experimental or simulation techniques, sometimes combining both as needed. There 25 studies are based on building energy Simulation method [14, 15, 19, 22, 23, 29, 31, 33, 34, 37, 39, 40, 42, 45, 46, 48, 50, 51, 53, 58–60, 66, 67] and out of 10 research 7 number of literatures are combined building energy simulation method with other methodologies like statistical analysis, optimization and case study method [24, 32, 41, 49, 52, 63, 65]. The 6 studies are based on case studies [16, 38, 44, 54, 69, 71], and 9 studies [35,

36, 43, 55–57, 61, 62, 64] employed a statistical analysis of the energy performance investigation. 4 number of studies are exclusively based on multi-objective optimization [20, 47, 68, 70]. A detailed analysis of annual EPB for the case buildings was performed using a computerized simulation to explore energy performance shortcomings as a base case [49]. Building geometry, space layout, the grouping of rooms in thermally homogeneous zones, building orientation, building construction, thermal properties of all building components, building usage, internal loads and schedules for lighting, occupants, and equipment, HVAC system type and operating characteristics are some of the input data required for energy simulation of buildings [100]. In recent years, thermal dynamic simulation has been widely employed in the design phase to assess the appropriateness of the intended project to thermal and energy performance objectives. This simulation assumes that the findings accurately represent the actual behavior of the buildings. A comparison of site measurements and numerical simulation results is required to demonstrate this idea [101]. Guo et al. [65] employed a mixed-method approach evaluation as well as intensive computer simulations to discover the ideal design approaches within the energy as well as thermal comfort constraints. Five separate benchmark geometric models were constructed in OpenStudio, indicative of diverse climates, while using the EnergyPlus engine to examine the coupling relationship between energy usage and thermal comfort, according to local energy conservation codes. Using the dynamic simulation method and calibrating the simulated energy consumption against the building's actual energy use. Chedwal et al. [46] concluded that there is a significant energy saving potential of up to 27.9 kWh/year in hotel buildings in India by implementing ECBC (Energy Conservation Building Code) along with other energy efficiency measures. Lu et al. [55] through statistical regression analysis, assessed that standardized energy consumption intensity of the HVAC system is significantly related to the gross floor area. Adamu et al. [37] used four natural ventilation systems intended for single-bed hospital wards to assess the viability of buoyancy-driven airflows. These tactics include single-window opening, inflow and stacking,

Fig. 7 Various research methodologies adapted in the reviewed articles



same-side dual-opening, and ceiling-based natural ventilation, which is a revolutionary concept. As a case study, these solutions were investigated using a dynamic thermal simulation model and computational fluid dynamics on a new ward in a London hospital Pisello et al. [36] presented post-occupancy evaluation by in-situ analysis to achieve an average monthly energy savings of 20.5% for lighting, heating, cooling, lighting, additional sources, and types of equipment, of overall primary energy demands for electricity, decreasing from 385.8 to 306.7 kWh/m² year via calibrated and validated dynamic simulation model. Zou et al. [72] developed a comprehensive technique for enhancing building performance by improving the design of typical architectural spaces. The optimization process is divided into three stages. The first step is to build a database by generating research objects at random and stimulating their development. The second phase of multi-objective optimization is to construct artificial neural network models as an alternative to time-consuming building simulations to predict building performance quickly. Finally, perform multi-objective optimization based on the actual design limitations. Delgarm et al. [23] combined a mono- and multi-objective particle swarm optimization algorithm with EnergyPlus building energy simulation software to find a set of non-dominated solutions to improve EPB, resulting in a powerful and useful tool that can save time when searching for optimal solutions with competing for objective functions. EnergyPlus is one of the most robust, trustworthy building simulation tools that can model energy consumption for heating, cooling, ventilation, lighting, as well as plug and process loads [33]. Echenagucia et al. [47] with the help of a multi-objective search using genetic algorithms, reduced the energy required for heating, cooling, and lighting an open space office building by changing the quantity, placement, form, and type of windows and thus the thickness of masonry walls using the NSGA-II algorithm in conjunction with EnergyPlus building energy simulation tool. Norbert Harmathy et al. [53] developed an integrated approach, a multi-criterion optimization method, in conjunction with extremely detailed Building Information Modelling programs and dynamic energy simulation engines, to achieve better energy performance of offices by relating building envelope optimization and comfort of users in a wide range of climatic conditions and for varying construction types. Zhang et al. [20] presented the results of a simulated optimization study of numerous spatial configurations to determine the best trade-off between reducing energy use for heating and lighting, reducing summer discomfort time, and maximizing useable daylight luminous flux. Lighting load, HVAC load, thermal load, and ventilation methods are among the software that can be used in conjunction with various simulation engines to evaluate the EPB. The energy plus simulation engine, when combined with other simulation software, produces an upgraded

building model that can be used to evaluate the energy, thermal, heating, cooling, lighting, and ventilation performance of different building types. Current computer simulation resources can largely predict energy usage by HVAC, lighting fixtures, and appliances, among other things. EnergyPlus, OpenStudio, Revit, DesignBuilder, eQUEST, and other simulation tools are used to create these energy use figures [66]. The trustworthy results encouraged many researchers to use Energy Plus in their studies. Different simulation engines are developed to investigate the energy performance of the building with advanced plug-in software. Energyplus engine coupled with different software like an OpenStudio and DesignBuilder is utilized in most of the research. Ecotect software was used to simulate daylight. Where it offers vital information about the architectural aspects that affect the current situation's sunshine. This includes elements such as windows, as well as their characteristics such as position and size, as well as their impact on the amount of daylight that enters the area and the duration of daylighting [28]. Although DesignBuilder is based on a complex simulation program, it attempts to address the architect's specific language with a visually orientated interface and inputs in different levels for developing and evaluating comfort as well as energy-efficient architecture from concept to completion [102]. Bawaneh et al. [64] proposed a mathematical formulation for efficient assessment of the optimal healthcare building floor area, which anticipates their yearly energy consumption and can be used as a source of reference for project planning and as an indication to monitor the energy management of such buildings. Liu Yang [30] examined the cooling and heating requirements of the office building envelope in five major climate zones of China using the total thermal transfer value method and the heating degree-days method to develop standard building envelopes based on information collected from building surveys, local energy codes, and the ASHRAE Standard. Musau et al. [14] used the TAS, Lightscape, and Excel computer programs to evaluate the possible implications of typical open, mixed, as well as closed configurations and their space usage densities/intensities on a base case.

Sample design to assess the energy performance of the buildings

The number of samples considered in the various methodologies for the investigation of energy performance are ranging from a single building to 119 buildings [57]. The entire building samples to single rooms like classrooms [72] and patient wards [59] were investigated to analyze the various energy performance indicators like cooling, heating, ventilation, lighting, electricity consumption, and thermal comfort in different building typologies. Adamu et al. [37] explored



ventilation strategies via dynamic simulation and computational fluid dynamics, by investigating different departments of the Great Ormond street hospital located in the United Kingdom. Wang et al. [45] focused on the investigation of the impacts of window control on building performance for various types of ventilation techniques in a medium-size reference office building where the floor is divided into 5 functional zones to develop a simulation model. Many researchers considered typical floors [47] to multistorey buildings [40, 77] in their research to develop an experimental framework or to create a simulation model as well as a base case [58, 73]. Aunio-Villa et al. [95] analyzed energy consumption of HVAC, medical types of equipment in an energy-intensive department like radiology, catering, nuclear medicine, operation theatres, and intensive care units of a hospital with a 182-bed capacity and an area of 25,177 m². Different instruments are used to collect energy consumption data in various departments. The sample used in the simulation-based projects is either an actual case study building or reference model [17] or a hypothetical model [22]. Most of the simulation models of an actual building, reference buildings, or hypothetical models are developed using software like AutoCAD, DesignBuilder, OpenStudio, rhino grasshopper, etc. To examine the room energy consumption under different temperature circumstances, a typical hospital structure representing the Italian healthcare buildings was chosen as a case study and placed in 4 Italian cities, Milan, Bologna, Rome, and Naples. Cesari et al. [67] collected the data for the investigation process of energy consumption of any building gather from field studies, technical reports, energy audits, measurements using instruments, etc. There are several articles focused on the investigation of space layout by developing space layout variants which were found to be effective in assessing the EPB. Different variants are created based on the climatic considerations [17], spatial arrangement [22], envelope parameters [42]. Rajagopalan et al. [44] created 10 variants of space layout of two buildings selected out of 30 hospitals based on age, location, and size of the building to investigate the energy consumption in medium-sized hospitals in Australia. Du et al. [17] designed 11 variants based on the existing reference space layout of the office which was simulated in 3 different climatic zones to measure the effect of spatial layout on EPB in different climates. Zhang et al. [20] selected a common form of classroom space with 30 design characteristics and was selected as a case study to demonstrate the optimization process. The optimization targets were set at energy demand, thermal performance, and daylight environment. It can be observed that some of the researchers are focused on mixed building typologies as the sample frame to investigate the energy usage in the buildings. Ma et al. [57] considered the 119 public buildings in which 99 office buildings, 11 hospital buildings, and 9 school buildings are considered as samples for the energy

consumption investigation in China. García-Sanz-Calcedo et al. [12] evaluated the physical and functional elements that have the greatest impact on sizing healthcare facilities, as well as the practical correlations between energy use and emissions by considering 70 health centers in Extremadura (Spain) for research. Whereas Bawaneh et al. [64] provided an analytic overview of end-use energy consumption statistics in healthcare systems in the United States hospitals. Shahzad et al. [56] compared the building performance of the two buildings, they are an office building in Norway constructed in 2000 and a British office building constructed in 2011 against the standards and benchmarks. It included energy consumption, thermal performance, carbon dioxide, and light levels. Short et al. [21] examined more than 1000 room types of clinical and non-clinical spaces to suggest the typical environmental design strategies for hospitals to enhance the EPB. He collected electricity consumption of 28 departments of 8 medium to large critical hospitals in England through a field survey.

Results and discussions

The literature survey mainly focused on the energy performance of hospitals and their parameters along with other functional requirements of buildings. The space layout is an integrated part of architectural design, and many works of literature identified the whole architectural design effect on energy consumption patterns and suggested alternative technology, passive strategies, building form, and orientation. The geographical location and climate play an important role in energy-efficient buildings. There is more research concentrated on climates of warm humid, hot and dry, and moderate climates in various locations like the USA, UK, and Asia. The HVAC, lighting, and electricity consumption are regulated using effective strategies like design optimization, passive strategies, and alternative building methods. The most selected case study building typology is an office building with a 42% rate and healthcare buildings have been studied with a rate of 14%. The least studied building typology that complies with Fig. 3 is mixed-use buildings with a 2% rate. 5% of the whole studies are not specific to any building typologies. Table 2 demonstrates that most of the studies have been done theoretically with a 45% rate in the literature in which simulation tools are used to analyze energy performance and 10% of works of literature considered mixed methodologies [103]. Building simulation helped to evaluate the building model for energy performance very accurately within a shorter period and many alternate energy optimization solutions can be generated based on the necessity and the context. 44% of the research depended on EnergyPlus as a simulation engine and out of which 25% of studies considered DesignBuilder as software. EnergyPlus software is



considered in much research to get more accurate results compared to other simulation engines, as it is validated by the Department of Energy, USA. From the review, it can be concluded that 27% of articles studied the effectiveness of the layout along with other perimeter parameters. The next major part of the study concentrated on occupancy, orientation, and glazing parameters with 25% each. 29% of the study highlighted the importance of shading devices and details on the energy performance of the building [55]. Also, different user activities and systems against space-to-space environmental diversity are significant determinants of the energy performance of any complex buildings [14]. 25% of the studies addressed the methodological system to investigate the energy consumption and performance of different design variables of the buildings and also resulted in significant variation in the energy load including HVAC, lighting, and electricity [23, 30, 40, 46, 48–51, 53, 63, 68, 72]. HVAC efficacy is most rewarding in structures that operate 24 hours like hotels, hospitals, etc. [41].

The review also explored the future research direction where many of the papers investigated the energy consumption and building design elements of particular buildings and suggested the same criteria or methodology for other complex buildings like hospitals, hotels, etc. [20, 23, 46]. The single-room experiments can be extended to complex buildings considering the building envelope parameters along with more environmental factors as decision variables and the building energy demands along with cost functions through multi-objective optimization [20, 23]. There is further scope to develop an optimal model-based control approach to achieve the space layout and thermal zone configuration in complex structures where there is flexible occupancy as well as space use intensities [14, 19, 36]. More research can be towards adapting effective adaptive thermal control and passive strategies along with the consideration of HVAC components' operation, type, and control for solar optimization to reduce the HVAC energy consumption in buildings giving special emphasis to individual departments of hospitals [29, 54, 71]. Energy use in hospitals is higher than compared other public buildings, so it is essential to investigate its energy consumption performance to develop a comprehensive strategy to reduce the mechanical load [104]. But there is limited research on the impact of space layout of hospital buildings on building energy performance. There is a lack of the proper energy consumption calculation methodology for multi-dimensional functions, activities, and the management systems of hospital buildings. There is a concern about the diverse functional requirements in varied departments and zones of the hospitals, as well as their investigation of energy performance along with suggestions for an effective research framework to analyze actual energy data [54]. In hospitals, combining lighting and ventilation system for energy simulation can be a great solution

to calculate a wide-ranging energy performance considering the architectural design emphasizing space layout and building perimeter.

Conclusion

The systematic literature review was carried out to identify the variables, their assessment criteria, methodology for evaluation, and optimization strategies for the energy performance of the buildings from selected 55 articles. Many works of the literature identified the impact of the architectural design and space layout effect on energy consumption along with the building perimeter variables. Three are suggestions for alternative technology, passive strategies, enhancing envelope parameters improving building form and orientation, and focusing on climatic parameters. In recent years, the methodologies to investigate energy performance in buildings is mainly focused on simulation-based study with multiple objectives, which gives accurate results, and analysis can be conducted in lesser time. Exterior window WWR, door opening size, type, and location/orientation, as well as frame types and insulation, all have a significant impact on influencing the energy load. According to the study, proper sizing of the building will reduce around 17–35% of energy consumption. Choosing the correct glazing system will reduce the 35–40% energy load of the building. Enhanced Window detailing can bring a 30–60% energy consumption difference in a building. Despite much research on the design of energy-efficient windows, there is still a lack of information on the mutual impact of the orientation of windows along with size and position on energy loads. Literature review shows a lack of insight into the correlation between space layout and energy performance framework which needs to be studied further, especially in terms of multiple energy performance indicators like heating, cooling, lighting, and thermal comfort, especially in the health-care-built environment. Compared to other buildings such as public buildings, offices, commercial and hotels, hospitals consume more energy because of their diversified functional requirement and activities. There is a lack of studies on the effect of hospital architecture design on energy consumption and related costs and it is very much necessary to conduct interventional studies, investigate the effect of using different methods on reducing energy consumption, and choose effective economical practices. There is varied energy consumption in each space or zones of a hospital since there can be a detailed analysis of each department individually to explore the energy efficiency of the hospital like outpatient department, inpatient department, offices, day-care units, operation theatres, intensive care unit, kitchen, radiology department, emergency wards, etc. along with geographical and climatic conditions. In India, the study on the energy performance



of hospitals is inadequate, so precise analysis is required. Implementing the ECBC building code and advanced energy efficiency techniques can be used to analyze energy-saving potential in hospitals in India. The impact of climates such as composite and warm humid climates need to be explored to integrate the functional objectives in the process of investigation for the EPB with relation to space layout which is scarcely mentioned in the previous research. Future research could be directed toward the spatial configuration of the energy performance of hospital buildings with multiple parameters simultaneously. Well-thought-out layout design may prevent unreasonable energy consumption to enhance the overall sustainability of the building and contribute to climate change mitigation.

Funding Open access funding provided by Manipal Academy of Higher Education, Manipal. The authors have no financial or proprietary interests in any material discussed in this article.

Declarations

Conflict of interest The authors declare no conflict of interest regarding the publication of this manuscript.

Open Access This article is licensed under a Creative Commons Attribution 4.0 International License, which permits use, sharing, adaptation, distribution and reproduction in any medium or format, as long as you give appropriate credit to the original author(s) and the source, provide a link to the Creative Commons licence, and indicate if changes were made. The images or other third party material in this article are included in the article's Creative Commons licence, unless indicated otherwise in a credit line to the material. If material is not included in the article's Creative Commons licence and your intended use is not permitted by statutory regulation or exceeds the permitted use, you will need to obtain permission directly from the copyright holder. To view a copy of this licence, visit <http://creativecommons.org/licenses/by/4.0/>.

References

- Rahman, N.M.A., Haw, L.C., Fazlizan, A.: A literature review of naturally ventilated public hospital wards in tropical climate countries for thermal comfort and energy saving improvements. *Energies (Basel)* **14**, 435 (2021). <https://doi.org/10.3390/en14020435>
- Mirabella, N., Röck, M., Saade, M.R.M., Spirinckx, C., Bosmans, M., Allacker, K., Passer, A.: Strategies to improve the energy performance of buildings: a review of their life cycle impact. *Buildings* **8**(8), 105 (2018)
- Global Energy and CO2 Status Report 2019, IEA, Paris (2019)
- Santamouris, M., Vasilakopoulou, K.: Present and future energy consumption of buildings: challenges and opportunities towards decarbonisation. *e-Prime*. 100002 (2021). <https://doi.org/10.1016/j.prime.2021.100002>
- Pérez-Lombard, L., Ortiz, J., Pout, C.: A review on buildings energy consumption information. *Energy Build.* **40**, 394–398 (2008). <https://doi.org/10.1016/j.enbuild.2007.03.007>
- Sun, Z., Cao, Y., Wang, X., Yu, J.: Multi-objective optimization design for windows and shading configuration: consenergy consumption, thermal environment, visual performance and sound insulation effect. *Int. J. Energy Environ. Eng.* **12**, 805–836 (2021). <https://doi.org/10.1007/s40095-021-00413-0>
- Du, T., Jansen, S., Turrin, M., van den Dobbelen, A.: Effects of architectural space layouts on energy performance: a review. *Sustainability* **12**(5), 1829 (2020). <https://doi.org/10.3390/su12051829>
- Forcael, E., Nope, A., García-Alvarado, R., Bobadilla, A., Rubio-Bellido, C.: Architectural and management strategies for the design, construction and operation of energy efficient and intelligent primary care centers in Chile. *Sustainability (Switzerland)* **11**, 464 (2019). <https://doi.org/10.3390/su11020464>
- Du, T., Jansen, S., Turrin, M., van den Dobbelen, A.: Impact of space layout on energy performance of office buildings coupling daylight with thermal simulation. In: CLIMA 2019At: Bucharest, Romania. (2019). <https://doi.org/10.1051/e3sconf/2019111030>
- Coakley, D., Raftery, P., Keane, M.: A review of methods to match building energy simulation models to measured data. *Renew. Sustain. Energy Rev.* **37**, 123–141 (2014). <https://doi.org/10.1016/j.rser.2014.05.007>
- Wright, J.: Factors influencing the design of spatial layouts in healthcare buildings. In: Proceedings of the 25th Annual ARCOM Conference (ARCOM 2009), Nottingham, UK, vol. 2 (2009)
- García-Sanz-Calcedo, J.: Analysis on energy efficiency in healthcare buildings. *J. Healthc. Eng.* **5**, 361–374 (2014). <https://doi.org/10.1260/2040-2295.5.3.361>
- Zhang, A., Huang, Q., Sun, Y., Zhang, Q.: Multi-objective window optimization of school buildings for thermal and daylight performance in the cold climate of China. In: Proceedings of 33rd PLEA International Conference: Design to Thrive, PLEA 2017, pp. 4461–4468 (2017)
- Musau, F., Steemers, K.: Space planning and energy efficiency in laboratory buildings: the role of spatial, activity and temporal diversity. *Archit. Sci. Rev.* **50**, 281–292 (2007). <https://doi.org/10.3763/asre.2007.5034>
- Musau, F., Steemers, K.: Space planning and energy efficiency in office buildings: the role of spatial and temporal diversity. *Archit. Sci. Rev.* **51**, 133–145 (2008). <https://doi.org/10.3763/asre.2008.5117>
- Bano, F., Sehgal, V.: Evaluation of energy-efficient design strategies: comparison of the thermal performance of energy-efficient office buildings in composite climate, India. *Sol. Energy.* **176**, 506–519 (2018). <https://doi.org/10.1016/j.solener.2018.10.057>
- Du, T., Jansen, S., Turrin, M., van den Dobbelen, A.: Effect of space layouts on the energy performance of office buildings in three climates. *J. Build. Eng.* **39**, 102198 (2021). <https://doi.org/10.1016/j.jobe.2021.102198>
- Shahzad, S., Brennan, J., Theodossopoulos, D., Hughes, B., Calautit, J.K.: A study of the impact of individual thermal control on user comfort in the workplace: Norwegian cellular vs. British open plan offices. *Archit. Sci. Rev.* **60**, 49–61 (2017). <https://doi.org/10.1080/00038628.2016.1235544>
- Gärtner, J.A., Massa Gray, F., Auer, T.: Assessment of the impact of HVAC system configuration and control zoning on thermal comfort and energy efficiency in flexible office spaces. *Energy Build.* **212**, 109785 (2020). <https://doi.org/10.1016/j.enbuild.2020.109785>
- Zhang, A., Bokel, R., van den Dobbelen, A., Sun, Y., Huang, Q., Zhang, Q.: Optimization of thermal and daylight performance of school buildings based on a multi-objective genetic algorithm in the cold climate of China. *Energy Build.* **139**, 371–384 (2017). <https://doi.org/10.1016/j.enbuild.2017.01.048z>



21. Short, C.A., Al-Maiyah, S.: Design strategy for low-energy ventilation and cooling of hospitals. *Build. Res. Inf.* **37**, 264–292 (2009). <https://doi.org/10.1080/09613210902885156>
22. Aldawoud, A.: The influence of the atrium geometry on the building energy performance. *Energy Build.* **57**, 1–5 (2013). <https://doi.org/10.1016/j.enbuild.2012.10.038>
23. Delgarm, N., Sajadi, B., Kowsary, F., Delgarm, S.: Multi-objective optimization of the building energy performance: a simulation-based approach by means of particle swarm optimization (PSO). *Appl. Energy* **170**, 293–303 (2016). <https://doi.org/10.1016/j.apenergy.2016.02.141>
24. Lavy, S., Kiss, C.W., Fernandez-Solis, J.L.: Linking design and energy performance in U.S. military hospitals. *Archit. Eng. Des. Manage.*
25. Raghu, S.J., Rodrigues, L.L.R.: Behavioral aspects of solid waste management: a systematic review. *J. Air Waste Manag. Assoc.* **70**(12), 1268–1302 (2020). <https://doi.org/10.1080/10962247.2020.1823524>
26. Skoczek-Rubińska, A., Bajerska, J., Menclawicz, K.: Effects of fruit and vegetables intake in periodontal diseases: a systematic review. *Dent. Med. Probl.* **4**, 55 (2018). <https://doi.org/10.17219/dmp/99072>
27. Borgstein, E.H., Lamberts, R., Hensen, J.L.M.: Evaluating energy performance in non-domestic buildings: a review. *Energy Build.* **128**, 734–755 (2016). <https://doi.org/10.1016/j.enbuild.2016.07.018>
28. Aksoy, U.T., Inalli, M.: Impacts of some building passive design parameters on heating demand for a cold region. *Build. Environ.* **41**, 1742–1754 (2006). <https://doi.org/10.1016/j.buildenv.2005.07.011>
29. Tzempelikos, A., Athienitis, A.K.: The impact of shading design and control on building cooling and lighting demand. *Sol. Energy* **81**, 369–382 (2007). <https://doi.org/10.1016/j.solener.2006.06.015>
30. Yang, L., Lam, J.C., Tsang, C.L.: Energy performance of building envelopes in different climate zones in China. *Appl. Energy* **85**, 800–807 (2008)
31. Aldawoud, A., Clark, R.: Comparative analysis of energy performance between courtyard and atrium in buildings. *Energy Build.* **40**, 209–214 (2008). <https://doi.org/10.1016/j.enbuild.2007.02.017>
32. Poirazis, H., Blomsterberg, Å., Wall, M.: Energy simulations for glazed office buildings in Sweden. *Energy Build.* **40**, 1161–1170 (2008). <https://doi.org/10.1016/j.enbuild.2007.10.011>
33. Sozer, H.: Improving energy efficiency through the design of the building envelope. *Build. Environ.* **45**, 2581–2593 (2010). <https://doi.org/10.1016/j.buildenv.2010.05.004>
34. Nielsen, M.V., Svendsen, S., Jensen, L.B.: Quantifying the potential of automated dynamic solar shading in office buildings through integrated simulations of energy and daylight. *Sol. Energy* **85**, 757–768 (2011). <https://doi.org/10.1016/j.solener.2011.01.010>
35. García Sanz-Calcedo, J., Cuadros Blázquez, F., López Rodríguez, F., Ruiz-Celma, A.: Influence of the number of users on the energy efficiency of health centres. *Energy Build.* **43**, 1544–1548 (2011). <https://doi.org/10.1016/j.enbuild.2011.02.012>
36. Pisello, A.L., Bobker, M., Cotana, F.: A building energy efficiency optimization method by evaluating the effective thermal zones occupancy. *Energies (Basel)* **5**, 5257–5278 (2012). <https://doi.org/10.3390/en5125257>
37. Adamu, Z.A., Price, A.D.F., Cook, M.J.: Performance evaluation of natural ventilation strategies for hospital wards—a case study of Great Ormond Street Hospital. *Build. Environ.* **56**, 211–222 (2012). <https://doi.org/10.1016/j.buildenv.2012.03.011>
38. Ascione, F., Bianco, N., de Masi, R.F., Vanoli, G.P.: Rehabilitation of the building envelope of hospitals: achievable energy savings and microclimatic control on varying the HVAC systems in Mediterranean climates. *Energy Build.* **60**, 125–138 (2013). <https://doi.org/10.1016/j.enbuild.2013.01.021>
39. Schulze, T., Eicker, U.: Controlled natural ventilation for energy efficient buildings. *Energy Build.* **56**, 221–232 (2013). <https://doi.org/10.1016/j.enbuild.2012.07.044>
40. Zhou, S., Zhao, J.: Optimum combinations of building envelop energy-saving technologies for office buildings in different climatic regions of China. *Energy Build.* **57**, 103–109 (2013). <https://doi.org/10.1016/j.enbuild.2012.11.019>
41. Tulsyan, A., Dhaka, S., Mathur, J., Yadav, J.V.: Potential of energy savings through implementation of Energy Conservation Building Code in Jaipur city, India. *Energy Build.* **58**, 123–130 (2013). <https://doi.org/10.1016/j.enbuild.2012.11.015>
42. Susorova, I., Tabibzadeh, M., Rahman, A., Clack, H.L., Elnmeiri, M.: The effect of geometry factors on fenestration energy performance and energy savings in office buildings. *Energy Build.* **57**, 6–13 (2013). <https://doi.org/10.1016/j.enbuild.2012.10.035>
43. García-Sanz-Calcedo, J., López-Rodríguez, F., Cuadros, F.: Quantitative analysis on energy efficiency of health centers according to their size. *Energy Build.* **73**, 7–12 (2014). <https://doi.org/10.1016/j.enbuild.2014.01.021>
44. Rajagopalan, P., Elkadi, H.: Energy performance of medium-sized healthcare buildings in Victoria, Australia—a case study. *J. Healthc. Eng.* **5**(2), 247–260 (2013). <https://doi.org/10.1260/2040-2295.5.2.247>
45. Wang, L., Greenberg, S.: Window operation and impacts on building energy consumption. *Energy Build.* **92**, 313–321 (2015). <https://doi.org/10.1016/j.enbuild.2015.01.060>
46. Chedwal, R., Mathur, J., Agarwal, G.D., Dhaka, S.: Energy saving potential through energy conservation building code and advance energy efficiency measures in hotel buildings of Jaipur city, India. *Energy Build.* **92**, 282–295 (2015). <https://doi.org/10.1016/j.enbuild.2015.01.066>
47. Méndez Echenagucia, T., Capozzoli, A., Cascone, Y., Sassone, M.: The early design stage of a building envelope: multi-objective search through heating, cooling, and lighting energy performance analysis. *Appl. Energy* **154**, 577–591 (2015). <https://doi.org/10.1016/j.apenergy.2015.04.090>
48. Zahiri, S., Altan, H.: The effect of passive design strategies on thermal performance of female secondary school buildings during warm season in a hot and dry climate. *Front. Built Environ.* **2**, 3 (2016). <https://doi.org/10.3389/fbuil.2016.00003>
49. Taleb, H.M.: Enhancing the skin performance of hospital buildings in the UAE. *J. Build. Eng.* **7**, 300–311 (2016). <https://doi.org/10.1016/j.job.2016.07.006>
50. Yang, Z., Ghahramani, A., Becerik-Gerber, B.: Building occupancy diversity and HVAC (heating, ventilation, and air conditioning) system energy efficiency. *Energy* **109**, 641–649 (2016). <https://doi.org/10.1016/j.energy.2016.04.099>
51. Amaral, A.R., Rodrigues, E., Rodrigues Gaspar, A., Gomes, A.: A thermal performance parametric study of window type, orientation, size and shadowing effect. *Sustain. Cities Soc.* **26**, 456–465 (2016). <https://doi.org/10.1016/j.scs.2016.05.014>
52. Goia, F.: Search for the optimal window-to-wall ratio in office buildings in different European climates and the implications on total energy saving potential. *Sol. Energy* **132**, 467–492 (2016). <https://doi.org/10.1016/j.solener.2016.03.031>
53. Harmathy, N., Magyar, Z., Folić, R.: Multi-criterion optimization of building envelope in the function of indoor illumination quality towards overall energy performance improvement. *Energy* **114**, 302–317 (2016). <https://doi.org/10.1016/j.energy.2016.07.162>
54. Morgenstern, P., Li, M., Raslan, R., Ruyssevelt, P., Wright, A.: Benchmarking acute hospitals: Composite electricity targets



- based on departmental consumption intensities? *Energy Build.* **118**, 277–290 (2016). <https://doi.org/10.1016/j.enbuild.2016.02.052>
55. Lu, S., Zheng, S., Kong, X.: The performance and analysis of office building energy consumption in the west of Inner Mongolia Autonomous Region, China. *Energy Build.* **127**, 499–511 (2016). <https://doi.org/10.1016/j.enbuild.2016.06.008>
 56. Shahzad, S., Brennan, J., Theodosopoulos, D., Hughes, B., Calautit, J.K.: Energy and comfort in contemporary open plan and traditional personal offices. *Appl. Energy* **185**, 1542–1555 (2017). <https://doi.org/10.1016/j.apenergy.2016.02.100>
 57. Ma, H., Du, N., Yu, S., Lu, W., Zhang, Z., Deng, N., Li, C.: Analysis of typical public building energy consumption in northern China. *Energy Build.* **136**, 139–150 (2017). <https://doi.org/10.1016/j.enbuild.2016.11.037>
 58. Alhuwayil, W.K., Abdul Mujeebu, M., Algarny, A.M.M.: Impact of external shading strategy on energy performance of multi-story hotel building in hot-humid climate. *Energy* **169**, 1166–1174 (2019). <https://doi.org/10.1016/j.energy.2018.12.069>
 59. Wagdy, A., Sherif, A., Sabry, H., Arafa, R., Mashaly, I.: Daylighting simulation for the configuration of external sun-breakers on south oriented windows of hospital patient rooms under a clear desert sky. *Sol. Energy* **149**, 164–175 (2017). <https://doi.org/10.1016/j.solener.2017.04.009>
 60. Bayoumi, M.: Impacts of window opening grade on improving the energy efficiency of a façade in hot climates. *Build. Environ.* **119**, 31–43 (2017). <https://doi.org/10.1016/j.buildenv.2017.04.008>
 61. Prieto, A., Knaack, U., Auer, T., Klein, T.: Passive cooling and climate responsive façade design exploring the limits of passive cooling strategies to improve the performance of commercial buildings in warm climates. *Energy Build.* **175**, 30–47 (2018). <https://doi.org/10.1016/j.enbuild.2018.06.016>
 62. González González, A., García-Sanz-Calcedo, J., Salgado, D.R.: A quantitative analysis of final energy consumption in hospitals in Spain. *Sustain. Cities Soc.* **36**, 169–175 (2018). <https://doi.org/10.1016/j.scs.2017.10.029>
 63. Omar, O., García-Fernández, B., Fernández-Balbuena, A.Á., Vázquez-Moliní, D.: Optimization of daylight utilization in energy saving application on the library in faculty of architecture, design and built environment Beirut Arab University. *Alex. Eng. J.* **57**, 3921–3930 (2018). <https://doi.org/10.1016/j.aej.2018.10.006>
 64. Bawaneh, K., Nezami, F.G., Rasheduzzaman, M., Deken, B.: Energy consumption analysis and characterization of healthcare facilities in the United States. *Energies (Basel)* **12**, 3775 (2019). <https://doi.org/10.3390/en12193775>
 65. Guo, Y., Bart, D.: Optimization of design parameters for office buildings with climatic adaptability based on energy demand and thermal comfort. *Sustainability (Switzerland)* **12**, 3540 (2020). <https://doi.org/10.3390/SU12093540>
 66. William, M.A., Elharidi, A.M., Hanafy, A.A., Attia, A., Elhelw, M.: Energy-efficient retrofitting strategies for healthcare facilities in hot-humid climate: parametric and economical analysis. *Alex. Eng. J.* **59**, 4549–4562 (2020). <https://doi.org/10.1016/j.aej.2020.08.011>
 67. Cesari, S., Valdiserri, P., Coccagna, M., Mazzacane, S.: The energy saving potential of wide windows in hospital patient rooms, optimizing the type of glazing and lighting control strategy under different climatic conditions. *Energies (Basel)* **13**, 2116 (2020). <https://doi.org/10.3390/en13082116>
 68. Fang, Y., Cho, S.: Design optimization of building geometry and fenestration for daylighting and energy performance. *Sol. Energy* **191**, 7–18 (2019). <https://doi.org/10.1016/j.solener.2019.08.039>
 69. Kyritsi, E., Michael, A.: An assessment of the impact of natural ventilation strategies and window opening patterns in office buildings in the Mediterranean basin. *Build. Environ.* **175**, 106384 (2020). <https://doi.org/10.1016/j.buildenv.2019.106384>
 70. Pilechiha, P., Mahdavejad, M., Pour Rahimian, F., Carnemolla, P., Seyedzadeh, S.: Multi-objective optimisation framework for designing office windows: quality of view, daylight and energy efficiency. *Appl. Energy* **261**, 114356 (2020). <https://doi.org/10.1016/j.apenergy.2019.114356>
 71. Aunió-Villa, J., Gómez-Chaparro, M., García-Sanz-Calcedo, J.: Study of the energy intensity by built areas in a medium-sized Spanish hospital. *Energy Effic.* **14**, 1–15 (2021). <https://doi.org/10.1007/s12053-021-09944-1>
 72. Zou, Y., Zhan, Q., Xiang, K.: A comprehensive method for optimizing the design of a regular architectural space to improve building performance. *Energy Rep.* **7**, 981–996 (2021). <https://doi.org/10.1016/j.egyr.2021.01.097>
 73. Dorrah, D.H., Marzouk, M.: Integrated multi-objective optimization and agent-based building occupancy modeling for space layout planning. *J. Build. Eng.* **34**, 101902 (2021). <https://doi.org/10.1016/j.job.2020.101902>
 74. Noshin, S., Kanwal, H., Aslam, M.S., Mushtaq, U.: Evaluation of daylight performance on the selected design parameters of light shelves. *Int. J. Eng. Res.* **9** (2018)
 75. Hafiz, D.: Daylighting, space, and architecture: a literature review. *J. Archit.* **12** (2015). <https://doi.org/10.17831/enq:arcc.v12i1.391>
 76. Edwards L., Torcelliniv, P.: Literature review of the effects of natural light on building occupants. In: U.S. Department of Energy Office of Scientific and Technical Information (2002)
 77. Haq, M.A.U., Hassan, M.Y., Abdullah, H., Rahman, H.A., Abdullah, M.P., Hussin, F., Said, D.M.: A review on lighting control technologies in commercial buildings, their performance and affecting factors. *Renew. Sustain. Energy Rev.* **33**, 268–279 (2014)
 78. Bhatnagar, M., Mathur, J., Garg, V.: Development of reference building models for India. *J. Build. Eng.* **21**, 267–277 (2019). <https://doi.org/10.1016/j.job.2018.10.027>
 79. Darwish, M.A.: Building air conditioning system using fuel cell: case study for Kuwait. *Appl. Therm. Eng.* **27**, 2869–2876 (2007). <https://doi.org/10.1016/j.applthermaleng.2006.06.001>
 80. Solgi, E., Kari, B.M., Fayaz, R., Taheri, H.: The impact of phase change materials assisted night purge ventilation on the indoor thermal conditions of office buildings in hot-arid climates. *Energy Build.* **150**, 488–497 (2017). <https://doi.org/10.1016/j.enbuild.2017.06.035>
 81. Artmann, N., Manz, H., Heiselberg, P.: Climatic potential for passive cooling of buildings by night-time ventilation in Europe. *Appl. Energy* **84**, 187–201 (2007). <https://doi.org/10.1016/j.apenergy.2006.05.004>
 82. Haase, M., Amato, A.: An investigation of the potential for natural ventilation and building orientation to achieve thermal comfort in warm and humid climates. *Sol. Energy* **83**, 389–399 (2009). <https://doi.org/10.1016/j.solener.2008.08.015>
 83. Hemsath, T.L., Alagheband Bandhosseini, K.: Sensitivity analysis evaluating basic building geometry's effect on energy use. *Renew. Energy* **76**, 526–538 (2015). <https://doi.org/10.1016/j.renene.2014.11.044>
 84. Raji, B., Tenpierik, M.J., van den Dobbelsteen, A.: Early-stage design considerations for the energy-efficiency of high-rise office buildings. *Sustainability (Switzerland)* **9**, 623 (2017). <https://doi.org/10.3390/su9040623>
 85. Xu, X., Luo, F., Wang, W., Hong, T., Fu, X.: Performance-based evaluation of courtyard design in China's cold-winter hot-summer climate regions. *Sustainability (Switzerland)* **10**, 3950 (2018). <https://doi.org/10.3390/su10113950>
 86. Halawa, E., Ghaffarianhoseini, A., Ghaffarianhoseini, A., Trombly, J., Hassan, N., Baig, M., Yusoff, S.Y., Azzam



- Ismail, M.: A review on energy conscious designs of building façades in hot and humid climates: lessons for (and from) Kuala Lumpur and Darwin. *Renew. Sustain Energy Rev.* **82**(3), 2147–2161 (2018). <https://doi.org/10.1016/j.rser.2017.08.061>
87. Luo, Y., Zhang, L., Bozlar, M., Liu, Z., Guo, H., Meggers, F.: Active building envelope systems toward renewable and sustainable energy. *Renew. Sustain Energy Rev.* **104**, 470–491 (2019). <https://doi.org/10.1016/j.rser.2019.01.005>
 88. Hammad, F., Abu-Hijleh, B.: The energy savings potential of using dynamic external louvers in an office building. *Energy Build.* **42**, 1888–1895 (2010). <https://doi.org/10.1016/j.enbuild.2010.05.024>
 89. Gan, W., Cao, Y., Jiang, W., Li, L., Li, X.: Energy-saving design of building envelope based on multiparameter optimization. *Math. Probl. Eng.* **2019**, 1–11 (2019). <https://doi.org/10.1155/2019/5261869>
 90. Kheiri, F.: A review on optimization methods applied in energy-efficient building geometry and envelope design. *Renew. Sustain. Energy Rev.* **92**, 897–920 (2018). <https://doi.org/10.1016/j.rser.2018.04.080>
 91. Minne, E., Wingrove, K., Crittenden, J.C.: Influence of climate on the environmental and economic life cycle assessments of window options in the United States. *Energy Build.* **102**, 293–306 (2015). <https://doi.org/10.1016/j.enbuild.2015.05.039>
 92. Lee, J.W., Jung, H.J., Park, J.Y., Lee, J.B., Yoon, Y.: Optimization of building window system in Asian regions by analyzing solar heat gain and daylighting elements. *Renew. Energy* **50**, 522–531 (2013). <https://doi.org/10.1016/j.renene.2012.07.029>
 93. Guan, L.: The influence of glass types on the performance of air-conditioned office buildings in Australia. *Adv. Mater. Res.* **346**, 34–39 (2012). <https://doi.org/10.4028/www.scientific.net/AMR.346.34>
 94. Gustavsen, A., Griffith, B.T., Arasteh, D.: Natural convection effects in three-dimensional window frames with internal cavities. *ASHRAE Trans.* **107**(2), 527–537 (2001)
 95. Jia, L.R., Han, J., Chen, X., Li, Q.Y., Lee, C.C., Fung, Y.H.: Interaction between thermal comfort, indoor air quality and ventilation energy consumption of educational buildings: a comprehensive review. *Buildings* **11**, 591 (2021). <https://doi.org/10.3390/buildings11120591>
 96. Lee, D., Jo, J.H., Koo, S.-H., Lee, B.: Development of climate indices using local weather data for shading design. *Sustainability* **7**, 1884–1899 (2015). <https://doi.org/10.3390/su7021884>
 97. Lim, H.S., Kim, G.: Predicted performance of shading devices for healthy visual environment. *Indoor Built Environ.* **19**, 486–496 (2010). <https://doi.org/10.1177/1420326X10376440>
 98. ISO 50006:2014: Energy management systems—general principles and guidance (2014)
 99. Nourdine, B., Saad, A.: Energy consumption in hospitals. In: 2020 International Conference on Electrical and Information Technologies, ICEIT 2020. Institute of Electrical and Electronics Engineers Inc. (2020)
 100. Bahar, Y.N., Pere, C., Landrieu, J., Nicolle, C.: A thermal simulation tool for building and its interoperability through the building information modeling (BIM) platform. *Buildings* **3**(2), 380–398 (2013). <https://doi.org/10.3390/buildings3020380>
 101. Bencheikh, D., Bederina, M.: Assessing the duality of thermal performance and energy efficiency of residential buildings in hot arid climate of Laghouat, Algeria. *Int. J. Energy Environ. Eng.* **11**, 143–162 (2020). <https://doi.org/10.1007/s40095-019-00318-z>
 102. Weytjens, L., Attia, S., Verbeeck, G., Herde, A.: The ‘Architect-friendliness’ of six building performance simulation tools: a comparative study. *Int. J. Sustain. Build. Technol. Urban Dev.* **2**, 237–244 (2012). <https://doi.org/10.5390/SUSB.2011.2.3.237>
 103. Kiritmat, A., Koyunbaba, B.K., Chatzikonstantinou, I., Sariyildiz, S.: Review of simulation modeling for shading devices in buildings. *Renew. Sustain. Energy Rev.* **53**, 23–49 (2016)
 104. Ji, R., Qu, S.: Investigation and evaluation of energy consumption performance for hospital buildings in China. *Sustainability (Switzerland)* **11**, 1724 (2019). <https://doi.org/10.3390/su11061724>

Publisher's Note Springer Nature remains neutral with regard to jurisdictional claims in published maps and institutional affiliations.





Study of a solar HDH desalination unit powered greenhouse for water and humidity self-sufficiency

Karima Hijjaji¹ · Nader Frikha^{1,2} · Slimane Gabsi^{1,2} · Abdelhamid Kheiri³

Received: 4 May 2022 / Accepted: 13 August 2022 / Published online: 26 August 2022
© The Author(s), under exclusive licence to Islamic Azad University 2022

Abstract

This study investigates the performances of a self-sufficient greenhouse powered by a solar humidification–dehumidification desalination unit. It aims to achieve an overall integrated system that produces enough fresh water to cover the irrigation demand as well as the air humidification needs of the greenhouse. The humidification–dehumidification operation was numerically simulated using the developed model along with the greenhouse microclimate. The greenhouse model was validated through an experimental real-scale greenhouse. To make the proposed system more flexible, an auxiliary control system is used to easily monitor the greenhouse needs and ensure its satisfaction. The findings revealed that the integrated system, with its two main subsystems and its regulation device, successfully ensures the greenhouse irrigation, the humidification needs and provides an optimal plant growth. For the case study, i.e. cucurbit greenhouse situated at El Hamma (Tunisia), the desalination system can cover more than 200% of the greenhouse water irrigation needs while keeping the greenhouse inside air at a humidity level of 60% at least. The maximum productivity and the best energy efficiency are respectively 5.1 m³/day and 63.25%.

Keywords Solar energy · Saltwater greenhouse · HDH desalination · Process control · Irrigation

List of symbols

A	Area (m ²)	h	Heat transfer coefficient (W/m ² K)
a	Specific gas–liquid interfacial area (m ² /m ³)	h_c	Convective heat transfer coefficient (W/m ² K)
C_p	Specific heat capacity (J/kg K)	h_e	Evaporative heat transfer coefficient (W/m ² K)
D	Molecular diffusion coefficient (m ² /s)	h_r	Radiative heat transfer coefficient (W/m ² K)
d_p	Diameter of packing (m)	I	Solar radiation intensity (W/m ²)
$E\lambda$	Evapotranspiration flux (W/m ²)	K	Thermal conductivity (W/m K)
e	Water content of the air (kg/m ³)	k, k_m	Mass transfer coefficient (kg/s m ³ atm)
e^*	Saturated water content of the air at surface (kg/m ³)	L	Water flow rate (kg/m ² s)
f_g	Ventilation flux correction coefficient	LAI	Leaf area index
G	Air flow rate (kg/m ² s)	Le	Lewis number
H	Greenhouse height (m)	L_{CL}	Characteristic leaf length (m)
H_L	Enthalpy liquid (kJ/kg)	L_v	Latent heat of vaporization (kJ/kg)
		M	Molar mass (kg/mol)
		m	Mass (kg)
		P_p	Proportion of area covered by plants (m ² /m ²)
		P_t	Total pressure (Pa)
		P_v	Partial pressure (Pa)
		P_{vs}	Saturated vapor pressure (Pa)
		Q	Mass flow rate (kg/m ² h)
		q	Heat flux (W/m ²)
		r	Crop resistance (s/m)
		Ra	Rayleigh number
		Re	Reynolds number
		Rn	Net shortwave radiation (W/m ²)
		Sc	Schmidt number

✉ Karima Hijjaji
karimahijjaji@gmail.com

¹ Laboratory Energy, Water, Environment and Process, National Engineering School of Gabes, University of Gabes, Gabes, Tunisia

² Higher Institute of Biotechnology of Sfax & National Engineering School of Sfax, University of Sfax, Street Omar Ibn ElKhattab, 6029 Gabes, Tunisia

³ Lemta, CNRS, Université de Lorraine, Nancy, France



T	Temperature ($^{\circ}\text{C}$ or K)
U	Overall heat transfer coefficient between the water and air ($\text{W}/\text{m}^2 \text{K}$)
V	Wind speed (m/s)
VPD	Vapour pressure deficit (Pa)
w, y	Absolute humidity (kg/kg dry air)
y^*	Saturation humidity (kg/kg dry air)
Z	Sprayer height (m)

Greek letters

ρ	Density (kg/m^3)
Φ	Relative humidity (%)
α	Absorptivity (–)
α_{ct}	Cover absorptivity of thermal radiation (–)
γ	Psychrometric constant (Pa/C)
δ	Slope of the saturation curve of the psychrometric chart (Pa/C)
ϵ	Emissivity (–)
τ	Transmissivity of greenhouse cover material to solar irradiation (Pa s)
μ	Dynamic viscosity ($\text{kg}/\text{m s}$)

Subscripts

a	Air/vapor mixture
am	Ambient
b	Solar still basin
c	Cover
cond	Condensate water
e	External, exterior air
g	Glassed cover
i	Internal, interior air
in	Inlet
is	Insulation
out	Outlet
p	Plant
s	Top soil
s0	Soil at a depth of 0.5 m
w	Water

Introduction

Disasters, including pandemics like COVID 19, prove the importance of food security, especially in arid regions that lack freshwater resources. Thus, a relentless quest for a sustainable agriculture system producing food with reduced consumption of water is a vital priority [1]. Within this context, greenhouse agriculture emerges as an ideal option that has shown a good adaptation to climate change while intending to reduce energy and water consumption making it hence a sustainable option for food production [2]. However, it is mandatory to control and maintain the microclimatic parameters inside the greenhouse at the desired ranges for optimal plant growth by

maximizing the photosynthetic and ensuring the irrigation requirements too. Maintaining an optimal relative humidity level in the greenhouses ensures optimal plant transpiration and less water irrigation needs.

Mpusia [3] suggested that water consumption in greenhouses can reduce by up to 50% compared to the outdoor conventional farming. Fernandes et al. [4] estimated that ensuring the required humidity inside greenhouse results in a 60–80% reduction in water consumption compared to the irrigation within outside fields. The average value of the main parameters required for crop growth includes a relative humidity within the range of 60 to 90%, an air temperature within the temperature range of 10 to 30 $^{\circ}\text{C}$ [5, 6], a carbon dioxide concentration in the range of 700–900 $\mu\text{mol mol}^{-1}$ [7] and a sufficient flow of photosynthetic photons inside the greenhouse. Humidity is the hardest controlling variable in a greenhouse, and even the most advanced equipment cannot entirely control the humidity levels because it fluctuates with air temperature changes, the plant transpiration, which adds an extra steam to the air, and the solar radiation too [8]. High inside air humidity induces many agricultural issues such as leaf and root diseases, slow but permanent drying of the substrate, plant stress, and loss of quality and yield. Besides, the plants tend to be weaker and stretched [9]. Consequently, more pesticides must be used to counteract these diseases and stress. Conversely, if the humidity level is too low, the plant's growth is affected and it takes much longer to reach the desired size. Hence, whether the humidity is too high or too low, it is not favorable for the plant's growth [10].

Several systems are integrated into greenhouse in order to provide the desired microclimate by heating, cooling, or giving sufficient CO_2 and artificial lighting, in some cases [11]. Seawater greenhouses SWGH are becoming more and more popular nowadays. They consist in supplying fresh water and cooling the greenhouse inside air in one structure. Besides the greenhouse structure, the SWGH unit includes two humidifiers (evaporators) and one condenser (dehumidifier) placed in the greenhouse [12]. However, many authors argue that this type of integrated greenhouse SWGH is not economically profitable. Furthermore, they can neither cover the total irrigation need nor do they maintain the greenhouse humidification requirements in the desired ranges for a convenient growth of the plant [13]. Therefore, several modifications of the SWGH have been proposed in the literature. Farrell et al. [14] investigated a sustainable integrated greenhouse that encompasses a dehumidification desalination system, a reverse osmosis system, a reverse electro dialysis apparatus, and a dehumidification desalination system in an attempt to generate freshwater to cover the irrigation load of the greenhouse, cool the greenhouse inside environment to adequate temperatures while being energy self-sufficient using the electric energy produced by the reverse electro dialysis apparatus.



The authors show that producing a part of the irrigation needs by the reverse osmosis powered by the reverse electro-dialysis apparatus ensures an economically efficient system. Akrami et al. [15] developed a zero liquid discharge desalination system coupled with an agricultural greenhouse. They demonstrated the feasibility of using wicked solar still, HDH and a rainwater storage to ensure the needed irrigation water. Their findings show that the greenhouse they develop may be autonomous for its water requirement under different climates and in different countries. Radhwan [16] developed a stepped solar still for heating and humidifying an agriculture greenhouse. The performances of the still parameters were analyzed and presented. The results show that the average daily efficiency of the still is approximately 63%; and the total daily yield is approximately 4.92 l/m². Zamen et al. [17] suggested integrating and enhancing humidification–dehumidification unit (HDH) into an SWGH system, including a direct contact dehumidifier and a solar water heater. Results show a freshwater production of 450 L per day for a greenhouse area of 200 m². Salah et al. [18] studied the design performance of a new integrated self-sufficient agricultural greenhouse with transparent solar stills (TSS) on the roof to be self-sufficient in irrigation by using both excess solar energy via direct solar desalination in the TSS and the humidification–dehumidification (HDH) process as two sources for water production. The results reveal that system can only generate a maximum of 2.44 l/m² of fresh water on the coldest day, indicating a requirement to install additional solar stills if more water is needed.

Most studies in this field have focused on using a desalination system that can be operated with renewable energy [19, 20] to show that this system is economically viable. However, most of these systems are greenhouse dependent and therefore they work only during the greenhouse growing seasons.

The present research focuses on studying the feasibility of new proposed integrated saltwater greenhouse where an independent solar HDH desalination unit is coupled with an agriculture greenhouse. The characteristics of the proposed system that make its unicity are the independence of the HDH unit from the greenhouse which makes it more flexible to choose the HDH system and its dimensions and operates throughout the year. The HDH system is composed of a modified solar still operating with solar energy as humidifier and packed bed condenser as a dehumidifier. In order to make the HDH system simple and economically viable, some modifications are made to the solar still compared to the conventional solar still. Water forced evaporation is achieved by injecting air and water into the solar still, where the hot saline water is pulverized on the top, and the air is forced from the bottom, coming in indirect contact with the hot water, the produced humid air may be directed totally or partially to the agriculture greenhouse or the condenser to

produce freshwater. Furthermore, a control system is developed and used to drive the humid air part directed to the greenhouse and to control the whole system. Finally, the dehumidification is undergone in a packed bed condenser.

The main objective of this work is to study the performances of the proposed system using a comprehensive unsteady-state mathematical model of the several parts that constitute the system. The greenhouse model is experimentally evaluated using a real-scale greenhouse, and the simulation result of the whole model, driven by the developed control system, will permit to evaluate its performance in terms of ensuring the greenhouse humidification and irrigation needs.

Experimental

The integrated greenhouse considered in this study is composed of two independent but coupled main subsystems: the HDH and the greenhouse itself. The HDH subsystem encompasses mainly a condenser and solar stills (Fig. 1). Furthermore, a control auxiliary system is used to drive the whole system to meet the desired condition for the plant growing in the greenhouse. Contrary to the classical systems, here the humid air from the solar still may completely or partially be redirected to the greenhouse. The control system will manage the quantity of humid air at the solar still outlet. It will give the necessary to set the desired humidity in the greenhouse and the rest of the humid air will be redirected to the packed bed condenser to produce freshwater for the irrigation needs of the greenhouse plants.

In the following section (“[The HDH subsystem](#)” and “[The greenhouse subsystem](#)” sections) the HDH and the greenhouse considered subsystems in the present work are described.

The HDH subsystem

The irrigation water production is based on the well-known humidification and dehumidification (HDH) process. The humidification operation is ensured by a solar-powered and double-sloped desalination solar still where the saltwater is pulverized at the top of the still, as shown in Fig. 2. It is noted that the high of this solar still may be limited to a maximum of 60 cm. Compared to classic stills, pulverizing the saltwater enhances the surface contact between the pulverized droplets and the crossing flow of the inside blown air, and hence increases their mass and heat transfers.

- To ensure the dehumidification process, a packed bed direct contact condenser is used. In fact, this recently developed condensation technology shows more efficient results and is currently undergoing a dynamic growing



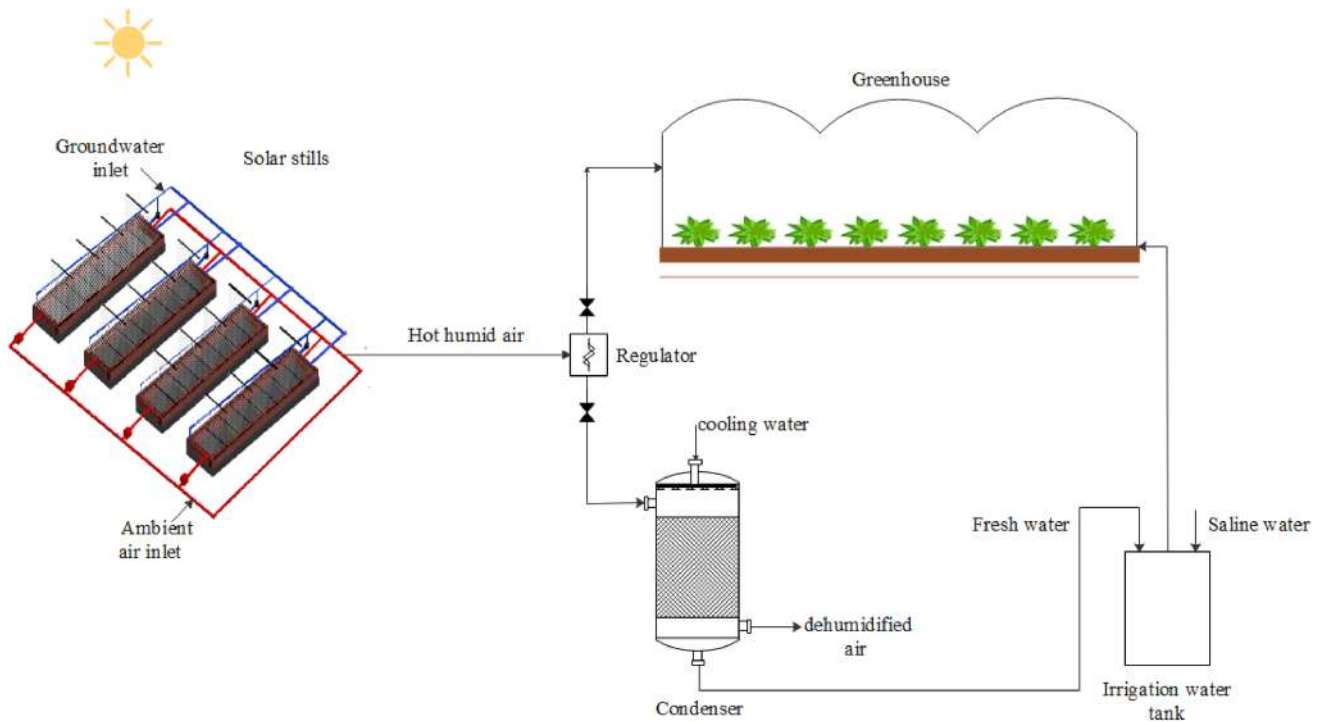


Fig. 1 Process schematic of HDH desalination system integrated into a greenhouse

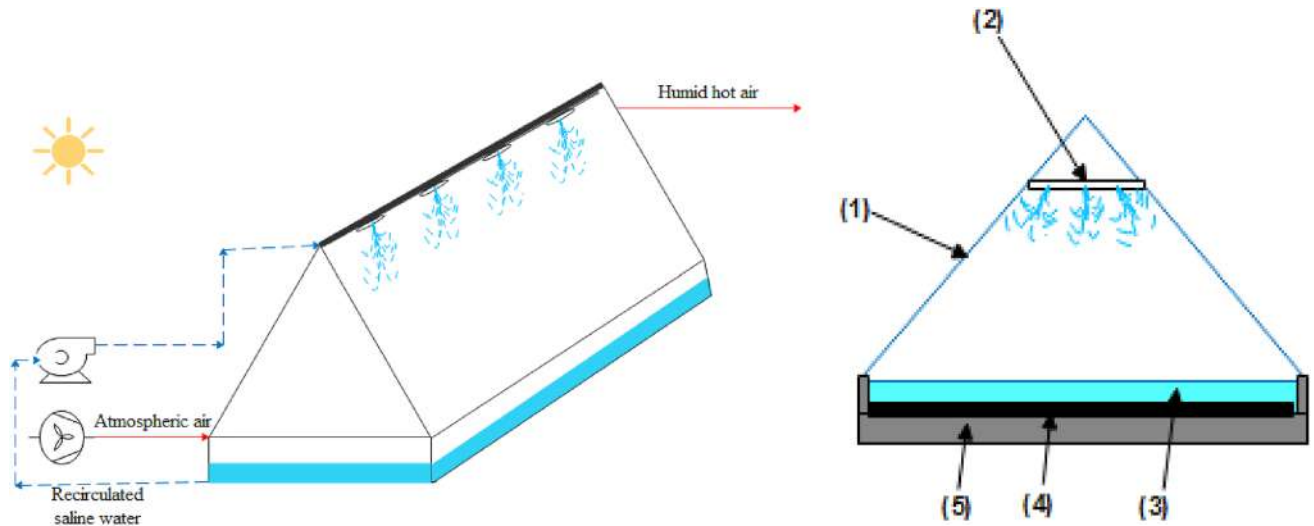


Fig. 2 Schematic diagram of the solar still of the HDH desalination system: (1)-transparent cover, (2)-sprayer, (3)-saline water, (4)-absorber, (5)-insulation layer

trend of interest and actual use [21]. Further details of the solar still working conditions are as follows:

- The sprayed saltwater water is continuously recirculated from the basin that stands at the bottom of the still where it is directly heated by the solar radiation.
- The ambient air is blown in the still and comes into contact with the droplets of the sprayed saltwater, which increases its relative humidity level and temperature. The

humidified air is extracted at the top of the solar still. Then, a part of the extracted humidified air enters the greenhouse to create the suitable humidity and temperature environment for the plant's growth, while the rest is redirected to the condenser to produce freshwater. The control auxiliary that drives the extracted humidified air flows is programmed to give the priority to covering the humidification needs of the greenhouse.

- In the irrigation water tank, the produced freshwater may be mixed with a saline water to obtain the desired salinity for the irrigation water of the greenhouse plants. In the present study, to achieve a desired salinity of the irrigation water of 1.6 g/l for cucurbit crop, the produced freshwater is mixed with a saline groundwater with a salinity of 3 g/l.

The considered HDH system for the further simulations is constituted to four solar stills with an area of 16 m² for each one, and by a condenser with a cross-section area of 0.36 m². The latter includes a 1 m height polypropylene packing bed. The density, specific heat and void fraction of the packed bed are 850 kg/m³, 2350 J/kg K, and 87.5%, respectively. The condenser is cooled by a deep groundwater with an incoming temperature assumed to be 15 °C for January and February and at 20 °C for the rest of the considered early crop season.

The greenhouse subsystem

The considered greenhouse in this work is a real-scale multi-span greenhouse type situated in El Hamma in south Tunisia. It is used both for the experimental validation of the developed models and for the simulation of the whole integrated system. It was constructed in East–West directions with a footprint of 500 m². Its dimensions include a length of 31 m, a width of 19.2 m and a height of 4 m. Cucurbit crops are cultivated in this greenhouse during two crop seasons: the early season from January to May, and a late season from Sept to December. Hygrometer Digital temperature sensors are used to measure the inside and outside air temperature and the relative humidity. The variation of air parameters as a function of time is recorded using an acquisition chain every 30 min.

A hydroponics system distributes the required irrigation load in a mass flow rate assumed to be equivalent to 110% of the mass rate of the evapotranspiration of the plants [22]. This water supply is assumed to be achieved between 8:00 a.m. and 6:00 p.m., and there is no water supply out of this period.

The Irrigation Load Coverage (ILC) of the whole system is its capability of covering the irrigation load. The ILC is computed irrespective of the fact that a part of the humidified air may be directly introduced into the greenhouse. Hence, considering that the irrigation need of the greenhouse crop corresponds to 110% of the evapotranspiration, the ILC is calculated as follows:

Irrigation Load Coverage

$$= \frac{\text{mass of condensate recovered by the condenser}}{\text{mass of evapotranspired water vapour} * 1.1} * 100$$

Mathematical modeling

Modeling is an effective way to examine the functioning of a system under various conditions. In order to model the integrated greenhouse system, mass and energy balance equations are formulated for each part, i.e. mainly for the solar still, the agriculture greenhouse and the condenser. The unsteady state global model leads to coupled differential equations that have been numerically solved using the fourth-order Runge Kutta method and a dedicated Matlab[®] code has been developed. The whole system behavior is simulated using this developed model.

The greenhouse model

The inside microclimate of the greenhouses is represented by the inside air temperature and its relative humidity, and results from complex mechanisms involving several heat and mass exchange processes of the soil, the air and the crop and of the greenhouse cover, as shown in Fig. 3. It depends strongly on the external conditions on the solar radiation and on the feeding air [22]. Furthermore, the water vapor plays a key role in this microclimate, and hence its mass balance is involved in the greenhouse models. It hence appears that the greenhouse global model is constituted by four energy balance equations and by at least one mass balance when the soil and the plant's mass balances are not considered.

These balances are presented below in “Greenhouse cover temperature” and “Plant temperature” sections assuming the following assumptions:

- The air and the topsoil temperatures are uniform in the greenhouse.
- The crop temperature depends only on the solar radiation and the air temperature inside the greenhouse.
- Soil temperature at 0.5 m depth is constant throughout the year.
- No evaporation occurs from the soil.
- Radiation energy is neither absorbed, emitted nor diffused by the inside air.

Greenhouse cover temperature

The energy balance equation for the greenhouse cover in unsteady state conditions is given by [22]:

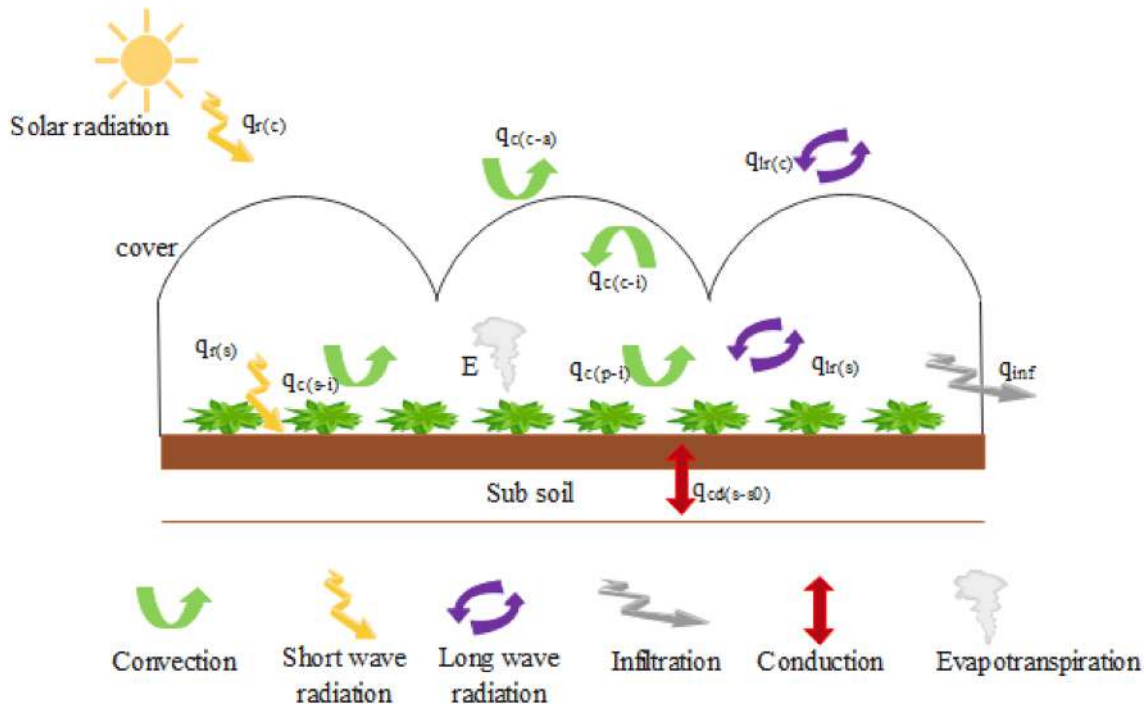


Fig. 3 Schematic of the greenhouse and its exchange with surroundings

$$\begin{aligned} \rho_c c p_c x_c \frac{dT_c}{dt} &= \alpha_c I (1 + \tau_c (1 - \alpha_s)) \\ &+ \frac{-\epsilon_c \gamma T_c^4 A_c + \alpha_{ct} \gamma T_{sky}^4 \epsilon_{sky} A_c + \epsilon_s \gamma T_s^4 \alpha_{ct} A_s}{A_s} \\ &- h_{c(c-a)} (T_c - T_{am}) + h_{c(c-i)} (T_c - T_i) \end{aligned} \quad (1)$$

where T_{sky} [23] is the so-called sky temperature. $h_{c(c-a)}$ is the convective heat transfer coefficient between the cover and the exterior ambient air and $h_{c(c-i)}$ is the convection heat transfer coefficient between the cover and the inside air [24].

The sky temperature and these two convection coefficients were computed using the followings equations [25]:

$$T_{sky} = 0.0552 (T_{am}^{1.5}) \quad (2)$$

$$h_{c(c-a)} = 7.2 + 3.8v \quad (3)$$

$$h_{c(c-i)} = 1.75 |T_c - T_i|^{1/3} \quad (4)$$

Greenhouse inside air temperature

The unsteady air state temperature inside the greenhouse obeys the following equation that describes the energy balance:

$$\begin{aligned} \rho_a c p_a H \frac{dT_i}{dt} &= -h_{c(s-i)} (T_i - T_s) - \frac{\rho_a G c p_a (T_i - T_{am})}{3600 A_s} \\ &- h_{c(c-i)} (T_c - T_i) + P_p L A I h_{c(p-i)} (T_p - T_i) \end{aligned} \quad (5)$$

where $h_{c(s-i)}$ and $h_{c(p-i)}$ are respectively the convective heat transfer coefficients between the inside air and the topsoil and between the inside air and the plants and are calculated by [23]:

$$h_{c(s-i)} = 1.75 |T_s - T_i|^{1/3} \quad (6)$$

$$h_{c(p-i)} = 1.4 \left(\frac{|T_p - T_i|}{L_{cl}} \right)^{0.25} \quad (7)$$

Plant temperature

As stated in the general assumptions, the plant temperature is estimated directly from the interior air temperature T_i and the global solar radiation I using the multiple linear regression model proposed by Wang and Deltour [26]:

$$T_p = -2.05 + 1.01 T_i + 0.00425 \tau_c I \quad (8)$$

Greenhouse soil temperature

The soil energy balance leads to the following differential equation [27]:

$$\rho_s c p_s x_{s0} \frac{dT_s}{dt} = \alpha_s I \tau_c + h_{c(s-i)}(T_i - T_s) - k_{s0}(T_s - T_{s0}) - \frac{\alpha_s \gamma \epsilon_s S_s T_c^4 - \epsilon_s \gamma T_s^4 S_s}{S_s} \tag{9}$$

where T_{s0} is the soil temperature at a depth of 0.5 m

Greenhouse inside air humidity

The mass balance of the water vapor of the greenhouse inside air leads to the following differential equation [25]:

$$l_v H \frac{de_i}{dt} = E \lambda - \frac{L_v}{\rho_a c p_a} L e^{\frac{1}{3}} h_{si}(e_i - e_s^*) - \frac{L_v}{\rho_a c p_a} L e^{\frac{1}{3}} h_{ci}(e_i - e_c^*) \frac{S_c}{A_s} - G f_g \frac{L_v}{A_s}(e_i - e_e) \tag{10}$$

where $E \lambda$ is the evapotranspiration rate given by Penman–Monteith [28]:

$$E \lambda = \frac{\delta R n + \left(\frac{2 L A l \rho_a C_A}{r_c}\right) VPD}{\gamma \left(1 + \left(\frac{\delta}{\gamma}\right) + \left(\frac{r_i}{r_c}\right)\right)} \tag{11}$$

The solar still model

The solar still bottom part consists of a simple insulated basin filled with the salt water and of a galvanized plate which constitutes the still’s absorber. The still is double-sloped with two glass cover and includes several water nozzles set up at the top. A fan blows the ambient air at the bottom of the still to create a crossing flow and also counter-current with the falling saltwater droplets. The air and the sprayed water are in close contact in such a way that the mass transfer is enhanced inducing a rapid enhancement of the relative humidity of the air. The humid air is extracted at the upper opposite side regarding the still feeding air. It was proven in a former study [29] that this enhanced solar still is more efficient than the simple stills.

Glassed cover temperature

The still top glassed covers temperature obeys the following equation that describes their energy balance:

$$m_g C_{pg} \frac{dT_g}{dt} = I \alpha_g A_g + \left[0.09 \sigma (T_w^4 - T_g^4) + h_{e(w-g)}(T_w - T_g) + h_{c(w-g)}(T_w - T_g)\right] A_b - \left[h_{c(g-a)}(T_g - T_{amb}) + h_{r(g-sky)}(T_g - T_{sky})\right] A_g \tag{12}$$

The Dunkle model is used to calculate the convective $h_{c(w-g)}$, evaporative $h_{e(w-g)}$, and radiative $h_{r(g-sky)}$ heat transfer coefficients between water and the glassed covers [30, 31].

$$h_{e(w-g)} = \frac{M_e L_v}{M_a c p_a} h_{c(w-g)} \frac{(P_w - P_g)}{(T_w - T_g)} \tag{13}$$

$$h_{c(w-g)} = 0.884 \left[(T_w - T_g) + \frac{(P_w - P_g) T_w}{268.10^3 - P_w} \right]^{1/3} \tag{14}$$

where P_w : saturation vapour pressure at water temperature T_w , P_g : saturation vapour pressure at glassed cover temperature T_g .

$$P_w = \exp\left(25.217 - \frac{5144}{T_w}\right) \tag{15}$$

$$P_g = \exp\left(25.217 - \frac{5144}{T_g}\right)$$

$$h_{r(g-sky)} = \frac{7.803 \cdot 10^{-3} [T_g^4 + T_{sky}^4]}{T_g - T_{sky}} \tag{16}$$

The convective heat transfer coefficient between the cover and the ambient exterior air is given by [25]:

$$h_{c(g-a)} = 5.7 + 3.8V \tag{17}$$

Saltwater temperature

The following equation gives the energy balance for the salt-water in the still’s basin:

$$m_w C_{pw} \frac{dT_w}{dt} = \left[\tau_g \alpha_w I + h_{c(b-w)}(T_b - T_w) - h_{c(w-g)} A_b (T_w - T_g) - 0.09 \sigma (T_w^4 - T_g^4) - h_{e(w-g)}(T_w - T_g) - h_{c(w-a)}(T_w - T_a)\right] A_b \tag{18}$$

The convection heat transfer coefficient between the salt water and the absorber plate is computed from the following relations [32]:

$$h_{c(b-w)} = \frac{k_w}{x_w} \quad Ra < 10^4 \tag{19}$$

$$h_{c(b-w)} = 0.54 \frac{k_w \text{Ra}_w^{1/4}}{x_e} \quad \text{Ra} = 10^4 - 10^7 \quad (20)$$

$$h_{c(b-w)} = 0.14 \frac{k_w \text{Ra}_w^{1/3}}{x_w} \quad \text{Ra} = 10^7 - 10^{11} \quad (21)$$

The evaporative heat transfer between the sprayed water and the air is given by [29]:

$$h_{e(w-a)} = -12.20 - 0.060G + 0.000923L + 0.3152T_w + 26.32Z + 0.00668G^2 + 0.000264GL + 0.00760GT_w - 0.6228GZ - 0.493T_wZ \quad (22)$$

Still inside air temperature

The following equation gives the energy balance for the still inside air:

$$m_a C_{pa} \frac{dT_a}{dt} = h_{e(w-a)}(T_w - T_a) - GC_{pa}(T_a - T_{amb}) \quad (23)$$

Absorber temperature

The following equation gives the energy balance for the still's absorber [33]:

$$m_b C_{pb} \frac{\partial T_b}{\partial t} = (\tau_g \tau_w \alpha_b I - h_{c(b-w)} A_b (T_b - T_w) - U_b (T_b - T_{is})) A_b \quad (24)$$

where the heat loss coefficient through the absorber is found from [32]:

$$U_b = \left(\frac{x_{is}}{k_{is}} + \frac{1}{h_{c(g-a)}} \right)^{-1} \quad (25)$$

Insulation temperature

To reduce heat loss through the still's basin, a thermal insulation is used. The following equation gives the energy balance for the insulation:

$$m_{is} C_{pis} \frac{\partial T_{is}}{\partial t} = U_b (T_b - T_{is}) - U_{is} A_b (T_{is} - T_a) \quad (26)$$

where the heat loss coefficient through the insulation is [32]:

$$U_{is} = \left(\frac{e_b}{k_b} + \frac{e_{is}}{k_{is}} + \frac{1}{h_{c(is-a)}} \right)^{-1} \quad (27)$$

$$h_{c(is-a)} = h_{c(g-a)}$$

Still inside air humidity

The following equation gives the mass balance for the air humidity inside the still:

$$m_a \frac{dy_a}{dt} = k_{m,a} (y_w - y_a) - G(y_a - y_0) \quad (28)$$

The mass transfer between the water and the air is given by [29]:

$$k_{m,a} = 10^{-3} (-6.9 + 2.221G - 0.00040L - 0.023T_w + 0.4Z - 0.01777G^2 + 0.000159GL + 0.00699GT_w - 1.060GZ) \quad (29)$$

$$y_w = 0.62 \frac{P_w}{P_{atm} - P_w}; \quad P_w = 25.317 - \frac{5144}{T_w} \quad (30)$$

The packed bed direct contact condenser model

In the used packed bed direct contact condenser [33], the cooling liquid and the humid air are in direct close contact in co-current flows. The heat is removed by the condensing cooling water (Fig. 4) that is sprayed over the cross-section on the top of the packing bed at the level where the humid air is injected. Following Li et al. [33], a two-fluid model is used where the energy and mass balance conservation unsteady state conditions are applied to a differential control volume leading to the humidity of the air and of the respective temperature of the air, the water and the packed bed material according to the vertical axis (z -axis). Air and water vapor are modelled as ideal gases, and heat losses are neglected.

Air humidity in the condenser

The conservation of mass applied to the liquid and vapor phases of the control volume is given by the following equation [34, 35]:

$$\frac{dw}{dz} = \frac{dT_a}{dz} \frac{P}{P - P_{sat}(T_a)} w (b - 2cT_a + 3dT_a^2) \quad (31)$$

where $P_{sat}(T)$ is the saturation pressure related to temperature T . This pressure is computed as [33]:

$$P_{sat}(T) = a \exp(bT - cT^2 + dT^3) \quad (32)$$

where empirical constants are: $a = 0.611379$, $b = 0.0723669$, $c = 2.78793 \cdot 10^{-4}$, $d = 6.76138 \cdot 10^{-7}$.

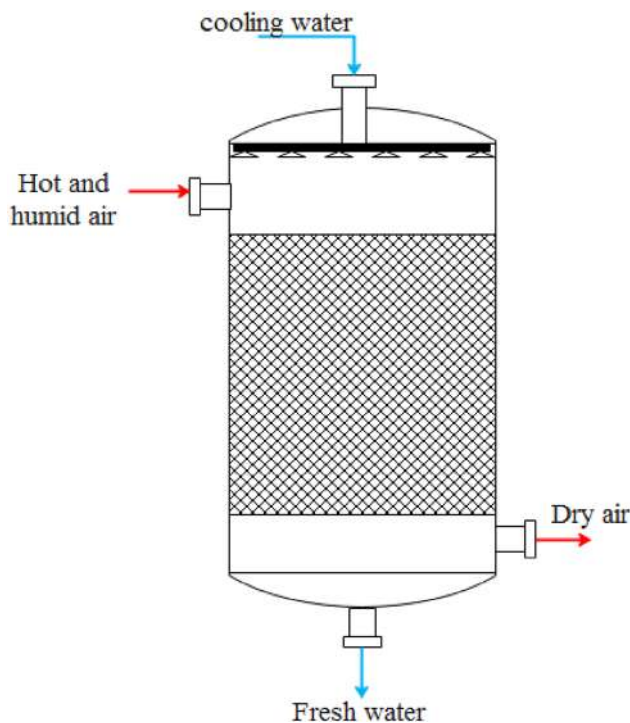


Fig. 4 Schematic representation of the dehumidification system

Condenser cooling water temperature

The conservation of energy applied to the cooling water of the control volume is given by the following equation [34, 35]:

$$\frac{dT_1}{dz} = \frac{G}{L} \frac{dw}{dz} \frac{(L_v - H_1)}{C_{pl}} + \frac{Ua(T_1 - T_a)}{C_{pL}L} \quad (33)$$

where the mass and heat transfer coefficients are given by [36, 37]:

$$k_1 = 0.0051 \text{Re}_1^{\frac{2}{3}} \text{Sc}_1^{-0.5} (ad_p)^{0.4} \left(\frac{\mu_1 g}{\rho_w} \right)^{\frac{1}{3}} \quad (34)$$

$$k_a = C \text{Re}_a^{0.7} \text{Sc}_a^{\frac{1}{3}} (ad_p)^{-2} a D_a \quad \begin{cases} C = 5.23 & \text{For } d_p > 0.015 \\ C = 2 & \text{For } d_p \leq 0.015 \end{cases} \quad (35)$$

$$U = (U_1^{-1} + U_a^{-1})^{-1} \quad (36)$$

$$U_1 = k_1 \left(\rho_w C_{pw} \frac{k_1}{D_1} \right)^{\frac{1}{2}} \quad (37)$$

$$U_a = k_a (\rho_a C_{pa})^{\frac{1}{3}} \left(\frac{K_a}{D_a} \right)^{\frac{2}{3}} \quad (38)$$

Condenser inside air temperature

The conservation of energy applied to the air/vapor mixture over a differential e-control volume leads to the following equation [33]:

$$\frac{dT_a}{dz} = \frac{-1}{(1+w)} \frac{dw}{dz} \frac{h_1(T_a)}{C_{pa}} + \frac{Ua(T_1 - T_a)}{C_{pa}G(1+w)} \quad (39)$$

The condensation rate in the condenser is calculated as:

$$m_{\text{cond}} = G(w_{\text{in}} - w_{\text{out}}) \quad (40)$$

L_v , c_p , and ρ are calculated as a function of the temperature.

The control auxiliary system model

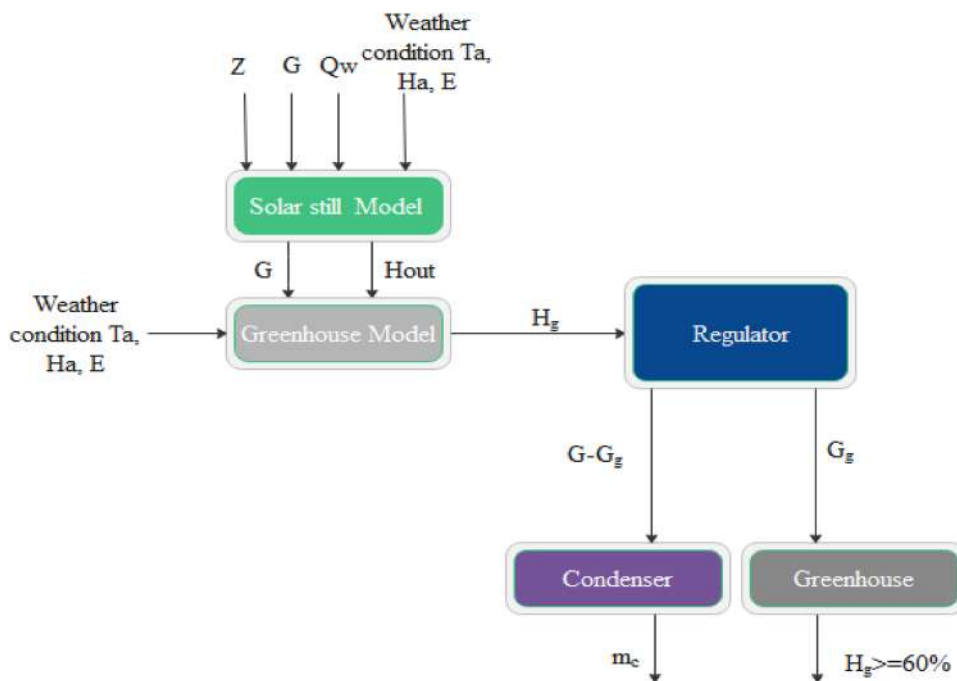
The idea behind the controller proposed in this study is to maintain the desired humidity inside the greenhouse. A control model was added to the set of above-developed equation for the integrated greenhouse. The only variable of the control model was the humid air mass flows ratio. The latter is the ratio between the flow directed to the greenhouse and the total flow at outlet solar. It was noticed that this ratio is zero during the nighttime since there is no fair flow directed to the greenhouse.

The various steps involved in the simulation process are presented in the scheme of Fig. 5. First, the meteorological data, air and water flow rates were introduced in the solar still model as inputs. Three parameters can be controlled, the water and air mass flow rates and the sprayer height inside the solar still. These parameters were set when the humidity of air, at the outlet solar still, reaches the optimal value. At this level, in order to regulate the humidity inside the greenhouse, the flux of humid air will be introduced in the greenhouse model as input. The exterior climate conditions parameters are also introduced into the greenhouse model.

The coupled equations [Eqs. (1) to (40)] of the whole model of the integrated saltwater greenhouse are solved through a Runge Kutta procedure using a unique code developed under Matlab® software. The models resolution outcome is, among others, the humidity value in the greenhouse over 24 h.

Then, control action is taken as follows: If the humidity inside the agricultural greenhouse is less than 60%, the regulation performs the suitable action on tree control parameters, i.e. the water and the airflow rates inside the solar still and the humid air ratio, that permit the greenhouse humidity to be equal or superior to 60%. While giving the priority to satisfying the humidity set point of the greenhouse, the control system directs the rest of the humid air to the packed

Fig. 5 The proposed control scheme for the integrated greenhouse system



bed condenser to produce freshwater for the irrigation needs of the greenhouse plants. This supervisory action is repeated every 6 min.

Results and discussions

At first, the model of the greenhouse is validated through the cucurbit experimental greenhouse of El Hamma. Then the numerical models of the greenhouse and of the solar still are run to obtain the functioning parameters of the whole integrated system. Finally, the ability of the proposed system to supply the greenhouse irrigation water requirements and the greenhouse air humidity level are studied.

Validation of the greenhouse model

The greenhouse model accuracy was evaluated by comparing the predicted and the measured air temperature and humidity data for three non-successive days covering the cucurbit crop first season. These typical days are January 1st, March 1st and May 1st.

The fit average relative error (Fig. 6) doesn't exceed 15%. The model applies better to the data during the night than during the day. This is related to the more complex day energy balances, and to the fact that the irrigation operations occur only during the daytime.

Air relative humidity is the most difficult challenging parameter to estimate as stated by several authors [8, 9]. Figure 7 shows the good performance of the model over the 24 h simulation period over the three simulated days with

a fit average relative error that doesn't exceed 15%. This figure shows that the hourly air humidity is less during the daytime than the nighttime due to the greenhouse day–night air temperature difference (Fig. 6) on the one hand, and the fact that the plant transpiration varies between the day and the night [38] on the other hand.

The accordance with the predicted results with the experimental data using the R^2 , the RMSE and the MAPE factors show that the proposed model estimates the inside greenhouse temperature and humidity by R^2 0.97–0.98 and by RMSE 1–2 °C for the temperature and R^2 of 0.84–0.96 and RMSE of 3–5% for the humidity and a MAPE of 4–7%.

Evaluation of the HDH system components

The simulation results are presented in the following “[Solar still simulation results](#)” and “[The condenser simulation results](#)” sections.

Solar still simulation results

Figure 8 depicts the effect of the modified solar still parameters on the saltwater evaporated rate. As shown in the figure, at a constant spray height, the evaporated water increases with the increase of the ratio between the sprayed saltwater mass flow rate and the blown air mass flow rate. Nevertheless, this increase declines when the ratio value increases. This is due to less difference between the air actual humidity and the value of its saturation humidity when the water mass flow rate is high. Furthermore, this figure shows that increasing the spraying height decreases

Fig. 6 Comparison of predicted air temperature inside greenhouse with experimental results

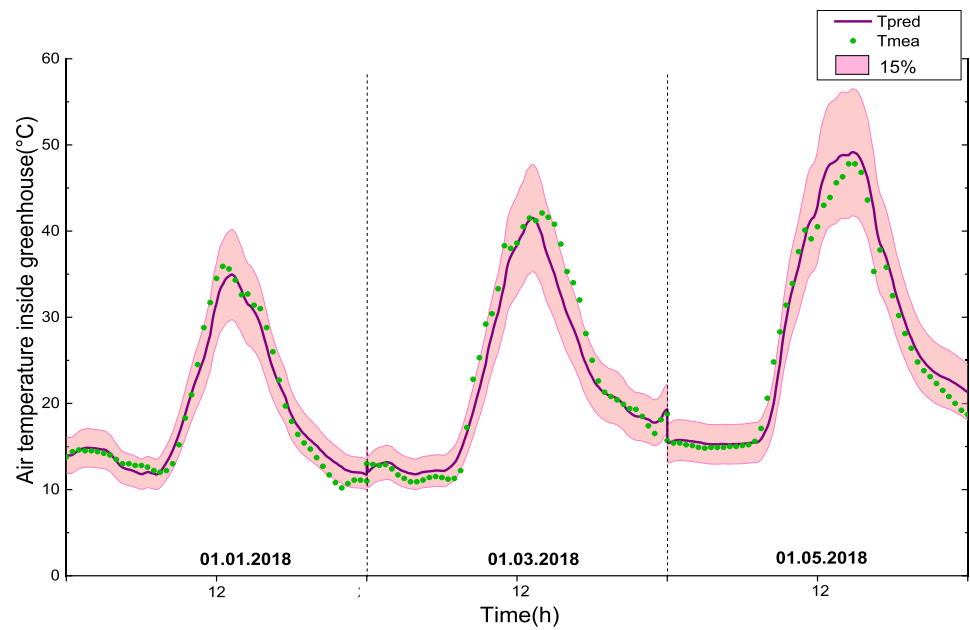
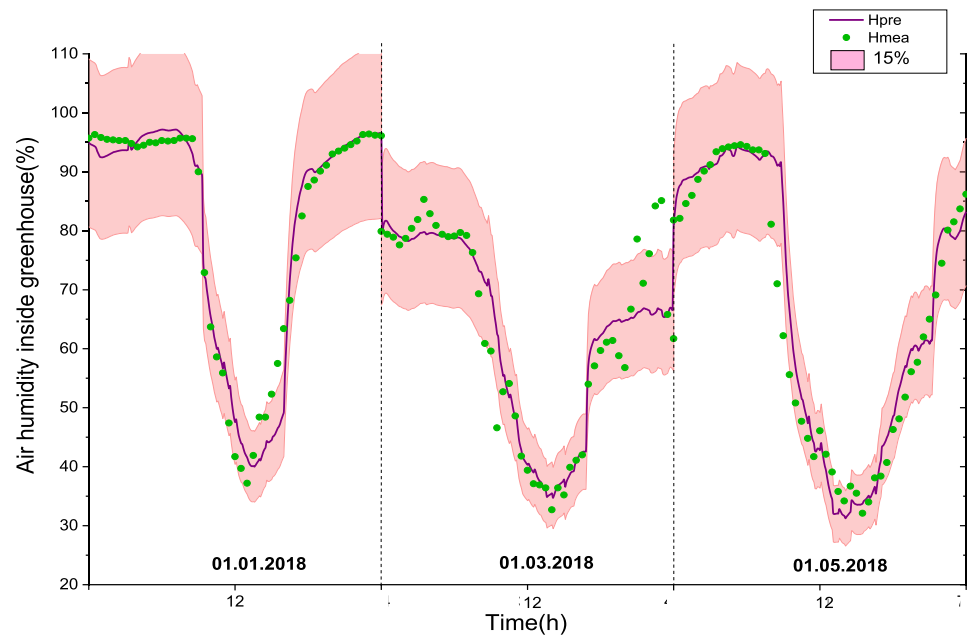


Fig. 7 Comparison of predicted air humidity inside greenhouse with experimental results



the water evaporated rate for constant air and water flow rates. This is explained by the fact that the mass and heat transfer coefficients drop with the increase of the spraying height [29], although the contact time between air and water rises with the increase of height, the temperature of pulverized water decreases all along the way. Figure 8 shows also that the attained values of the water evaporated rate per day are higher than those reached in conventional solar stills [30].

The condenser simulation results

The simulation of the condenser operation was performed by varying the cooling water temperature and flow rate and by varying the humid air mass flow rate. Figure 9 shows that, at constant cooling water temperature and a constant humid air mass flow rate, increasing the cooling water flow rate enhances the freshwater production and consequently boosts

Fig. 8 Effect of water mass flow rate to air mass flow rate ratio in solar still on irrigation load coverage for different spray height (1 May)

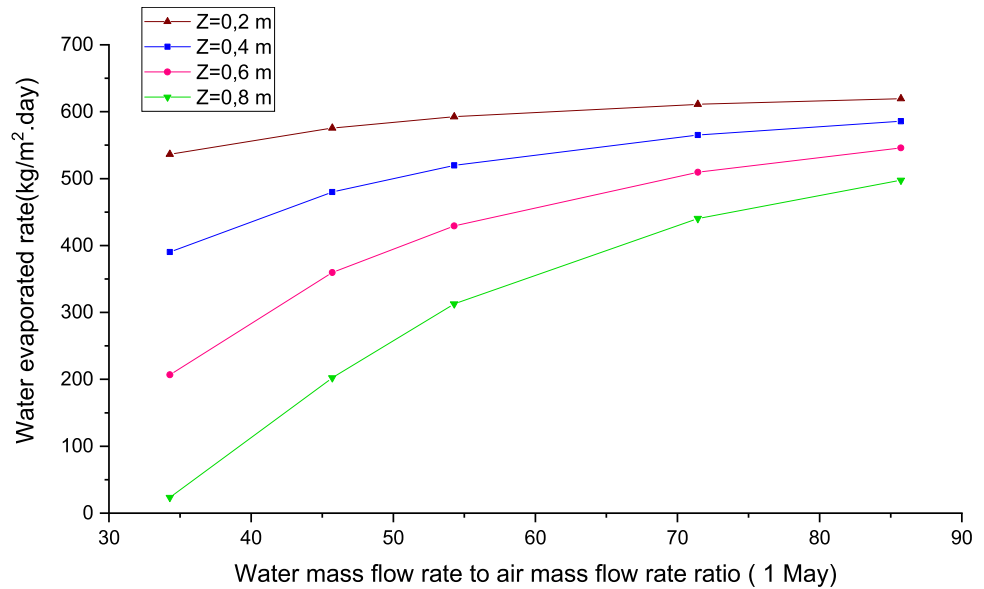
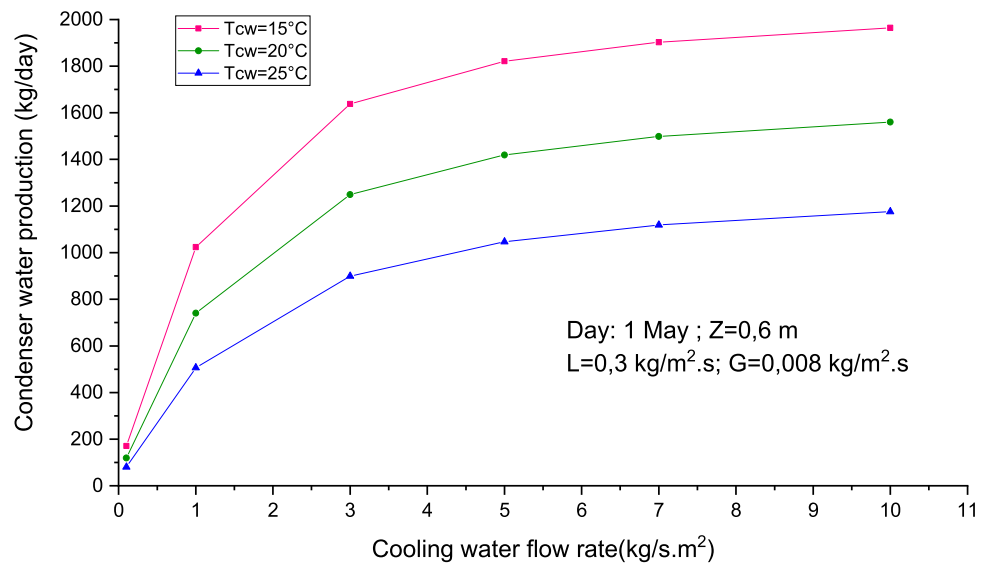


Fig. 9 Effect of the cooling water temperature and flow rate on the freshwater production by the condenser (1 May)



the irrigation load coverage. However, above a cooling water flow rate value of 7 kg/s m^2 , the freshwater production rising trend decreases. Figure 9 also shows that, reducing the condenser cooling water temperature resulted in a very significant increase in condenser water production and consequently an increase in the irrigation load coverage.

Thus, to cover both the total irrigation needs and the air humidification requirements of the greenhouse, an appropriate water mass flow has to be chosen according to the water temperature to reduce the pumping costs.

Evaluation of the greenhouse needs meeting and the performance of the control system

Humidity inside the greenhouse

The control system is used to set the greenhouse humidity at the desired levels that allow the best conditions for plants growth. Figure 8 shows the humid air ratio effect supplied in the greenhouse on the humidity inside the greenhouse.

The control system is used to set the greenhouse humidity at the desired levels that allow the best conditions for



the plants growth. It acts on the humid air mass flow ratio between the flow directed to the greenhouse and the total flow at outlet of solar stills (Fig. 1).

The control and the whole system results are presented for the chosen day of March 1st. Figure 10 shows the humid air ratio effect on the humidity inside the greenhouse. It is shown that when the supplied humid air ratio increases, the inside air humidity enhances. With 100% of humid air ratio, the humidity can be set at a level up to 80% throughout the day. Figure 10 also reveals that during the nighttime, the humidity remains at high levels without any humid air supply. So, as showed in Fig. 10, by the curve related to the case of no air supplying the green house, the regulation will be performed just during the day period and will have to start with the beginning of the decrease of humidity at 9:00 am until it reaches its minimum at 1:00 p.m. The control is set to maintain a humidity level inside the greenhouse at a level that is superior to 60% through the 24 h of the day. This level is sufficient for the optimal plant growth [5, 6]. In fact, enhancing this inside required humidity minimum level induces higher supply of humid air ratio to the greenhouse and consequently decreases the humid air mass flow directed to the condenser to produce freshwater for irrigation. Figure 11 depicts the timely variation for the day of March 1st the humid air ratio provided by the control/regulation system to permit the greenhouse humidity to be maintained at a humidity level of a minimum of 60% is zero during the nighttime and it reaches a maximum of 58% at nearly 12:30 a.m. and at 20:00 p.m.

Fig. 10 Effect of humid air ratio on greenhouse indoor humidity (1 March)

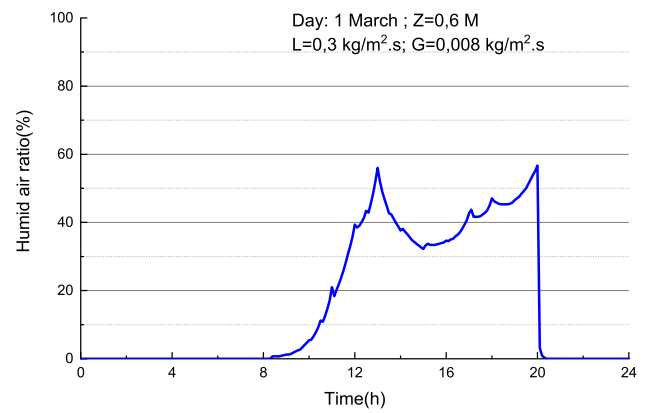
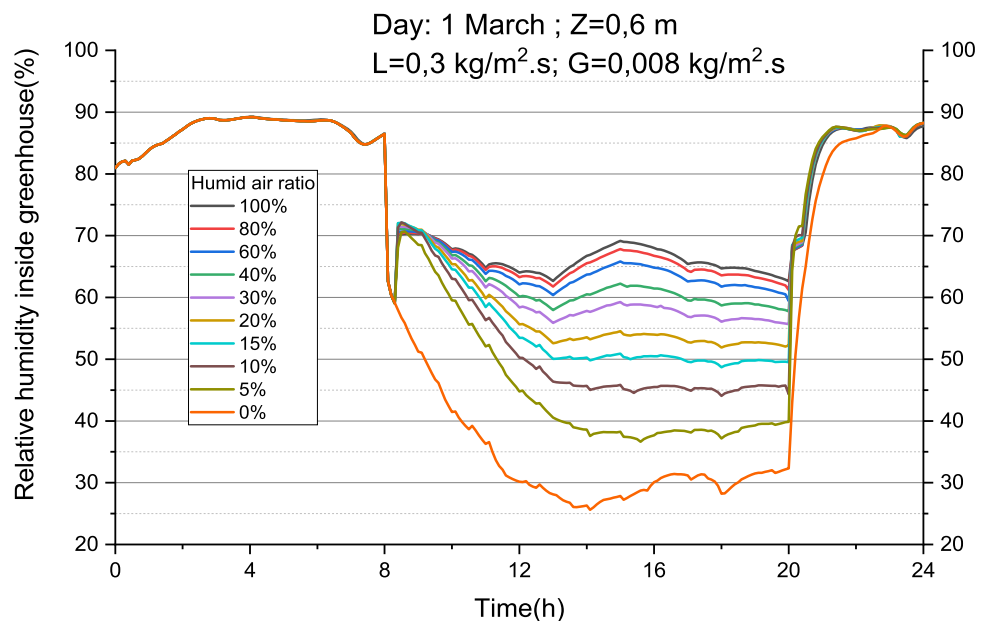


Fig. 11 Regulation profile of the humid air ratio fed the greenhouse (1 March)

The greenhouse requirement covering evaluation

The innovation in this work consists in the fact that the proposed system is a 100% autonomous; it provides both the optimal greenhouse microclimate and irrigation needs. However, these two objectives are closely related to each other because they depend on outdoor weather conditions, solar radiation intensity, and plant evapotranspiration. Therefore; it would impossible to study or control each parameter separately. Furthermore, the developed model [Eqs. (1) to (40)] shows the close relationship between these parameters.

Setting all the input parameters at their own optimal values, the simulations achieved in this section aim at studying the air humidity in the greenhouse and the irrigation water production with its related ILC ratio. For the conducted simulations, the respective values at which the parameters

Fig. 12 Effect of greenhouse integration on irrigation load coverage over early crop season

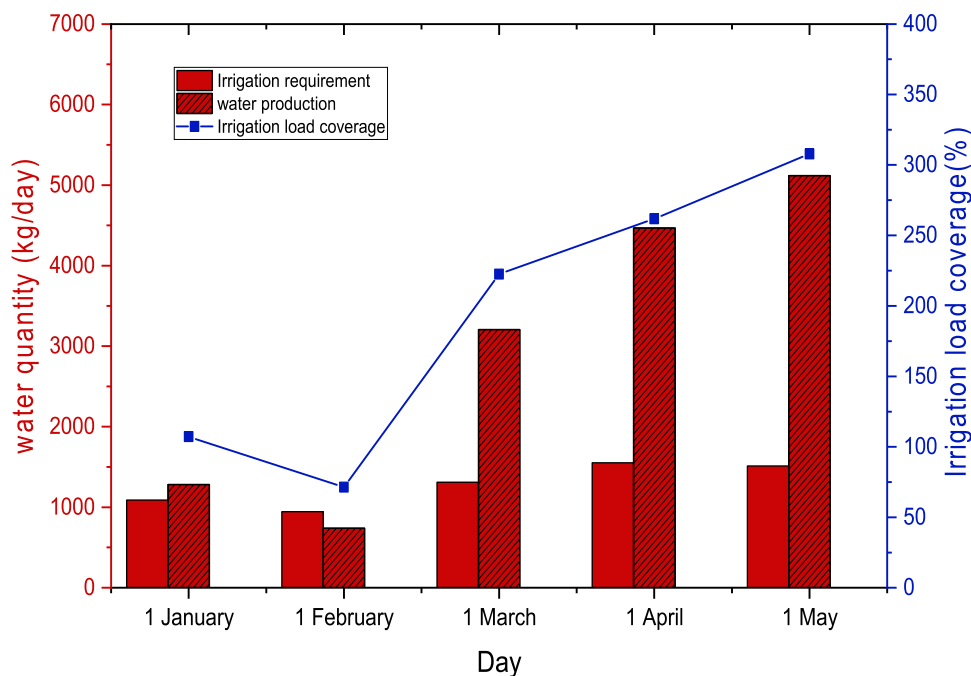
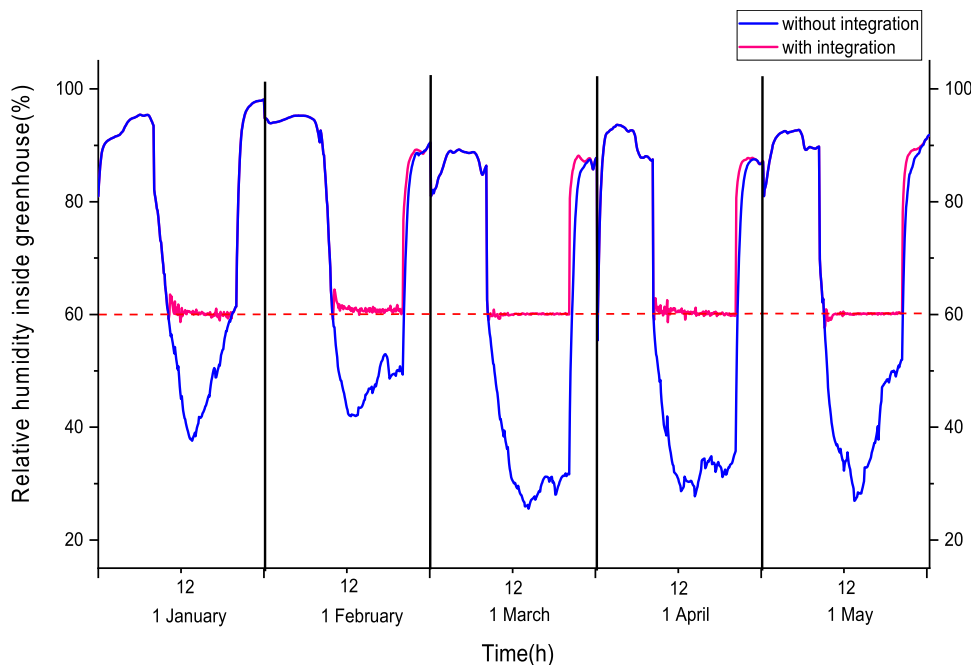


Fig. 13 Greenhouse humidity regulation over early crop season



are set are as follow the spraying height at 0.4 m, the air mass flow at 0.035 kg/s m², spraying the water flow rate at 1.9 kg/s m², the cooling water temperature at 15 °C for January and February and at 20 °C for the other season months, and the cooling water flow rate at 7 kg/s m².

Figure 12 shows the effect of the integration of the HDH system with the greenhouse structure over the early cucurbit season cultivation (Jan–May). The results are given for five representative days that are the first days of the month January to May.

For February, 1st, the day with the lowest values in terms of temperature and solar radiation, as the air at the outlet of the solar still is not saturated and therefore the condensation efficiency is weak, the proposed system with the chosen stills dimensions can cover only 70% of the irrigation needs as shown in Fig. 12. However, it monitors the greenhouse humidity successfully and actually ensures that it exceeds 60% during the day as shown in Fig. 13.

For March, 1st, that is the most unfavorable day in terms of humidity level, the system sets the greenhouse at its just necessary humidity level as shown in Fig. 13. On this same

day, the system covers more than 200% of the needed irrigation water.

For May 1st, the hottest day among the three, the system permits the humidity continuous adjustment to a value that is always greater than 60%, and at the same time, it covers more than 300% of the greenhouse irrigation needs. It can be concluded thus that the chosen input parameters in this section are convenient.

Notice that one may extend the still surface to cover 100% of the greenhouse even during the day of February, 1st, but in this case, the produced irrigation water will be greater than the value calculated above for the days March 1st and May 1st.

Figure 14 compares the condenser freshwater hourly production during the cucurbit cultivation season, taking into account the humidity regulation, i.e. the part of the humid air that is supplied to the greenhouse. The maximum productivity is reached when the solar irradiation is the highest, and the freshwater production period is between 8:00 a.m. and 8:00 p.m.

One may also notice that during the closed periods of the greenhouse, i.e out of the cultivation seasons, the proposed system can produce only fresh water and store it for the use in the following season during the low production periods. Storing the freshwater permits the reduction of the dimension of the HDH subsystem as well as the cost too.

Further simulation of the whole along the Jan-May cultivation seasons shows that the proposed system offers 460

m³ of irrigation water with a salinity of 1.6 g/l. This total amount of irrigation water production represents more than 200% of the greenhouse irrigation requirement.

Integrated system energy efficiency

The energy efficiency of a desalination process is defined as the ratio between the energy used to produce a unit of mass of drinking water and that required by a distillation system. For a solar-powered desalination system, energy efficiency is determined by the following equation [39]:

$$\eta = \frac{m_{\text{dist}} * L_v}{S_{\text{abs}} * E}$$

with m_{dist} is the mass flow rate of the distillate (kg/s), L_v is the latent heat of vaporization (kJ/kg), S_{abs} is the surface the solar still's absorber (m²) and E is the global solar irradiation (W/m²). The energy efficiency of a HDH desalination system translates the efficiency in producing pure water.

The variation of energy efficiency during the cucurbit cultivation for the solar still and all the HDH system is presented in Table 1. The best efficiency was achieved on the hottest day May 1st for both systems and the lowest was achieved on the coldest day February 1st for the solar still. However, the lowest efficiency for the overall HDH system was achieved on March, 1st, which corresponds to the most unfavorable day in terms of humidity level. This

Fig. 14 Hourly condenser productivity for three defined days

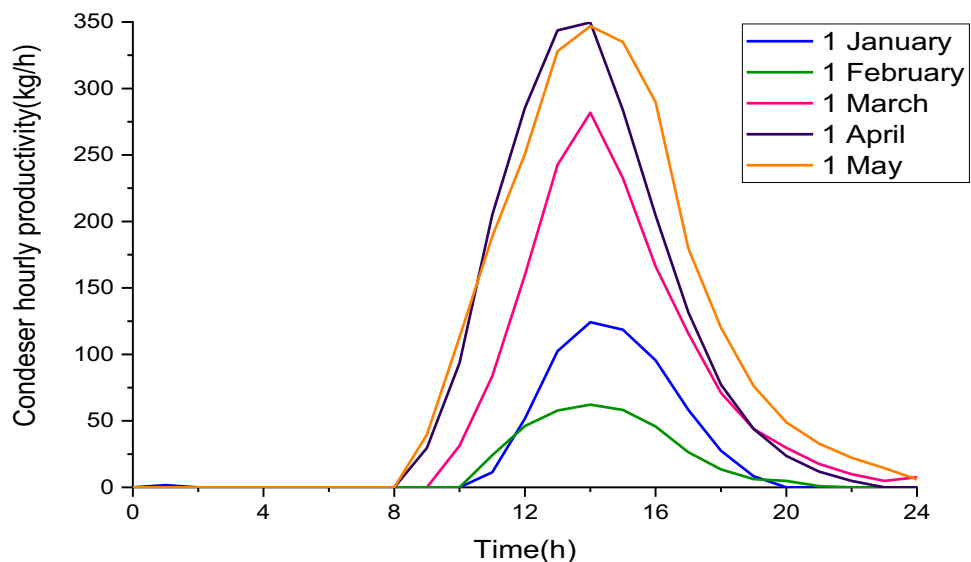


Table 1 Integrated system energy efficiency

Day	January 1st (%)	February 1st (%)	March 1st (%)	April 1st (%)	May 1st (%)
Solar still efficiency	42.57	32.81	57.56	59.79	71.29
HDH efficiency	29.78	15.75	11.78	49.34	63.25

shows that the solar still efficiency is strongly linked to the density of solar flux and that the HDH efficiency is also affected by the humidity level.

Conclusion

The main objective of this work is to study a novel integrated saltwater greenhouse concept that provides the greenhouse microclimate and irrigation requirement in arid regions with saline groundwater. Findings show that the proposed system covers the humidity requirements of the greenhouse during all these typical days with a set point of 60% as the minimum air humidity level in the greenhouse. With the HDH system chosen dimension, the irrigation needs are satisfied for these days except for February 1st for which the irrigation covering ratio is only 70%.

However, it was noticed that extending the solar still surface permits covering the irrigation need at a level of 100% even during February 1st. During the considered cultivation season of cucurbit, the irrigation production of the system covers more than 200% of the greenhouse water irrigation needs. As the proposed HDH is independent of the greenhouse, the produced fresh water during the inter-seasonal can be stored as to serve the bad days. The water storage may reduce the dimension of the HDH subsystem while satisfying all the microclimate and irrigation needs of the greenhouse.

The current study can be further improved by implementing temperature model regulation. In addition, optimization efforts must be taken to improve the HDH system especially when an inter-seasonal freshwater storage is considered. Later studies involving various locations and crop types can reveal the potential effectiveness of the suggested integrated greenhouse under various climates and world regions. Furthermore, the proposed system's functioning and installation cost need to be studied and optimized regarding the location region and the desired crops.

Declarations

Conflict of interest On behalf of all authors, the corresponding author states that there is no conflict of interest.

References

- Béné, C.: Resilience of local food systems and links to food security—a review of some important concepts in the context of COVID-19 and other shocks. *Food Secur.* **12**, 1–18 (2020)
- Muñoz, P., Antón, A., Nuñez, M., Paranjpe, A., Ariño, J., Castells, X., Montero, J.I., Rieradevall, J.: Comparing the environmental impacts of greenhouse versus open-field tomato production in the Mediterranean region. In: *International Symposium on High Technology for Greenhouse System Management: Greensys2007* 801, pp. 1591–1596 (2007, October)
- Mpusia, P.T.O.: *Comparison of Water Consumption Between Greenhouse and Outdoor Cultivation*. ITC, Enschede (2006)
- Fernández, M.D., Gallardo, M., Bonachela, S., Orgaz, F., Thompson, R.B., Fereres, E.: Water use and production of a greenhouse pepper crop under optimum and limited water supply. *J. Hortic. Sci. Biotechnol.* **80**(1), 87–96 (2005)
- Yohannes, T., Fath, H.E.: Novel agriculture greenhouse that grows its water and power: thermal analysis. In: *Proceedings of the 24th Canadian Congress of Applied Mechanics (CANCAM 2013)*, Saskatoon, Saskatchewan, Canada (2013, June)
- Shamshiri, R.R., Jones, J.W., Thorp, K.R., Ahmad, D., Che Man, H., Taheri, S.: Review of optimum temperature, humidity, and vapour pressure deficit for microclimate evaluation and control in greenhouse cultivation of tomato: a review. *Int. Agrophys.* **32**(2), 287–302 (2018)
- De Pascale, S., Maggio, A.: Plant stress management in semiarid greenhouse. In: *International Workshop on Greenhouse Environmental Control and Crop Production in Semi-Arid Regions 797*, pp. 205–215 (2008, October)
- Rabbi, B., Chen, Z.H., Sethuvenkatraman, S.: Protected cropping in warm climates: a review of humidity control and cooling methods. *Energies* **12**(14), 2737 (2019)
- BC Ministry of Agriculture, Fisheries and Food: *Understanding Humidity Control in Greenhouses Floriculture*. Fact Sheet file no 400-5 (1994)
- Shelton, S.: “Sweating High Humidity” *Greenhouse Product News* (2005)
- Gorjian, S., Ebadi, H., Najafi, G., Chandel, S.S., Yildizhan, H.: Recent advances in net-zero energy greenhouses and adapted thermal energy storage systems. *Sustain. Energy Technol. Assess.* **43**, 100940 (2021)
- Garg, H.P., Adhikari, R.S., Kumar, R.: Experimental design and computer simulation of multi-effect humidification (MEH)–dehumidification solar distillation. *Desalination* **153**(1–3), 81–86 (2003)
- Bait-Suwailam, T.K., Al-Ismaili, A.M.: Review on seawater greenhouse: achievements and future development. *Recent Patents Eng.* **13**(4), 312–324 (2019)
- Farrell, E., Hassan, M.I., Tufa, R.A., Tuomiranta, A., Avci, A.H., Politano, A., Curcio, E., Arafat, H.A.: Reverse electro dialysis powered greenhouse concept for water-and energy-self-sufficient agriculture. *Appl. Energy* **187**, 390–409 (2017)
- Akrami, M., Salah, A.H., Dibaj, M., Porcheron, M., Javadi, A.A., Farmani, R., Fath, H.E., Negm, A.: A zero-liquid discharge model for a transient solar-powered desalination system for greenhouse. *Water* **12**(5), 1440 (2020)
- Radhwan, A.M.: Transient analysis of a stepped solar still for heating and humidifying greenhouses. *Desalination* **161**(1), 89–97 (2004)
- Zamen, M., Amidpour, M., Firoozjaei, M.R.: A novel integrated system for fresh water production in greenhouse: dynamic simulation. *Desalination* **322**, 52–59 (2013)
- Salah, A.H., Hassan, G.E., Fath, H., Elhelw, M., Elsherbiny, S.: Analytical investigation of different operational scenarios of a novel greenhouse combined with solar stills. *Appl. Therm. Eng.* **122**, 297–310 (2017)
- Mahmoudi, H., Abdul-Wahab, S.A., Goosen, M.F.A., Sablani, S.S., Perret, J., Ouagued, A., Spahis, N.: Weather data and analysis of hybrid photovoltaic–wind power generation systems



- adapted to a seawater greenhouse desalination unit designed for arid coastal countries. *Desalination* **222**(1–3), 119–127 (2008)
20. Mahmoudi, H., Spahis, N., Goosen, M.F., Ghaffour, N., Drouiche, N., Ouagued, A.: Application of geothermal energy for heating and fresh water production in a brackish water greenhouse desalination unit: a case study from Algeria. *Renew. Sustain. Energy Rev.* **14**(1), 512–517 (2010)
 21. Mamouri, S.J., Tan, X., Klausner, J.F., Yang, R., Bénard, A.: Performance of an integrated greenhouse equipped with light-splitting material and an HDH desalination unit. *Energy Convers. Manag.* **X** **7**, 100045 (2020)
 22. Hashem, F., Medany, M.A., Abd El-Moniem, E.M., Abdallah, M.M.F.: Influence of green-house cover on potential evapotranspiration and cucumber water requirements. *Arab Univ. J. Agric. Sci.* **19**(1), 205–215 (2011)
 23. Abdel-Ghany, A.M., Kozai, T.: Dynamic modeling of the environment in a naturally ventilated, fog-cooled greenhouse. *Renew. Energy* **31**(10), 1521–1539 (2006)
 24. Garzoli, K.V., Blackwell, J.: An analysis of the nocturnal heat loss from a single skin plastic greenhouse. *J. Agric. Eng. Res.* **26**(3), 203–214 (1981)
 25. Fatnassi, H., Boulard, T., Bouirden, L.: Development, validation and use of a dynamic model for simulate the climate conditions in a large scale greenhouse equipped with insect-proof nets. *Comput. Electron. Agric.* **98**, 54–61 (2013)
 26. Wang, S., Deltour, J.: An experimental model for leaf temperature of greenhouse-grown tomato. *Acta Hortic.* **491**, 101–106 (1999). <https://doi.org/10.17660/ActaHortic.1999.491.13>
 27. Joudi, K.A., Farhan, A.A.: A dynamic model and an experimental study for the internal air and soil temperatures in an innovative greenhouse. *Energy Convers. Manag.* **91**, 76–82 (2015)
 28. Villarreal-Guerrero, F., Kacira, M., Fitz-Rodríguez, E., Kubota, C., Giacomelli, G.A., Linker, R., Arbel, A.: Comparison of three evapotranspiration models for a greenhouse cooling strategy with natural ventilation and variable high pressure fogging. *Sci. Hortic.* **134**, 210–221 (2012)
 29. Hijjaji, K., Frikha, N., Gabsi, S., Kheiri, A., Khalij, M.: Using DOE and RSM procedures to analyze and model a spray evaporation type solar still. *Int. J. Energy Environ. Eng.* **12**, 1–11 (2021)
 30. El-Agouz, S.A., El-Samadony, Y.A.F., Kabeel, A.E.: Performance evaluation of a continuous flow inclined solar still desalination system. *Energy Convers. Manag.* **101**, 606–615 (2015)
 31. Dev, R., Abdul-Wahab, S.A., Tiwari, G.N.: Performance study of the inverted absorber solar still with water depth and total dissolved solid. *Appl. Energy* **88**(1), 252–264 (2011)
 32. Aybar, H.Ş., Assefi, H.: Simulation of a solar still to investigate water depth and glass angle. *Desalin. Water Treat.* **7**(1–3), 35–40 (2009)
 33. Li, Y., Klausner, J.F., Mei, R., Knight, J.: Direct contact condensation in packed beds. *Int. J. Heat Mass Transf.* **49**(25–26), 4751–4761 (2006)
 34. Alnaimat, F., Klausner, J.F., Mei, R.: Transient analysis of direct contact evaporation and condensation within packed beds. *Int. J. Heat Mass Transf.* **54**(15–16), 3381–3393 (2011)
 35. Klausner, J.F., Li, Y., Mei, R.: Evaporative heat and mass transfer for the diffusion driven desalination process. *Heat Mass Transf.* **42**(6), 528–536 (2006)
 36. Onda, K., Takeuchi, H., Okumoto, Y.: Mass transfer coefficients between gas and liquid phases in packed columns. *J. Chem. Eng. Jpn.* **1**(1), 56–62 (1968)
 37. Eckert, E.R.G.: Analogies to Heat Transfer Processes. Measurements in Heat Transfer, p. 399412. Hemisphere, Washington, DC (1976)
 38. De Dios, V.R., Roy, J., Ferrio, J.P., Alday, J.G., Landais, D., Milcu, A., Gessler, A.: Processes driving nocturnal transpiration and implications for estimating land evapotranspiration. *Sci. Rep.* **5**(1), 1–8 (2015)
 39. Ibrahim, A.G., Dincer, I.: A solar desalination system: exergetic performance assessment. *Energy Convers. Manag.* **101**, 379–392 (2015)

Publisher's Note Springer Nature remains neutral with regard to jurisdictional claims in published maps and institutional affiliations.

Springer Nature or its licensor holds exclusive rights to this article under a publishing agreement with the author(s) or other rightsholder(s); author self-archiving of the accepted manuscript version of this article is solely governed by the terms of such publishing agreement and applicable law.





Simple analytical considerations on a thermal-flow operating parameters of a heat storage tank

Oktawia Dolna¹ · Weronika Wiśniewska²

Received: 7 February 2022 / Accepted: 28 June 2022 / Published online: 31 July 2022
© The Author(s) 2022

Abstract

A heat storage tank (HST), described in this paper, may be applied to numerous systems used for thermal energy generation and storage. Working principle and heat-flow processes of the HST remain the same and are independent of the systems in which the HST is being used. This paper presents a thermal-flow analysis of a heat storage tank (HST) operating in an air compressor heat pump (ACHP) and a dry cooler (DC) combined cycle. The HST is operated under transient conditions for four different ACHP steady states. The HST was analysed using lumped capacitance method. The heating power of a single coil varied from 2.2 to 3.2 kW. 50% increase in mass flow rate of heating water in the coils increased the HST water mean temperature by 5.6 °C. A differential equation for the HST water temperature variation was solved analytically and it was presented with the use of dimensionless numbers. The presented solution is of a general form. An important parameter such as number of the coils may be varied easily. Additionally, a Mathcad computational program was proposed for the estimation of HST-ACHP-DC system thermodynamic and thermal-flow parameters. System dynamics was studied using MATLAB/Simulink. An optimal operating parameters of the HST were found and are presented in the paper. The aforementioned parameters are as follows: mass flow rates of heating and cooling media in all three coils, mass flow rate of freshwater supplying the HST, number of loops in coils and resulting heat transfer area, diameter of the loops of the coils, diameter of the coils, time after which water in the HST reaches a steady value, time period within which the HST may fulfil demand for central heating and domestic hot water (DHW) preparation without being charged simultaneously. The presented analytical model was validated based on the available data in the field literature and a high compliance was reached. For this purpose theoretical model results were compared to results of HST computational fluid dynamics (CFD) simulations. The temperature calculated using the presented model differed from the one obtained by the CFD analysis by 2.96 K.

Keywords Heat storage tank · Lumped capacitance method · Dimensionless numbers

List of symbols

Latin symbols

A_{coil}	External surface of the coil, m ²
A_{hst}	External surface of the HST, m ²
D_{coil}	Diameter of a single whorl of the coil, m

D_{int}	HST internal diameter, m
D_{ext}	HST external diameter, m
$d_{\text{mean.coil}}$	Mean diameter of the coil, m
$d_{\text{i.coil}}$	Internal diameter of the coil, m
$d_{\text{e.coil}}$	External diameter of the coil, m
h	Specific enthalpy, J/kg
h_{coil}	Height of the coil, m
K_{hst}	Overall heat transfer coefficient of the HST, W/m ² K
k_{coil}	Overall heat transfer coefficient of the coil
L_{hst}	HST height, m
L_{coil}	Length of the coil, m
\dot{m}_{11}	Mass flow rate of the freshwater supplying the HST, kg/s
\dot{m}_{12}	Mass flow rate of the heating medium in the coil ₁₂ , kg/s

✉ Oktawia Dolna
odolna@imp.gda.pl

Weronika Wiśniewska
wwisniewska@imp.gda.pl

¹ Heat Transfer Department, Centre of Heat and Power Engineering, Institute of Fluid-Flow Machinery of Polish Academy of Sciences, Fiszerza 14 st., 80-231 Gdańsk, Poland

² Turbine Department, Centre of Heat and Power Engineering, Institute of Fluid-Flow Machinery of Polish Academy of Sciences, Fiszerza 14 st., 80-231 Gdańsk, Poland



m_{34}	Mass flow rate of the heating medium in the coil ₃₄ , kg/s
m_{56}	Mass flow rate of the cooling medium in the coil ₅₆ , kg/s
M_{11}	Mass of the water in the HST, kg
N	Number of the loops in the coil, –
\dot{Q}_0	HST heat losses to the surrounding, W
\dot{Q}_{11}	The heat flux which is directly harvested from the HST, W
\dot{Q}_{12}	Heat flux transferred via coil ₁₂ , W
\dot{Q}_{34}	Heat flux transferred via coil ₃₄ , W
\dot{Q}_{56}	Heat flux harvested from the HST via coil ₅₆ , W
\dot{Q}_{hst}	Resultant heat flux transferred to the HST, W
q_{con}	Specific thermal load of the condenser, J/kg
R_{hst}	Overall thermal resistance of the HST (water in the HST–HST wall air outside the HST), m ² K/W
s	Entropy, J/K
t_{con}	Condensation temperature, °C
t_{ev}	Evaporation temperature, °C
T_1	Heating medium inlet temperature of the coil ₁₂ , °C
T_2	Heating medium outlet temperature of the coil ₁₂ , °C
T_3	Heating medium inlet temperature of the coil ₃₄ , °C
T_4	Heating medium outlet temperature of the coil ₃₄ , °C
T_5	Cooling medium inlet temperature of the coil ₅₆ , °C
T_6	Cooling medium outlet temperature of the coil ₅₆ , °C
T_9	Freshwater supply temperature, °C
$T_{11} = T_{\text{hst}}$	Resultant HST water mean temperature, °C
w_t	Specific theoretical work, J/kg

Greek symbols

α	Heat transfer coefficient, W/m ² K
δ_{is}	Thickness of the thermal insulation of the HST, m
ϵ_{con}	ACHP coefficient of performance, –
τ	Time, s
λ_{hst}	Thermal conductivity of the wall of the HST, W/m K
λ_{is}	Thermal conductivity of thermal insulation, W/m K
λ_r	Thermal conductivity of coil, W/m K
λ	Thermal conductivity, W/m Kf
τ_0	Characteristic time

Sub- and superscripts

*	Denotes for dimensionless variables
11 and w.hst	Correspond to the water in the HST
12	Corresponds to the heating coil 12
34	Corresponds to the heating coil 34
56	Corresponds to the cooling coil 56
i, int	Internal
i	Initial
e, ext	External
hst	Heat storage tank
crit	Critical
con	Condensation
ev	Evaporation, evaporator
red	Reduced
sat	Saturation
sh	Super heated
'	Liquid, inlet
"	Vapour, outlet

Highlights

- HST-ACHP-DC design and verification analysis is presented.
- The solution of time-dependent HST water temperature variation is of a general form.
- Optimal thermal-flow operating parameters of the HST coils are proposed.
- An increase in \dot{m}_{air} by 48% implies an increase in temperature by 5.6 °C.

Introduction

This article studies the analytical and numerical analysis of a heat storage tank (HST). The HST is coupled with an air compressor heat pump (ACHP) and a dry cooler (DC). This study concentrates on a detailed analysis of the operating parameters of all components of the system, namely the HST, ACHP and DC. However, the HST is the main objective of the presented research. The ACHP and the DC operate as the HST heat supplier and consumer, respectively. The topic of the HST which is taken up within the paper is an important one as increasing the energy efficiency, by means of thermal energy storage, is a desirable effect. The HST operation was therefore studied in terms of the parametric analysis aiming at improving the heat transfer coefficient inside the coils and inside the HST. The HST with two coils was briefly analysed by Dolna [1]. This paper presents



further development of HST mathematical model mentioned in [1]. The differential equation describing the HST water temperature variation over time is presented using dimensionless numbers. The HST model assumes that one or two coils, depending on the case, are thermally charging the HST while an additional coil (second or third) operates as a heat sink. In the paper, the analysis of the dimensionless numbers is also included. The differential equation that describes the time-dependent HST water temperature variation was therefore presented in a form including the following dimensionless numbers like Reynolds, Prandtl and Nusselt numbers. However, other dimensionless numbers, such as the Grashof and Rayleigh, were also calculated as they are of a substantial importance in the studied problem. The Grashof number is a measure of the ratio of buoyancy forces to viscous forces acting on a fluid. Additionally, the Grashof number plays the same role in free convection as the Reynolds number plays in forced convection. The Rayleigh number is a product of the Grashof and the Prandtl numbers. As it is known, free convection is not restricted to laminar flow. With the increase in the value of the Rayleigh number, the transition from laminar to turbulent flow occurs. More detailed analysis on dimensionless numbers regarding their values is presented further in the paper. The present paper demonstrates the HST unsteady operation under four distinct steady-state operating conditions of the ACHP. By these means, the HST operation dynamics at the varying heat loads was studied. All calculations of the HST-ACHP-DC system were carried out using Mathcad software. Moreover, the system dynamics was analysed using MATLAB/Simulink environment. The goal was also to couple the HST with the ACHP and DC. Accomplishment of the latter one has led to creating an author's computational program allowing for a complex thermodynamic and heat-flow analysis of the HST-ACHP-DC system. In work by Chang et al. [2], a single-tank thermocline (STTC) thermal energy storage (TES) was analysed. Authors have proposed an advanced one-dimensional (1D) two- and one-phase (2D) analytical models of the STTC. The STTC was filled up with encapsulated phase change materials (PCM). MicroSol-R plant and STTC TES were studied empirically in PROMES laboratory. The laboratory bench and experimental data are also presented in paper [2]. Both analytical models were validated using the available empirical results provided by PROMES. Computational fluid dynamics (CFD) analysis of the studied system was also carried out. Authors of [2] have stated that the results obtained on the way of 1D-2P analytical model considerations were more exact than CFD results when compared with empirical data. Authors of [2] have introduced dimensionless discharging time and discharging efficiency among others. A multi-parametric optimisation design procedure was proposed as well as numerous cases were studied. Authors of [2] have also introduced a critical value of Peclet number

at which the final discharging efficiency increases in a line with the output power of the STTC. In the work by Xu et al. [3], 1D analytical model of a thermocline storage tank (TCST) was presented. The fluid-flow TCST did not contain any heating nor cooling coils. The hot water inlet was localised at the top of the TCST while the cold water outlet was placed at the bottom of the tank. The analytical model presented in [3] captured the temperature variation over time, and the TCST height as transient 1D energy equation was employed. In the paper by Zachár [4], transient heat transfer process as well as temperature distribution in a hot water storage tank was analysed theoretically, among others. Author of [4] has solved the aforementioned problem by applying a coupled system of a first-order partial and a first-order ordinary differential equation (PDE-ODE). Based on the developed analytical solutions, a temperature distribution within the water in the hot storage tank may be obtained. It is commonly known that the HST operates at high thermal energy storage efficiency whenever a thermal stratification within the liquid is obtained. The formation of the thermocline closely depends on such geometric and flow parameters of the HST as its shape, inlet, hydrodynamics and the characteristics of the liquid mixing in the tank [5, 6]. The mixing of liquids occurs due to high-temperature gradients and the buoyancy force acting [7]. Additionally, in many fluid-flow HSTs, the water movement results from charging and discharging processes which is obvious. In the work by Li et al. [6], the Authors concentrate on the HST integrated with the solar installation and they focus on the HST optimisation due to the influence of its external geometry on a thermal stratification in the heated water and on the heat capacity of the tank. It is obvious that the HST, working as a specific heat storing unit, ought to be sensitive and of a proper dynamics in response to the time-dependent solar irradiance. The HSTs studied by Li et al. [6] were of a classical internal geometry; namely, one coil was localised at the bottom of the HST. However, general geometry of studied HSTs differed much due to spherical, cylindrical or circular truncated cone shape of the tank. According to the content of the work by Li et al. [6], the tank geometry has a significant impact on the increase in thermal energy storing efficiency of the HST. In paper [6], the authors have concentrated on the HST optimisation as well as influence of geometry on a thermal stratification in the heated water and on the heat storage capacity. Smusz et al. in paper [8] analyse a coil-type heat exchanger performance in terms of Dean dimensionless number and corresponding Reynolds critical value. They conclude that the heat transfer phenomenon can be intensified in the coil-type heat exchangers by means of inertial and centripetal forces and the viscous forces in the liquid which lead to emergence of reversed flow [8]. The reversed flow is perpendicular to the main flow direction and it can be intuitively concluded that the heat transfer would be intensified.



Nowadays, a rapid increase in the interest of the use of PCM in the thermal energy storage units can be noticed [9–11]. However, the efficient operation of a system containing the PCM strongly depends on the characteristics of a charging–discharging process dynamics which need to be well known [9]. As it is emphasised in paper by Okten et al. [12], HSTs are widely used in various industries as they improve thermal energy generation, storage and utilisation efficiency. As it is mentioned in [5, 6, 13], the value of the Richardson number in the HST water thermal stratification description is of a significant importance. Its low value denotes for a complete mixing of the liquid masses of diverse temperatures. Consequently, its high value implies a thermal stratification of the liquid which is a desirable phenomenon according to the HST operation efficiency [14, 15]. In paper by Koçak et al. [16], it was reported that a perfect stratification in the HST which was used in a solar collectors system has led to the growth in thermal energy generated by 38% compared to the case of a fully mixed water in the HST. It is stated in the papers [17–19] that when the ratio H/D (HST height, H , to its diameter, D) reaches 4 then further increase in this value does not imply any significant thermal efficiency improvement. Furthermore, Lavan et al. [20] indicated that a HST, which fulfils the condition presented through the ratio $H/D \in (3, 4)$, is a reasonable compromise between its efficiency and its cost. Castell et al. [5] have presented a relation allowing for estimation of the HST discharging efficiency. The aforementioned efficiency was defined as a ratio of a useful thermal energy, accumulated over time, which can be extracted from the HST, to a total amount of a recoverable thermal energy [5, 21, 22]. This relation allows for an evaluation of the thermal stratification in the HST during a discharging process. As it is mentioned in paper by Fertahi et al. [23], a sensible thermal storage based on the stratified heat storage tank is characterised by technical simplicity which stays in line with low investment and maintenance costs. Therefore, as it is aforementioned, many researchers still concentrate on improving the HST operation parameters such as the proper thermal stratification or a charging/discharging efficiency, different configurations of insulation and other [23]. In the paper by Kurşun [24] an important numerical work on the influence of the HST insulation was carried out. Author of [24] has stated that significant improvement of the thermal stratification was reached for low values of the HST aspect ratio, bottom-to-top insulation diameter ratio and bottom-to-top insulation thickness, with negligible decrease in exergy efficiency as against the HST with a conventional insulation.

The novelty of the presented article is a new simple HST analytical model which enables estimation of the HST water mean temperature variation over time, among others. The model proposed can be used in engineering practice and is of a general character. Hereafter, it can be used to analyse

similar technical problems (i.e. coil-type heat exchangers). The model based on which a computational program was prepared allows for a complex heat-flow and thermodynamic analysis of a system containing HST, ACHP and DC. Therefore, the program captures, i.e. the HST response (i.e. water temperature variation, variation of the heat transfer area of the coils, etc.) to the variation of the air mass flow rate in the ACHP primary cycle. The program can be used for design and verification calculations.

Methodology

Theoretical analysis

Within this paragraph, the definition of an investigated problem and simple analytical considerations are presented. As it is commonly known, the left-hand Linde cycle is realised in a compressor heat pump. Therefore, the ACHP cycle was modelled based on a known procedure. All needed calculations were carried out using the Mathcad environment. The Mathcad CoolProp library was used to estimate working fluid thermophysical properties (i.e. thermal conductivity, density, kinematic and dynamic viscosity, specific heat). HST and ambient air served as high- and low-ACHP-heat sources, respectively. Original computational program has been prepared that coupled all subcomponents of the HST-ACHP-HST system. Heat-flow and thermodynamic analysis of the studied system was carried out using the original computational program. This program enables thermodynamic analysis of the ACHP. Additionally, heat-flow analysis of the HST and DC can be carried out. Moreover, this program couples all mentioned devices in a way providing automatic recalculation of all of the resultant parameters of the whole system after applying new input data (i.e. change in mass flow rate of air at the ACHP low-heat source side results in change of the heat transfer area of the heating coils, etc.).

Boundary conditions

In the analytical model, it was assumed that the ambient temperature equals to 25 °C. This temperature value was applied to reflect conditions of a planned HST-ACHP-DC system laboratory bench. The temperature at which the evaporation proceeded was 15 °C lower than the ambient temperature [25]. Condensation temperature was equal to 43 °C or 60 °C. Both cases were compared, and further analysis was carried out for the latter one. The present analysis is about estimating the optimal parameters of the ACHP which supplied thermally the HST. The aim was to provide the most appropriate heat source to supply the HST. Regarding this fact, higher condensation temperature was used for further analysis. R32 working fluid critical temperature and pressure



are as follows: $T_{crit} = 78.11\text{ }^\circ\text{C}$ and $P_{crit} = 57.8\text{ bars}$. Therefore, assuming the condensation temperature and pressure at the level of $60\text{ }^\circ\text{C}$ and 39.33 bar , respectively, is appropriate. It was assumed that the refrigerant vapour is being superheated by $5\text{ }^\circ\text{C}$ at the compressor suction side. The working fluid condensate was also subcooled by $5\text{ }^\circ\text{C}$ upstream of the throttle valve. The presented computational program allows for the temperature and pressure variation according to users' needs. Additionally, the air mass flow rate of the primary cycle of the ACHP may be set to the designated value. This results in change of the R32 and condenser cooling water mass flow rates. The studied HST contains two (coil₁₂, coil₅₆) or three (coil₁₂, coil₃₄, coil₅₆) coils. In the HST with three coils, two of them are heating ones (coil₁₂ and coil₃₄) while coil₅₆ is a cooling one. Both heating coils are coupled with ACHP which operates as the HST heat supplier. Coil₅₆ is coupled with DC to provide a heat intake from the HST. The following temperature boundary conditions were applied to the HST (see Fig. 4): $T_1 = 66.64\text{ }^\circ\text{C}$, $T_2 = 30\text{ }^\circ\text{C}$, $T_3 = 66.64\text{ }^\circ\text{C}$, $T_4 = 30\text{ }^\circ\text{C}$, $T_5 = 30\text{ }^\circ\text{C}$, $T_6 = 50\text{ }^\circ\text{C}$, $T_9 = 15\text{ }^\circ\text{C}$, $T_i = 15\text{ }^\circ\text{C}$. Temperatures T_1 and T_2 were obtained based on the ACHP cycle thermodynamic analysis. Their values are the same as t_4'' water temperature (see Fig. 3). It was assumed that the heating water is cooled down in the heating coils to $30\text{ }^\circ\text{C}$ (T_2 and T_4). Temperatures T_2 and T_4 were also estimated based on the ACHP cycle analysis. The cooling coil outlet temperature was assumed to be $50\text{ }^\circ\text{C}$ to provide DHW preparation in real conditions. The analytical model which is presented in the paper is a preliminary study

for further experimental work. Therefore, parameters values applied ought to reflect both laboratory and real conditions in which the HST would operate. Hence, the inlet temperature of the cooling coil was set to $30\text{ }^\circ\text{C}$. Mass flow rate of the freshwater \dot{m}_{11} supplying the HST varied from 0.06 to 0.135 kg/s (see Table 7, Fig. 4). Mass flow rate of the cooling water in coil₅₆ was constant and equal to 0.024 kg/s . Mass flow rates \dot{m}_{12} , \dot{m}_{34} , \dot{m}_{R32} and \dot{m}_{air} also varied depending on the case applied (see Table 3).

HST-ACHP-DC combined cycle

HST-ACHP-DC combined cycle presented within Fig. 1 reflects a planned laboratory bench. The purpose of the current studies was to investigate it theoretically. In this paragraph, the heat pump cycle calculations were presented intentionally, for the sake of formalities, even though they are of a fundamental character, just to ensure that the whole analysis was performed based on the right theoretical foundations.

Figure 1 presents the system which was analysed. Starting from the ACHP evaporator outlet (point 1 in Fig. 2), on the R32 side, one can compute a saturation pressure at a given evaporation temperature, $t_{ev} = 10\text{ }^\circ\text{C}$ when the quality, $x = 1$. The extensive working fluid parameters, such as enthalpy and entropy, were also obtained at the same conditions.

In Fig. 2, the ACHP cycle is presented in the P–h diagram. The figure was obtained using Python and a Cool-Prop module. The set of formulas presented in Table 1, Eqs.

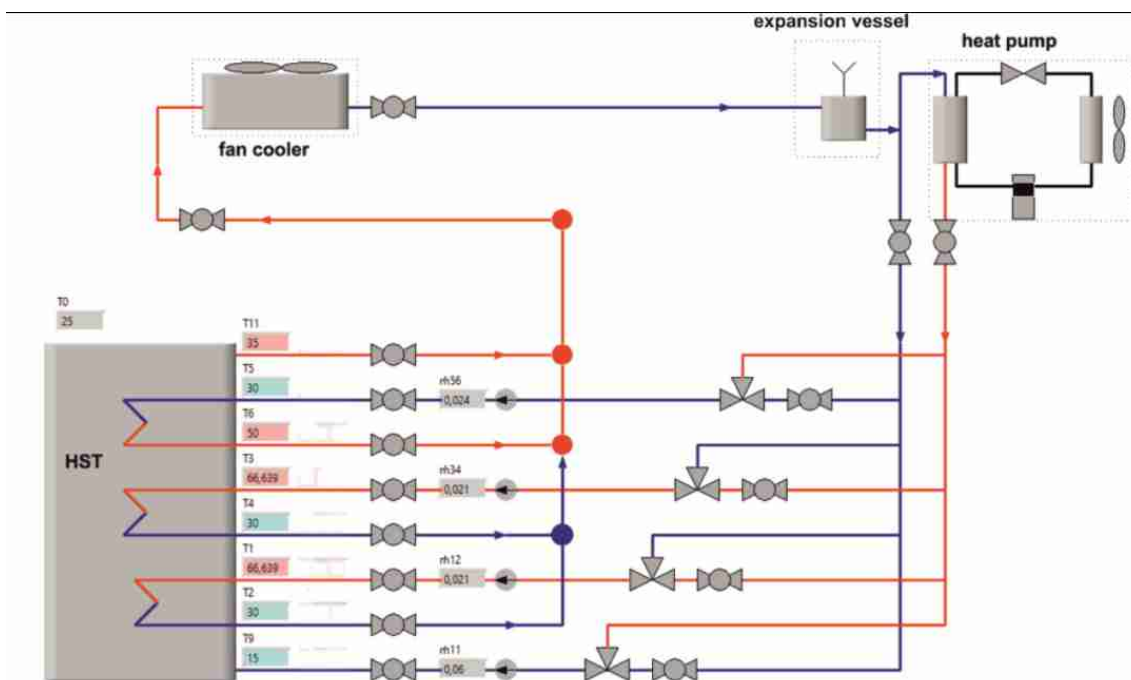


Fig. 1 Scheme of the system which was studied analytically

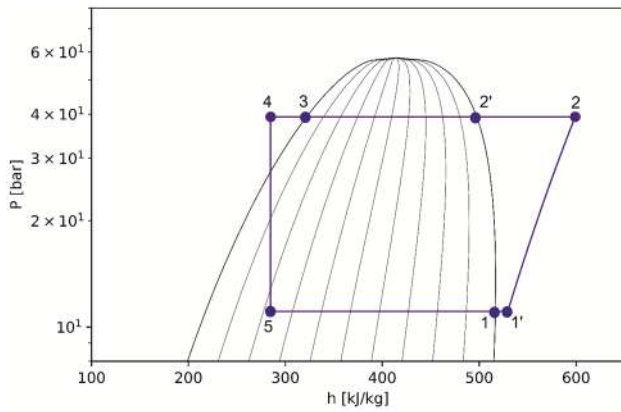


Fig. 2 Pictorial view of the ACHP cycle presented in P–h diagram for R32

(2)–(3) and Eqs. (6)–(8) reveal a method of calculating an extensive and intensive parameters of the R32 working fluid. Evaporation temperature was assumed to be 15 °C lower than the ambient temperature [25]. Therefore, evaporation occurred in $t_{ev} = 10$ °C. Values of evaporation pressure, enthalpy and entropy in point 1 of the Linde cycle (Fig. 2) are presented in Table 1. At the compressor suction (point 1' in Fig. 2) side, the working fluid is superheated by $t_{sh} = 5$ °C. At the compressor discharging side (point 2 in Fig. 2), the enthalpy for an isentropic compression ($h_{2_{is}}$) was calculated first. The temperature in point 2 could be obtained based on estimated $h_{2_{is}}$ and known condensation pressure P_{con} . The CoolProp procedure was used to calculate discussed temperature. However, as the non-isentropic compression was assumed, the estimated temperature at point 2 was set to be 10 °C higher than the temperature at which $h_{2_{is}}$ was computed. Consequently, the real temperature has reached the value of $t_2 = 111$ °C.

Based on the computed enthalpy values, an isentropic efficiency was calculated according to the definition [26]

$$\eta_{is} = \frac{h_{2_{is}} - h_{1'}}{h_2 - h_{1'}} \quad (1)$$

The computed value of the isentropic efficiency was around 0.79 which corresponds well with the real operating conditions [26]. It was assumed that temperature at the compressor discharging side was approximately equal to 111 °C. This result is based on the calculated temperature at point 2 with P_{con} pressure and assuming an isentropic compression. This temperature was calculated using CoolProp for given enthalpy $h_{2_{is}}$ and condensation pressure P_{con} . The resultant value was simply increased by 10 °C which makes that the final value is 111 °C. Usually, the isentropic efficiency is assumed and the temperature at the compressor discharging side is a resulting one.

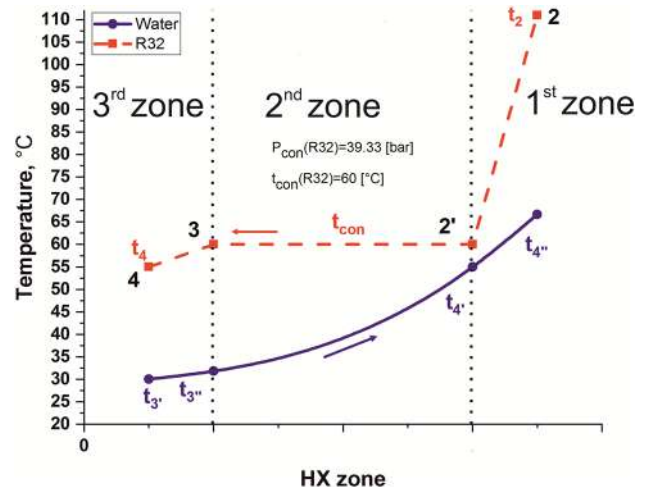


Fig. 3 Temperature variation of the water and R32 along the condenser length; P_{con} (R32) = 39.33 [bar], t_{con} (R32) = 60 [°C]

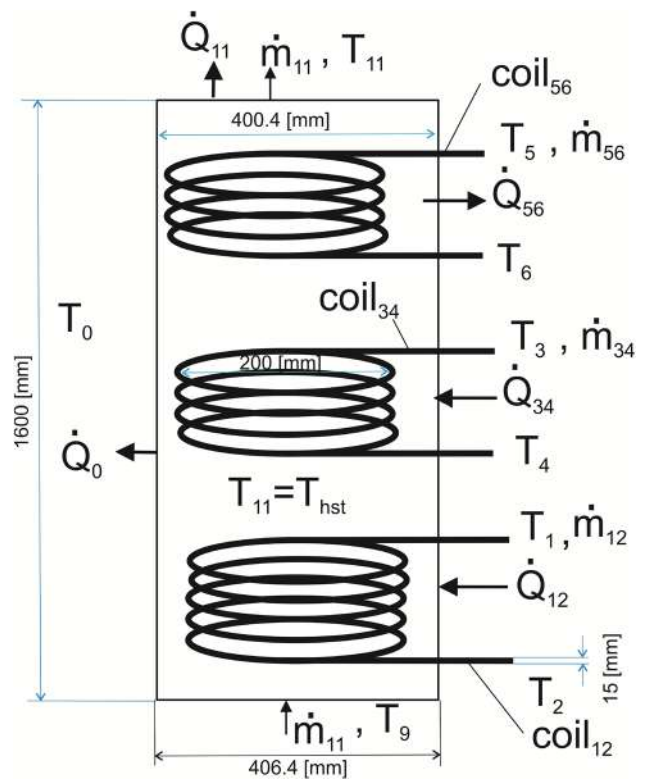


Fig. 4 Geometry of the studied HST

$$h_3(t_{con}, x) = 3.2 \cdot 10^5 \text{ [J/kg]} \quad (2)$$

$$s_3(t_{con}, x) = 1.4 \cdot 10^3 \text{ [J/(kg K)]} \quad (3)$$

where $x = 0$.

Table 1 Parameters of the cycle in points 1, 1' and 2 (Fig. 2)

	Point 1	Point 1'	Point 2
P [bar]	$P_{\text{sat}}(t_{\text{ev}}) = 11.07$	$P_{1'} = P_1$	$P_2 = P_{\text{con}}$
h [J/kg]	$h_1(t_{\text{ev}}, x) = 5.2 \cdot 10^5$	$h_{1'}(t_{1'}, P_1) = 5.23 \cdot 10^5$	$h_2(t_2, P_{\text{con}}) = 5.9 \cdot 10^5$
s [J/(kg K)]	$s_1(t_{\text{ev}}, x) = 2.1 \cdot 10^3$	$s_{1'}(t_{1'}, P_1) = 2.14 \cdot 10^3$	$s_2(h_2, P_{\text{con}}) = 2.18 \cdot 10^3$
t [°C]	$t_1 = 10$	$t_{1'} = t_1 + t_{\text{sh}}$	$t_2 = 111$

Where $x = 1$ is the quality; $P_{\text{sat}}(t_{\text{ev}})$ R 32 saturation pressure at t_{ev} temperature; h_1 enthalpy calculated at evaporation conditions, J/kg; and s_1 entropy calculated at evaporation conditions

$$w_t = h_2 - h_{1'} \tag{4}$$

The counter flow condenser was divided into three zones (see Fig. 3). In the first one, the superheated R32 vapour was cooled down from the temperature t_2 to t_{con} . In the second zone, the condensation process occurred while in the third one the condensate was cooled down from the temperature t_{con} to t_4 . The specific thermal load of the condenser was therefore estimated as:

$$q_{\text{con}} = h_2 - h_4 \tag{5}$$

Finally, the coefficient of performance (COP), $\epsilon_{\text{con}} = \frac{h_2 - h_4}{h_2 - h_{1'}} = 4.2$ was obtained. The calculated value of the COP stays in line with the COP of the ACHP (KAISAI KHC-10RY1) [27] which was bought for further empirical investigations.

$$P_4 = P_{\text{sat}}(t_{\text{con}}) \text{ [bar]} \tag{6}$$

$$h_4(t_4, P_4) = 3.08 \cdot 10^5 \text{ [J/kg]} \tag{7}$$

$$s_4(t_4, P_4) = 1.35 \cdot 10^3 \text{ [J/(kg K)]} \tag{8}$$

Figure 3 presents the temperature profiles of the condenser cooling water and R32 working medium along the condenser length. The zone numbering starts from the side of the hot R32 vapour inflow (1st zone). At the end of the first zone, there was assumed a minimal temperature difference $\Delta t = 5$ °C. Temperature value of the heated water at the inlet $t_{3'}$ of the condenser was equal to 30 °C.

$$h_{2'}(t_{\text{con}}, x = 1) = 4.97 \cdot 10^5 \text{ [J/kg]} \tag{9}$$

Working fluid enthalpy in point 2' (in Fig. 3) was, therefore, calculated using the CoolProp at a given temperature and quality (Eq. 9).

$$h_{4''} = (h_2 - h_{2'}) \cdot m_{\text{red}} + h_{4'} \tag{10}$$

Equation (10) allows for the calculation of the outlet temperature of the water heated in the condenser

$$t_{4''} = \frac{h_{4''}}{Cp_w} \tag{11}$$

which equals 66.64 °C. The water temperature at the end of the second zone $t_{3''}$ was calculated in the same way.

$$h_{3''} = (h_3 - h_4) \cdot m_{\text{red}} + h_{3'} \tag{12}$$

$$t_{3''} = \frac{h_{3''}}{Cp_w} \tag{13}$$

where $m_{\text{red}} = \frac{\dot{m}_{\text{R32}}}{\dot{m}_w}$ and h_3, h_4 apply to the R32 working fluid (Figs. 2, 3) and $h_{3''}, h_{3'}, t_{3''}$ refer to the heated water (Fig. 3).

The estimation of an appropriate mass flow rate of the R32 working fluid and the water in the secondary ACHP cycle was carried out based on Eqs. (14) and (20), respectively. The air mass flow rate in the primary ACHP cycle was an input value that varied by 0.025 kg/s from 0.06 to 0.135 kg/s. This enabled estimation ACHP operating parameters at four separate steady states. These parameters, namely the heating water mass flow rate and the temperature, were used as input data in the HST analysis.

Assumption of an ideal thermal energy transfer through the evaporator has led to derivation of the equation defining the R32 working fluid mass flow rate:

$$\dot{m}_{\text{R32}} = \frac{\dot{m}_{\text{air}} \cdot (h_{\text{ev.air}'} - h_{\text{ev.air}''})}{h_1 - h_5} \tag{14}$$

The mass flow rate of the cooling water in the condenser was estimated from the following relationship:

$$\frac{\dot{Q}_{\text{con_ext}}}{\dot{Q}_{\text{ev_ext}}} = \frac{\dot{Q}_{\text{con_int}}}{\dot{Q}_{\text{ev_int}}} \tag{15}$$

where int denotes an internal ACHP cycle and ext corresponds to the primary or secondary cycle.

$$\dot{Q}_{\text{con_ext}} = \dot{m}_w \cdot (h_{4''} - h_{3'}) \tag{16}$$

$$\dot{Q}_{\text{ev_ext}} = \dot{m}_{\text{air}} \cdot (h_{\text{ev.air}'} - h_{\text{ev.air}''}) \tag{17}$$

$$\dot{Q}_{\text{con_int}} = \dot{m}_{\text{R32}} \cdot (h_2 - h_4) \tag{18}$$

$$\dot{Q}_{\text{ev_int}} = \dot{m}_{\text{R32}} \cdot (h_1 - h_5) \tag{19}$$

By substituting Eqs. (16)–(19) to (15) one may determine the water mass flow rate depending on the air and R32 mass flow rates and the enthalpies of these fluids at relevant points of the cycle,

$$\dot{m}_w = \frac{\dot{m}_{\text{air}} \cdot (h_{\text{ev,air}'} - h_{\text{ev,air}}) \cdot (h_2 - h_4)}{(h_{4''} - h_{3'}) \cdot (h_1 - h_5)} \tag{20}$$

Mathematical model description of the HST

Internal geometry of the HST is presented schematically in Fig. 4. In this paper, the authors concentrate on a detailed analysis of the HST internal geometry as well as its operating parameters and dynamics at varying thermal loads. The heat-flow and the geometrical parameters have been analysed precisely. It has led to the estimation of the optimal operating conditions. The following parameters were analysed among others: coil length, number of the loops in a single coil, height of the coil, heat transfer area of the coil, heat fluxes transferred through the coils, heat transfer coefficient at the heating water side, mass flow rate of the freshwater supplying the HST, air mass flow rate in the ACHP primary cycle and diameter of a single loop of the coil (Tables 5, 6, 7, 8). Two modes of the HST operation were studied, namely continuous and intermittent. Intermittent operation mode of the HST reposed on alternating charging and discharging process occurrence. The main aim was to examine the ability of the HST to fulfil demand for heat for central heating and DHW preparation in a case of not being charged thermally. This paragraph presents the balance equations based on which the HST analysis was carried out. External geometry of the HST is presented in [1] and in Table 2. The internal geometry of the HST varies in terms of the number of loops in the coils. As the HST total volume remains constant, variation in the number of loops in the coils results in variation in the volume of water inside the tank.

The radius of a single whorl of the coil, D_{coil} , was assumed to vary from 0.2 to 0.3 m, while the internal diameter of

all of the coils was 0.015 m and the pipe thickness was $\delta_{\text{coil}} = 0.0015$ m.

$$\dot{Q}_{\text{hst}} = \dot{Q}_{12} + \dot{Q}_{34} - \dot{Q}_{56} - \dot{Q}_{11} - \dot{Q}_0 \tag{21}$$

where \dot{Q}_{hst} is the overall heat flux transferred to the HST, kW.

$$\dot{Q}_{\text{hst}} = M_{\text{hst}} \cdot C_{p11} \cdot \frac{dT_{11}}{d\tau} \tag{22}$$

where M_{hst} is the mass of the water in the HST, kg.

The presented HST-ACHP-DC system is described mathematically using lumped parameters model and its energy balance is described through Eq. (21). As it is known, the essence of the lumped parameters model is that the temperature is spatially uniform at any time during the unsteady process. The heat fluxes \dot{Q}_{12} and \dot{Q}_{34} correspond to the heating coils denoted as coil₁₂ and coil₃₄, respectively. The heat source, for two coils 12 and 34 is the ACHP. Therefore, further in the paper, there are listed considerations on the influence of the ACHP varying heating power on the HST operation. The heat flux \dot{Q}_{56} refers to the cooling coil₅₆. The DC is cooling receiver for the HST. The fresh cold water supply, into the fluid-flow HST, at the temperature lower than the mean HST liquid temperature influences the energy balance of the HST. Therefore, supplying the tank with cold water is regarded as the HST heat loss \dot{Q}_{11} . The last term in the balance equation \dot{Q}_0 denotes the heat losses from the HST to its surrounding.

$$\dot{Q}_{12} = \dot{m}_{12} \cdot C_{p12} \cdot (T_1 - T_2) = A_{12} \cdot K_{12} \cdot \Delta T_{\text{log},12} \tag{23}$$

$$\dot{Q}_{34} = \dot{m}_{34} \cdot C_{p34} \cdot (T_3 - T_4) = A_{34} \cdot K_{34} \cdot \Delta T_{\text{log},34} \tag{24}$$

$$\dot{Q}_{56} = \dot{m}_{56} \cdot C_{p56} \cdot (T_6 - T_5) = A_{56} \cdot K_{56} \cdot \Delta T_{\text{log},56} \tag{25}$$

$$\dot{Q}_{11} = \dot{m}_{11} \cdot C_{p11} \cdot (T_{11} - T_9) \tag{26}$$

$$\dot{Q}_0 = K_{\text{hst}} \cdot A_{\text{hst}} \cdot (T_{11} - T_0) \tag{27}$$

Overall heat transfer coefficient of the coil is calculated as follows:

$$K_{ij} = \frac{1}{R_{\text{coil},ij,\text{hst}}} \tag{28}$$

Total thermal resistance $R_{\text{coil},ij,\text{hst}}$ is defined as

$$R_{\text{coil},ij,\text{hst}} = \frac{1}{\alpha_{c,ij}} + \frac{d_{\text{mean,coil}}}{\lambda_r} + \frac{1}{\alpha_{11}} \tag{29}$$

where $i = 1, 3, 5$ and $j = 2, 4, 6$.

Table 2 Geometrical parameters of the HST taken from the project assumptions [1]

Height, L_{hst} [m]	External diameter, D_{ext} [m]	Internal diameter, D_{int} [m]
1.6	0.4064	0.4004

$$Nu = 0.023 \cdot Re^{0.8} \cdot Pr^{0.4} \tag{30}$$

$$\alpha = Nu \cdot \frac{\lambda}{d_{i,coil}} \tag{31}$$

$$\epsilon_c = 1 + 3.54 \cdot \frac{d_{i,coil}}{D_{coil}} \tag{32}$$

$$\alpha_{c_{ij}} = \alpha \cdot \epsilon_c \tag{33}$$

Overall heat transfer coefficient calculated for the HST in terms of the total thermal resistance to heat transfer between the water in the HST and its surrounding air was calculated using Eqs. (34) and (35):

$$K_{hst} = \frac{1}{R_{hst}} \tag{34}$$

Total thermal R_{hst} is presented through a following formula:

$$T_{11}^* = \frac{\{(D + G \cdot T_0^* \cdot \tau_0 + H \cdot T_9^* \cdot \tau_0 + T_i^* \cdot \tau_0 \cdot (-H - G)) \cdot e^{\tau^* \cdot \tau_0 \cdot (-H - G)}\} - D - \tau_0 \cdot (G \cdot T_0^* + H \cdot T_9^*)}{\tau_0 \cdot (-H - G)} \tag{37}$$

$$R_{hst} = \frac{1}{\alpha_{air}} + \frac{\ln\left(\frac{D_{ext}}{D_{int}}\right)}{2 \cdot \pi \cdot \lambda_{hst}} + \frac{\ln\left(\frac{D_{ext} + 2 \cdot \delta_{is}}{D_{ext}}\right)}{2 \cdot \pi \cdot \lambda_{is}} + \frac{1}{\alpha_{11}} \tag{35}$$

The heat transfer coefficient α at the heating water side in all three coils was computed using the classical Dittus–Boelter correlation for Nusselt number for turbulent flow (Eq. 30). Additionally, a correction coefficient (Eq. 32) taking into account the coil shape was applied to provide the most accurate heat transfer coefficient value. Finally the heat transfer coefficient of the medium inside the coils was calculated using Eq. (33).

Equations (22)–(27) can be substituted into Eq. (21) and then, the resulting equation can be solved for temperature T_{11} . The time and the temperature were introduced in a dimensionless form defined as $\tau^* = \frac{\tau}{\tau_0}$, $T^* = \frac{T}{T_0 - T_i}$ respectively. Hence, physical dimensional Eq. (21) was transformed into a non-dimensional mathematical equation which was solved. Appearance of the dimensionless numbers results from the transformation the physical equation into mathematical (Eq. 36):

$$\frac{dT_{11}^*}{d\tau^*} = A^* + B^* - C^* - D^* - E^* \tag{36}$$

where

$$A^* = Re_{12} \cdot Pr \cdot \frac{\pi \cdot d_{i,coil} \cdot \lambda_{12}}{4 \cdot M_{11} \cdot Cp_{11}} \cdot (T_1^* - T_2^*) \cdot \tau_0$$

$$B^* = Re_{34} \cdot Pr \cdot \frac{\pi \cdot d_{i,coil} \cdot \lambda_{34}}{4 \cdot M_{11} \cdot Cp_{11}} \cdot (T_3^* - T_4^*) \cdot \tau_0$$

$$C^* = Re_{56} \cdot Pr \cdot \frac{\pi \cdot d_{i,coil} \cdot \lambda_{56}}{4 \cdot M_{11} \cdot Cp_{11}} \cdot (T_6^* - T_5^*) \cdot \tau_0$$

$$D^* = Re_{119} \cdot Pr \cdot \frac{\pi \cdot d_{i,pipe} \cdot \lambda_{119}}{4 \cdot M_{11} \cdot Cp_{11}} \cdot (T_{11}^* - T_9^*) \cdot \tau_0$$

$$E^* = \frac{\left(\frac{L_{hst}}{\lambda_{11}} + \frac{\ln\left(\frac{D_{ext}}{D_{int}}\right)}{2 \cdot \pi \cdot \lambda_{hst}} + \frac{L_{hst}}{Nu_{air}}\right)^{-1} \cdot A_{hst} \cdot \frac{\mu_{11}}{\lambda_{11}}}{M_{11} \cdot Pr_{11}} \cdot (T_{11}^* - T_0^*) \cdot \tau_0$$

The solution of the differential Eq. (36) was found analytically and is expressed by formula (37):

where

$$M_{11} = M_{hst} \text{ is the total mass of the water in the HST, kg}$$

$$H = Re_{119} \cdot Pr \cdot \frac{\pi \cdot d_{i,pipe} \cdot \lambda_{119}}{4 \cdot M_{11} \cdot Cp_{11}}$$

$$G = \frac{\left(\frac{L_{hst}}{\lambda_{11}} + \frac{\ln\left(\frac{D_{ext}}{D_{int}}\right)}{2 \cdot \pi \cdot \lambda_{hst}} + \frac{L_{hst}}{Nu_{air}}\right)^{-1} \cdot A_{hst} \cdot \frac{\mu_{11}}{\lambda_{11}}}{M_{11} \cdot Pr_{11}}$$

$$D = A^* + B^* - C^*$$

Equations (21) and (36) describe the energy balance for the HST containing three coils, two heating and one cooling. The energy balance for the HST with two coils assumes that one heating coil is removed (in this case it is coil₃₄) and it takes the form as follows:

$$\dot{Q}_{hst} = \dot{Q}_{12} - \dot{Q}_{56} - \dot{Q}_{11} - \dot{Q}_0 \tag{38}$$

and

$$\frac{dT_{11}^*}{d\tau^*} = A^* - C^* - D^* - E^* \tag{39}$$

Shifting between two HST models, namely the first one with three coils and the second one with two coils, can be performed easily in the equations presented above. The variable D contains the terms corresponding to each heating and cooling coil. Therefore, the coil number may be arbitrarily varied. The only limiting condition is the HST height. Therefore, Eq. (37) can also be used for HST water temperature estimation in the case of the HST with two coils. In such case, the variable D should be replaced with $D_{2_coils} = A^* - C^*$.

In this place, it is worth mentioning dimensionless numbers which play a meaningful role in HST operation analysis, namely the Grashof and Rayleigh numbers. They were calculated for the water inside the studied HST.

$$Gr_{w,hst} = \frac{g \cdot L_{hst}^3 \cdot \rho_{w,hst}}{\mu_{w,hst}} \cdot \beta_{w,hst} \cdot \Delta T \tag{40}$$

where ΔT , °C, stands for the temperature difference between the water and the wall of the heating coil. In this case, $Gr_{w,hst} = 5.51 \cdot 10^9$. The value of the Grashof number $Gr_{w,hst}$ indicates that the buoyancy force dominates the viscous forces. Additionally, the value of the following ratio, $\frac{Gr_{w,hst}}{Re_{w,hst}}$, implies that in the HST occurs a free convection as this ratio value is $3.1 \cdot 10^4$. Moreover, the calculated Rayleigh number, defined as $Ra_{w,hst} = Gr_{w,hst} \cdot Pr_{w,hst}$, reached the value of $2.34 \cdot 10^{10}$. If the Rayleigh number is lower than 10^8 , the flow is laminar. However, when the Rayleigh number value exceeds 10^{10} , the flow is turbulent [7]. Therefore, the Rayleigh number value implies that within the investigated HST the water movement is of a turbulent character.

$$Nu_{w,hst} = 0.6 \cdot 0.33 \cdot Re_{w,hst}^{0.6} \cdot Pr_{w,hst}^{0.33} \tag{41}$$

Equation (41) represents a correlation for the Nusselt number for a shell–tube heat exchanger which was found to be the most suitable for the HST with the internal coils. At the beginning of the correlation Eq. (41), there stands a correction coefficient which equals 0.6. This coefficient accounts for the leakage and a non-perpendicular water inflow to the coils external surface.

$$\alpha_{w,hst} = Nu_{w,hst} \cdot \frac{\lambda_{w,hst}}{d_{e,coil}} \tag{42}$$

Therefore, the heat transfer coefficient at the HST internal water side was calculated using formula (42).

Validation of the analytical model

The validation of the HST analytical model was carried out based on the data made available by Li et al. [6]. The presented model of the HST is based on the lumped capacitance

method approach, as already mentioned, that essentially comes down to the assumption that the temperature is spatially uniform in the whole computational domain. The work by Li et al. [6] presents the CFD analysis assuming that the water velocity through the HST during its charging is set at 0 m/s. Additionally, the HST heating coil velocity inlet boundary condition was set in the commercial computational software. Hence, the heating medium (ethylene glycol) velocity was equal to 0.45 m/s. The geometrical and fluid-flow conditions of the CFD analysis presented in [6] were also used for the present HST analytical model validation. This refers to the height and diameter of the HST as well as to the coil and the heating medium mass flow rates. The validation of the present model was carried out for the case No 1 described in [6]. The reference results for the cylindrical HST are presented in Fig. 6b in [6]. For the purpose of the validation, in the present model it was assumed that there is no fluid flow through the HST and that it is heated by one coil. Regarding that only inlet temperature of the heating medium (ethylene glycol) is known, and that there is no fluid flow through the HST, the balance Eq. (21) simplifies to

$$\dot{Q}_{hst} = \dot{Q}_{12} - \dot{Q}_0 \tag{43}$$

where $\dot{Q}_{12} = \dot{m}_{12} \cdot Cp_{12} \cdot (T_{12} - T_{11})$. In this particular case, all parameters indexed with 12 correspond to the ethylene glycol. The terms \dot{Q}_{hst} and \dot{Q}_0 are defined by Eqs. (22) and (27), respectively. Taking this into account, Eq. (43) may be rewritten as

$$M_{hst} \cdot Cp_{11} \cdot \frac{dT_{11}}{d\tau} = \dot{m}_{12} \cdot Cp_{12} \cdot (T_{12} - T_{11}) - K_{hst} \cdot A_{hst} \cdot (T_{11} - T_0) \tag{44}$$

Therefore, T_{11} depends on time while T_{12} depends on the coil length. T_{12} is a mean temperature of the ethylene glycol at x length of the coil.

On the other hand, \dot{Q}_{12} can be presented as

$$\dot{m}_{12} \cdot Cp_{12} \cdot dT_{12} = K_{12,e} \cdot O_{coil,12} \cdot (T_{12} - T_{11}) \cdot dx \tag{45}$$

where $O_{coil,12}$ is the circumference of coil₁₂, m; T_{12} is a temperature of the ethylene glycol at the x length of the coil, K; and $K_{12,e}$ is the overall heat transfer coefficient calculated for the heating coil with ethylene glycol. By solving Eq. (45) for T_{12} at $x=0$, $T_{12}=T_1$ boundary conditions applied, one obtains:

$$T_{12} - T_{11} = (T_1 - T_{11}) \cdot e^{A \cdot x} \tag{46}$$

where $A = \frac{k_{coil,12} \cdot O_{coil,12}}{\dot{m}_{12} \cdot Cp_{12}}$.

By substituting Eqs. (44)–(46) and after solving the differential equation, one can obtain a solution allowing for computing temperature variation of the water in the HST, namely T_{11} , over time.

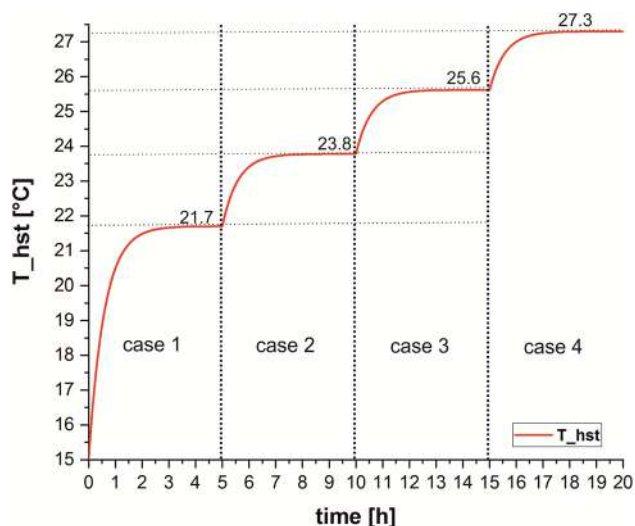


Fig. 5 HST water temperature (T_{hst}) variation over time at four ACHP steady states for constant values of $\dot{m}_{11}=0.085$ kg/s and $\dot{m}_{56}=0.024$ kg/s; for each case, the following conditions are fulfilled: $\dot{m}_w = \dot{m}_{12} + \dot{m}_{34}$ and $\dot{m}_{12} = \dot{m}_{34}$, $D_{\text{coil}} = 0.2$ m; values of the mass flow rates are presented in Table 3

Table 3 Values of the mass flow rates corresponding to all studied cases

	Case 1	Case 2	Case 3	Case 4
\dot{m}_{12} [kg/s]	0.014	0.017	0.019	0.021
\dot{m}_{air} [kg/s]	0.63	0.73	0.83	0.93
\dot{m}_{R32} [kg/s]	0.015	0.018	0.02	0.023

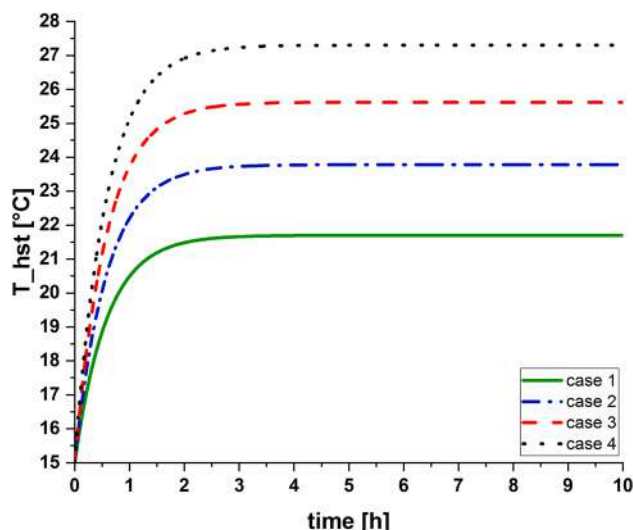


Fig. 6 Time-dependent HST water temperature (T_{hst}) variation at four ACHP steady states; $D_{\text{coil}}=0.2$ m

Table 4 An increase in T_{hst} temperature as an answer to the percentage growth in \dot{m}_{12} , \dot{m}_{34} mass flow rates for all studied cases

Case	$\dot{m}_{12}, \dot{m}_{34}$, kg/s	T_{hst} , °C
1 versus 2	↑ 21.4%	↑ 2.1
2 versus 3	↑ 11.8%	↑ 1.8
3 versus 4	↑ 10.5%	↑ 1.7

$$T_{11} = \frac{\left\{ e^{x \cdot (-B \cdot e^{A \cdot x} - W)} \cdot [B \cdot T_1 \cdot e^{A \cdot x} + W \cdot T_0 + T_i \cdot (-B \cdot e^{A \cdot x} - W)] \right\} - B \cdot T_1 \cdot e^{A \cdot x} - W \cdot T_0}{-B \cdot e^{A \cdot x} - W} \tag{47}$$

where $B = \frac{\dot{m}_{12} \cdot C_{p12}}{M_{11} \cdot C_{p11}}$, $W = \frac{K_{\text{hst}} \cdot A_{\text{hst}}}{M_{11} \cdot C_{p11}}$ and x is the length of the coil, m.

The temperature computed using formula (47) for the second hour of the HST operation time reached the value of 316.96 K. It was compared with the temperature value shown in Fig. 6b in [6] in which the layout of the isothermal surfaces in a longitudinal section of the cylindrical HST is depicted. The results differ by only 2.96 K which is considered satisfactory accordance between the values.

Results and discussion

The dynamics of the HST-ACHP-FC system was carried out using the MATLAB/Simulink. As it is presented in Fig. 5, the HST operated under transient conditions while

the ACHP worked at four subsequent steady states (Table 3). The heating coils coil₁₂ and coil₃₄ were provided the same heating power as the mass flow rates \dot{m}_{12} and \dot{m}_{34} were set to be equal at a constant temperature difference at the inlets and outlets of both coils. In this way, the influence of the ACHP heating power variation on the HST operation was studied. The following analysis was conducted for the D_{coil} equal to 0.2 m and 0.3 m.

The increase in the mass flow rate of the air in the primary ACHP cycle has obviously resulted in T_{hst} temperature increase (see Fig. 5). By comparing cases 1 and 4, one may conclude that the increase of $\dot{m}_{\text{air}}=0.63$ kg/s by about 48% leads to increase in T_{hst} by 5.6 °C, in \dot{m}_{12} and \dot{m}_{R32} by 50% and 53%, respectively. When two previously mentioned cases are compared, it is rather clear that the difference in T_{hst} temperature at the level of 5.6 °C leads to the growth

Table 5 Thermal and geometrical parameters of coil₁₂ and coil₃₄ of the HST for case 1–case 4 marked in Figs. 5 and 6

	Case 1	Case 2	Case 3	Case 4
$\alpha_{12,34} \left[\frac{W}{m^2 K} \right]$	959.1	1079	1196	1310
$\dot{Q}_{coil,12,34}$ [kW]	2.2	2.5	2.9	3.2
$Re_{12,34}$	2122	2458	2795	3132
$Nu_{12,34}$	17.8	20	22.2	24.3
$L_{coil12,34}$ [m]	8.9	10	11	12.2
N	14	16	18	20
$h_{coil12,34}$ [m]	0.25	0.29	0.32	0.35
$A_{coil12,34}$ [m ²]	0.5	0.56	0.63	0.7

of the stored thermal energy by 4.45 MJ in the case 4 against the case 1. Therefore, by comparing the electric power used to supply the circulation pumps to the benefit of the thermal energy storage one may decide whether it is worthy or not. In the current paper, the presented system was not investigated regarding its economics.

Each of the cases, 1, 2, 3 and 4, depicted in Figs. 5 and 6 is of different HST thermal and geometrical parameters which are listed in Table 5. Equality of \dot{m}_{12} and \dot{m}_{34} causes that all parameters presented in Table 5 are also the same for both heating coils. In the paper, design HST calculations are disclosed; therefore, the coil geometrical parameters differ in all cases, which are presented through Table 5. By comparing all instances, it can be noticed that the highest growth in both temperature T_{hst} and \dot{m}_{12} , \dot{m}_{34} mass flow rates was detected for case 1 and 2 (see Table 4). The 21.4% increase in the mass flow rates has led to increase in the HST water temperature by 2.1 °C.

As it is presented in Table 4, the overall growth in \dot{m}_{12} and \dot{m}_{34} mass flow rates by 50% has resulted in the HST water mean temperature increase by 5.6 °C. At this point, it is to be considered whether the growth in the temperature is worth the growth of demand for electrical energy of the circulating pump.

Table 6 An example extended analysis results carried out for each of the studied cases

	Case 1	Case 2	Case 3	Case 4
	$A_{coil12,34}$ [m ²]			
	0.5	0.56	0.63	0.7
\dot{m}_{air} [kg/s]	$\dot{Q}_{coil,12,34}$ [kW]			
0.1	1.2	1.3	1.5	1.6
0.5	2.1	2.3	2.6	2.9
1	2.4	2.6	3	3.3
1.5	2.5	2.8	3.1	3.5

Within Table 5, design analysis results of the HST heating coils are presented.

Extended calculations were carried out for the geometrical parameters which were previously estimated for four studied cases based on design analysis. In design calculations, the geometrical parameters values were derived. In extended calculations, the values of the geometrical parameters were input data.

Based on the aforementioned, the geometrical parameters such as the heat transfer surface area of the heating coils $A_{coil12,34}$ the length of the coils $L_{coil12,34}$ and their height take now constant values which are case-dependent. Extended calculations were carried out for geometrical parameters presented in Table 5. It is obvious that the growth in the air mass flow rate at the ACHP low-heat source side implies the growth in the heat flux transferred through the HST heating coils. For the purpose of extended calculations, each of four cases can be chosen. Keeping constant geometrical parameters and varying heating medium mass flow rate, one may find the quantity of thermal energy transferred through a particular heating coil. An example of the extended analysis results is presented through Table 6.

Table 6 presents the results of the extended analysis which was carried out by applying particular geometrical parameters of the coils. The geometrical parameters were constant for each case (case 1–4). Nevertheless, they differed when compared one case to another. As the coil geometry was kept constant for a given case (case 1–4), the overall heat transfer coefficient was varying due to variation of the heat transfer coefficient which resulted from varying Reynolds and Nusselt numbers.

Obviously, the highest heat flux values are observed for the fourth case as the coil heat transfer surface area is

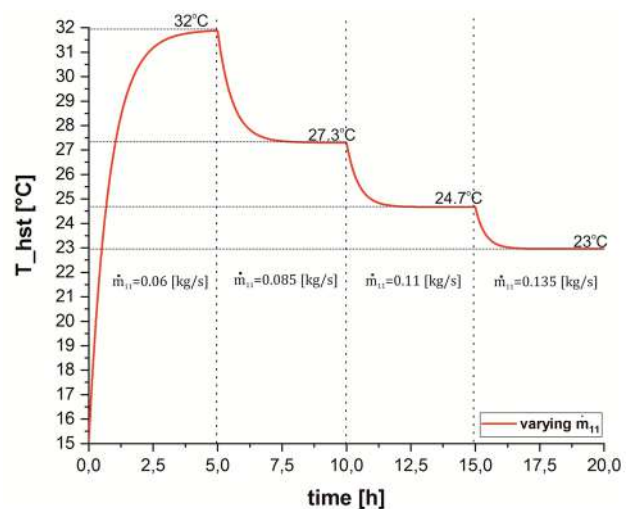


Fig. 7 T_{hst} temperature variation over time and over increasing \dot{m}_{12} at constant \dot{m}_{air} ; $D_{coil} = 0.2$ m

the highest. The content of Table 6 allows for choosing an appropriate heating power of the coil which results from the user’s needs.

The case 4 (Table 5) was chosen for further analysis due to highest heat transfer area of the heating coils. Figure 7 shows how the HST mean water temperature varies over time after altering mass flow rate of the freshwater supplying the HST. The mass flow rate of the water \dot{m}_{11} that is heated while flowing through the HST, may vary according to the actual consumer needs. In the case of a minimal usage of the thermal energy stored in the HST by harvesting it through \dot{m}_{11} , there is still 4.2 kW transferred by the flow and the HST water temperature is the highest in this case (32 °C). When HST reaches the steady state, the \dot{m}_{11} is increased by 0.025 kg/s that results in T_{hst} drop by about 4.6 °C. The heat flux which is transferred from the HST reaches 4372 W in this case. Further increase of \dot{m}_{11} to the value of 0.11 kg/s leads to slight growth of the transferred heat flux to 4447 W. The water outflow of $\dot{m}_{11}=0.135$ kg/s carries the heat flux at the level of 4.5 kW; however, the HST water temperature decreases significantly in this case as it is only 8 °C higher in value than the initial temperature (15 °C).

The analysis of the HST operation under varying \dot{m}_{11} mass flow rate was carried for the fourth case which was found to be the most appropriate from an energetic point of view.

Figure 8 and Table 7 show the time after which the HST temperature reaches a steady value for selected values of \dot{m}_{11} . It is evident that the change of the value of \dot{m}_{11} affects the temperature of the liquid inside the HST. This temperature decreases in time after \dot{m}_{11} is increased which is rather obvious. However, the analysis which was carried out is of a design and a verification character. Therefore, after

Table 7 Time required to reach the steady state in the HST with selected values of \dot{m}_{11} mass flow rate (see Fig. 8)

\dot{m}_{11} [kg/s]	T_{hst} [°C]	t [h]
0.135	22.96	2.6
0.11	24.66	3
0.085	27.29	3.9
0.06	31.85	4.5

defining the optimal heat-flow and the geometrical parameters (Table 5, case 4) further analysis was conducted.

Figure 9 shows the characteristics of an intermittent HST operation. The aforementioned characteristics were obtained for the following operating conditions. Blue dashed line applies to the case in which simultaneous HST charging through both heating coils (coil₁₂, coil₃₄) and discharging through coil₅₆ was assumed. During this HST charging–discharging process \dot{m}_{11} mass flow rate was constant and equal to 0.06 kg/s. After 5 h of charging, the mass flow rates were set to 0 kg/s in both heating coils which naturally resulted in the commencement of the discharging process as both, \dot{m}_{11} and \dot{m}_{56} , mass flow rates were kept at constant values, namely 0.06 kg/s and 0.024 kg/s, respectively. The red solid line also presents T_{hst} temperature variation over time during intermittent charging–discharging process. However, in contrast to the former case the mass flow rate in the coil₅₆, intended to fulfil demand on domestic hot water (DHW) preparation, was turned down to 0 kg/s. In this case, T_{hst} increased in value by about 7.2 °C relative to the previous case. Nevertheless, Fig. 9 shows that even when the HST prepares DHW during its charging process, it can still accumulate thermal energy at the level that allows for its further continuous operation for the next 1 h without being charged. In this case, the HST water temperature reaches the same value as in the case without DHW preparation which

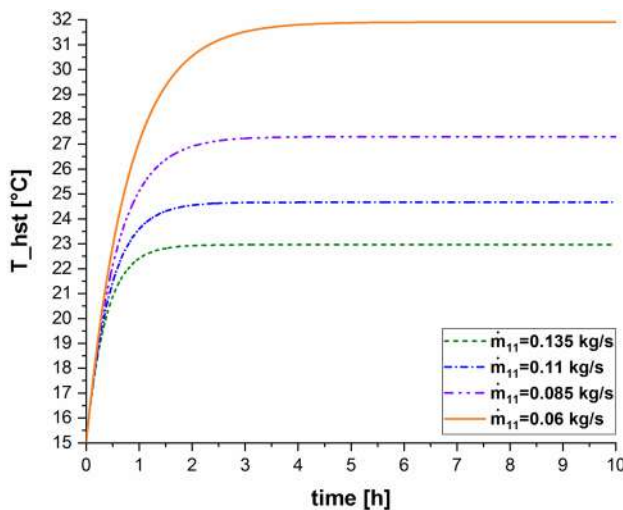


Fig. 8 T_{hst} temperature variation over time at constant \dot{m}_{air} at four different \dot{m}_{11} values; $D_{\text{coil}}=0.2$ m

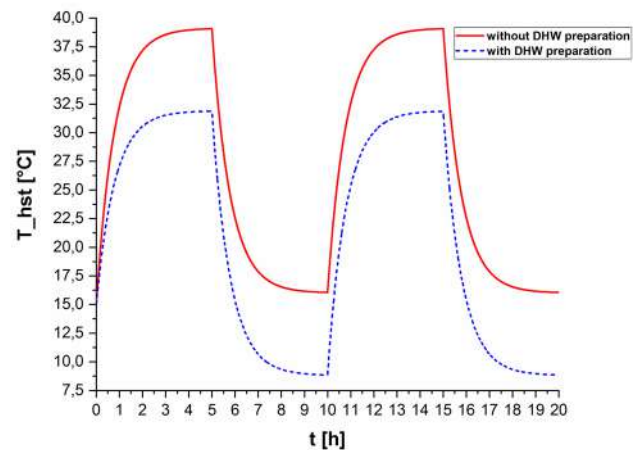


Fig. 9 Intermittent HST charging–discharging process under the conditions of the 4th case (see Table 5) and the lowest \dot{m}_{11} mass flow rate of 0.06 kg/s (see Table 7); DHW, domestic hot water

Table 8 Thermal and geometrical parameters of coil₁₂ and coil₃₄ of the HST for the same input parameters as in case 4 but for the coil diameter D_{coil} equal 0.3 m

$\alpha_{12,34} \left[\frac{\text{W}}{\text{m}^2 \text{K}} \right]$	1236
$\dot{Q}_{\text{coil},12,34} \text{ [kW]}$	3.3
$\text{Re}_{12,34}$	3190
$\text{Nu}_{12,34}$	24.7
$L_{\text{coil},12,34} \text{ [m]}$	12.5
N	14
$h_{\text{coil},12,34} \text{ [m]}$	0.24
$A_{\text{coil},12,34} \text{ [m}^2\text{]}$	0.71

Table 9 Thermal and geometrical parameters of coil₁₂ for the case of the HST with two coils and $\dot{Q}_{12} = 2 \cdot 3.2 \text{ kW}$

$\alpha_{12} \left[\frac{\text{W}}{\text{m}^2 \text{K}} \right]$	2280
$\dot{Q}_{\text{coil},12} \text{ [kW]}$	6.4
Re_{12}	6264
Nu_{12}	42.3
$L_{\text{coil},12} \text{ [m]}$	22.2
N	36
$h_{\text{coil},12} \text{ [m]}$	0.64
$A_{\text{coil},12} \text{ [m}^2\text{]}$	1.23

is about 16.3 °C. The HST operation period without being charged may be enlarged to 5 h. Unfortunately, in this case the HST water temperature decreases significantly and its final value reaches 8 °C.

Further on, a comparison to the HST with the coils diameter D_{coil} equal to 0.3 m is presented. The input data are the same as in case 4 described previously. The results are compared to those presented in Table 5 (case 4). As given in Table 5 (case 4) and in Table 8, 0.1 m increase in the coil diameter D_{coil} causes a decrease by 100 W/(m² K) in the value of the heat transfer coefficient. In general, lowering the coil diameter implies the growth of curvature of the coil which obviously results in the heat transfer coefficient growth (see Eqs. (31)–(33)). The heat transfer coefficient calculated using Eq. (33) is higher in value than the one calculated using Eq. (31). However, along with the decrease in the coil diameter, its height increases which also must be taken into account if the HST height is kept constant. In the previously studied case, $D_{\text{coil}} = 0.2 \text{ m}$ and this value seems to be the most appropriate from the heat transfer and geometrical points of view.

The comparison of the HST with varying number of the coils was made. In all cases being examined, the initial temperature of the liquid in the HST was equal to 15 °C. The reference case was the one with 3 coils from which two heating coils (i.e. coil₁₂ and coil₃₄) and operated at the same level of heat-flow rate, namely 3.2 kW. In the second instance, one heating coil (coil₁₂) operated at varying heating power of 3.2 kW or 6.4 kW. It was found out that the presented model did capture the change in T_{hst} when the coil number changed from 2 to 3 in the case of

$\dot{Q}_{\text{coil},12} = 3.2 \text{ kW}$. It was noticed that for this assumption, T_{hst} for the HST with 2 coils reached the value of 18.47 °C while with three coils the temperature in the HST grew to the value of 27.33 °C. When the heating power of the coil₁₂ was increased from $\dot{Q}_{\text{coil},12} = 3.2 \text{ kW}$ to $\dot{Q}_{\text{coil},12} = 2 \cdot 3.2 \text{ kW}$ in the case of the HST containing 2 coils, the water temperature in the HST reached the same value as in the reference case, namely 27.33 °C. In the case of the HST with 2 coils and $\dot{Q}_{\text{coil},12} = 2 \cdot 3.2 \text{ kW}$, the temperature in the HST was the same as in the reference case, namely 27.33 °C. Additionally, in the case of 2 coils, a heat transfer area was somewhat lower than in the reference case which could negatively affect the heat transfer against the reference case. On the other hand, in the case of two coils, the heat transfer coefficient increased by 74% (Table 9) when compared to the reference case which, obviously, improved the thermal energy transfer. Obviously, increasing the heating medium mass flow rate and keeping the same coil diameter d_{coil} results in the increase in the Reynolds number that implies the increment in Nusselt number and the heat transfer coefficient values.

To capture a more precise variation in T_{hst} for the aforementioned case, the HST domain ought to be divided into minimum 3 zones and the T_{hst} should be calculated for all zones, giving more adequate results. Such analysis was not carried out within the current study as the goal was not to provide a local but general view on the T_{hst} variation. The aim was also to introduce a methodology allowing for the HST thermal-flow analysis and the presented model is sufficient for it.

Conclusions

HST-ACHP-FC combined cycle was analysed in this paper. The HST response to the varying operating parameters was analysed. The differential equation describing the HST water temperature variation over time was proposed based on the lumped capacitance method. Solution of this equation enables calculation of the time-dependent temperature of the water in the HST using even a calculator. Additionally, a correlation of the aforementioned temperature variation over time and with the coil length was proposed. The analytical model validation was carried out. The model presented gave proper results, and an excellent accordance with the literature data was reached. The results of the analysis led to the following conclusions. Essential information on the HST operation at varying thermal-flow conditions is presented. Hence, when both border cases are compared, namely the case 1 and case 4, it is seen that the increase in the air mass flow rate of the primary cycle and of the heating water mass flow rate in the coil by 48% and 50%, respectively, implied a growth in the HST water temperature by 5.6 °C. It was

observed that the change in heating coils mass flow rate from 0.014 to 0.021 kg/s has resulted in the growth of the heat transfer coefficient from 959.1 to 1310 W/m² K. Simultaneously an increase in the heat flux transferred through the heating coils from 2.2 to 3.2 kW was obtained. Additionally, it was noticed that 0.1 m increase in the coil diameter D_{coil} caused a decrease by 100 W/(m² K) in the value of the heat transfer coefficient. The proposed solution for the time-dependent temperature variation reveals the dimensionless numbers which dominate in the studied problem. Based on the knowledge about the dimensionless numbers that play a key role in the HST operation, one may identify which parameters should be measured during empirical investigations. Based on the analysis carried out, it was concluded that an increase in diameter of a single loop of the coil D_{coil} by 50% implied a decrease in the heat transfer coefficient inside the coil by about 6%. Additionally, it was noticed that the increase in the coil heat transfer surface area by 40% has resulted in the increase in heat flux transferred through the coil by 33–40% depending on the heating medium mass flow rate. Optimal thermal-flow operating parameters of the HST coils were proposed due to highest heat flux transferred to the HST. Based on the analysis carried out, the time after which the HST reaches steady state at varying freshwater mass flow rate was estimated. Intermittent HST charging–discharging process was carried out for case 4 with the freshwater mass flow rate $\dot{m}_{11} = 0.06$ kg/s. The analysis was performed at DHW simultaneous preparation enabled and disabled. When DHW preparation was disabled, the HST water mean temperature increased by 7.2 °C with reference to the other case. Nevertheless, the HST could fulfil demand for heat for central heating and DHW preparation even for 5 h without charging. Future work on the HST may be carried out as there exists a turbulent mixing within the water inside the HST. This phenomena is important due to efficiency of thermal energy storage as it influences the stratification in water. Further works may also concern CFD analysis which would provide valuable data about isothermal surfaces distribution. Additionally, based on CFD analysis multiple geometrical and heat-flow parameters could be more precisely estimated. The speech is about the heat transfer coefficient in the coils and in the HST, the shape and localisation of the freshwater inlet, localisation of eddies and many others.

A simple analytical computational algorithm for the HST is presented. It allows for examining the effect of heat-flow and geometrical parameters variation on the HST operation. The algorithm was employed for few different cases and satisfactory results were obtained.

Appendix

Derivations of $A^* - D^*$ present in Eq. (36):

$$X^* = \frac{\dot{m}_{ij} \cdot Cp_{ij} \cdot \frac{\mu_{ij}}{\lambda_{ij}}}{M_w \cdot Cp_w \cdot \frac{\mu_{ij}}{\lambda_{ij}}} \cdot \Delta T_{ij}^* \cdot \tau_0 \tag{48}$$

where $X^* = A^*, B^*, C^*, D^*$; $\Delta T_{ij}^* = T_i^* - T_j^*$, $i = 1, 3, 6, 11; j = 2, 4, 5, 9$

$$Pr_{ij} = Cp_{ij} \cdot \frac{\mu_{ij}}{\lambda_{ij}} \tag{49}$$

$$X^* = \frac{\dot{m}_{ij} \cdot Pr_{ij}}{M_w \cdot Cp_w \cdot \frac{\mu_{ij}}{\lambda_{ij}}} \cdot \Delta T_{ij}^* \cdot \tau_0 \tag{50}$$

$$\dot{m}_{ij} = \rho_{ij} \cdot A_{coil} \cdot w_{ij} \tag{51}$$

where Pr_{ij} is the Prandtl number, \dot{m}_{ij} mass flow rate, kg/s; ρ_{ij} density, kg/m³; $A_{coil} = \pi \cdot \left(\frac{d_{i,coil}}{2}\right)^2$ cross-sectional area of the coil and w_{ij} velocity, m/s.

$$\mu_{ij} = \nu_{ij} \cdot \rho_{ij} \tag{52}$$

where μ_{ij} is the dynamic viscosity, Pa s, and ν_{ij} kinematic viscosity, m²/s.

By substituting Eqs. (51) and (52) to (50), a following formula is obtained:

$$X^* = \frac{\rho_{ij} \cdot d_{i,coil} \cdot w_{ij} \cdot Pr_{ij}}{\nu_{ij} \cdot \rho_{ij} \cdot \frac{M_w \cdot Cp_w}{\lambda_{ij}}} \cdot \frac{\pi \cdot d_{i,coil}}{4} \cdot \Delta T_{ij}^* \cdot \tau_0 \tag{53}$$

$$Re_{ij} = \frac{d_{i,coil} \cdot w_{ij}}{\nu_{ij}} \tag{54}$$

Consequently Eq. (53) can be presented through Eq. (55):

$$X^* = \frac{Re_{ij} \cdot Pr_{ij}}{\frac{M_w \cdot Cp_w}{\lambda_{ij}}} \cdot \frac{\pi \cdot d_{i,coil}}{4} \cdot \Delta T_{ij}^* \cdot \tau_0 \tag{55}$$

Finally, Eq. (55) takes the following form:

$$X^* = Re_{ij} \cdot Pr_{ij} \cdot \frac{\pi \cdot d_{i,coil} \cdot \lambda_{ij}}{4 \cdot M_{11} \cdot Cp_{11}} \cdot (T_i^* - T_j^*) \cdot \tau_0 \tag{56}$$

Derivation of E^* present in Eq. (36):

$$E^* = -T_0^* \cdot \tau_0 \tag{57}$$

$$E^* = \frac{K_{\text{hst}} \cdot A_{\text{hst}} \cdot \frac{\mu_{11}}{\lambda_{11}}}{M_{11} \cdot \text{Pr}_{11}} \cdot (T_{11}^* - T_0^*) \cdot \tau_0 \quad (58)$$

Overall heat transfer coefficient of the HST (water in the HST–HST wall air outside the HST):

$$K_{\text{hst}} = \frac{1}{R_{\text{hst}}} \quad (59)$$

Overall thermal resistance of the HST (water in the HST–HST wall air outside the HST):

$$R_{\text{hst}} = \frac{1}{\alpha_{\text{air}}} + \frac{\ln\left(\frac{D_{\text{ext}}}{D_{\text{int}}}\right)}{2 \cdot \pi \cdot \lambda_{\text{hst}}} + \frac{1}{\alpha_{11}} \quad (60)$$

Nusselt number calculated for the water in the HST:

$$\text{Nu}_{11} = \alpha_{11} \cdot \frac{L_{\text{hst}}}{\lambda_{11}} \quad (61)$$

Nusselt number calculated for the air outside the HST:

$$\text{Nu}_{\text{air}} = \alpha_{\text{air}} \cdot \frac{L_{\text{hst}}}{\lambda_{\text{air}}} \quad (62)$$

$$R_{\text{hst}} = \frac{1 \cdot \frac{L_{\text{hst}}}{\lambda_{\text{air}}}}{\alpha_{\text{air}} \cdot \frac{L_{\text{hst}}}{\lambda_{\text{air}}}} + \frac{\ln\left(\frac{D_{\text{ext}}}{D_{\text{int}}}\right)}{2 \cdot \pi \cdot \lambda_{\text{hst}}} + \frac{1 \cdot \frac{L_{\text{hst}}}{\lambda_{11}}}{\alpha_{11} \cdot \frac{L_{\text{hst}}}{\lambda_{11}}} - \frac{b \pm \sqrt{b^2 - 4ac}}{2a} \quad (63)$$

$$R_{\text{hst}} = \frac{1 \cdot \frac{L_{\text{hst}}}{\lambda_{11}}}{\text{Nu}_{11}} + \frac{\ln\left(\frac{D_{\text{ext}}}{D_{\text{int}}}\right)}{2 \cdot \pi \cdot \lambda_{\text{hst}}} + \frac{1 \cdot \frac{L_{\text{hst}}}{\lambda_{\text{air}}}}{\text{Nu}_{\text{air}}} \quad (64)$$

After substituting Eqs. (58)–(64) a final version defining E^* is obtained:

$$E^* = \frac{\left(\frac{L_{\text{hst}}}{\lambda_{11}} + \frac{\ln\left(\frac{D_{\text{ext}}}{D_{\text{int}}}\right)}{2 \cdot \pi \cdot \lambda_{\text{hst}}} + \frac{L_{\text{hst}}}{\text{Nu}_{\text{air}}}\right)^{-1} \cdot A_{\text{hst}} \cdot \frac{\mu_{11}}{\lambda_{11}}}{M_{11} \cdot \text{Pr}_{11}} \cdot (T_{11}^* - T_0^*) \cdot \tau_0 \quad (65)$$

Acknowledgements The work was partially financed by the National Centre for Research and Development (NCBR) in Poland. The grant number is as follows: POIR.01.01.01-00-1519/19. The work was also partially financed from the statutory funds of the Institute of Fluid-Flow Machinery of PAS.

Author contributions OD was responsible for conceptualisation, methodology, software (Mathcad and Python), validation, visualisation, writing the original draft, writing, reviewing and editing, investigation, and supervision. WW contributed to software (MATLAB/Simulink, LabVIEW).

Declarations

Conflict of interest The authors declare that they have no known competing financial interests or personal relationships that could have appeared to influence the work reported in this paper.

Open Access This article is licensed under a Creative Commons Attribution 4.0 International License, which permits use, sharing, adaptation, distribution and reproduction in any medium or format, as long as you give appropriate credit to the original author(s) and the source, provide a link to the Creative Commons licence, and indicate if changes were made. The images or other third party material in this article are included in the article's Creative Commons licence, unless indicated otherwise in a credit line to the material. If material is not included in the article's Creative Commons licence and your intended use is not permitted by statutory regulation or exceeds the permitted use, you will need to obtain permission directly from the copyright holder. To view a copy of this licence, visit <http://creativecommons.org/licenses/by/4.0/>.

References

- Dolna, O.: Operation of a ground thermal energy storage supplied by different sources in a low-temperature district heating network. *Renew. Energy* **180**, 586–604 (2021)
- Chang, Z., Li, X., Falcoz, Q., Wang, Z., Neveu, P., Fasquelle, T.: Approximate analytical characterization and multi-parametric optimization design of single-tank thermozone heat storage system. *Appl. Therm. Eng.* **181**, 116010 (2020)
- Xu, C., Liu, M., Jiao, S., Tang, H., Yan, J.: Experimental study and analytical modeling on the thermozone hot water storage tank with radial plate-type diffuser. *Int. J. Heat Mass Transf.* **186**, 122478 (2022)
- Zachár, A.: Analytical solution for convection dominant heat transport induced by buoyant jet entrainment inside hot fluid storage tanks. *Sol. Energy* **195**, 239–248 (2020)
- Castell, A., Medrano, M., Sole, C., Cabeza, L.F.: Dimensionless numbers used to characterize stratification in water tanks for discharging at low flow rates. *Renew. Energy* **35**(10), 2192–2199 (2010)
- Li, A., Cao, F., Zhang, W., Shi, B., Li, H.: Effects of different thermal storage tank structures on temperature stratification and thermal efficiency during charging. *Sol. Energy* **173**, 882–892 (2018)
- Oosthuizen, P.H., Naylor, D.: *An Introduction to Convective Heat Transfer Analysis*. McGraw-Hill Science, Engineering & Mathematics Press, New York (1999)
- Smusz, R., Wilk, J.: Dimensionless numbers in the coil-type heat exchanger characteristics. *Sci. Noteb. Rzeszow Univ. Technol. Mech.* **91**, 67–78 (2019)
- Karwacki, J.: Cooling system with PCM storage for an office building: experimental investigation aided by a model of the office thermal dynamics. *Materials* **14**, 1356 (2021)
- Nchelatebe Nkwetta, D., Vouillamoz, P.E., Haghghat, F., El-Mankibi, M., Moreau, A., Daoud, A.: Impact of phase change materials types and positioning on hot water tank thermal performance: using measured water demand profile. *Appl. Therm. Eng.* **67**, 460–468 (2014)
- Wang, Z., Zhang, H., Dou, B., Zhang, G., Wu, W., Zhou, L.: An experimental study for the enhancement of stratification in heat-storage tank by equalizer and PCM module. *J. Energy Storage* **27**, 101010 (2020)



12. Ökten, K., Kurşun, B., Toksöz, A., Kara, M.: Analysis of coiled tube waste heat storage tank under water injection. *J. Energy Storage* **26**, 100979 (2019)
13. Chandra, Y.P., Matuska, T.: Numerical prediction of the stratification performance in domestic hot water storage tanks. *Renew. Energy* **154**, 1165–1179 (2020)
14. Han, Y.M., Wang, R.Z., Dai, Y.J.: Thermal stratification within the water tank. *Renew. Sustain. Energy Rev.* **13**(5), 1014–1026 (2009)
15. Castro Gerhardt, F.L., de Vasconcelos Salvo, R., deMarchi Neto, I., Sene de Lima, R., da Silva, R.C.: Computational modelling of a thermal energy storage tank coupled to a water-cooled household refrigerator. *J. Energy Storage* **41**, 102961 (2021)
16. Koçak, B., Fernandez, A.I., Paksoy, H.: Review on sensible thermal energy storage for industrial solar applications and sustainability aspects. *Sol. Energy* **209**, 135–169 (2020)
17. Hahne, E., Chen, Y.: Numerical study of flow and heat transfer characteristics in hot-water stores. *Sol. Energy* **64**, 9–18 (1998)
18. Al-Najem, N.M., Al-Marafie, A., Ezuddin, K.Y.: Analytical and experimental investigation of thermal stratification in storage tanks. *Int. J. Energy Res.* **17**, 77–88 (1993)
19. Ismail, K.A.R., Leal, J.F.B., Zanardi, M.A.: Models of liquid storage tanks. *Int. J. Energy Res.* **22**, 805–815 (1997)
20. Lavan, Z., Thompson, J.: Experimental study of thermally stratified hot storage tanks. *Sol. Energy* **19**(5), 519–524 (1977)
21. Zurigat, Y.H., Ghajar, A.J., Dincer, I.: Heat transfer and stratification in sensible heat storage, chapter 6. In: *Thermal Energy Storage*. Wiley (2002)
22. Shah, L.J., Andersen, E., Furbo, S.: Theoretical and experimental investigations of inlet stratifiers for solar energy storagetanks. *Appl. Therm. Eng.* **25**, 2086–2099 (2005)
23. Fertahi, S.E.-D., Jamil, A., Benbassou, A.: Review on solar thermal stratified storage tanks (STSST): insight on stratification studies and efficiency indicators. *Sol. Energy* **176**, 126–145 (2018)
24. Kurşun, B.: Thermal stratification enhancement in cylindrical and rectangular hot water tanks with truncated cone and pyramid shaped insulation geometry. *Sol. Energy* **169**, 512–525 (2018)
25. Bohdal, T., Charun, H., Czapp, M.: *Compressor and Vapour Type Cooling Devices* (textbook in Polish). Scientific and Technical Publishing House, Warsaw (2003)
26. Borgnakke, C., Sonntag, R.E.: *Fundamentals of Thermodynamics*. Wiley, Hoboken (2013)
27. <https://docplayer.net/198161539-Arctic-series-heat-pumps-energy-efficient-solutions-for-your-home.html>

Publisher's Note Springer Nature remains neutral with regard to jurisdictional claims in published maps and institutional affiliations.





Investigation on the cost-effective optimal dimensions of a solar chimney with the Bees Algorithm

Recep Emre Unal¹ · Muhammed Huseyin Guzel¹ · Muhammed Arif Sen² · Faruk Kose² · Mete Kalyoncu²

Received: 3 June 2022 / Accepted: 2 September 2022 / Published online: 20 September 2022
© The Author(s), under exclusive licence to Islamic Azad University 2022

Abstract

Solar chimney systems which consist of three main parts (collector, chimney, turbine) are one of the main thermal methods that produce electricity using solar energy. In a solar chimney, the high-power generation that can be obtained by increasing the design dimensions can also cause ineffective high investment costs. In this study, differing from the traditional design approach, a heuristic optimization method based on the Bees Algorithm is present to obtain the optimum design parameters (the chimney and collector dimensions) that are provided the more effective solutions. It is made for 3 configurations in order to prove the accuracy of the optimization study using different algorithm parameters. By using the obtained mathematical equations and the defined non-currency investment cost unit for a traditional solar chimney, the optimum design parameters that can provide more power output with acceptable costs are investigated. Two main objectives are taken into consideration namely maximizing efficiency of solar chimney system and minimizing investment cost. In the optimization process, within the ranges determined for the decision variables, the maximum and minimum dimensions are determined as 1293.05–1330.47 m for the collector diameter, 94–99 m for the chimney diameter and 783–792 m for the chimney height. The obtained results showed that this open to develop approach proposed within the scope of the study can be useful in the optimal design of solar chimney systems.

Keywords Optimization · Renewable energy · Solar chimney · Solar energy · The Bees Algorithm

List of symbols

η	Efficiency
\dot{Q}	Heat energy (J/s)
A	Cross-sectional area (m ²)
I	Solar radiation (W/m ²)
\dot{m}	Mass flow rate (kg/s)
c_p	Specific heat (J/kg K)
ΔT	Temperature increase in the collector (K)
ρ	Density (kg/m ³)
V	Velocity (m/s)
H	Height (m)
T	Temperature (K)
P	Power (W)
D	Diameter (m)
p	Percentage (%)

J	Objective function
w	Weighted gain constants

Subscripts

c	Collector
ch	Chimney
t	Turbine
e	Electrical
m	Mechanical
g	Generator
1	Inlet of collector
2	Inlet of chimney
cu	Currency unit

Abbreviations

SCS	Solar chimney system
TGP	Turbine generator part
GA	Genetic algorithm
PSO	Particle swarm optimization
IC	Investment cost
BA	The Bees Algorithm

✉ Recep Emre Unal
reunal@ktun.edu.tr

¹ Vocational School of Technical Sciences, Konya Technical University, Konya, Turkey

² Faculty of Engineering and Natural Sciences, Konya Technical University, Konya, Turkey



Introduction

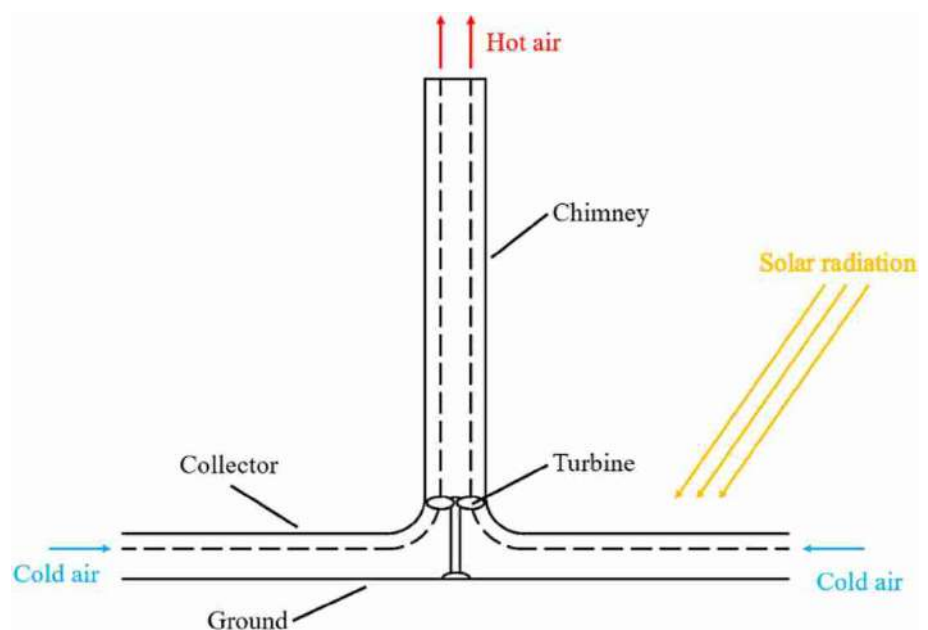
In the last century, there has been a dramatic increase in energy demand and this energy need are been met from various sources [1]. The determinant supply of energy is fossil fuels such as coal, oil and natural gas. Accordingly, the demand for renewable energy sources emerged and solar energy are been seen as an important source that can meet this [2]. The interest in solar chimney systems (SCSs) is started to increase again due to environmental concerns caused by greenhouse gas emissions from fossil fuels in the world [3]. Considering the current energy problems, SCS can take its place in the sector as an alternative solution as a clean renewable energy source, especially in barren lands. SCSs have significant advantages over other systems that convert solar energy into electrical energy, such as: it can use both direct and diffuse solar radiation in the collector, the ground can store heat, it is reliable due to the low number of rotating parts, the cooling water is not required for its operation, reachable materials and known technologies are used in its construction, and it can be applied without expensive technological efforts [4]. As seen in Fig. 1, a traditional SCS consists of three main parts: collector, chimney and Turbine-Generator Part (TGP). The kinetic energy of the heated air is converted into mechanical energy in the turbine and electrical energy in the generator [5]. The amount of electrical power obtained depends on the design parameters of SCSs.

Toghraie et al. numerically examined the effects of geometric properties on the SCS performance and found that its efficiency is directly proportional to the increase in the

collector diameter and the chimney height and inversely proportional to the increase in the collector height [6]. Khalil et al. used two different collector surfaces, namely the glass surface collector and the PV panel surface collector. They determined that the system with the PV panel surface collector is lower thermal energy and higher power output [7]. Guo et al. stated that the research and development of new materials and technologies related to SCSs will play an important role in preventing environmental problems [8]. Onyeka et al. conducted a feasibility study for the installation of a SCS and stated that 24.840 tons of CO₂ released to the atmosphere in a year could be avoided when an equivalent SCS is used instead of any system with a 30 MW electricity generation [9].

Tian et al. proposed a hybrid model for nighttime energy storage and used deer hunting algorithm, genetic algorithm (GA) and particle swarm optimization (PSO) algorithms for optimization of SCSs [10]. Muhammed et al. used computational fluid dynamics to model the relationship between heat and convection in the chimney and collector regions from SCS parts and performed an optimization study to examine the system when the design parameters of chimney height and diameter, collector height and diameter are changed [11]. Asayesh et al. used the area under the collector as a desalination pond and determined the benefit that could be obtained by applying the PSO algorithm [12]. Dehghani et al. applied a multi-objective optimization method, whose objective functions are the power output of the system and the capital cost, to determine the optimum design parameters of an SCS [13]. In order to obtain fresh water from seawater by provide the best ratio between the power output of system and freshwater production, Azad et al. are optimized the

Fig. 1 Schematic representation of a traditional SCS



collector height and diameter, chimney height and diameter and curvature of the chimney outer wall of SCS [14]. The reinforced concrete chimney, floating chimney and collector are considered by Ali as a design parameter for an SCS and a comparison between the actual payback time and the optimized payback time for 12 different SCSs is presented. In addition, sensitivity analysis is performed to evaluate the effects of operating cost, solar radiation and electricity price on payback periods [15]. Abdeen et al. are aimed to optimize the system design in order to maximize the air velocity transferred indoors by natural convection [16].

There is very limited study to use a heuristic algorithm for the optimization of solar chimney dimensions in literature. The novelty and significance of this study is the determination of optimum SCS dimensions using the Bee Algorithm. The scope of this paper is to present a way to find the optimum dimensions of the solar chimney, minimum investment cost and maximum efficiency of solar chimney. So, the Bees Algorithm-based optimization study is carried out in order to obtain the most cost-effective geometric dimensions of the chimney and collector to provide an optimal solution between the investment cost and the efficiency of a SCS. In “General methodology and experimental setup of the SCS” section, after the introduction, the experimental studies of SCS are given. In “The mathematical modeling of system” section, the SCS is modeled mathematically and in “The economic modeling of investment cost” section economically. “The Bees Algorithm optimization” section describes the optimization with the Bees Algorithm for the system. In “Results and discussion” section, optimization and

mathematical-economic modeling calculation results and discussions are provided. End of the paper, in “Conclusion” section, conclusions are given.

General methodology and experimental setup of the SCS

Numerous laboratory-scale and modeling studies related to SCS have been examined in the literature. The largest prototype among these systems is constructed in Manzanares, Spain. This prototype, which can generate 50 kW of electrical power, is the first large-scale pilot plant in the field of SCSs. The chimney height of this system is 194.6 m, the chimney diameter is 10.16 m and the collector diameter is 244 m. In some of the other experimental studies, Ketlogetswe et al. built a solar chimney prototype with a chimney height of 22 m and a collector diameter of 15 m in Botswana, Africa [17]. Also, Ucgul and Koyun built a prototype with a chimney height of 15 m, a chimney diameter of 1.2 m and a collector diameter of 16 m in Isparta, Turkey [18]. In Fig. 2a, the general view of the Manzanares prototype is given and Fig. 2b shows the experimental setup that by the authors constructed in our previous work [19]. In the experiments carried out in Konya Technical University, the temperature, radiation and air velocity values are examined with the measuring devices placed in the collector and chimney. Although the first prototype and the experimental setup in by the authors' previous work reach significantly experimental findings, it presents results that are dependent on



Fig. 2 a General view of the Manzanares prototype, b general and schematic view of the experimental setup

the design parameters. Therefore, it is required to evaluate SCSs of different sizes theoretically and to determine the optimum dimensions.

The mathematical modeling of system

In order for the SCS to be applied economically, the optimum design parameters of each part must be determined. The main design parameters of system for mathematical modeling are shown in Fig. 3. Some assumptions have been made in the calculation of the airflow and energy conversions that occur between the collector inlet and the chimney outlet due to the effect of solar radiation [20]:

- Although the heat transfer from the outside to the collector is taken into account, the heat transfer between the ground and the air inside the collector is neglected.
- It is assumed that heat storage in the ground is ignored.
- Although the solar radiation varies with time along to a day, the constant value is assumed as an average of 800 W/m^2 for steady-state conditions.
- The Mach number is less than 0.3, since the air velocity in the system is much lower than the speed of sound, and therefore, the flow is assumed to be incompressible.
- Although the specific heat at constant pressure and air density varies slightly depending on temperature and height, they are considered constant as $c_p = 1006 \text{ J/kgK}$ and $\rho = 1.16 \text{ kg/m}^3$.
- The ambient temperature is taken as $T_1 = 25 \text{ }^\circ\text{C}$.
- The turbine efficiency is $\eta_t = 0.8$, and the generator efficiency is $\eta_g = 0.8$.

The efficiency of the collector is found by the ratio of the amount of energy transferred to the air at the outlet of the

collector to the amount of energy entering the system with the effect of solar radiation [21]. In order to obtain the efficiency in Eq. 1, heat energy, mass flow rate and velocity at the inlet of chimney should be calculated, respectively, from Eqs. 2, 3 and 4. Accordingly, the efficiency of the collector (η_c) is obtained as in Eq. 5.

$$\eta_c = \frac{\dot{Q}_c}{A_c \cdot I} \quad (1)$$

$$\dot{Q}_c = \dot{m}_2 \cdot c_p \cdot \Delta T_1 \quad (2)$$

$$\dot{m}_2 = \rho \cdot V_2 \cdot A_{ch} \quad (3)$$

$$V_2 = \sqrt{2 \cdot g \cdot H_{ch} \cdot \frac{\Delta T_2}{T_2}} \quad (4)$$

$$\eta_c = \frac{\rho \cdot V_2 \cdot A_{ch} \cdot c_p \cdot \Delta T_1}{A_c \cdot I} \quad (5)$$

The air heated by solar radiation in the collector is directed to the inlet of the chimney and leaves the SCS through the outlet of the chimney after passing through the turbine [22]. During this process, the heated air turns into mechanical energy and the hot air begins to rise due to the density difference of the air. Thanks to the pressure drop in the turbine, power output that will provide electricity production in the generator is obtained. The chimney height and the chimney efficiency are directly proportional to each other. However, the efficiency of the chimney is very low. Therefore, the overall efficiency of the SCS will be significantly reduced. The efficiency of the chimney (η_{ch}) is given in Eq. 6–8. To calculate the efficiency of the chimney in Eq. 6, firstly the temperature difference between the inlet of the chimney and the outlet of the chimney is specified in Eq. 8 so that $0.5 \text{ }^\circ\text{C}$ drops for every 100 m height. Then, the air temperature at the inlet of the chimney is obtained by Eq. 7.

$$\eta_{ch} = \frac{\rho \cdot H_{ch}}{c_p \cdot T_2} \quad (6)$$

$$T_2 = T_1 + \Delta T_2 \quad (7)$$

$$\Delta T_2 = H_{ch} \cdot 0.005 \quad (8)$$

There is an axially placed turbine at the inlet of the chimney. The task of the turbine is to convert the kinetic energy of the air into mechanical energy. The efficiency of the turbine (η_t) and the electrical power (P_e) are given in the following equations. The efficiency of the turbine is

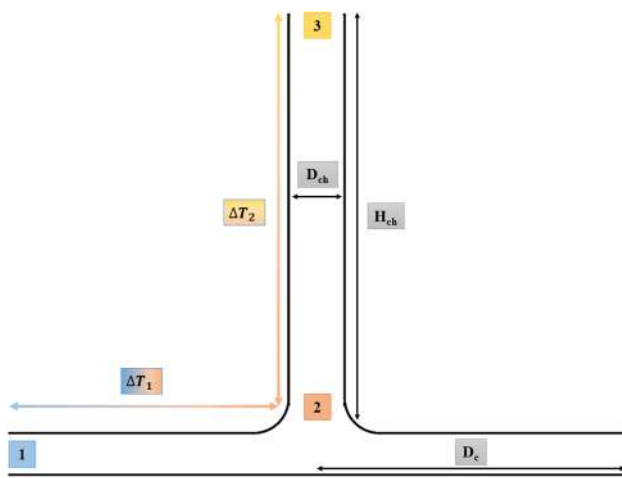


Fig. 3 The main design parameters of system



calculated as stated in Eq. 9, using the previously obtained efficiency of the chimney and the air velocity at the chimney inlet, together with the temperature difference between the inlet and outlet of the collector. Electrical power is found by multiplying the solar energy coming to the collector, the efficiency of SCS in Eq. 11 and the mechanical efficiency in Eq. 12, which states the total efficiency in TGP. Accordingly, electrical power is obtained as in Eq. 13.

$$\eta_t = 1 - \frac{V_2^2}{2 \cdot c_p \cdot \Delta T_1 \cdot \eta_{ch}} \quad (9)$$

$$P_e = \dot{Q} \cdot \eta_{SCS} \cdot \eta_m \quad (10)$$

$$\eta_{SCS} = \eta_c \cdot \eta_{ch} \quad (11)$$

$$\eta_m = \eta_t \cdot \eta_g \quad (12)$$

$$P_e = A_c \cdot I \cdot \eta_c \cdot \eta_{ch} \cdot \eta_t \cdot \eta_g \quad (13)$$

The economic modeling of investment cost

To investigate optimum configurations, the power output of system should be considered with the cost of each of the design parameters altogether. Therefore, by defining a non-currency unit, the investment cost of the system is parametrically included in the optimization algorithm. It can be done by considering the cost model approach created by Pretorius et al. [23] a non-currency unit (IC_{cu}) in C is defined for the investment cost (IC) to be created for all parts used in the SCS. All capital costs of SCS are defined using this currency. Hence, the specific capital cost of the system due to the construction, which will be determined by the size of the dimensions of the SCS, is established in a unit of cost per cubic meter of the volume of the SCS, as Eq. 14.

$$IC_{cu} = 1C/m^3 \quad (14)$$

For the chimney, it has been assumed that the chimney wall thickness increases by 1 mm for every 1 m increase in the height of the chimney. Thus, IC of the chimney (IC_{ch}) is as follows:

$$IC_{ch} = \frac{\pi}{4} \left((D_{ch} + 0.001 \cdot H_{ch})^2 - D_{ch}^2 \right) \cdot H_{ch} \cdot IC_{cu} \quad (15)$$

IC of the collector (IC_c) is calculated using Eq. 16. p_c is taken as 8% in the calculation of IC per square meter of the collector. IC of TGP is approximately equal to 10% of the total IC of the collector and chimney [13]. Accordingly, IC for TGP (IC_{TGP}) can be as in Eq. 17.

$$IC_c = A_c \cdot p_c \cdot H_c \cdot IC_{cu} \quad (16)$$

$$IC_{TGP} = p_{TGP} \cdot (IC_c + IC_{ch}) \quad (17)$$

$$IC_{SCS} = IC_{ch} + IC_c + IC_{TGP} \quad (18)$$

The Bees Algorithm optimization

In SCS, the increase in the chimney height and the collector diameter is directly proportional to the power output of the system. However, SCS has downsides in terms of manufacturing difficulties and IC when it comes to very large sizes. For this reason, many optimization studies have been carried out. It is not possible to make solely dimension optimization because the increase in dimensions of design parameters also increases the power output. In order to balance this situation at an acceptable point, it is necessary to include the investment cost factor in the optimization study. In the literature, there are a limited number of studies based on GA [24] and PSO [25] on the optimization of SCS with meta-heuristic methods. The aim of this study is to contribute to the literature by using BA optimization that a different approach in determining the cost-effective design parameters for the chimney and the collector.

The most appropriate value or best solution can be found in the optimization process. It can be maximum or minimum values can be found in optimization problems, also single or multi-objective problems can also be solved [26]. In many fields, such as mechanical and civil engineering, there are various problems with multiple objectives [27]. In this study, two main objectives are taken into account, namely maximizing the efficiency and minimizing of IC. Equations 11 is used to define the efficiency (η_{SCS}) and Equations 18 is used to define the IC of SCS (IC_{SCS}) [13].

In a traditional SCS, three decision variables are contained the main dimension parameters. These are the collector diameter, the chimney height and the chimney diameter. There is no combination of decision variables values that optimizes both objectives at the same time. The following ranges (Eqs. 19–21) are used for the decision variables used for solving the optimization problem. Both experimental and theoretical studies are taken into account in determining these ranges. Although there are many experimental studies, such as in Ghalamchi et al. study D_c 3 m and H_{ch} 3 m, D_{ch} 0.25 m [28], in Ucgul and Koyun study D_c 16 m, H_{ch} 15 m, D_{ch} 1.2 m [18] at the laboratory-scale, only the Manzanares prototype is available on a large-scale. The maximum and minimum dimensions in theoretical studies, 500–8000 m [10] and 60–800 m [14] ranges for the chimney height and 5000–8500 m [29] and 200–600 m [30] intervals for the



collector diameter are similarly examined. According to, it seems that there is no limit to the dimensions solar chimney in theoretical studies. Thus, these ranges are determined by considering physical constraints such as construction, safety, operational difficulties and by reference to experimental and theoretical studies [31, 32]. In the optimization process, the decision variables change within the specified ranges.

$$750 \leq D_c \leq 2250(m) \tag{19}$$

$$200 \leq H_{ch} \leq 800(m) \tag{20}$$

$$20 \leq D_{ch} \leq 100(m) \tag{21}$$

The Bees Algorithm (BA) [33] is used to determine the best dimensions of design parameters of SCS for optimization. BA is a population-based, heuristic search algorithm that mimics the sourcing behavior of honeybees and the

sharing of information with each other [34–36]. Consisting of scout and recruit bees performing different tasks, BA is both a local and global optimization method combined with a random neighborhood search [37, 38]. Scout bees search for new sources independently without using any information, while recruit bees transmit information about the source to other bees in the hive with a movement called ‘waggle dance’ [39]. The performance of the ‘waggle dance’ proposed for local search in the BA as a heuristic method, which gives successful results in different applications, on this system has been investigated. The general flowchart of optimization with BA is shown in Fig. 4, and the basic parameters used in BA are given in Table 1. To examine and verify the performance of the proposed method, three times runs are made for the BA parameter values determined in different configurations. The objective function for this study, which is aimed to have high η and low IC, is as follows:

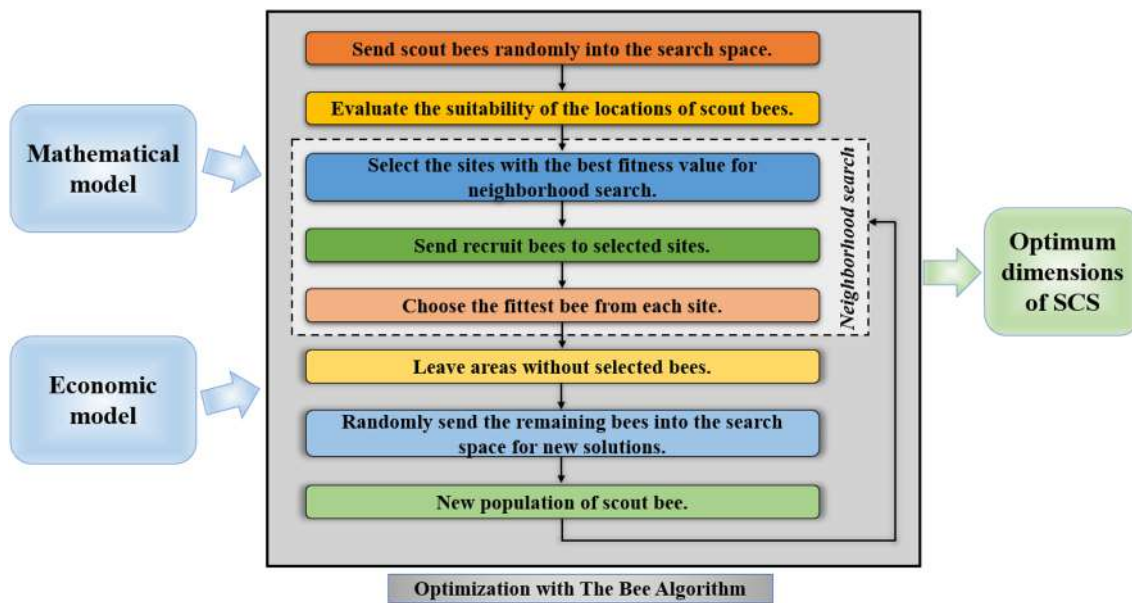


Fig. 4 General flowchart of optimization with BA

Table 1 The parameters used in BA

BA parameters	Configuration 1	Configuration 2	Configuration 3
Number of scout bees (n)	20	40	60
Number of optimal sites selected from n sites visited (m)	10	12	14
Number of elite sites in m selected sites (e)	8	10	12
Number of bees sent to the best e site (nep)	12	16	20
Number of bees sent to the remaining (m-e) site (nsp)	10	12	14
Site size (ngh)	0.01	0.005	0.001
Iteration (itr)	50	100	150

$$J = w_1 \cdot IC_{SCS} + w_2 \cdot \frac{1}{\eta_{SCS}} \tag{22}$$

The weight gains are used to ensure that each unit change in the cost and efficiency of the system affects the objective function at the same rate. In the determination of the weight gains, the average values between the investment cost and efficiency of the widely used systems of different dimensions are taken into account and the trial-and-error methods which based on the experience of the authors from their previous studies [40]. The constant gains ($w_1 = 0.017, w_2 = 12.19$) which weighted the changes in IC_{SCS} and η_{SCS} values to each other are defined based on the previous studies of authors by considering various the diameters of collector and chimney and the height of chimney values. The objective function convergence performances of BA are shown graphically in Fig. 5. The diversified iteration numbers in each configuration are determined as the stopping criteria. As can be clearly seen from the figure, BA has well-converged solutions for all configurations after a global and local search.

Results and discussion

In this section, three important design parameters for solar chimneys are analyzed. These three parameters, which are the collector diameter, chimney diameter and chimney

height, are determined by combining the efficiency of the solar chimneys with the ideal investment cost, and their optimum dimensions are determined. For this purpose, the results section is divided into two parts. Optimization results are presented in the first part. In the second part, the validation of these results is explained in detail.

The optimization results

The main scope of this study is to determine the optimum design parameters of SCS. A code specially developed with BA is used in the optimization process of determining the SCS dimensions. Optimal dimensions of SCS are found as indicated in Table 2. The purpose of the existence of 3 different configurations is to show that the results obtained are not affected by independent changes in BA parameters. For this purpose, it has been observed that the optimum dimensions of the SCS are quite compatible with each other in all 3 cases. As a result, 1293.05 m, 1323.94 m and 1330.47 m for the diameter of collector, 94.62 m, 95.39 m and 98.16 m for the diameter of chimney and 783.77 m, 791.04 m and 789.35 m for the diameter of chimney are found to be very close to each other. At the same time, these results are similar to the values of 844.52 m [30] for the chimney height, 1345 m [10] and 1384.6 m [14] for the collector diameter, and 72 m [10] for the chimney diameter, which are among the other optimization results in the literature.

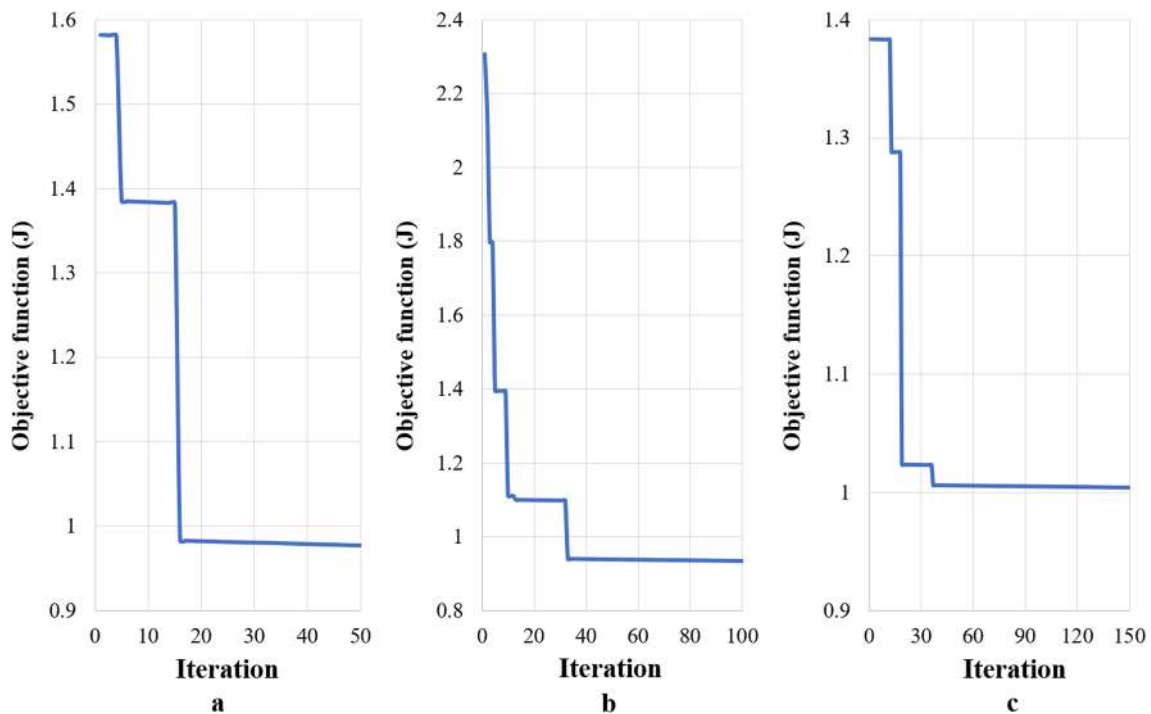


Fig. 5 Objective function convergence performances of BA a For configuration 1, b For configuration 2, c For configuration 3

In order to better understand the optimization results, Table 3 has been prepared. In this table, the calculation results of electrical power, investment cost, efficiency and objective function values for SCS with optimum geometric dimensions are given. Accordingly, the electrical power is 56.75 MW, 62.21 MW and 58.50 MW for all configurations, respectively. It is indicated that both investment cost and efficiency, which are used to obtain objective functions, and electrical power are in better agreement. In addition, the objective function values obtained according to Eq. 23 are consistent in all configurations.

The validation of obtained optimal dimensions

In this section, in order to validate the obtained optimization results numerically, if any of the design parameters of the SCS is constant, the effects of other design parameters on the efficiency and IC in various dimensions are calculated and shown in graphs. Accordingly, Eqs. 1–11 and Eqs. 14–18 are used in the calculations of efficiency and investment cost, respectively.

The variation of efficiency and investment cost at different dimensions of collector diameter, changing in the range of 750–2250 m, is given in Table 4 and Fig. 6 when the chimney height is constant at 400 m and the chimney diameter is 50 m. According to this table and figure, it is consistent with the values obtained in the optimization results

(1293.05–1330.47 m), within 1200–1400 m of the optimum dimension for the collector diameter.

The variation of efficiency and investment cost at different dimensions of chimney diameter, changing in the range of 20–100 m, is given in Table 5 and Fig. 7 when the chimney height is constant at 400 m and the collector diameter is 1500 m. According to this table and figure, it is consistent with the values obtained in the optimization results (94.62–98.16 m), within 90–100 m of the optimum dimension for the chimney diameter.

The variation of efficiency and investment cost at different dimensions of chimney height, changing in the range of 200–800 m, is given in Table 6 and Fig. 8 when the collector diameter is constant at 1500 m and the chimney diameter is 50 m. According to this table and figure, it is consistent with the values obtained in the optimization results (783.77–791.04 m), within 700–800 m of the optimum dimension for the chimney diameter.

Thanks to the equations purposed in the mathematical and economical modeling, using these tables and figures, appropriate dimensions can be suggested for the design parameters. Accordingly, it is clearly seen that the investment cost increases with the increase in the dimensions of SCS. Also, although the power output increases as collector diameter enlarges, the efficiency decreases. Finally, it can be said that the design parameter that most affects the alteration of both investment cost and efficiency is collector diameter.

Table 2 The optimal design parameters of SCS

Design parameter	Results for configuration 1	Results for configuration 2	Results for configuration 3
Diameter of collector (D_c) (m)	1293.05	1323.94	1330.47
Diameter of chimney (D_{ch}) (m)	94.62	98.16	95.39
Height of chimney (H_{ch}) (m)	783.77	791.04	789.35

Table 3 The optimization results of BA in different configurations

	Configuration 1	Configuration 2	Configuration 3
Electrical power (P_e) (MW)	56.75	62.21	58.50
Investment cost (IC) (C)	33.19	34.88	34.78
Efficiency (η_{SCS})	0.0844	0.0882	0.0822
Objective function (J)	144.99	138.80	148.89

Table 4 The efficiency and IC for different dimensions of collector diameter ($H_{ch} = 400$ m ve $D_{ch} = 50$ m)

	D_c (m)							
	800	1000	1200	1400	1600	1800	2000	2200
η_{SCS}	0.016	0.010	0.007	0.005	0.004	0.003	0.003	0.002
IC _{SCS} (C)	102,346	152,108	212,930	284,809	367,747	461,744	566,799	682,912

Bold values indicate optimum results

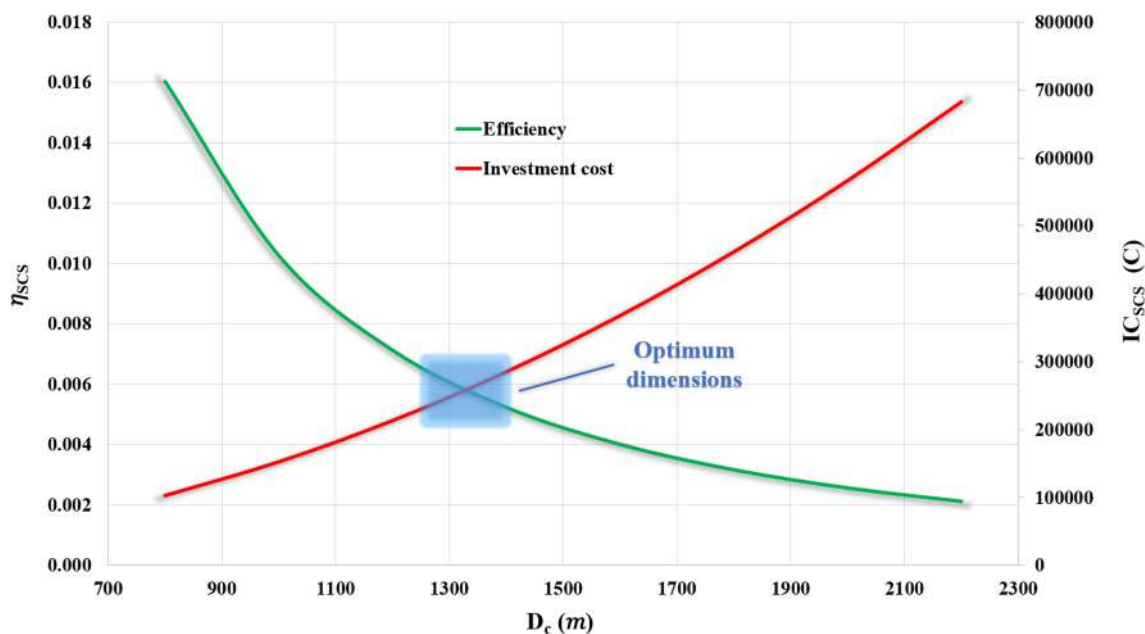


Fig. 6 The variation of IC and efficiency of SCS according to collector diameter ($H_{ch} = 400$ m ve $D_{ch} = 50$ m)

Table 5 The efficiency and IC for different dimensions of chimney diameter ($H_{ch} = 400$ m ve $D_c = 1500$ m)

	D_{ch} (m)									
	20	30	40	50	60	70	80	90	100	
η_{SCS}	0.001	0.002	0.003	0.005	0.007	0.009	0.012	0.015	0.018	
$IC_{SCS}(C)$	316,602	319,367	322,131	324,896	327,661	330,425	333,190	335,954	338,719	

Bold values indicate optimum results

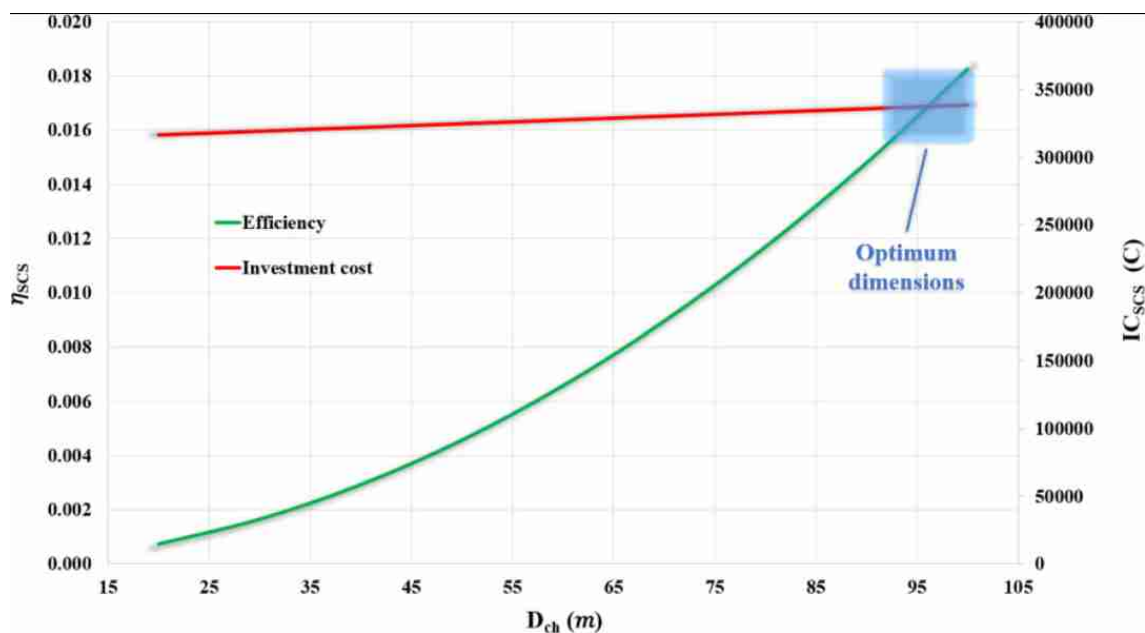


Fig. 7 The variation of IC and efficiency of SCS according to chimney diameter ($H_{ch} = 400$ m ve $D_c = 1500$ m)

Table 6 The efficiency and IC for different dimensions of chimney height ($D_c = 1500$ m ve $D_{ch} = 50$ m)

	$H_{ch}(m)$						
	200	300	400	500	600	700	800
η_{SCS}	0.001	0.003	0.005	0.007	0.010	0.014	0.018
$IC_{SCS}(C)$	314,480	318,816	324,896	332,724	342,306	353,647	366,752

Bold values indicate optimum results

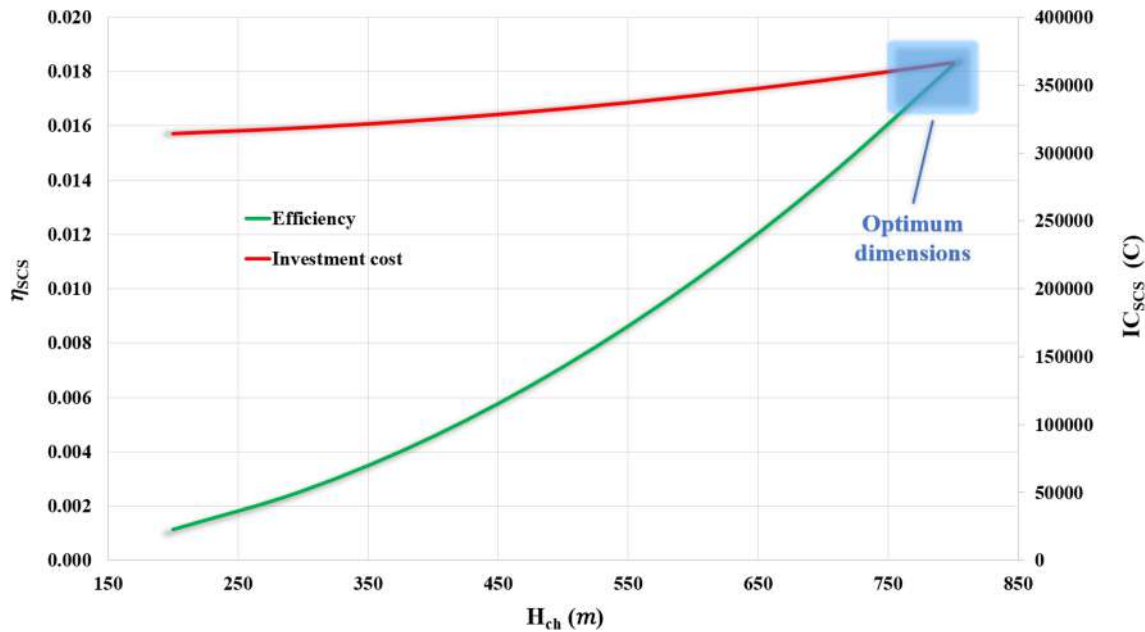


Fig. 8 The variation of IC and efficiency of SCS according to chimney height ($D_c = 1500$ m ve $D_{ch} = 50$ m)

Conclusion

In this study, the optimization is carried out for the geometric dimension and the IC for SCS. The diameter of the collector and chimney and the height of the chimney ranges are determined by using the research in the literature. Optimum dimensions are found by using BA for the design parameters. In order to determine the consistency of the optimization, three different configurations for the parameters of BA are taken and the results are obtained. The efficiency and the IC are calculated by mathematical and economic modeling. If the diameter of the chimney and collector is constant, it is seen that the efficiency increases as the height of the chimney enlarges. Similarly, when merely the diameter of the chimney is various, the efficiency is directly proportional. Optimization and mathematical-economic modeling calculation results are found to be compatible. According to this study, it is concluded that the IC should also be taken into account in determining the optimum dimensions for the collector and chimney in the manufacture of an SCS. This study can

lead to optimization studies for solar chimneys and can be developed using different algorithms.

In future studies, the results obtained here can be compared using different algorithms and optimization methods. Dimension optimization can also be performed by considering computational fluid dynamics analyzes and results to provide a reference for the construction of the SCS. The use of heuristic methods for dimension optimization of renewable energy systems, such as solar chimneys, is likely to become more common in the future.

References

1. Yuliza, E., Lizalidiawati, L., Ekawita, R.: The effect of tilt angle and orientation of solar surface on solar rooftop miniature system in Bengkulu University. *Int. J. Energy Environ. Eng.* **12**(3), 589–598 (2021)
2. Buyukzeren, R., et al., Experimental validation of performance parameters of an air source heat pump model. *Gazi Univ. J. Sci. Part C Des. Technol.* **9**(4): 739–748
3. Kaya, M.N., Aksoy, M.H., Kose, F.: Renewable energy in Turkey: potential, current status and future aspects. *Ann. Faculty Eng. Hunedoara* **15**(1), 65 (2017)



4. dos Santos Bernardes, M.A.: Solar chimney power plants—developments and advancements. *Sol. Energy* **84**(6), 978–953 (2010)
5. Guzel, M.H., et al.: The fuzzy logic-based modeling of a micro-scale sloped solar chimney power plant. *J. Mech. Sci. Technol.* **35**(3), 1301–1308 (2021)
6. Toghraie, D., et al.: Effects of geometric parameters on the performance of solar chimney power plants. *Energy* **162**, 1052–1061 (2018)
7. Ahmed, O.K., Hussein, A.S.: New design of solar chimney (case study). *Case Stud. Therm. Eng.* **11**, 105–112 (2018)
8. Guo, P., et al.: Questions and current understanding about solar chimney power plant: a review. *Energy Convers. Manage.* **182**, 21–33 (2019)
9. Okoye, C.O., Atikol, U.: A parametric study on the feasibility of solar chimney power plants in North Cyprus conditions. *Energy Convers. Manage.* **80**, 178–187 (2014)
10. Tian, M.-W., et al.: New optimal design for a hybrid solar chimney, solid oxide electrolysis and fuel cell based on improved deer hunting optimization algorithm. *J. Clean. Prod.* **249**, 119414 (2020)
11. Muhammed, H.A., Atrooshi, S.A.: Modeling solar chimney for geometry optimization. *Renew. Energy* **138**, 212–223 (2019)
12. Asayesh, M., Kasaeian, A., Ataei, A.: Optimization of a combined solar chimney for desalination and power generation. *Energy Convers. Manage.* **150**, 72–80 (2017)
13. Dehghani, S., Mohammadi, A.H.: Optimum dimension of geometric parameters of solar chimney power plants—A multi-objective optimization approach. *Sol. Energy* **105**, 603–612 (2014)
14. Azad, A., et al.: Multi-objective optimization of a solar chimney for power generation and water desalination using neural network. *Energy Convers. Manage.* **238**, 114152 (2021)
15. Ali, B.: Techno-economic optimization for the design of solar chimney power plants. *Energy Convers. Manage.* **138**, 461–473 (2017)
16. Abdeen, A., et al.: Solar chimney optimization for enhancing thermal comfort in Egypt: An experimental and numerical study. *Sol. Energy* **180**, 524–536 (2019)
17. Ketlogetswe, C., Fiszdon, J.K., Seabe, O.O.: Solar chimney power generation project—The case for Botswana. *Renew. Sustain. Energy Rev.* **12**(7), 2005–2012 (2008)
18. Ucgul, I., Koyun, A.: Experimental investigations on performance and design parameters of solar chimney. *Pamukkale Univ. J. Eng. Sci.* **16**(3), 255–264 (2010)
19. Guzel, M.H., Unal, R.E., Kose, F.: Experimental study of a micro-scale sloped solar chimney power plant. *J. Mech. Sci. Technol.* **35**(12), 5773–5779 (2021)
20. Köse, F.: Comparison of solar chimney power systems with PV and wind power systems. *Acad. Platform-J. Eng. Sci.* **6**(3), 121–129 (2018)
21. Schlaich, J.R., et al.: Design of commercial solar updraft tower systems—utilization of solar induced convective flows for power generation. *J. Sol. Energy Eng.* **127**(1), 117–124 (2005)
22. Dewangan, S.K.: Effect of collector roof cum chimney divergence and exhaust fan on solar chimney power plant performance. *Int. J. Energy Environ. Eng.*, 1–18 (2021)
23. Pretorius, J.P., Kröger, D.G.: Thermo-economic optimization of a solar chimney power plant. *J. Solar Energy Eng.* **130**(2) (2008)
24. Habibollahzade, A., et al.: Exergoeconomic assessment and multi-objective optimization of a solar chimney integrated with waste-to-energy. *Sol. Energy* **176**, 30–41 (2018)
25. Habibollahzade, A., et al.: Continuous power generation through a novel solar/geothermal chimney system: Technical/cost analyses and multi-objective particle swarm optimization. *J. Clean. Prod.* **283**, 124666 (2021)
26. Gunantara, N.: A review of multi-objective optimization: Methods and its applications. *Cogent Eng.* **5**(1), 1502242 (2018)
27. Esleman, E.A., Onal, G., Kalyoncu, M.: Optimal PID and fuzzy logic based position controller design of an overhead crane using the Bees Algorithm. *SN Appl. Sci.* **3**(10), 1–13 (2021)
28. Ghalamchi, M., et al.: An experimental study on the thermal performance of a solar chimney with different dimensional parameters. *Renew. Energy* **91**, 477–483 (2016)
29. Cottam, P., et al.: Solar chimney power plants—Dimension matching for optimum performance. *Energy Convers. Manage.* **194**, 112–123 (2019)
30. Azimlu, F., et al.: Designing solar chimney power plant using meta-modeling, multi-objective optimization, and innovization. In: *International Conference on Evolutionary Multi-Criterion Optimization*. Springer (2019)
31. Sangi, R.: Performance evaluation of solar chimney power plants in Iran. *Renew. Sustain. Energy Rev.* **16**(1), 704–710 (2012)
32. Gholamalazadeh, E., Mansouri, S.: A comprehensive approach to design and improve a solar chimney power plant: a special case—Kerman project. *Appl. Energy* **102**, 975–982 (2013)
33. Pham, D.T., et al.: The bees algorithm—a novel tool for complex optimisation problems. In: *Intelligent Production Machines and Systems*. Elsevier, pp. 454–459 (2006)
34. Onder, A., et al.: Heuristic optimization of impeller sidewall gaps-based on the bees algorithm for a centrifugal blood pump by CFD. *Int. J. Artif. Organs* **44**(10), 765–772 (2021)
35. Pham, D., et al.: Application of the bees algorithm to the training of radial basis function networks for control chart pattern recognition. In: *Proceedings of 5th CIRP International Seminar on Intelligent Computation in Manufacturing Engineering (CIRP ICME'06)*, Ischia, Italy (2006)
36. Zeybek, S., et al.: An improved bees algorithm for training deep recurrent networks for sentiment classification. *Symmetry* **13**(8), 1347 (2021)
37. Bilgic, H.H., et al.: Meta-heuristic tuning of the LQR weighting matrices using various objective functions on an experimental flexible arm under the effects of disturbance. *Arab. J. Sci. Eng.* **46**(8), 7323–7336 (2021)
38. ArifSen, M., Tinkir, M., Kalyoncu, M.: Optimisation of a PID controller for a two-floor structure under earthquake excitation based on the bees algorithm. *J. Low Freq. Noise Vib. Active Control* **37**(1), 107–127 (2018)
39. Sen, M.A., Bilgic, H.H., Kalyoncu, M.: Determination of LQR controller parameters for stabilization and position control of double inverted pendulum using the bees algorithm. *Mühendis ve Makina* **57**(679), 53–62 (2016)
40. Fahmy, A., Kalyoncu, M., Castellani, M.: Automatic design of control systems for robot manipulators using the bees algorithm. *Proc. Inst. Mech. Eng. Part I: J. Syst. Control Eng.* **226**(4), 497–508 (2012)

Publisher's Note Springer Nature remains neutral with regard to jurisdictional claims in published maps and institutional affiliations.

Springer Nature or its licensor holds exclusive rights to this article under a publishing agreement with the author(s) or other rightsholder(s); author self-archiving of the accepted manuscript version of this article is solely governed by the terms of such publishing agreement and applicable law.





Optimization of balcony's glazed enclosure with spectrally selective coatings regarding heating demand and thermal comfort in a multifamily building

Magdalena Grudzińska¹

Received: 12 April 2022 / Accepted: 22 May 2022 / Published online: 22 June 2022
© The Author(s), under exclusive licence to Islamic Azad University 2022

Abstract

Sunspaces in the form of enclosed balconies are a frequently used solution to reduce heat loss from adjacent rooms, protect against noise or create additional usable space. Deterioration of thermal comfort in summer caused by impeded heat outflow from living spaces may be their disadvantage. Internal conditions in the greenhouse and adjacent rooms can be influenced by using spectrally selective coatings on the balcony enclosure glazing. The subject of the research was the analysis of the effects caused by such modifications throughout the year (distinguishing between the heating and cooling season). Computer simulations allowed choosing the optimal solution from the point of view of three scenarios, namely: minimisation of heat demand, the number of overheating hours, and energy demand determined based on various climate data. Glazing with a high solar transmittance coating in a thermally insulated balcony's casing, allowing for a good buffer effect of the enclosure, proved to be the optimal solution.

Keywords Passive solar systems · Glazed balconies · Spectrally selective coatings · Energy demand · Thermal comfort

Introduction

Passive methods of solar energy acquisition enable the conversion of solar radiation into thermal energy [1, 2]. This reduces the demand for heat in buildings and shortens the heating season, reducing the consumption of energy produced from traditional non-renewable sources. Passive systems include, among others, greenhouse systems implemented as winter gardens (mainly in single-family buildings) or glazed balconies (the solution prevailing in multifamily buildings). They are of particular interest not only because of the possibility to obtain renewable energy but also due to their high architectural attractiveness, additional usable area, and noise protection in urban areas [3].

Many studies, based both on in situ studies and simulation analyses, confirmed the possibility of reducing energy demand owing to the unheated, glazed space adjacent to

the living spaces [3–6]. The effectiveness of such solutions may vary considerably, depending on the location, type of buildings, and greenhouse enclosure, as well as the manner of conducting analyses. Simulations of a residential building in Belgrade presented the savings related to the use of greenhouses amounting to 2% for the entire building (which was assessed as an effective strategy to increase energy efficiency) [7]. The glazing of the balcony in an apartment in a multifamily building located in Umbria (Italy) allowed reducing the energy demand during the heating season by about 20% [8]. The numerical modelling results of a multifamily building in Korea showed that the heating energy demand was higher by nearly 40% in an apartment without solar space, compared to a version with a separate loggia [9]. The reduction of energy needs was much more considerable in the rooms directly adjacent to the glazed buffer space. The simulations carried out on the example of an apartment in Bucharest showed the energy savings of 77% [10].

As far as the single-family buildings are concerned, energy savings there may be lower than in multifamily buildings due to the larger area of the heated residential zone in relation to the area of the greenhouse. For example, the computer modelling results of a single-family building in China confirmed such dependencies, showing that the reduction

✉ Magdalena Grudzińska
m.grudzinska@pollub.pl

¹ Department of Construction, Faculty of Civil Engineering and Architecture, Lublin University of Technology, Nadbystrzycka St. 40, 20-618 Lublin, Poland



of demand for energy owing to enclosed loggia amounted to about 12% [11].

Simulation research on greenhouse systems enabled not only to confirm their energy efficiency but also to assess the impact of various factors on the effectiveness of solar space as a collector of solar radiation. Numerical analyses were used, i.e. to compare material solutions or to analyse the effects of climatic conditions on energy gains. The findings proved that solar radiation conversion efficiency of sunspaces was influenced by [3, 12–14]:

- Thermal insulation and tightness of balcony enclosures,
- Optical properties of the glazing and its area,
- The radiation absorption capacity of an opaque greenhouse enclosure,
- Integration of the glazed space into the ventilation system of a building.

Numerous publications have dealt with the relationship between the surface area, type of glazing, shape of the greenhouse enclosure, and the energy demand in adjacent spaces. Based on the analyses conducted for the climate of Jordan, it was found that increasing the proportion of glazing in the total enclosure area and using double glazing had a positive effect on reducing the heating demand during the heating season, but caused overheating problems in summer [13]. Similar conclusions were presented in studies, according to which increasing the glazing area of the greenhouse resulted in a decrease in the residential heat demand (though to a small extent) and a significant increase in the cooling needs [14, 15]. A simple linear relationship between the quantities was not found.

Computer simulations confirmed that in exemplary multifamily buildings, the use of glazing with better thermal insulation in the enclosure of balconies allowed more efficient use of the available solar radiation [15, 16]. Another paper presented the greenhouse enclosure solutions differing in the number of panes and the type of gases filling the gap between them [17]. Single and double glazing (the latter filled with air, argon, or krypton) were analysed to determine the energy demand of a building with a greenhouse addition, located in a rural area in a severely cold region of China. The results showed that double glazing was more effective in reducing the heat demand of the building, and also helped to determine the optimum glazing cavity widths for each gas.

Adapting a building to passive solar energy acquisition during the heating season can have different effects on the indoor conditions in the summer. In some publications, via simulations, it was found that the enclosed greenhouse reduced the cooling demand of adjacent rooms through their additional shading [8, 9, 18]. However, in most reported cases, it has been observed that during higher radiation supply, passive systems may result in the need for more intensive cooling

due to overheating and periodic thermal discomfort [19–22]. These phenomena may be intensified during the heat waves resulting from anthropogenic climate change and increased air temperature due to the greenhouse effect [23]. Therefore, it is important that the analysis of the effects of greenhouses is not limited to the modification of the energy demand in the heating season, but is carried out concerning thermal comfort and elimination of the need for cooling during summer.

Previous research has confirmed the possibility of shaping greenhouse energy efficiency and thermal conditions in adjacent spaces through structural and material solutions of the sunspace enclosure [13, 15–17]. However, there is a lack of broader analyses in the related literature on the effects of optical properties of greenhouse glazing on the conditions in the living zone. Modification of solar transmittance and reflectance in specific spectral ranges can be achieved by using spectrally selective coatings, applied during glass manufacturing or afterward. These are designed to increase reflectivity in the near and far infrared while maintaining the highest possible transmittance in the visible range [24]. These solutions offer the possibility of reducing solar gains and protecting rooms against overheating. Their effective use in direct gain systems indicates the potential of internal climate control also in combination with passive greenhouse systems.

The present article aimed to partially fill the gap in the current state of knowledge by analysing the conditions in the apartment adjacent to the glazed balcony, located in the warm-summer humid continental climate conditions. The research was carried out with the use of dynamic simulation analyses performed in the BSim software [25]. The scope of work included analysis of the energy demand for heating and cooling in the apartment for various types of glazing and balcony enclosures and analysis of thermal comfort during heat waves in the summer based on the concept of adaptive comfort.

The main objectives of the study were to find the relationship between the optical and thermal properties of the balcony casing and the thermal conditions in the adjacent living zone together with the energy demand throughout the year. The analysed glazing types varied with thermal transmittance, reflectance, and insulating properties, which influenced internal temperature in the balcony area and, indirectly, heat inflow and outflow from the apartment. These allowed the selection of optimal casing solutions from the point of view of reducing the heating and cooling demand as well as eliminating the need for mechanical cooling.

Research methodology

As an example, the flat with a net usable area of 75 m² was analysed, with an external balcony of approx. 5 m² (Fig. 1). The flat was located in the middle part of a floor, having two



external and two internal walls dividing it from the neighbouring apartments of the same function.

The thermal insulation of the external partitions of the apartment complied with the requirements in force in Poland since 2014 (external walls: $U \leq 0.25 \text{ W}/(\text{m}^2 \cdot \text{K})$, roofs: $U \leq 0.20 \text{ W}/(\text{m}^2 \cdot \text{K})$, windows: $U \leq 1.30 \text{ W}/(\text{m}^2 \cdot \text{K})$). In the flat there were defined three thermal zones, differing by internal conditions and the air exchange with the surrounding environment. The residential zone (zones 2 and 3) was air-conditioned, and the assumed heating and cooling settings are $20 \text{ }^\circ\text{C}$ and $26 \text{ }^\circ\text{C}$. The possibility of ventilating the rooms and shading the windows was assumed in summer, if the internal temperature exceeded $24 \text{ }^\circ\text{C}$ and $25 \text{ }^\circ\text{C}$, respectively. Solar transmittance of the shadings was 50%. If these methods of removing excess heat did not yield the expected results and the internal temperature exceeded $26 \text{ }^\circ\text{C}$, cooling was started. The ventilation of the apartment was gravitational, and it was assumed that the airflow in the rooms of zone 3 was directly from the outside. The room adjacent to the balcony (zone 2) was supplied with outdoor air preheated in the sunspace. Creating an additional thermal zone 2 allowed for a more adequate modelling of the air exchange between the building and the external environment.

The balcony was a non-conditioned zone, the temperature of which was the result of the influence of solar radiation and the ambient temperature. The balcony enclosure was glazed on all exterior walls. The glazing heights were assumed to be 1.80 m, 2.20 m, or 2.60 m, in combination with a wall under the window with a height of 1.00, 0.60, or 0.20 m, respectively. To maximize passive gains, the balcony glazing was closed and exposed in winter. During the summer and transitional periods, it was possible to ventilate the balcony by opening the windows if the temperature of the indoor air exceeded $22 \text{ }^\circ\text{C}$. It was also assumed that limiting overheating by using curtains with radiation permeability of 50%

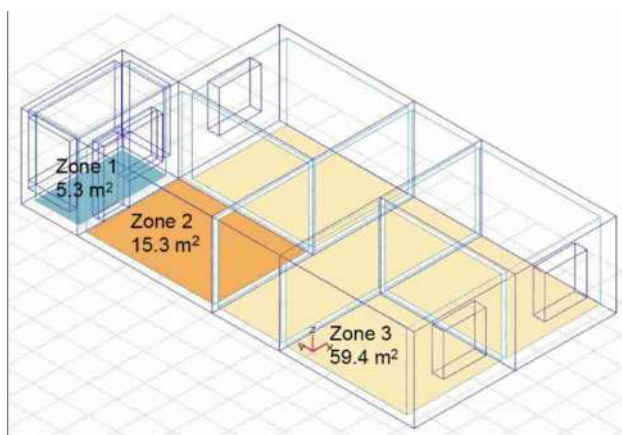


Fig. 1 Outline of the apartment with thermal zones: zone 1—balcony, zone 2—room adjacent to the balcony, zone 3—remaining part of the apartment

was possible if the internal temperature exceeded $24 \text{ }^\circ\text{C}$ or the solar radiation intensity transmitted by the glazing was greater than $300 \text{ W}/\text{m}^2$.

Due to the greater efficiency of double glazed windows in the conversion of solar energy, which was confirmed in the literature [15–17], it was assumed that this type of glazing, filled with argon or krypton, will be used in the greenhouse enclosure. Glazing differing in optical and insulating properties was marked with symbols from O2.0 to O 2.4. The O2.0 glazing was made of plane glass, the others had spectrally selective coatings applied on one or two panes (O2.4). The associated rise in infrared reflectivity has increased thermal insulation but at the expense of decreasing solar energy permeability.

The thermal insulation of the whole balcony enclosure was related to the thermal insulation of the glazing (Table 1). In the case of glazing without spectrally selective coatings (O2.0), an enclosure with lower thermal insulation ($U = 0.65 \text{ W}/(\text{m}^2 \cdot \text{K})$) was used, maintaining the proportions between the insulation of the glazed and the full part, which were used in the case of coated glazing. This version of the enclosure was conducive to maximizing the solar gains owing to glazing with lower thermal insulation and higher solar radiation permeability. In other cases (O2.1—O2.4), the operation of the greenhouse was aimed at minimising heat loss by increasing thermal insulation, associated with the reduction of solar gains. The thermal transmittance coefficient of the full casing amounted to $0.30 \text{ W}/(\text{m}^2 \cdot \text{K})$.

Taking into account the variability of individual parameters, a total of 75 calculation cases described in Table 2. were analysed. The simulation results were compared with the results obtained for an apartment with an open balcony.

Climate data used in simulations

Poland is situated in a temperate climate zone, with a transient character between the oceanic climate in the west (Cfb) and the continental climate in the east (Dfb—continental climate with warm summer) [27]. Two types of climate data were used in the simulations. The first is the Typical Meteorological Year (TMY) for the Warsaw Okęcie station (latitude $52^\circ 10' \text{ E}$, longitude $20^\circ 58' \text{ N}$, the height of station 107 m a.s.l.), which was used to assess the annual energy demand in apartments. The second is the actual measurement data from the period 2001–2020, coming from the Warsaw Bielany (latitude $52^\circ 17' \text{ E}$, longitude $20^\circ 58' \text{ N}$, the height of the post 98 m a.s.l) and Warsaw Okęcie weather stations. They were used to assess the need for cooling and the risk of overheating the rooms in summer when mechanical cooling is not used. The stations belong to the Meteorology and Water Management—National Research Institute (IMGW—PIB) measurement stations.

Table 1 Thermal and optical properties of the glazing [26]

No	Sym-bol	No of panes	Spectrally selective coating	U_g [W/(m ² ·K)]	g [-]	τ_{vis} [-]	τ_s [-]	ρ_s [-]	g/U_g [(m ² ·K)/W]
1	O2.0	2	—	2.7	0.80	0.83	0.77	0.14	0.30
2	O2.1	2	+	1.4	0.74	0.81	0.66	0.19	0.53
3	O2.2	2	+	1.3	0.63	0.80	0.56	0.29	0.48
4	O2.3	2	+	1.2	0.53	0.72	0.48	0.40	0.44
5	O2.4	2	+	1.1	0.42	0.63	0.38	0.48	0.38

U_g —thermal transmittance coefficient of the glazing

g —total solar energy transmittance

τ_{vis} —visible radiation transmittance (in the range 380 nm–780 nm)

τ_s —beam solar radiation transmittance (in the range 300 nm–2500 nm)

ρ_s —beam solar radiation reflectance (in the range 300 nm–2500 nm)

Table 2 Basic parameters in the simulation

No	Parameter	No of variants	Range
1	Building's location	1	Warsaw
2	Balcony's orientation	5	S, SE, E, SW, W
3	Apartment's location	1	Middle part of the building
3	Thermal insulation of the apartment's external partitions	1	0.25 W/(m ² ·K)/0.20 W/(m ² ·K)/1.30 W/(m ² ·K) (walls/roof/windows)
5	Air exchange rate	1	0.5 1/h/0.3 1/h/0.8 1/h (zone 3/2/1)
6	Type of the balcony	1	External, glazed on three walls
7	Balcony's glazing type	5	Description in Table 1
8	Glazing height	3	1.80 m, 2.20 m, 2.60 m
9	Absorptivity of the internal surfaces of the balcony's enclosure	1	0.5

Typical Meteorological Years were developed in 2004 for energy certification of buildings [28]. According to TMY, the average outside air temperatures were the lowest in January (-1.2 °C), and the highest in July (19.2 °C) for Warsaw Okęcie. Extreme temperatures occurred in January and August, amounting to -12.3 °C and 33.2 °C, respectively. The average temperature of the heating season (from September to May) is 5.1 °C. The smallest insolation occurred from November to January, whereas the largest was from May to July. The predominant share of total radiation was the diffused component, which represented on average 76% in the heating season and 65% in the remaining months.

The method of developing Typical Years took into account the fact that they are to be used to determine the characteristics which do not deviate from long-term average energy needs [29]. As a result, a set of parameters was obtained, which may not reliably illustrate the risk of

overheating the rooms, being a rather short-term phenomenon related to the extreme values of the external temperature.

By the end of the twenty-first century, it is expected that progressive climate change may cause an increase in outdoor temperature, combined with the occurrence of milder winters and warmer summer periods [23, 30]. This may translate into changes in the use and energy consumption of buildings, i.e. above all, an increase in the share of space cooling in the energy demand structure [31]. To assess the risk of overheating the rooms operating without mechanical cooling and the possible need for their cooling, the simulations used the actual climate data covering the months from June to August from the period 2001–2020, provided by IMGW—PIB.

While choosing the year with the greatest risk of overheating, the following data were analysed (Table 3) [32]:

- Mean air temperature,
- Mean air temperature during astronomical summer,
- Maximum air temperature,
- The number of hours with temperatures above 26 °C, 28 °C, and 30 °C,
- Occurrence and length of heatwaves.

The heatwave is most often defined by the limit temperature and the minimum duration [33]. In this work, a sequence of at least three consecutive days in which the maximum temperature exceeds 30 °C was adopted as a heatwave, being the criteria proposed for the climatic conditions of Poland [34].

The year 2015 recorded the longest periods of elevated temperature and the longest heatwaves, including the maximum 10-day heatwave which occurred between the 3rd and 12th of August. This period was assessed as exceptionally burdensome not only in Poland but also in Western Europe [35]. It was also the year with the third-highest average temperature from June to August and the second-highest



Table 3 Characteristics of the TMY and the period 2001–2020, taking into account the possibility of overheating

No	Year	Average temperature June–August [°C]	Average summer temperature [°C]	Maximum temperature [°C]	No. of hours with the temperature above:			Heatwaves [no. of days]
					26°C	28°C	30°C	
1	TMY	17.6	15.8	33.2	114	50	21	0
2	2001	18.4	17.4	33.9	154	72	19	3
3	2002	19.8	18.6	32.1	236	97	26	0
4	2003	19.0	17.9	31.3	155	59	13	0
5	2004	17.6	17.4	31.6	79	21	4	0
6	2005	18.1	17.5	32.1	154	43	13	3
7	2006	19.9	18.4	34.7	317	200	90	9
8	2007	18.9	16.8	35.0	163	72	31	3
9	2008	19.0	17.1	29.8	154	26	0	0
10	2009	18.2	18.0	30.4	106	39	5	0
11	2010	19.8	17.2	34.1	288	157	71	4+3+3
12	2011	18.6	17.4	31.0	80	36	5	0
13	2012	19.2	18.0	34.1	228	123	53	3
14	2013	19.5	17.8	36.7	199	98	45	3
15	2014	18.7	18.2	32.7	224	90	17	3
16	2015	20.3	20.0	36.2	395	249	132	4+10+3
17	2016	19.4	18.8	33.0	195	88	33	3
18	2017	19.0	17.9	34.1	158	76	24	0
19	2018	20.8	20.3	32.3	353	151	54	6+3
20	2019	21.1	19.0	35.2	375	186	82	3+3+4
21	2020	19.7	18.8	32.5	214	75	18	3

temperature during the astronomical summer (21st July–23rd September).

Results and discussion

Validation of computer software

During the preliminary works, the software was validated using temperature measurements from helioenergetic chambers of the Rzeszów University of Technology, designed to conduct research on passive solar systems under the actual climatic conditions [36]. For validation, the measurements taken from the 18th May 2016 to 9th June 2016 were used, during which the temperature of the indoor air, the temperature on the surface of full and glazed partitions, as well as the heat fluxes flowing through the glazing, were recorded at 10-min intervals. At the same intervals, the measurements of the external environment parameters were taken, such as temperature and humidity of the external air, pressure, direction, and speed of the wind, as well as the intensity of solar radiation on the

horizontal plane. During the measurements, the chamber was not air-conditioned, and the validation consisted in comparing the course of the temperature inside it, determined based on simulations and experimental tests (Fig. 2) [37, 38].

The basic statistical parameters did not exceed the values recommended by the American Society of Heating Refrigerating and Air-Conditioning Engineers (ASHRAE) [39], the International Performance Measurement and Verification Protocol Committee (IPMVP) [40], or the Federal Energy Management Program [41] for the calibrated models:

- Mean Bias Error (MBE) = 0.57% < ±5% (according to [40]) and < ±10% (according to [39, 41])

$$\text{MBE} = \frac{\sum_{i=1}^n (S_i - M_i)}{n} \cdot 100\%, \quad (1)$$

- Coefficient of Variation of Root Mean Square Error (Cv(RMSE)) = 5.22% < 20% (according to [40]) and < 30% (according to [39, 41])

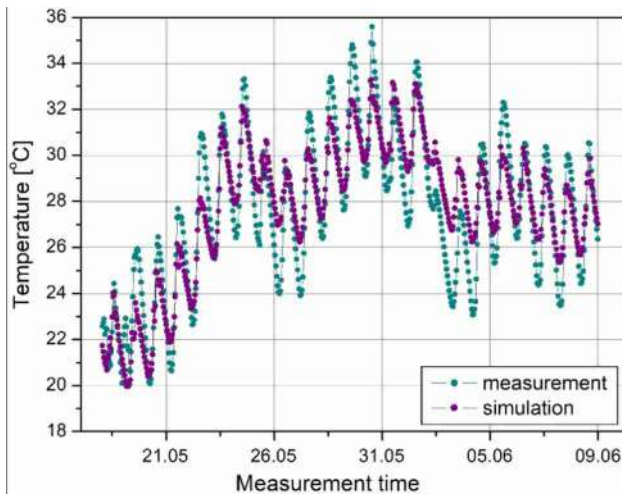


Fig. 2 Temperature time series coming from measurements and simulations, 18th May–9th June 2016

$$Cv(RMSE) = \frac{\sqrt{\frac{\sum_{i=1}^n (S_i - M_i)^2}{n}}}{M'} \cdot 100\% \tag{2}$$

Moreover, the Mean Absolute Percentage Error (MAPE) value equalled 4.38% and did not exceed 5%, which allowed the model to be assessed as good [42],

$$MAPE = \frac{\sum_{i=1}^n \left| \frac{S_i - M_i}{M_i} \right|}{n} \cdot 100\% \tag{3}$$

where

- M—measured value,
- M'—mean measured value,
- S—value determined based on simulation,
- n—number of observations.

Energy demand as a derivative of glazing properties, analyses using TMY

The basic parameters for assessing the efficiency of solar radiation energy acquisition were the demand for heat and cold in the entire apartment (zones 2 and 3). The results were presented depending on the proportion of the effective solar collecting area of glazed elements and the heat transfer coefficient of the balcony enclosure, calculated as [43]:

$$A_{sol} = F_{sh,gl} \cdot g \cdot A_g \tag{4}$$

where

- A_{sol} —effective solar collecting area of glazed elements [m^2].

- $F_{sh,gl}$ —shading reduction factor for movable shading provisions (blinds, curtains), $F_{sh,gl} = 1$,
- g —total solar energy transmittance, $g = 0.9 \cdot g_n$,
- g_n —total solar energy solar transmittance for radiation perpendicular to the glazing,
- A_g —an overall projected area of the glazed element [m^2],

$$H_{tr} = \sum_i A_i \cdot U_i + \sum_j l_j \cdot \psi_j \tag{5}$$

where

- H_{tr} —heat transfer coefficient of the balcony enclosure [W/K]

- A_i —the area of the i-th partition surrounding the heated space, calculated according to the external dimensions of the partition [m^2],

- U_i —total thermal transmittance coefficient of the i-th partition [W/($m^2 \cdot K$)],

- l_j —length of the j-th linear thermal bridge [m],

- ψ_j —linear thermal transmittance coefficient of the j-th thermal bridge [W/($m \cdot K$)].

A_{sol}/H_{tr} was well-correlated with the energy demand (for heat demand, the correlation coefficient was approx.

–0.95, for the cooling demand 0.90). It also allowed taking into account the optical characteristics and thermal insulation of individual parts of the housing using a single indicator, which was very beneficial for the transparency of the analyses.

The demand for heat during the heating season depended very little on the height of the glazing, so it was decided to present the results only for an intermediate height of 2.20 m (the differences between the results obtained for glazing with a height of 1.80 m and 2.60 m did not exceed 3%). Heating needs in the entire apartment were also relatively little differentiated depending on the type of casing or the orientation of the greenhouse (Fig. 3).

Along with the increase in the A_{sol}/H_{tr} ratio, a slight decrease in energy needs was observed (by a maximum of about 11%). Between the glazing types O2.4 and O2.1 there was almost a 30% loss in insulation properties, and an approximately 75% rise in solar radiation transmittance, giving a small reduction in heating demand as a result. Despite significant differences in the permeability of solar radiation for uncoated glazing O2.0 and coated glazing O2.4 (g equal to 0.80 and 0.42, respectively), the obtained heat demand in the apartment was very similar, and the differences did not exceed 2.3%. The similarity of the final results was derived from various mechanisms of heat exchange. In the first variant of the casing, the high g coefficient was combined with worse thermal insulation, i.e. higher heat gains were not fully utilised as a result of their outflow through the enclosure. In the second one, the thermal insulation of the glazed

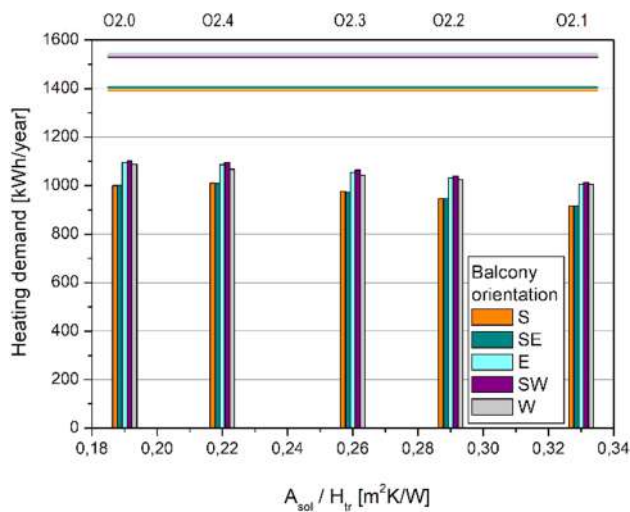


Fig. 3 Energy demand depending on the type of the casing and the balcony's orientation (bars depict energy demand in the flat with a glazed balcony, lines—in the flat with an open balcony)

and full part was higher, but with lower solar gains a similar level of energy demand was achieved.

The heating demand for the entire apartment was the lowest if the balcony was facing south or south-east. The vertical planes of these orientations received the highest amount of insolation during the heating season, which, connected with the biggest area of the front glazing, caused favourable conditions for the conversion of solar energy. The southwest side proved to be the worst location of the balcony, and the results obtained for the eastern and western orientations were similar. The changes resulting from the balcony orientation in relation to the most favourable direction reached about 12%.

The balcony enclosure in each of the presented variants resulted in reduced heat demand compared to an apartment with an open balcony. Energy savings amounted to about 35% (the O2.1 glazing with a height of 2.60 m, balcony facing the southeast), which is certainly a result that translates into real benefits while using the facility. For the glazing types O2.0 and O2.4, the heating reduction was the smallest (in the range of 27%–31%).

The cooling demand in the apartment proved to be more dependent on the type and height of the glazing used in the solar space, however, the amount of energy demand was much lower than in the heating season (Fig. 4). Maximum energy needs reached 80 kWh/year, while in the case of heating demand—1113 kWh/year. These values corresponded to primary energy demand for cooling equal to 51 kWh/year, and primary energy demand for heating equal to 1841 kWh/year, calculated assuming the use of split air conditioners and a district heating system in the building.

Along with the increase in A_{sol}/H_{tr} , the cooling needs in the group of glazing with spectrally selective coatings have been increasing from over twofold to almost fourfold. Here the higher solar transmittance played a crucial role in the growth of solar gains, surpassing the effects of higher heat transmission to the outside caused by the lower glazing insulation. The less insulated enclosure with the O2.0 type glazing differed from this trend and the cooling demand was higher than it would be expected for the glazing with a similar A_{sol}/H_{tr} proportion. This indicated the higher usefulness of the glazing with spectrally selective coatings combined with greater insulation, as in the case of heat demand.

The impact of the height of the glazing on the energy demand was more visible than before, and the differences between the results for the extreme heights of the glazing ranged from 20 to 135% (the greatest disproportions occurred in the case of the southern orientation, mainly due to the lowest values of the cold demand itself).

The southern orientation of the balcony was the most favourable, which was due to small solar gains in the north-facing part of the apartment and relatively small insolation of the vertical plane facing south during summer. The worst results were obtained for the eastern and western directions, possibly south-eastern or south-western (in some cases of glazing with a height of 2.60 m). Due to the change in the position of the balcony in relation to the southern orientation, the demand for cold increased from about 5% to 278%.

The glazing with a total radiation permeability of less than 0.5 allowed reducing the energy demand below the level characteristic of an apartment with an open balcony (O2.4, except for a height of 2.60 m). In other cases, the balcony enclosure increased the cold demand, even more than four times for double glazing with the greatest height.

The Polish climate is more oriented towards heating than cooling; hence, the results characterising the heating season were consistent with the results covering the total annual energy demand. The final result of the balcony enclosure installation proved to be beneficial, despite the periodic increase in cooling needs in the summer. At best, the energy demand was reduced by almost 33% compared to an apartment with an open balcony.

Assessment of cooling demand and risk of room overheating based on 2015 climate data

In the second stage of the analysis, the cooling needs were simulated using climate data from 2015, as the TMY was not recommended for a reliable assessment of the demand for cold, due to anthropogenic climate changes observed since the beginning of the twenty-first century [44]. The same dataset was used to assess the risk of rooms overheating without the possibility of cooling.

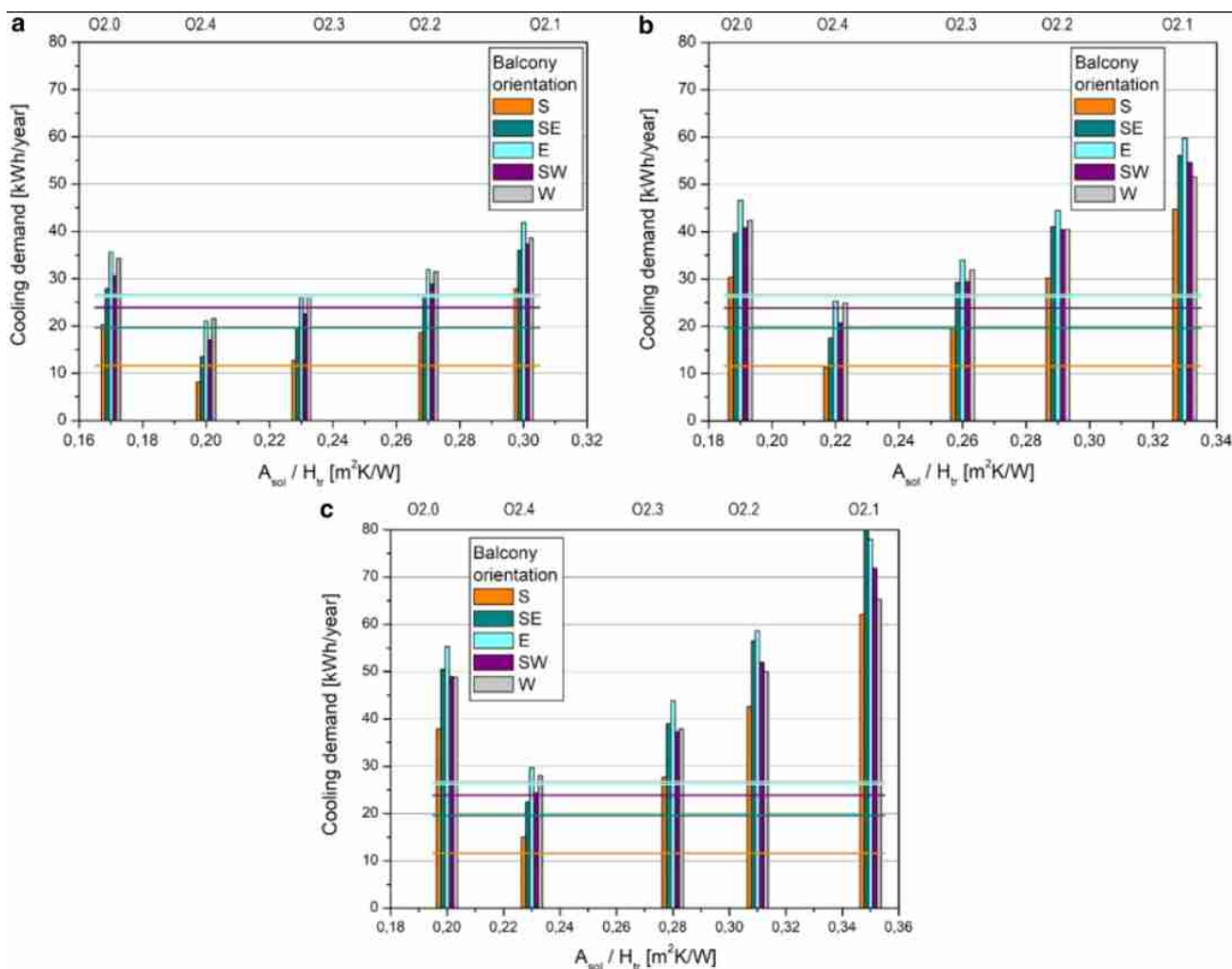


Fig. 4 Energy demand depending on the type of the casing and the balcony's orientation (bars depict energy demand in the flat with a glazed balcony, lines—in the flat with an open balcony): a) glazing

height 1.80 m, b) glazing height 2.20 m, c) glazing height 2.60 m. Climate data—TMY

The analysis based on current climate data displayed an average tenfold increase in cooling demand compared to the results based on TMY (reaching 397 kWh/year, which corresponds to primary energy use 253 kWh/year), confirming the great importance of the type of climate data in the analysis of phenomena occurring in buildings in summer (Fig. 5). However, the course of the graphs showed some similarities with the previous results. Among the coated glazing, there was an increase in energy demand with the rise in A_{sol} / H_{tr} , and the casing with O2.0 glazing deviated from this regularity. The southern balcony orientation was the most advantageous, whereas the eastern and western were the least. The reasons for these effects were the same as in the case of cooling demand calculated based on TMY. In most situations, the enclosure of balconies caused an increase in the demand for cold above the level set for an apartment with an open balcony (13% on average). Exceptions were the O2.4

glazing with a height of up to 2.20 m, and the O2.3 glazing with a height of up to 1.80 m. These solutions decreased the demand for cold by 4.5% on average.

Living quarters in Poland are rarely cooled. An alternative method of assessing the summer conditions was to examine the possibility of overheating the rooms, assuming that the internal temperature was regulated by low-energy passive methods, i.e. mainly by opening or closing windows and using curtains, blinds, night ventilation, etc. based on the criteria of adaptive comfort [45] specified in EN 16,798–1:2019 "Energy performance of buildings—Ventilation for buildings—Part 1: Indoor environmental input parameters for design and assessment of energy performance of buildings addressing indoor air quality, thermal environment, lighting and acoustics" [46]. The assessment was made based on the operating temperature, being the weighted average of the indoor air temperature

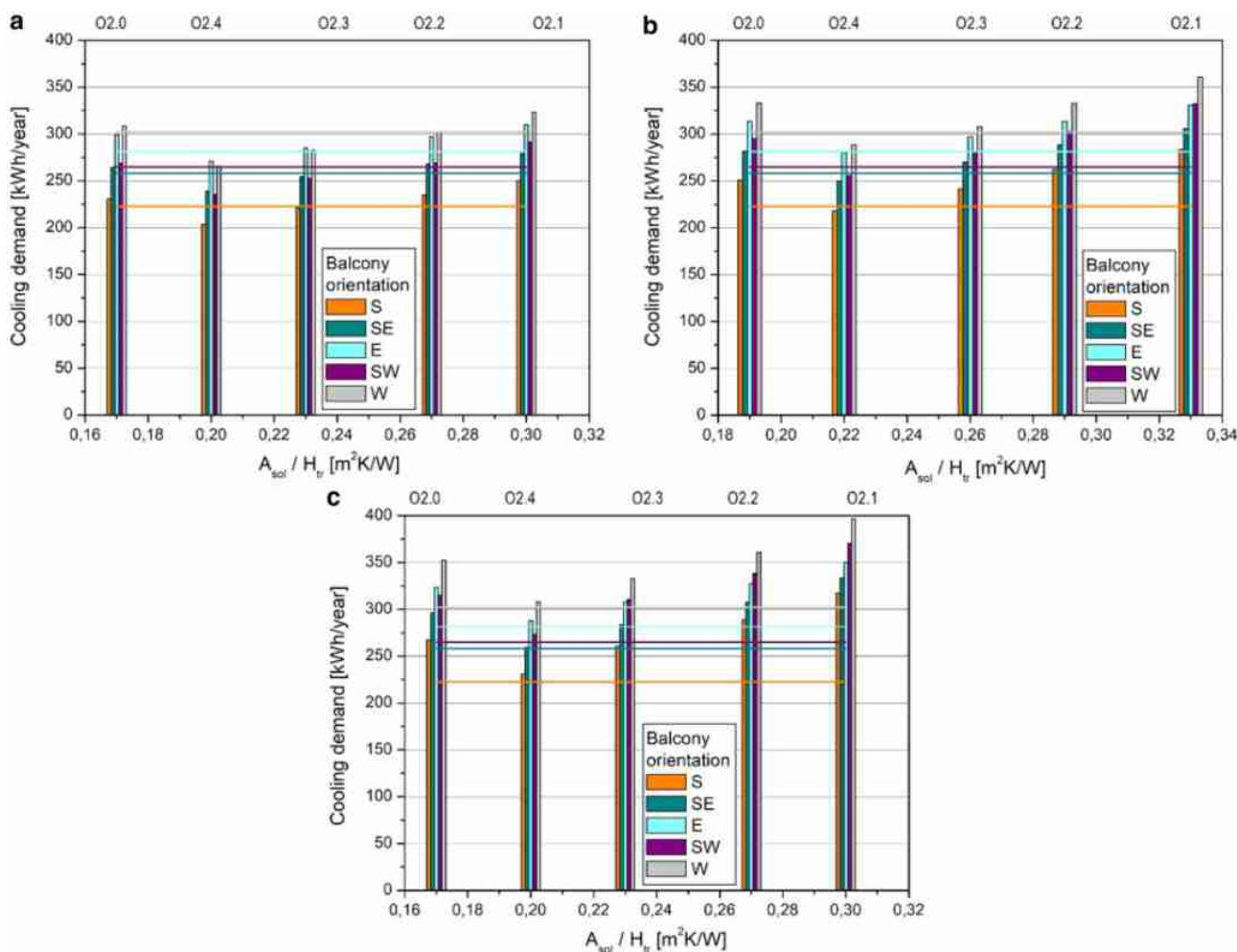


Fig. 5 Energy demand depending on the type of the casing and the balcony’s orientation (bars depict energy demand in the flat with a glazed balcony, lines—in the flat with an open balcony): a) glazing

height 1.80 m, b) glazing height 2.20 m, c) glazing height 2.60 m. Climate data—the year 2015

and the average radiation temperature. The outdoor running mean temperature is calculated as:

$$\begin{aligned} \theta_{rm} &= (1 - \alpha) \cdot (\theta_{ed-1} + \alpha \cdot \theta_{ed-2} + \alpha \cdot \theta_{ed-3}^2) \\ &= (1 - \alpha) \cdot \theta_{ed-1} + \alpha \cdot \theta_{rm-1}, \end{aligned} \tag{6}$$

where

θ_{rm} —outdoor running mean temperature for the considered day [°C],

θ_{rm-1} —running mean outdoor air temperature for the previous day [°C],

θ_{ed-1} —running mean outdoor air temperature for the second previous day [°C],

θ_{ed-2} —running mean outdoor air temperature for the third previous day, etc. [°C],

α —constant between 0 and 1 (recommended value is 0,8),

$$\theta_c = 0.33 \cdot \theta_{rm} + 18.8, \tag{7}$$

θ_c —comfort temperature.

The standard defines four categories of an indoor environment, differing in the level of user expectations and permissible deviations from the comfort temperature. They are marked as IEQ_I (high level of expectation), IEQ_{II} (medium level of expectation), IEQ_{III} (moderate level of expectation), IEQ_{IV} (low level of expectation). The limit temperature values in the particular categories are:

category I - upper limit : $\theta_{imax} = 0.33 \cdot \theta_{rm} + 18.8 + 2,$
 lower limit : $\theta_{imin} = 0.33 \cdot \theta_{rm} + 18.8 - 3,$

category II - upper limit : $\theta_{imax} = 0.33 \cdot \theta_{rm} + 18.8 + 3,$
 lower limit : $\theta_{imin} = 0.33 \cdot \theta_{rm} + 18.8 - 4,$

category III - upper limit : $\theta_{i\max} = 0.33 \cdot \theta_{rm} + 18.8 + 4$,
 lower limit : $\theta_{i\min} = 0.33 \cdot \theta_{rm} + 18.8 - 5$,

$\theta_{i\max}$ —maximum temperature for the given category [°C].

where

$\theta_{i\min}$ —minimum temperature for the given category [°C],

The number of hours outside individual categories of the indoor environment was determined depending on the type of casing, the area of the glazing, and the orientation of the balcony. The results were compared with the conditions

Table 4 Number of hours beyond the specific categories of the internal environment.

Glazing type	Glazing height	Categories of an indoor environment									
		I					II				
		Balcony's orientation					Balcony's orientation				
		E	SE	S	SW	W	E	SE	S	SW	W
O2.0	1.80	215	180	170	246	297	32	2	4	51	79
	2.20	257	234	213	321	363	53	24	28	93	116
	2.60	274	261	261	383	428	68	56	57	119	145
O2.1	1.80	245	226	225	316	342	47	19	30	93	103
	2.20	294	285	313	441	456	89	79	92	146	161
	2.60	341	388	426	545	562	119	118	135	215	217
O2.2	1.80	212	194	181	248	281	30	5	8	51	67
	2.20	259	255	264	356	368	55	45	57	104	113
	2.60	285	295	344	455	456	79	82	106	151	156
O2.3	1.80	193	159	148	212	235	26	2	0	27	39
	2.20	211	197	205	281	297	31	16	25	73	83
	2.60	238	241	260	368	370	42	32	61	116	111
O2.4	1.80	172	120	102	167	200	20	1	0	5	10
	2.20	185	146	137	218	250	23	2	0	36	48
	2.60	196	170	170	263	300	26	2	7	68	81
Open balcony		199	165	139	209	259	22	3	5	64	75

Glazing type	Glazing height	Categories of an indoor environment				
		III				
		Balcony's orientation				
		E	SE	S	SW	W
O2.0	1.80	0	0	0	0	0
	2.20	0	0	0	2	3
	2.60	0	0	0	6	12
O2.1	1.80	0	0	0	0	2
	2.20	0	0	0	22	21
	2.60	0	0	10	58	57
O2.2	1.80	0	0	0	0	0
	2.20	0	0	0	2	3
	2.60	0	0	1	22	19
O2.3	1.80	0	0	0	0	0
	2.20	0	0	0	0	0
	2.60	0	0	0	3	3
O2.4	1.80	0	0	0	0	0
	2.20	0	0	0	0	0
	2.60	0	0	0	0	0
Open balcony		0	0	0	1	3

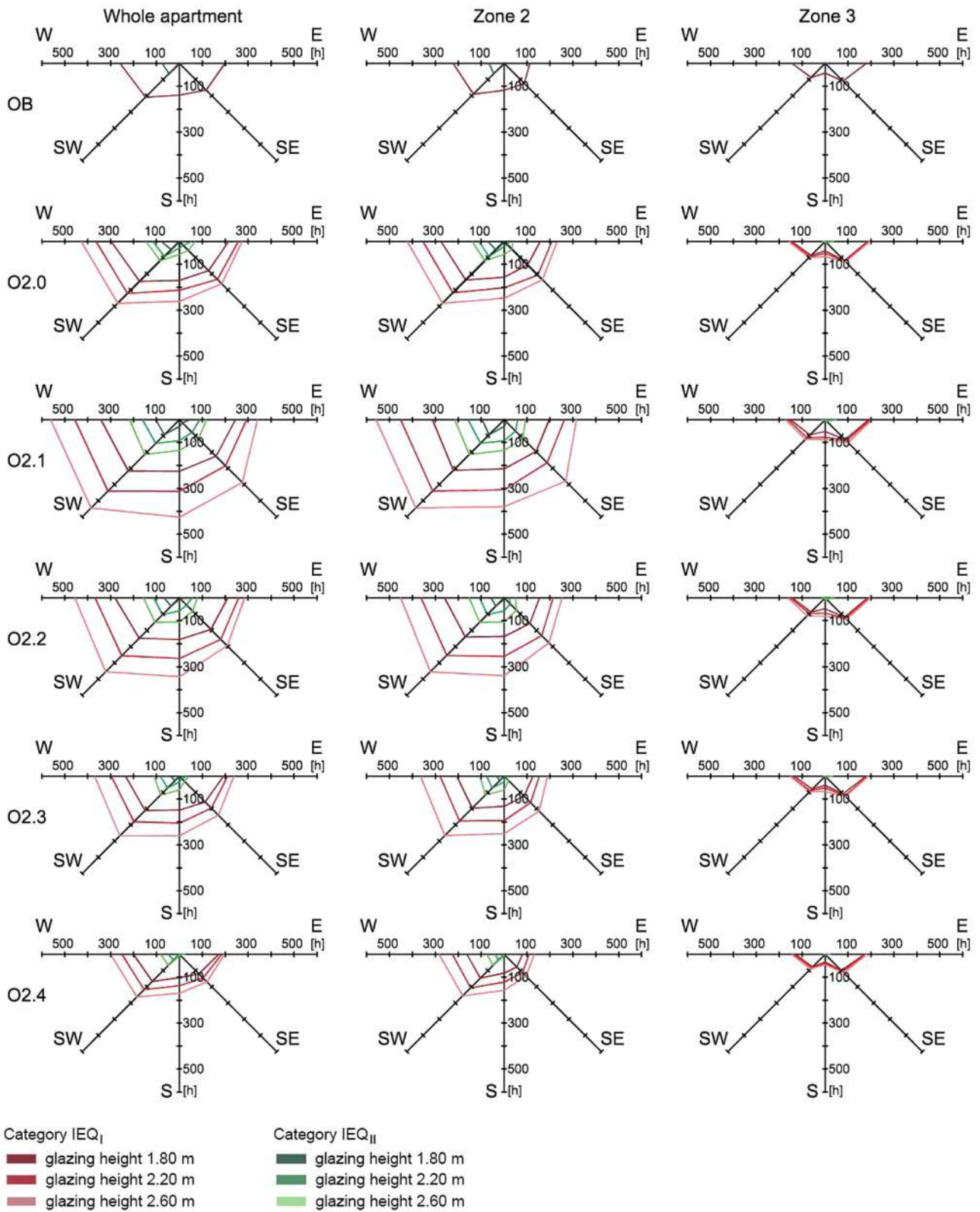


Fig. 6 Number of hours beyond categories IEQ_I and IEQ_{II}, depending on the type of the casing and the balcony’s orientation (OB—open balcony)

prevailing in an analogous apartment with an open balcony (Table 4, Fig. 6).

In an apartment with an open balcony, the room adjacent to the balcony was in most cases more exposed to the occurrence of high temperature than the rest of the apartment (except for the eastern orientation). This was influenced, among others, by the larger area of the glazing—the proportion of the glazing surface area to the floor surface area in zone 2 was 18.3%, and in zone 3—8.5%. Part of the windows of zone 3 was generally directed to the northern part of the sky, so the intensity of solar radiation reaching them was also lower. In both zones, as in the entire apartment, the distribution of the number of hours outside the comfort categories was not symmetrical concerning the sides of the world, which resulted from the asymmetry of the intensity of radiation falling on vertical planes. In zone 2, the western and south-western directions were unfavourable, whereas in zone 3—the eastern and western. Considering the whole apartment, the southern and south-eastern directions should be preferred. This was consistent with the regularities observed for the cooling demand, caused by the smallest summer insolation of the vertical planes facing south. The requirements of category II of the internal environment for these orientations were slightly exceeded (by 3 and 5 h), while the requirements of category III were met in the entire apartment, also for the eastern orientation.

The spatial nature of the results for apartments with a built-in balcony was similar—in zone 2 and the entire apartment, the shortest periods of overheating occurred when the balcony was directed east, southeast or south. For the south-western and western directions, the number of hours outside category I rose significantly. Increasing the height of the glazing and radiation permeability were also factors enhancing discomfort in the room adjacent to the balcony. To some extent, the glazing without spectrally selective coatings in a worse thermally insulated casing (O2.0) deviated from this regularity. Despite the highest permeability ($g=0.80$), the results obtained for higher heat dissipation capacity outside the enclosure were between those obtained for the O2.2 and O2.3 glazing ($g=0.63$ and 0.53 , respectively).

In zone 3 (the rest of the apartment outside the room adjacent to the balcony), the dependence of the results on the orientation of the balcony was the same as in an apartment with an open balcony—the least favourable directions are eastern and western, whereas the most favourable was the southern direction. Balcony enclosure in most cases contributed to the extension of overheating periods, with this effect being less visible than in zone 2.

There were no possibilities to meet the requirements of category I of the internal environment, but the same was true in an apartment with an open balcony. Its enclosure in most cases resulted in an increase in the time of overheating, about threefold in the worst situation (O2.1 glazing, height

2.60 m, southern orientation). It was possible to shorten the overheating periods for type O2.4 glazing with a height of 1.80 m, compared to an apartment with an open balcony, by an average of about 20%. Beneficial phenomena were also observed in the case of a glazing height of 2.20 m (except for the south-western orientation).

The less restrictive requirements of category II were met in the apartment in individual cases for the O2.3 and O2.4 glazing with a lower height (for the southern orientation). These types of glazing allowed for reducing the number of hours with excessive temperature compared to the basic version of the apartment (with an open balcony), in particular for the glazing height of 1.80 m. It was also possible when using higher glazing (2.20 m), but with some limitations related to the type of glazing and the orientation of the balcony—this only applied to the O2.4 glazing, except for the eastern orientation.

The internal conditions expected from rooms in category III of the environment for the O2.0, O2.1, and O2.2 glazing can be provided throughout the apartment at a glazing height of 1.80 m, practically regardless of the balcony orientation, and at a height of 2.20 m—for the eastern, south-eastern, and southern directions. For other glazings, with lower radiation permeability, the apartment qualified for category III in almost all cases. The exception was the variant of the balcony enclosure with the O2.3 glazing with a height of 2.60 m facing south-west or west, but in these cases, the number of hours with excessive temperature was only 3.

Summing up the above-mentioned analyses in terms of selecting the type of glazing and balcony enclosure due to their impact on the possibility of overheating the rooms, it can be concluded that:

- Balcony enclosures may increase or decrease the number of hours exceeding the limits of a comfortable use of the premises compared to an apartment with an undeveloped balcony; these effects were felt the most in the room adjacent to the solar space;
- The use of glazing with high radiation transmittance and large surface area has had adverse effects; in the case of glazing with the smallest solar aperture, the results may be beneficial, due to the reduction of solar gains in the room adjacent to the balcony;
- Regardless of the material solutions, the requirements for rooms in category I of the indoor environment were not met; this was not due to the balcony enclosure since the same restrictions existed in an apartment with an open balcony;
- Due to the appropriate selection of the elements of the enclosure, the height of the glazing, and the orientation of the balconies concerning the cardinal directions, the requirements of category II can be met for certain types



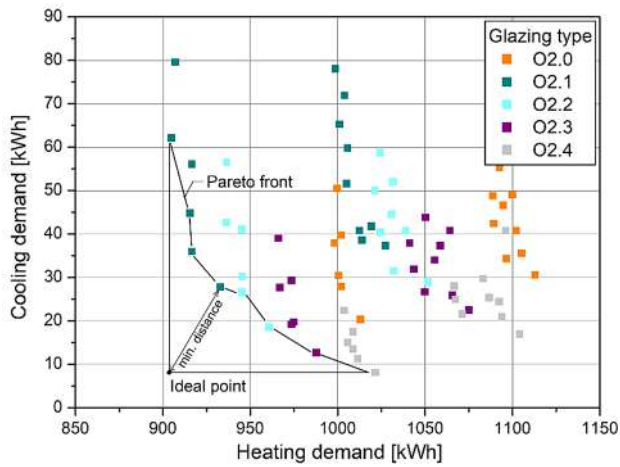


Fig. 7 Choice of the optimal solution for scenario I

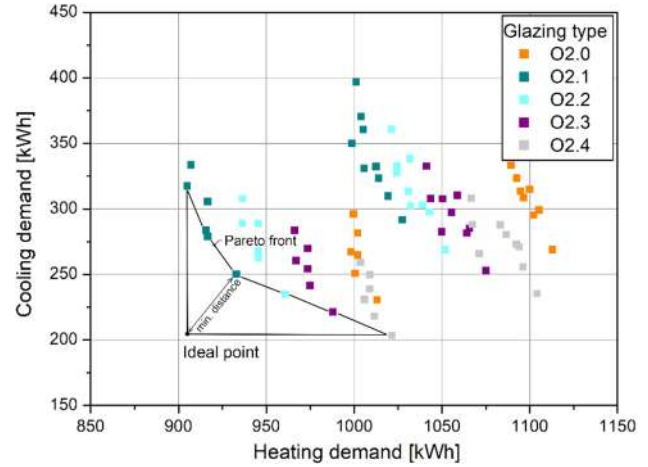


Fig. 8 Choice of the optimal solution for scenario II

of glazing (O2.3 and O2.4), except that these were single configurations in the analysed variants;

- Category III requirements can be met for most of the analysed cases (77%);
- The lowest risk of overheating existed if the balcony was facing east, south-east or south; the south and south-west orientations were the least favourable.

Selecting the optimal solution

Aiming at reducing heat demand in the heating season and reducing the need for cooling or the possibility of overheating in the summer are opposing goals. Increased radiation permeability and glazing area are conducive to increasing heat gains, which is a beneficial phenomenon in the heating period, but not in the cooling period. The search for the optimal solution will consist in seeking the best compromise from the point of view of both criteria.

The optimisation objectives are as follows:

- Obtaining the lowest demand for heat and cold according to the analyses carried out based on TMY—scenario I (Fig. 7),
- Obtaining the lowest demand for heat and cold according to the analyses performed based on TMY (heating season) and data from the year with extreme periods of heat (cooling season)—scenario II (Fig. 8),
- Obtaining the lowest heat demand according to the analyses conducted based on TMY and the lowest number of hours of overheating based on data from the year with extreme periods of heat—scenario III (Fig. 9, 10).

To choose the best solution, the Pareto method was used, according to which "the solution is a Pareto solution if there

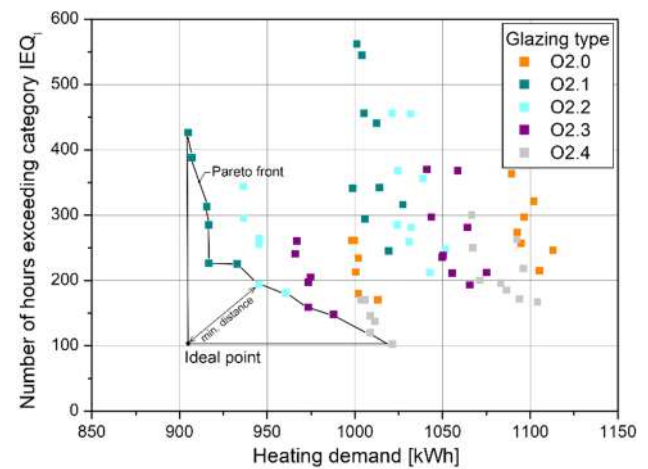


Fig. 9 Choice of the optimal solution for scenario III (category IEQI)

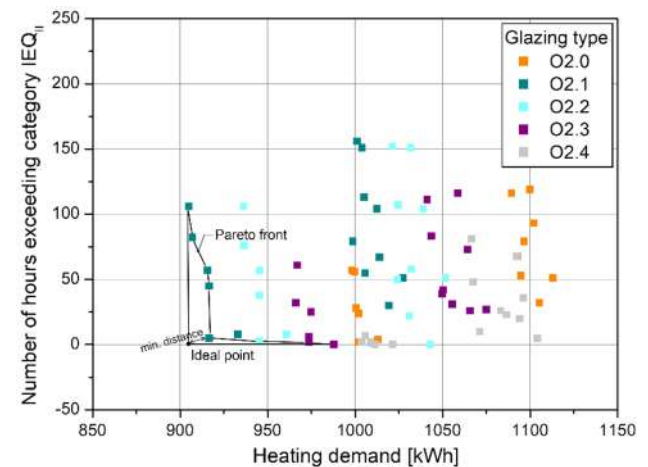


Fig. 10 Choice of the optimal solution for scenario III (category IEQII)

is no other feasible solution that would improve one optimisation goal without endangering another" [47]. If there are two objective functions, then solutions in the sense of Pareto form the front, and the final choice of the best one requires a specific decision-making process. Because the Pareto front in all scenarios was a curve comprising concave fragments, the optimal solution was the point characterised by the smallest distance from the ideal solution, described as:

$$\text{Minimum } D = \sqrt{\lambda_1 (C_1 - C_{1id})^2 + \lambda_2 (C_2 - C_{2id})^2} \quad (8)$$

where

λ_1, λ_2 —weighting coefficients for the criteria C_1 and C_2 ,

$\sum_{i=1}^2 \lambda_i = 1$, in the analysed cases it was assumed that $\lambda_1 = \lambda_2 = 0.5$,

C_1, C_2 —optimization criteria, namely demand for heat and demand for cold/number of hours of overheating,

C_{1id}, C_{2id} —ideal solutions for the optimization criteria C_1, C_2 .

In the first two scenarios, comparing the heating and cooling demand, the most recommended type of glazing was the O2.1 glazing, regardless of the climate datasets used in the simulations of the summer conditions. It had the highest radiation permeability and the lowest thermal insulation among glazing with selective coatings, as well as the highest A_{sol}/H_{tr} ratio for the entire casing. In the optimal variant, the glazing was 1.80 m high and the balcony was facing south. At the same time, this solution minimised the demand for energy in the heating season, which indicated that the heating season under the Polish climate conditions was of the greatest importance for the thermal operation of the considered apartment.

In scenario III, comparing heating demand and the number of overheating hours, the optimal solution differed depending on the desired category of the internal environment. Considering category IEQ_I, the recommended variant included the casing with the O2.2 glazing, with the smaller solar radiation transmittance compared to the glazing O2.1. The remaining characteristics of the casing were the same as in the previous case, namely the glazing height equal to 1.80 m and the southern orientation of the balcony. If the category IEQ_{II} was considered, admitting higher internal temperature, the optimal solution was as in scenarios I and II.

Conclusions

The conducted research confirmed the significant impact of spectrally selective coatings used in the glazed space enclosure (balcony) on the energy demand and thermal conditions

in the residential zone. The final decisions regarding the choice of glazing should be made taking into account primarily the energy savings that can be achieved during the heating season, but also analysing the impact of material solutions on the summer comfort of use. The research indicated the intentional use of double glazing and thermally insulated enclosures, due to the greater buffer effect of the solar space. Selective coatings on the glass allowed for shaping heat gains and losses so that their mutual proportion is as beneficial as possible for the year-round operation of the facility.

The lowest total energy demand (heat and cold), calculated based on Typical Meteorological Year and actual climate data, was obtained for the O2.1 glazing in a well-insulated casing. At the same time, it is glazing for which the risk of overheating and discomfort of use in the absence of mechanical cooling during heat waves may be the greatest. If it was necessary to maintain a lower internal temperature due to user requirements, the O2.2 glazing type should also be considered, provided that a balcony facing east, southeast, or south can be designed.

It was difficult to compare the research results with findings available in the literature on the subject, because of many differences in the simulation assumptions, mainly concerning the types of the buildings (single- and multi-family ones), the scope of the analyses (regarding a whole apartment, a whole building, or only a space adjacent to the greenhouse), location, types of sunspace casing, etc. However, some similarities could be found relating to the publication [7, 9, 14], where the reduction in demand for heating in exemplary flats with sunspaces (being a part of multi-family buildings) ranged approximately from 20 to 55%. The presented results reporting the reduction of heating demand between 27 and 35% fell within this range.

Acknowledgements The source of the climatic data used in the research was the Institute of Meteorology and Water Management—National Research Institute in Poland.

Funding The work was financially supported by the Ministry of Science and Higher Education in Poland within the statutory research number FD-20/IL-4/022 at the Lublin University of Technology.

Declarations

Conflict of interest On behalf of all authors, the corresponding author states that there is no conflict of interest.

References

1. Chwieduk, D.: *Solar Energy in Buildings. Thermal Balance for Efficient Heating and Cooling*. Academic Press, Elsevier Inc.: San Diego, CA (2014)

2. Duffie, J.A., Beckman, W.A.: *Solar Engineering of Thermal Processes*. Wiley, Hoboken, New Jersey (2013)
3. Albatici, R., Passerini, F., Pfaffert, J.: Energy performance of verandas in the building retrofit process. *Energies* **9**, 365 (2016)
4. Ribeiro, C.F.T., Ramos, N.M.M., Flores-Colen, I.: Spaces in-between impacts on indoor environment and energy efficiency in dwellings. *MATEC Web of Conf.* **282**, 020202071 (2019)
5. Yang, Q., Li, N., Chen, Y.: Energy saving potential and environmental benefit analysis of application of balcony for residence in the hot summer and cold winter area of China. *Sustain. Energy Technol. Assess.* **43**, 100972 (2021)
6. Amoako-Attah, J., B-Jahromi, A.: Impact of conservatory as a passive solar design of UK dwellings. In: *Proceedings of the Institution of Civil Engineers Engineering Sustainability* 169, 198–213 (2016)
7. Ignjatović, D., Jovanović, P.M., Kavran, J.: Application of sunspaces in fostering energy efficiency and economical viability of residential buildings in Serbia. *Energ. Build.* **98**, 3–9 (2015)
8. Asdrubali, F., Cotana, F., Messineo, A.: On the evaluation of solar greenhouse efficiency in building simulation during the heating period. *Energies* **5**, 1864–1880 (2012)
9. Song, D., Choi, Y.I.: Effect of building regulation on energy consumption in residential buildings in Korea. *Renew. Sust. Energ. Rev.* **16**, 1074–1081 (2012)
10. Catalina, T., Bortis, D., Vartires, A., Lungu, C.: Glazed balconies impact on energy consumption of multi-story buildings. *E3S Web of Conferences* **111**, 06079 (2019)
11. Ma, Q., Fukuda, H., Lee, M., Kobatake, T., Kuma, Y., Ozaki, A., Wei, X.: Experimental analysis of the thermal performance of a sunspace attached to a house with a central air conditioning system. *Sustainability* **10**, 1428 (2018)
12. Hilliaho, K., Mäkitalo, E., Lahdensivu, J.: Energy saving potential of glazed space: sensitivity analysis. *Energ. Build.* **99**, 87–97 (2015)
13. Bataineh, K.M., Fayed, N.: Analysis of thermal performance of building attached sunspace. *Energ. Build.* **43**, 1863–1868 (2011)
14. Vukadinović, A., Radosavljević, J., Đorđević, A., Petrović, N.: Effects of the geometry of residential buildings with a sunspace on their energy performance. *Facta Universitatis, Series: Architecture and Civil Engineering* **1**, 105–118 (2019)
15. Vukadinović, A., Radosavljević, J., Đorđević, A., Protić, M., Nikolić, Z.: Analysis and optimisation of energy performance in residential buildings with sunspaces. In: *Proceedings of the VIII International Conference Industrial Engineering and Environmental Protection* (2018); October 11–12th, Zrenjanin, Serbia (2018)
16. Chiesa, G., Simonetti, M., Ballada, G.: Potential of attached sunspaces in winter season comparing different technological choices in Central and Southern Europe. *Energ. Build.* **138**, 377–395 (2017)
17. Ma, L., Zhang, X., Li, D., Arıcı, M., Yıldız, Ç., Li, Q., Zhang, S., Jiang, W.: Influence of sunspace on energy consumption of rural residential buildings. *Sol. Energy* **211**, 336–344 (2020)
18. Monge-Barrio, A., Sánchez-Ostiz, A.: Energy efficiency and thermal behaviour of attached sunspaces in the residential architecture in Spain. *Summer Conditions. Energ. Build.* **108**, 244–256 (2015)
19. Sánchez-Ostiz, A., Monge-Barrio, A., Domingo-Irigoyen, S., González-Martínez, P.: Design and experimental study of an industrialized sunspace with solar heat storage. *Energ. Build.* **80**, 231–246 (2014)
20. Saleh, P.H.: Thermal performance of glazed balconies within heavy weight/thermal mass buildings in Beirut. Lebanon's hot climate. *Energ. Build.* **108**, 291–303 (2015)
21. Song, D., Choib, Y.J.: Effect of building regulation on energy consumption in residential buildings in Korea. *Renew. Sust. Energ. Rev.* **16**, 1074–1081 (2012)
22. Vukadinović, A., Radosavljević, J., Đorđević, A., Protić, M., Petrović, N.: Multi-objective optimization of energy performance for a detached residential building with a sunspace using the NSGA-II genetic algorithm. *Sol. Energy* **224**, 1426–1444 (2021)
23. Solomon, S., Qin, D., Manning, M., Marquis, M., Averyt, K., Tignor, M., Miller, H.L., Chen, Z.: *Climate Change 2007: The Physical Science Basis. Part of the Working Group I Contribution to the Fourth Assessment Report of the Intergovernmental Panel on Climate Change*. Cambridge University Press, Cambridge (2007)
24. Piegari, A., Flory, F.: *Optical Thin Films and Coatings. From Materials to Applications*. Woodhead Publishing, Oxford (2013)
25. Wittchen, K.B., Johnsen, K., Grau, K.: *BSim user's guide*. Danish Building Research Institute, Hørsholm (2004)
26. Calumen II v. 1.3.1, Saint Gobain Glass
27. Kottek, M., Grieser, J., Beck, C., Rudolf, B., Rubel, F.: World map of the Köppen-Geiger climate classification updated. *Meteorol. Z.* **15**, 259–263 (2006)
28. Narowski, P., Janicki, M., Heim, D.: Comparison of untypical meteorological years (umy) and their influence on building performance simulations. In: *The Proceedings of BS 2013: 13th Conference of International Building Performance Simulation Association, Chambéry, France, August 26–28* (2013)
29. ISO 15927-4: 2005 Hygrothermal performance of buildings—calculation and presentation of climatic data—part 4: hourly data for assessing the annual energy use for heating and cooling. International Organization for Standardization, Geneva (2005)
30. Hulme, M., Jenkins, G.J., Lu, X., Turnpenny, J.R., Mitchell, T.D., Jones, R.G., Lowe, J., Murphy, J.M., Hassell, D., Boorman, P., McDonald, R., Hill, S.: *Climate Change Scenarios for the United Kingdom: The UKCIP02 Scientific Report*. School of Environmental Sciences, University of East Anglia, Norwich, Tyndall Centre for Climate Change Research (2002)
31. Chow, D., Levermore, G.J.: The effects of future climate change on heating and cooling demands in office buildings in the UK. *Build. Serv. Eng. Res. T.* **31**, 307–323 (2010)
32. Hacker, J., Belcher S., White A.: *Design summer years for London*. CIBSE TM 49. Chartered Institution of Building Services Engineers, London (2014)
33. Della-Marta, P.M., Luterbacher, J., Von Weissenfluh, H., Xoplaki, E., Brunet, M., Wanner, H.: Summer heat waves over western Europe 1880–2003, their relationship to large-scale forcings and predictability. *Clim. Dyn.* **29**, 251–275 (2007)
34. Krzyżewska, A., Bartoszek, K., Wereski, S.: The meteorological conditions during particularly severe heatwave in Lublin in August 2015 (in Polish). *Przegląd Geofizyczny* **3–4**, 239–249 (2016)
35. Muthers, S., Laschewski, G., Matzarakis, A.: The summers 2003 and 2015 in South-West Germany: heat waves and heat-related mortality in the context of climate change. *Atmosphere* **8**, 224–237 (2017). In: Krasoń J., Lichołai, L.: Thermal efficiency of a modified thermal storage wall containing phase change material in comparative test periods. In: *E3S Web of Conferences* 49, 00059 (2018)
36. Krasoń, J., Lichołai, L.: Thermal efficiency of a modified thermal storage wall containing phase change material in comparative test periods. In: *E3S Web of Conferences* 49, 00059 (2018)
37. Grudzińska, M.: *Glazed balconies as passive greenhouse systems. Evaluation of functioning in Polish climatic conditions*. Lublin University of Technology Publishing House, Lublin (2020).
38. Grudzińska, M.: Thermal and optical properties of the sunspace casing as factors influencing temperature rise in greenhouse systems. *Mater.* **14**, 7411 (2021)
39. ASHRAE Guideline 14–2002: *Measurement of Energy and Demand Savings*. American Society of Heating, Refrigerating and Air-Conditioning Engineers, Atlanta, GA (2002)



40. International performance measurement and verification protocol: concepts and options for determining energy and water savings, Vol. I, International Performance Measurement and Verification Protocol Committee, Oak Ridge, TN (2002)
41. Measurement and verification guidelines in measurement and verification for performance-based contracts, Version 4.0. U.S. Department of Energy, Federal Energy Management Program, Washington, DC (2015)
42. Rogalska, M.: Multi-factor models in evaluating the time of building processes Lublin University of Technology Publishing House, Lublin (2016)
43. ISO 52016–1:2017 Energy performance of buildings—energy needs for heating and cooling, internal temperatures and sensible and latent heat loads—part 1: calculation procedures. International Organization for Standardization, Geneva (2017)
44. Grudzińska, M., Jakusik, E.: Energy performance of buildings in Poland on the basis of different climatic data. *Indoor Built Environ.* **26**, 551–566 (2017)
45. Humphreys, M.A., Nicol, J.F.: Understanding the adaptive approach to thermal comfort. *ASHRAE Trans.* **104**, 991–1004 (1998)
46. EN 16798–1:2019 Energy performance of buildings—ventilation for buildings—Part 1: Indoor environmental input parameters for design and assessment of energy performance of buildings addressing indoor air quality, thermal environment, lighting and acoustics. European Committee For Standardization, Brussels (2019)
47. Delgarm, N., Sajadi, B., Kowsary, F., Delgarm, S.: Multi-objective optimization of the building energy performance: A simulation-based approach by means of particle swarm optimization (PSO). *Appl. Energ.* **170**, 293–303 (2016)

Publisher's Note Springer Nature remains neutral with regard to jurisdictional claims in published maps and institutional affiliations.





Performance study of a new type of collection equipment for unorganized fumes from aluminum electrolysis

Shuichang Liu¹ · Qingyu Wang¹ · Yong Zhang² · Zhengguo Zheng³ · Yelong Jiang⁴

Received: 17 May 2022 / Accepted: 24 August 2022 / Published online: 5 September 2022
© The Author(s), under exclusive licence to Islamic Azad University 2022

Abstract

To address the deterioration of workshop air quality due to free emission of unorganized fumes from multiple surface sources of residual anode carbon blocks during electrolytic cell opening and anode changing operations, new unorganized fumes collecting equipment based on negative pressure suction was designed. Take a workshop as an example, by the CFD coupled DPM simulation method for unorganized fumes, the influence of the negative pressure P of the fan, and the distance h between the upper surface of the residual carbon block and the exhaust hood on the collection efficiency was investigated. The results showed that the collection efficiency of flue gas and dust increased with the increase in negative pressure and increased at first and then decreased with the rise in the distance between the upper surface of the residual carbon block and the exhaust hood. The collection efficiency of flue gas and dust was the highest when the negative pressure was 5000 Pa, and the distance was 176 mm; at this time the collection efficiency of flue gas was 85.06%, and the dust was 72.58%. Further, validation tests in practical applications were carried out. The experimental results consistently demonstrate that the established CFD coupled DPM simulation method had a good agreement with the experimental results. The error of flue gas collection efficiency was less than 3.1%, and the error of dust collection efficiency was less than 1.2%. The research conducted had critical engineering application values for achieving high cleanliness and low energy consumption operation of unorganized fumes.

Keywords CFD · DPM · Unorganized fumes · Exhaust hood · Collection efficiency

Introduction

Aluminum is a chemically very active element, which exists in nature mostly in the form of alumina [1]. Since 1886, when Hall–Heroult invented the method of producing aluminum by electrolysis of cryolite-alumina molten salt and formed the stage of large-scale production, this method has been the only method for producing metallic aluminum [2]. The electrolysis technology of aluminum has developed from chemical production to the modern application of

electrolysis. In China, the production of primary aluminum increased from approximately 5.55 million tonnes in 2003 to 22.06 million tonnes in 2013, showing an average of 14.8% annual increase during a span of 10 years [3]. In 2020, the production of alumina, primary aluminum and carbon for aluminum in China was 7313 [4], 3708 [4] and 20 million tonnes [5], accounting for 54.6%, 56.8% and 61.0% of the total world production in that year, respectively. As the world's largest producer and consumer of aluminum, China's aluminum electrolysis industry is an important pillar of the national economy, but at the same time, it has the issues of high energy consumption and heavy pollution [6, 7].

Modern aluminum electrolysis production is a process that uses cryolite—alumina as the electrolyte and carbon material as the electrode to prepare metallic aluminum [8]. In the process of electrolysis, liquid aluminum metal is precipitated from the cathode, and CO₂-based gas is produced from the anode [9]. As shown in Fig. 1, after the anode is consumed, it is necessary to open the cell and change the anode, during which a large number of harmful gases, mainly HF, CO₂, SO₂ and dust [10, 11], are emitted from the

✉ Yong Zhang
289714423@qq.com

¹ School of Civil Engineering, Hunan University of Technology, Zhuzhou 412007, China

² School of Mechanical Engineering, Hunan University of Technology, Zhuzhou 412007, China

³ Zhuzhou Tianqiao Crane Co., Ltd., Zhuzhou 412001, China

⁴ Hunan Special Equipment Inspection and Testing Institute, Changsha 410116, China



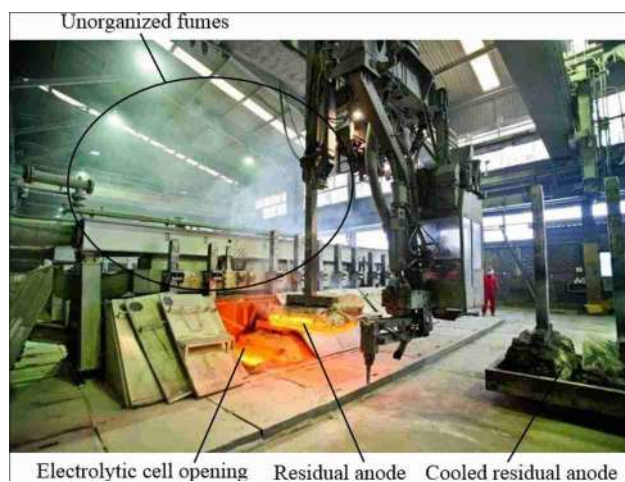


Fig. 1 Aluminum electrolysis workshop production operations

surface of the electrolytic cell and the residual anode, which are dispersed in the air with the movement of the crane and are called unorganized fumes [12]. In continuous production, the air quality in the workshop gradually deteriorates, which threatens the life, health and safety of operators for a long time [13, 14]. Therefore, it is of great engineering importance to find ways to efficiently clean unorganized fumes and reduce energy consumption.

In the research of industrial workshop unorganized fumes collection technology and structure, Liu et al. [15] proposed three types of exhaust hood structures: up-draft, side-draft and air-curtain, which were applied to the collection of unorganized fumes from open dust sources, and the results showed that the air-curtain hood had the highest capture efficiency, which proved that the exhaust hood structure was effective in collecting unorganized fumes. Lin et al. [16] proposed a cyclone curtain-type exhaust hood collection technique for the unorganized fumes generated during welding operations and established the optimal design parameters. It was shown that the airflow organization of the exhaust hood had an effect on the collection efficiency. Jing et al. [17] used closed dust hood and vortex blowing and suction dust removal technology to solve the problem of dust diffusion caused by the formation of induced airflow in the conveyor belt during the transportation of coal. It demonstrated that the combination of exhaust hood structure and airflow organization can effectively collect unorganized fumes. The above studies showed that exhaust hoods can play a good role in the collection of unorganized fumes in industrial workshops, but they have not been applied to the collection of aluminum electrolysis unorganized fumes. For unorganized fumes from aluminum electrolysis residual anodes, in 2011, Wang et al. [18] were the first to propose an exhaust hood structure based on local suction technology for residual anodes stacked at fixed points. They carried out CFD numerical simulations

under pure air conditions, which provided a better research idea for the solution of this problem. In 2017, Vincent Verin et al. [19] designed a residual anode tray with a restrictive cover to facilitate residual anode placement while reducing unorganized fumes emissions, the residual anodes were sealed and cooled to reduce unorganized fumes emission. In 2018, Song et al. [20] proposed a mobile dust collection hood structure for fixed residual carbon blocks, which can be moved to a fixed position to collect the unorganized fumes emitted from the residual carbon blocks.

In summary, the current collection technology for aluminum electrolysis unorganized fumes can only collect the fumes emitted from fixed residual carbon blocks, but there are still no better solutions for the unorganized fumes emitted during the opening of the electrolytic cell, the lifting of the residual carbon block from the electrolytic cell, and transit by the crane.

In this regard, we propose an aluminum electrolysis unorganized fumes collection technology and mobile fumes collection equipment based on negative pressure suction, which can collect the unorganized fumes emitted from the residual carbon block in the process of lifting and transiting. Taking a workshop as an example, we establish a CFD coupled DPM simulation method to study the collection efficiency of flue gas and dust (both contained by fumes), the influence of the negative pressure P of the fan and the distance h between the upper surface of the residual carbon block and the exhaust hood on the collection efficiency is investigated, and the optimized parameters for the highest collection efficiency are derived and experimental verification is carried out.

Model and methodology

Aluminum electrolysis unorganized fumes collection equipment

During the aluminum electrolysis operation, the crane is equipped with special tools to complete many operational tasks such as new and old anode replacement, dressing addition, and aluminum liquid extraction in the cell in different locations of the electrolytic cell according to the electrolysis process and cycle, thus the crane is called Pot Tending Machine (PTM) for aluminum electrolysis. In this regard, in order to realize the fumes collection of carbon block in the mobile state, the principle of negative pressure suction can be used to wrap the source of fumes emitted from the surface of the high-temperature residual anode through the liftable exhaust hood, and lift the fumes through the negative pressure fan suction to the telescopic pipe fixed on the PTM tool. The end of the telescopic pipe is connected with the designed fumes delivery trolley. The fumes delivery trolley moves simultaneously with the PTM in the fixed

flow channel on the workshop wall. The fume is pumped through the flow channel to the adsorption unit device such as cyclone dust removal fixed in the workshop to complete the purification, consequently forming a new collection technology and equipment for mobile fumes.

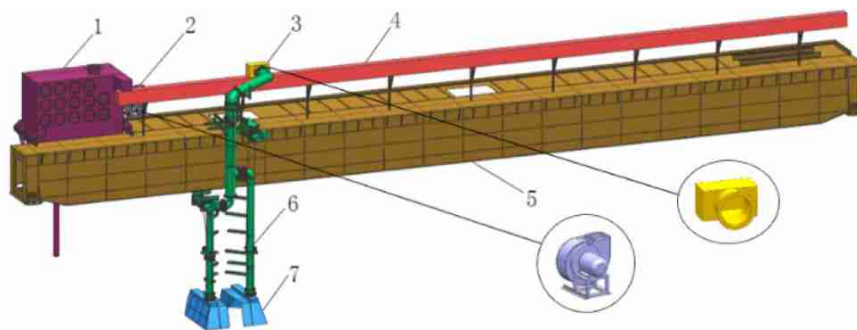
Its structure is shown in Fig. 2. The aluminum electrolysis unorganized fumes collection equipment contains an up-draft exhaust hood, telescopic pipe (supporting winch mechanism), PTM track, flow channel and fumes delivery trolley, purification device, negative pressure fan, and supporting electric control system.

Up-draft exhaust hood structure

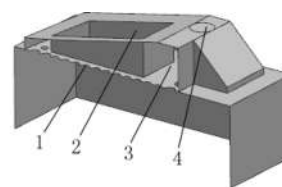
The up-draft exhaust hood is a crucial component for fume collection, and its size should be compatible with the size of the residual anode carbon block. At present, the standard size of residual anode carbon block commonly used in the industry is 1570×660×520 mm, and the residual anode carbon blocks are lifted in pairs during electrolysis. According to the size of the carbon block of the residual anode group and the obstacle avoidance requirements of the anode changing fixture operation, the overall size of the two-flap type exhaust hood used is 2.1×0.8×1.06 m, and the structure of the exhaust hood is shown in Fig. 3. The fumes enter the hood chamber through the hood hole, the fixture holes for telescoping are available for the anode changing fixture to telescope, and the fumes in the hood chamber enter the telescopic pipe through the pipe inlet.

The hood holes are arranged according to the shape of the residual anode group, which is rectangular, and the middle of the hood holes should be reserved for fixture holes for telescoping. According to the requirements of the code [21], the wind speed in the telescopic pipe should not be less than 15 m/s and not more than 28 m/s. The diameter of the hood holes affects the air volume and air velocity in the pipe. To keep the air velocity in the pipe within a suitable range, the diameter of the hood holes is therefore set to 60 mm and 90 mm.

Fig. 2 Aluminum electrolysis unorganized fumes collection equipment

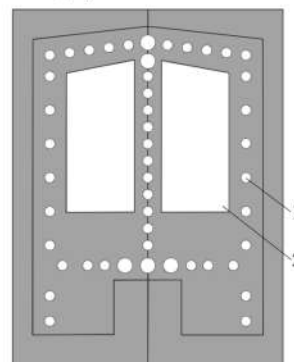


1-purification device 2-negative pressure fan 3-fumes delivery trolley 4-flow channel 5- PTM track 6- telescopic pipe 7-up-draft exhaust hood



1-hood holes 2-fixture holes for telescoping 3-hood chamber 4-pipe inlet

(a)Up-draft exhaust hood



1-hood holes 2-fixture holes for telescoping

(b)Distribution of hood holes

Fig. 3 Up-draft exhaust hood structure

Collection efficiency evaluation index

According to the characteristics of fumes components, the effectiveness of the new collection technology and equipment is evaluated by the collection efficiency index of flue gas and dust respectively.

(1) Flue gas collection efficiency.

On the basis of the reference [22], the flue gas collection efficiency is calculated from Eq. (1)

$$\eta = \frac{QC}{q_m} \times 100\% \tag{1}$$

where η is the flue gas collection efficiency, %; Q is the air volume of the exhaust hood, the hood inlet is the bottom horizontal surface of the exhaust hood, m^3/s ; C is the average concentration of flue gas at the hood inlet, kg/m^3 ; q_m is the volatilization rate of the volatile surface of the flue gas, kg/s .

(2) Dust collection efficiency.

On the basis of the reference [15], the dust collection efficiency is calculated from Eq. (2)

$$\eta_m = \frac{m_b}{m_a} \times 100\% \quad (2)$$

where η_m is the dust collection efficiency, %; m_b is the total mass of dust inhaled from the hood inlet, kg ; m_a is the total mass of dust emitted from the source, kg .

Numerical simulation methods

The basic process of CFD calculations can be viewed as the numerical solution of the nonlinear flow governing equations (mass conservation equation, momentum conservation equation, energy conservation equation) and other subsidiary physical equations in fluid mechanics. Through the above computational process, the distribution of the fundamental physical quantities within the flow field of a complex geometric or complex fluid model with geometric space or time can be obtained [23].

In order to further determine the installation position of the equipment and the negative suction pressure during operation, CFD numerical simulation is applied to an aluminum electrolysis workshop as an example to study the influence law of negative fan pressure P , the distance h between the upper surface of the residual carbon block and the exhaust hood of the equipment installation parameters on the collection efficiency.

Physical model

The space size of the workshop is $75 \times 30 \times 23$ m, taking into account the fumes free drift rate, combined with the size of the exhaust hood, taking into account the calculation efficiency, the calculation domain is taken as $L \times W \times H = 6.1 \times 4.8 \times 4.0$ m, and the original equipment model is simplified, the main pipe is kept and the fine parts are deleted, as a physical model for CFD analysis, as shown in Fig. 4.

Governing equations

The governing equations of the airflow employed are the time-averaged Navier–Stokes equations. After Reynolds averaging, the governing equations of the continuity,

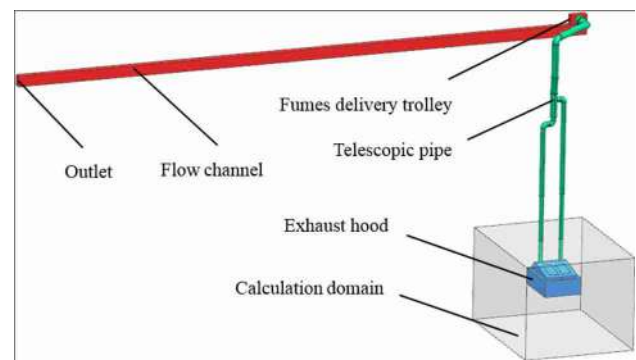


Fig. 4 Physical model

momentum, energy and species are given in tensor forms as follows.

Assuming that the fume is incompressible flow, the governing equations [23] are.

(1) Continuity equation

$$\frac{\partial \rho}{\partial t} + \text{div}(\rho \vec{u}) = 0 \quad (3)$$

where ρ is the density, kg/m^3 ; t is the time, s ; and \vec{u} is the velocity vector, m/s .

(2) Momentum equation

$$\frac{\partial(\rho u_i)}{\partial t} + \text{div}(\rho u_i \vec{u}) = \text{div}(\mu \text{grad } u_i) - \frac{\partial p}{\partial x_i} + S_{u_i} \quad (4)$$

where u_i is the component of the velocity vector, m/s ; μ is the dynamic viscosity, Pa s ; p is the static pressure, Pa ; x_i is the coordinate component; and S_{u_i} is the generalized source term of the momentum conservation equation.

(3) Energy equation

$$\frac{\partial(\rho T)}{\partial t} + \text{div}(\rho \vec{u} T) = \text{div}\left(\frac{k}{c_p} \text{grad } T\right) + S_T \quad (5)$$

where c_p is the specific heat capacity, kJ/kg ; T is the temperature, K ; k is the heat transfer coefficient, $\text{W}/(\text{m}^2 \text{K})$; and S_T is the viscous dissipation term.

(4) Species transport equation

$$\frac{\partial(\rho c_A)}{\partial t} + \text{div}(\rho \vec{u} c_A) = \text{div}(D_A \text{grad}(\rho c_A)) + S_A \quad (6)$$

where c_A is the volume concentration of component A , m^3/m^3 ; D_A is the diffusion coefficient of component A , m^2/s ; S_A is the source term, i.e., the release intensity of component A at any point.

(5) Discrete phase equations of motion.

The DPM is used to simulate the dust motion process [24]. The theory of the Discrete Phase Model is based on

the Euler–Lagrange method, i.e., the Eulerian method is applied to describe the continuous phase of the fluid and the Lagrange method is devoted to describe the discrete phase of the particles [25], where the transport equations of the continuous phase are solved first and then the discrete phase is calculated in Lagrange coordinates [26], taking into account the coupling between the discrete and continuous phases.

The trajectory of the discrete phase particles is obtained by solving the differential equation for the particle forces in Lagrangian coordinates [27]. The equilibrium equation for the particle force [28] is

$$\frac{du_p}{dt} = F_D(u - u_p) + \frac{g_x(\rho_p - \rho)}{\rho_p} \tag{7}$$

where u is the velocity of the continuous phase, m/s; u_p is the velocity of the discrete phase particles, m/s; ρ is the density of the continuous phase, kg/m³; ρ_p is the density of the discrete phase particles, kg/m³; F_D is the drag force per unit mass of the particles, N .

The expression of F_D is

$$F_D = \frac{18\mu C_D Re}{\rho_p d_p^2} \frac{C_D Re}{24} \tag{8}$$

where μ is the continuous-phase dynamic viscosity Pa s; d_p is the discrete-phase particle diameter, mm; Re is the Reynolds number, and C_D is the drag coefficient.

The expression of C_D is

$$C_D = a_1 + \frac{a_2}{Re} + \frac{a_3}{Re} \tag{9}$$

where a_1 , a_2 and a_3 are constants [29], and all take the value of 1 in the context of this paper.

Mesh division and boundary conditions

The unstructured tetrahedral mesh and the prismatic mesh can both have a better fit. For this purpose, ICFM CFD 2021

is used to mesh the carbon block and the exhaust hood with a spacing of 216 mm as an example. It is verified that the number of meshes does not affect the calculation results at about 6 million by the mesh-independence verification (Fig. 5).

The Fluent 2021 solver is applied to carry out the steady-state calculations, and the gravity and energy equations are turned on considering the effects of dust gravity and thermal pressure of the residual carbon block [30], and the RNG k – ϵ model is chosen for the turbulence model [31]. The SIMPLE algorithm is used, and the second-order upwind with a convergence residual of 10^{-6} .

Adopt negative pressure suction, the carbon block is surrounded by natural air inlet, and the surface of the carbon block is the fumes emitting surface, the outlet of the flow channel is the pressure outlet, the initial temperature of the fume is 200 °C, the ambient temperature is 27 °C, the velocity of the fumes emitted from the surface of the residual carbon block after it is pulled out from the electrolysis cell is measured to be 0.284 m/s, and the maximum negative pressure that the fan can provide is 5000 Pa. The boundary conditions of the species transport model are set as shown in Table 1.

The boundary conditions of the DPM are set as shown in Table 2 below. The diameter of the dust particles is measured by a laser particle size analyzer, and the true density of the dust particles is measured by the liquid phase substitution method [32].

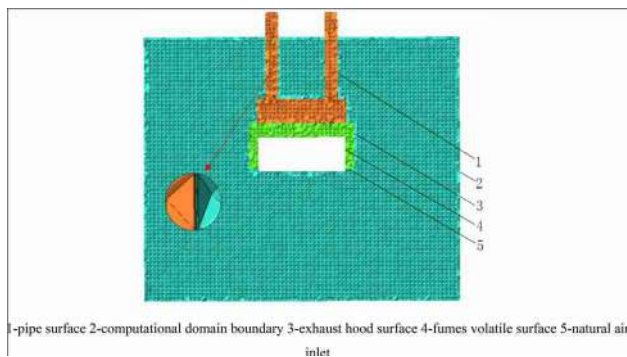


Fig. 5 Schematic diagram of grid division (including boundary layer)

Table 1 Species transport model setup

Name	Type	Parameters
Natural air inlet	Pressure inlet	–
The outlet of the flow channel	Pressure outlet	–3000 – 5000 Pa
Fumes volatile surface	Velocity inlet	0.284 m/s
Exhaust hood and pipe surface	Wall	–
Computational domain boundary	Wall	–

Table 2 Discrete phase model setup

Boundary conditions	Parameters
Injection type	Surface
Mass flow rate	2×10^{-6} kg/s
Particle density	2.5×10^3 kg/m ³
Diameter distribution	Rosin–Rammler
Diameter	0.3–130 μ m
Turbulent dispersion	Discrete random walk model
Outlet	Trap
Computational domain boundary	Escape

Results and discussion

Effect of different negative pressure on collection efficiency

In this regard, the collection efficiency of the equipment is investigated at a distance of 216 mm between the upper surface of the residual carbon block and the exhaust hood when the negative pressure P is 3000 Pa, 3500 Pa, 4000 Pa, 4500 Pa and 5000 Pa, respectively. Using the above simulation scheme, a contour of the flue gas concentration field can be obtained as shown in Fig. 6.

Figures a, b, c, d and e are the flue gas concentration fields at pressures P of 3000 Pa, 3500 Pa, 4000 Pa, 4500 Pa and 5000 Pa, respectively.

As is seen from Fig. 6, when the negative pressure is from 3000 to 4000 Pa, the flue gas escapes from the bottom of the exhaust hood to all around. This indicates that when the negative pressure is small, the thermophoretic force plays a dominant role and the flue gas drifts into the hood chamber under the action of thermal pressure, resulting in a high concentration of flue gas in the hood chamber and the pipes. When the negative pressure is from 4500 to 5000 Pa, the flue gas only partially leaks at the bottom of the exhaust hood. This indicates that when the

negative pressure increases, the effect of wind pressure is greater than the thermal pressure. When the pressure-gradient force increases, the initial momentum of the flue gas increases [33], the flue gas in the hood chamber is more extracted and collected, and the concentration of flue gas in the hood chamber and the pipe is significantly reduced.

As shown in Fig. 7, the dust concentration fields (unit: kg/m^3) from Figures a, b, c, d and e are at negative pressures of $P = 3000$ Pa, 3500 Pa, 4000 Pa, 4500 Pa and 5000 Pa, respectively.

As is seen from Fig. 7, when the negative pressure is from 3000 to 4000 Pa, the dust escapes from the bottom of the exhaust hood under the action of gravity. This indicates that when the negative pressure is small, gravity and buoyancy play a dominant role, and the dust is dispersed in all directions under the action of buoyancy. When the negative pressure is from 4500 to 5000 Pa, the concentration of dust escaping from the surroundings of the exhaust hood is relatively reduced as the negative pressure increases. This indicates that when the negative pressure increases, the pressure-gradient force plays a dominant role, when the dust enters the exhaust hood under the action of wind pressure and is collected, and the escaping dust is relatively reduced.

Figure 8 shows the average concentration of flue gas at the hood inlet and the number of particles captured at the outlet obtained by numerical simulation. As the

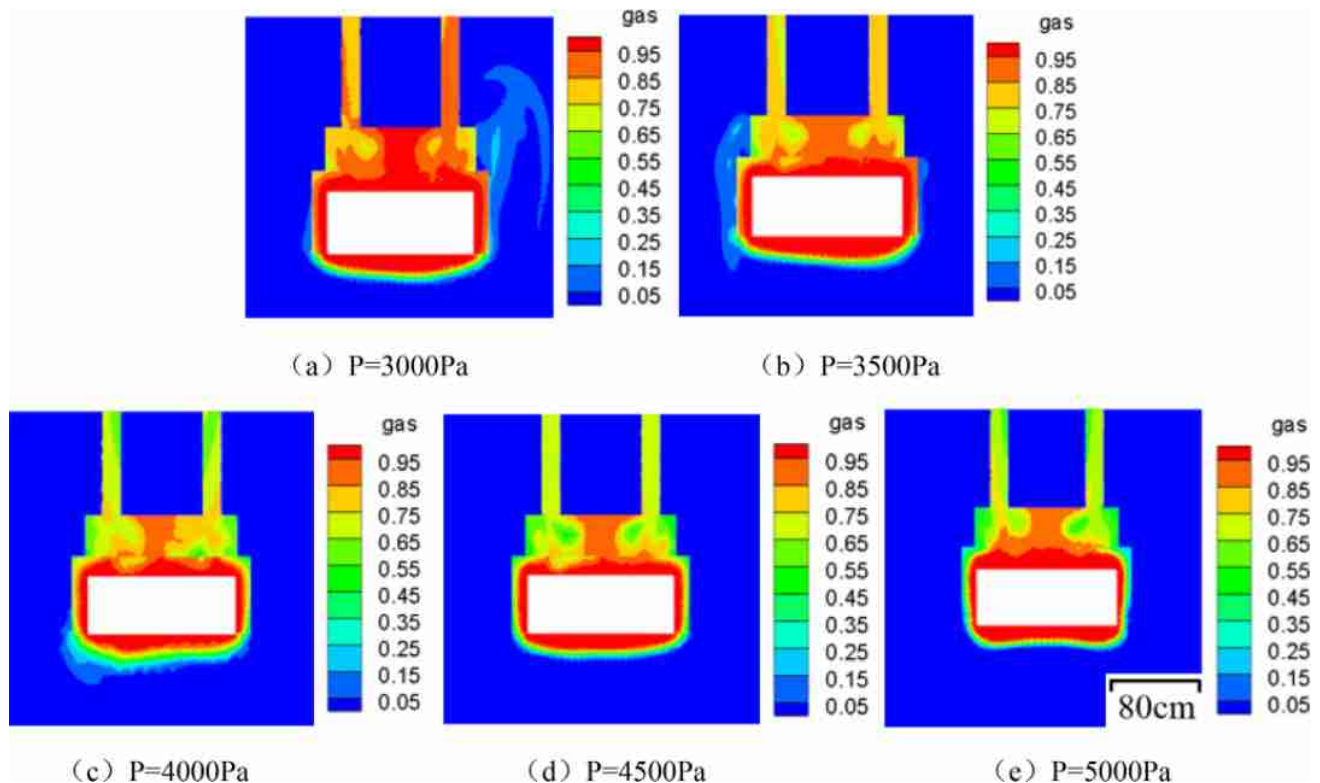


Fig. 6 Flue gas concentration field at different pressure conditions

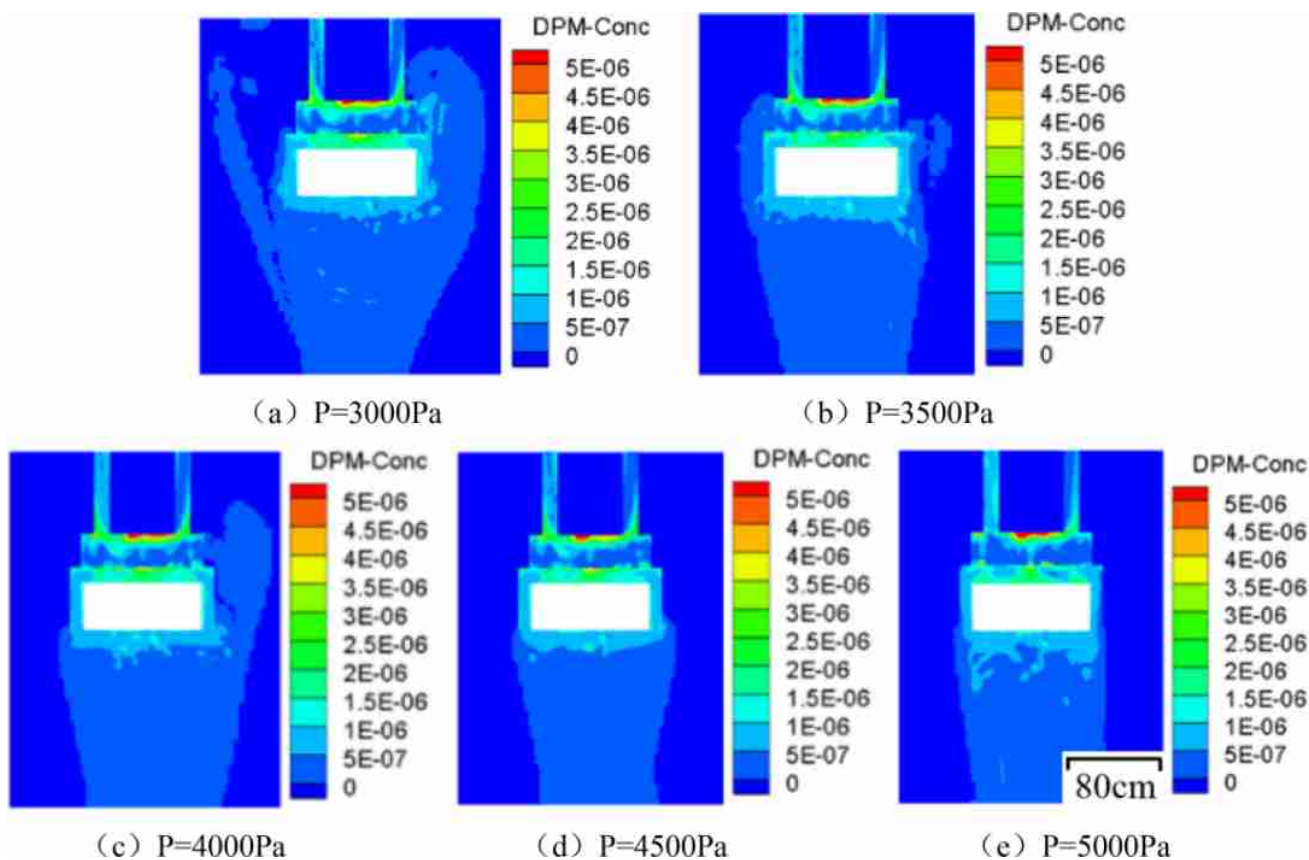
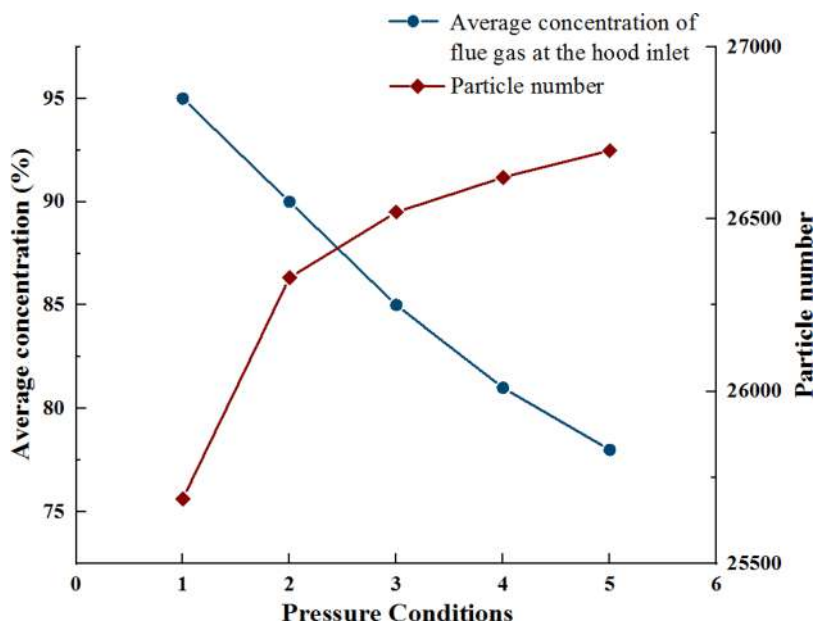


Fig. 7 Dust concentration field at different pressure conditions

Fig. 8 Different pressure conditions



negative pressure of the fan increases, the average concentration of flue gas decreases, and when the negative pressure is 5000 Pa, the average concentration of flue gas is the lowest. Because when the negative pressure is

small, the thermophoretic force plays a dominant role. When the negative pressure increases, the pressure-gradient force increases, the initial momentum of the flue gas increases, and more of the flue gas in the hood chamber

is extracted and collected. As the negative pressure of the fan increases, more dust particles are collected by the equipment, and the maximum number of particles are captured at the outlet when the negative pressure is 5000 Pa. Because when the negative pressure is small, gravity and buoyancy play a dominant role, when the negative pressure increases, the pressure-gradient force plays a dominant role, the dust enters the exhaust hood under the action of wind pressure is collected, and the escaping dust is reduced.

By substituting the data in Fig. 8 into Eqs. (1) and (2), the effect of negative pressure P on the flue gas and dust collection efficiency can be obtained.

As shown in Fig. 9, the horizontal coordinates 1, 2, 3, 4 and 5 are the pressure conditions at the distance $h=216$ mm when $P=3000$ Pa, 3500 Pa, 4000 Pa, 4500 Pa and 5000 Pa respectively, with the increase in negative pressure, the flue gas collection efficiency rises, and when the negative pressure is 5000 Pa, the flue gas collection efficiency is the highest, up to 83.86%. With the increase in negative pressure, the dust collection efficiency rises slowly, and when the negative pressure is 5000 Pa, the dust collection efficiency is the highest, up to 71.65%. When the negative pressure increases, the pressure-gradient force plays a dominant role, which results in an increase in the collection efficiency of flue gas and dust. The dust collection efficiency increases insignificantly with increasing negative pressure, which may be due to the limitations of the equipment structure, resulting in dust deposition on the upper surface of the hood chamber and in the pipes.

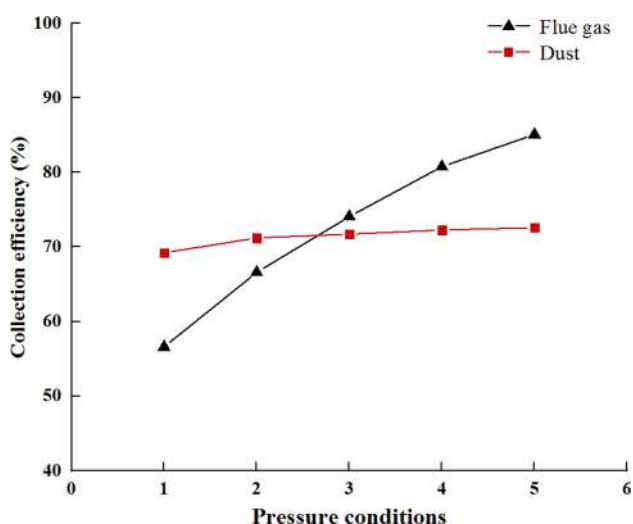


Fig. 9 Flue gas and dust collection efficiency at different pressure conditions

Effect of different distance on collection efficiency

As shown in Fig. 10, from Figures a, b, c, d, e are the flue gas concentration fields of the equipment at the distance $h=96$ mm, 136 mm, 176 mm, 216 mm, 256 mm between the upper surface of the residual carbon block and the exhaust hood at the negative pressure $P=5000$ Pa, respectively.

As is seen from Fig. 10, when the distance between the upper surface of the residual carbon block and the exhaust hood is 96 mm, the concentration of flue gas inside the hood chamber is lower. This is because the distance between the upper surface of the residual carbon block and the exhaust hood is closer, the wind pressure along the resistance loss is lower, the initial momentum of the flue gas is larger, and the flue gas inside the hood chamber is more easily collected. When the distance between the upper surface of the residual carbon block and the exhaust hood is from 136 to 256 mm, as the distance increases, the concentration of flue gas in the hood chamber becomes higher and higher, and at the same time, the flue gas is partially leaked at the bottom of the exhaust hood. This is because the distance between the upper surface of the residual carbon block and the exhaust hood is getting farther and farther, the wind pressure along the resistance loss is increasing, and as the area outside the exhaust hood exposed at the bottom of the carbon block is increasing, the flue gas is influenced by the thermophoretic force to escape from the exhaust hood.

As shown in Fig. 11, from Figures a, b, c, d and e are the dust concentration fields (unit: kg/m^3) of the equipment at the distance $h=96$ mm, 136 mm, 176 mm, 216 mm and 256 mm between the upper surface of the residual carbon block and the exhaust hood at the negative pressure $P=5000$ Pa, respectively.

As can be seen from Fig. 11, the dust escapes relatively more when the distance is 96 mm and 256 mm, and less dust escapes when the distance is 136–216 mm. When the distance between the upper surface of the residual carbon block and the exhaust hood is small, the air volume entering the exhaust hood is insufficient, the initial momentum of the dust is low, which makes it challenging to collect the dust; when the distance between the upper surface of the residual carbon block and the exhaust hood is large, the area of the residual carbon block exposed outside the exhaust hood is more extensive, which causes the dust to escape under the action of buoyancy.

Figure 12 shows the average concentration of flue gas at the hood inlet and the number of particles captured at the outlet obtained by numerical simulation. With the increase in the distance between the upper surface of the residual carbon block and the exhaust hood, the average concentration of flue gas at the hood inlet first decreases and then increases, and when the distance is 176 mm, the average concentration of flue gas at the hood inlet is the

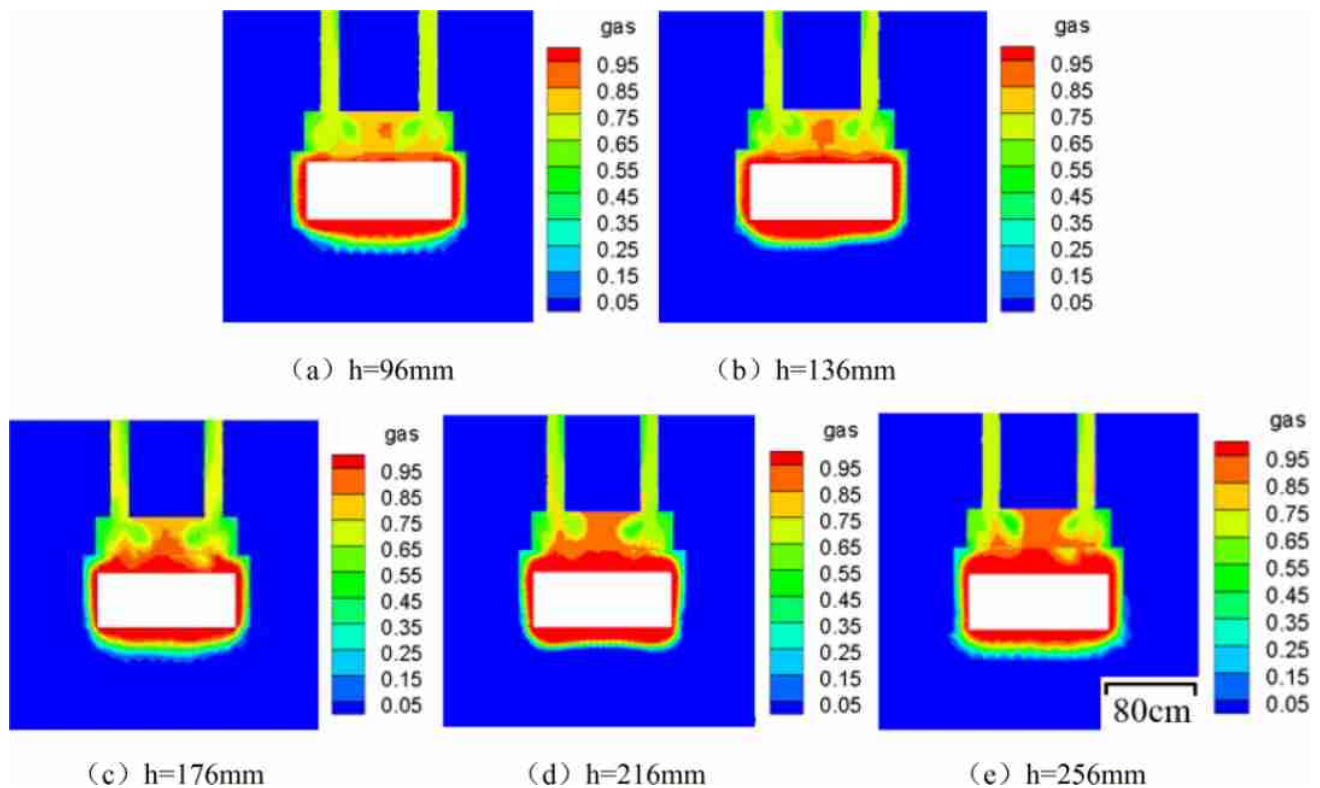


Fig. 10 Flue gas concentration field at different distance conditions

smallest and the collected flue gas is the largest. This is because when the distance between the upper surface of the residual carbon block and the exhaust hood is small, the air volume entering the hood is insufficient and the initial momentum of the flue gas is small, at which time the flue gas escapes under the action of thermophoretic force; when the distance between the upper surface of the residual carbon block and the exhaust hood is large, the residual carbon block exposes more area outside the exhaust hood, thus causing the flue gas to escape under the action of thermophoretic force. With the increase in the distance between the upper surface of the residual carbon block and the exhaust hood, the number of particles captured at the outlet first increases and then decreases, and the number of particles captured at the outlet is the highest when the distance is 176 mm. This is because when the distance between the upper surface of the residual carbon block and the exhaust hood is small, the air volume entering the collection hood is insufficient, and the initial momentum of the dust is small, so the dust escapes under the effect of buoyancy, which makes it difficult to be collected; when the distance between the upper surface of the residual carbon block and the exhaust hood is large, the residual carbon block exposes more area outside the exhaust hood, which causes the dust to escape under the effect of buoyancy.

By substituting the data in Fig. 12 into Eqs. (1) and (2), the effect of distance h on the flue gas and dust collection efficiency can be obtained.

As shown in Fig. 13, the horizontal coordinates 1, 2, 3, 4 and 5 indicate the pressure conditions when the distance between the upper surface of the residual carbon block and the exhaust hood is 96 mm, 136 mm, 176 mm, 216 mm and 256 mm at negative pressure $P = 5000$ Pa, respectively. When the distance between the upper surface of the residual carbon block and the exhaust hood is lower than 176 mm, the air volume entering the hood holes is insufficient, the initial momentum of the flue gas is small, and the flue gas escapes under the action of thermophoretic force at this time, resulting in low flue gas collection efficiency; while when the distance exceeds 176 mm, the surface area of the residual carbon block exposed outside the exhaust hood increases, hence increasing the flue gas dissipation under the action of thermophoretic force. When the distance between the upper surface of the residual carbon block and the exhaust hood is 176 mm, the highest flue gas collection efficiency is achieved, reaching 85.08%. When the distance between the upper surface of the residual carbon block and the exhaust hood is lower than 176 mm, the air volume entering the exhaust hood is insufficient, the initial momentum of the dust is small, and the dust escapes under the action of buoyancy at this



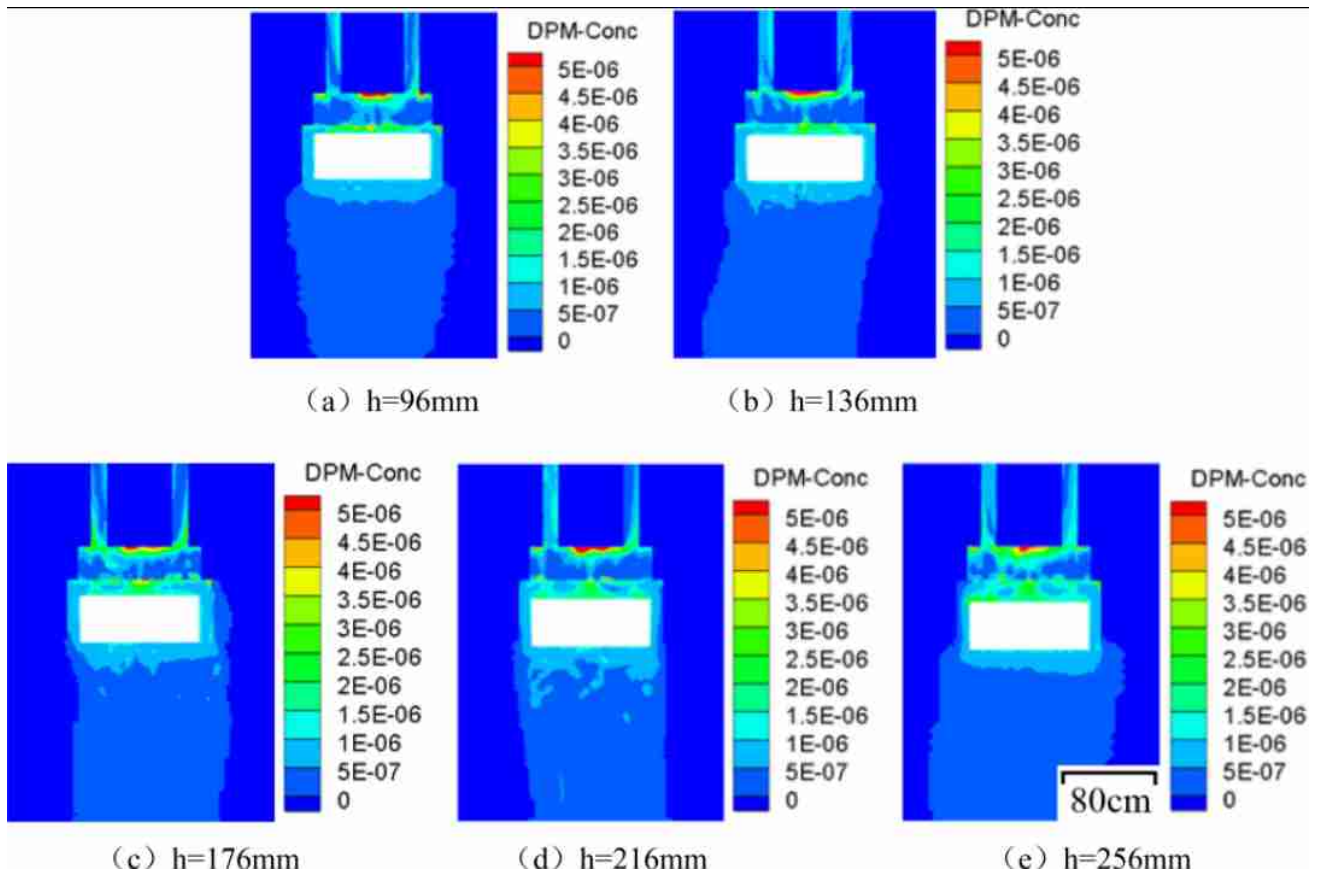


Fig. 11 Dust concentration field at different distance conditions

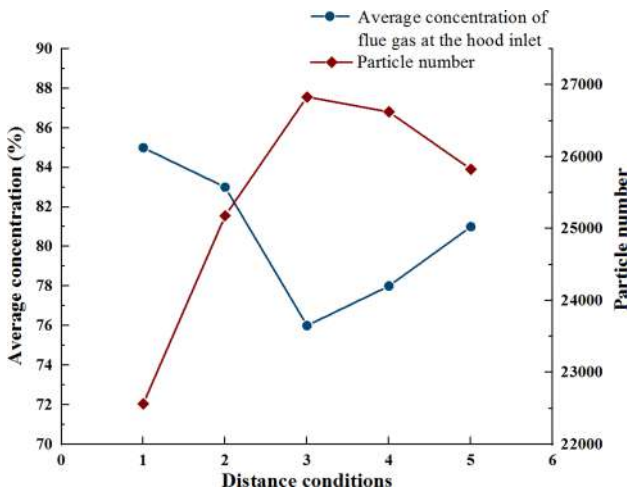


Fig. 12 Different distance conditions

time, resulting in a low dust collection efficiency; and as the distance increases, the surface area of the residual carbon block exposed outside the gas collector increases, so that more dust is dissipated under the action of buoyancy and the collection efficiency is slightly reduced. When

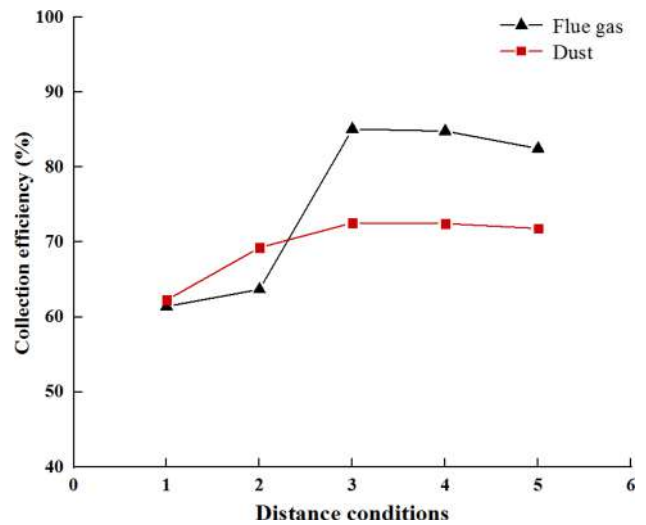


Fig. 13 Flue gas and dust collection efficiency at different distance conditions

the distance between the upper surface of the residual carbon block and the exhaust hood is 176 mm, the dust collection efficiency is the highest, reaching 72.58%.

After the above analysis, it is known that the highest collection efficiency of flue gas and dust is achieved when the negative pressure of the exhaust hood is $P = 5000$ Pa and the distance between the upper surface of the residual carbon block and the exhaust hood is $h = 176$ mm. Therefore, the collection equipment is installed and operated with

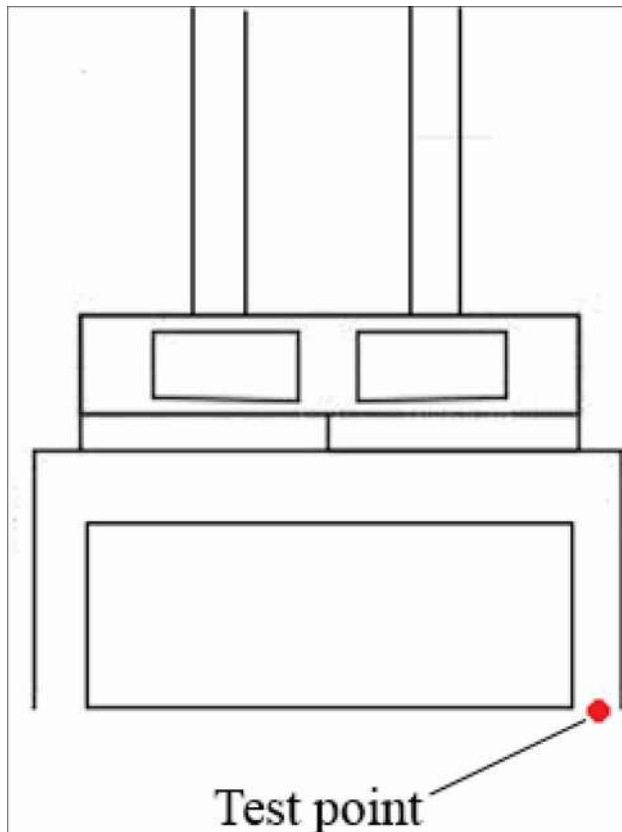


Fig. 14 Distribution of measurement points

these parameters, and experimental tests are conducted. The flue gas and dust concentrations are tested with a gas chromatograph and a dust concentration detector, respectively (Fig. 14).

The experimentally measured data are shown in Table 3.

The collection efficiency obtained from the numerical simulation is compared with the experiment, as shown in Fig. 15

As shown in Fig. 15, the flue gas collection efficiency of the equipment is 82.45% and the dust collection efficiency is 71.72% as measured experimentally, so the new collection equipment can effectively collect unorganized fumes.

Comparing the experimentally measured collection efficiency with the maximum collection efficiency of flue gas and dust in Fig. 13, the error of flue gas collection efficiency is less than 3.1% and the error of dust collection efficiency is less than 1.2%, indicating that the established CFD coupled DPM simulation method has a good agreement with the experimental results.

Summary and limitations

Now we will further provide an extended discussion on the collection efficiency of the aluminum electrolysis unorganized fumes collection equipment influenced by the negative pressure P of the fan and the distance h between the upper surface of the residual carbon block and the exhaust hood. The collection efficiency of flue gas and dust increases as the negative pressure increases, and the collection efficiency of flue gas increases more significantly than the collection efficiency of dust. When the negative pressure is 5000 Pa, the flue gas and dust collection efficiency are the greatest. Furthermore, as the distance h increases, the average concentration of flue gas at the hood inlet first decreases and

Table 3 Test point data

Number of experiments	Flue gas concentration in natural state (mg/m^3)	Dust concentration in natural state (mg/m^3)	Flue gas concentration after collection (mg/m^3)	Dust concentration after collection (mg/m^3)
1	200.36	12.41	35.28	3.48
2	201.28	13.25	34.66	3.21
3	200.85	12.69	35.11	3.43
4	202.53	13.68	36.11	3.82
5	199.76	12.12	34.85	3.13
6	201.58	13.73	36.73	2.97
7	202.34	11.28	33.86	3.86
8	198.67	12.33	35.86	4.23
9	200.39	11.34	34.71	3.34
10	200.87	12.07	35.43	3.85
Average	200.86	12.49	35.26	3.53



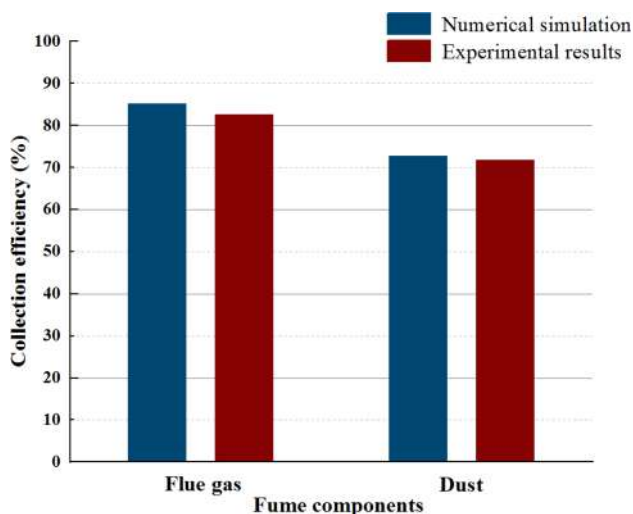


Fig. 15 Numerical simulation and experimental comparison

then increases, the number of particles captured at the outlet first increases and then decreases, and when the distance is 176 mm, the average concentration of flue gas at the hood inlet is the smallest, the number of particles captured at the outlet is the greatest, and the flue gas and dust collection efficiency are the greatest. Therefore, appropriately increasing the negative pressure of the fan within the allowed range, while reasonably controlling the distance between the residual carbon block and the exhaust hood can improve the collection efficiency of the flue gas and dust. Previous studies [34] have also found that the height of the exhaust hood from the pollution source and the exhaust hood suction pressure can affect the collection efficiency of aluminum electrolysis fumes, and increasing the suction pressure can improve the collection efficiency of fumes at the optimal exhaust hood height. In general, among the two factors in this study, the negative pressure P and distance h have some influence on the performance of the aluminum electrolysis unorganized fumes collection equipment. The variation of negative pressure P and distance h has a relatively obvious effect on the collection efficiency of flue gas. In contrast, the effect on the collection efficiency of dust is relatively less significant.

Nevertheless, the limitations of our current study are as follows:

Only the effect of negative pressure P on the collection efficiency of unorganized fumes from aluminum electrolysis at a fixed distance h and the effect of distance h on the collection efficiency of unorganized fumes from aluminum electrolysis at a fixed negative pressure P were discussed, and the collection efficiency of flue gas and dust did not reach the optimal value because of the structural limitation of the equipment. Next, the interaction effects of two or more factors on the collection efficiency can be investigated, the structural parameters of the equipment can be improved, and

multi-objective optimization for maximizing the collection efficiency can be carried out.

Conclusions

In this paper, we proposed an aluminum electrolysis unorganized fumes collection technology and mobile fumes collection equipment based on negative pressure suction, which could collect the unorganized fumes emitted from the residual carbon block in the process of lifting and transiting. The performance of the new collection equipment was investigated, the influence of the negative pressure P of the fan and the distance h between the upper surface of the residual carbon block and the exhaust hood on the collection efficiency was investigated. The main conclusions obtained are as follows:

When the negative pressure P is small, the thermophoretic force and buoyancy play a dominant role and more flue gas and dust escape. When the negative pressure P increases, the pressure-gradient force plays a dominant role and the collection efficiency of flue gas and dust increases. When the distance h is small, the air volume into the exhaust hood is insufficient and the initial momentum of the flue gas and dust is low, resulting in more flue gas and dust escaping. When the distance h is larger, the residual carbon block exposes more area outside the exhaust hood, and the flue gas is influenced by thermophoretic force and dust is influenced by buoyancy to escape.

Among the two factors in this study, the negative pressure P and distance h have some influence on the performance of the aluminum electrolysis unorganized fumes collection equipment. The variation of negative pressure P and distance h has a relatively obvious effect on the collection efficiency of flue gas. In contrast, the effect on the collection efficiency of dust is relatively less significant. The collection efficiency of flue gas and dust increased with the increase in negative pressure P . The collection efficiency of flue gas and dust increased at first and then decreased with the increase in the distance h . When the negative pressure $P = 5000$ Pa and the distance between the upper surface of the residual carbon block and the exhaust hood $h = 176$ mm, the collection efficiency of flue gas and dust is the highest, and the collection efficiency of flue gas is 85.08% and the collection efficiency of dust is 72.58% at this time.

The influencing factors of the equipment's flue gas and dust collection efficiency are analyzed and experiments are carried out. The error of flue gas collection efficiency is less than 3.0% and the error of dust collection efficiency is less than 1.0%. The simulation and experimental results have a good agreement, indicating that the numerical simulation results can be used as a reference basis for theoretical analysis.



Funding This research was completed with the support of the Key Research and Development Program of Hunan Province (2022GK2065) and the Scientific Research Program of Education Department of Hunan Province (20A157).

Data availability Data sharing not applicable to this article as no datasets were generated or analyzed during the current study.

Declarations

Conflict of interest The authors declare that they have no conflict of interest.

References

- Cheng, Q.W., Yu, S.R.: Promotion and inhibition of overcapacity in the electrolytic aluminum industry: based on the perspective of land resource and environmental regulation. *J. Central South Univ.* **24**(4), 107–116 (2018)
- Zhang, Y.L., Sun, M.X., Hong, J.L., et al.: Environmental footprint of aluminum production in China. *J. Clean. Prod.* **133**, 1242–1251 (2016)
- CSY, 2004e2014. China Statistical Yearbook. China Statistics Press, Beijing
- National Bureau of Statistics. Statistics on production of primary aluminum and alumina [J/OL]. National Bureau of Statistics (2021-01-17) [2021-03-09]
- Liu, F.Q.: Review & outlook of Chinese aluminum industry[C]. International Tar Association 2020 Annual Conference. Webinar (2020)
- Yu, B.Y., Zhao, Z.H., Zhang, S., et al.: Technological development pathway for a low-carbon primary aluminum industry in China. *Technol. Forecast. Soc. Chang.* **173**, 1–15 (2021)
- Liu, F.Q., Qiu, D.F., Gu, S.Q., et al.: Analysis of competitiveness of China's aluminum industry in the world and its development trend. *Chin. J. Eng.* **44**(4), 561–572 (2022)
- Liang, X.M., Zhang, S.J.: *Modern Aluminum Electrolysis Production Technology and Management*. Central South University Press, Changsha (2011)
- Zhou, K.C., He, Y., Li, Z.Y., et al.: Research progress of inert anode materials and technology for aluminum electrolysis. *Chin. J. Nonferrous Metals* **31**(11), 3010–3023 (2021)
- Li, S.P., Niu, L.P., Qiang, Y., et al.: Trajectory, driving forces, and mitigation potential of energy-related greenhouse gas (GHG) emissions in China's primary aluminum industry. *Energy* **239**, 1–11 (2022)
- Zhang, Y.S., Yan, Q., Wang, J., et al.: Emission characteristics and potential toxicity of polycyclic aromatic hydrocarbons in particulate matter from the rebaked anode industry. *Sci. Total Environ.* **722**, 137–177 (2020)
- Chen, J.C., Chen, Q.S.: Preliminary exploration on effect of aluminum electrolysis fume upon plant air and human health. *Environ. Sci. Technol.* **34**(S2), 444–446 (2011)
- Wannaz, E., Rodriguez, J., Wolfsberger, T., et al.: Accumulation of aluminium and physiological status of tree foliage in the vicinity of a large aluminium smelter. *Sci. World J.* (2012). <https://doi.org/10.1100/2012/865927>
- Li, X., Yang, Y., Xu, X., et al.: Air pollution from polycyclic aromatic hydrocarbons generated by human activities and their health effects in China. *J. Clean. Prod.* **112**, 1360–1367 (2016)
- Liu, Y., Xia, T.J., Wang, Y., et al.: Simulation and experimental investigation of dust-collecting performances of different dust exhaust hoods. *J. Air Waste Manag. Assoc.* **70**(12), 1367–1377 (2020)
- Lin, D.J., Li, L.F., Zhou, H.: Numerical simulation for the welding fume collection with the cyclone air curtain exhausting hood. *J. Saf. Environ.* **19**(1), 226–231 (2019)
- Jing, D.J., Jia, X., Ge, S.C., et al.: Numerical simulation and experimental study of vortex blowing suction dust control in a coal yard with multiple dust production points. *Powder Technol.* **388**, 554–565 (2021)
- Wang, S.P., Wang, H.N., Bian, Y.L.: Numerical simulation of airflow field of local exhaust hood used in aluminum electrolysis anode scrap cleaning. *J. Shenyang Jianzhu Univ.* **27**(1), 157–162 (2011)
- Verin, V., Bouhabila, E.H., Neveu, J., et al.: Potroom HF emission reduction by anode inert tray technology performance of ALRO industrial 1st of class. In: Ratvik, A.P. (ed.) *Light Metals. The Minerals, Metals & Materials Society, United States of America* (2017)
- Song, H.C., Kong, Y.: Analysis and measures of fluoride inorganizing emission from butts in pot rooms. *Light Metals* **4**, 20–23 (2018)
- GB51020-2014: Code for Design of Ventilation Dedusting and Fume Scrubbing of Aluminum Smelter. China Planning Press, Beijing (2014)
- Zheng, H.C., Dang, X.Q., Li, S.J., et al.: Selection and optimization of VOCs exhaust gas collection method inprinting process. *Chin. J. Environ. Eng.* **14**(10), 2786–2795 (2020)
- Wang, F.J.: *Computational Fluid Dynamics Analysis: Principles and Applications of CFD Software*. Tsinghua University Press, Beijing (2004)
- Song, S.Z., Zhou, G., Duan, J.J., et al.: CFD simulation of multiphase and multi-component diffusion of air-dust-gas in a fully mechanized mining face. *Environ. Sci. Pollut. Res.* **28**, 18260–18275 (2021)
- Eveline, L.T., Pawel, K., Boris, V.B., et al.: A numerical study of flow field and particle deposition in nasal channels with deviant geometry. *Eng. Appl. Comput. Fluid Mech.* **15**(1), 180–193 (2021)
- Jiang, Z.A., Deng, Q.L., Shi, X.X., et al.: Numerical simulation of dust mass concentration distribution in screening workshop of asbestos concentrator. *J. Hunan Univ.* **44**(12), 135–141 (2017)
- Li, J.Y., Xu, L.S., Xu, M.: Flow characteristic analysis of grout in new type differential pressure densimeter based on CFD–DPM coupling method. *J. Central South Univ.* **48**(5), 1308–1315 (2017)
- Liu, X., Yang, Y., Wang, Z., et al.: CFD modeling of alumina diffusion and distribution in aluminum smelting cells. In: Chesonis, C. (ed.) *Light Metals 2019*. Springer, Switzerland (2019)
- Fan, H.: *The Research of Air Entrainment and Particle Movement Characteristic in Free Falling Particle Stream*. X'ian University of Architecture and Technology, X'ian (2015)
- Xiong, R., Liu, K.Q., Sun, G.C., et al.: Integrated technology and equipment for deep cleaning of high temperature flue gas and recovery of high-grade waste heat. *J. Eng. Thermophys.* **40**(6), 1418–1425 (2019)
- Mao, Y.Q., Pu, W.H., Cai, L., et al.: Numerical simulation of the particle-wall collision strength and swirling effect on the performance of the axial flow cyclone separator. *Int. J. Chem. Reactor Eng.* **19**(10), 1009–1022 (2021)
- Liu, X.C.: *Cleaning Technology for Fluorine-containing Flue Gas Control in Electrolytic Aluminum Process Based on Bag Filter*. Donghua University, Shanghai (2019)
- Huang, Y.Q., Lu, K., Guo, J.W.: Study on ventilation performance of lateral exhaust hood under the influence of two high-temperature buoyant jets. *Build. Environ.* **177**, 106849 (2020)



34. Li, F.Q.: Study on the Control of Air Contaminants in Smelting Workshop Based on CFD Technology. Hunan University of Technology, Zhuzhou (2016)

Publisher's Note Springer Nature remains neutral with regard to jurisdictional claims in published maps and institutional affiliations.

Springer Nature or its licensor holds exclusive rights to this article under a publishing agreement with the author(s) or other rightsholder(s); author self-archiving of the accepted manuscript version of this article is solely governed by the terms of such publishing agreement and applicable law.





NO and NO₂ emissions of waste tire pyrolysis oil (TPO) blended with diesel in a flameless combustor

Raul G. Chumpitaz¹ · Jean A. Barbosa² · José C. Andrade² · Cláudia G. Azevedo³ · Ricardo A. Andrade² · Christian J. R. Coronado¹

Received: 12 May 2022 / Accepted: 7 September 2022 / Published online: 20 September 2022
© The Author(s), under exclusive licence to Islamic Azad University 2022

Abstract

Combustion systems can use tire pyrolysis oil (TPO) due to its high energy content. The amount of nitrogen and sulfur present in the TPO should result in NO_x and SO₂ emissions when combustion occurs. A flameless combustion regime can reduce pollutant emissions, mainly NO_x, with greater thermal efficiency. This work aims to analyze the NO and NO₂ emission in different diesel fuel mixtures with TPO, 5% (TPO5), and 10% (TPO10) by mass, in a flameless regime. A combustor was used operating with a maximum heat input of 13 kW and an effervescent injector promoting an average Sauter diameter of $33.89 \pm 3.77 \mu\text{m}$. The uniform temperature profile within the combustor characterizes the flameless combustion regime that was reached after 50 min for diesel and after 40 min for TPO5 and TPO10 from the ignition. TPO5 and TPO10 have similar NO emissions in flameless combustion. The NO₂ emission increases with the TPO content in the mixture.

Keywords Pyrolysis oil · Waste tires · Diesel · Flameless · Emissions

Introduction

In 2019, the production of tires was 5 million tons [1]. This production would eventually become undesirable waste without proper treatment, which could become an environmental problem. In the same year, almost 95% of the waste tire were used in energy recovery, recycling, civil engineering application, and other minor applications, including pyrolysis [2]. Pyrolysis is a thermal degradation process in an inert ambient, resulting in fuel gas, fuel oil, and solid waste as products [3–5]. Tire pyrolysis oil (TPO) has the potential to be used in combustion systems because of its calorific value and physicochemical properties that are similar to diesel [6, 7]. Even though its great potential, TPO has

the drawback of having a high sulfur and nitrogen content that will generate pollutant emissions, such as NO_x and SO₂, when used in a combustion process [5, 7].

William et al. [7] measured the gas emissions of TPO in a combustor chamber. Their measurements show that TPO has higher emissions of NO_x and SO₂ than pure diesel due to the nitrogen and sulfur content in TPO. Frigo et al. [5] use a single-cylinder diesel engine to study the blends of TPO with diesel in 20% and 40% of TPO. When the engine is at full load and 3000 rpm, the NO_x emissions were lower for the TPO blends compared to pure diesel, and with blends of 50%, the emissions were practically the same as pure diesel. They claimed that this was due to the increase in the ignition delay, resulting in lower pressure and temperature combustion. In another study, Murugan et al. [6] analyzed the performance characteristics of TPO blended with diesel in 10%, 30%, and 50% in a single-cylinder diesel engine. Their results show that in brake power below 3.25 kW, the mixture of 10% of TPO has higher emissions of NO_x than the pure diesel, and in brake powers above 3.25 kW, the NO_x emission is practically the same. For the other blends, NO_x emissions increase with the brake power. In aeronautical applications, the emissions of TPO blended with kerosene in a small gas turbine were analyzed by Suchocki et al. [4], which shows that the emissions of NO_x increase with the

✉ Jean A. Barbosa
jean.barbosa@inpe.br

¹ Mechanical Engineering Institute–IEM, Federal University of Itajubá–UNIFEI, BPS Ave. 1303, Itajubá, MG CEP 37500903, Brazil

² Combustion and Propulsion Laboratory, National Space Research Institute, Cachoeira Paulista, SP CEP 12630000, Brazil

³ São Paulo State University–UNESP, Campus of Rosana, Barrageiros Ave. 1881, Rosana, SP CEP 19274000, Brazil



TPO content in the mixture; however, the SO_2 emission decreases with the TPO content.

One way to reduce pollutant combustion emissions, especially NO_x , is through a flameless regime [8–12]. Flameless combustion regime has received several acronyms over the years, such as HiTAC (high-temperature air combustion) [13, 14], Flameless Oxidation (FLOX) [15, 16], CDC (colorless distributed combustion) [17, 18], and MILD (moderate or intense low oxygen diffusion) combustion [19, 20]. In all these cases, the recirculation of exhaust gases within the combustion chamber characterizes the flameless regime, resulting in a higher turbulence level than conventional combustion [19, 21, 22]. In addition, the injection of the oxidizer at high temperatures leads to a lean, stable, and distributed reaction throughout the combustion chamber, obtaining a homogeneous temperature profile inside it [23]. The higher level of turbulence increases fuel's residence time to a value greater than the chemical time. This residence time allows the fuel to burn completely inside the combustion chamber, which results in high-efficiency combustion. NO_x emissions in MILD combustion were studied numerically by Mohamed and Hmaeid [24], who concluded that the NO_x emission after complete combustion depends slightly on the mixing combustion.

Therefore, this work's goal is to measure the NO and NO_2 emissions of TPO with Diesel, in 5% and 10% on a mass basis, in a combustion chamber that operates in a flameless regime which was built based on the acquired knowledge of the previous works of this research group [25, 26] and will operate with a power input of 13 kW. An effervescent

injector will atomize the fuel. A homogeneous temperature profile within the combustion chamber indicates the achievement of a flameless regime. Eleven thermocouples type K placed along with the combustion chamber measures the temperature profile. The chemiluminescence analyzer measures the emissions of NO and NO_2 during the entire test.

Experimental

Figure 1 shows the experimental setup. A 32 HP Schulz air compressor provides the necessary combustion air. Nitrogen pressurizes the fuel's tank, and synthetic air is the atomization gas. An effervescent injector makes the fuel mixture atomization. It consists of a twin fluid atomizer with an internal mix.

Figure 2 presents a scheme of the effervescent injector. The injector has a length of 40 mm and diameter of 27 mm and comprises two concentric regions. The inner region with a diameter of 6.35 mm is for the fuel. The outer is for the atomization's air and has a diameter of 19 mm. The inlet of the atomization air also has a diameter of 6.35 mm. The air was injected into the fuel by two lines of 4 concentric aeration holes placed at the inner tube. The aeration holes have a diameter of 0.5 mm. The exit nozzle has a diameter of 0.5 mm.

The stainless-steel combustion chamber has a diameter of 130 mm and a length of 500 mm. Figure 3 depicts a scheme of the combustion chamber. It has two observation windows of ROBAX[®] ceramic glass. The combustor was isolated by



Fig. 1 Experimental setup

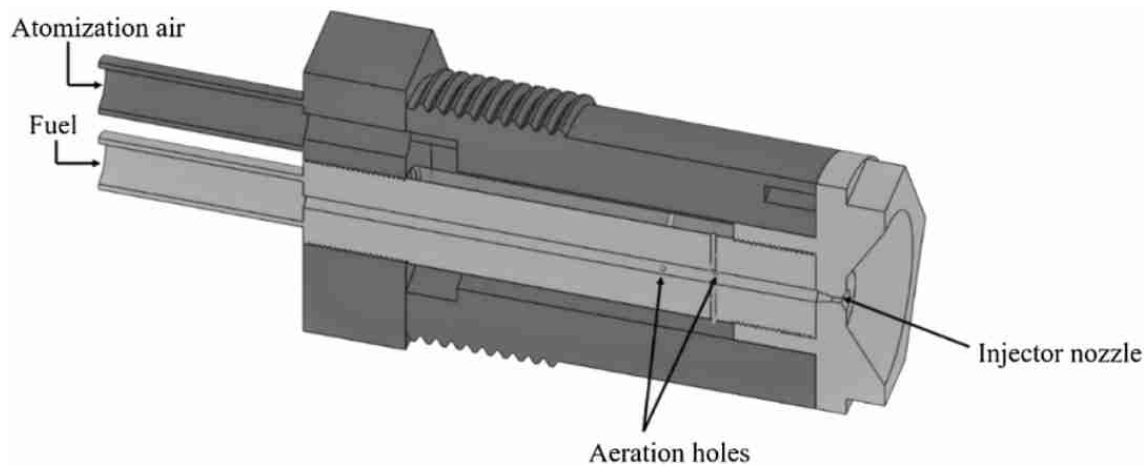


Fig. 2 Scheme of the effervescent injector

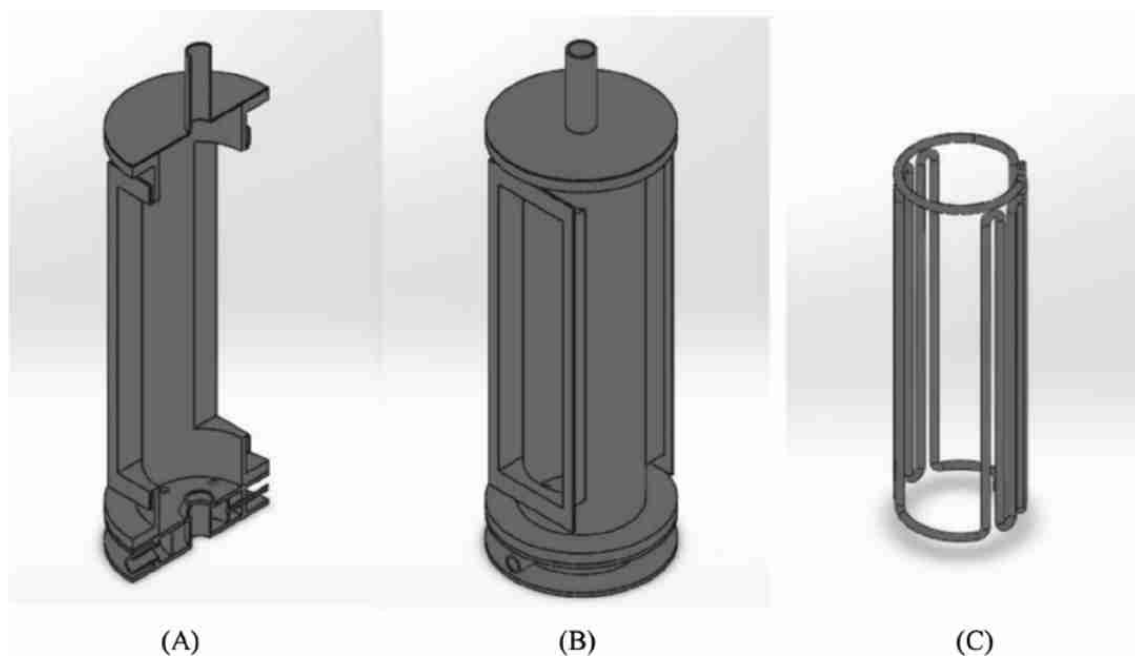


Fig. 3 Scheme of the combustion chamber. **A** Cross section of the combustion chamber; **B** combustion chamber; **C** heat exchanger

a ceramic blanket to minimize heat loss to the environment. The combustion air passes through a 9 mm diameter serpentine welded in the outlet wall before entering the combustor. This serpentine acts like a heat exchanger and uses the generated heat inside the combustor to heat the combustion air to the desired temperature. The injector is concentric with the combustor and placed at the bottom of it. The combustion air enters through 6 holes of 1.5 mm diameter equally spaced radially from the fuel injection center.

A National LabVIEW software interface records temperature and gas emissions during the tests. The

temperature profile inside the combustion chamber was measured by 11 thermocouples K type. One is placed at the bottom of the combustor; the other ten thermocouples are placed along the combustion chamber, equally spaced by 50 mm. The top of the combustion chamber has a 28 mm diameter duct with a length of 100 mm for gas exhaustion. A stainless-steel probe placed at the exhaustion duct withdraws the emissions gases samples. An electric plug spark of 450 W placed at the bottom of the chamber ignites the fuel/oxidant mixture. Table 1 presents the range and uncertainty of all measuring instruments.

Table 1 Range and uncertainty of the measuring instruments

Parameters	Measure instrument	Ranges	Accuracy* (%)
Atomization air mass flow rate	GFM	0–5 l/min	±1
Combustion air mass flow rate	Rotameter	0–200 l/min	±5
Fuel mass flow rate	Rotameter	0–5 l/min	±5
Temperature	K-type thermocouple	– 200–1260 °C	±0.1
Injector Pressure	Pressure transducer	0–10 bar	±0.5
NO, and NO ₂ concentration	Chemiluminescence analyzer	0–5000 ppm	±3

*The accuracy is in full scale

Table 2 Properties of Diesel and TPO [27]

Property	TPO	Diesel
Autoignition temperature(K)	–	498
Density (kg/m ³) at 293 K	920.7	820–865
Viscosity (cSt) at 413 K	5.153	2.5–5.5
Carbon (wt%)	87.1	86.499
Hydrogen (wt%)	9.65	13.5
Nitrogen (wt%)	0.6	–
Sulfur (wt%)	0.89	<0.001
Oxygen (wt%)	1.76	–
Ash (wt%)	<0.01	–
Higher heating value (MJ/kg)	42.015	46
Lower heating value (MJ/kg)	39.891	43

Results and discussion

Test conditions

The fuels tested are diesel with low sulfur content with maximum value of 10 ppm, and mixtures with TPO in 5 and 10% on a mass basis. Table 2 presents the physical–chemical properties of diesel and TPO. A previous work [27] measured the TPO's physical–chemical properties used here.

Atomization efficiency is fundamental in the combustion of liquid fuels. Atomization should be efficient to promote vaporization, mixing, and fuel combustion inside the combustion chamber [28]. In an effervescent atomizer, the air is forced directly into the liquid fuel inside the mixing chamber inner to the injector. It creates pressurized “bubbles” that quickly expand when it passes through the exit nozzle, and it will break the liquid fuel into a fine spray. The advantages of this injector are that it can produce homogenous spray in

an ample range of operations and use a smaller quantity of atomizer air than the other types of injectors, and its performance is insensitive to the fluid viscosity [29, 30].

Atomization efficiency is quantified through the Sauter mean diameter (SMD) together with the measurement span in a specific air–liquid mass ratio (ALR). A Malvern's Spraytech© with an accuracy of ± 1% in full scale measured the SMD. Table 3 presents the atomization parameters. It was considered an average value for SMD, span, and cone angle in the three tested fuels because the difference between them is in the second decimal place.

At the beginning of the tests, the combustion chamber operates in a conventional regime with stoichiometric proportion. In this regime, the combustion air was heated up through the combustor walls until reaches the fuel's autoignition temperature. To achieve flameless combustion, it is also necessary to increase the equivalence ratio (λ). For that, the air combustion volumetric rate increases, consequently, the inlet momentum rate inside the combustion chamber. The latter increases entrainment and recirculation inside the combustion chamber, parameters necessary for achieving flameless combustion [21, 31, 32]. Also, inlet momentum will affect the residence time [33]. Indeed, the characteristic length will increase with the recirculation inside the combustor resulting in a high residence time. The total inlet momentum rate can be calculated as

$$M = (\dot{m}_l + \dot{m}_g)v + \dot{m}_{air}v_{CA} \quad (1)$$

\dot{m}_l and \dot{m}_g are the injector's fuel and air mass flow rates, respectively. It was considered that the liquid and the air at the injector have the same velocity v . \dot{m}_{air} and v_{CA} are the mass flow rate and velocity of the combustion air, respectively. As $v_{CA} \gg v$, combustion air velocity controls the total inlet momentum rate.

Table 3 Atomization parameters

Fuel	P_{air} (bar)	P_{liq} (bar)	ALR (kg/kg)	SMD (μ m)	Span (-)	Cone angle (°)
Diesel	0.25	0.19	0.191	33.89	3.77	18
TPO5	0.29	0.20	0.190			
TPO10	0.34	0.28	0.192			



Another important parameter in the flameless combustion regime is the combustor thermal input because the amount of injected fuel is proportional to the average temperature inside the combustor [33]. However, the recirculation will spread the reaction along the combustor, and the temperature will not increase anymore. Thermal input can be calculated by the fuel mass flow rate (\dot{m}_f) multiplied by the low heat value. Table 4 shows the test parameters.

Flameless regime characterization

The temperature profile measurement in the combustion chamber characterizes the flameless regime. Figure 4 presents the temperature profile for the three different fuels tested. AC is the combustion air thermocouple, and the number of the other thermocouples (TC_XX) shows their axial locations (in mm) on the combustion chamber, with reference at the bottom. The thermocouples are near the combustor wall where the temperature is lower than the center because of the system heat loss. So, when these thermocouples reach a homogenous temperature, it is possible to say that the reaction is homogeneous throughout the entire combustion chamber.

Before flameless regime achievement, the combustion chamber passes through two phases: conventional and transition. The Supplemental material has photographs of the fuel’s combustion in the different stages (Fig. 4A–C). In the first phase, the temperature grows up with time, as shown on the left side of each figure in Fig. 4. Figure 4 shows that the temperature of the AC rises with a different rate than the others. AC is at the supply line of the combustion air (bottom of the combustor), so the increase in temperature in this location comes from the heat exchange presented in Fig. 3C. The heat generated in the combustor heats by conduction of the serpentine that carries the combustion air. Therefore, this stage can be called as “heat up stage” in this experimental apparatus.

The other thermocouples are inside the combustion chamber where the combustion actuals occur. Hence, it should be elevated temperatures gradients and an accentuated temperature increase rate, even though these temperatures are lower than the actual flame temperature because they are near the wall and not in the flame itself due to heat loss and the recirculation inside the combustor. However, once the flameless regime is achieved, the difference between these temperatures reduces to a maximum value of 50 K [33–35].

Table 4 Test parameters

Fuel	\dot{m}_f (g/s)	λ (-)	Thermal input (kW)	\dot{m}_{air} (kg/s)	v_{CA} (m/s)	M (N)
Diesel	0.244	3.66	10.49	0.19	136.41	26.30
TPO5	0.303	4.54	13.01	0.14	97.32	13.39
TPO10	0.280	4.17	12.01	0.23	165.52	38.73

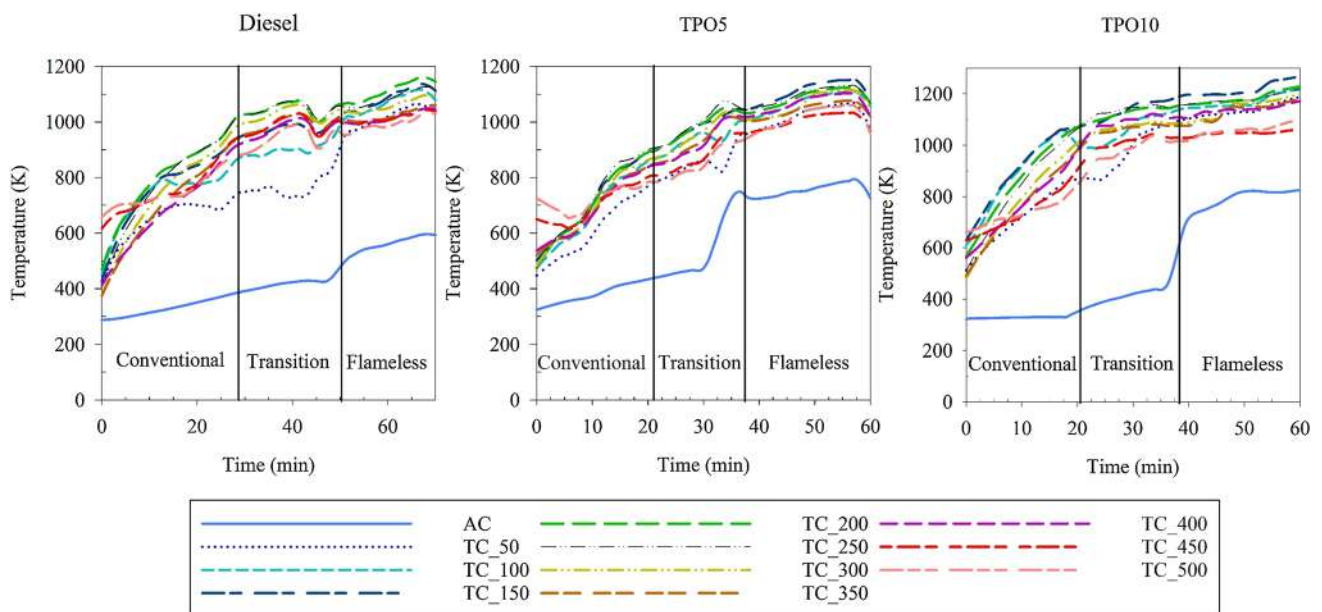


Fig. 4 Temperature profile in the combustion chamber for different test fuels. Thermocouples are placed near the combustor chamber’s wall

Therefore, if the temperature near the wall is constant along the combustor, the reaction is already homogenized inside it.

In the transition stage, the combustion chamber has almost all the necessary parameters to achieve flameless conditions, i.e., high recirculation rate and an air combustion temperature above the fuel auto-ignition temperature. Figure 4 shows that in the transition stage, the air combustion temperature is near the auto-ignition for all fuels, so it is necessary to increase the recirculation rate by raising the air combustion velocity. This phenomenon is shown in Fig. 4 by the sudden increase in the AC for all tested fuels. With the increment of the air combustion velocity, more mass is injected into the combustor resulting in a sudden elevation in AC's temperature.

The flameless regime was achieved with a combustion air temperature of 500 K (above the auto-ignition temperature of the tested fuels) and a high equivalence ratio. It occurred for diesel after 50 min, for the 5% and 10% TPO blend after 35 min, all from the ignition. The results showed a uniform temperature profile in flameless combustion. For diesel, the average temperature was 1029.56 ± 87.25 K in 50 to 70 min (flameless regime). The average temperature for TPO5 was 1054.21 ± 70.43 K in 36 to 60 min. An average temperature of 1149.04 ± 57.51 K was measured for TPO10 in 35 to 60 min.

In the flameless regime, the temperature inside the combustor is uniform because the recirculation of products mass spreads the reaction inner it [20, 23, 36, 37], contrary to the transition stage where the temperature profile is not uniform. Therefore, in this way, flameless combustion was characterized by the tested fuels.

Emissions

Figure 5 depicts the emission of NO and NO₂ for Diesel, TPO5, and TPO10.

NO emissions increase with time in the conventional combustion regime for all the tested fuels due to the temperature rise inside the combustor that enhances the thermal mechanism of NO formation. In the transition stage, there are peaks in the measurement of NO emission that can be related to a non-stable condition inside the combustor because this stage is the intermediate one between the conventional and the lean and stable combustion (flameless regime). NO emissions reduce for all teste fuels after the achievement of the flameless regime.

For Diesel, NO emission increased to 60 ppm in the conventional combustion and decreased in the flameless stage. For TPO5, NO emissions increase from 30 to 50 ppm, followed by a reduction to an average value of 18.58 ± 2.45 ppm in the flameless regime. TPO10 shows similar behavior for NO emissions, increases to 60 ppm in the transition regime,

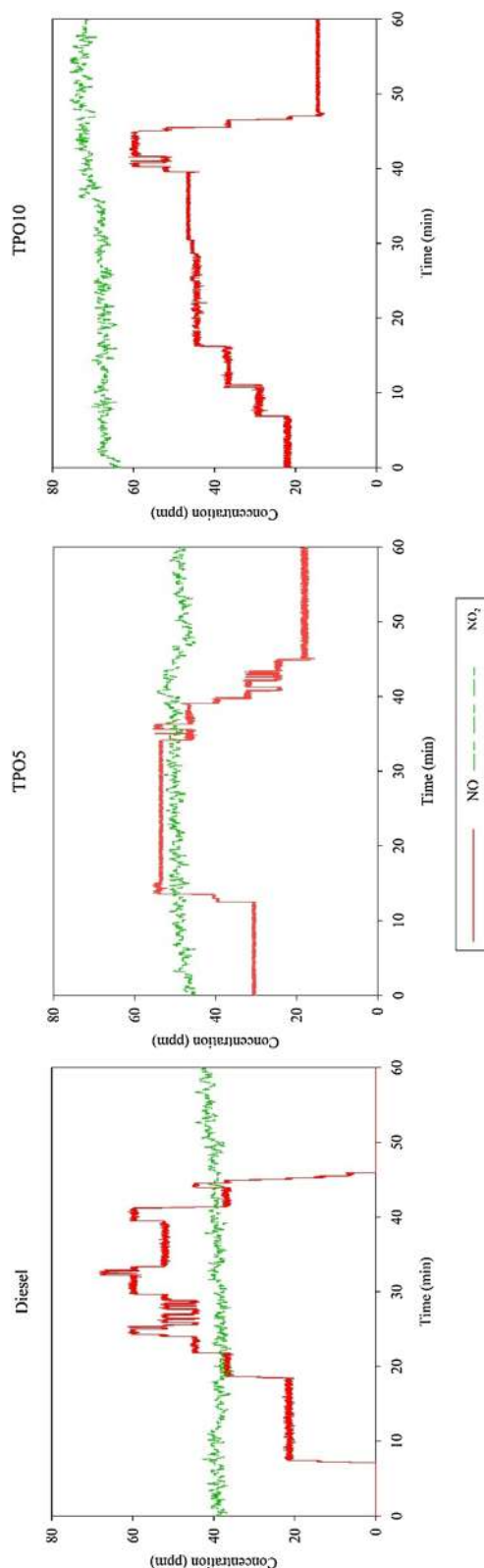


Fig. 5 NO and NO₂ emissions in the combustion chamber



and reduces to an average value of 14.49 ± 0.29 ppm in the flameless stage.

In a combustion reaction, the principal source of NO emissions is related to the N_2 present in the air at high temperatures (a thermal mechanism) [38, 39]. However, the fuels tested here have a high nitrogen content, enhancing NO formation. According to Barlow and Carter [40], the NO formation via nitrogen compounds has the same scale that the combustion reaction. Therefore, it has two mechanisms enhancing the NO formation, thermal and nitrogenated fuel. The thermal mechanism is reduced in flameless combustion because the temperature is lower than 1800 K [41, 42], but it does not affect the other formation mechanism. Even though, for all the tested fuels, the NO emissions decrease.

To have a detailed explanation, it is necessary to analyze the NO_2 emissions because NO_2 emission is related to the quick conversion of NO to NO_2 mainly by $NO + HO_2 \rightarrow NO_2 + OH$. The region with a temperature gradient between the hot gases' circulation and the combustion air, which enters the combustion chamber at a relatively lower temperature than the recirculated gases, enhances HO_2 formation, leading to a part conversion of NO into NO_2 [43].

In general, there are no significant changes in NO_2 emissions for all tested fuels. Diesel in the two first stages had a NO_2 emission of 38.9 ppm, and the emission was 41.23 ± 1.22 ppm in the flameless regime. TPO5 practically does not have any change in the average value of 48.99 ± 1.49 ppm for the NO_2 emissions. TPO10 in the conventional and transition regimes has an emission of 67.67 ppm and passes to 72.60 ± 1.32 ppm in the flameless regime.

These results for NO_2 emissions collaborate with the previous possible explanation about the transformation of NO to NO_2 . Average NO_2 emissions increased with TPO content; in other words, the increase in nitrogen content increases its emissions. Therefore, it can be inferred that part of the NO formed in the reaction had converted to NO_2 . Also, this conversion can explain why there was no detection of NO emission for diesel in the flameless regime. However, a numerical detail study, which is not the focus of this work, is necessary to estimate how much NO has converted into NO_2 and how significant is the nitrogen content of the fuel to the formation of NO in flameless combustion.

It is important to point out that once the flameless regime is achieved, NO and NO_2 emissions do not change with time anymore because the reaction is already stable with a constant temperature, so the mechanism of NO and NO_2 should not change without an external mechanism.

Considering NOx as $NO + NO_2$, the NOx emission for TPO5 and TPO10 is 67.57 ppm and 87.09 ppm, respectively. The reduction of NOx emission when the combustion chamber enters in flameless regime was 33.9% for TPO5 and 26.5% for TPO10. The reduction of the NOx emission in

flameless combustion is following other data in the literature [33, 34, 44, 45].

It is not so simple to compare the results that come from TPO because its composition depends on the production chemical path. However, qualitatively, the emissions found in this work are lower than other data in the literature. Wilians et al. [7] measure for pure TPO an emission of 343 ppm of NOx for 7.6% excess of oxygen in a furnace of 1.6 m long that operates in a conventional regime. In addition, Murugan et al. [6] found a NOx emission of 2000 ppm for Diesel and TPO10 in a diesel engine with a brake power of 4.329 kW. The temperature for these works is probably higher than the flameless regime, which results in a higher NOx emission.

It is essential to point out that even though SO_2 emissions were not measured here, they can be formed in the combustion of TPO, even in a flameless regime, because of the oxidation of the sulfur content present in the fuel. A detailed study of SO_2 formation in flameless combustion is necessary to guarantee that the use of TPO in this specified condition meets the environmental criteria of reduction in pollutant gases.

Conclusions

This work demonstrates the possibility to achieve a flameless regime using a mixture of 5 (TPO5) and 10% (TPO10) of tire pyrolysis oil (TPO) with diesel and pure diesel. It used a combustion chamber that operates with a thermal input between 10 and 15 kW. The average temperature inside the combustion chamber in the flameless regime was 1029.56 ± 87.25 K for diesel, 1054.21 ± 70.43 K for TPO5, and 1149.09 ± 57.51 K for TPO10.

The emission of NO increases in the first two stages of the combustion (conventional and transition); after the flameless regime is achieved, the NO emissions are reduced for all the tested fuels. On other hand, the NO_2 emissions increase with the TPO content in the mixture. Two hypotheses can explain this increase in NO_2 emissions: nitrogen content in the fuel or the part conversion of NO into NO_2 . However, a detailed numerical study that includes the reaction mechanism is necessary to guarantee which one of these two factors is the most significant in the flameless regime.

NO and NO_2 emissions do not significantly change, once the flameless regime was achieved, because of the stable reaction inside the combustor and its low-temperature gradients. Considering NOx as the sum of NO and NO_2 , each fuel has NOx emission reduced in the flameless regime. Therefore, the use of the energy content in TPO in combustion systems generating low NO and NO_2 emissions is the main implication of this work. The combustion of TPO can generate SO_2 because of the sulfur present in its composition. A further study of the SO_2 emission in the flameless regime



is also necessary to guarantee the environmental criteria of pollutant emissions.

Supplementary Information The online version contains supplementary material available at <https://doi.org/10.1007/s40095-022-00529-x>.

Acknowledgements Funding for this study was provided by the Fundação de Amparo à Pesquisa do Estado de Minas Gerais, FAPEMIG – Brazil. FAPEMIG (Proc. N° TEC-APQ-00467–11) and CNPq-Brazil (Proc. No. 305741/2019-5). This study was financed in part by the Coordenação de Aperfeiçoamento de Pessoal de Nível Superior-Brasil (CAPES)-Finance Code 001.

Data availability The datasets generated during and/or analyzed during the current study are available from the corresponding author upon reasonable request.

Declarations

Conflict of interest The authors declare that they have no known competing financial interests or personal relationships that could have appeared to influence the work reported in this paper.

References

- ETRMA: The ETRMA Statistics Report. Eur. tyre rubber Manuf. Assoc. 48 (2019)
- Tyre, T.E.: In Europe 95% of all End of Life Tyres were collected and treated in 2019 Brussels, 11th May 2021-ETRMA, the European Tyre and Rubber Manufacturers' Association, has consolidated data on the management of End of Life Tyres (ELTs) for ELTs (2021)
- Williams, P.T.: Pyrolysis of waste tyres: a review. *Waste Manag.* **33**, 1714–1728 (2013). <https://doi.org/10.1016/j.wasman.2013.05.003>
- Suchocki, T., Witanowski, L., Lampart, P., Kazimierski, P., Januszewicz, K., Gawron, B.: Experimental investigation of performance and emission characteristics of a miniature gas turbine supplied by blends of kerosene and waste tyre pyrolysis oil. *Energy* **215**, 119125 (2021). <https://doi.org/10.1016/j.energy.2020.119125>
- Frigo, S., Seggiani, M., Puccini, M., Vitolo, S.: Liquid fuel production from waste tyre pyrolysis and its utilisation in a Diesel engine. *Fuel* **116**, 399–408 (2014). <https://doi.org/10.1016/j.fuel.2013.08.044>
- Murugan, S., Ramaswamy, M.C., Nagarajan, G.: The use of tyre pyrolysis oil in diesel engines. *Waste Manag.* **28**, 2743–2749 (2008). <https://doi.org/10.1016/j.wasman.2008.03.007>
- Williams, P.T., Bottrill, R.P., Cunliffe, A.M.: Combustion of tyre pyrolysis oil. *Process Saf. Environ. Prot.* **76**, 291–301 (1998). <https://doi.org/10.1205/095758298529650>
- Wünning, J.A., Wünning, J.G.: Flameless oxidation to reduce thermal no-formation. *Prog. Energy Combust. Sci.* (1997). [https://doi.org/10.1016/S0360-1285\(97\)00006-3](https://doi.org/10.1016/S0360-1285(97)00006-3)
- Wang, Y.D., McIlveen-Wright, D., Huang, Y., Hewitt, N., Eames, P., Rezvani, S., McMullan, J., Roskilly, A.P.: The application of FLOX/COSTAIR technologies to reduce NO_x emissions from coal/biomass fired power plant: a technical assessment based on computational simulation. *Fuel* **86**, 2101–2108 (2007). <https://doi.org/10.1016/j.fuel.2007.01.013>
- Mahendra Reddy, V., Kumar, S.: Development of high intensity low emission combustor for achieving flameless combustion of liquid fuels. *Propuls. Power Res.* **2**, 139–147 (2013). <https://doi.org/10.1016/j.jprr.2013.04.006>
- Plessing, T., Peters, N., Wünning, J.G.: Laseroptical investigation of highly preheated combustion with strong exhaust gas recirculation. *Symp. Combust.* **27**, 3197–3204 (1998). [https://doi.org/10.1016/S0082-0784\(98\)80183-5](https://doi.org/10.1016/S0082-0784(98)80183-5)
- Levy, Y., Sherbaum, V., Arfi, P.: Basic thermodynamics of FLOX-COM, the low-NO_x gas turbines adiabatic combustor. *Appl. Therm. Eng.* **24**, 1593–1605 (2004). <https://doi.org/10.1016/j.applthermaleng.2003.11.022>
- Weber, R., Gupta, A.K., Mochida, S.: High temperature air combustion (HiTAC): HOW it all started for applications in industrial furnaces and future prospects. *Appl. Energy* **278**, 115551 (2020). <https://doi.org/10.1016/j.apenergy.2020.115551>
- Katsuki, M., Hasegawa, T.: The science and technology of combustion in highly preheated air. In: *Symposium (International) on Combustion* (1998)
- Cho, E.S., Danon, B., de Jong, W., Roekaerts, D.J.E.M.: Behavior of a 300kWth regenerative multi-burner flameless oxidation furnace. *Appl. Energy* **88**, 4952–4959 (2011). <https://doi.org/10.1016/j.apenergy.2011.06.039>
- Cho, E.S., Shin, D., Lu, J., de Jong, W., Roekaerts, D.J.E.M.: Configuration effects of natural gas fired multi-pair regenerative burners in a flameless oxidation furnace on efficiency and emissions. *Appl. Energy* **107**, 25–32 (2013). <https://doi.org/10.1016/j.apenergy.2013.01.035>
- Karyeyen, S., Feser, J.S., Jahoda, E., Gupta, A.K.: Development of distributed combustion index from a swirl-assisted burner. *Appl. Energy* **268**, 114967 (2020). <https://doi.org/10.1016/j.apenergy.2020.114967>
- Arghode, V.K., Gupta, A.K.: Effect of flow field for colorless distributed combustion (CDC) for gas turbine combustion. *Appl. Energy* (2010). <https://doi.org/10.1016/j.apenergy.2009.09.032>
- Dally, B.B., Riesmeier, E., Peters, N.: Effect of fuel mixture on moderate and intense low oxygen dilution combustion. *Combust. Flame* (2004). <https://doi.org/10.1016/j.combustflame.2004.02.011>
- Cavaliere, A., Joannon, M.: Mild Combustion. *Prog. Energy Combust. Sci.* **30**, 329–366 (2004)
- Szegö, G.G., Dally, B.B., Nathan, G.J.: Operational characteristics of a parallel jet MILD combustion burner system. *Combust. Flame* (2009). <https://doi.org/10.1016/j.combustflame.2008.08.009>
- Mancini, M., Schwöppe, P., Weber, R., Orsino, S.: On mathematical modeling of flameless combustion. *Combust. Flame* **150**, 54–59 (2007). <https://doi.org/10.1016/j.combustflame.2007.03.007>
- Maruta, K., Muso, K., Takeda, K., Niioka, T.: Reaction zone structure in flameless combustion. *Proc. Combust. Inst.* **28**, 2117–2123 (2000). [https://doi.org/10.1016/S0082-0784\(00\)80621-9](https://doi.org/10.1016/S0082-0784(00)80621-9)
- Mohamed, H., Hmaeid, B.: Influence of turbulent mixing intensity on the MILD combustion and the pollutant formation. *Int. J. Energy Environ. Eng.* **3**, 1–6 (2012). <https://doi.org/10.1186/2251-6832-3-22>
- de Azevedo, C.G., de Andrade, J.C., de Souza Costa, F.: Flameless compact combustion system for burning hydrous ethanol. *Energy* (2015). <https://doi.org/10.1016/j.energy.2015.07.049>
- Barbosa, J.A., de Andrade, J.C., de Souza Costa, F., Coronado, C.J.R., de Azevedo, C.G., de Andrade, R.A.: Temperature profile and gas emissions of jet fuel using a low power flameless combustor. *J. Braz. Soc. Mech. Sci. Eng.* **44**, 1–13 (2022). <https://doi.org/10.1007/s40430-021-03305-w>
- Chumpitaz, G.R.A., Coronado, C.J.R., Carvalho, J.A., Andrade, J.C., Mendiburu, A.Z., Pinto, G.M., de Souza, T.A.: Design and study of a pure tyre pyrolysis oil (TPO) and blended with Brazilian diesel using Y-Jet atomizer. *J. Braz. Soc. Mech. Sci. Eng.* **41**, 1–20 (2019). <https://doi.org/10.1007/s40430-019-1632-z>



28. Lefebvre, A.H., McDonell, V.G.: Atomization and sprays. CRC Press, Boca Raton (2017)
29. Konstantinov, D., Marsh, R., Bowen, P., Crayford, A.: Effervescent atomization for industrial energy-technology review. *At. Sprays* **20**, 525–552 (2010). <https://doi.org/10.1615/AtomizSpr.v20.i6.40>
30. Sovani, S.D., Sojka, P.E., Lefebvre, A.H.: Effervescent atomization. *Prog. Energy Combust. Sci.* **27**, 483–521 (2001). [https://doi.org/10.1016/S0360-1285\(00\)00029-0](https://doi.org/10.1016/S0360-1285(00)00029-0)
31. Veríssimo, A.S., Rocha, A.M.A., Costa, M.: Importance of the inlet air velocity on the establishment of flameless combustion in a laboratory combustor. *Exp. Therm. Fluid Sci.* **44**, 75–81 (2013). <https://doi.org/10.1016/j.expthermflusci.2012.05.015>
32. Mi, J., Li, P., Dally, B.B., Craig, R.A.: Importance of initial momentum rate and air-fuel premixing on moderate or intense low oxygen dilution (MILD) combustion in a recuperative furnace. *Energy Fuels* (2009). <https://doi.org/10.1021/ef900866v>
33. Reddy, V.M., Katoch, A., Roberts, W.L., Kumar, S.: Experimental and numerical analysis for high intensity swirl based ultra-low emission flameless combustor operating with liquid fuels. *Proc. Combust. Inst.* (2015). <https://doi.org/10.1016/j.proci.2014.05.070>
34. Derudi, M., Rota, R.: 110th anniversary: MILD combustion of liquid hydrocarbon-alcohol blends. *Ind. Eng. Chem. Res.* (2019). <https://doi.org/10.1021/acs.iecr.9b02374>
35. Rebola, A., Costa, M., Coelho, P.J.: Experimental evaluation of the performance of a flameless combustor. *Appl. Therm. Eng.* **50**, 805–815 (2013). <https://doi.org/10.1016/j.applthermaleng.2012.07.027>
36. Kumar, S., Paul, P.J., Mukunda, H.S.: Studies on a new high-intensity low-emission burner. *Proc. Combust. Inst.* **29**, 1131–1137 (2002)
37. Reddy, V.M., Trivedi, D., Kumar, S.: Experimental investigations on lifted spray flames for a range of coflow conditions. *Combust. Sci. Technol.* **184**, 44–63 (2012). <https://doi.org/10.1080/00102202.2011.615770>
38. Ali, G., Zhang, T., Wu, W., Zhou, Y.: Effect of hydrogen addition on NO_x formation mechanism and pathways in MILD combustion of H₂-rich low calorific value fuels. *Int. J. Hydrog. Energy.* **45**, 9200–9210 (2020). <https://doi.org/10.1016/j.ijhydene.2020.01.027>
39. Miller, J.A., Bowman, C.T.: Mechanism and modeling of nitrogen chemistry in combustor. *Prog. Energy Combust. Sci.* **15**, 287–338 (1989)
40. Barlow, R.S., Carter, C.D.: Raman/Rayleigh/LIF measurements of nitric oxide formation in turbulent hydrogen jet flames. *Combust. Flame* **97**, 261–280 (1994). [https://doi.org/10.1016/0010-2180\(94\)90020-5](https://doi.org/10.1016/0010-2180(94)90020-5)
41. Khidr, K.I., Eldrainy, Y.A., EL-Kassaby, M.M.: Towards lower gas turbine emissions: flameless distributed combustion. *Renew. Sustain. Energy Rev.* **67**, 1237–1266 (2017). <https://doi.org/10.1016/j.rser.2016.09.032>
42. Cameretti, M.C., Tuccillo, R., Reale, F., Piazzesi, R.: Liquid bio-fuels in an EGR equipped micro gas turbine. In: Proceedings of the ASME Turbo Expo (2011)
43. Hori, M.: Experimental study of nitrogen dioxide formation in combustion systems. *Symp. Combust.* **21**, 1181–1188 (1988). [https://doi.org/10.1016/S0082-0784\(88\)80349-7](https://doi.org/10.1016/S0082-0784(88)80349-7)
44. Derudi, M., Rota, R.: Experimental study of the mild combustion of liquid hydrocarbons. *Proc. Combust. Inst.* (2011). <https://doi.org/10.1016/j.proci.2010.06.120>
45. Mahendra Reddy, V., Sawant, D., Trivedi, D., Kumar, S.: Studies on a liquid fuel based two stage flameless combustor. *Proc. Combust. Inst.* (2013). <https://doi.org/10.1016/j.proci.2012.06.028>

Publisher's Note Springer Nature remains neutral with regard to jurisdictional claims in published maps and institutional affiliations.

Springer Nature or its licensor holds exclusive rights to this article under a publishing agreement with the author(s) or other rightsholder(s); author self-archiving of the accepted manuscript version of this article is solely governed by the terms of such publishing agreement and applicable law.





Techno-economic optimization of packed-bed thermal energy storage system combined with CSP plant using DOE: design of experiment technique and Taguchi method

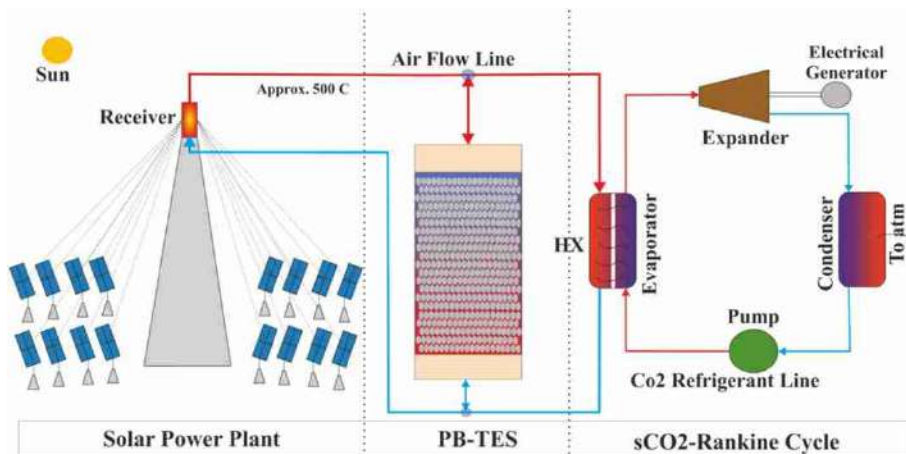
Amit Sharma¹ · Pankaj K. Pandey² · Mukesh Didwania³

Received: 7 March 2022 / Accepted: 26 August 2022 / Published online: 15 October 2022
© The Author(s), under exclusive licence to Islamic Azad University 2022

Abstract

Three distinct sensible thermal energy storage (STES) mediums were researched in order to optimize the packed-bed thermal energy storage (PB-TES) system for a combined CSP and CO₂ Rankine plant. PB-TES was studied using various particle types, including alumina, steel particles, and a hybrid of the two. The PB-TES system for various STES media has been simulated using CFD models. The experiments were confirmed by a prior investigation with constant mass flow rate air as a heat transfer fluid. In the present study, a cylindrical tank containing porous STES material was used for CFD modeling using the Ansys Fluent program. Using a transient two-phase model equation for fluid and solid phases, simulations of charging and discharging are performed for the current study. For more accurate simulation outcomes, the thermal dispersion and conductivity of the STES in the PB-TES system were taken into account. After confirming the CFD simulation, the combined solar thermal and Rankine cycle plant sizing and design cost for the PB-TES is required. Using the design of experiment approach (“Taguchi method”), a techno-economic analysis is conducted for an optimized PB-TES system employing the dynamic cycling methodology. In this study, geometric modifications of the PB-TES system with respect to cost assumptions were also examined. Hybrid STES media predict optimal outcomes for the PB-TES system at a significant cost.

Graphical abstract



Keywords Packed-bed thermal energy storage (PB-TES) · CFD simulation · Techno-economic analysis · Solar thermal plants · Sensible thermal energy storage (STES) media

✉ Amit Sharma
amit_king@ymail.com

Extended author information available on the last page of the article

List of symbols

ANOVA	Analysis of variance
CAPEX	Capital expenditure
CD	Composite desirability



ch	Charging
Ch-pump	Pump for charging
CT	Cold temperature of HTF
D-ch	Design charging
D-dis	Design discharge
dis	Discharge
Dis-pump	Pump for discharging
DNI	Direct normal irradiation
DOE	Design of experiment
G	Mass flow rate per cross section [$\text{kg}/(\text{m}^2 \text{ s})$]
H	Height of PB-TES
HT	Hot temperature of HTF
HTF	Heat transfer fluid
HTT	Height of tank
LCOE	Levelized cost of energy
N	Number of PB-TES units
NTP	Number of parallel tanks
OPEX	Operational cost of energy
PB-TES	Packed-bed thermal energy storage
Pre	Preliminary
S/N ratio	Signal-to-noise ratio
S/NS	Significance/nonsignificance
Season-ch	Seasonal charging
SF	Solar field
T	Temperature
t	Time
TC	Thermocline
therm	Thermal
VF	Void fraction
x	Height of PB-TES as per temperature profile in PB-TES

Introduction

Thermal energy storage (TES) is the optimal CSP component. Due to thermal energy storage (TES), it is now feasible to maximize the utilization of CSP plants, making TES a crucial component. Combining thermal energy storage with a CSP plant makes it superior and unique among all other renewable energy production options [1, 2]. Integrating thermal energy storage into a CPS plant is crucial for its economic viability. A great deal of research is being conducted worldwide to determine the commercial feasibility of combined TES and CSP power stations [EASE] [3].

The combination of thermal energy storage with a CSP plant has been shown to be revolutionary. Globally, thermal energy storage and CSP plants will generate around 5.1 GW of electrical energy by 2017. This magnitude continues to grow as a result of its industrial viability [ITP]. This technique has several advantages.

Due to thermal energy storage, the CSP plant is capable of providing optimal levels of both thermal energy and electrical energy. Utilizing thermal energy storage components increases the CSP systems' capacity factor. Cost-effective thermal energy storage is packed-bed TES, which employs mostly waste materials such as sand, stone, and pebbles. PB-TES makes the CSP plant more efficient and economical than other renewable energy generating facilities. For high-temperature CSP facilities, packed-bed thermal energy storage uses sensible storage materials and air as the heat transmission fluid [4]. Packed-bed thermal energy storage has various benefits, including inexpensive and abundant sensible storage material, a temperature range from low to high, and sensible heat distribution among STES and HTF. There are no safety requirements for this technology, low maintenance, no chemical reactions, and no rusting [5, 6]. Other electrical energy generation methods, like the Rankine power cycle, can be integrated with the CSP plant to maximize its efficiency. With thermal energy storage capacity, the thermal energy receiver of the CSP plant may operate at output temperatures of about 800 °C. According to Dostal et al. [7], super-critical alternative power cycles are compatible with CSP reactors. Numerous studies indicate that combining CSP plants with sCO_2 power cycles increases the total system efficiency, particularly at higher temperatures. They [4] analyzed the thermal and economic performance of the sCO_2 power cycles when paired with CSP and PB-TES facilities. Packed-bed TES is a basic concept that requires more study to enhance its thermal performance. It requires optimization (both single and multiple) of several design and process factors in order to optimize its thermal performance. For improved functioning of TES components integrated with CSP plants [3, 8–10], it is necessary to adjust geometrical and operational parameters. Due to the availability of multiple input factors (geometrical, operational, and thermo-physical), the experimental investigation of the PB-TES is both extensive and time-consuming. As a result, the majority of researchers do simulation-based research (modeling, optimization, sensitivity) for large input parameters [45]. In a sensitivity study, researchers alter a number of factors before analyzing the effect of indicator parameters that have been utilized in prior investigations. These sensitivity analyses allow for a robust design of the CSP system and contribute to the optimization of the TES components. Hänchen et al. [11] reported that several researchers have examined the temperature distribution and charging and discharging of the PB-TES in order to maximize its thermal efficiency. Researchers select various input parameters, including charging and discharging temperatures, efficiency, capacity factor, thermal-to-electrical conversion, energy loss, materials, economic analysis, and the geometrical shape of TES plants, including height, aspect ratio, and insulation thickness, among others.



This paper presents the techno-economic optimization of coupled PB-TES and CSP facilities. The LCOE is chosen as the economic parameter for optimizing the TES in accordance with the geometrical and operational parameters of the TES. In order to demonstrate the significance of numerical modeling, the present work does experiment validation with earlier studies. A dynamic modeling technique is adopted for the techno-economic optimization of the packed-bed thermal energy storage device. In the initial segment, three distinct sensible thermal energy storage (STES) media were examined in order to optimize the packed-bed thermal energy storage (PB-TES) system for a combined CSP and CO₂ Rankine plant. PB-TES was studied using alumina particles, steel particles, and a hybrid of the two. The PB-TES system was simulated using CFD models for these STES media. Experiments with constant mass flow rate air as a heat transfer fluid were validated using prior research (HTF). Then, techno-economic optimization is done using the design of experiment approach and the Taguchi method selected for the best STES medium. In multi-objective optimization, a composite desirability function method is chosen.

In this investigation Jamshidian et al. [12], it was anticipated that a thermal multi-effect distillation (MED) facility would be coupled with a reverse osmosis (RO) desalination system. This integration would fulfill the heat and energy demands of the hybrid RO-MED facility using a solar CHP system comprised of parabolic trough concentrators (PTCs). Consequently, Bushehr's climate patterns. First, new algorithms were developed to integrate RO and MED desalination plants, and then, MATLAB was used to develop an integrated TES system. Second, new algorithmic implementations were made. The performance of both the RO-MED plant and the solar CHP system was evaluated using a mathematical model of the entire system. To achieve impartial comparisons of energy performance and life-cycle costs, it [13] was recommended to conduct a systematic analysis (LCC). Particular focus was placed on practical concerns such as TES charging power. Most LCC cost reductions result from peak load reduction. Among TES technologies, BTM has the lowest total cost of ownership, but WT has a larger heat loss rate and lower storage density. Good insulation minimizes energy use, resulting in cost savings. Reduced discharge power is to blame for this. A higher price or stricter regulations may promote residential adoption of TES technology.

This study Desai et al. [14] examines packed-bed rock storage, two-tank indirect storage, and two-tank direct storage for a solar cogeneration system based on foil. Determine the optimal energy storage design and technology. The study of two types of rocks and three heat transfer fluids is observed. Solar field heat transfer fluid operational and economic considerations influence the selection of a storage system. Using packed-bed rock (including quartzite) with

Therminol 55 as the heat transfer fluid appears to offer the lowest levelized cost of energy. Some other authors [15–18] are also studied on the TES optimization for different boundary conditions and found the best outcome of the research study. No literature available in which DOE (design of experiment) method is used for the techno-economic optimization was performed.

Modeling

Numerical modeling

A three-dimensional numerical model of PB-TES (packed-bed thermal energy storage) has been developed to perform experimental validation of Cascetta et al. [15] published research work. The PB-TES system has a length of 1800 mm and a diameter of 580 mm, according to Cascetta et al. [15] previous published research work. The modeling of HTF flow in a cylinder with varied boundary conditions is detailed in Table 1. According to Cascetta et al. [15–17], the sensible thermal energy storage (STES) medium “Alumina” is selected for numerical modeling. Experimental validation aids in the development of additional numerical models for various STES media, such as steel and hybrids of both (alumina and steel). Validation results are shown in Fig. 1 with an approximate error of 10% with experiment results [15–17]. The validation of CFD simulation results is for the charging and discharging of PB-TES.

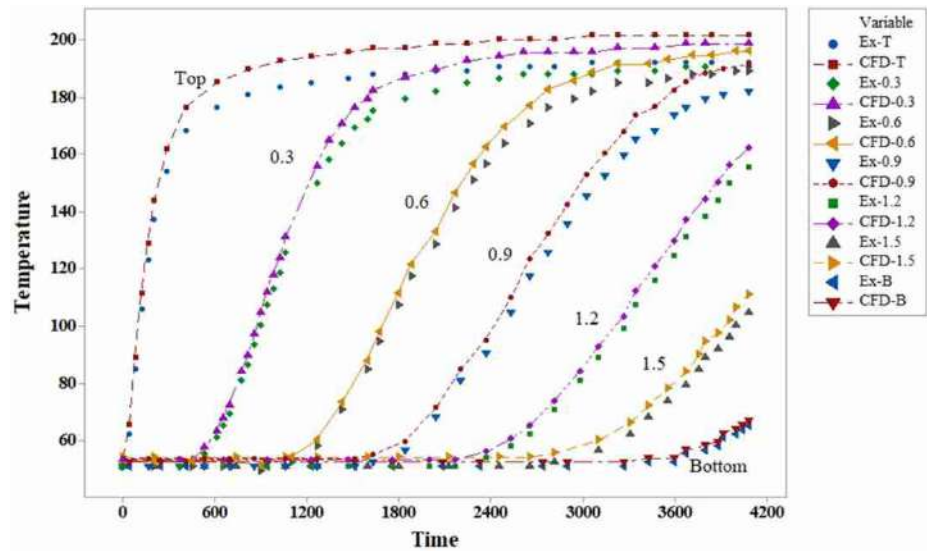
Using accessible pre-configured models, Ansys Fluent software [19] is used to construct a numerical model. Because fluid and solid phases are involved in PB-TES numerical modeling, user-defined functions (UDF) are utilized to generate more accurate energy equation models. With an average mesh size of 1 mm, grid independence tests have also been done, and the results have been encouraging. In Table 2 are mentioned the thermo-physical characteristics of the STES medium.

Table 1 Input data for numerical modeling [15, 16]

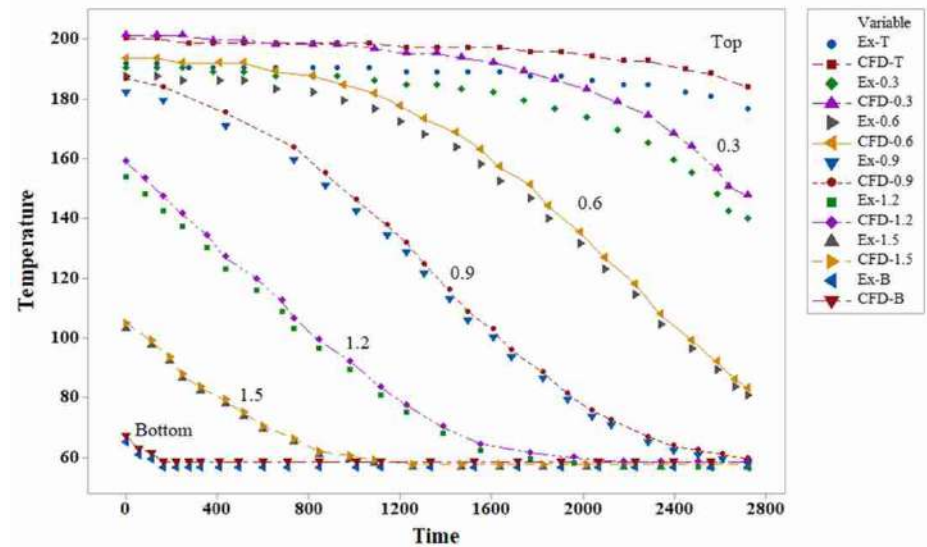
Input boundary	Value	Unit
BED height	1800	[mm]
BED diameter	584	[mm]
Aspect ratio	3.1	[–]
Air flow rate	0.2	[kg/s]
Alumina particle diameter	8	[mm]
BED void fraction	0.395	[–]
Insulation thickness	100	[mm]



Fig. 1 Validation of PB-TES against references experimental studies [15–17]



(a) Charging validation of PB-TES at different time and length of PB-TES



(b) Discharging validation of PB-TES at different time and length of PB-TES

Comparison of three different sensible thermal energy storage (STES) media

In this work, three STES materials were chosen for the PB-TES simulation: alumina, steel, and a hybrid of the two materials. After the successful validation of the alumina material, a numerical model was constructed for the remaining materials, and the results for these three STES materials are depicted in Fig. 2.

Figure 2 depicts the charging of PB-TES at various device heights. As demonstrated in Fig. 2a, the highest heat gain

is achieved by a hybrid of both STES media, and the same findings are displayed for 0.6 m, 0.9 m, 1.2 m, and the bottom of the bed.

Optimum STES media then used for techno-economic modeling for 25 MW_e CSP plant attached with CO₂ Rankine generator [16, 20–22].

Alumina and steel materials thermo-physical properties are gathered from [15–17, 23] which are listed in Table 2. Hybrid material is the combination of both materials and it was assumed that both materials have same volume in PB-TES device.

Table 2 Thermo-physical properties of STES media used in numerical modeling

STES media	Unit	Alumina	Steel	References
Density	[kg/m ³]	3550	8030	[15–17, 17]
Specific heat	[J/(kg K)]	902	502.48	
Thermal conductivity	[W/(mK)]	30	16.27	
Particle average diameter	[mm]	7–10	7–10	

Boundary conditions for thermal model development (steady and dynamic both)

According to the author’s best knowledge, most research investigations on PB-TES have utilized constant formulations for techno-economic optimization [24], particularly when PB-TES is coupled with concentrated solar power plants [25–27]. For techno-economic optimization, a constant heat transfer fluid (mainly air) is chosen in the majority of research [28, 29]. Solar energy does not have a constant DNI every day; thus, the modeling of continuous heat

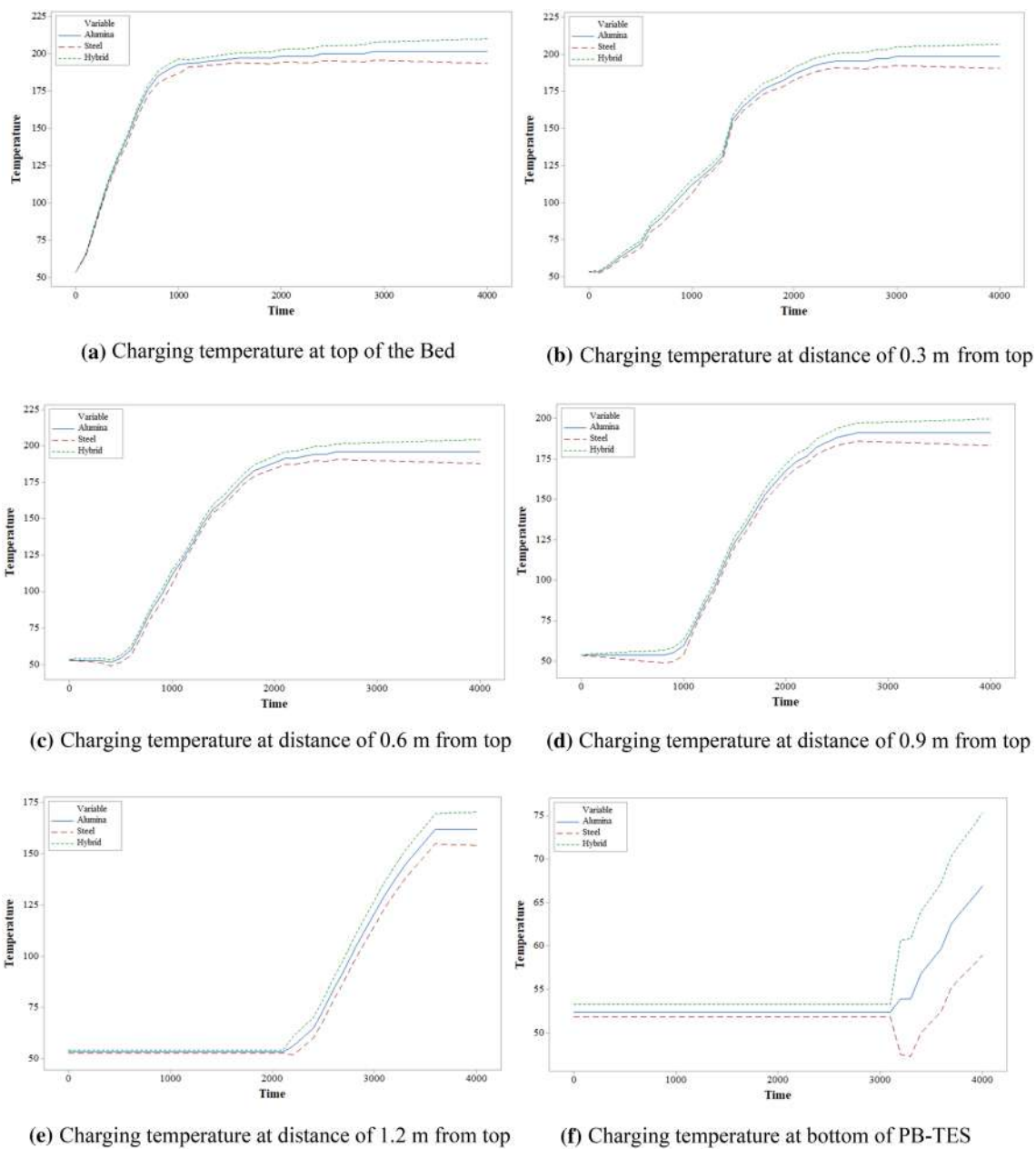


Fig. 2 Charging temperature comparison for three materials (alumina, steel, and hybrid of both)

transfer fluid is not entirely warranted. Real-time modeling of TES in a CSP plant is only possible when the mass flow rate of HTF is modeled based on real DNI values [24].

The majority of CSP facilities provide steady electricity. Hence, the CSP plants produce more thermal energy throughout the day, so the PB-TES is increased. The PB-TES releases this extra energy at night. The Rankine generator may use the discharged energy. The charging and discharging of the PB-TES system are governed by a temperature limit chosen by the author based on past research [24]. For more real-time modeling of PB-TES system, DNI-dependent HTF mass flow rate is selected for current study. Design mass flow rate of HTF \dot{m}_{D-ch} for full cycle charging of the PB-TES is shown in Eq. (1)

$$\dot{m}_{D-ch} = \frac{E_{PB-TES}}{(\bar{c}_p)_{air} (T_{ch} - T_{dis})t_{ch}} \tag{1}$$

where T_{ch} and T_{dis} are charging and discharging temperature of the PB-TES device. E_{PB-TES} is designed energy capacity which can be produced by PB-TES during full cycle. $(\bar{c}_p)_{air}$ is average specific heat capacity of the HTF. It was calculated by average temperature of charge and discharge temperature.

Dynamic mass flow rate of HTF was calculated by $(\dot{m}_{season-ch})_t$ and shown in Eq. (2) for single day (15th) from each month.

$$(\dot{m}_{monthly-ch})_t = (\dot{m}_{D-ch}) \left(\frac{(DNI)_t (\eta_{SF})_t}{DNI \bar{\eta}_{SF}} \right) \tag{2}$$

where t represents the time, and DNI and $(\eta_{SF})_t$ are direct normal irradiance and solar field efficiency. The city of Jaipur (Rajasthan, India) was chosen for this study due to its year-round sunshine availability. Jaipur’s latitude and longitude are 26.82° north and 75.8° east. All calculations pertaining to the solar field are conducted using the commercially available, free software SAM (system Adviser Model) [NREL 30]. The input values necessary for SAM computations are outlined in Table 3. The monthly mass flow rate of HTF is calculated based on the DNI and solar field efficiency. Results for DNI $(\eta_{SF})_t$ and monthly mass flow rate profiles are shown in Fig. 3a–c, respectively. 15th day of each month is selected for calculating the thermo-economic modeling.

The energy-plus simulation software gathers Jaipur weather information from the ISHARE, India data repository. In Table 3 is presented the essential information necessary for techno-economic analysis.

The operating temperature for electrical power cycle analysis using CSP and PB-TES is between 600 and 100 °C. In the present study, the Rankine cycle is supposed

Table 3 Input boundary conditions for techno-economic model development

<i>(a) Weather information-Jaipur [NREL]</i>		
Direct normal	2165	[kWh/m ²]
Global horizontal	2070.8	[kWh/m ²]
Dry bulb temperature	25.7	[°C]
Wind speed	1.5	[m/s]
Latitude	26.82	[°]
Longitude	75.8	[°]
<i>(b) CSP information</i>		
Solar multiple	2.5	[–]
Turn-down fraction	0.25	[–]
Maximum operation fraction	1.3	[–]
Receiver design thermal power	100	[MW _t]
Design HTF Temperature	600	[°C]
Maximum receiver flux	1000	[kW _t /m ²]
<i>(c) Thermal storage system (TES)</i>		
Storage type	Thermocline	[–]
Tank diameter	10–13	[m]
Tank height	10–17	[m]
Parallel tank	2–6	[–]
Void fraction	0.3–0.5	[–]
Materials	Hybrid	[–]

to be selected for generating electricity from PB-TES thermal energy (as shown in Fig. 4).

The design mass flow rate is required to compute the actual mass flow rate of HTF, and a preliminary design study is necessary to determine HTF’s capacity to transmit the necessary thermal energy. Maximum field enthalpy Δh change is necessary to calculate the charge and discharge mass flow rates, as demonstrated by Eqs. (3) and (4), respectively.

$$\dot{m}_{ch} = \frac{E_{PB-TES}}{\Delta h \cdot t_{D-ch} \cdot N_{PB-TES} \cdot \eta_{pre}} \tag{3}$$

$$\dot{m}_{dis} = \frac{E_{PB-TES}}{\Delta h \cdot t_{D-dis} \cdot N_{PB-TES} \cdot \eta_{pre}} \tag{4}$$

where t represents time required for full cycle (charging and discharging) of the thermal energy storage device. N represents the number of storage tanks in system. η_{pre} is the preliminary efficiency, and in present study, author was assumed it equal to 0.85 [24].

Effective volume of PB-TES is evaluated by using Eq. (5) where ΔT_D is maximum temperature difference in PB-TES as per design considerations. Total 2–4 PB-TES tanks (N_{PB-TES}) are assumed for present study as per authors experience.

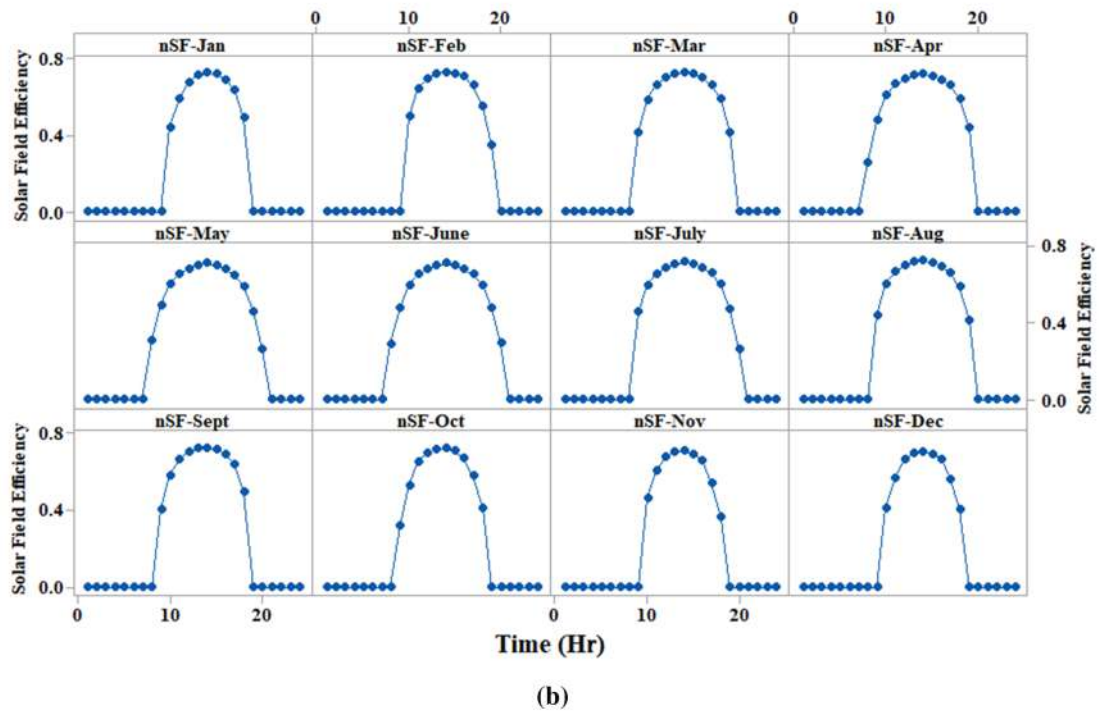
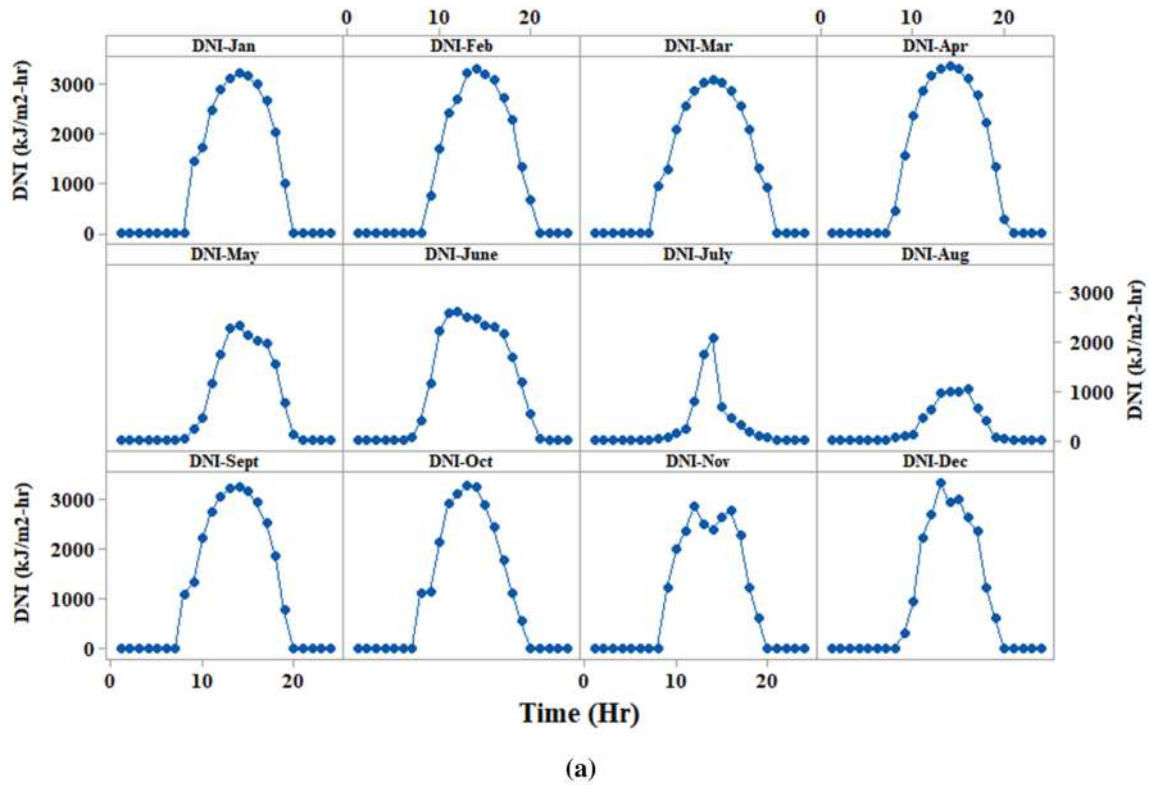


Fig. 3 a DNI profile for 15th day of each month during 24 h time period. b (η_{SF}) profile for 15th day of each month during 24 h time period. c $m_{monthly-ch}$ profile for 15th day of each month during 24 h time period

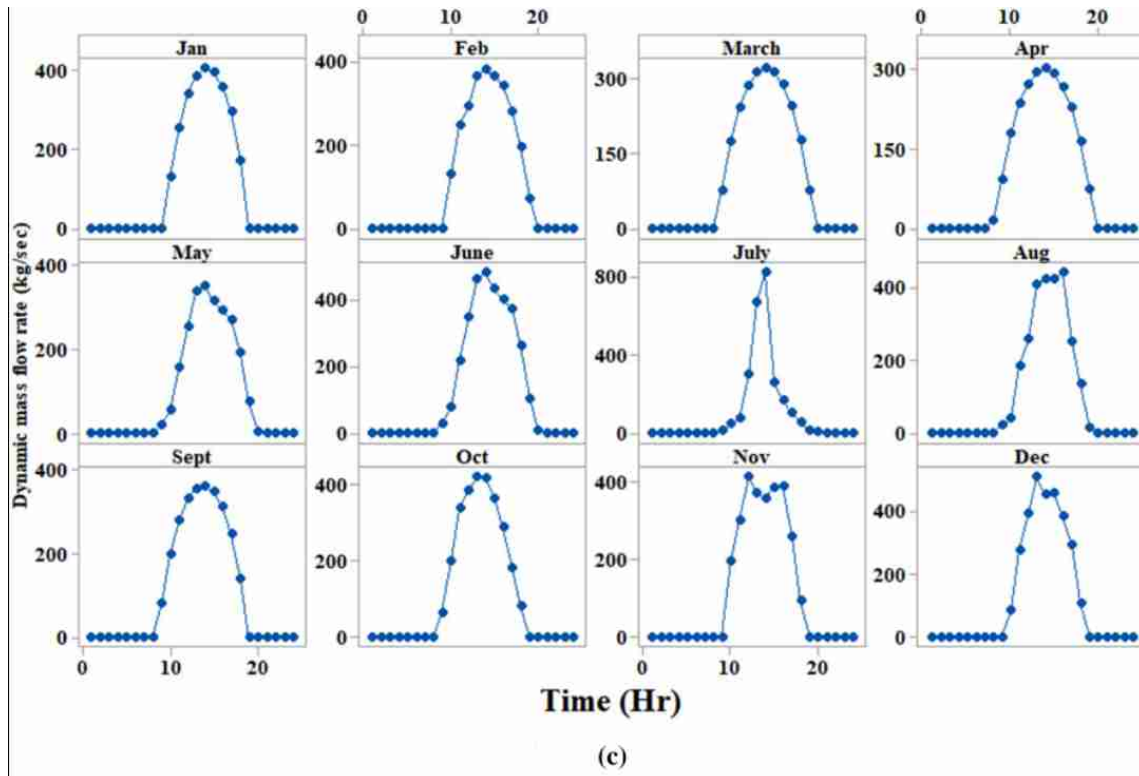


Fig. 3 (continued)

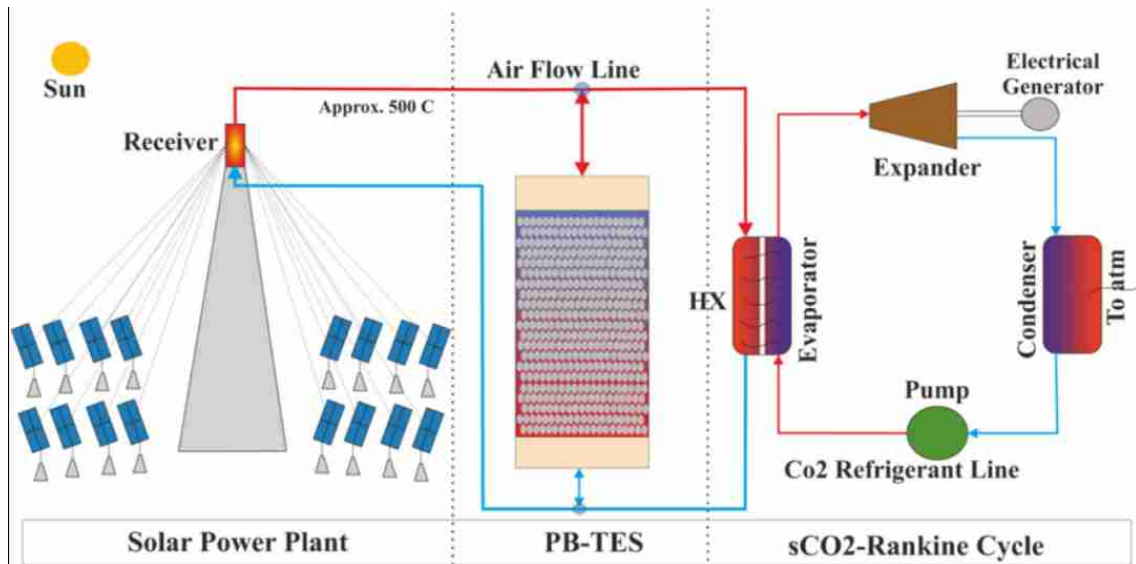


Fig. 4 Combined CSP and Rankine generator run with PB-TES component

$$V_{PB-TES} = \frac{E_{PB-TES}}{(\rho c_p)_{air} \cdot \Delta T_D \cdot N_{PB-TES} \cdot \eta_{pre}} \tag{5}$$

Ergun’s correlation is used to calculate the pressure drop in packed-bed thermal energy storage during flow conditions. Equation (6) is directly used in present study where H is height of the packed-bed thermal energy storage.

$$\frac{\Delta p}{H} = 1.75 \left(\frac{1 - \epsilon}{\epsilon^3} \right) \frac{G^2}{\rho_{air} d_p} + 150 \left(\frac{(1 - \epsilon^2)^2}{\epsilon^3} \right) \frac{G \mu_{air}}{\rho_{air} d_p^2} \tag{6}$$

Energy required for pumping the HTF fluid at required mass flow rate is shown in Eq. (7).

$$E_{pump} = E_{ch-pump} + E_{dis-pump} \tag{7}$$

Different pumping power is required for charging and discharging mode, and detailed power calculations for full cycle are present in Eq. (8).

$$E_{pump} = \left[\int_0^{t_{ch}} \frac{A \cdot N_{PB-TES} \cdot (G_{ch})_t (\Delta p_{ch})_t}{\rho_{air}} dt + \int_0^{t_{dis}} \frac{A \cdot N_{PB-TES} \cdot (G_{dis})_t (\Delta p_{dis})_t}{\rho_{air}} dt \right] \frac{1}{\eta_{comp}} \tag{8}$$

where G is mass flow rate of HTF per cross-sectional area for full cycle analysis. t is charging and discharging time for PB-TES. η_{comp} is compressor efficiency and assumed equal to 0.90.

Preliminary designs calculations under dynamic boundary conditions

In present investigation, dynamic modeling is considered for calculation of thermo-economic parameters. Energy stored during charging cycle and discharging cycle is evaluated from Eqs. (9) and (10), respectively.

$$(E_{PB-TES})_{dis} = \int_0^{t_{dis}} (A) (N_{PB-TES}) (G_{dis})_t (c_{p-air})_t [((T_{out})_t - T_{in})]_{dis} dt \tag{9}$$

where $[((T_{out})_t - T_{in})]_{dis}$ and $[((T_{in}) - (T_{out})_t)]_{ch}$ are in and out temperature from PB-TES during discharging and charging mode. Temperature-dependent specific heat of HTF fluid is evaluated as per time fraction parameters. A is cross-sectional area of the PB-TES unit.

$$(E_{PB-TES})_{ch} = \int_0^{t_{ch}} (A) (N_{PB-TES}) (G_{ch})_t (c_{p-air})_t [((T_{in}) - (T_{out})_t)]_{ch} dt \tag{10}$$

Overall thermal efficiency of the PB-TES is shown in Eq. (11) where discharge energy is output of the PB-TES and charging energy and pumping energy is input of the PB-TES.

$$\eta_{ther} = \frac{(E_{PB-TES})_{dis}}{(E_{PB-TES})_{ch} + (E_{ch-pump}) + (E_{dis-pump})} \tag{11}$$

During charging of the PB-TES, the equation for thermo-cline thickness is evaluated in Eq. (12), where x is height of the PB-TES tanks as per temperature variations during charging and discharging.

$$TC_{dis} = \frac{|x_{T-50} - x_{T+50}|}{H} \tag{12}$$

Boundary conditions for economic model development

Using the following equations for CAPEX and LCOE financial indicators, a simple constant model for calculating economic parameters is formulated. The CAPEX is

derived from Eq. (13) [24] where C is the cost of materials and V is the total volume of materials. Table 4 contains the costs of all the components necessary for economic modeling. Data collection for material pricing and thermal attributes is derived from earlier research [31] and local area of study region quotes.

$$CAPEX = \sum_{i=1}^{N_{mat}} C_i V_i \tag{13}$$

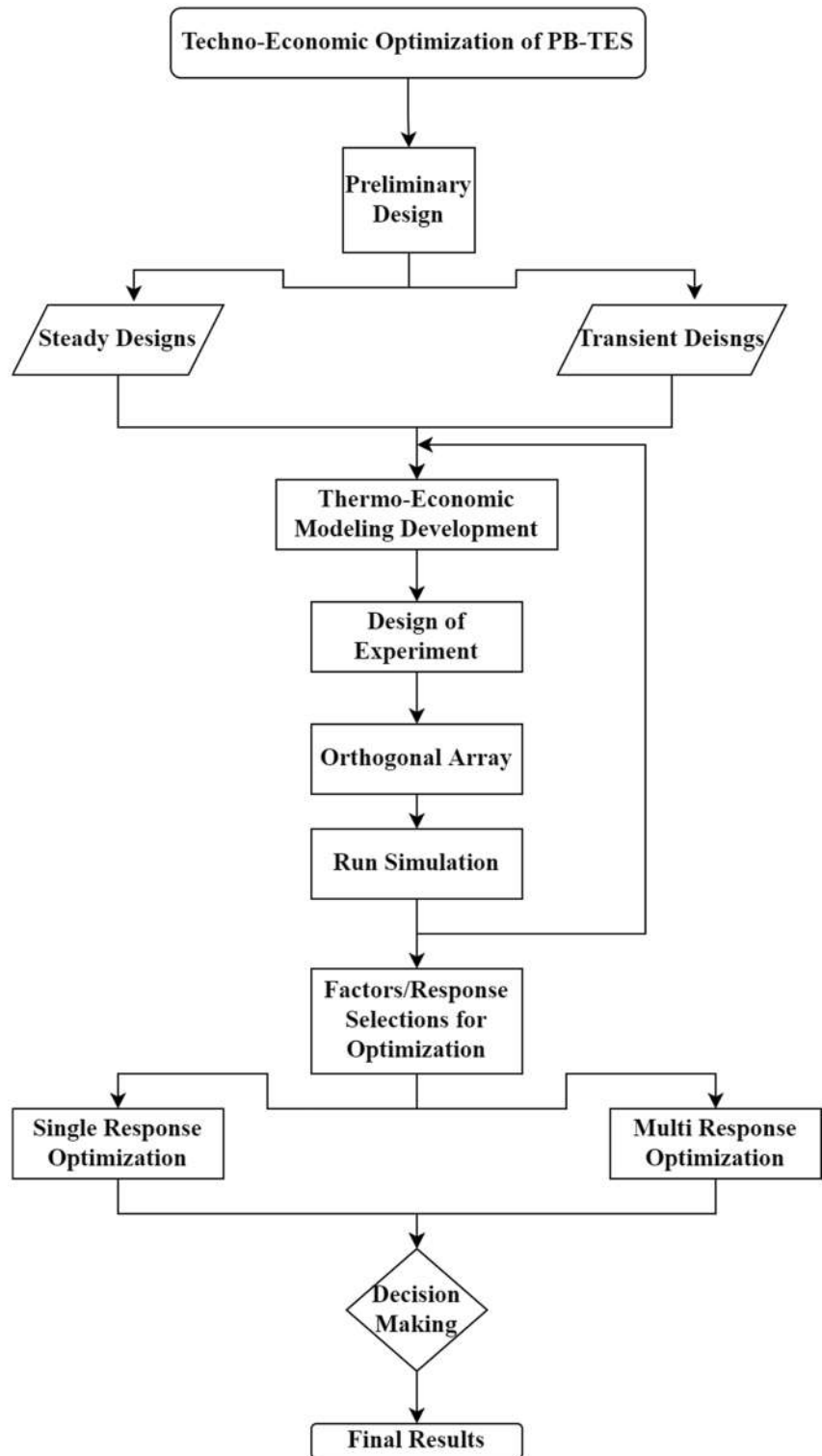
The operational cost of the system is calculated using Eq. (14), where 5% of the CAPEX cost is assumed for calculations including pumping power and the regional electricity rate (0.12 \$/kWh). All economic calculations are made on an annual basis.

$$OPEX = (0.05 * CAPEX) + (E_{pump} C_{ele} N_{PB-TES} (365)) \tag{14}$$

Table 4 Cost of main components required for techno-economic

Component	Value	Unit
Alumina	50–60	[\$/m ³]
Insulation material	4000–5000	[\$/m ³]
Tank steel	40,000–50,000	[\$/m ³]
Foundation	500–1000	[\$/m ³]
Steel balls (wastage)	100–200	[\$/m ²]

Fig. 5 Proposed research methodology required for optimization of PB-TES component combined with CSP plant



Pumping power is evaluated from Eq. (8). LCOE (Levelized cost of energy) is calculated using formula show in Eq. (15).

$$LCOE = \frac{\sum_{n=1}^N \frac{Plant_Cost}{(1+r)^n}}{\sum_{n=1}^N \frac{E_{net}}{(1+r)^n}} \tag{15}$$

ENET is the recoverable net electrical production of the TES unit. LCOE was created by Short et al. [32]. For NREL, it is evaluated using Eq. (15), where plant cost is the total of plant installation, operation and maintenance costs, and other plant-related costs. In the current analysis, a 25 MW_e electrical capacity plant is considered, and all expenditures are calculated accordingly.

Design methodology

Figure 5 proposes the research technique necessary for the optimization of PB-TES. In this section, we will talk about the four most important parts of the research process.

In the first phase, an initial steady-state model is created to assess the thermal behavior of the packed-bed thermal energy storage device during a full charging and discharging cycle. At this stage, it was assumed that the mass flow rate and design temperature of the charge were fixed. For these steady-state computations, the TES volume Eq. (5) is employed and an initial efficiency of 0.85 is used. Using Eqs. (3) and (4), the mass flow rate under charging and discharging circumstances is calculated (4). A temperature cutoff is necessary to determine the discharge time for the cycle analysis. This modeling research is based on the idea of a simple CO₂-based Rankine generator with a maximum working temperature of 600 °C and a minimum working temperature of 100 °C.

As in the second stage, the thermo-financial performance of the TES must be evaluated with respect to suitable strong limit constraints. In typical operating settings, the mass flow rate of the charge depends on the energy input from upstream. Consideration must now be given to the thermo-financial KPIs obtained during the TES under consistent and dynamic limit settings. During the subsequent phases of development, the dynamic limit conditions should be addressed if a significant difference is found between them. Significant plan factors (mathematical and operational boundaries) and competing objectives should be differentiated as a last step. Then, a comprehensive multi-objective development should be conducted to study the extent of variation in the distinguished plan boundaries. Multiple objectives are optimized utilizing the CD function approach, which is advantageous.

Design of experiment (DOE)–Taguchi method theory

Techno-economic performance of PB-TES combined with CSP plants necessitates an efficient design and depends on a variety of input parameters, such as number of tanks, tank height, charging and discharging temperature design, and tank porosity. All of these elements contribute to the optimization of thermal energy systems for CSP facilities. The Taguchi method is a strategy for optimizing the PB-TES system for certain parameters. For optimization, the Taguchi technique utilizes an orthogonal array. Several control variables with fixed values are found using the Taguchi approach. The construction of an experiment table necessitates the selection of a specific orthogonal array (OA) based on these factors [33]. This OA includes optimal runs for certain parameters and their values, indicating that the Taguchi method is a reliable methodology that works on the principle of minimal experiments to save money during trials.

In Taguchi technique, results from OA are analyzed using the “signal-to-noise ratio” parameter, depending on the condition of the response parameters; three criteria are stated in Table 5 for signal-to-noise ratio (*S/N*).

n is the number of observations collected during simulation, *Y* is the simulated response value, and *I* is the number of simulation repeats. *I* is equal to one in all situations for this research. For optimal results, “Analysis of Variance” (ANOVA) is used to determine the contribution of every input parameter. ANOVA facilitates the identification of flaws in simulation or experiment data.

Optimum runs for orthogonal array are selected by Eq. (16) generated by Ross [34], as per this equation *N*_{min} is minimum number of DOE runs required for any study, *NV* represents total variables selected for study, and *l* represents total number of levels.

$$(N_{Min}) = 1 + NV(L - 1) \tag{16}$$

The control variables and their chosen values for the present investigation are presented in Table 6. As seen in the table, a total of five criteria, each with three levels, are selected. The selection of the components and levels is based on prior studies published by several scholars [24, 35–41]. After analyzing all of these research articles, the final

Table 5 Signal-to-noise ratio for different conditions [Minitab help]

<i>S/N</i> ratio	Formula
Larger is better	$\left[S/N_{large} = -10\log \left[\frac{1}{n} \sum \frac{1}{Y_i^2} \right] \right]$
Smaller is better	$\left[S/N_{large} = -10\log \left[\frac{1}{n} \sum Y_i^2 \right] \right]$

Table 6 Control factors and their levels

No.	Factors	Labels	Unit	Level-I	Level-II	Level-III
1	Void fraction	VF	[–]	0.3	0.4	0.5
2	Number of parallel tanks	NPT	[–]	2	3	4
3	Height of tank	HTT	[m]	12	15	17
4	Hot temperature	HT	[°C]	560	565	570
5	Cold temperature	CT	[°C]	280	290	300

Table 7 Formulas required for ANOVA table

Description	Formula	–
Sum of square (SS-mean)	$SS = n(x_1 - \bar{m})^2 + n(x_2 - \bar{m})^2 + n(x_3 - \bar{m})^2$	Where n total trials of experiment/simulation, x represent mean S/N ratio values, m is mean of all S/N ratio
Sum of square (SS-total)	$SS_{total} = \sum_{i=1}^{n=27} (x_i - \bar{\omega})^2$	Where $\bar{\omega}$ is total mean of all experiment trials
Sum of square (SS-error)	$SS_{error} = SS_{total} - SS_{mean}$	–
Degree of freedom	$DOF = Level - 1$	Where DOF is degree of freedom
Variance/MS (mean square)	$Variance = \frac{SS_{error}}{DOF}$	–
F -ratio	$F - Ratio = \frac{MS_{factor}}{MS_{error}}$	–
% of contribution	$\frac{SS_{mean}}{SS_{Total}} \times 100$	–

components and levels for the PB-TES techno-economic analysis are picked.

Analysis of variance (ANOVA)

The greatest benefit of the Taguchi technique is the variance analysis table, which predicts the contribution of each input parameter and the mistakes associated with orthogonal array-generated outputs [33]. In the ANOVA table, the total of squares, the mean of squares, the variance, the contribution, and the F -factor are the essential indicators that assist in identifying faults and improving optimizations [34]. Table 7 lists all the formulae necessary for generating ANOVA tables.

Orthogonal array

When factor and level are fixed in the Taguchi technique, an orthogonal array is required to finish the runs. The Minitab [42] is utilized to conduct appropriate simulation tests for the PB-TES system. There are a total of 27 experiment runs, which are listed in Table 8. All simulations are executed according to this orthogonal array. In the present analysis, three response parameters are selected: the capacity factor of CSP plants paired with PB-TES (CF), thermal energy generated by PB-TES (TE-TES), and the levelized cost of energy (LCOE) (LCOE). LCOE is an economic metric of the plant that includes significant plant costs, such as TES building and maintenance costs.

Table 8 Orthogonal array (L_{27})

Run	VF	NPT	HTT	HT	CT
1	0.3	2	12	560	280
2	0.3	2	12	560	290
3	0.3	2	12	560	300
4	0.3	3	15	565	280
5	0.3	3	15	565	290
6	0.3	3	15	565	300
7	0.3	4	17	570	280
8	0.3	4	17	570	290
9	0.3	4	17	570	300
10	0.4	2	15	570	280
11	0.4	2	15	570	290
12	0.4	2	15	570	300
13	0.4	3	17	560	280
14	0.4	3	17	560	290
15	0.4	3	17	560	300
16	0.4	4	12	565	280
17	0.4	4	12	565	290
18	0.4	4	12	565	300
19	0.5	2	17	565	280
20	0.5	2	17	565	290
21	0.5	2	17	565	300
22	0.5	3	12	570	280
23	0.5	3	12	570	290
24	0.5	3	12	570	300
25	0.5	4	15	560	280
26	0.5	4	15	560	290
27	0.5	4	15	560	300

Result and discussion

Various thermo-physical factors, such as tank size, charging and discharging temperatures, affect the techno-economic optimization of packed-bed thermal energy storage. The main goal of this analysis is to find relationships between variables and responses using the signal-to-noise ratio and to do optimization research for single-response and multi-response parameters using the Taguchi and CD function approaches.

Signal-to-noise ratio analysis: capacity factor of CSP plant, thermal energy of BT-TES and LCOE

For the research of techno-economic optimization of a CSP plant integrated with PB-TES, the following five elements have been selected as control parameters: (1) VF, (2) NPT, (3) HTT, (4) HT, and (5) CT. The nomenclature of HT and

CT is collected from the SAM software theory handbook [NREL]. Table 6 displays these five control parameters and their respective values. Equation (16) was used to determine the total number of trial runs for this research project, and Table 8 lists the 27 best runs. This combination of variables and levels is the same for each of the three response parameters used for this investigation. After the production of the orthogonal array, the simulation of the technological-economic system will be undertaken using the equations described in the preceding portion of this study. The input values necessary to solve these equations must be obtained from Table 6. Using the formulae shown in Table 5, the S/N ratio is calculated for three response parameters. Larger is the best choice when selected for CP and TE-TES, but smaller is the best option when chosen for LCOE. The signal-to-noise ratio for each of the three response characteristics is displayed in Tables 9, 10, and 11 accordingly.

Table 9 Mean signal-to-noise ratio analysis for capacity factor (CF) of CSP plant

Run	VF	NPT	HTT	HT	CT	CF	S/N
1	0.3	2	12	560	280	69.20	36.80
2	0.3	2	12	560	290	68.70	36.74
3	0.3	2	12	560	300	67.70	36.61
4	0.3	3	15	565	280	69.30	36.81
5	0.3	3	15	565	290	68.50	36.71
6	0.3	3	15	565	300	67.50	36.59
7	0.3	4	17	570	280	69.20	36.80
8	0.3	4	17	570	290	68.40	36.70
9	0.3	4	17	570	300	67.10	36.53
10	0.4	2	15	570	280	69.80	36.88
11	0.4	2	15	570	290	68.70	36.74
12	0.4	2	15	570	300	67.40	36.57
13	0.4	3	17	560	280	69.70	36.86
14	0.4	3	17	560	290	68.80	36.75
15	0.4	3	17	560	300	68.10	36.66
16	0.4	4	12	565	280	69.30	36.81
17	0.4	4	12	565	290	68.20	36.68
18	0.4	4	12	565	300	67.40	36.57
19	0.5	2	17	565	280	69.70	36.86
20	0.5	2	17	565	290	69.10	36.79
21	0.5	2	17	565	300	67.50	36.59
22	0.5	3	12	570	280	69.30	36.81
23	0.5	3	12	570	290	68.60	36.73
24	0.5	3	12	570	300	67.60	36.60
25	0.5	4	15	560	280	69.80	36.88
26	0.5	4	15	560	290	68.90	36.76
27	0.5	4	15	560	300	68.20	36.68



Table 10 Mean signal-to-noise ratio analysis for thermal energy produced by PB-TES

Run	VF	NPT	HTT	HT	CT	TE-TES	S/N
1	0.3	2	12	560	280	83.88	38.47
2	0.3	2	12	560	290	81.39	38.21
3	0.3	2	12	560	300	81.06	38.18
4	0.3	3	15	565	280	85.92	38.68
5	0.3	3	15	565	290	83.37	38.42
6	0.3	3	15	565	300	80.69	38.14
7	0.3	4	17	570	280	85.56	38.65
8	0.3	4	17	570	290	84.24	38.51
9	0.3	4	17	570	300	82.28	38.31
10	0.4	2	15	570	280	81.98	38.27
11	0.4	2	15	570	290	80.35	38.10
12	0.4	2	15	570	300	80.67	38.13
13	0.4	3	17	560	280	83.10	38.39
14	0.4	3	17	560	290	84.15	38.50
15	0.4	3	17	560	300	80.67	38.13
16	0.4	4	12	565	280	83.54	38.44
17	0.4	4	12	565	290	81.37	38.21
18	0.4	4	12	565	300	79.67	38.03
19	0.5	2	17	565	280	82.78	38.36
20	0.5	2	17	565	290	80.81	38.15
21	0.5	2	17	565	300	77.68	37.81
22	0.5	3	12	570	280	82.28	38.31
23	0.5	3	12	570	290	81.17	38.19
24	0.5	3	12	570	300	80.21	38.08
25	0.5	4	15	560	280	83.26	38.41
26	0.5	4	15	560	290	82.37	38.32
27	0.5	4	15	560	300	81.49	38.22

Discussion of results

Discussion of signal-to-noise ratio (S/N)

After selecting a total of five parameters with three levels each and generating a total of 27 trials using Minitab, the next step is to calculate the signal-to-noise ratio for each of the three response parameters. Individual S/N ratios for CF, TE-TES, and LCOE are detailed in Tables 9, 10, and 11, respectively. Signal-to-noise ratio analysis has the benefit of ranking the identification of response parameter variables. Tables 12, 13, and 14 accordingly display the ranking for each answer parameter.

The larger is better option chosen for the CF and TE-TES replies, while the smaller is better option chosen for the LCOE response. Table 12's average S/N ratio is calculated by picking each component for each level and then averaging the individual S/N ratios. The average S/N ratios are then displayed in Tables 12, 13, and 14. For rank

identification, users need to figure out Delta. Equation (17) shows how to figure out Delta.

$$\text{Delta} = (\text{Avg}^{S/N})_{\text{Max}} - (\text{Avg}^{S/N})_{\text{Min}} \quad (17)$$

As shown in Table 12, for each factor three average values of S/N ratio are calculated so maximum and minimum of these average S/N ratios are used in Eq. (17).

According to Table 12, the first-ranked parameter is the cold temperature of the thermal energy storage system, the second-ranked parameter is the void fraction of the tank, the third-ranked parameter is the hot temperature of the TES, and the fourth- and fifth-ranked parameters are the height of the tank and the number of tanks, respectively. Average S/N ratios are displayed in the main impact plots of the CSP plant's capacity factor.

As shown in Fig. 6, the highest contribution of input parameters is calculated for cold temperature of the thermal energy storage.

Table 11 Mean signal-to-noise ratio analysis for LCOE (levelized cost of energy)

Run	VF	NPT	HTT	HT	CT	LCOE	S/N
1	0.3	2	12	560	280	167.23	-44.47
2	0.3	2	12	560	290	169.50	-44.58
3	0.3	2	12	560	300	170.84	-44.65
4	0.3	3	15	565	280	168.40	-44.53
5	0.3	3	15	565	290	169.27	-44.57
6	0.3	3	15	565	300	172.80	-44.75
7	0.3	4	17	570	280	167.10	-44.46
8	0.3	4	17	570	290	168.50	-44.53
9	0.3	4	17	570	300	172.69	-44.75
10	0.4	2	15	570	280	166.80	-44.44
11	0.4	2	15	570	290	167.40	-44.48
12	0.4	2	15	570	300	171.31	-44.68
13	0.4	3	17	560	280	166.32	-44.42
14	0.4	3	17	560	290	168.50	-44.53
15	0.4	3	17	560	300	169.34	-44.58
16	0.4	4	12	565	280	167.80	-44.50
17	0.4	4	12	565	290	170.20	-44.62
18	0.4	4	12	565	300	172.90	-44.76
19	0.5	2	17	565	280	166.20	-44.41
20	0.5	2	17	565	290	167.90	-44.50
21	0.5	2	17	565	300	168.34	-44.52
22	0.5	3	12	570	280	167.10	-44.46
23	0.5	3	12	570	290	170.61	-44.64
24	0.5	3	12	570	300	172.29	-44.73
25	0.5	4	15	560	280	167.21	-44.47
26	0.5	4	15	560	290	169.20	-44.57
27	0.5	4	15	560	300	170.71	-44.65

Table 12 Factors rank identification table for CF (average S/N values)

Level	VF	NPT	HTT	HT	CT
1	36.70	36.73	36.71	36.75	36.84
2	36.73	36.73	36.74	36.71	36.73
3	36.74	36.71	36.73	36.71	36.60
Delta	0.04	0.02	0.03	0.04	0.24
Rank	2	5	4	3	1

Table 14 Factors rank identification table for LCOE (average S/N values)

Level	VF	NPT	HTT	HT	CT
1	-44.59	-44.53	-44.6	-44.55	-44.46
2	-44.55	-44.58	-44.57	-44.57	-44.56
3	-44.55	-44.59	-44.52	-44.57	-44.67
Delta	0.04	0.06	0.08	0.03	0.21
Rank	4	3	2	5	1

Table 13 Factors rank identification table for TE-TES (average S/N values)

Level	VF	NPT	HTT	HT	CT
1	38.4	38.19	38.23	38.31	38.44
2	38.25	38.32	38.3	38.25	38.29
3	38.2	38.34	38.31	38.28	38.11
Delta	0.19	0.16	0.08	0.07	0.33
Rank	2	3	4	5	1

According to Table 13, the parameter with the highest rank is the cold temperature of the thermal energy storage, followed by the void percentage of the tank, the number of tanks, the height of the tank, and then the hot temperature of the thermal energy storage. Figure 7 shows the average S/N ratios for the main effect plots of thermal energy made by a thermal energy storage system.

According to Table 14, the first rank of the parameter is the cold temperature of the thermal energy storage; the

Fig. 6 Main effect plot for mean S/N ratio of CF (capacity factor)

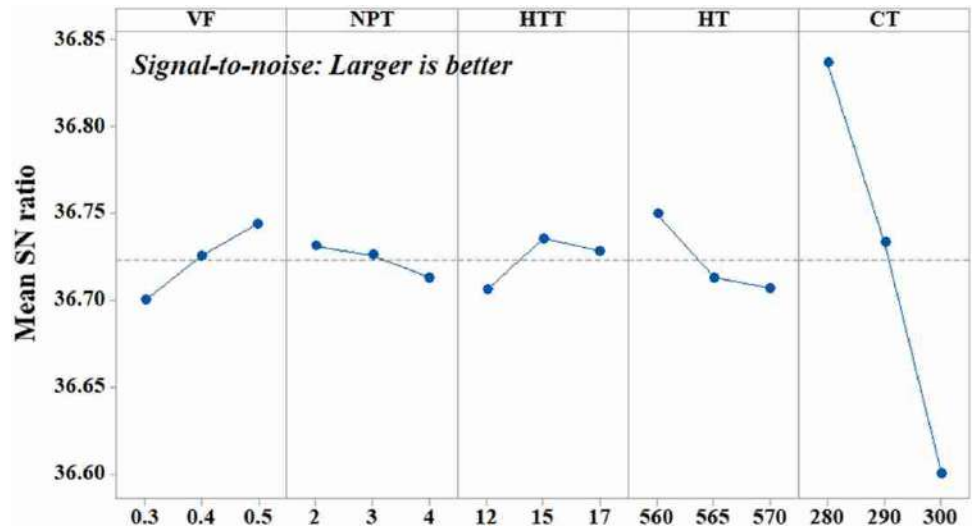


Fig. 7 Main effect plot for mean S/N ratio of TE-TES (thermal energy)

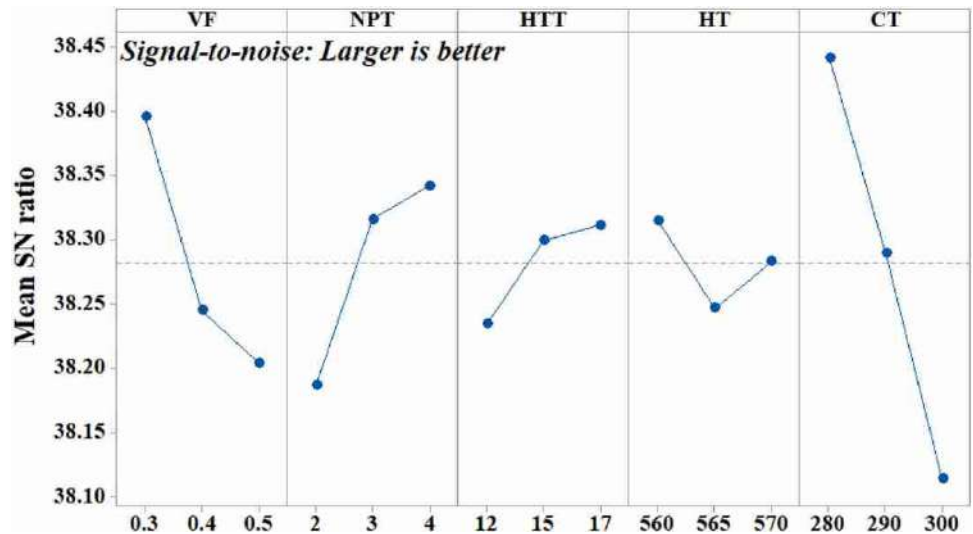


Fig. 8 Main effect plot for mean S/N ratio of LCOE (levelized cost of energy)

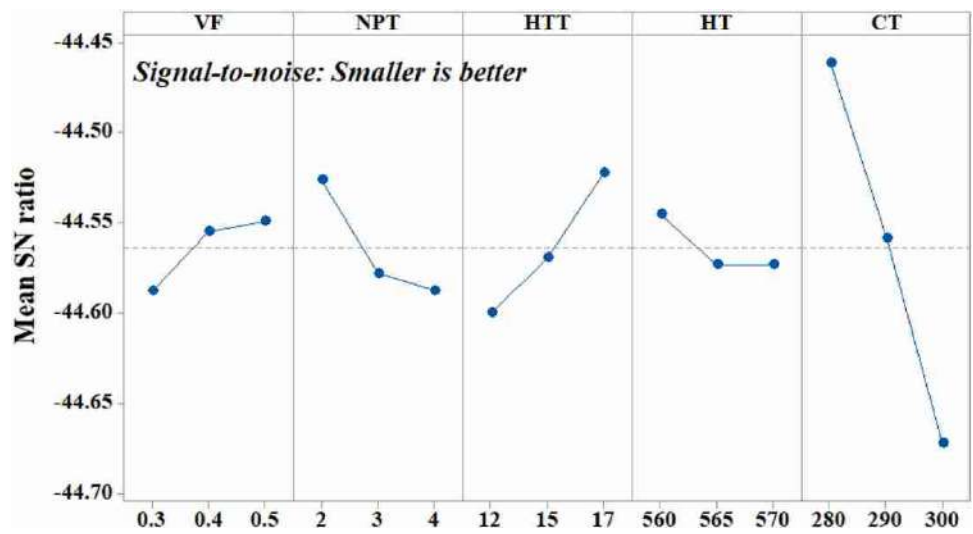


Table 15 ANOVA tale for CF (capacity factor)

Source	<i>df</i>	SS	Contribution	MS	<i>F</i> value	<i>P</i> value	S/NS
Regression	5	0.27	94.99%	0.054	79.61	0	S
VF	1	0.008	2.98%	0.0085	12.47	0.002	S
NPT	1	0.0015	0.52%	0.0015	2.19	0.154	NS
HTT	1	0.0027	0.95%	0.0027	3.96	0.06	S
HT	1	0.0081	2.83%	0.0081	11.85	0.002	S
CT	1	0.251	87.72%	0.2519	367.59	0	S
Error	21	0.014	5.01%	0.0006			
Total	26	0.287	100.00%				

Table 16 ANOVA tale for TE-TES (thermal energy)

Source	<i>df</i>	SS	Contribution	MS	<i>F</i> value	<i>P</i> value	S/NS
Regression	5	70.7476	80.08%	14.1495	16.89	0	S
VF	1	14.832	16.79%	14.832	17.7	0	S
NPT	1	9.6515	10.92%	9.6515	11.52	0.003	S
HTT	1	2.6771	3.03%	2.6771	3.19	0.058	S
HT	1	0.3836	0.43%	0.3836	0.46	0.506	NS
CT	1	43.2035	48.90%	43.2035	51.56	0	
Error	21	17.5972	19.92%	0.838			
Total	26	88.3449	100.00%				

Table 17 ANOVA tale for LCOE (levelized cost of energy)

Source	<i>df</i>	SS	Contribution	MS	<i>F</i> value	<i>P</i> value	S/NS
Regression	5	96.509	87.95%	19.3017	30.66	0	S
VF	1	2.546	2.32%	2.5463	4.04	0.057	S
NPT	1	6.468	5.89%	6.468	10.27	0.004	S
HTT	1	9.831	8.96%	9.8306	15.62	0.001	S
HT	1	1.361	1.24%	1.3613	2.16	0.156	NS
CT	1	76.302	69.54%	76.3024	121.21	0	S
Error	21	13.22	12.05%	0.6295			
Total	26	109.728	100.00%				

Table 18 Percentage contribution (PC) for all three response parameters

Factors	CF	TE-TES	LCOE
VF	2.98	16.79	2.32
NPT	0.52	10.92	5.89
HTT	0.95	3.03	8.96
HT	2.83	0.43	1.24
CT	87.72	48.90	69.54

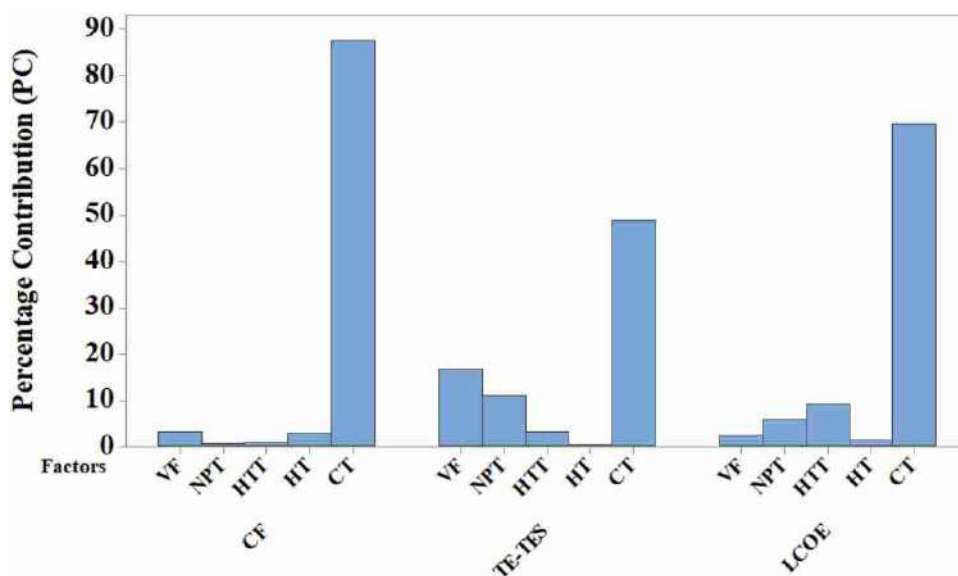
second rank is the height of the tank; the third rank is the number of tanks; and the fourth and fifth ranks are the void fraction of the TES and the hot temperature of the thermal energy storage, respectively. Figure 8 depicts average *S/N* ratios for LCOE main effect plots (levelized cost of energy).

If horizontal profile is present in effects plots of three response parameters, then particular parameters and its levels should be omitted from study [33], but in present study, there is no horizontal line present in any effect plots (Figs. 6, 7, 8).

Discussion of analysis of variance (ANOVA)

Analysis of variance (ANOVA) may be used to determine the significance (S) or nonsignificance (NS) of each component. In the present study, an ANOVA test was conducted for the five control variables and three response parameters listed in Table 6. In Table 7, the necessary formula is provided. The ANOVA tables for CF, TE-TES, and LCOE are presented in Tables 15, 16, and 17, respectively. *df* (degree of freedom), SS (sum of square), percentage contribution, MS (mean of square), *F* and *P* values with

Fig. 9 Percentage contribution (PC) for all three response parameters



significance and nonsignificance columns are provided in the ANOVA table. Selective response parameters are the most effective factors for determining F value and P value. The P value is used in ANOVA calculations to calculate the 95% confidence interval. If the P value is less than or equal to 0.05, the input parameter is significant; otherwise, the parameter is not significant. Another essential aspect is “percentage contribution,” which demonstrates the effect of the factors on one another in relation to the selected response parameter. The maximum contribution percentage of the input parameter is chosen as the top-rated parameter for the selective response parameter. Table 18 and Fig. 9 illustrate the percentage contribution (PC) for each of the three response parameters. As depicted in Fig. 9, the highest PC for CF is found at a cold temperature of 87.72%, while the highest PC for TE-TES is discovered at a cold temperature of 48.90%, and the maximum PC for the final response parameter is found at a cold temperature of 69.54%.

Minimum PC for CF is 0.52% for number of tanks used for thermal energy storage device, for TE-TES the minimum PC is 0.43% for hot temperature, and for the last response LCOE the minimum PC is 1.24 for the same hot temperature. As seen in Tables 15, 16 and 17, only one NS (nonsignificant) is present like for CF response parameter, the nonsignificant parameter is number of parallel tanks, for TE-TES the nonsignificant parameter is hot temperature, and for last response LCOE, the nonsignificant parameter is hot temperature.

Single- and multi-objective optimization

Single optimal solution for three response parameters is done by using average signal-to-noise ratio analysis performed for these responses. The average signal-to-noise ratio is listed in Tables 12, 13 and 14 for CF, TE-TES, and LCOE, respectively. Optimal solutions using Taguchi method are only possible to select the maximum optimum values for each level and each factors. Optimal solution for capacity factor is “ $(VF)^{0.5}(NPT)^2(HTT)^{15}(HT)^{560}(CT)^{280}$,” optimal solution for thermal energy production using thermal energy storage is “ $(VF)^{0.3}(NPT)^4(HTT)^{17}(HT)^{560}(CT)^{280}$,” and optimal solution for last response LCOE is “ $(VF)^{0.5}(NPT)^2(HTT)^{17}(HT)^{560}(CT)^{280}$.”

Multi-objective optimization

For the present techno-economic analysis of thermal energy storage, the CD function (composite desirability) multi-objective optimization approach is chosen. Two response parameters, capacity factor and thermal energy of TES, are selected as “want to maximum” objective selection criterion, whereas one response parameter is selected as “want to lowest” objective selection criteria. This optimization is performed using Minitab (Table 19).

In the CD function, the D function value is the most crucial; therefore, the higher the CD function value, the more precise the optimization outcomes. The highest CD function value is one and the lowest CD function value is zero. CD function value for all 27 trials is shown in Table 20.



Table 19 Objective goals required for CD function optimization

Response	Goal	Lower	Upper	Weight	Importance
LCOE	Minimum	150	175	1	1
TE-TES	Maximum	70	90	1	1
CF	Maximum	60	75	1	1

Three best optimum results for multi-objective design criteria (as seen in Table 19) are listed in Table 21, in which all CD values are more than 0.9 and approach to one value.

As seen in Table 21, the best multi-objective solution is found at void fraction of 0.3, number of tanks is equal to 3,

height of the tank is equal to 17 m, and hot and cold temperature is equal to 560 °C and 280 °C, respectively.

Conclusions

A comprehensive thermo-economic analysis of packed-bed thermal energy storage (PB-TES) was conducted to analyze and improve the entire system. In the present work, the Taguchi method is utilized for the analysis and optimization of response parameter designs. Using SAM input data, a numerical model of packed-bed thermal energy storage is created and solved for Jaipur, India. This PB-TES is coupled with a CSP plant that is capable of generating 25 MWe of electricity using a CO₂-based Rankine generator. The

Table 20 Composite desirability values for individual trials

Run	VF	NPT	HTT	HT	CT	CF	TE-TES	LCOE	CD value
1	0.3	2	12	560	280	69.20	83.88	167.23	0.80
2	0.3	2	12	560	290	68.70	81.39	169.50	0.53
3	0.3	2	12	560	300	67.70	81.06	170.84	0.24
4	0.3	3	15	565	280	69.30	85.92	168.40	0.83
5	0.3	3	15	565	290	68.50	83.37	169.27	0.55
6	0.3	3	15	565	300	67.50	80.69	172.80	0.24
7	0.3	4	17	570	280	69.20	85.56	167.10	0.83
8	0.3	4	17	570	290	68.40	84.24	168.50	0.54
9	0.3	4	17	570	300	67.10	82.28	172.69	0.20
10	0.4	2	15	570	280	69.80	81.98	166.80	0.79
11	0.4	2	15	570	290	68.70	80.35	167.40	0.52
12	0.4	2	15	570	300	67.40	80.67	171.31	0.24
13	0.4	3	17	560	280	69.70	83.10	166.32	0.92
14	0.4	3	17	560	290	68.80	84.15	168.50	0.65
15	0.4	3	17	560	300	68.10	80.67	169.34	0.36
16	0.4	4	12	565	280	69.30	83.54	167.80	0.75
17	0.4	4	12	565	290	68.20	81.37	170.20	0.46
18	0.4	4	12	565	300	67.40	79.67	172.90	0.14
19	0.5	2	17	565	280	69.70	82.78	166.20	0.83
20	0.5	2	17	565	290	69.10	80.81	167.90	0.59
21	0.5	2	17	565	300	67.50	77.68	168.34	0.31
22	0.5	3	12	570	280	69.30	82.28	167.10	0.71
23	0.5	3	12	570	290	68.60	81.17	170.61	0.44
24	0.5	3	12	570	300	67.60	80.21	172.29	0.16
25	0.5	4	15	560	280	69.80	83.26	167.21	0.86
26	0.5	4	15	560	290	68.90	82.37	169.20	0.59
27	0.5	4	15	560	300	68.20	81.49	170.71	0.31

Table 21 Optimum solution for three response parameters using CD function technique

Solution	VF	NPT	HTT	HT	CT	LCOE fit	TE-TES fit	CF fit	Composite desirability
1	0.3	2.5	17	560	280	166.20	84.68	69.63	0.93
2	0.3	2	17	560	280	165.89	84.30	69.67	0.91
3	0.5	4	17	560	280	166.33	83.95	69.87	0.91

primary objective of the present study is to determine the ranking of factors for selective response parameters. The significance of the factors is the second objective of the present study. The final objective of the study is to determine the single- and multi-objective optimization of the PB-TES component via Taguchi optimization and CD function optimization. The very first phase of the investigation is to identify the most effective STES medium for usage in thermal energy systems. In this experiment, three distinct types of STES media are used, and CFD simulations for these three media types (alumina, steel, and hybrid of both) are performed. The thermal energy system based on alumina is confirmed by previously published research. A thorough techno-economic study will be conducted after identifying the most cost-effective STES medium.

The following five input parameters, each with three levels, have been selected for this study: the parameters include volume fraction of thermal energy tank (VF), number of parallel tanks (NPT), tank height (HTT), hot temperature of HTF (HT), and cold temperature of HTF (CT) (CT). Each component has three levels that are determined after a review of past research. The following three response parameters are selected: capacity factor, thermal energy generated by thermal energy system, and lastly, levelized energy cost (LCOE). In the current study, rank identification is done using the signal-to-noise ratio, the significance of each parameter is solved using analysis of variance (ANOVA), and in the last step, three response parameters (CF, TE-TES, and LCOE) are optimized using the CD function approach. The following are the study's principal findings:

1. Three STES media are selected for CFD simulation for constant mass flow rate and the best result was shown by hybrid of alumina and steel. This hybrid is equal mixture of the particles. These hybrid media are then used for techno-economic optimization study.
2. Based on the analysis of variance (ANOVA), the best influence parameter for capacity factor is cold temperature of HTF (87.72%), for thermal energy production by PB-TES the most influence parameter is cold temperature of HTF (48.90%), and the most influence parameter for last response LCOE is cold temperature of HTF (69.54%).
3. Second influence parameter for capacity factor is void fraction (2.98%), for TE-TES the second influence parameter is void fraction (16.79%), and for LCOE the second influence parameter is height of tank (8.96%).
4. Least influence parameter for capacity factor is NPT (0.52%), for TE-TES the least influence parameter is heating temperature of HTF (0.43%), and for LCOE the least influence parameter is heating temperature of HTF (1.24%).
5. Optimal solution for capacity factor is “ $(VF)^{0.5}(NPT)^2(HTT)^{15}(HT)^{560}(CT)^{280}$,” optimal solution for thermal energy production using thermal energy storage is “ $(VF)^{0.3}(NPT)^4(HTT)^{17}(HT)^{560}(CT)^{280}$,” and optimal solution for last response LCOE is “ $(VF)^{0.5}(NPT)^2(HTT)^{17}(HT)^{560}(CT)^{280}$.”
6. The best multi-objective solution is found at void fraction of 0.3, number of tanks is equal to 3, height of the tank is equal to 17 m, and hot and cold temperature is equal to 560 °C and 280 °C, respectively.

References

1. Kuravi, S., Trahan, J., Goswami, D.Y., Rahman, M.M., Stefanakos, E.K.: Thermal energy storage technologies and systems for concentrating solar power plants. In *Progress in Energy and Combustion Science*, vol. 39, no. 4, pp. 285–319 (2013). <https://doi.org/10.1016/j.pecs.2013.02.001>
2. Liu, M., Riahi, S., Jacob, R., Belusko, M., Bruno, F.: Design of sensible and latent heat thermal energy storage systems for concentrated solar power plants: thermal performance analysis. *Renewable Energy* **151**, 1286–1297 (2020). <https://doi.org/10.1016/j.renene.2019.11.115>
3. Steinmann, W.-D.: Thermal energy storage systems for concentrating solar power (CSP) plants. In: *Concentrating Solar Power Technology*, pp. 362–394. Elsevier (2012). <https://doi.org/10.1533/9780857096173.2.362>
4. Mehos, M., Turchi, C., Vidal, J., Wagner, M., Ma, Z., Ho, C., et al.: Concentrating solar power generation demonstration road-map (2017)
5. Zanganeh, G., Pedretti, A., Zavattoni, S., Barbato, M., Steinfeld, A.: Packed-bed thermal storage for concentrated solar power - pilot-scale demonstration and industrial-scale design. *Sol. Energy* **86**, 3084–3098 (2012). <https://doi.org/10.1016/j.solener.2012.07.019>
6. Zanganeh, G., Pedretti, A., Haselbacher, A., Steinfeld, A.: Design of packed bed thermal energy storage systems for high-temperature industrial process heat. *Appl. Energy* **137**, 812–822 (2015). <https://doi.org/10.1016/j.apenergy.2014.07.110>
7. Dostal, V., Hejzlar, P., Driscoll, M.J.: High-performance supercritical carbon dioxide cycle for next-generation nuclear reactors. *Nucl. Technol.* **154**, 265–282 (2006). <https://doi.org/10.13182/NT154-265>
8. Guedéz, R., Ferruzza, D., Arnaudo, M., Rodríguez, I., Perez-Segarra, C.D., Hassar, Z., Laumert, B.: Techno-economic performance evaluation of solar tower plants with integrated multi-layered PCM thermozone thermal energy storage—a comparative study to conventional two-tank storage systems. In: *AIP Conference Proceedings*, p. 1734 (2016). <https://doi.org/10.1063/1.4949159>
9. Erkinaci, T., Baytas, F.: CFD investigation of a sensible packed bed thermal energy storage system with different porous materials. *Int. J. Heat Technol.* **35**(1), S281–S287 (2017). <https://doi.org/10.18280/ijht.35Sp0138>
10. Gasia, J., Tay, N.H.S., Belusko, M., Cabeza, L.F., Bruno, F.: Experimental investigation of the effect of dynamic melting in a cylindrical shell-and-tube heat exchanger using water as PCM. *Appl. Energy* **185**, 136–145 (2017). <https://doi.org/10.1016/j.apenergy.2016.10.042>



11. Hänchen, M., Brückner, S., Steinfeld, A.: High-temperature thermal storage using a packed bed of rocks—heat transfer analysis and experimental validation. *Appl. Therm. Eng.* **31**(10), 1798–1806 (2011). <https://doi.org/10.1016/j.applthermaleng.2010.10.034>
12. Jamshidian, F.J., Gorjian, S., Shafieefar, M.: Techno-economic assessment of a hybrid RO-MED desalination plant integrated with a solar CHP system. In: *Energy Conversion and Management*, Vol. 251, p. 114985 (2022). ISSN:0196-8904. <https://doi.org/10.1016/j.enconman.2021.114985>
13. Zhang, Y., Johansson, P., Kalagasidis, A.S.: Techno-economic assessment of thermal energy storage technologies for demand-side management in low-temperature individual heating systems. *Energy* **236**(C), 121496 (2021)
14. Desai, N.B., Mondejar, M.E., Haglind, F.: Techno-economic analysis of two-tank and packed-bed rock thermal energy storages for foil-based concentrating solar collector driven cogeneration plants. *Renew. Energy* **186**, 814–830 (2022). <https://doi.org/10.1016/j.renene.2022.01.043>
15. Cascetta, M., Cau, G., Puddu, P., Serra, F.: A comparison between CFD simulation and experimental investigation of a packed-bed thermal energy storage system. *Appl. Therm. Eng.* **98**, 1263–1272 (2016). <https://doi.org/10.1016/j.applthermaleng.2016.01.019>
16. Cascetta, M., Serra, F., Cau, G., Puddu, P.: Comparison between experimental and numerical results of a packed-bed thermal energy storage system in continuous operation. *Energy Procedia* **148**, 234–241 (2018). <https://doi.org/10.1016/j.egypro.2018.08.073>
17. Cascetta, M., et al.: Thermocline vs. two-tank direct thermal storage system for concentrating solar power plants: a comparative techno-economic assessment. *Int. J. Energy Res.* **45**(12), 17721–17737 (2021)
18. Lasing, F., Hirsch, T., Odenthal, C., Bauer, T.: Techno-economic optimization of molten salt concentrating solar power parabolic trough plants with packed-bed thermocline tanks. *ASME. J. Sol. Energy Eng.* **142**(5), 051006 (2020). <https://doi.org/10.1115/1.4046463>
19. Ansys® Academic Research Fluid: Release 18.2, Help System, Ansys Fluent theory Guide, ANSYS, Inc.
20. Wilson, G., Sahoo, S., Sabharwal, P., Bindra, H.: Packed bed thermal storage for LWRs. In *Storage and Hybridization of Nuclear Energy: Techno-economic Integration of Renewable and Nuclear Energy*, pp. 229–248. Elsevier (2018). <https://doi.org/10.1016/B978-0-12-813975-2.00007-7>
21. Al-Azawii, M.M.S., Jacobsen, D., Bueno, P., Anderson, R.: Experimental study of thermal behavior during charging in a thermal energy storage packed bed using radial pipe injection. *Appl. Therm. Eng.* (2020). <https://doi.org/10.1016/j.applthermaleng.2020.115804>
22. Kumar Rai, R., Rekha Sahoo, R.: Taguchi-Grey method optimization of VCR engine performance and heat losses by using *Shorea robusta* biodiesel fuel. *Fuel* (2020). <https://doi.org/10.1016/j.fuel.2020.118399>
23. Andreozzi, A., Bianco, N., Manca, O., Nardini, S., Naso, V.: Numerical investigation of sensible thermal energy storage in high temperature solar systems. *WIT Trans. Model. Simul.* **48**, 461–472 (2009). <https://doi.org/10.2495/CMEM090421>
24. Trevisan, S., Guédez, R., Laumert, B.: Thermo-economic optimization of an air driven supercritical CO₂ Brayton power cycle for concentrating solar power plant with packed bed thermal energy storage. *Sol. Energy* **211**, 1373–1391 (2020). <https://doi.org/10.1016/j.solener.2020.10.069>
25. Mao, Q., Zhang, Y.: Thermal energy storage performance of a three-PCM cascade tank in a high-temperature packed bed system. *Renewable Energy* **152**, 110–119 (2020). <https://doi.org/10.1016/j.renene.2020.01.051>
26. Guo, H., Xu, Y., Guo, C., Chen, H., Wang, Y., Yang, Z., Huang, Y., Dou, B.: Thermodynamic analysis of packed bed thermal energy storage system. *J. Therm. Sci.* **29**(2), 445–456 (2020). <https://doi.org/10.1007/s11630-019-1115-7>
27. Gbadago, D.Q., Oh, H.T., Oh, D.H., Lee, C.H., Oh, M.: CFD simulation of a packed bed industrial absorber with interbed liquid distributors. *Int. J. Greenh. Gas Control* (2020). <https://doi.org/10.1016/j.ijggc.2020.102983>
28. Kocak, B., Paksoy, H.: Performance of laboratory scale packed-bed thermal energy storage using new demolition waste based sensible heat materials for industrial solar applications. *Sol. Energy* **211**, 1335–1346 (2020). <https://doi.org/10.1016/j.solener.2020.10.070>
29. Gautam, A., Saini, R.P.: Experimental investigation of heat transfer and fluid flow behavior of packed bed solar thermal energy storage system having spheres as packing element with pores. *Sol. Energy* **204**, 530–541 (2020). <https://doi.org/10.1016/j.solener.2020.05.024>
30. NREL, SAM, CSP Models—System Advisor Model (SAM) (2022).
31. Choudhury, C., Chauhan, P.M., Garg, H.P.: Economic design of a rock bed storage device for storing solar thermal energy. *Sol. Energy* **55**, 29–37 (1995). [https://doi.org/10.1016/0038-092X\(95\)00023-K](https://doi.org/10.1016/0038-092X(95)00023-K)
32. Short, W., Packey, D.J., Holt, T.: *A Manual for the Economic Evaluation of Energy Efficiency and Renewable Energy Technologies* (1995).
33. Kumar, S., Murugesan, K.: Optimization of geothermal interaction of a double U-tube borehole heat exchanger for space heating and cooling applications using Taguchi method and utility concept. *Geothermics* (2020). <https://doi.org/10.1016/j.geothermics.2019.101723>
34. Ross, P.J.: *Taguchi technique for quality engineering: loss function, orthogonal experiments, parameter and tolerance design*. McGraw-Hill, New York (1988)
35. Majumdar, R., Saha, S.K.: Computational study of performance of cascaded multi-layered packed-bed thermal energy storage for high temperature applications. *J. Energy Storage* (2020). <https://doi.org/10.1016/j.est.2020.101930>
36. Khor, J.O., Yang, L., Akhmetov, B., Leal, A.B., Romagnoli, A.: Application of granular materials for void space reduction within packed bed thermal energy storage system filled with macro-encapsulated phase change materials. *Energy Convers. Manage.* (2020). <https://doi.org/10.1016/j.enconman.2020.113118>
37. Jemmal, Y., Zari, N., Asbik, M., Maaroufi, M.: Experimental characterization and thermal performance comparison of six Moroccan rocks used as filler materials in a packed bed storage system. *J. Energy Storage* (2020). <https://doi.org/10.1016/j.est.2020.101513>
38. Hrifech, S., Agalit, H., Jarni, A., Mougouina, E.M., Grosu, Y., Faik, A., Bennouna, E.G., Mimet, A.: Characterization of natural rocks as filler materials for medium-temperature packed bed thermal energy storage system. *J. Energy Storage* (2020). <https://doi.org/10.1016/j.est.2020.101822>
39. Nguyen, T.A., Byrne, R.H.: Software tools for energy storage valuation and design. In: *Current Sustainable/Renewable Energy Reports*, Vol. 8, No. 3, pp. 156–163. Springer (2021). <https://doi.org/10.1007/s40518-021-00186-4>
40. Walayat, K., Duesmann, J., Derks, T., Houshang Mahmoudi, A., Cuypers, R., Shahi, M.: Experimental and numerical investigations for effective thermal conductivity in packed beds of thermochemical energy storage materials. *Appl. Therm. Eng.* (2021). <https://doi.org/10.1016/j.applthermaleng.2021.117006>
41. Gutiérrez, R.E., Haro, P., Gómez-Barea, A.: Techno-economic and operational assessment of concentrated solar power plants with a dual supporting system. *Appl. Energy* (2021). <https://doi.org/10.1016/j.apenergy.2021.117600>



42. Minitab, LLC. (Version 18): Minitab. Retrieved from <https://www.minitab.com>
43. EASE/EERA: European Energy Storage Technology Development Roadmap (2017)
44. ITP Thermal Pty Limited: Concentrating Solar Thermal Power Technology Status, p. 160 (2018)
45. Trevisan, S., Jemmal, Y., Guedez, R., Laumert, B.: Packed bed thermal energy storage: a novel design methodology including quasi-dynamic boundary conditions and techno-economic optimization. *J. Energy Storage* (2021). <https://doi.org/10.1016/j.est.2021.102441>

Publisher's Note Springer Nature remains neutral with regard to jurisdictional claims in published maps and institutional affiliations.

Springer Nature or its licensor holds exclusive rights to this article under a publishing agreement with the author(s) or other rightsholder(s); author self-archiving of the accepted manuscript version of this article is solely governed by the terms of such publishing agreement and applicable law.

Authors and Affiliations

Amit Sharma¹  · Pankaj K. Pandey² · Mukesh Didwania³

¹ Department of Mechanical Engineering, Amity University, Jaipur, Rajasthan, India

² Department of Chemical Engineering, Amity University, Jaipur, Rajasthan, India

³ Department of Mechanical Engineering, Poornima College of Engineering, Jaipur, Rajasthan, India





Simulation and comprehensive technical, economic, and environmental assessments of carbon dioxide capture for methanol production through flue gas of a combined cycle power plant

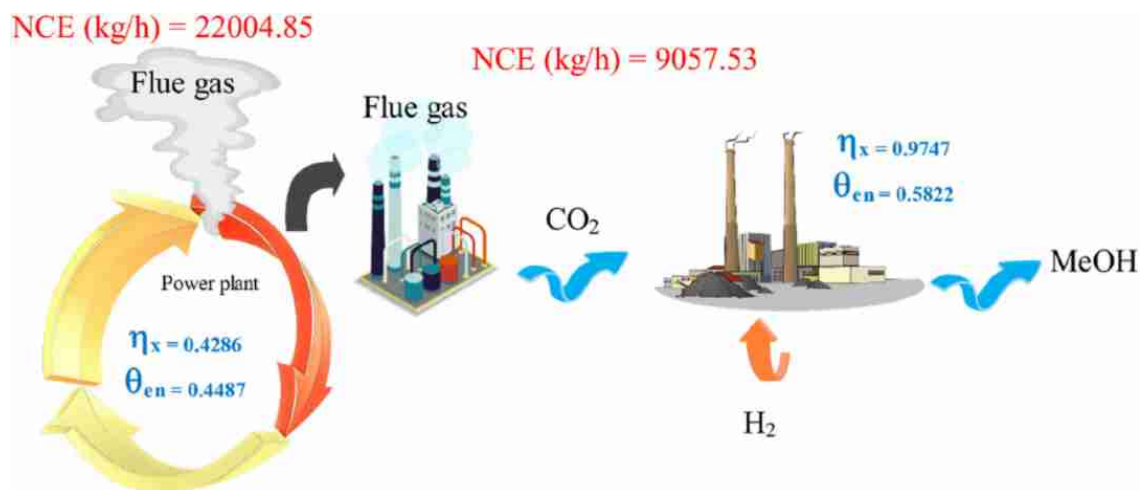
Hao Qi¹ · Xuewen Wu¹ · Hehuan Huan¹

Received: 9 March 2022 / Accepted: 2 July 2022 / Published online: 8 August 2022
© The Author(s), under exclusive licence to Islamic Azad University 2022

Abstract

Although it is an environmental threat, the flue gas of a combined cycle power plant can be a good motivation to produce methanol due to its high carbon dioxide richness. This paper includes a simulation and comprehensive technical, economic, and environmental analyses of the methanol production process through CO₂ capture. In other words, an improved and modified power plant (plus version) is introduced through structural optimization. At first, the combined cycle power plant was simulated, and thermoeconomic and environmental evaluations were performed. Then, it was found that its energy and exergy efficiencies were 44.87 and 42.86%, respectively, and its annual profit was approximately equal to 1.96 M\$. In the second stage, in addition to the power generation section, two sections of carbon dioxide capture and methanol production were simulated, which showed that the performance of the power plant plus was improved compared to the conventional system. Energy and exergy analysis for the power plant plus demonstrated that the total energy and exergy efficiency, in this case, was 58.22 and 97.47%, respectively. From the environmental viewpoint, it was found that the power plant plus could reduce the net carbon dioxide emission by 58.84% compared to the simple system. Economic estimations explained that despite the 116.09% increase in the investment cost of the power plant plus compared to the combined cycle power plant, the annual revenue and profit increased by 182.03 and 116.08%, respectively, and the payback period also decreased by 0.66 years.

Graphical abstract



Keywords Power plant · Methanol production · CO₂ capture · Thermodynamic analysis · Thermoeconomic and environmental assessment

Extended author information available on the last page of the article

Abbreviations

A	Area [m ²]
D	Diameter [m]
\dot{E}	Exergy rate [kW]
\dot{E}_D	Exergy destruction rate [kW]
\dot{G}	Molar flow rate [mol/h]
h	Specific enthalpy [kJ/kg]
J	Interest rate [%]
\dot{m}	Mass flow rate [kg/h] or [ton/h]
P	Pressure [Pa]
\dot{Q}	Heat [kW]
S	Specific entropy [kJ/kg-K]
T	Temperature [K]
U	Overall heat transfer coefficient [W/m ² .K]
V	Volume [m ³]
\dot{W}	Work or power [kW]

Greek symbols

θ	Energy efficiency [%]
η	Exergy efficiency [%]

Subscripts

CH	Chemical
e	Exit
f	Fuel
i	Inlet
L	Loss
P	Product
PH	Physical

Introduction

Environmental issues such as greenhouse gas emissions, global warming, and ozone depletion motivate companies and countries to modify and optimize the structure of conventional power plants [1]. Indeed, many traditional power plants use fossil or hydrocarbon fuels as the input fuel to run the cycle [2]. Moreover, they are usually associated with low efficiency and high irreversibility [3]. In this way, several techniques can be applied to these setups to improve their capabilities, which the operational optimization, structural modification, and the use of the waste heat of the plant are appropriate works [4]. Accordingly, the utilization of the waste heat and carbon dioxide (CO₂) leaving the power plants can be considered for producing energy-based products [5].

One of the proposed ways to improve and ameliorate the power plant's performance is recovering waste energies and materials. Flue gas in a cycle, including CO₂, is one of the potential sources for the recovery processes. Through the hydrogenation of CO₂, methane, hydrocarbons, ethanol, methanol, dimethyl ether, and syngas can be delivered as by-products [6].

Carbon capture and use of heat recovery frameworks are standing out enough to be noticed by scientists recently. Pak et al. [7] described that at a condenser, the CO₂ gas in the flue gas could be easily separated from the condensate. The recovered CO₂ gas is condensed, moved by a CO₂ tanker, and utilized again to produce methanol. Overall energy efficiency was assessed to be 54.60%. Foncillier et al. [8] recovered carboxylates effectively from fermented organic waste. In their examination, an anion-exchange resin was utilized and followed by desorption with CO₂-extended methanol. Sarp et al. [9] compared renewable energy-powered CO₂ to methanol technologies. They examined the CO₂ hydrogenation frameworks and the impetuses that drive them. Hermen et al. [10] devised a novel methanol production from renewable-based power plants combined with hydrogenation. In their work, a new non-combusting heat-carrier biomass gasifier framework was proposed, combined with a solar power plant and alkaline water electrolysis framework, for methanol production from syngas, water, and CO₂. Aspen Plus, MATLAB, and TRNSYS softwares were utilized to model and evaluate the efficiency of each component of the proposed framework in various climatic conditions of Toronto, Canada, and Crotone, Italy.

Multiple advantages of multigeneration energy systems include their ability to integrate with a range of processes, such as CO₂ capture. Li et al. [11] comparatively investigated CO₂ power cycles for the waste heat recovery of the gas turbines. Four classifications and six cycles were picked to address the common design of the supercritical CO₂ power cycle. In another work, Li et al. [12] proposed a hybrid cooling, heating, and power plant, which comprised of CO₂ power system, absorption chiller, and heaters for waste heat recovery of the gas turbine. In the described new framework, the chiller and heaters were driven by the excess energy of the CO₂ power procedure and chimney flue gas simultaneously. A trigeneration plant was proposed by Nazerifard et al. [13] to diminish environmental CO₂-caused pollution and generate methanol, hydrogen (H₂), and electricity. The setup was made out of an organic Rankine cycle, a direct methanol fuel cell, a carbon capture unit, a proton-exchange membrane (PEM) electrolyzer, and a methanol synthesis section. Castellani et al. [14] concentrated on surveying the carbon and energy footprint of a novel cycle for CO₂ recycling, with chimney flue gas as the feedstock of nitrogen (N₂) and CO₂. N₂ was changed into ammonia (NH₃) through the Haber–Bosch cycle and CO₂ into methane (CH₄) utilizing a Sabatier reaction utilizing H₂ generated by renewable energy. Yuan et al. [15] studied the favorable conditions for CH₄ recovery from hydrate supply with gaseous CO₂. The trial results demonstrated that a hydrate supply with underlying free gas, high saturation of free gas, and low saturation of water was suitable for the recovery of the methane with CO₂. Abdelaziz et al. [16] developed effective cycles that

were proper for converting/using CO₂ streams into energy-rich liquid products (fuels).

To increase efficiency, the recently proposed strategy for Heat Recovery Steam Generator (HRSG) Flue-Gas Injection (FGI) into the Heller tower of the power plant was developed by Sharif et al. [17]. At that point, the CO₂ captured plant (utilizing MEA mechanical Absorption), which was installed inside the Heller towers, was explored. Energy and exergy investigation was done for every segment and lastly for the entire power plant under crosswind conditions. León and Martín [18] assessed the power generation utilizing a combined gas turbine/steam turbine cycle. In their investigation, the gas was cleaned up to eliminate humidity, H₂S, CO₂, and NH₃. Fu and Gundersen [19] represented three CO₂ capture procedures. They showed that critical energy saving could be accomplished by appropriate heat and work combination. Leonzio [20] analyzed producing methanol and dimethyl ether from CO₂ hydrogenation. The social considerations about carbon capture and use frameworks were reported. Deng and Adams et al. [21] proposed a new process for coke oven gas and blast furnace gas to methanol with CO₂ capture. They utilized the Aspen Plus software pack to simulate the represented process. Wiesberg et al. [22] used a novel structure for exergy analysis of cycles with chemical reactions, which was utilized to assess the efficiency of two methanol production methods from CO₂ of flue gas. Their investigation included direct hydrogenation and indirect conversion. The exergy efficiency of the direct method was 66.3%, while it was 55.8% for the indirect process, demonstrating the lower sustainability of the latter. They showed that carbon capture and storage had the worst exergy proficiency, even lower than the emission scenario. Alsayegh et al. [23] showed the economic feasibility of a novel methanol production process using captured CO₂ and H₂ obtained from water splitting unit. Ultimately, they compared their method to an alternate sustainable methanol synthesis technique from the literature in order to emphasize the distinctions between electrochemical and thermochemical approaches. Parigi et al. [24] represented energy and economic analyses for the CO₂ re-utilization procedure to produce methanol. To create an economically attractive market for methane and methanol, it was determined that the production plants should maintain a utilization factor of approximately 50%, the cost of SOECs should be close to 1050 €/kW, and the electricity required to operate the system must come from renewable sources at a very low cost (below 40–50 \$/MWh).

Main novelties and contributions

Technology for carbon capture and utilization (CCU) has the potential to make industrial and power production operations more sustainable and generate additional revenue from the conversion of carbon dioxide (CO₂) to commercial products.

To reduce global warming while possibly replacing fossil fuel feedstocks in the chemical and energy sectors, CCU stands as a significant option. The literature review proves that the CO₂ gas exiting the power cycles can be recovered and captured for technical ameliorations. Concerning this fact, the present work is motivated to incorporate a CO₂ capture unit into a combined power plant and use the captured CO₂ for methanol production. Hence, all simulation processes are completely performed using the Aspen Hysys software [25]. Based on the simulation, the comprehensive energy, exergy, economic, and environmental analyses have been implemented to examine the feasibility of the optimized structure with CO₂ capture and methanol production units (power plant plus) compared to the base power plant. Also, a sensitivity analysis of the system is carried out, in which the effect of the reflux ratio of the solvent recovery tower on the performance criteria is measured.

Process overview

Figure 1 shows the diagram of the methanol production process using CO₂ captured from the power plant's flue gas. Operational components include the combined cycle power plant as the principal source of flue gas production and the carbon source required for methanol conversion, chemical absorption, flue gas purification, methanol synthesis, and separation. The combined cycle power plant, which uses natural gas as inlet fuel and steam turbines to generate electricity, regularly releases flue gas into the atmosphere. This flue gas stream contains a significant amount of CO₂ resulting from the combustion of natural gas (methane in this study) in the combustion chamber of the gas turbine.

Contrary to the usual trend, the flue gas produced from the heat recovery section of the power plant enters the CO₂ capture process, wherewith a technology called post-combustion, CO₂ is 90% absorbed and provided to the methanol production system. The recovered CO₂ enters the methanol synthesis and separation process, where it reacts directly with H₂ to produce methanol. H₂ can be supplied in various ways, including natural gas reform, coal gasification, biomass gasification, and electrolyzer [16]. This study considers that the H₂ needed to react with CO₂ is provided through the reforming of natural gas. As shown in Fig. 1, to provide a part of the energy of the carbon capture unit, the energy released from the methanol synthesis and separation section through the methanol reactor and cooling of the methanol reactor products is sent to the stripper tower's reboiler. Likewise, in the CO₂ capture section, at the beginning of the process, a part of the energy from the flue gas cooling is provided to the reboiler, which has a total of three energy flows used for optimization to minimize energy consumption for solvent recovery and create thermal integration.



Fig. 1 Process of methanol production from power plant's flue gas

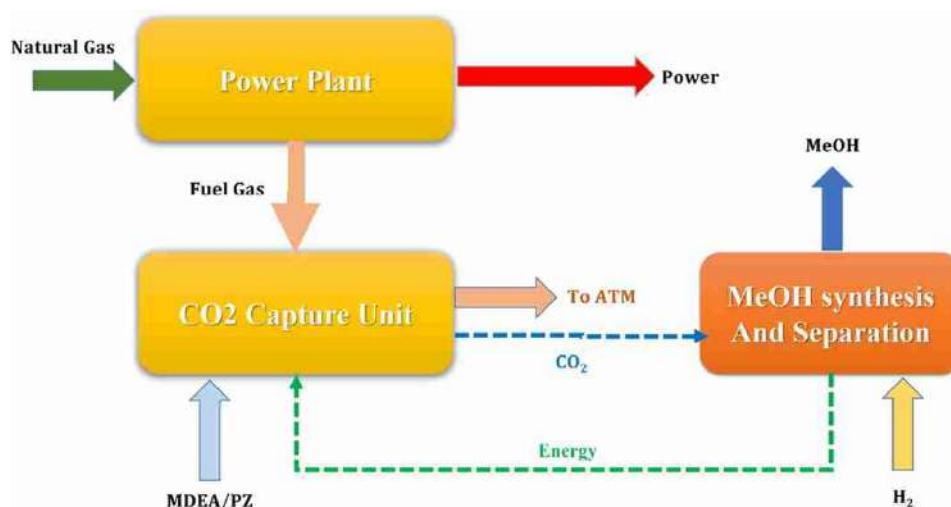


Table 1 Comparison of energy consumption for recovery of different amino solvents (single and mixed)

Work	Solvent	$E_{\text{regen}}(\text{GJ}_{\text{reb}}/\text{t}_{\text{CO}_2})$
Zhao et al. [26]	MDEA-PZ	2.74
Dubois and Thomas [27]	MEA	3.36
Osagie et al. [28]	AMP	2.9
Pérez-Fortes et al. [29]	MEA	4.95
Nwaoha et al. [30]	AMP-PZ-MEA	3.86
Ozcan et al. [31]	Hybrid System	3.2
Laribi, et al. [32]	DEA-PZ	3.03

Since the post-combustion process is performed at a pressure between 101.3 kPa and 120 kPa, the solvent flow and the energy consumption are high. Therefore, choosing a suitable solvent to absorb CO_2 can greatly help reduce costs and increase overall energy efficiency. According to Table 1, which shows a comparison between energy consumption for solvent recovery based on a wide range of chemical solvents, the use of activated methyl diethanolamine solvent (MDEA-PZ) can be a good option to recover CO_2 .

As mentioned, the methanol is produced through hydrogenation of CO_2 captured from the flue gas of the combined cycle power plant. Initially, the simulation of the conventional combined cycle power plant with natural gas feed, illustrated in Fig. Figs. 12, is carried out. Figure Figs. 13 demonstrates the simulation of the power plant plus, using CO_2 capture, synthesis, and methanol production unit.

Figure Figs. 14 shows a complete plot with details, including all parts of the process (combined cycle power plant, CO_2 capture, methanol synthesis, and separation) for methanol production from the combined cycle power plant's flue gas. Subsequently, all three sections are described in detail.

Combined cycle power plant

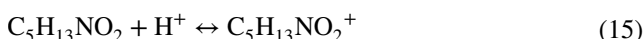
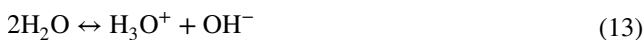
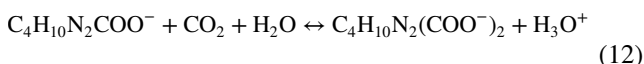
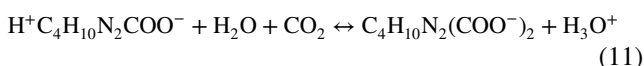
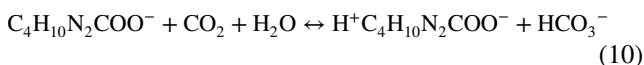
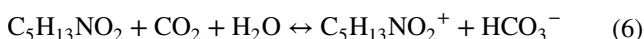
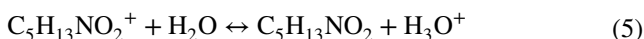
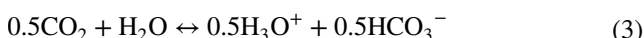
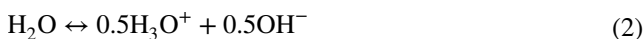
The natural gas is considered methane with an intensity of 500 kmol/h, a pressure of 2000 kPa, and a temperature of 30 °C, which is mixed with the airflow supplied from the atmosphere. The K-100–K-103 compressors and E-100–E-102 intermediate coolers are responsible for air conditioning. Finally, a mixture of air and methane enters the combustion chamber, where methane is completely burned, and high energy is released from combustion according to Eq. (1) [33].



Combustion products enter the gas turbine (GT) at a temperature of 2361 °C and a pressure of 2000 kPa and leave this equipment at a pressure of 120 kPa and enter the producing steam heat exchangers. The E-103–E-105 heat exchangers generate high-pressure, medium-pressure, and low-pressure steam streams, respectively, and each feeds HP-ST, MP-ST, and LP-ST turbines for power generation, individually. The outlet pressure of these turbines is equal to 101.1 kPa. The condensate flow coming out of the turbines is mixed by a mixer and enters the AC-100 air cooler with a total intensity of 5321 kmol/h so that the condensate temperature in this equipment reaches 90 °C at a constant pressure of 101.1 kPa. The outlet current from the air cooler enters the P-100 pump and in this equipment, the water pressure increases up to 4000 kPa. Considering that apart from high-pressure turbines, two other turbines operate at pressures of 2000 and 1000 kPa; therefore, the water flow is passed through the reducing valve before entering the medium and low-pressure turbines.

Carbon dioxide capture from flue gas

As Figure Figs. 14 displays, the flue gas that leaving the E-105 heat exchanger is the feed of the CO₂ capture unit. In the chemical absorption unit, the formulated solvent MDEA-PZ reacts with CO₂ and this is the main mechanism in this process. The capture reactions are presented in Eqs. (2)–(16) [34]. These equations display MDEA with the chemical formula C₅H₁₃NO₂ and PZ activator with the chemical formula C₄H₁₀N₂ [34].



Due to its temperature, the flue gas is a desirable heat source to supply a part of the energy of the stripper tower's reboiler. Hence, before entering the absorption tower, it is passed through the Side Reboiler and E-109 heat exchangers. The amount of energy released through the Side Reboiler heat exchanger is equal to 5,372,000 kJ/h, which reduces

the flue gas temperature to 128 °C, and in the second stage, using cooling water, the flue gas temperature reaches 45 °C in the E-109 heat exchanger. In the output of the E-109 heat exchanger, a part of the water in the condensate flue gas flow is separated by V-100 two-phase separator. The vapors above this separator enter the absorption column from below, where a parallel and counter contact is established between the MDEA-PZ solvent and the CO₂-rich flue gas.

The absorption and stripper towers are designed so that 90% of the CO₂ in the flue gas is captured (see Eq. 17) and sent to the methanol synthesis and separation section through the reflux of the stripper tower drum. The sizing and specifications of these two towers, which are primarily responsible for mass transfer in the post-combustion absorption process, are presented in Table 2. Compensatory water flow is injected from the highest point of the absorption tower to prevent solvent losses. Thus, there is no solvent in the purified gas stream, and there is no need for compensatory water for reflux in the stripper tower.

In Eq. (17), the calculation of CO₂ capture is presented, in which CO_{2,ABS} is the percentage of the CO₂ capture, $\dot{G}_{\text{CO}_2,\text{in}}$ is the molar flow rate of the CO₂ in the feed gas, and $\dot{G}_{\text{CO}_2,\text{out}}$ is the molar flow rate of CO₂ in the purified gas [16].

$$\text{CO}_{2,\text{ABS}} = \frac{\dot{G}_{\text{CO}_2,\text{in}} - \dot{G}_{\text{CO}_2,\text{out}}}{\dot{G}_{\text{CO}_2,\text{in}}} \times 100 \quad (17)$$

The solvent flow exiting the bottom of the absorption tower has a high concentration of CO₂ (Riched Amine), and its load ($\alpha_{\text{CO}_2}^{\text{Rich}}$) is equal to 0.3154 (see Eq. (18)) [35]. The Riched Amine flow enters the E-110 heat exchanger through a P-103 pump at a pressure of 250 kPa, where the temperature of the rich solvent flow is increased and preheated by the hot solvent produced in the stripper tower's reboiler [16].

$$\alpha_{\text{CO}_2}^{\text{Rich}} = \frac{\text{mole}_{\text{CO}_2}}{\text{mole}_{\text{Amine}}} \quad (18)$$

A stream of gas-rich Amines is fed from the top of the stripper tower. The stripper tower has a partial condenser with liquid and steam products. From the top of the reflux drum, the recovered CO₂ product is sent to the methanol synthesis and separation section, and a clean solvent flow

Table 2 Specifications and sizing of absorption and stripper towers

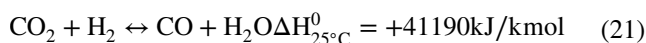
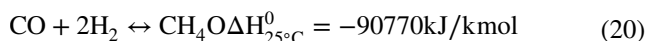
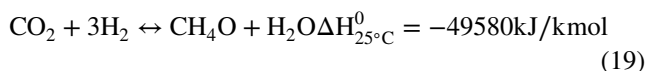
Stripper(T-101)	Absorber (T-100)	Term
4.015	4.015	Diameter (m)
1	1	Filling height (m)
FLEXIPAC	FLEXIPAC	Filling type
10	10	Tower height (m)
10	10	Number of equilibrium steps
plastic	plastic	Filling material



or Lean Amine is generated from the reboiler, which has less CO₂ compared to the Riched Amine flow. Lean Amine current temperature is slightly reduced by passing through the E-110 heat exchanger, and to send it to the absorption tower, it is necessary for its temperature to reach 45 °C, so after the E-110 heat exchanger by cooling water flow in the heat exchanger E-111, the solvent flow temperature reached the desired value of 45 °C, and the solvent was used again in the T-100 absorption tower.

Synthesis and separation of methanol

This section starts with the K-108 compressor and ends with the T-103 distillation column (see Appendix. A. 3). Two streams of captured CO₂ and H₂ are the main feeds. In the synthesis section, based on the hydrogenation of CO₂ on commercial Cu/ZnO/Al₂O₃ catalyst, methanol production has been done [35]. The reactor in this study is simulated as a plug, and the LHHV kinetic model is used to define the reactions. The hydrogenation reaction of CO₂ with excess H₂ is the main reaction. Also, two reactions, namely reverse water–gas shift (RWGS) and hydrogenation of carbon monoxide, occur at lower rates. Reaction equations are presented in Eqs. (19)–(21) [36]. Also, the velocity equation for methanol synthesis under operating conditions of 250 °C and pressure between 5000 kPa and 10,000 kPa are presented by Bussche and Froment [37]. The dimensions and specifications of the methanol synthesis reactor used in this simulation can be seen in Table 3 [37].



H₂ and CO₂, the main feed for methanol synthesis, are compressed in a network of compressors and heat exchangers with phase separators and at a temperature of 118.8 °C

Table 3 Dimensions and specifications of the methanol synthesis reactor [37]

Parameter	Value
Diameter (mm)	0.0055
Catalyst	Cu/ZnO/Al ₂ O ₃
Number of Tubes	3026
Reactor Length (m)	10
Reactor Total Volume (m ³)	0.72
Void Fraction	0.39
Reactor Type	Plug

and a pressure of 5000 kPa constitute synthetic gas. As shown in Fig. Figs. 14, compressors K-108 to K-111 and K-112 to K-117 are used to compress CO₂ and H₂. After each stage of gas compression, due to the increase in temperature, heat exchangers are used to reduce the temperature of the next compression. Owing to the presence of water in the CO₂ stream, after compaction and cooling, the condensed water is separated by V-103 to V-105 phase separators. The resulting gas mixture enters the E-128 heat exchanger before entering the methanol synthesis reactor, where the temperature of this flow is increased by the hot product leaving the reactor and enters the plug reactor. The reactor product releases its energy by passing through the E-128 heat exchanger in the Side Reboiler 2 heat exchanger and provides it to the solvent recovery tower reboiler in the post-combustion section. The output flow from the Side Reboiler 2 enters the E-129 heat exchanger, which reduces the flow temperature of the methanol reactor product to 45 °C. This matter allows the methanol and water to be partially separated from light gases at high pressures. The separation of gases and raw methanol was performed in the V-106 phase separator, and the gases above this separator formed a single purge. The liquid produced from the V-106 phase separator enters the methanol separation distillation column at a pressure of 120 kPa. The distillation tower consists of 30 trays, and a methanol is produced from a condenser at a temperature of 60 °C. Wastewater also comes out of the reboiler of this distillation tower. Methanol distillation tower reboiler heating was performed using a steam utility (saturated steam at a pressure of 500 kPa).

Simulation and analyses

The simulation method of the project is to select the equation of state, select the reactant components, determine the reactions and set the reaction settings up, enter the simulation environment and install the operational units (such as reactor, gas compression, absorption, and stripper towers, methanol synthesis and its separation). Simulation with software is a major part of this study. Simulation software such as Aspen Hysys [25] contains various components, such as a composition database, a thermodynamic model database, a flow plate constructor, a single operating model database, and a flow plate convergence. Note that other elements, such as other levels of the flow plate, financial analysis tools, and the engineering unit option, are part of the dependent software category included in the Aspen One package. The purpose of the process simulation is to predict how a process will behave in a given operating situation. To simulate the process of methanol production from the flue gas of the aforementioned power plants, several assumptions have been considered, which are mentioned below:



- Isentropic efficiency of pumps, turbines, and compressors is equal to 75%.
- The combustion chamber of the gas turbine is simulated as the Gibbs reactor.
- The cooling water flow temperature is 30 °C, and its pressure is 500 kPa in all parts of the process.
- The inlet pressure of the high-pressure (HP), medium-pressure (MP), and low-pressure (LP) turbines are equal to 4000 kPa, 2000 kPa, and 1000 kPa, respectively.
- To simulate the heat exchangers producing steam in a combined cycle power plant, the characteristic of steam flows is 100% of complete steam.
- The ambient air temperature for cooling in the AC-100 air cooler is equal to 35 °C.
- The operating pressure and temperature of the natural gas inlet (CH₄) for combustion in the gas turbine are 2000 kPa and 30 °C, respectively.
- There are no Carry Over phase separators.
- The pressure of the CO₂ capture tower is 120 kPa, and the amount of pressure loss is zero.
- The pressure of the stripper tower (distillation tower) is 230 kPa, and the pressure drop between the reboiler and the condenser is 50 kPa.
- The condensing temperature of the distillation tower (CO₂ outlet) is equal to 45 °C.
- The pressure of the methanol synthesis reactor is 5000 kPa [38].
- The temperature of the methanol synthesis reactor is 250 °C [30].
- The condensing temperature of the methanol separation tower is 60 °C.
- The number of methanol distillation tower trays is calculated based on the Short Cut design, and the concentration of methanol in the solution is equal to 0.1 mol%.
- The simulation conditions are steady state.
- The composition of the forming components of the solvent for CO₂ capture is 40% by weight of methyl diethanol amine (MDEA) and 10% by weight of piperazine (PZ).
- Combustion products exit the gas turbine at a pressure of 120 kPa.
- The outlet pressure of the HP, MP, and LP turbines is equal to 100 kPa.
- Methane’s combustion in the combustion chamber is 100%.

Process analysis

Evaluation of methanol production process through hydrogenation of CO₂ captured from the flue gas of combined cycle power plant in this section has been done generally in three sections of Thermodynamic-Economic-Environmental Analysis (TEEA). Thermodynamic evaluation has

been performed in both energy and exergy modes. In the economic evaluation section, basic parameters such as Total Investment Cost (TIC), Return On Investment (ROI), Min Annualized Total Cost (MATC), Minimum Selling Price (MSP), and Payback Period are calculated. Environmental assessment has dealt heavily with CO₂ emissions based on power plant and power plant plus products.

Energy analysis

In this study, the main goal is to improve thermo-environmentally the combined cycle power plant with natural gas fuel. In this regard, one of the essential thermodynamic analyzes is to evaluate the energy of the power plant and the power plant plus (along with methanol production). For this purpose, the amount of energy efficiency must be formulated for two cases. The general mass rate and energy rate equations for a component are written as Eqs. (22) and (23) [39]:

$$\sum \dot{m}_i = \sum \dot{m}_e \tag{22}$$

$$\sum \dot{m}_i h_i + \dot{Q}_i + \dot{W}_i = \sum \dot{m}_e h_e + \dot{Q}_e + \dot{W}_e \tag{23}$$

In the above correlations, \dot{m}_i is the input mass flow rate and \dot{m}_e is the output mass flow rate. \dot{Q}_i is the heat input rate and \dot{Q}_e is the heat output rate. Also, h is the specific enthalpy. Based on the general relation (23), the energy efficiency for a cycle or component (θ_{en}^{system}) can be shown as Eq. (24) [40]:

$$\theta_{en}^{system} = \frac{\sum \dot{m}_e h_e + \dot{Q}_e + \dot{W}_e}{\sum \dot{m}_i h_i + \dot{Q}_i + \dot{W}_i} \tag{24}$$

According to this equation, the energy efficiency of the power plant ($\theta_{en}^{powerplant}$) is defined as Eq. (25) for when is only operating and no other cycle has been added to it [40]:

$$\theta_{en}^{powerplant} = \frac{\dot{W}_{prod}^{GT} + \dot{W}_{prod}^{HP-ST,LP-ST,MP-ST}}{\dot{m}_{fuel} LHV_{fuel} + \dot{W}_{used}^{aircomps}} \tag{25}$$

Subsequently, the relationship between the energy efficiency of the methanol production process through direct hydrogenation of recovered CO₂ from the flue gas of a combined cycle power plant (power plant plus) is as follows [41]:

$$\theta_{en}^{powerplant+} = \frac{\dot{m}_{MeOH} LHV_{MeOH} + \dot{Q}_{prod} + \dot{W}_{prod}}{\dot{m}_{fuel} LHV_{fuel} + \dot{m}_{H2} LHV_{H2} + \dot{W}_{used} + \dot{Q}_{used}} \tag{26}$$

In the methanol synthesis and separation unit (direct hydrogenation of CO₂), the energy efficiency relationship can be defined specifically according to Eq. (27) [41].

$$\theta_{\text{en}}^{\text{MeOHSynandSep}} = \frac{\dot{m}_{\text{MeOH}} \text{LHV}_{\text{MeOH}} + \dot{Q}_{\text{fromR101}} + \dot{Q}_{\text{fromSideReb2}}}{\dot{m}_{\text{H}_2} \text{LHV}_{\text{H}_2} + \dot{W}_{\text{comps}}^{\text{H}_2} + \dot{W}_{\text{comps}}^{\text{CO}_2} + \dot{Q}_{\text{T103Reb}}} \quad (27)$$

In this equation, $\dot{Q}_{\text{fromR101}}$ is the net given heat-based energy to the reboiler of the methanol separation distillation tower, $\dot{Q}_{\text{fromR101}}$ is the generated heat by the methanol synthesis reactor, $\dot{Q}_{\text{fromSideReb2}}$ is the released energy through side reboiler 2 heat exchanger, $\dot{W}_{\text{comps}}^{\text{H}_2}$ is the power consumption in H_2 compression compressors, and $\dot{W}_{\text{comps}}^{\text{CO}_2}$ is the power consumption in CO_2 compression compressors.

Exergy analysis

The concept of exergy applies to many processes. Exergy is used for thermo-environmental studies and process optimization. Exergy rate balance in a system is the basis of exergy assessment. For static processes and systems, exergy destruction rate (\dot{E}_D) can be explained as the difference between the sum of input exergy rates ($\sum \dot{E}_i$) to the system and the sum of output exergy rates ($\sum \dot{E}_e$) from that as follows [42]:

$$\dot{E}_D = \sum \dot{E}_i - \sum \dot{E}_e \quad (28)$$

With regard to the use of fuel (\dot{E}_F) and product (\dot{E}_P) concepts, the exergy rate balance for a stable process or system can be written as a function of exergy destruction rate, exergy loss rate, and fuel and product exergy rates, which is consistent with Eq. (29) [37]:

$$\dot{E}_F = \dot{E}_D + \dot{E}_L + \dot{E}_P \quad (29)$$

The exergy efficiency can be defined and calculated based on Eq. (30) [40] for the i th component of the system and according to Eq. (31) for the whole cycle [43].

$$\eta_{\text{ex}}^i = \frac{\dot{E}_P^i}{\dot{E}_F^i} = 1 - \frac{\dot{E}_D + \dot{E}_L}{\dot{E}_F} \quad (30)$$

$$\eta_{\text{ex}}^{\text{cycle}} = \frac{\sum \dot{E}_e}{\sum \dot{E}_i} \quad (31)$$

where $\sum \dot{E}_i$ and $\sum \dot{E}_e$ are the total input exergy rate and total output exergy rate, respectively.

In this study, the methanol is produced through hydrogenation of CO_2 captured from the flue gas of a combined cycle power plant. Considering that in different parts of the process such as power plant, CO_2 capture by chemical solvent, and methanol synthesis, there is a chemical reaction, so

in addition to physical exergy (\dot{E}_i^{PH}), chemical exergy (\dot{E}_i^{CH}) must be considered. Thus, the total exergy of the i^{th} state (\dot{E}_i) is defined as Eq. (32) [40].

$$\dot{E}_i = \dot{E}_{\text{PH},i} + \dot{E}_{\text{CH},i} \quad (32)$$

In addition, Table 4 represents the exergy equilibrium equations for each component of the methanol production process and the whole cycle.

Economic analysis

A comprehensive economic analysis has been performed for the methanol production process. Almost all the basic and competitive parameters that are important for a chemical process have been measured in this work. It is assumed that the economic lifetime (N) of the project is 30 years, the interest rate (J) is 8%, and the tax rate (T_{Rate}) is 35% [44]. Also, the operating hours of the system for one year are equal to 8150 h [16]. In this study, the Total Operating Cost (TOC) is obtained through the Aspen Process Economic Analyzer (APEA) tool, which is the sum of the fixed and variable operating costs. Also, the Total Equipment Cost (TEC) has been calculated through the same tools and Aspen Hysys software [40].

$$\begin{aligned} \text{Total Operating Cost (TOC)} \\ = \text{Fixed Operating Cost} + \text{Variable Operating Cost} \end{aligned} \quad (33)$$

Moreover, the Total Investment Cost (TIC) of the system has been calculated regarding the following equation [40]:

$$\text{Total Investment Cost} = \text{Total Equipment Cost} \left(1 + \sum_{j=1}^m \text{RF}_j \right) \quad (34)$$

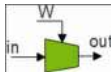
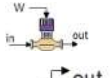
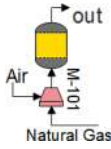
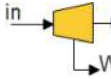
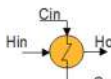
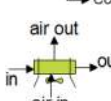
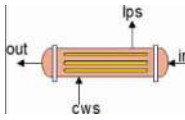
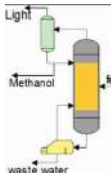
For this purpose, the values for the relative factors (RF_j) are presented in Table 5 [45, 46].

The Return On Investment (ROI) rate, which is a function of plant's lifetime and interest rate, is calculated based on Eq. (35) [47]. By obtaining the ROI parameter, the value of the competitive parameter of the Minimum Annual Total Cost (MATC) can be determined by Eq. (36) for the proposed design. The MATC includes the total operating and investment costs [47].

$$\text{ROI} = \text{Total Investment Cost} \left(\frac{J(J+1)^N}{(1+J)^N - 1} \right) \quad (35)$$



Table 4 Exergy equations and relations for the components and whole cycle of the methanol production system

Component	Schema	\dot{E}_F^i (kW)	\dot{E}_P^i (kW)
Compressors		\dot{W}_{used}	$\dot{E}_{out} - \dot{E}_{in}$
Pumps		\dot{W}_{used}	$\dot{E}_{out} - \dot{E}_{in}$
Chamber		\dot{E}_{out}	$\dot{E}_{inlets}^{PH} - \dot{E}_{out}^{PH}$
Turbine		$\dot{E}_{in} - \dot{E}_{out}$	\dot{W}_{prod}
Heat Exchangers		$(\dot{E}_{in} - \dot{E}_{out})_{hot}$	$(\dot{E}_{out} - \dot{E}_{in})_{cold}$
Air Cooler		$(\dot{E}_{in} - \dot{E}_{out})_{hot} + W$	$(\dot{E}_{out} - \dot{E}_{in})_{air}$
R-101		$\dot{E}_{inletstream}$	$\dot{E}_{outlet} + (\dot{E}_{LPS} - \dot{E}_{CWS})$
T-103		$\dot{E}_{feed} + (\dot{E}_{LPS2} - \dot{E}_{LPC2})$	$\sum \dot{E}_{prods}$
Cycle Efficiency	$\sum \dot{E}_i$ (KW)		$\sum \dot{E}_c$ (KW)
Methanol Synthesis and Separation	$\dot{E}_{H2} + \dot{E}_{CO2} + (\dot{E}_{LPS2} - \dot{E}_{LPC2}) + \dot{W}_{used}$		$\dot{E}_{MeOH} + (\dot{E}_{LPS3} - \dot{E}_{CWS19})$
Power Plant	$\dot{W}_{used} + \dot{E}_{NatGas}$		\dot{W}_{prod}
CO ₂ Capture nit	$\dot{E}_{FlueGas} + \dot{E}_{Reb} + \dot{W}_{used}$		$\dot{E}_{CO2Capture} + \dot{E}_{LowCarbon}$
Power Plant Plus	$\dot{W}_{used} + \dot{E}_{NatGas} + \dot{E}_{Reboilers}$		$\dot{E}_{MeOH} + \dot{W}_{prod}$

$$\begin{aligned}
 MATC &= TOC + ROI \\
 &= TOC + \text{Total Investment Cost} \\
 &\left(\frac{J(J + 1)^N}{(1 + J)^N - 1} \right)
 \end{aligned}
 \tag{36}$$

The second important parameter that has been calculated for the methanol production scheme by hydrogenation of CO₂ from power plant’s flue gas is the Minimum Selling Price (MSP), which can be calculated from [47]:

$$\text{MinimumSellingPrice} \left(\frac{\text{USD}}{\text{kg}_{MeOH}} \right) = \frac{ROI + TOC + \text{Tax}}{\dot{m}_{MeOHProd}}
 \tag{37}$$

This parameter is calculated at the point of equality of costs and revenues and is a direct function of the rate of return on capital, costs, and taxes. In Eq. (37), the parameter $\dot{m}_{MeOHProd}$ is the annual flow rate of the methanol production (kg/year).

Equation (38) can be used to calculate the amount of annual tax, while the amount of depreciation for 30 years is assumed to be linearly constant. As can be seen in this equation, the amount of tax over a year depends on the project Annual Profit (A.P) and the tax rate. The profit of the project can be calculated through Eq. (39), where it is necessary to have the amount of revenue of the methanol production plan to calculate the value of the A.P parameter. To compute

Table 5 Relative factors for investment cost [37]

Type	Item (j)	RF _j
Direct cost	Purchased equipment	0.21
	Purchased equipment installation	0.10
	Piping	0.12
	Buildings	0.15
	Electrical systems	0.06
	Field	0.01
	Instrumentation and Controls	0.05
	Engineering and supervision	0.1
Indirect cost	Working Capital	0.17
	Construction expenses	0.09
	Contingency	0.07
Fixed-capital investment	Contractor's fee	0.04
		1
Working capital		0.17

revenue, Eq. (40) should be used. Finally, the payback period can be measured in terms of years based on Eq. (41) [47].

$$\text{Tax} = (\text{A.P}) \times T_{\text{Rate}} \tag{38}$$

$$\text{A.P} = \text{Revenue} - \text{Total Operating Cost} \tag{39}$$

$$\text{Revenue} = \frac{(\text{ROI} \times T_{\text{Rate}}) + \text{Total Operating Cost}(1 - T_{\text{Rate}})}{1 - T_{\text{Rate}}} \tag{40}$$

$$\text{PaybackPeriod} = \frac{\text{Total Investment CostRevenue}}{=} \frac{\text{Total Equipment Cost}(1 + \sum_{j=1}^m \text{RF}_j)}{\frac{(\text{ROI} \times T_{\text{Rate}}) + \text{Total Operating Cost}(1 - T_{\text{Rate}})}{1 - T_{\text{Rate}}}} \tag{41}$$

Environmental analysis

The process based on the use of CO₂ must be environmentally capable of reducing the emission of this greenhouse gas compared to the base state. Therefore, in this manner, the methanol production process can be acceptable in terms of environmental features. The Net CO₂ Emission (NCE) should be evaluated to determine the position of the proposed process relative to the baseline. The NCE parameter can be calculated from the total emission of CO₂ through the flue gas (CO_{2,fluegas}), utility gas (CO_{2,utility}), and the CO₂ introduced into the process through the feed (CO_{2,feed}) [40].

$$\text{NCE} \left(\frac{\text{kg}}{\text{h}} \right) = \text{CO}_{2,\text{fluegas}} + \text{CO}_{2,\text{utility}} - \text{CO}_{2,\text{feed}} \tag{42}$$

Table 6 Simulation results for the combined cycle power plant

Parameter	Value
Polytropic efficiency of K-100 (%)	77.63
Polytropic efficiency of K-101 (%)	77.18
Polytropic efficiency of K-102 (%)	77.25
Polytropic efficiency of K-103 (%)	77.56
Energy consumption of K-100 (kJ/h)	11590000
Energy consumption of K-101 (kJ/h)	9901000
Energy consumption of K-102 (kJ/h)	10260000
Energy consumption of K-103 (kJ/h)	12000000
Gas turbine production capacity (kW)	44120
Electricity generated from gas turbines (kWh/day)	1059000
Polytropic efficiency of GT (%)	69.33
Polytropic efficiency of HP-ST (%)	72.16
Polytropic efficiency of MP-ST (%)	72.73
Polytropic efficiency of LP-ST (%)	73.2
Power generation of HP-ST (kW)	8250
Electricity generated from HP-ST (kWh/day)	198000
Power generation of MP-ST (kW)	1931
Electricity generated from MP-ST (kWh/day)	46340
Power generation of LP-ST (kW)	1203
Electricity generated from LP-ST (kWh/day)	28880

Results and discussion

This chapter is prepared in six different subsections including the results attained from the energy, exergy, economic, and environmental analyses, comparison of the results, and

sensitivity analysis results.

Energy analysis results

Table 17 presents the thermodynamic properties for each stream of the combined cycle power plant illustrated in Fig. Figs. 14 Also, Table 6 represents its simulation results, wherein the polytropic efficiency of the compressors and turbines, energy consumption capacity of the compressors, and power produced by the turbines attained from the Aspen Hysys software are reported. Based on Table 6, the total energy consumption capacity of the compressors is computed to be 43,751,000 kJ/h, which is equal to 12,153 kW. Here, the gas turbine and steam turbines provide 44,120 kW and 11,384 kW power for the grid, respectively.

Figure 2 reveals a schematic illustration of the energy results attained from the simulation process specifically

Fig. 2 Input and output energy flow rates for the methanol production process through CO₂ capture

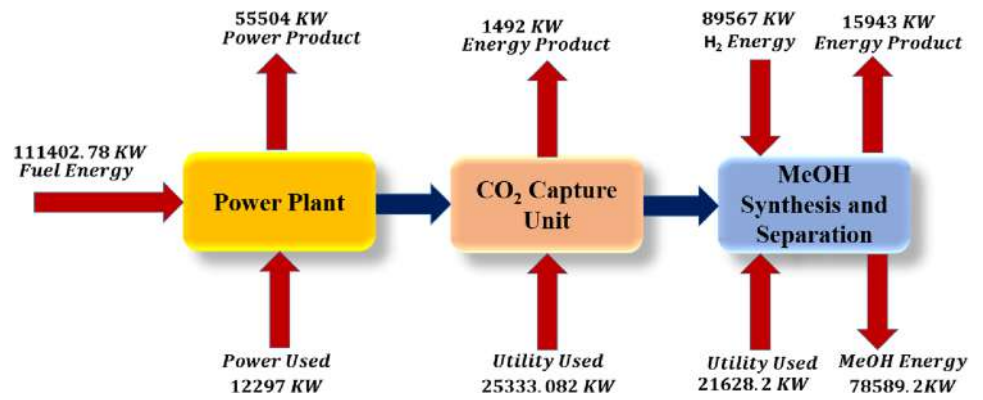


Table 7 Composition of formation components for streams of the CO₂ capture unit (Molar fraction)

Stream Name	CO2	N2	O2	H2O	PZ	MDEA
Mole Fraction						
Flue Gas-2	0.1163	0.6274	0.0237	0.2326	0.0	0.0
STM30	0.1163	0.6274	0.0237	0.2326	0.0	0.0
STM31	0.1163	0.6274	0.0237	0.2326	0.0	0.0
STM32	0.1393	0.7516	0.0284	0.0807	0.0	0.0
Low Carbon	0.0128	0.7658	0.0209	0.1924	0.0	0.0
STM34	0.0419	0.0	0.0	0.8254	0.0341	0.0986
STM35	0.0419	0.0	0.0	0.8254	0.0341	0.0986
STM36	0.0419	0.0	0.0	0.8254	0.0341	0.0986
STM38	0.0059	0.0	0.0	0.8551	0.0357	0.1033
STM39	0.0059	0.0	0.0	0.8551	0.0357	0.1033
STM39	0.0059	0.0	0.0	0.8551	0.0357	0.1033
L-Amine	0.0059	0.0	0.0	0.8551	0.0357	0.1033
CO2 Captured	0.9456	0.0002	0.0	0.0541	0.0	0.0

for the power plant plus (power plant with methanol production). In the power plant section, inlet streams include methane gas fuel and energy consumed by the air compressors. Likewise, the power generated by the gas turbine and three steam turbines is the total produced energy. Indeed, the power plant receives 111,402 kW of fuel energy rate and 12,297 kW of power and generates 55,504 kW of power. Similarly, the stripper tower and pumps of the CO₂ capture unit are recognized as energy-consuming components. But in the same unit, energy is released through the cooling of the flue gas in the Side Reboiler heat exchanger, which is provided for the reboiler. The utility used in the CO₂ capture unit is equal to 25,333.1 kW and its output energy rate is computed to be 1492 kW. In the methanol synthesis and separation unit, the input energies to the process include H₂ as feed, power consumption in the H₂ compressors and captured CO₂, and reboiler of the methanol separation distillation tower. The energies produced in the methanol synthesis and separation unit also include the energy released by cooling the reactor product in the Side Reboiler2 heat exchanger and the energy released by controlling the reactor

Table 8 Composition of formation components for streams of the methanol synthesis and separation unit (Molar fraction)

Stream Name	CO2	N2	H2O	H2	MeOH
Mole Fraction					
H2 Feed	0.0	0.0	0.0	1	0.0
STM72	0.254	0.0001	0.0016	0.7443	0.0
STM74	0.0118	0.0001	0.4956	0.0	0.4925
Purge Gas	0.8327	0.0087	0.0318	0.0007	0.1255
STM80	0.0013	0.0	0.5016	0.0	0.4972
Methanol	0.0023	0.0	0.0	0.0	0.9977
waste water	0.0	0.0	0.999	0.0	0.0001
Light Gas	0.1149	0.0004	0.0	0.0	0.2083

temperature and producing low-pressure steam to supply the power of the stripper tower reboiler in the recovery of CO₂ from the flue gas section. Consequently, by receiving 21,628.2 kW of utility used, and 89,567 kW of energy from the H₂, the methanol is generated with an energy generation rate of 78,589.2 kW.

Table 9 Technical results for carbon dioxide absorption section

Parameters	Value
Rich Amine Loading ($\alpha_{CO_2}^{Rich}$)	0.3154
Lean Amine Loading ($\alpha_{CO_2}^{Lean}$)	0.043
L/G Ratio ($\frac{mole_{solvent}}{mole_{recdgas}}$)	3.34
*Reboiler Heat Duty (kJ/h)	91,130,000
Condenser Heat Duty (kJ/h)	-17,520,000
p_{CO_2} in Treated Gas (kPa)	1.536
T-101 Reflux Ratio (mol/mol)	0.5

Table 10 The exergy analysis results for the components of the combined cycle power plant

Component	\dot{E}_i^F (kW)	\dot{E}_i^P (kW)	\dot{E}_i^D (kW)	η_{ex}^i (%)
K-100	3220	2601	619	80.78
E-100	439	96.24	342.76	21.92
LP-ST	1669.31	1203	466.31	72.07
K-101	2750	2230	520	81.1
E-101	477	96.24	380.76	20.18
K-102	2849	2315	534	81.26
MP-ST	2680.6	1931	749.6	72.04
E-102	508	101.73	406.27	20
K-103	3333	2727	606	81.82
Chamber	127334	86318	41016	67.79
G.T	46669	44120	2549	94.54
E-103	34325	28558	5767	83.2
HP-ST	11495	8250	3245	71.77
E-104	11418	6904.5	4513.5	60.47
P-100	144.8	131.22	13.58	90.62
AC-100	10932	3167	7765	28.97
Power Plant	260098.91	190750	69348.91	
$\eta_{ex}^{powerplant} = 42.86\%$				

In Table 7, the composition of the components of each stream is reported as a result of the simulation with Aspen Hysys. Likewise, Table 8 shows the composition of the components of each stream in the methanol synthesis and separation section. In Table 9 the technical results for the Post-Combustion section are also presented.

* This value does not take into account energy integration.

Exergy analysis results

In this study, a comprehensive exergy analysis has been performed for different parts of the methanol production process through the hydrogenation of CO₂ recovered from the power plant’s flue gas. These results are presented in Table 18 for all streams connected to the equipment that ultimately formed the whole system. Indeed, the physical,

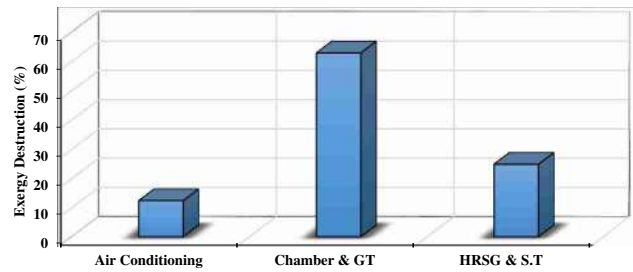


Fig. 3 Comparison of the share of exergy destruction rate in different parts of the combined cycle power plant

Table 11 The exergy analysis results for the components of the CO₂ capture unit

Component	\dot{E}_i^F (kW)	\dot{E}_i^P (kW)	\dot{E}_i^D (kW)	η_{ex}^i (%)
E-109	1378.91	442.5	936.41	32.1
T-100	1677998.42	1678023.06	0	100
P-103	17.6	11.87	5.73	67.44
E-110	2664.48	2090.47	574.01	78.46
T-101	1680287.47	1678078.33	2209.14	99.87
P-102	5.482	3.66	1.822	66.6
E-111	1551.6	566	985.6	36.48
CO ₂ capture unit	3363904	3359216	4688.11	–
$\eta_{ex}^{CO_2 Capture} = 51.94\%$				

chemical, and total exergy rates for the streams are presented in this table.

Table 10 presents the results of the exergy rate balance for the combined cycle power plant. According to the calculations, the total exergy of the fuel and product of the power plant is 260098.91 kW and 190,750 kW, respectively, which the total amount of exergy destruction rate is estimated to be 69,349.91 kW. In addition, the total exergy loss of the combined cycle power plant ($\dot{E}_L^{powerplant}$) has been calculated, which is equal to 79,272 kW. Based on a comparison between the three components of a combined cycle power plant, including compression and cooling of air conditioning, gas turbine and its combustion chamber, heat recovery, HRSG, and ST, the share of exergy destruction rate for the second part is equal to 62.82%. In other words, in a combined cycle power plant, the combustion chamber and the gas turbine destroy more exergy, the amount of which is 43565 kW. It should be noted that the combustion chamber alone has the highest exergy destruction rate among other equipment. Lastly, the exergy efficiency of this section is computed to be 42.86%. Additionally, according to Fig. 3, the combustion chamber and gas turbine section has the highest share of exergy destruction with a value of 59.14%.

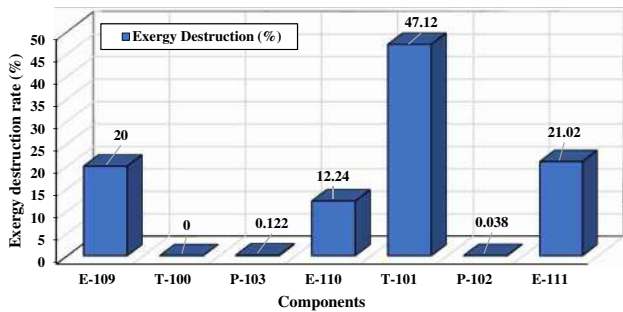


Fig. 4 Comparison of the share of exergy destruction rate in different parts of the CO₂ capture unit

Table 12 The exergy analysis results for the components of the synthesis and separation of methanol unit

Component	\dot{E}_i^F (kW)	\dot{E}_i^P (kW)	\dot{E}_i^D (kW)	η_{ex}^i (%)
R-101	96488.19	96244.34	243.85	99.75
T-103	96477.55	89475.23	7002.32	92.74
K-112	838	671.3	166.7	80
E-123	136.66	27.57	109.09	20.17
K-113	1005	817.99	187.01	81.39
E-124	180.46	32.35	148.11	17.93
K-114	961	780.55	180.45	81.22
K-108	406.4	328.06	78.34	80.72
E-125	168.68	32.35	136.33	19.18
K-115	1009	821.77	187.23	81.44
E-126	180.64	32.35	148.29	17.91
K-116	1014	825.52	188.48	81.41
E-127	181.37	32.35	149.02	17.84
K-117	842.4	679.96	162.44	80.72
E-120	82.35	18.64	63.71	22.64
K-109	396.7	320.62	76.08	80.82
E-121	75.78	15.62	60.13	20.61
K-110	375.4	303.07	72.33	80.73
E-122	72.69	14.81	57.88	20.37
K-111	409.9	328.71	81.19	80.19
E-128	690.62	527.27	163.35	76.35
E-129	450.59	87.67	362.92	19.46
Methanol Synthesis and Separation	202443.38	191560.23	10883.15	-

$\eta_{ex}^{MeOHplant} = 85.39\%$

Table 11 shows the results of exergy calculations for the CO₂ capture unit. According to the calculations, the total exergy rate of fuel and product for this section is equal to 3,363,904 kW and 3,359,216 kW, respectively. Moreover, the calculated total exergy destruction rate and exergy loss rate of this unit are 4688.11 kW and 1,612,004.15 kW, respectively. The solvent recovery tower has the highest

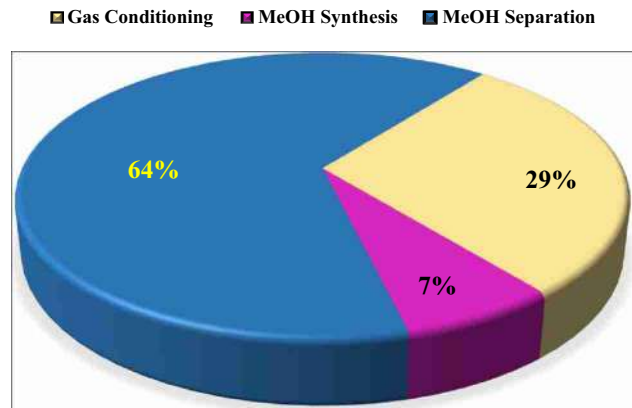


Fig. 5 Comparison of the share of exergy destruction rate in different parts of the methanol synthesis and separation unit

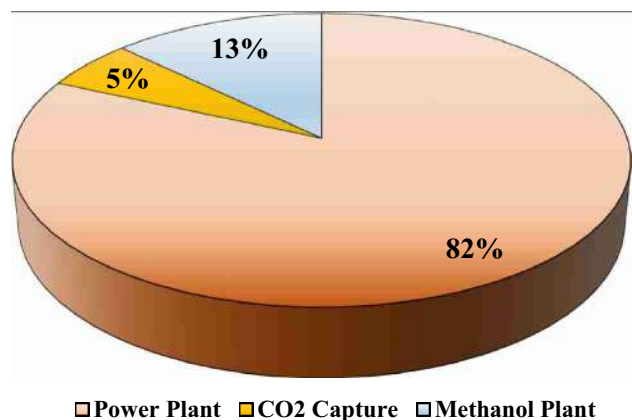


Fig. 6 Comparison of the share of exergy destruction rate for each unit of the power plant plus

exergy efficiency (99.87%) due to preheating operation in E-110 heat exchanger but has more share in exergy destruction rate than other types of equipment. This section has an exergy efficiency of 51.94%. According to Fig. 4, the share of the exergy destruction rate of the T-101 tower is equal to 47.12%, which is the highest amount.

Table 12 shows the results of exergy calculations for the synthesis and separation of methanol. According to the estimates, the exergy rate of the fuel and product in this part of the process is 202443.38 kW and 191,560.23 kW, respectively. Also, the total exergy destruction rate of the synthesis and separation of the methanol unit is equal to 10,883.15 kW. The exergy efficiency of this unit is found to be 85.39%. Also, the total exergy loss rate for this section is equal to 18,693.83 kW. Here, the distillation column T-103 has the largest share of exergy destruction rate with a share of 64% (see Fig. 5).

Table 12 represents the basic parameters of exergy analysis. Also, in Fig. 6, the comparison of the share of

Table 13 Comparison of exergy results for different parts of the power plant plus

parameter	unit	power plant	CO ₂ capture	Methanol production
Fuel exergy	kW	260098.91	3363904	202443.38
Product exergy	kW	190750	3359216	191560.23
Exergy destruction	kW	69348.91	4688.11	10883.15
Exergy efficiency	%	42.86	51.94	85.39

exergy destruction rate of the power plant, CO₂ capture unit, and methanol production unit is performed. According to the study, the combined cycle power plant section has the highest share of the total exergy destruction rate as 69,348.91 kW, which is equal to 82%. This means that the combustion chamber of the gas turbine must be optimized to reduce the overall exergy destruction of the power plant. Because according to Table 13, the combustion chamber's exergy destruction rate is very high and it is considered an exergy challenge.

In terms of exergy efficiency, the evaluations indicate that the methanol production sector is in a better position (85.39%). In the methanol production section, the heat generated from the heat of the reaction, heat production through cooling of methanol reactor's products, and pre-heating the methanol reactor's feed are three significant factors that have led to the most utilization of fuel exergy. Moreover, in the methanol production part, the highest share of the total exergy destruction rate belongs to the T-103 tower (64%). Due to the integrated performance of the reactor and Side Reboiler 2 heat exchanger, this challenge is not much considerable in general and it is overshadowed by the good performance of the entire methanol production sector.

Economic analysis results

Initially, the calculated purchase cost for each component of the whole system is reported in Table 19. The purchase cost of the equipment is calculated using the APEA tool.

Accordingly, Table 14 shows the results of the comprehensive economic estimate performed for the power plant and the power plant plus. Based on the obtained values, the total investment cost of the power plant is almost 40.89 M\$, and the amount of income from annual electricity production is approximately 14.55 M\$. Likewise, its profit is approximately equal to 1.96 M\$/year. However, when the CO₂ capture unit and methanol production section are added to the power plant, the annual revenue increased by 182.03% and reached 40.77 M\$/year. Also, based on the calculations, it is found that the annual profit of power plant plus increases by 116.08% compared to the combined power plant and reaches 4.23 M\$/year. The payback period for the power plant plus is 2.17 years and for the combined cycle power plant is 2.83 years, which shows that using the process of

Table 14 Results of the economic calculations

Parameters	Value
<i>a: Combined power Plant</i>	
TotalOperatingCost(USD/year)	12501700
TotalEquipmentCost(USD)	18842140
TotalInvestmentCost(USD)	40887443.8
Revenue(USD/year)	14457352.83
Profit(USD/year)	1955653
PaybackPeriod(year)	2.83
<i>b: CO₂ Capture Unit</i>	
TotalOperatingCost(USD/year)	9035250
TotalEquipmentCost(USD)	1878600
TotalInvestmentCost(USD)	4076562
<i>c: Methanol synthesis and separation unit</i>	
TotalOperatingCost(USD/year)	15011450
TotalEquipmentCost(USD)	19995020
TotalInvestmentCost(USD)	4338919.34
<i>d: Power Plant Plus</i>	
TotalOperatingCost(USD/year)	36548400
TotalEquipmentCost(USD)	40715760
TotalInvestmentCost(USD)	88353199.2
MATC(USD/year)	44396587.92
Revenue(USD/year)	40774347.38
Profit(USD/year)	4225947.39
Tax (USD/year)	1479081.59
MSP (USD/kg _{MeOH})	0.396
PaybackPeriod(year)	2.17

capturing CO₂ from the power plant's flue gas and converting it to methanol can reduce the payback period.

In the following, the results of economic estimates for the three mentioned sectors of the power plant plus are compared (see Fig. 7).

According to Fig. 7, among the sectors of the power plant plus, the methanol production sector (synthesis and separation) has the highest share of costs (operating costs, equipment costs, and investment costs). The CO₂ capture unit is much less expensive than a power plant and methanol production. It should be noted that in the methanol production section, two factors have a strong effect on increasing investment costs. First, in this section, a two-stage compressor is used for compression and cooling of CO₂ and H₂ gases, and the second factor is the distillation tower of methanol separation.



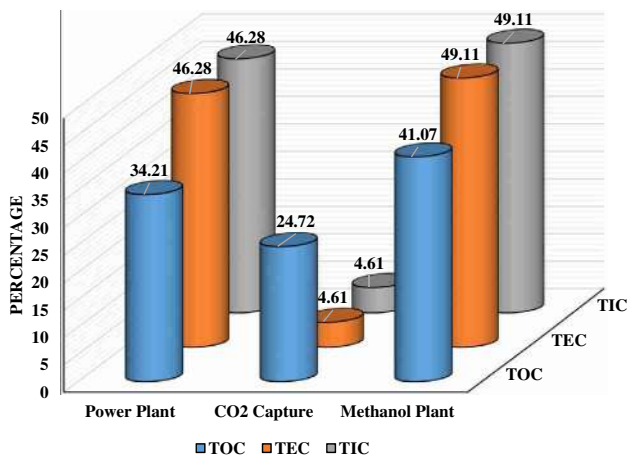


Fig. 7 Comparison of the cost-share of different parts of the power plant plus

Table 15 Summary of the environmental analysis results

Parameters	Vale
<i>a. Power Plant</i>	
CO _{2,fluegas} (kg/h)	22004.85
CO _{2,utility} (kg/h)	0
CO _{2,feed} (kg/h)	0
NCE(kg/h)	22004.85
<i>b. Power Plant Plus</i>	
CO _{2,fluegas} (kg/h)	1990.53
CO _{2,utility} (kg/h)	7067
CO _{2,feed} (kg/h)	0
NCE(kg/h)	9057.53

Environmental analysis results

To calculate the parameter CO_{2,utility}, it should be considered that this item has a section of electricity and heat generation. That is, the amount of CO₂ emitted through utility is obtained from the total amount of emissions by generating electricity and generating heat. However, considering that the case study

is a combined cycle power plant, so a part of the generating capacity of the power plant is used to supply power to pumps and compressors. As a result, the CO_{2,utility} term for the power plant is zero. But in connection with the methanol production process through the hydrogenation of the CO₂ captured from the power plant, a part of the energy of the solvent recovery tower’s reboiler (equivalent to 26.87 $\frac{\text{MMBtu}}{\text{h}}$) and all energy of the methanol separation tower’s reboiler (equivalent to 49.02 $\frac{\text{MMBtu}}{\text{h}}$) are provided by heat production. It should be noted that the amount of CO₂ emission per MMBtu of heat is equal to 205.3 pounds (lb) [45]. Table 15 summarizes the amount of CO₂ emissions in various forms for the power plant and the methanol production process through captured CO₂ (power plant plus). According to the results of the environmental assessment, the power plant has a net CO₂ emission of 22,004.85 kg/h in the baseline state, while with the addition of the methanol production process and utilization of CO₂, the value of the NCE parameter has been reduced to 9057.53 kg/h, which indicates a reduction of 58.84% of CO₂.

Comparison of power plant and power plant plus

The comparison between the combined power plant and power plant plus is presented here. According to Fig. 8, when the power plant is only operating, the amount of energy consumed and produced is equal to 1236.78 kW and 55,504 kW, respectively. In this case, the total energy efficiency for the power plant is equal to 44.87%. With the addition of two sections of CO₂ capture unit and synthesis and separation of methanol, the amounts of energy produced and consumed are changed, the values of which are compared in Fig. 8. When the methanol process was added to the power plant to reduce the CO₂ emission, the energy produced is 173% higher than that of the simple power plant. This structural optimization improves thermodynamically the power plant and increases its overall energy efficiency to 58.22%. The use of two heat exchangers of Side reboiler 1 and 2, the production of methanol, utilization of released heat from the methanol synthesis reactor, are the main factors for increasing the energy efficiency.

Fig. 8 Comparison of energy consumption and production for power plant and power plant plus

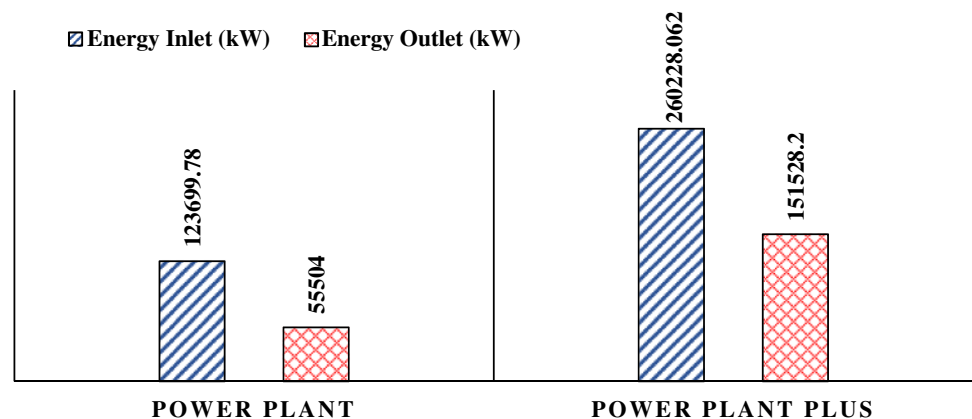


Table 16 Comparison of the results between combined power plant and power plant plus

Parameter	Power Plant	Power Plant Plus
θ_{en} [%]	44.87	58.22
η_{ex} [%]	42.86	97.47
PaybackPeriod(year)	2.83	2.17
Profit(USD/year)	1955653	4225947.39
NCE(kg/h)	22004.85	9057.53

Table 16 compares the triple thermodynamic, economic, and environmental results for both systems evaluated in the present study. According to this table, the use of power plant plus is far superior to the power plant. Because it has been able to improve the technical, economic, and environmental indicators well. The energy efficiency of the power plant plus is 58.22% and the

combined cycle power plant is 44.87%. The exergy efficiency of power plant plus is 97.47%, while this value is 42.86% for the combined cycle power plant, which indicates a thermodynamic improvement. Economically, the annual profit of the power plant plus is 2.27 M\$ more than the combined cycle power plant, and the payback period for the power plant plus shows a decrease of 0.66 years. Also, in terms of environment, the NCE index for the power plant is 9057.53 kg/h and for the combined cycle power plant is 22004.85 kg/h, which shows that methanol production through hydrogenation of the flue gas leads to a reduction of 58.84% for the CO₂ emission (Table 17, Table 18, Table 19).

Sensitivity analysis results

Figure 9 investigates the effect of the reflux ratio of solvent recovery tower on energy consumption of T-101 and T-103 towers in the CO₂ capture section. According to this

Fig. 9 Investigation of the effect of reflux ratio of solvent recovery tower on energy consumption of methanol stripper and separation towers

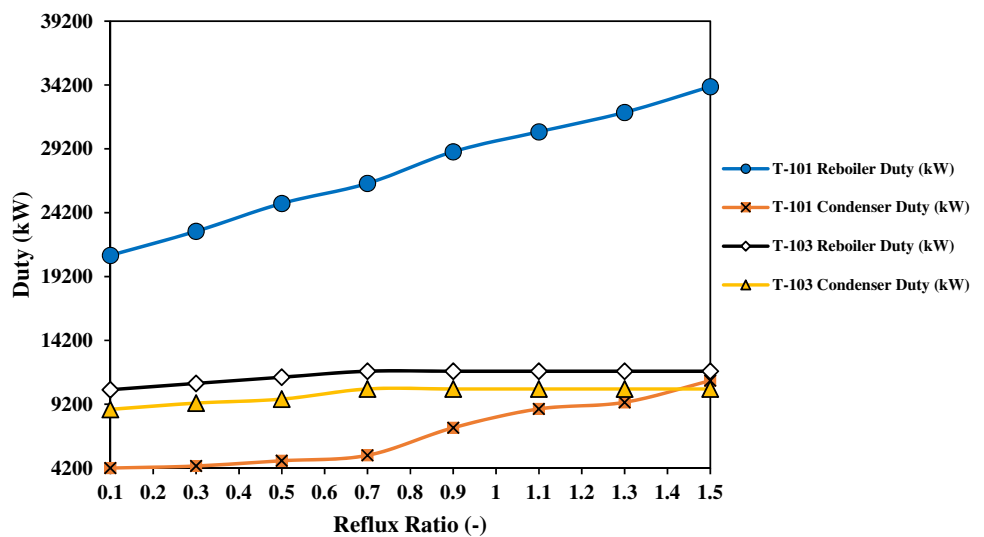


Fig. 10 Investigation of the effect of the reflux ratio of solvent recovery tower on the percentage of CO₂ uptake from the flue gas, net carbon dioxide emissions, and intensity of the methanol production

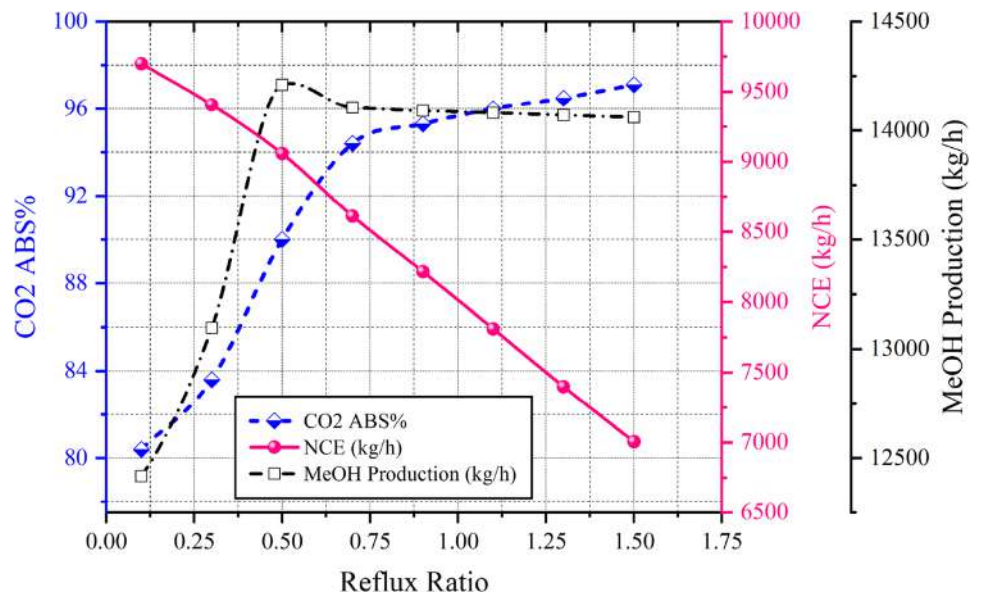
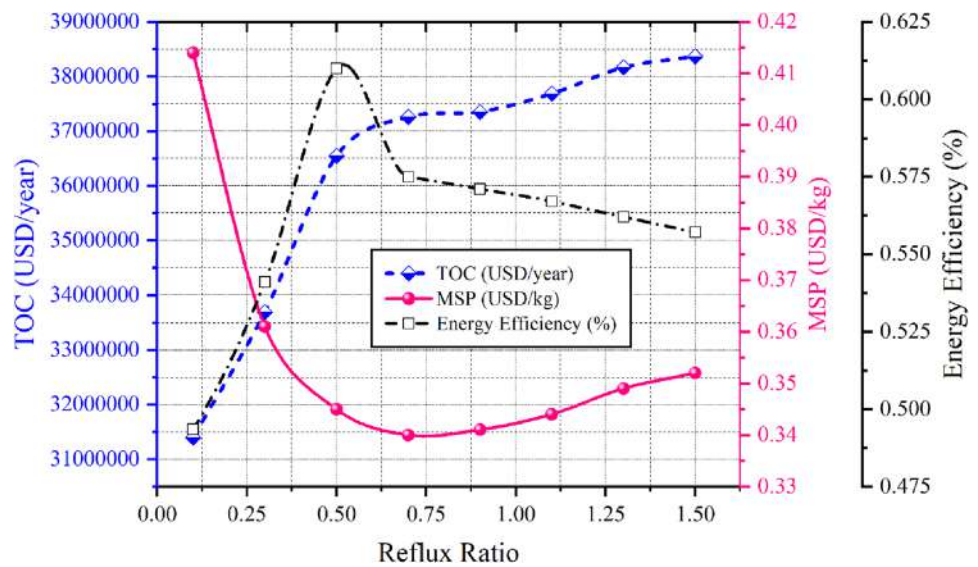


Fig. 11 Investigation of the effect of the reflux ratio of solvent recovery tower on TOC, MSP, and overall energy efficiency of the methanol production process



figure, with increasing the reflux ratio from 0.1 to 1.5, the energy consumption of the T-101 solvent recovery tower in the reboiler and condenser has taken an upward trend. When the reflux ratio of the T-101 tower increases, more moles of water evaporate in the reboiler, and for this, it is necessary to increase the energy consumption of the T-101 tower. On the other hand, by increasing the evaporation of water moles in the reboiler, more mass of steam is produced to emit the CO_2 , and more energy must be used in the condenser to condense the vapors. According to Fig. 9, when the reflux ratio of the T-101 distillation tower increases, the energy consumption of the methanol separation distillation tower (T-103) in both reboiler and condenser equipment also rises. According to the curves, this upward trend to Reflux Ratio of 0.7 continued and from this amount onwards the energy consumption in the reboiler and condenser has been fixed.

Figure 10 shows the effect of the reflux ratio of the T-101 tower on the percentage of CO_2 uptake. It is an uptrend because with the increase in the reflux ratio parameter, the CO_2 stripper operation in the T-101 tower is better and finally the produced amine by the reboiler has a lower load ($\alpha_{\text{CO}_2}^{\text{Lean}}$). When the $\alpha_{\text{CO}_2}^{\text{Lean}}$ parameter decreases, more CO_2 is released in the absorption tower, which eventually leads to an increase in the absorption percentage. But it is noteworthy that in this study, the absorption of 90% of CO_2 was considered. Therefore, 90% absorption in a reflux ratio of 0.5 has been achieved. Increasing the percentage of CO_2 capture causes the amount of $\text{CO}_{2,\text{fluegas}}$ parameter to decrease in NCE. By reducing this parameter, which has a stronger effect on the net CO_2 emission, the amount of NCE for the whole process also takes an upward trend, which is shown in Fig. 10. According to Fig. 10, with increasing the reflux ratio in the solvent recovery tower (T-101), the amount of methanol production also has an upward trend.

According to the simulation, when the reflux ratio value exceeds 0.5, the $\frac{\text{H}_2}{\text{CO}_2}$ ratio in the methanol synthesis reactor will decrease (at a constant amount of H_2). By reducing this ratio, the conversion rate of CO_2 decreases due to the lack of excess H_2 . Finally, the efficiency of methanol production in the methanol synthesis reactor decreases, which results in a lower methanol production flow rate.

Figure 11 examines the influence of the reflux ratio of the stripper tower in the CO_2 recovery section on the total operating cost. According to this study, with the increase in the reflux ratio parameter of T-101 tower, fixed and variable operating costs and in general, TOC parameter has taken an upward trend. Because according to Fig. 9 with increasing the reflux ratio, the amount of energy consumption in distillation towers increases. Moreover, this trend of increasing energy is also present for CO_2 compressors, but it is very significant for reboilers and condensers of T-101 and T-103 distillation towers. Figure 11 displays that increasing the reflux ratio of the T-101 tower to 0.5 causes the overall energy efficiency to experience an upward trend and above this value has reduced the process energy efficiency. Likewise, the amount of methanol production and the resulting energy have a significant effect on the overall value of the $\theta_{\text{en}}^{\text{powerplant+}}$. However, referring to Fig. 10, methanol production has a maximum value when the reflux ratio is 0.5. After this amount, methanol production has a downward trend due to the decrease in the conversion of CO_2 in the methanol reactor. As a result, when the reflux ratio of the T-101 tower is greater than 0.5, firstly, the conversion rate of CO_2 in the methanol reactor decreases, and secondly, the intensity of the methanol production decreases, and with decreasing methanol production, the overall energy efficiency will decrease (Fig. 12, Figure 13, Figure 14.)

Conclusions

Designing an efficient methanol production process and calculating its performance and life cycle GHG emissions were the primary goals of this work, which aimed for a minimal carbon footprint. Accordingly, a comprehensive study on methanol production through direct hydrogenation of captured CO₂ from a combined cycle power plant has been performed. Thus, in two modes of the power plant and power plant plus (power plant that was associated with the production of methanol), energy, exergy, economic, and environmental assessments have been carried out. Also, a sensitivity analysis based on the effect of the reflux ratio of the solvent recovery tower on the performance criteria has been conducted. The main outcomes of the present work are summarized below:

- The simulation results revealed showed that the exergy and energy efficiencies were 42.86% and 44.87%, respectively, while the CO₂ emission through the combined cycle was equal to 22,004.85 kg/h that was an important motivation to define this research.
- According to the results, the exergy efficiency of the power plant plus was 97.47%, and its energy efficiency was equal to 58.22%, which indicated a thermodynamic improvement.
- According to the survey conducted among the power plant plus sectors, the power and steam generation sector (power plant) had the highest exergy destruction rate (82%).
- The economic analysis showed that despite an increase of 116.09% in investment costs in the power plant plus system, annual income and profits increased by 182.03% and 116.08%, respectively, compared to the base system. The payback period was also reduced by 0.66 years, which exhibited the significant advantage of the power plant plus compared to the combined cycle power plant.

- From an environmental viewpoint, the CO₂ in the flue gas was used for methanol synthesis; the power plant plus could reduce the net emission by about 58.84%.
- Finally, adding a methanol production plant to the combined cycle power plant is completely positive in terms of technology, economy, and environment.

Future directions

Commercial use of captured CO₂ is an alternate approach for reducing industrial GHG emissions and perhaps meeting the Paris Agreement obligations. CO₂ is utilized as a chemical commodity in this option to make value-added fuels, chemicals, and other goods that would otherwise be made with fossil fuels, enhancing the financial and societal acceptability of CO₂ capture. The possibility of using CO₂ in methanol production systems raises significant concerns. Which of the CO₂-methanol pathways is the most environmentally friendly? Is it always necessary to use direct CO₂ hydrogenation technology? Is it preferable to integrate the CO₂ collection plant into the existing natural gas-based methanol plants? Despite the fact that multiple papers on the CO₂ to methanol conversion process have been published, there is still a dearth of comprehensive design and life cycle comparisons of alternative conversion paths. As a result, full process development and extensive modeling, energy integration, and life cycle evaluation for multiple methanol production paths can be considered in the upcoming works.

Appendix

See Figs. 12, 13 and 14 and Tables 17, 18 and 19.

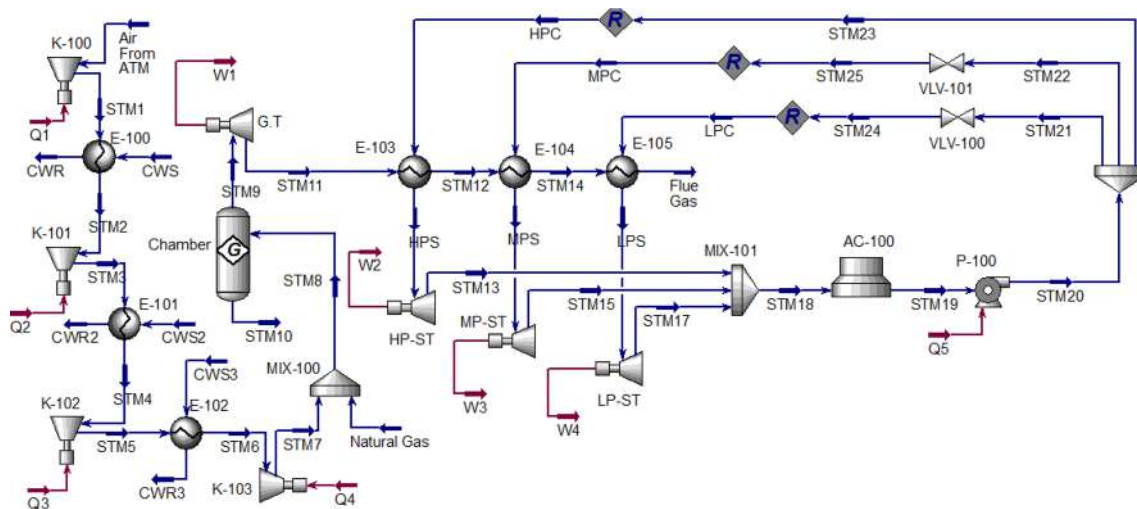


Fig. 12 The plot of the combined cycle power plant with natural gas as fuel simulated in the current work

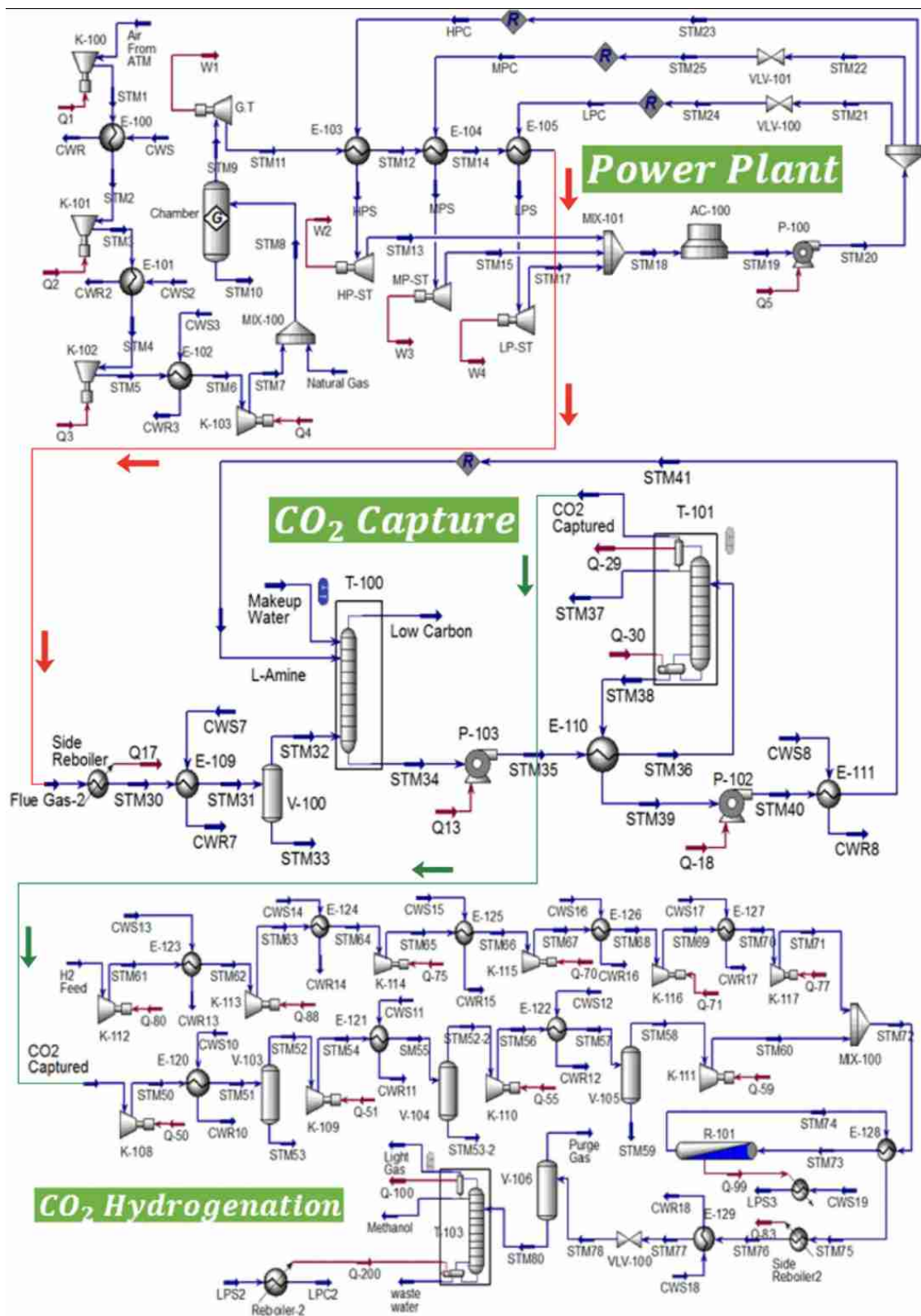


Fig. 13 The plot of the power plant plus simulated in the current work

Table 17 Thermodynamic properties for the streams of the power plant plus

Stream	T(°C)	P(kPa)	F(kmol/h)	Stream	T(°C)	P(kPa)	F(kmol/h)
<i>a: Combined power plant</i>							
Natural Gas	30	2000	500	STM1	128.5	230	3800
Air From ATM	25	101.3	3800	STM2	45	230	3800
STM3	133.2	450	3800	STM4	45	450	3800
STM5	136.3	900	3800	STM6	45	900	3800
STM7	151.7	2000	3800	STM8	133.7	2000	4300
STM9	2361	2000	4300	STM11	1616	120	4300
STM12	699.4	120	4300	STM14	411.7	120	4300
Flue Gas	166.9	120	4300	HPS	250.4	4000	3511
STM13	99.78	101.3	3511	HPC	90.52	4000	3511
MPC	90.52	2000	1000	MPS	212.4	2000	1000
STM15	99.78	101.3	1000	LPC	91.14	1000	810
LPS	179.9	1000	810	STM17	99.78	1000	810
STM18	99.78	101.3	3511	STM19	90	101.3	3511
<i>b: CO₂ capture unit</i>							
STM30	128	120	4300	STM31	45	120	4300
STM32	45	120	3589	STM33	45	120	710.5
STM34	60.76	120	12,570	STM35	60.79	250	12,570
STM39	86.83	210	12,000	STM36	100	230	12,570
STM40	86.84	250	12,000	STM40	45	120	12,000
L-Amine	45	120	12,000	Makeup Water	45	120	500
Low Carbon	63.06	120	3523	STM38	124.7	230	12,000
STM37	44.99	180	85.29	CO ₂ Captured	44.99	180	481.1
<i>c: Methanol synthesis and separation unit</i>							
H ₂ Feed	45	100	1333	STM61	124.2	180	1333
STM62	45	180	1333	STM63	139.8	180	1333
STM64	45	180	1333	STM65	135.6	700	1333
STM66	45	700	1333	STM67	139.8	1400	1333
STM68	45	1400	1333	STM69	139.8	2800	1333
STM70	45	2800	1333	STM71	123.1	5000	1333
CO ₂ Captured	44.99	180	481.1	STM50	122.5	400	481.1
STM51	45	400	481.1	STM52	45	400	467
STM54	123.7	900	467	SM55	45	900	467
STM56	122.9	2000	460.6	STM57	45	2000	460.6
STM60	136.6	5000	457.9	STM72	118.8	5000	1791
STM73	220	5000	1791	STM74	250	5000	902.2
STM75	243.2	5000	902.2	STM76	128	5000	902.2
STM77	45	5000	902.2	STM78	45.14	120	902.2
Purge Gas	45.14	120	11.44	STM80	45.14	120	890.8
Light Gas	60	110	0.3236	Methanol	60	110	443.2
waste water	104.6	120	447.2	LPS2	151.8	500	1240



Table 18 Physical, chemical, and total exergy rates for each stream of the power plant plus

Stream	$\dot{E}_{PH,i}$ (kW)	$\dot{E}_{CH,i}$ (kW)	\dot{E}_i (kW)
<i>a: Combined cycle power plant</i>			
Air From ATM	0	1755	1755
STM1	2601	1755	4356
STM2	2162	1755	3917
STM3	4392	1755	6147
STM4	3915	1755	5670
STM5	6230	1755	7985
STM6	5722	1755	7477
STM7	8449	1755	10,204
CWS	32	8667	8699
CWR	128.24	8667	8795.24
CWS2	32	8667	8699
CWR2	128.24	8667	8695.24
CWS3	38.27	10,400	10,438.27
CWR3	140	10,400	10,540
Natural Gas	1013.1	116,182	117,195.1
STM8	9397	117,937	127,334
STM9	95,715	6702	102,417
STM11	49,046	6702	55,748
STM12	14,721	6702	21,423
STM14	3303	6702	10,005
Flue Gas	2322	6702	9024
HPC	529	3043	872
HPS	18,009	11,421	29,430
STM13	7557	10,378	17,935
MPC	140.5	867	1007.5
MPS	4659	3253	7912
STM15	2213	3018.4	5231.4
LPC	110	702	812
LPS	3358	2634.75	5992.75
STM17	1834	2489.44	4323.44
STM18	11,602	15,883	27,485
STM19	670	4612	5282
STM20	801.22	4612	5413.22
<i>b: CO₂ capture unit</i>			
Flue Gas-2	2322	6702	9024
STM30	1895.46	6702	8597.46
STM31	516.55	6702	7218.55
STM33	10.6	615.77	626.37
STM32	506	6086.23	6592.23
L-Amine	248.4	1,670,717	1,670,965.4
STM41	248.4	1,670,717	1,670,965.4
STM40	1800	1,670,717	1,672,517
STM39	1796.34	1,670,717	1,672,513.34
STM38	4460.82	1,670,717	1,675,177.82
Makeup Water	7.46	433.33	440.79
Low Carbon	963.48	3110.45	4073.93
STM34	583.13	1,673,366	1,673,949.13
STM35	595	1,673,366	1,673,961

Table 18 (continued)

Stream	$\dot{E}_{PH,i}$ (kW)	$\dot{E}_{CH,i}$ (kW)	\dot{E}_i (kW)
STM36	2685.47	1,673,366	1,676,051.47
CO ₂ Captured	194.29	2631	2825.29
STM37	1.3	73.92	75.22
CWS7	216.5	52,000	52,216.5
CWR7	659	52,000	52,659
CWS8	271	65,000	65,271
CWR8	837	65,000	65,837
<i>c: Methanol synthesis and separation unit</i>			
H ₂ Feed	0	88,307.55	88,307.55
STM61	671.3	88,307.55	88,978.85
STM62	534.64	88,307.55	88,842.19
STM63	1352.46	88,307.55	89,660.01
STM64	1172	88,307.55	89,479.55
STM65	1952.55	88,307.55	90,260.1
STM66	1783.87	88,307.55	90,091.42
STM67	2605.64	88,307.55	90,913.19
STM68	2425	88,307.55	90,732.55
STM69	3250.52	88,307.55	91,558.07
STM70	3069.15	88,307.55	91,376.7
STM71	3749.11	88,307.55	92,056.66
CO ₂ Captured	194.29	2631	2825.29
STM50	522.35	2631	3153.35
STM51	440	2631	3071
STM52	439.38	2631	3070.38
STM53	0.21	12.26	12.47
STM54	760	2631	3391
SM55	684.22	2631	3315.22
STM52-2	682.18	2631	3313.18
STM53-2	0.12	5.53	5.65
STM56	985.25	2631	3616.25
STM57	912.56	2631	3543.56
STM58	910.29	2631	3541.29
STM60	1239	2631	3870
STM59	0.07	2.35	2.42
STM72	5022.37	90,938.55	95,960.92
STM73	5549.64	90,938.55	96,488.19
STM74	4379	90,664	95,043
STM75	3688.38	90,664	94,352.38
STM76	525.38	90,664	91,189.38
STM77	74.79	90,664	90,738.79
STM78	22.57	90,664	90,686.57
STM80	20.66	89,255.261	89,275.921
waste water	82.65	387.7	470.35
Methanol	38.73	88,923.16	88,961.89
Light Gas	0.21	42.78	42.99
CWS19	22.66	3467	3489.66
LPS3	1224	3467	4691
LPS2	4494	4033.44	8527.44
LPC2	251.14	1074.67	1325.81
CWS13	12.76	3467	3479.76

Table 18 (continued)

Stream	$\dot{E}_{PH,i}$ (kW)	$\dot{E}_{CH,i}$ (kW)	\dot{E}_i (kW)
CWR13	40.33	3476	3516.33
CWS14	15.93	4333.33	4349.26
CWR14	48.28	4333.33	4381.61
CWS15	15.93	4333.33	4349.26
CWR15	48.28	4333.33	4381.61
CWS16	15.93	4333.33	4349.26
CWR16	48.28	4333.33	4381.61
CWS17	15.93	4333.33	4349.26
CWR17	48.28	4333.33	4381.61
CWS10	9.57	2600	2609.57
CWR10	28.21	2600	2628.21
CWS11	8.29	2253.33	2261.62
CWR11	23.94	2253.33	2277.27
CWS12	7.5	2036.67	2044.17
CWR12	22.31	2036.67	2058.98
CWS18	41.46	11,267	11,308.46
CWR19	129.13	11,267	11,396.13

Table 19 Purchase cost for each component obtained from APEA.

Component	Purchased cost from APEA(USD)
E-111	154,200
T-103	455,900
V-105	18,500
P-102	12,400
E-109	33,700
K-108	807,800
E-127	25,500
AC-100	622,600
K-109	841,400
E-123	50,200
K-111	927,700
E-103	737,760
K-110	878,800
E-110	251,500
E-125	22,900
K-101	3,037,200
E-128	32,600
K-102	2,011,300

Table 19 (continued)

Component	Purchased cost from APEA(USD)
P-100	90,800
E-101	80,800
K-113	3,198,700
LP-ST	225,000
E-104	202,000
G.T	360,000
MP-ST	270,000
E-122	11,200
HP-ST	370,000
V-100	73,100
K-114	1,882,400
P-103	13,900
K-117	1,612,400
K-116	1,606,400
E-129	55,700
E-121	11,000
V-103	18,000
K-112	5,962,600
E-126	23,600
T-100	781,800
Chamber	1580
K-100	8,870,300
E-102	58,300
Side Reboiler	25,900
E-105	182,800
Reboiler-2	29,800
E-100	126,100
K-115	1,564,900
T-101	532,100
E-100	33,100
R-101	22,500
V-104	15,600
Side Reboiler2	21,500
E-120	11,100
E-124	31,700
V-106	23,100
K-103	1,595,600



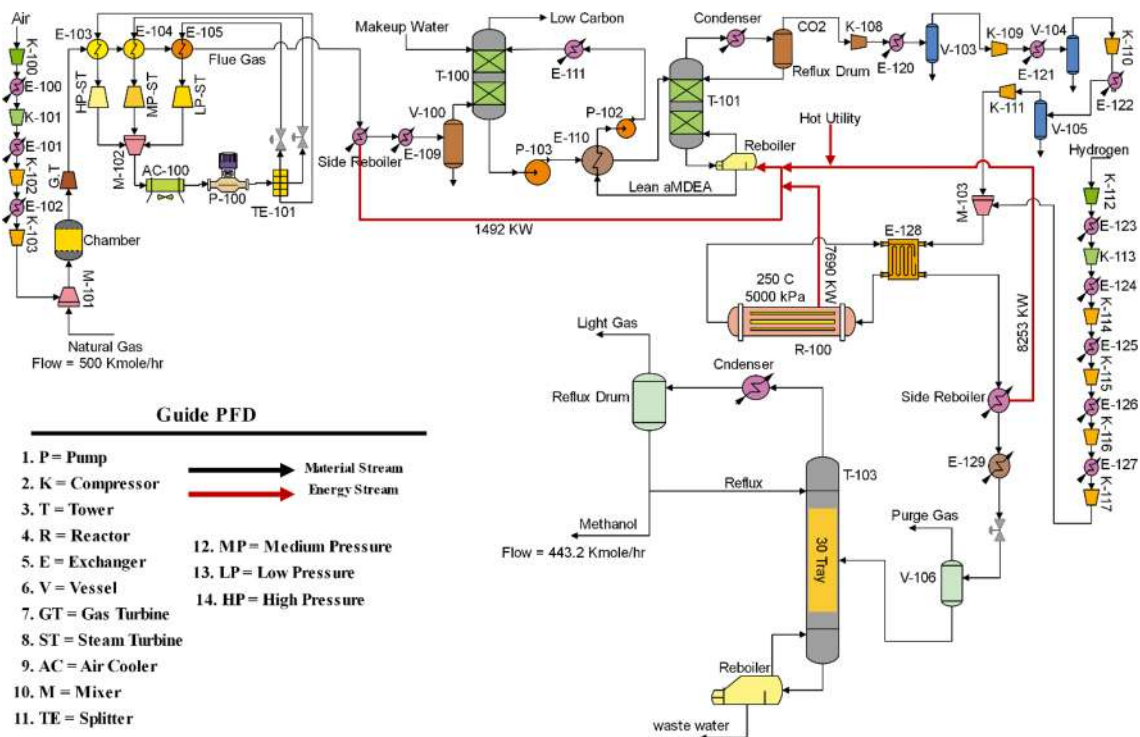


Fig. 14 Schematic of the methanol production process from flue gas leaving the combined cycle power plant

References

- Hamrang, F., Shokri, A., Mahmoudi, S.M.S., Ehghaghi, B.: Performance analysis of a new electricity and freshwater production system based on an integrated gasification combined cycle and multi-effect desalination. *Sustainability*. **12**(19), 7966 (2020)
- Ziapour, B.M., Saadat, M., Palideh, V., Afzal, S.: Power generation enhancement in a salinity-gradient solar pond power plant using thermoelectric generator. *Energy Convers. Manag.* **136**, 283–293 (2017)
- Ahmadi, S., Ghaebi, H., Shokri, A.: A comprehensive thermodynamic analysis of a novel CHP system based on SOFC and APC cycles. *Energy* **186**, 115899 (2019)
- Cao, Y., Mohamed, A.M., Dahari, M., Delpisheh, M., Haghghi, M.A.: Performance enhancement and multi-objective optimization of a solar-driven setup with storage process using an innovative modification. *J. Energy Storage*. **32**, 101956 (2020)
- Haghghi, M.A., Shamsaiee, M., Holagh, S.G., Chitsaz, A., Rosen, M.A.: Thermodynamic, exergoeconomic, and environmental evaluation of a new multi-generation system driven by a molten carbonate fuel cell for production of cooling, heating, electricity, and freshwater. *Energy Convers. Manag.* **199**, 112040 (2019)
- Huang, C.-H., Tan, C.-S.: A review: CO₂ utilization. *Aerosol Air Qual. Res.* **14**, 480–499 (2014)
- Pak, P.S., Suzuki, Y., Tazaki, Y.: CO₂-recovering power generation system in a CO₂-recycling global energy system based on solar energy. *IFAC Proc.* **26**, 821–824 (1993)
- Fernando-Foncillas, C., Cabrera-Rodríguez, C.I., Caparrós-Salvador, F., Varrone, C., Straathof, A.J.J.: Highly selective recovery of medium chain carboxylates from co-fermented organic wastes using anion exchange with carbon dioxide expanded methanol desorption. *Bioresour. Technol.* **319**, 124178 (2021)
- Sarp, S., Hernandez, S.G., Chen, C., Sheehan, S.W.: Alcohol production from carbon dioxide: methanol as a fuel and chemical feedstock. *Joule*. **5**, 59–76 (2021)
- Herdem, M.S., Mazzeo, D., Matera, N., Wen, J.Z., Nathwani, J., Hong, Z.: Simulation and modeling of a combined biomass gasification-solar photovoltaic hydrogen production system for methanol synthesis via carbon dioxide hydrogenation. *Energy Convers. Manag.* **219**, 113045 (2020)
- Li, B., Wang, S., Wang, K., Song, L.: Comparative investigation on the supercritical carbon dioxide power cycle for waste heat recovery of gas turbine. *Energy Convers. Manag.* **228**, 113670 (2021)
- Mohammadi, A., Ahmadi, M.H., Bidi, M., Joda, F., Valero, A., Uson, S.: Exergy analysis of a combined cooling, heating and power system integrated with wind turbine and compressed air energy storage system. *Energy Convers. Manag.* **131**, 69–78 (2017)
- Nazerifard, R., Khani, L., Mohammadpourfard, M., Mohammadi-Ivatloo, B., Akkurt, G.G.: Design and thermodynamic analysis of a novel methanol, hydrogen, and power trigeneration system based on renewable energy and flue gas carbon dioxide. *Energy Convers. Manag.* **233**, 113922 (2021)
- Castellani, B., Rinaldi, S., Morini, E., Nastasi, B., Rossi, F.: Flue gas treatment by power-to-gas integration for methane and ammonia synthesis—energy and environmental analysis. *Energy Convers. Manag.* **171**, 626–634 (2018)
- Yuan, Q., Sun, C.-Y., Yang, X., Ma, P.-C., Ma, Z.-W., Liu, B., Ma, Q.-L., Yang, L.-Y., Chen, G.-J.: Recovery of methane from hydrate reservoir with gaseous carbon dioxide using a three-dimensional middle-size reactor. *Energy* **40**, 47–58 (2012)
- Abdelaziz, O.Y., Hosny, W.M., Gadalla, M.A., Ashour, F.H., Ashour, I.A., Hultberg, C.P.: Novel process technologies for

- conversion of carbon dioxide from industrial flue gas streams into methanol. *J. CO2 Util.* **21**, 52–63 (2017)
17. Sharif, A., Jahangiri, A., Ameri, M.: CO2 capturing from flue gases injected into the NDDCT: feasibility study, exergy and economic investigation of simultaneously MEA-solvent chemical absorption and flue gas injection. *Sustain. Energy Technol. Assessments.* **45**, 101102 (2021)
 18. León, E., Martín, M.: Optimal production of power in a combined cycle from manure based biogas. *Energy Convers. Manag.* **114**, 89–99 (2016)
 19. Fu, C., Gundersen, T.: Heat and work integration: Fundamental insights and applications to carbon dioxide capture processes. *Energy Convers. Manag.* **121**, 36–48 (2016)
 20. Leonzio, G.: State of art and perspectives about the production of methanol, dimethyl ether and syngas by carbon dioxide hydrogenation. *J. CO2 Util.* **27**, 326–354 (2018)
 21. Deng, L., Adams, T.A., II.: Techno-economic analysis of coke oven gas and blast furnace gas to methanol process with carbon dioxide capture and utilization. *Energy Convers. Manag.* **204**, 112315 (2020)
 22. Wiesberg, I.L., Brigagão, G.V., Ofélia de Queiroz, F.A., de Medeiros, J.L.: Carbon dioxide management via exergy-based sustainability assessment: carbon capture and storage versus conversion to methanol. *Renew. Sustain. Energy Rev.* **112**, 720–732 (2019)
 23. Alsayegh, S., Johnson, J.R., Ohs, B., Wessling, M.: Methanol production via direct carbon dioxide hydrogenation using hydrogen from photocatalytic water splitting: process development and techno-economic analysis. *J. Clean. Prod.* **208**, 1446–1458 (2019)
 24. Parigi, D., Giglio, E., Soto, A., Santarelli, M.: Power-to-fuels through carbon dioxide re-utilization and high-temperature electrolysis: a technical and economical comparison between synthetic methanol and methane. *J. Clean. Prod.* **226**, 679–691 (2019)
 25. Haydary, J.: Chemical process design and simulation: Aspen Plus and Aspen Hysys applications. John Wiley & Sons (2019)
 26. Zhao, B., Liu, F., Cui, Z., Liu, C., Yue, H., Tang, S., Liu, Y., Lu, H., Liang, B.: Enhancing the energetic efficiency of MDEA/PZ-based CO2 capture technology for a 650 MW power plant: process improvement. *Appl. Energy.* **185**, 362–375 (2017)
 27. Dubois, L., Thomas, D.: Comparison of various configurations of the absorption-regeneration process using different solvents for the post-combustion CO2 capture applied to cement plant flue gases. *Int. J. Greenh. Gas Control.* **69**, 20–35 (2018)
 28. Osagie, E., Biliyok, C., Di Lorenzo, G., Hanak, D.P., Manovic, V.: Techno-economic evaluation of the 2-amino-2-methyl-1-propanol (AMP) process for CO2 capture from natural gas combined cycle power plant. *Int. J. Greenh. Gas Control.* **70**, 45–56 (2018)
 29. Pérez-Fortes, M., Moya, J.A., Vatopoulos, K., Tzimas, E.: CO2 capture and utilization in cement and iron and steel industries. *Energy Procedia.* **63**, 6534–6543 (2014)
 30. Nwaoha, C., Beaulieu, M., Tontiwachwuthikul, P., Gibson, M.D.: Techno-economic analysis of CO2 capture from a 1.2 million MTPA cement plant using AMP-PZ-MEA blend. *Int. J. Greenh. Gas Control.* **78**, 400–412 (2018)
 31. Ozcan, D.C., Brandani, S., Ahn, H.: A hybrid carbon capture system of indirect calcination and amine absorption for a cement plant. *Energy Procedia.* **63**, 6428–6439 (2014)
 32. Laribi, S., Dubois, L., De Weireld, G., Thomas, D.: Study of the post-combustion CO2 capture process by absorption-regeneration using amine solvents applied to cement plant flue gases with high CO2 contents. *Int. J. Greenh. Gas Control.* **90**, 102799 (2019)
 33. Cengel, Y.A., Boles, M.A., Kanoglu, M.: Thermodynamics: an engineering approach. McGraw-hill New York (2011)
 34. Abd, A.A., Naji, S.Z., Barifcani, A.: Comprehensive evaluation and sensitivity analysis of regeneration energy for acid gas removal plant using single and activated-methyl diethanolamine solvents. *Chinese J. Chem. Eng.* **28**, 1684–1693 (2020)
 35. Nwaoha, C., Smith, D.W., Idem, R., Tontiwachwuthikul, P.: Process simulation and parametric sensitivity study of CO2 capture from 115 MW coal-fired power plant using MEA–DEA blend. *Int. J. Greenh. Gas Control.* **76**, 1–11 (2018)
 36. Bussche, K.M.V., Froment, G.F.: A steady-state kinetic model for methanol synthesis and the water gas shift reaction on a commercial Cu/ZnO/Al2O3Catalyst. *J. Catal.* **161**, 1–10 (1996)
 37. Gholamian, E., Zare, V., Mousavi, S.M.: Integration of biomass gasification with a solid oxide fuel cell in a combined cooling, heating and power system: a thermodynamic and environmental analysis. *Int. J. Hydrogen Energy.* **41**, 20396–20406 (2016)
 38. Nguyen, T.B.H., Zondervan, E.: Methanol production from captured CO2 using hydrogenation and reforming technologies: environmental and economic evaluation. *J. CO2 Util.* **34**, 1–11 (2019)
 39. Yao, Z., Yuxing, Z., Yaqian, K., Sobhani, B.: Research on an integrated power and freshwater generation system from natural gas energy and geothermal sources. *Desalination* **525**, 115494 (2022)
 40. Bejan, A., Tsatsaronis, G., Moran, M.: Thermal Design and Optimization John Wiley and Sons, Inc, New York (1996)
 41. Eisavi, B., Ranjbar, F., Nami, H., Chitsaz, A.: Low-carbon biomass-fueled integrated system for power, methane and methanol production. *Energy Convers. Manag.* **253**, 115163 (2022)
 42. Mahdavi, N., Ghaebi, H., Minaei, A.: Proposal and multi-aspect assessment of a novel solar-based trigeneration system; investigation of zeotropic mixture's utilization. *Appl. Therm. Eng.* **206**, 118110 (2022)
 43. Odejebi, J.O., Ayorinde, O.S.: Exergy and economic analyses of methanol production process. *Niger. J. Technol.* **37**, 365–373 (2018)
 44. Peters, M.S., Timmerhaus, K.D., West, R.E.: Plant design and economics for chemical engineers. McGraw-Hill New York (2003)
 45. Chen, J., Yang, S., Qian, Y.: A novel path for carbon-rich resource utilization with lower emission and higher efficiency: an integrated process of coal gasification and coking to methanol production. *Energy* **177**, 304–318 (2019)
 46. Dincer, I., Rosen, M.A.: Exergy: energy, environment and sustainable development. Newnes (2012)
 47. Do, T.N., Kim, J.: Process development and techno-economic evaluation of methanol production by direct CO2 hydrogenation using solar-thermal energy. *J. CO2 Util.* **33**, 461–472 (2019)

Publisher's Note Springer Nature remains neutral with regard to jurisdictional claims in published maps and institutional affiliations.

Springer Nature or its licensor holds exclusive rights to this article under a publishing agreement with the author(s) or other rightsholder(s); author self-archiving of the accepted manuscript version of this article is solely governed by the terms of such publishing agreement and applicable law.

Authors and Affiliations

Hao Qi¹ · Xuewen Wu¹ · Hehuan Huan¹

✉ Hao Qi
haoqi.022h@gmail.com

¹ Solar Energy Application Technology, Shenzhen BALUN
Technology Co., Ltd, Shenzhen 518053, Guangdong, China



Improved social network search algorithm coupled with Lagrange method for extracting the best parameter of photovoltaic modules and array

Patrick Juvet Gnetchejo¹ · Salomé Ndjakomo Essiane^{1,2} · Abdouramani Dadjé³ · Daniel Eutyche Mbadjoun Wapet⁴ · Pierre Ele^{1,3} · Zhicong Chen⁴

Received: 29 March 2022 / Accepted: 9 September 2022 / Published online: 28 September 2022
© The Author(s), under exclusive licence to Islamic Azad University 2022

Abstract

Optimizing the operation of a photovoltaic system involves a precise model. The current–voltage characteristic equation remains the best way to obtain its optimal parameters from the model. However, the transcendence of this equation remains a significant problem in the process of extracting these parameters. This paper presents a hybrid method comprised of the improved social network search algorithm and the Lagrange method for obtaining the best parameters for modeling a photovoltaic panel. The proposed method improves the basic algorithm by randomly adding a control parameter through Gaussian and Cauchy distributions, which aim to boost the search space agents to converge to the best solution. Then, the Lagrange method is used to solve the objective function's transcendental problem and to generate the best-estimated current. The proposed method has been applied to three different systems, viz., a photovoltaic array consisting of 18 modules (GL100), a photovoltaic panel (Photowatt PWP module), and a photovoltaic cell (RTC France). The difference in the results obtained vis-a-vis the other metaheuristic methods and those recently proposed for solving the transcendental of the I–V equation demonstrated the efficiency of the proposed algorithm. For the Photowatt PWP PV panel considered as the test system in the literature, the best parameters obtained are 1.0331 A for the photocurrent, 1.1863 μ A for the saturation current, 45.3535 for the diode ideality factor, 1.5002 Ω for the series resistance, and 683.8995 Ω for the parallel resistance. These parameters gave a root mean square error of 1.5410×10^{-3} , which converges at the 600th iteration.

Keywords Photovoltaic parameters · PV array · Lagrange · Optimization · Solar cell

Introduction

The development of new energy sources, such as solar energy, which is clean, accessible, and cost-free, has been prompted by the world's energy shortage [1]. The photovoltaic (PV) cell is the main constituent in solar energy generation [2]. The photovoltaic module is composed of cells arranged in series and parallel [3]. For the solar array to create sufficient electrical power, the modules are linked in series and/or parallel. The design, forecast, sizing, diagnosis, and maintenance of photovoltaic system installations need a dependable and accurate model of the cell, module, and PV array [4]. The literature has developed three distinct types with one, two, and three diodes [5]. These models are characterized by parameters that have to be extracted accurately.

✉ Patrick Juvet Gnetchejo
patrick.juvet.gnetchejo@uqtr.ca

✉ Abdouramani Dadjé
abdouramanid@yahoo.fr

¹ Laboratory of Technologies and Applied Sciences, University of Douala, Douala, Cameroon

² Signal, Image and Systems Laboratory, Higher Technical Teacher Training College of Ebolowa, University of Ebolowa, Ebolowa, Cameroon

³ School of Geology and Mining Engineering, University of Ngaoundéré, Ngaoundere, Cameroon

⁴ Laboratory of Electrical Engineering, Mechatronic and Signal Treatment, National Advanced School of Engineering, University of Yaounde 1, Yaoundé, Cameroon



Obtaining these different parameters remains a crucial and challenging problem. Several methods have been developed in the literature to estimate the best PV parameters. These methods can be numerical, analytical, evolutionary, and hybrid [6]. The current–voltage characteristic equation is the optimal approach for determining the features of a PV since it encompasses all of the PV's attributes and parameters. This equation is difficult to solve because of its transcendence, which leads to an optimization challenge. Metaheuristics are likely the most effective approach to resolving this issue, since their efficacy has been shown in the resolution of several issues in other domains. [7–9].

Using Lambert's W function, [10] provided a novel explicit approach to estimate the seven parameters of a two-diode model. The model is founded on two principles: Thevenin's theorem, which describes the linear portion of the PV cell model, and a piecewise linear function, which approximates the nonlinear portion of the cell. [11] extracted parameters from a single-diode model using a novel empirical relation. The empirical technique derives the starting value of the series resistance from the slope of the manufacturer-supplied current–voltage characteristic. In general, the numerical data of the current–voltage characteristic are never supplied at the time of purchase of a PV; thus, image processing will be required to get this data from the technical literature; however, these data are not always precise. Under normal weather circumstances, analytical procedures are effective, but changing atmospheric conditions render them ineffective [4]. Moreover, the approximation of the equations greatly reduces the precision of the results. Furthermore, [12] proposed a new approach with good accuracy of the one-diode model of a PV module; they developed a novel, very accurate method for the one-diode model of a PV module; the methodology is implemented in MATLAB/Simulink using the Levenberg–Marquardt algorithm. The approach used by [13] was predicated on the analysis of the current–voltage characteristic. The main disadvantage of numerical techniques such as Newton–Raphson is the need to perform extensive calculations for convergence; they do not give accurate results when the number of parameters to be estimated increases. The primary drawback of numerical approaches such as Newton–Raphson is the necessity to do long computations for convergence; they do not provide reliable answers as the number of parameters to be evaluated rises. Despite the efficacy of numerical approaches, their slow convergence does not necessarily ensure the optimal outcome, since they may converge to a local minimum and the selection of the starting condition is often not straightforward [4]. The five parameters of a single-diode model

are estimated using the penguin emperor optimization approach [14]; to lower the algorithm's execution time, two parameters (I_{ph} and I_s) were calculated analytically. The differential evolution approach is paired with an analytical method in [15] to predict the optimal parameters of a PV when atmospheric conditions vary. The authors of [16] adapted the Harris Hawk method with trigonometric persistence to minimize the global optimum search time; the algorithm effectively recovered the optimal parameters for one-, two-, and three-diode models. [17] suggested an adaptation of the three-diode model in which a new goal function is employed to estimate the various parameters using a heap-based approach. [18] suggested a novel application of the barnacles mating optimization algorithm (BMOA) for accurate parametrizing of the three-diode model of a PV cell. In [19], the modified bee colony algorithm was utilized in conjunction with a local search technique to enhance the exploration capabilities of the fundamental algorithm. Using a hybrid technique determined the parameters of a two-diode model; to increase the convergence of the wind-driven algorithm, another algorithm, the Fruit Fly, was incorporated to enhance the exploration capabilities of the former. In [20], a unique improved arithmetic optimization technique is used with the modified Newton–Raphson and Levenberg–Marquardt method to efficiently extract the optimal parameter of both single and double diodes. A differential method with a dynamic control parameter was presented by [21]; the control component consists of crossover and mutation, which allows the dynamic fit to converge on the optimal solution. [22] used the Grasshopper optimization algorithm (GOA) to estimate the parameters of a one- and two-diode model. Combining SNS and Secant method, [23] was able to determine the optimal modeling parameters for the design of solar PV modules and arrays. [24] used particle swarm optimization (PSO) and genetic algorithm (GA) to predict the optimal PV module settings in a thermal system.

Although metaheuristic algorithms are better suited for tackling optimization problems, many of them have downsides such as premature convergence to a local minimum, high execution time when the search space expands, and unstable solution after several trials. In order to solve the aforementioned limitations, a novel methodology based on the improved social network search (SNS) algorithm coupled with the Lagrange method (ISNS-LAG) is used in this research to determine the optimal parameters of a photovoltaic cell, module, and array. The social network search (SNS) algorithm replicates the popularity-seeking behavior of people in social networks. As with the majority of metaheuristics, the SNS algorithm sometimes falls locked



in a local minimum. To prevent this premature convergence, a random perturbation equation is introduced to the search space in order for the agents to converge on the optimum solution. Then, the Lagrange technique is included in the objective function to compute the most accurate estimated current.

This work’s novelty and principal contribution are as follows: The social network search algorithm and Lagrange technique are combined for the first time to extract the optimal parameters of a PV cell, module, and array. To enhance the research space of the social network search technique, a Gaussian and Cauchy distribution-based control parameter is randomly introduced to the search space to enable agents to converge on the ideal solution. The Lagrange technique is included into the objective function in order to compute the most accurately predicted currents. The suggested approach is applied to an actual PV array consisting of 18 PV modules. In comparison to earlier research, the obtained results demonstrate the superiority of the suggested methodologies. The specific objectives of this work are as follows: Improve the basic SNS algorithm by randomly adding a control parameter through Gaussian and Cauchy distributions to boost the search space agents to converge to the best solution; use the Lagrange method to solve the transcendental equation of the objective function's; generate the best-estimated current with the Lagrange method; combine the MSNS-LAG algorithm to estimate the optimal parameters of the photovoltaic cell, module, and array; compare the obtained results with current literature.

Materials and methods

Problem formulation

The goal is to develop a PV cell or module's mathematical model by precisely predicting its unknown characteristics, which are given as follows: $\theta = [I_{ph}, I_0, n, R_s, R_p]$ for the single-diode model (Fig. 1), and $\theta = [I_{ph}, I_{01}, I_{02}, n_1, n_2, R_s, R_p]$ for the double [25].

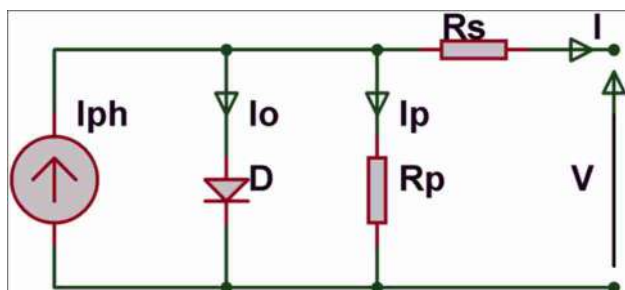


Fig. 1 One-diode PV cell

The root mean square error is often used to quantify the objective function, which is defined as the difference between measured and predicted currents. [26, 27].

$$RMSE = \sqrt{\frac{1}{N} \sum_{i=1}^N (I_{mes} - I_{ext})^2} \tag{1}$$

N : current–voltage measuring points; I_{mes} : the collection of empirically measured current values; I_{ext} : the estimated currents.

To get an estimated current–voltage characteristic (V_i, I_i) near to the measured (V_{mes}, I_{mes}), The one-diode model's predicted current expression is given as follows:

$$I_{i,ext} = I_{ph} - I_0 \left[\exp \left(\frac{q(V_i + I_{i,ext} \cdot R_s)}{n \cdot k \cdot T} \right) - 1 \right] - \frac{V_i + I_{i,ext} \cdot R_s}{R_p} \tag{2}$$

Since the nonlinearity of Eq. (2) precludes an explicit solution, it is rewritten as Eq. (3) as follows:

$$f_{i,ext} = I_{ph} - I_0 \left[\exp \left(\frac{q(V_i + I_{i,ext} \cdot R_s)}{n \cdot k \cdot T} \right) - 1 \right] - \frac{V_i + I_{i,ext} \cdot R_s}{R_p} - I_{i,ext} \tag{3}$$

where the equation is solved to get the total estimated currents ($I_{i,ext}$)

$$f(I_{i,ext}) = 0 \tag{4}$$

Equation (4) is solved using the Lagrange technique in this work.

The SNS algorithm

Inspiration

The SNS algorithm mimics social network users seeking popularity [28]. Like other metaheuristic algorithms, SNS's population reflects each user's social network views. By exchanging opinions, users boost their network standing.

Principle and model

Another user's perspective may influence one user's perspective in four ways [29]:

Imitation As the notion of one user improves, others will attempt to mimic it in their own expressions. This is the mathematical model definition::

$$X_{i,New} = X_j + \text{rand}(-1, 1) \cdot \text{rand}(0, 1) \cdot (X_j - X_i) \quad (5)$$

X_i : is the vector representing the i th user's perspective or position.

X_j : is the vector representing the j th user's perspective or position.

$X_{i,New}$: is the user's new location in the search space.

Conversation The conversation is the phase of exchange with other users to choose the best idea. The mathematical model of this viewpoint is defined by:

$$X_{i,New} = X_i + \text{rand}(0, 1) \cdot (X_j - X_i) \cdot \text{sign}(f_i - f_j) \quad (6)$$

X_i : denotes the randomly selected issue vector that will be addressed.

$\text{sign}(f_i - f_j)$: indicates the disparity between user viewpoints.

Dispute Conversation is the stage of exchanging ideas with other people to choose the best concept. The mathematical model for this perspective is described by:

$$X_{i,New} = X_i + \text{rand}(0, 1) \cdot \left(\frac{\sum_t^{N_r} X_t}{N_r} - (1 + \text{round}(\text{rand})) \cdot X_i \right) \quad (7)$$

$M = \frac{\sum_t^{N_r} X_t}{N_r}$: is the average of comments made by other users in the group AF: $1 + \text{round}(\text{rand})$: is the emphasis a user places on their opinion.

N_r : is the number of users in the group.

Innovation This is the fact that a user can share an idea from their new experience. The mathematical model for this is defined by:

$$X_{i,New}^d = \text{rand}_2 \cdot X_i^d + (1 - t) \cdot (lb_d + \text{rand}_1 \cdot (ub_d - lb_d)) \quad (8)$$

d : is the 10th variable selected at random from the interval of decision variables.

lb : is the minimum value for the variable d .

ub : represents the maximum value of the variable d .

In social networks, individuals must adhere to predetermined guidelines. These regulations include adhering to predetermined restrictions. Thus, the limit of each perspective is specified by:

$$\begin{aligned} x_i &= \min(x_i, ub_i) \\ x_i &= \max(x_i, lb_i) \end{aligned} \quad (9)$$

During the exchange process, a user's viewpoint might modify. The user may then embrace a novel concept. The objective function will assess the value of the new position, and the following equation will determine the best option:

$$X_i = \begin{cases} X_i, & f(X_i) < f(X_{i,new}) \\ X_{i,new}, & f(X_{i,new}) \geq f(X_i) \end{cases} \quad (10)$$

The starting locations are obtained using the following equation: $X_i = lb + \text{rand}(0, 1) \cdot (ub - lb)$ (11)

[29] provides exhaustive information on the SNS algorithm.

Proposed method: The ISNS-LAG algorithm

SNS algorithm is unstable, prematurely converges, and slow. This study proposes three solutions to these difficulties. Randomly adding a control parameter from the Gaussian and Cauchy distributions to the search space; adding a historical memory function; using Lagrange to minimize the error between observed and predicted currents.

Improvement

Randomly select one of the four equations (imitation, conversation, disputation, innovation) disperses the search space. In this paper, only the conversation equation (Eq. 6) is used from the original SNS algorithm model. By focusing only on the conversation, and choosing the user with the best point of view, the user's view at the end of these exchanges must be better.

Equation (6) of the conversation is therefore modified as shown as follows:

$$X_i = X_i + \text{rand} \cdot (X_{best} - X_i) \cdot \text{sign}(f_i - f_j) - P_i \quad (12)$$

X_{best} is the user's view vector following objective function assessment.

P_i is the equation for improved exploration and exploitation balance. This disturbance equation is given as follows:

$$P_i = G_i * (X_{M1} - X_{M2}) \quad (13)$$

G_i is a random function that is created using the Cauchy distribution.

$$G_i = \text{randch}_i(M_{C,ri}, 0.1) \quad (14)$$

with randch the Cauchy distribution, \mathbf{ri} a random integer between [1 100],

X_{M1} and X_{M2} are selected candidates in the search space.

The Lagrange method

Like the dichotomy, Lagrange method consists of the following principle. It is assumed that $f : [a, b] \rightarrow \mathbb{R}$ is continuous, $f(a) < 0$, and $f(b) > 0$. Consider the points $A(a, f(a))$ and $B(b, f(b))$ located on the representative curve C of f . A

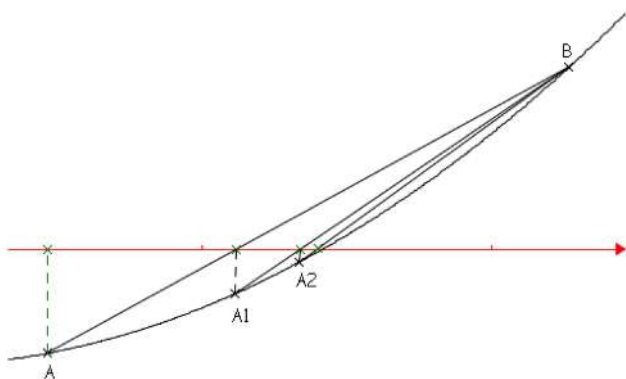


Fig. 2 Illustration of the Lagrange method

sequence (x_n) of real numbers is constructed using points A_n of C . To do this, $A_0 = A$ is posited and A_{n+1} is constructed by drawing the line (A_nB) which meets the axis (Ox) at a point of abscissa x_{n+1} . The point A_{n+1} is the point on C with abscissa x_{n+1} . This illustration can be observed in Fig. 2. The sequence (x_n) verifies the recurrence Eq. (15).

$$x_{n+1} = x_n - \frac{b - x_n}{f(b) - f(x_n)} f(x_n) \tag{15}$$

If f is convexly increasing, the sequence (x_n) converges to a solution of $f(x) = 0$ in the interval $[a, b]$, and furthermore, the convergence is geometric.

Application for the calculation of the best-estimated current

Considering Eq. 4, the solution of this equation is the estimated current I_{ext} . When calling the objective function

(Eq. 1), the images of the two points between which the best current is located are calculated by the following Eqs. (16) and (17):

$$f_i(a) = I_{ph} - I_0 \left[\exp \left(\frac{q(V_i + a.R_s)}{n.k.T} \right) - 1 \right] - \frac{V_i + a.R_s}{R_p} - a \tag{16}$$

$$f_i(b) = I_{ph} - I_0 \left[\exp \left(\frac{q(V_i + b.R_s)}{n.k.T} \right) - 1 \right] - \frac{V_i + b.R_s}{R_p} - b \tag{17}$$

Then, the estimated current is defined by Eq. (15), and its image by Eq. (3). The best estimate current can be determined by iterating Eqs. (3,15,16,17) with precision ϵ .

Lagrange method is used to solve the transcendental problem of Eq. (2). Compared to previous method like Lambert function and Newton method used, respectively, by [30] and [31], Lagrange method has two mains advantages. The first is its easy implementation; just Eq. (15) is enough to insert into Eq. (2). Secondly, as shown in Tables 1, 2 and 3, the obtained results are optimal than those obtained with previous methods.

The algorithm for calculating the best-estimated current based on Lagrange is given in Fig. 3. Algorithm 1 in appendix shows the pseudocode of the proposed ISNS-LAG method.

Experimental platform

To evaluate the proposed method, three case studies were conducted. The first example is the RTC France cell with two diodes, the second case is the Photowatt panel with one diode, and the third case is an experimental array of 18 PV modules (Fig. 4). For a fair assessment, the parameters were similar for each case study. The maximum number of

Table 1 Comparison of RTC with literature

Algorithms	Best parameters							
	Iph (A)	Io1 (µA)	Io2 (µA)	n1	n2	Rs(Ω)	Rp(Ω)	Best RMSE × 10 ⁻⁴
Proposed	0.7608	0.8800	11.3632	2.4977	1.3889	0.03902	61.5559	6.8635
SNS	0.7608	3.2303	0.2246	1.9963	1.4505	0.0368	55.4329	9.8261
DSO [31]	0.7608	0.0869	2.1772	1.3712	1.999	0.0380	58.3713	7.3255
DEDCE [21]	0.7608	0.0642	0.9999	1.3577	1.7869	0.0378	56.3793	7.4196
DE [32]	0.7605	0.4232	0.1872	1.8757	1.4360	0.02061	51.9345	7.6300
MPA [33]	0.7608	0.2704	0.2676	1.9488	1.4648	0.03667	53.5615	7.6499
GAMS [25]	0.7607	0.2259	0.7494	1.4510	2.0000	0.03674	55.4854	9.8248
OLGBO [34]	7.6078	0.7439	0.2265	2.0000	1.4512	1.4512	55.3151	9.8248
ABC-Ls [28]	0.7608	0.2279	0.7273	1.4518	1.9952	0.0367	53.5381	9.8257
ODGB [35]	0.7608	02,202	0.8020	1.4489	2.0000	0.0368	55.8326	9.8258
MABC [19]	0.7607	0.6306	0.2410	2.0000	1.4568	0.0367	54.7550	9.8276
ADHHO [16]	0.7607	2.4672	3.6648	1.4584	2.0000	0.0366	55.09	9.8398
HBO [17]	0.7606	0.6700	0.1970	1.9087	1.4407	0.0368	51.6761	10.4972

Table 2 Comparison of PWP with literature

Algorithms	Best parameters					
	I _{ph} (A)	I _o (μA)	<i>n</i>	R _s (Ω)	R _p (Ω)	Best RMSE × 10 ⁻³
Proposed	1.0331	1.18631	45.3535	1.5002	683.8995	1.5410
SNS	1.0318	3.2773	48.3488	1.20617	845.2469	2.4266
MSNS-SEC [23]	1.0331	1.1863	45.3536	1.5002	681.9921	1.5411
DSO [31]	1.0323	2.4965	47,3328	1.2405	748.3230	2.0399
MPA [33]	1.0323	2.5127	49,2804	1.2392	744.7016	2.0467
DEDCE [21]	1.0314	2.6380	47.5980	1.2356	821.6413	2.0529
DE [32]	1.0314	2.6380	47,3004	0.0343	22.8238	2.0529
NEPO [14]	NA	NA	48.4720	1.1720	982.4500	2.2000
FB-LLSEM [36]	1.0315	3.1436	48,2796	1.2181	858.4100	2.1321
EPO[14]	1.031	0.2090	48.4720	1.1720	982.450	2.2000
ODGB [35]	1.0305	3.4769	48.6369	1.2014	980.5942	2.4115
ABC-Ls [28]	1.0305	3.4742	48.6338	1.2016	984.1798	2.4250
OLGBO [34]	1.0305	3.48226	48.642	1.20127	981.9830	2.4250
ADHHO [16]	1.0304	3.5062	48.6690	1.2007	999.4300	2.4252
GAMS [25]	1.0320	3.2681	48.4020	1.2062	828.2928	2.4426
NLCWL [30]	1.0337	1.9119	46.3018	1.3792	825.8902	343.3

Table 3 Results of the experimental platform of 18 PV array

Operating condition		Algorithms	Best parameters					Best RMSE
G (w/m ²)	T (°C)		I _{ph} (A)	I _o (μA)	<i>n</i>	R _s (Ω)	R _p (Ω)	
553	41.4	ISNS-LAG	10.0076	0.0059	5.9975	2.6917	360.6267	0.0254
		ABC-TRR [37]	10.00	0.0057	215.87	2.699	368.2	0.0580
511	52.5	ISNS-LAG	9.2413	0.0098	6.1851	2.5401	412.1607	0.02213
		ABC-TRR [37]	8.00124	0.01276	6.4676	2.54568	426.17692	0.0580
442	36.7	ISNS-LAG	8.0012	1.2604	6.3684	2.5506	426.4955	0.0166
		ABC-TRR [37]	8.00	0.0099	230.29	2.568	419.8	0.0313
390	35.9	ISNS-LAG	7.0612	0.0036	6.0254	2.6665	487.4974	0.0128
		ABC-TRR [37]	7.06	0.0057	225.77	2.630	515.5	0.0291
333	32.4	ISNS-LAG	6.0219	0.0024	6.1708	2.6608	561.7872	0.0097
		ABC-TRR [37]	6.02	0.0034	225.75	2.634	580.2	0.0182
281	30.3	ISNS-LAG	5.0859	0.0022	6.2488	2.6531	603.3562	0.0069
		ABC-TRR [37]	5.08	0.0032	228.83	2.620	621.8	0.0134

G Irradiance, *T* Temperature

iterations was set to 1000, the number of users *N_u* was set to 50, and 10 runs were conducted for each scenario.

Details of the parameters of this experimental field are available in [37].

Results and discussion

Case study 1: RTC France PV cell

In the literature, the RTC France cell is utilized as the test set. The data of the current–voltage characteristic

are subjected to an irradiance $G = 1000 \text{ W/m}^2$ and a temperature $T = 33^\circ\text{C}$. The manufacturer's and characteristic information may be found in [15].

Table 1 shows the best results obtained by the proposed method. A comparative study is also made with [16, 17, 21, 25, 28, 31–35] on the basis of RMSE.

Table 1 reveals that the suggested algorithm yields the best results with an RMSE of 6.8635×10^{-4} , followed by 7.3255×10^{-4} for [31] and against 9.8248×10^{-4} for [25, 34] and lastly 10.4972×10^{-4} [17] for the worst. These various comparison findings are the best that are presently in the scientific literature.

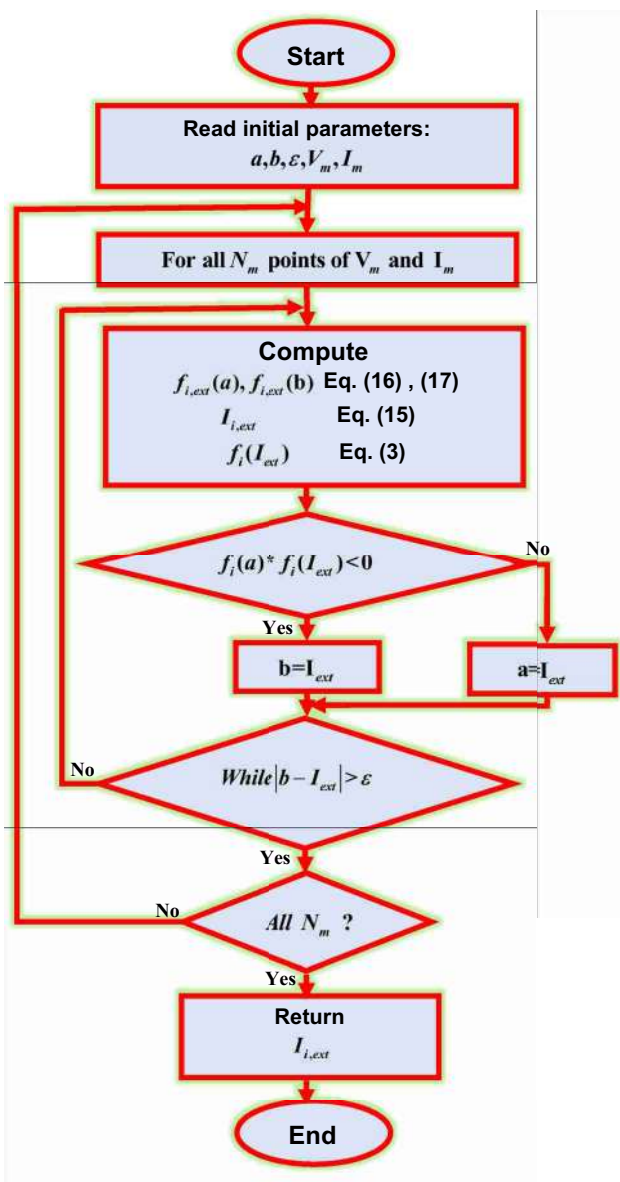


Fig. 3 Estimated current based on the Lagrange

The best parameters thus obtained were used to plot the current–voltage characteristic in Fig. 5. This curve represents the experimental measurement of the I–V characteristic (pink) and the algorithm's estimated I–V characteristic (green), which is shown from Eq. (2). These two qualities indicate that the ISNS-LAG algorithm has successfully improved parameters that are as near as feasible to the experimental measurement. It is also noted that the algorithm accurately predicts the experimental feature, as shown by the square root of the mean error provided in Table 1.

The closeness between the measurement (pink) and the estimate (green) indicates the correctness of the algorithm.

Case study 2: Photowatt PWP PV module

This model is an 11.5 W PV module, for which the current–voltage characteristic measure at a temperature $T = 45^{\circ}\text{C}$ and irradiance of $G = 1000 \text{ W/m}^2$.

Table 2 displays the optimal parameters determined by the ISNS-LAG method. The obtained is $\text{RMSE } 1.5410 \times 10^{-3}$. The gap between the original SNS and the suggested ISNS-LAG may be noted. Clearly, the addition of the Cauchy function to the search space and the Lagrange algorithm to the objective function improves the accuracy.

A comparison study with other recently published techniques, such as [16, 28, 21, 31, 33, 25, 34, 35, and 32] is undertaken in Table 2. Based on RMSE, it is obvious that the ISNS-LAG algorithm has the best optimum: 1.5410×10^{-3} , compared to 2.0399×10^{-3} and 2.4250×10^{-3} for the best recently proposed in the literature. It is also worth noting that the original SNS algorithm yields a value of 2.4242×10^{-3} , which is higher compared to the proposed method. It is also important to note that algorithms perform better the smaller the RSME.

The convergence curves of the basic SNS method and the ISNS-LAG algorithm are shown in Fig. 6.

The convergence curve of the ISNS-LAG algorithm is the first to achieve its minimum before the 600th iteration, as seen in the figure; this displays the algorithm's convergence speed. Even though the original SNS algorithm is the first to achieve its minimum before the 200th iteration, it stays stuck at a local minimum of 2.4242×10^{-3} until the completion of the iterations. Throughout this period, the ISNS-LAG algorithm continues to converge on its global optimal value of 1.5410×10^{-3} .

Case study 3: 18 PV experimental field

To validate the ISNS-LAG technique, the method is used to extract the five model parameters from one diode of the PV field of the experimental platform shown in Fig. 4 at various temperatures and irradiance levels. Table 3 presents the best retrieved characteristics of the PV field under various meteorological conditions.

The order of magnitude of the RMSEs is less in this table than in the reference publication [37]; this illustrates the accuracy of the ISNS-LAG method in predicting the parameters when the PVs are exposed to varying temperature and irradiation circumstances.

Fig. 4 Experimental platform. **a** Experimental of 18 PV array. **b** I–V sensor. **c** Incident irradiance and temperature sensor



Fig. 5 Current–voltage characteristic

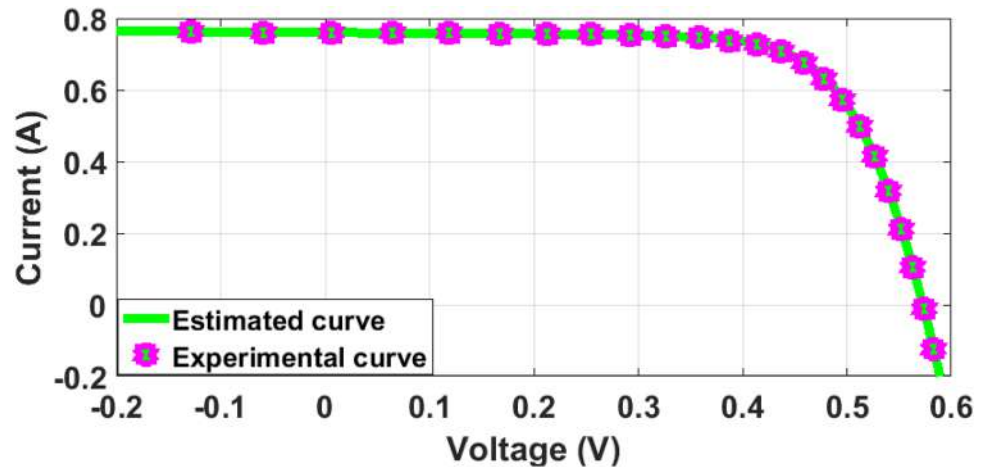


Figure 7 displays the experimentally determined and predicted current–voltage characteristics of the PV array.

The correctness of the results that were acquired can also be shown by the correlation that can be seen on the curves of Fig. 7. This correlation can be seen between the experimental curves and the estimated curves.

Conclusion

In this study, the optimal internal parameters of a photovoltaic cell, module, and array were determined using a novel technique based on the improved social network search



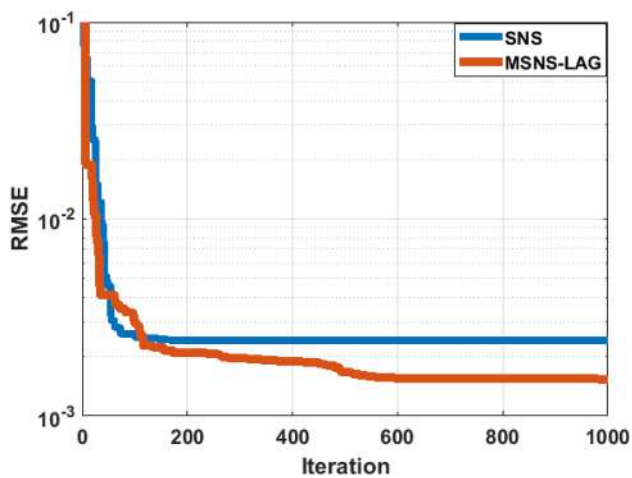


Fig. 6 Convergence curves

(SNS) algorithm and the Lagrange method (ISNS-LAG). There were three ways attempted to enhance the SNS algorithm. First, a random control parameter based on the Gaussian and Cauchy distributions was introduced to the search

space, followed by adding a historical memory function. The Lagrange approach was utilized to improve the accuracy of the best predicted current when the objective function was called. The approach was applied to three distinct systems: a PV cell, a PV panel, and a PV array of 18 modules. RMSE values of 6.8635×10^{-4} for the PV cell and 1.5410×10^{-3} for the PV module indicate that the suggested technique is much superior to all existing methods in the literature. These minimum errors were demonstrated by comparing the measured and estimated current curves. In addition, the convergence curves reaching the optimal before the 600th iteration illustrate the algorithm's speed, and the results of the experimental PV array consisting of 18 panels demonstrate the algorithm's resilience when panels are exposed to varying environmental conditions. The approach suggested in this research would aid in the optimum design of a PV cell, module, and system, which is necessary for the PV system's efficiency; the proposed method may be applied to more complex models, such as the dynamic model of the PV cell; and this technique may also be applied to other engineering problems to improve their performance.

Appendix

Algorithm 1: Pseudocode of ISNS-LAG algorithm

```

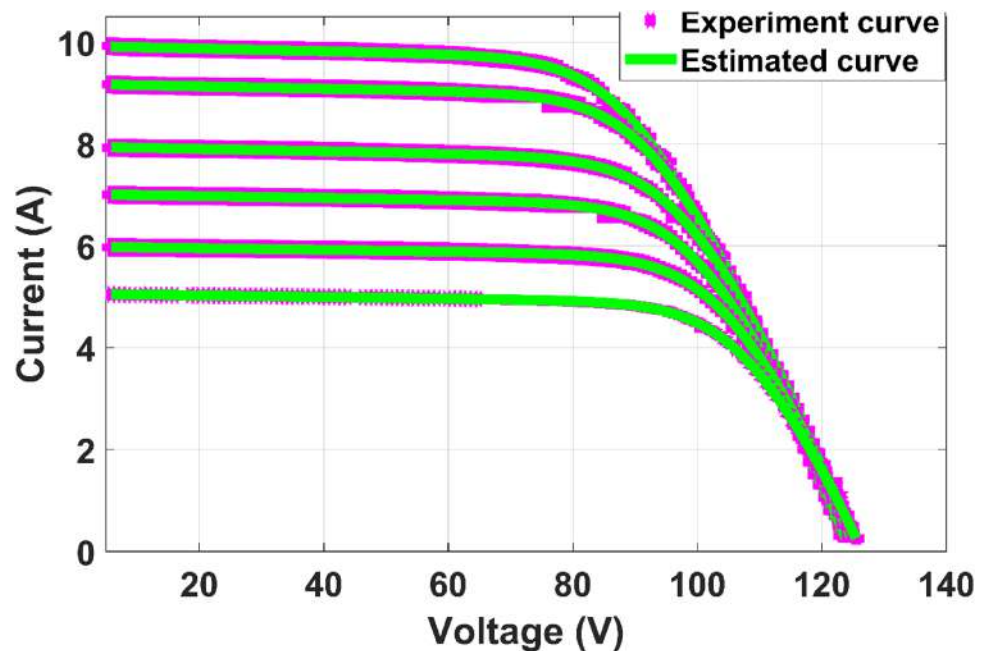
1: Define ISNS-LAG initial parameters (MaxIter, Nuser, UB, LB)
2: for i=1 to Nuser
3:   Generate initial population           Eq. (11)
4:   Evaluate objective function          Eq. (3)
5: End for
6: for i=1 to MaxIter
7:   initialise memory parameters
8:   for i=1 to Nuser
9:     generate the permutation function   Eq. (13) , Eq. (14)
10:    Update the new position              Eq. (12)
11:    Clamp the new solution              Eq. (9)
12:    Evaluate objective function.        Eq. (3)
13:    Calculate the best estimated currents Eq(4), Eq.(16) to Eq.(19)
14:    Update the best fitness
15:    Update the memory parameter with Cauchy and Gaussian distribution
16:    Select the best position and the best finest

17:      if NfBest < f(i)
18:        Update the new position         Eq. (10)
19:      end if
16:    Select the best position and the best finest
17:      if fBest < precision
18:        end if
19:    end for
20: end for

```



Fig. 7 I–V characteristic of PV array (GL100) at different temperature



Funding The authors declare that no funds, grants, or other support were received during the preparation of this manuscript.

Declarations

Conflict of interests The authors declare that they have no known competing financial interests or personal relationships that could have appeared to influence the work reported in this paper.

References

- Gnetchejo, P.J., Essiane, S.N., Ele, P., Dadjé, A., Chen, Z.: Faults diagnosis in a photovoltaic system based on multivariate statistical analysis. *Energy Sour. Part A Recovery Util. Environ. Effects* (2021). <https://doi.org/10.1080/15567036.2021.1919792>
- Gnetchejo, P.J., Ndjakomo Essiane, S., Ele, P.: Diagnostic des défauts d'un champ photovoltaïque par analyse statistique multivariée Fault detection in PV array based on statistical analysis. *Local Resour. Exploit.* **15**, 100273 (2021)
- Ndjakomo Essiane, S., Gnetchejo, P.J., Ele, P., Chen, Z.: Faults detection and identification in PV array using kernel principal components analysis. *Int. J. Energy Environ. Eng.* (2021). <https://doi.org/10.1007/s40095-021-00416-x>
- Gnetchejo, P.J., Essiane, S.N., Ele, P., Wamkeue, R., Mbadjoun Wapet, D., Perabi Ngoffe, S.: Enhanced vibrating particles system algorithm for parameters estimation of photovoltaic system. *JPEE* **07**, 1–26 (2019). <https://doi.org/10.4236/jpee.2019.78001>
- Qais, M.H., Hasanien, H.M., Alghuwainem, S.: Identification of electrical parameters for three-diode photovoltaic model using analytical and sunflower optimization algorithm. *Appl. Energy* **250**, 109–117 (2019). <https://doi.org/10.1016/j.apenergy.2019.05.013>
- Gnetchejo, P.J., Essiane, S.N., Dadjé, A., Ele, P., Wapet, D.E.M., Ngoffe, S.P., Chen, Z.: A Self-adaptive algorithm with newton raphson method for parameters identification of photovoltaic modules and array. *Trans. Electrical Electro. Mater.* **22**(6), 869–888 (2021). <https://doi.org/10.1007/s42341-021-00312-5>
- Wapet, D.E.M., Essiane, S.N., Wamkeue, R., Gnetchejo, P.J.: Hydropower production optimization from inflow: case study of songloulou hydroplant. *JPEE* **08**, 37–52 (2020). <https://doi.org/10.4236/jpee.2020.88003>
- Mbadjoun Wapet, D.E., Ndjakomo Essiane, S., Wamkeue, R., Bisso, D., Gnetchejo, P.J.: Optimal management of hydropower production: case of Memve'ele hydropower reservoir policy. *Energy Rep.* **8**, 1425–1456 (2022). <https://doi.org/10.1016/j.egy.2021.12.047>
- Mbadjoun Wapet, D.E., Ndjakomo Essiane, S., Wamkeue, R., Bisso, D., Gnetchejo, P.J., Bajaj, M.: Optimal policy of hydroelectric reservoir integrated spill flow. *J. Appl. Water Eng. Res.* (2022). <https://doi.org/10.1080/23249676.2022.2093794>
- Dehghanzadeh, A., Farahani, G., Maboodi, M.: A novel approximate explicit double-diode model of solar cells for use in simulation studies. *Renew. Energy* **103**, 468–477 (2017). <https://doi.org/10.1016/j.renene.2016.11.051>
- Senturk, A., Eke, R.: A new method to simulate photovoltaic performance of crystalline silicon photovoltaic modules based on datasheet values. *Renew. Energy* **103**, 58–69 (2017). <https://doi.org/10.1016/j.renene.2016.11.025>
- Tossa, A.K., Soro, Y.M., Azoumah, Y., Yamegueu, D.: A new approach to estimate the performance and energy productivity of photovoltaic modules in real operating conditions. *Sol. Energy* **110**, 543–560 (2014). <https://doi.org/10.1016/j.solener.2014.09.043>
- Ghani, F., Fernandez, E.F., Almonacid, F., O'Donovan, T.S.: The numerical computation of lumped parameter values using the multi-dimensional Newton-Raphson method for the characterisation of a multi-junction CPV module using the five-parameter approach. *Sol. Energy* **149**, 302–313 (2017). <https://doi.org/10.1016/j.solener.2017.04.024>
- Chauhan, A., Prakash, S.: A new emperor penguin optimisation-based approach for solar photovoltaic parameter estimation. *Int. Trans. Elect. Energy Syst.* (2021). <https://doi.org/10.1002/2050-7038.12917>



15. Mengue, F.D., Kammogne, A.S.T., Siewe, M.S., Yamapi, R., Fot-sin, H.B.: A new hybrid method based on differential evolution to determine the temperature-dependent parameters of single-diode photovoltaic cells. *J Comput. Electron.* **20**, 2511–2521 (2021). <https://doi.org/10.1007/s10825-021-01785-6>
16. Song, S., Wang, P., Heidari, A.A., Zhao, X., Chen, H.: Adaptive Harris hawks optimization with persistent trigonometric differences for photovoltaic model parameter extraction. *Eng. Appl. Artif. Intell.* **109**, 104608 (2022). <https://doi.org/10.1016/j.engappai.2021.104608>
17. AbdElminaam, D.S., Houssein, E.H., Said, M., Oliva, D., Nabil, A.: An efficient heap-based optimizer for parameters identification of modified photovoltaic models. *Ain Shams Eng. J.* **13**, 101728 (2022). <https://doi.org/10.1016/j.asej.2022.101728>
18. Agwa, A.M., Elsayed, S.K., Elattar, E.E.: Extracting the parameters of three-diode model of photovoltaics using barnacles mating optimizer. *Symmetry* **14**, 1569 (2022). <https://doi.org/10.3390/sym14081569>
19. Jamadi, M., Merrikh-Bayat, F., Bigdeli, M.: Very accurate parameter estimation of single- and double-diode solar cell models using a modified artificial bee colony algorithm. *Int. J. Energy Environ. Eng.* **7**, 13–25 (2016). <https://doi.org/10.1007/s40095-015-0198-5>
20. Ridha, H.M., Hizam, H., Mirjalili, S., Othman, M.L., Effendy Ya'acob, M.: Zero root-mean-square error for single- and double-diode photovoltaic models parameter determination. *Neural Comput. Appl.* **34**(14), 11603–11624 (2022). <https://doi.org/10.1007/s00521-022-07047-1>
21. Parida, S.M., Rout, P.K.: Differential evolution with dynamic control factors for parameter estimation of photovoltaic models. *J. Comput. Electron.* **20**, 330–343 (2021). <https://doi.org/10.1007/s10825-020-01617-z>
22. Montano, J., Tobón, A.F., Villegas, J.P., Durango, M.: Grasshopper optimization algorithm for parameter estimation of photovoltaic modules based on the single diode model. *Int. J. Energy Environ. Eng.* **11**, 367–375 (2020). <https://doi.org/10.1007/s40095-020-00342-4>
23. Gnetchejo, P.J., Ndjakomo Essiane, S., Dadjé, A., Mbadjoun Wapet, D., Ele, P.: Optimal design of the modelling parameters of photovoltaic modules and array through metaheuristic with Secant method. *Energy Convers. Manag.* **15**, 100273 (2022). <https://doi.org/10.1016/j.ecmx.2022.100273>
24. Bechouat, M., Younsi, A., Sedraoui, M., Soufi, Y., Youfsi, L., Tabet, I., Touafek, K.: Parameters identification of a photovoltaic module in a thermal system using meta-heuristic optimization methods. *Int. J. Energy Environ. Eng.* **8**, 331–341 (2017). <https://doi.org/10.1007/s40095-017-0252-6>
25. Gnetchejo, P.J., Ndjakomo Essiane, S., Ele, P., Wamkeue, R., Mbadjoun Wapet, D., Perabi Ngoffe, S.: Important notes on parameter estimation of solar photovoltaic cell. *Energy Convers. Manag.* **197**, 111870 (2019). <https://doi.org/10.1016/j.enconman.2019.111870>
26. Gnetchejo, P.J., Essiane, S.N., Ele, P., Wamkeue, R., Wapet, D.M., Ngoffe, S.P.: Reply to comment on “Important notes on parameter estimation of solar photovoltaic cell”, by Gnetchejo et al. *Energy Convers. Manag.* **201**, 112132 (2019). <https://doi.org/10.1016/j.enconman.2019.112132>
27. Gnetchejo, P.J., Ndjakomo Essiane, S., Dadjé, A., Ele, P.: A combination of Newton-Raphson method and heuristics algorithms for parameter estimation in photovoltaic modules. *Heliyon* **7**, e06673 (2021). <https://doi.org/10.1016/j.heliyon.2021.e06673>
28. Tefek, M.F.: Artificial bee colony algorithm based on a new local search approach for parameter estimation of photovoltaic systems. *J. Comput. Electron.* **20**, 2530–2562 (2021). <https://doi.org/10.1007/s10825-021-01796-3>
29. Talatahari, S., Bayzidi, H., Saraee, M.: Social network search for global optimization. *IEEE Access* **9**, 92815–92863 (2021). <https://doi.org/10.1109/ACCESS.2021.3091495>
30. Suwanarat, S., Phetphun, P., Prabpal, P., Yupapin, P.: Simple and efficient estimation of I–V photovoltaic using nonlinear curve fitting equivalent circuit model in Lambert W function form. *J. Comput. Electron.* **21**, 666–674 (2022). <https://doi.org/10.1007/s10825-022-01876-y>
31. Gnetchejo, P.J., Ndjakomo Essiane, S., Dadjé, A., Ele, P., Mbadjoun Wapet, D.E., Perabi Ngoffe, S., Chen, Z.: A self-adaptive algorithm with newton raphson method for parameters identification of photovoltaic modules and array. *Trans. Electr. Electron. Mater.* **22**, 869–888 (2021). <https://doi.org/10.1007/s42341-021-00312-5>
32. Kharchouf, Y., Herbazi, R., Chahboun, A.: Parameter's extraction of solar photovoltaic models using an improved differential evolution algorithm. *Energy Convers. Manag.* **251**, 114972 (2022). <https://doi.org/10.1016/j.enconman.2021.114972>
33. Sattar, M.A., Sumaiti, A.A., Ali, H., Diab, A.A.Z.: Marine predators algorithm for parameters estimation of photovoltaic modules considering various weather conditions. *Neural Comput. Appl.* **33**(18), 11799–11819 (2021). <https://doi.org/10.1007/s00521-021-05822-0>
34. Yu, S., Heidari, A.A., Liang, G., Chen, C., Chen, H., Shao, Q.: Solar photovoltaic model parameter estimation based on orthogonally-adapted gradient-based optimization. *Optik* **252**, 168513 (2022). <https://doi.org/10.1016/j.jpleo.2021.168513>
35. Premkumar, M., Jangir, P., Elavarasan, R.M., Sowmya, R.: Opposition decided gradient-based optimizer with balance analysis and diversity maintenance for parameter identification of solar photovoltaic models. *J. Ambient Intell. Human Comput.* (2021). <https://doi.org/10.1007/s12652-021-03564-4>
36. Sreekantha Reddy, S., Yammani, C.: Parameter extraction of single-diode photovoltaic module using experimental current–voltage data. *Circuit Theor. Apps.* **50**, 753–771 (2022). <https://doi.org/10.1002/cta.3133>
37. Wu, L., Chen, Z., Long, C., Cheng, S., Lin, P., Chen, Y., Chen, H.: Parameter extraction of photovoltaic models from measured I–V characteristics curves using a hybrid trust-region reflective algorithm. *Appl. Energy* **232**, 36–53 (2018). <https://doi.org/10.1016/j.apenergy.2018.09.161>

Publisher's Note Springer Nature remains neutral with regard to jurisdictional claims in published maps and institutional affiliations.

Springer Nature or its licensor holds exclusive rights to this article under a publishing agreement with the author(s) or other rightsholder(s); author self-archiving of the accepted manuscript version of this article is solely governed by the terms of such publishing agreement and applicable law.





Analytical MPPT for PV water heating system based on inverter input impedance

Henrique Pires Corrêa¹ · Flávio Henrique Teles Vieira¹

Received: 23 May 2022 / Accepted: 9 September 2022 / Published online: 20 September 2022
© The Author(s), under exclusive licence to Islamic Azad University 2022

Abstract

Carrying out maximum power point tracking (MPPT) is of utmost importance in photovoltaic (PV) systems to ensure high-efficiency power generation. A type of PV system which has not received much attention in MPPT literature is the photovoltaic water heating system (PWHS). The few existing PWHS-specific MPPT approaches in the literature suffer either from low efficiency, complex implementation or significant sensitivity to sample time. Taking this into account, the present work has the objective of proposing a novel MPPT approach for PWHSs that avoids all aforementioned difficulties. The proposed approach is analytical and its main innovation consists in estimating the PV inverter input impedance, which enables the direct computation of duty cycle. Validation is carried via computer simulations, in which comparison to three MPPT methods for PWHSs is considered. Obtained results show that the proposed method yields MPPT energy efficiency improvements of: (a) 0.79%, 1.18% and 11.12% with respect to the other three methods; (b) 0.59% and 0.90% under dynamic irradiance and temperature, respectively, compared to the second-best method; and (c) 7.55%, in average, for varying sample time when compared to the second-best method. At last, the proposed method is seen to be robust with respect to impedance estimation error and maintains peak efficiency for a 37% error margin.

Keywords Maximum power point tracking · Photovoltaic system · Analytical method · Input impedance · Water heating

Introduction

A recent technological trend in photovoltaic (PV) power generation is that of the photovoltaic water heating system (PWHS), which consists of an off-grid and batteryless PV array dedicated to feeding a resistive element that heats a water reservoir [1]. The emergence of PWHSs as a competitive alternative for sustainable water heating is explained by the continuously decreasing cost of PV modules and their simple installation [2, 3], which leads to significantly lower implementation costs when compared to more elaborate approaches such as the usage of photovoltaic-thermal systems [4].

As is also the case for other classes of PV systems, a maximum power point tracking (MPPT) function must be performed by electronic converters in the PWHS to ensure optimal PV power extraction for varying ambient conditions, i.e., irradiance and temperature [5]. The most common MPPT approach for off-grid systems is the two-stage topology [6–8]: the PV array is connected to a MPPT-controlled direct current (DC) converter, whose output feeds the DC bus of an inverter, which in turn powers the alternating current (AC) loads. In this sense, the inverter DC bus corresponds to an equivalent load which must be matched to the PV array maximum power point [9] by the DC converter.

For the particular case of PWHSs, DC bus voltage operates in an open loop and is, thereby, not regulated [10]. Furthermore, the resistive water heating element constitutes a constant impedance load fed by the inverter. Hence, from the MPPT viewpoint, the PWHS inverter presents a nonlinear (due to voltage and current harmonics) impedance load to the PV array. In this work, such unique load characteristic of PWHSs is used as basis for devising a novel PWHS-specific MPPT method that analytically matches PV panel maximum power point resistance and inverter input impedance.

Henrique Pires Corrêa and Flávio Henrique Teles Vieira contributed equally to this work.

✉ Henrique Pires Corrêa
pires_correa@ufg.br

¹ School of Electrical, Mechanical and Computer Engineering, Federal University of Goiás, Avenida Universitária 1488, Goiânia, GO 74605-010, Brazil



We now briefly review the existing MPPT schemes proposed for PWHSS; it is interesting to note that such PWHSS-specific approaches are relatively scarce in the literature and are all presented in patent documents [10–13]. The reader interested in extensive surveys of MPPT algorithms not specifically designed for PWHSS is pointed to the review papers [14–17].

In [10], the DC converter is controlled by means of a hill-climbing algorithm for carrying out MPPT. The specific algorithm is not disclosed, but a PWHSS implemented according to [10] has a nominal efficiency of 96% [18], from which it can be inferred that Perturb & Observe (P & O) was probably used [19]. It is worth noting that P & O has the problem of high sensitivity of efficiency with respect to sample time, which can complicate practical implementation.

Instead of hill-climbing MPPT, the constant voltage (CV) method is used in [11] to control the DC converter. Despite its simpler computations when compared to P & O, a problem of CV is its greater steady-state error [14], which makes it a less efficient method. Also, it requires a proportional-integral (PI) voltage controller, which increases implementation cost.

In [12], a variable resistance heater (VRH) is used for performing MPPT; the heating element resistance is switched between two possible values as a function of measured irradiance. This approach has the advantage of not requiring a DC converter, but it is clearly a very rough MPPT approximation which may result in exceedingly low tracking efficiency.

Similarly, a VRH approach is also proposed in [13]. The main difference with respect to [12] is that a heating element with more than two resistance values is assumed. However, as pointed out by [2], it remains an approximate MPPT strategy and implies a very bulky and complex heating load.

The above discussion shows that MPPT strategies for PWHSS are quite scarce in the literature, with the existing approaches suffering from significant performance and implementation problems. Taking this as motivation, this work aims at proposing a novel MPPT method for PWHSS that avoids the aforementioned difficulties associated with previous methods. Its innovation lies in using an expression deduced for inverter input impedance in combination with measurements from irradiance and temperature sensors, which enables analytical tracking to be performed. The proposed method is shown to have low implementation complexity and, as demonstrated by the experimental results, yields high efficiency and insensitivity to sample time.

Materials and methods

Materials

The typical implementation of a PWHSS is illustrated in Fig. 1, where a water reservoir with dual heating element is used for

enabling grid power demand when PV power is unavailable. This work focuses on the lower electric circuit of Fig. 1, which consists of PV module array, DC converter, inverter and heater.

PV module

The PV module is a source whose current-voltage characteristic is nonlinear and thereby has an operating point resistance R which varies with output voltage V . Furthermore, the characteristic is also modulated by irradiance S and temperature T , from which is clear that $R = R(V, S, T)$. For each pair of ambient conditions (S, T) , a single voltage $V = V_{mp}(S, T)$ and associated current $I = I_{mp}(S, T)$ exist which yield maximum power output. Hence, a maximum power point resistance $R_{mp}(S, T) = V_{mp}(S, T)/I_{mp}(S, T)$ exists for each (S, T) and must be matched to the PV module load via MPPT.

Unfortunately, the dependences of maximum power point voltage (MPPV) and maximum power point current (MPPC) on S and T are not documented on PV module datasheets. On the other hand, dependences of open circuit voltage (OCV) and short circuit current (SCC), which are, respectively, denoted by V_{oc} and I_{sc} , on ambient conditions are computed as [20, 21]:

$$I_{sc}(S, T) = I_{sc}(S_o, T_o) \cdot \frac{S}{S_o} [1 + \alpha_I(T - T_o)] \quad (1)$$

$$V_{oc}(S, T) = N_s m V_t \ln \left(\frac{S}{S_o} \right) + V_{oc}(S_o, T_o) \cdot [1 + \alpha_V(T - T_o)] \quad (2)$$

where T_o and S_o are the nominal values of temperature and irradiance, α_I and α_V are the SCC and OCV temperature coefficients, N_s is the number of series cells in the PV module, V_t is the cell thermal voltage and m is the ideality factor. We henceforth adopt the often-used procedure of assuming $m \approx 1$ [21].

The relations in (1) and (2) can be useful for MPPT purposes, since it is known that V_{mp} and I_{mp} are approximately

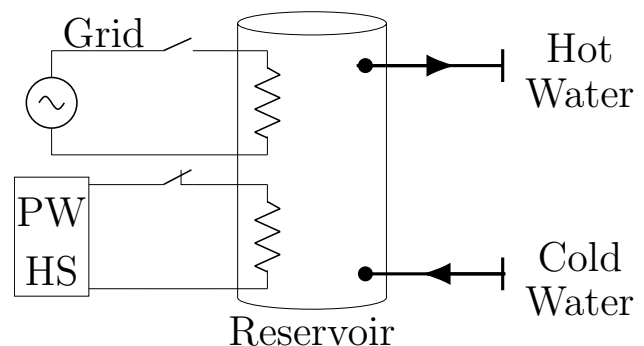


Fig. 1 Illustrative scheme of a photovoltaic water heating system with a dual heating element water reservoir

Table 1 PV module parameters

Parameter	Specification
T_o	25 °C
S_o	1000 W/m ²
$V_{mp}(S_o, T_o)$	29.0 V
$V_{oc}(S_o, T_o)$	36.3 V
$I_{mp}(S_o, T_o)$	7.35 A
$I_{sc}(S_o, T_o)$	7.84 A
α_v	-0.361%/°C
α_I	0.102%/°C
N_s	60

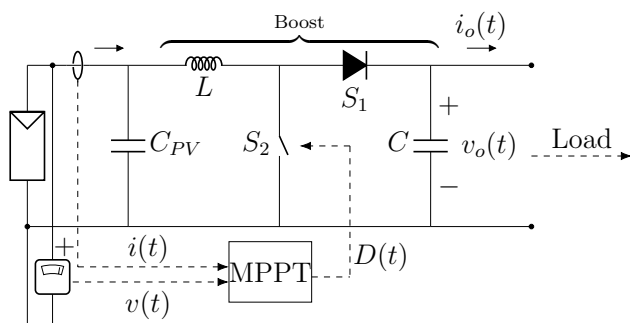


Fig. 2 Boost converter with MPPT control loop

proportional to V_{oc} and I_{sc} , respectively. Hence, it is possible to estimate MPPV and MPPC indirectly by using (1) and (2) if the proportionality constants are known.

In this study, we consider a 3 × 3 array of *1Soltech 1STH-215-P* modules, whose nominal data are taken from [22] and displayed in Table 1. The array has 1918.35 W peak power at 87 V and 22.05A for rated ambient conditions.

DC converter with MPPT control

Implementation of PWHs must be cost-effective, which requires usage of simple DC converter topologies [23]. Since the boost topology is most often employed in practice due to its higher efficiency [24], it is considered in this work. The connection of a PV module to an arbitrary load by means of a MPPT-controlled boost converter is illustrated in Fig. 2.

As depicted in Fig. 2, a general MPPT control loop consists in, at first, sampling PV output voltage $v(t)$ and current $i(t)$ with a sample time T_s . Then, the MPPT algorithm processes the obtained samples of according to its given logic and controls the pulse-width modulation (PWM) duty cycle $D(t)$ to track maximum PV power by matching R_{mp} and load resistance.

For clarity, we recall that the VRH-based methods [11, 12] do not require a DC converter, since they consist in measuring $S(t)$ and switching the load resistance accordingly.

On the other hand, the discussion in this section applies to CV, P &O and the MPPT approach proposed in “Proposed MPPT approach for PWHs” section.

A brief discussion of boost converter steady-state operation is now carried out. This topology yields a voltage conversion ratio given by:

$$M(D) = \frac{V_o}{V} = \frac{I}{I_o} = \frac{1}{1 - D} \tag{3}$$

where $V = \frac{1}{T_{sw}} \int_0^{T_{sw}} v(t)dt$ and analogous notations apply to the other voltage and current waveforms in Fig. 2, where T_{sw} is the PWM switching period.

Recall that, when maximum power point operation is achieved, the load resistance R_o is matched to $R_{mp}(S, T)$. This occurs when D is such that the load matching condition $M^2(D) = R_o/R_{mp}(S, T)$ is satisfied [25]. Hence, efficient MPPT performs rapid and accurate matching for varying S and T .

The converter components L and C are functions of the desired inductor current ripple ΔI_L and output voltage ripple ΔV_o as follows [25]:

$$L = \frac{DVT_{sw}}{2 \cdot \Delta I_L} \tag{4}$$

$$C = \frac{D I_o T_{sw}}{2 \cdot \Delta V_o} \tag{5}$$

To compute L and C , maximum power operation at nominal conditions S_o and T_o is assumed. Hence, $M^2(D) = R_o/R_{mp}(S_o, T_o)$, $V = V_{mp}(S_o, T_o)$ and $I = I_{mp}(S_o, T_o)$. Using such relations in (3)–(5), we obtain:

$$L = \frac{V_{mp}(S_o, T_o) \cdot T_{sw} \left[1 - \sqrt{\frac{V_{mp}(S_o, T_o)}{R_o I_{mp}(S_o, T_o)}} \right]}{2 \cdot \Delta I_L} \tag{6}$$

$$C = \frac{I_{mp}(S_o, T_o) \cdot T_{sw} \left[\sqrt{\frac{V_{mp}(S_o, T_o)}{R_o I_{mp}(S_o, T_o)}} - \frac{V_{mp}(S_o, T_o)}{R_o I_{mp}(S_o, T_o)} \right]}{2 \cdot \Delta V_o} \tag{7}$$

The input voltage ripple in boost converters is relatively small. Hence, in comparison to C , small values of C_{PV} are sufficient for suppressing it [26, 27]. For the sake of simplicity, it is henceforth assumed that $C_{PV} = C$.

Selected boost converter parameters are given in Table 2. The reactive components and switching period have been selected so as to yield ripples of $\Delta V_o \approx 180$ mV and $\Delta I_L \approx 125$ mA; such values have been selected since they represent about 1% of maximum power point voltage and current, thereby ensuring a high-quality power output [28]. A range of MPPT sample times from 50 to 1500 μ s

is considered, since the tracking performance may vary significantly with T_s and must thereby be assessed for different values of it; the selected range is similar to that considered in [29]. Switches S_1 and S_2 (see Fig. 2) are specified according to the most usual boost converter implementation, which employs a MOSFET and power diode pair. The switch parameters are taken from [28]. At last, when simulation of P &O is carried out, its duty cycle perturbation parameter is specified as $\Delta D = 0.01$. This is a commonly employed perturbation value when small T_s are used, as can be seen in [30].

Inverter with water heating load

A single-phase full-bridge inverter with bipolar PWM switching is considered. The nominal output and PWM switching frequencies are denoted as f_c and f_{swi} , respectively. Since PWHS voltage operates in open loop, a constant amplitude modulation m_a is assumed. As depicted in Fig. 3, the inverter feeds a load impedance $Z_l = |Z_l|\angle\theta_l$ (@ f_c), which is an equivalent of the heating load R_l and the inverter output filter. Since heaters do not require high power quality [10], a simple output inductor L_l is assumed as the output filter. Hence, $Z_l(\omega) = R_l + j\omega L_l$, where ω denotes frequency in radians per second. For a purely DC input $v_o(t) = V_o$, the inverter output voltage is [27]:

$$v_l(t) = V_l\sqrt{2} \cdot \left[\sin(\omega_c t) + \sum_{k \in \mathcal{H}} c_k \sin(k\omega_c t) \right] \tag{8}$$

where $\omega_c = 2\pi f_c$, V_l is the fundamental component root-mean-square (RMS) value of $v_l(t)$, \mathcal{H} is the set of voltage harmonic orders and c_k is the fixed ratio between the k -th harmonic RMS value and V_l . For bipolar PWM, the set $\mathcal{H} = \{a \cdot m_f \pm b; a, b \in \mathbb{N}^*\}$, where $m_f = f_{swi}/f_c$ is the frequency modulation.

As illustrated in Fig. 3, we define for later use the inverter DC input impedance $R_o = V_o/I_o$, where it is recalled that V_o and I_o are the DC components of $v_o(t)$ and $i_o(t)$, respectively.

Table 2 Boost converter parameters

Parameter	Specification
C, C_{PV}	1 mF
L	5 mH
S_1	On-resistance: $r_{on} = 1 \text{ m}\Omega$ Forward voltage: $V_{fwd} = 0.7 \text{ V}$
S_2	MOSFET On-resistance: $r_{on} = 100 \text{ m}\Omega$ Internal diode parameters: same as S_1
MPPT	$T_s \in [50, 1500] \text{ (}\mu\text{s)}$, $T_{sw} = 20 \text{ }\mu\text{s}$ $\Delta D = 0.01$ (P &O only)

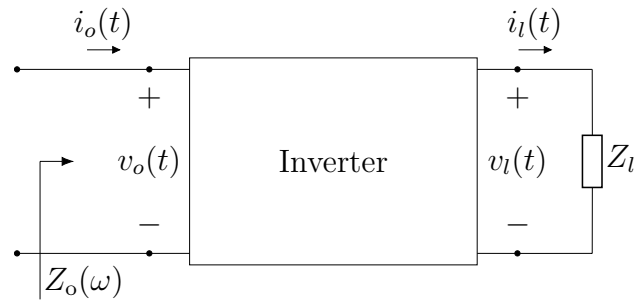


Fig. 3 Single-phase inverter with heating load

The selected inverter and heating load parameters are given in Table 3. Modulations satisfying $m_f \gg 1$ and $m_a \leq 1$ are used to avoid square-wave and low carrier frequency effects. The specific values of m_a , m_f and f_c are taken from [28], as are the inverter switch parameters, which are assumed to be MOSFETs identical to those considered for the boost converter. At last, load impedance is specified so that Z_l draws 1928.63 W (approximately matched to the PV array from “PV module” section) at 220 V and 0.99 power factor.

Proposed MPPT approach for PWHS

We now establish two theorems which will serve as basis for the proposed MPPT method. In Theorem 1, an expression for estimating the DC input impedance of the PWHS inverter is derived, whereas Theorem 2 provides an estimate of PV maximum power point resistance.

Theorem 1 *Let $Z_l = |Z_l|\angle\theta_l$ be an AC load connected to the output of a single-phase full-bridge PWM inverter. The DC input impedance R_o of this system is given by:*

$$R_o = \frac{2|Z_l|}{m_a^2 \cos \theta_l} \tag{9}$$

Proof Let V_o be the DC voltage applied to the inverter input and consider the computation of instantaneous power at the inverter DC and AC ports. If Z_l is not exceedingly reactive (i.e., $|\theta_l|$ is not close to 90°), conservation of instantaneous

Table 3 Inverter and heating load parameters

Parameter	Specification
Inverter	$m_a = 1, m_f = 29, f_c = 60 \text{ Hz}$ Full-bridge switches: same as S_2
Heating load	1928.63 W, 220 V, 0.99 power factor $Z_l = 25\angle 5 \text{ circ } \Omega$ (@ f_c)

power is approximately valid between the two ports and thus [31]:

$$V_o i_o(t) = v_l(t) i_l(t) \tag{10}$$

Since m_f is usually large, it is assumed that all output current harmonics are filtered even for small $|\theta_l|$. Hence, $i_l(t) = I_l \sqrt{2} \sin(\omega_c t - \theta_l)$, where I_l is the RMS value of load current. Substituting in (10) and manipulating, we obtain:

$$i_o(t) = \underbrace{\frac{V_l I_l}{V_o} \cos \theta_l}_{I_o} - \underbrace{\frac{V_l I_l}{V_o} \cos(2\omega_c t - \theta_l)}_{i_o^{(2)}(t)} + \underbrace{\frac{2V_l I_l}{V_o} \sum_{k \in \mathcal{H}} c_k \sin(k\omega_c t) \sin(\omega_c t - \theta_l)}_{i_o^*(t)} \tag{11}$$

where $i_o^{(2)}(t)$ is the double-frequency component associated with single-phase power oscillation at the inverter AC port and $i_o^*(t)$ is the sum of high frequency components associated with PWM switching. Using $R_o = V_o/I_o$, the expression for I_o in (11) and recalling that $V_l = \frac{1}{\sqrt{2}} m_a V_o$ for single-phase bipolar PWM [28], we arrive at (9). □

Theorem 2 The value of $R_{mp}(S, T)$ can be computed as:

$$R_{mp}(S, T) = K \cdot \frac{N_s m V_l \ln\left(\frac{S}{S_o}\right) + V_{oc}(S_o, T_o) \cdot [1 + \alpha_V(T - T_o)]}{I_{sc}(S_o, T_o) \cdot \frac{S}{S_o} [1 + \alpha_I(T - T_o)]} \tag{12}$$

where the constant $K = V_{mp}(S_o, T_o) I_{sc}(S_o, T_o) / V_{oc}(S_o, T_o) I_{mp}(S_o, T_o)$.

Proof For any S and T , $K_V = V_{mp}/V_{oc}$ and $K_I = I_{mp}/I_{sc}$ are approximately constant [32]. Hence, it follows that:

$$R_{mp}(S, T) = \frac{V_{mp}(S, T)}{I_{mp}(S, T)} = K \cdot \frac{V_{oc}(S, T)}{I_{sc}(S, T)} \tag{13}$$

where $K = K_V/K_I$ and K_V, K_I can be estimated from nominal PV values as $K_V = V_{mp}(S_o, T_o)/V_{oc}(S_o, T_o)$ and $K_I = I_{mp}(S_o, T_o)/I_{sc}(S_o, T_o)$. Combining (1), (2) and (13), the proof is complete. □

The assumptions used for proving Theorem 1 are that m_f is sufficiently large so that current harmonics are entirely filtered and $|\theta_l|$ is sufficiently small to ensure instantaneous power conservation. Such assumptions are valid for an ordinary PWHs, since the output filter is small and does not dominate load impedance at nominal frequency. Furthermore, a large m_f is always used in PWM inverters to avoid detrimental effects of low carrier frequency [28].

In any case, to further discuss the validity of instantaneous power conservation, an error assessment of (10) is carried out in Appendix A.

The proposed MPPT method, which we name PWHs-MPPT, is now described. It consists in using irradiance and temperature sensors in order to estimate $R_{mp}(S, T)$ via Theorem 2 and, subsequently, using Theorem 1 to estimate R_o . Given the estimated values, the D value that matches such resistance values is obtained analytically by solving the matching condition $M^2(D) = R_o/R_{mp}(S, T)$. To illustrate the proposed method, it is expressed in block diagram form in Fig. 4, where the sets $\mathcal{X}_o = \{m_a, Z_l\}$ and $\mathcal{X}_{mp} = \{m, N_s, S_o, T_o, K, \alpha_V, \alpha_I, V_{oc}(S_o, T_o), I_{sc}(S_o, T_o)\}$ contain the nominal heating load and PV array data for computing R_o and $R_{mp}(S, T)$, respectively.

At last, it should be observed that PWHs-MPPT provides a very simple implementation. In fact, it only requires specification of sample time T_s and two sensors for measuring S and T . It is thus noteworthy that its implementation is computationally simpler than that of P & O, which also is a two-sensor method but requires two parameters, i.e., T_s and ΔD . Since P & O is already considered a very simple MPPT algorithm, it is clear that PWHs-MPPT is even more so.

Methods

The methodology employed for validating the proposed method is now described. Four computer simulations were carried out in Scilab 6.1.0 to assess the performance of PWHs-MPPT under different ambient condition scenarios and while varying relevant MPPT parameters. In all simulations, we focus on evaluating the MPPT energy efficiency η , which is defined as:

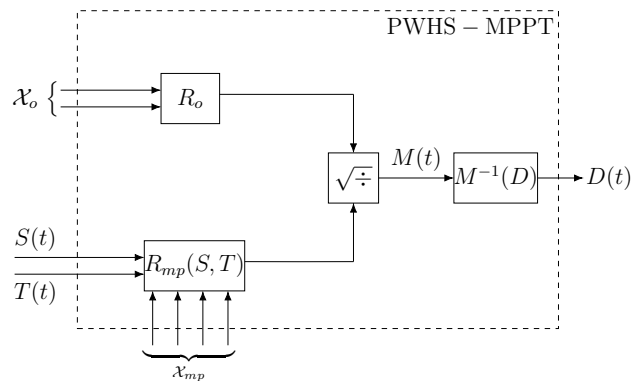


Fig. 4 Block diagram of the proposed PWHs-MPPT method, where $M^{-1}(D)$ is the conversion ratio inverse function. Sets \mathcal{X}_{mp} and \mathcal{X}_o contain nominal PV module and load data

$$\eta = \frac{\int_0^\tau p(t)dt}{\int_0^\tau p_{mp}(t)dt} \quad (14)$$

where τ designates total simulation time and $p_{mp}(t)$ is the time-varying maximum power associated with the maximum power point.

The listing of experiments and their respective descriptions follows.

1. *Comparison to other methods:* As a first validation step, this experiment compares the performance of PWS-MPPT to those yielded by the P & O [10], CV [11] and VRH [12] algorithms. In particular, VRH is considered in its version with two possible load resistance values, which functions by doubling the nominal value of R_l when $S < 500 \text{ W/m}^2$. Also, parameters of the PI controller required in CV are obtained with the Ziegler-Nichols method [19]. For each algorithm, a simulation scenario with $\tau = 1 \text{ s}$ duration is carried out in which irradiance begins at $S = 300 \text{ W/m}^2$, switches to $S = 1000 \text{ W/m}^2$ at $t = \frac{1}{3} \text{ s}$ and, at last, changes to $S = 700 \text{ W/m}^2$ at $t = \frac{2}{3} \text{ s}$. A sample time $T_s = 1000 \mu\text{s}$ is used and a constant temperature $T = 25^\circ\text{C}$ is assumed throughout the experiment.
2. *Dynamic ambient conditions:* Evaluating MPPT methods under varying S and T is of great importance, since efficiency is directly affected by tracking speed. This experiment compares P & O and PWS-MPPT when subject to periodic random-amplitude irradiance and temperature steps. Two simulations with durations $\tau = 30 \text{ s}$ are carried out. In the first one, a constant temperature $T = 25^\circ\text{C}$ is assumed and, at $t = 0.2j$, $j = 0, 1, \dots, 150$, irradiance is changed to a value randomly drawn, according to a uniform distribution, from set $\mathcal{S} = \{100j, j = 0, 1, \dots, 10\} (\text{W/m}^2)$. Analogously, the second simulation considers constant $S = 1000 \text{ W/m}^2$ with temperature being randomly drawn from set $\mathcal{T} = \{10j, j = 0, 1, \dots, 10\} (^\circ\text{C})$. An MPPT sample time of $T_s = 1000 \mu\text{s}$ is considered in this experiment.
3. *Effect of sampling time:* The sensitivity of MPPT algorithms to sample time must be assessed to ensure adequate performance can be obtained in practice for a large enough range of T_s values. This experiment compares the performances of PWS-MPPT and P & O, for varying T_s , in tracking a irradiance step. Sample time is varied in $50 \mu\text{s}$ increments inside the interval specified in Table 2 or each T_s , a simulation with $\tau = 1 \text{ s}$ duration and constant $T = 25^\circ\text{C}$ is carried out in which the system begins in complete shading ($S = 0 \text{ W/m}^2$) and, at $t = 0.5 \text{ s}$, transitions to $S = 1000 \text{ W/m}^2$.

4. *Effect of heating load mismatch:* The PWS-MPPT algorithm is based on the knowledge of R_l , which is used in (9) to obtain R_o . In this sense, we must assess the effects on performance due to a mismatch between the real R_l and the value assumed for it when computing (9), since this problem is prone to happen in practice. This experiment considers that R_l remains fixed and a value $\tilde{R}_l = R_l + \Delta R_l$ is used for computing R_o , with the resistance error ΔR_l being varied in the interval $[-R_l/2, R_l/2]$ at increments of $R_l/400$. For each \tilde{R}_l , the simulation scenario consists, as in the previous experiment, in a irradiance step transition from shading to $S = 1000 \text{ W/m}^2$. A sample time of $T_s = 1000 \mu\text{s}$ is adopted in this experiment.

It should be noted that only PWS-MPPT and P & O are compared in more detail from the second experiment onwards since the first experiment demonstrates that such methods are the best-performing ones.

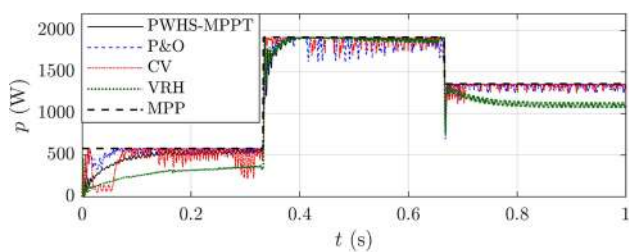
Results and discussion

Comparison to other methods

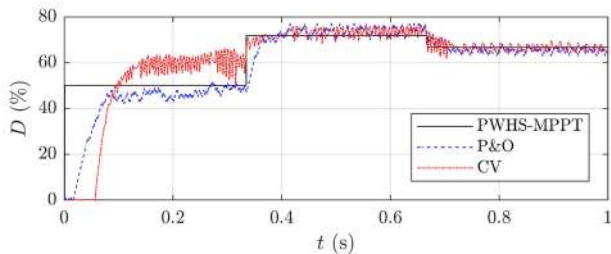
The obtained results are shown in Fig. 5, where computed efficiencies and time plots of $p(t)$, $D(t)$, $v(t)$ and $V_l(t)$ are presented for each considered MPPT method. For clarity, we recall that $V_l(t)$ denotes the RMS value associated with the fundamental component of $v_l(t)$.

As could be expected, the results show that VRH is the least competitive MPPT approach. It is seen to be very inefficient when the PV array is not subject to nominal conditions, i.e., when $S \neq 1000 \text{ W/m}^2$. This is explained by the fact that perfect source-load matching occurs with VRH only in two cases, namely nominal irradiance and $S = 500 \text{ W/m}^2$, which is the threshold used by VRH for doubling load resistance. For all other irradiance values, steady-state error and, as a consequence, efficiency losses occur.

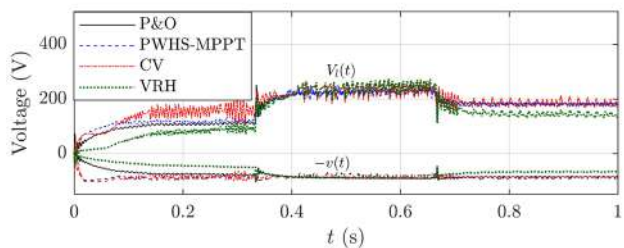
The CV algorithm has its efficiency reduced by two inherent problems, namely steady-state error and PI controller oscillations. The first issue is clearly seen from the $D(t)$ plots, which show that mismatch occurs with respect to the optimal duty cycle. Such error is caused by the fact that V_{mp} has a slight dependence on S , whereas CV attempts to maintain PV voltage at the nominal value $V_{mp}(S_o, T_o)$. Hence, a particularly large error occurs for $t < \frac{1}{3} \text{ s}$ since irradiance is far off the nominal S_o . The oscillation issue occurs due to interactions between DC converter and PI controller dynamics: the converter PWM switchings excite the PI response



(a) Plots of output power.



(b) Plots of converter duty cycle.



(c) Plots of PV and inverter output voltages.

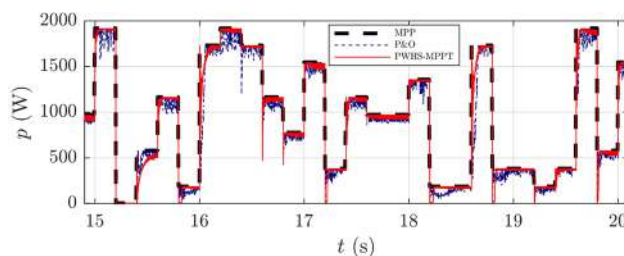
Fig. 5 Results for the MPPT algorithm comparison, which consist of time plots of **a** $p(t)$, **b** $D(t)$, **c** $v(t)$ and $V_i(t)$. The “MPP” line is the plot of $p_{mp}(t)$. Efficiencies yielded by PWHS-MPPT, P &O, CV and VRH were, respectively, 96.33%, 95.54%, 95.15% and 85.21%. Note that VRH does not use duty cycle control and therefore has no $D(t)$ curve

and thereby increase system oscillations, which further reduces efficiency.

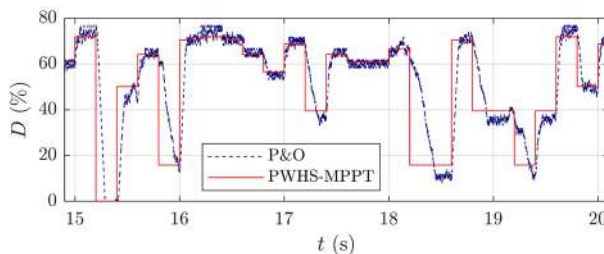
Contrastingly to VRH and CV, both P &O and PWHS-MPPT are seen to have negligible steady-state error and small oscillations. Consequently, such algorithms yielded the highest efficiency values. Despite the small oscillations of P &O, it is quite notable that it still oscillates significantly when compared to PWHS-MPPT. Since both algorithms presented similar tracking speeds, it is clear that the very small oscillations of PWHS-MPPT are the cause of its superior efficiency. Due to its importance, we discuss this phenomenon in greater detail in the next experiment.

Dynamic ambient conditions

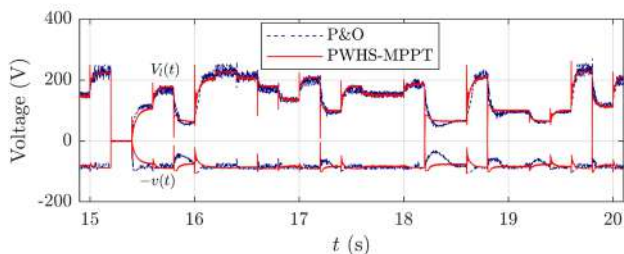
Results for the dynamic irradiance experiment are shown in Fig. 6, whereas the results for the dynamic temperature



(a) Plots of output power.



(b) Plots of converter duty cycle.



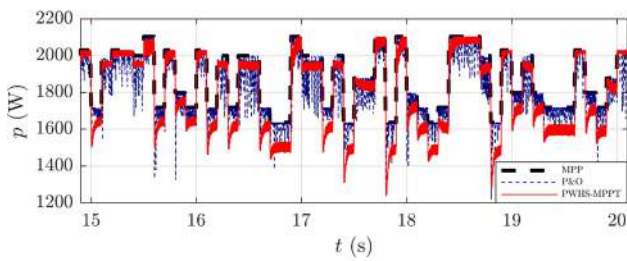
(c) Plots of PV and inverter output voltages.

Fig. 6 Results for dynamic S simulation, which consist of time plots ($14.9 \leq t \leq 20.1$) of **a** $p(t)$, **b** $D(t)$, **c** $v(t)$ and $V_i(t)$

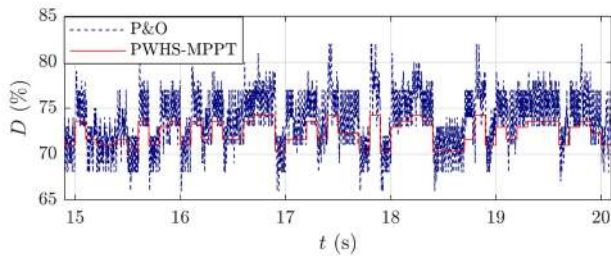
experiment are given in Fig. 7. Each figure displays the obtained time plots of $p(t)$, $D(t)$, $v(t)$ and $V_i(t)$.

As anticipated in the previous experiment, this comparison against P &O makes it particularly clear that a prominent feature of PWHS-MPPT is its very small steady-state oscillation. This is explained by the fact that, during steady-state, PWHS-MPPT yields constant duty cycle, whereas P &O oscillates around the maximum power point. Hence, only the very small oscillations associated with boost converter ripple affect PWHS-MPPT performance and steady-state efficiency is improved as a consequence. This is corroborated by the plots of $v(t)$ and $V_i(t)$ in Figs. 6 and 7, where the P &O voltage waveforms present significant oscillation when compared to PWHS-MPPT.

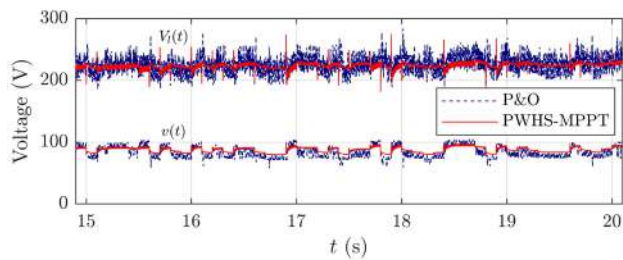
It is fair to note that some steady-state loss is introduced by PWHS-MPPT due to duty cycle estimation error. However, the $p(t)$ plots in Figs. 6 and 7 show that such loss is, in general, negligible. A single exception applies: from Fig. 7, it is seen that larger losses happen for smaller $p(t)$ values, which correspond to temperatures



(a) Plots of output power.



(b) Plots of converter duty cycle.



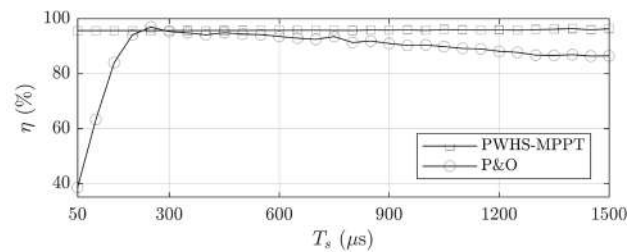
(c) Plots of PV and inverter output voltages.

Fig. 7 Results for dynamic T simulation of, which consist of time plots ($14.9 \leq t \leq 20.1$) of **a** $p(t)$, **b** $D(t)$, **c** $v(t)$ and $V_i(t)$

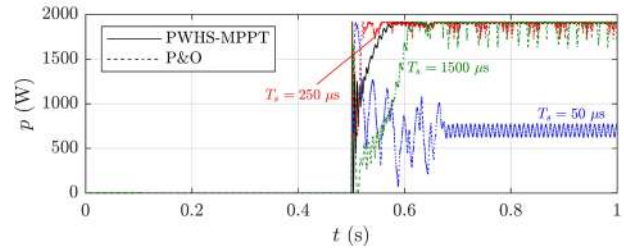
close to $T = 100^\circ\text{C}$. This indicates that (9) is less accurate for larger T . Fortunately, such loss increase happens for smaller $p_{mp}(t)$ whose associated T are very large and thereby not common in practice.

In any case, even with the aforementioned losses due to estimation error in the dynamic T simulation, PWHS-MPPT still performed better than P & O. In fact, as indicated in Figs. 6 and 7, the proposed method yielded higher efficiency values both for the dynamic irradiance (0.59% efficiency improvement) and temperature (0.90% efficiency improvement) simulations.

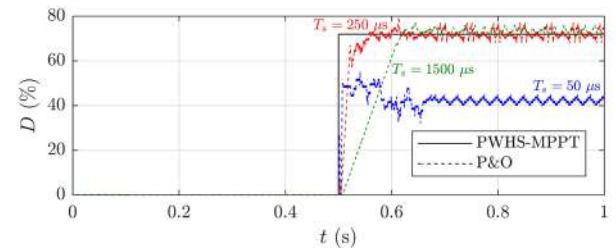
Aside from reduced steady-state oscillation, the good performance of PWHS-MPPT can also be attributed to its very fast tracking, which is clear from the $D(t)$ plots in Figs. 6 and 7, where the PWHS-MPPT duty cycle anticipates the trend followed by the $D(t)$ waveform yielded by P & O. This is explained by the fact that PWHS-MPPT computes duty cycle analytically, whereas P & O depends on a iterative perturbation routine. Hence, the proposed



(a) Plots of efficiency in terms of sample time.



(b) Plots of output power.



(c) Plots of converter duty cycle.

Fig. 8 Results for varying T_s simulation, which consist of **a** plot of efficiency in terms of T_s , **b** selected time plots of $p(t)$ and **c** selected time plots of $D(t)$

method compensates for varying S and T in a nearly instantaneous manner.

Effect of sampling time

The obtained results are displayed in Fig. 8, where a plot of efficiency as a function of T_s for each MPPT method is given, together with $p(t)$ and $D(t)$ plots for specific T_s values as further illustration.

The $\eta(T_s)$ plots in Fig. 8 show that PWHS-MPPT is much less sensitive to sample time than P & O, which is explained as follows. Each perturbation induced by P & O excites a transient response in the circuit, which implies that the tracking efficiency depends on the complex interaction between successive and possibly superposed transients. This phenomenon results in the existence, for a given ΔD , of an optimal T_s , whereas other values of sample time worsen efficiency. On the other hand, for each change in S or T , PWHS-MPPT induces a single electrical

transient in the system. Hence, complex superpositions do not occur and T_s becomes much less critical in determining tracking efficiency.

Insensitivity of PWHS-MPPT to T_s is a major advantage, since it does not require fine-tuning of sample time in order to achieve adequate performance. The exact opposite is true for P &O: extensive trial-and-error is required to determine an optimal efficiency T_s . The plots of $p(t)$ and $D(t)$ for $T_s = 50 \mu s$ and $T_s = 1500 \mu s$ in Fig. 8 further illustrate the difficulty of selecting T_s for P &O: a high sample time leads to excessive tracking delay, whereas small T_s causes drift due to the noise effect of output power ripple [19].

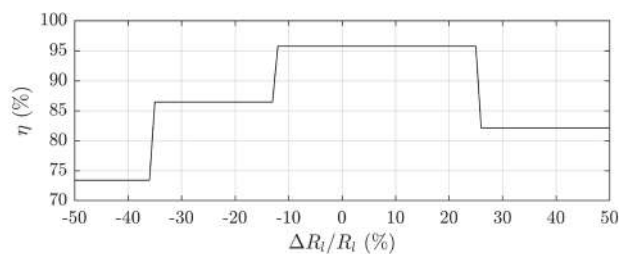
It is fair to note that a single value $T_s = 250 \mu s$ was obtained for which P &O efficiency slightly surpassed that of PWHS-MPPT; the $p(t)$ and $D(t)$ plots of P &O with $T_s = 250 \mu s$ are depicted in Fig. 8. This confirms the prior discussion that P &O requires much fine-tuning to attain optimal efficiency. Furthermore, it can be inferred that, in practical circumstances where a value of T_s would be selected without very extensive testing, PWHS-MPPT would perform better than P &O with very high probability. At last, by averaging over all T_s , it is concluded that PWHS-MPPT yielded an average efficiency improvement of 7.55% with respect to P &O.

Effect of heating load mismatch

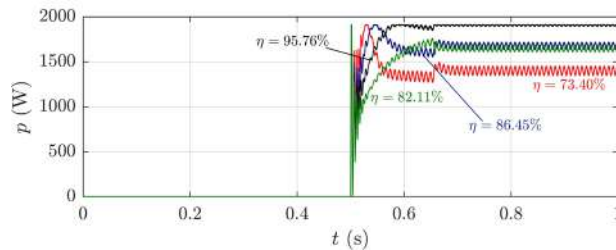
The results are given in Fig. 9, where a plot of efficiency against ΔR_l is displayed, together with $p(t)$ plots associated with different efficiency values.

It is seen that constant η values are obtained for different ranges of ΔR_l . This phenomenon is explained by boost converter dynamics: small variations in R_l are masked by power ripple, for which reason the system progresses as if no variation occurred at all. On the other hand, when a certain R_l variation threshold is surpassed which makes it distinguishable from ripple, the dynamics change and cause a corresponding variation in efficiency. This is advantageous for PWHS-MPPT, since it establishes a margin inside of which mismatch does not cause efficiency loss. In fact, the results in Fig. 9 show that optimal efficiency was obtained in the relatively wide range $\Delta R_l \in [-0.12 \cdot R_l, 0.25 \cdot R_l]$, i.e., a 37% error margin for no efficiency loss was obtained.

The $p(t)$ plots corresponding to each constant- η in Fig. 9 show that worst losses occur when R_l is severely underestimated. This is explained by comparing the nominal maximum power point resistance $R_{mp}(S_o, T_o) \approx 3.95 \Omega$, with the correct DC input impedance value $R_o \approx 50.2 \Omega$ computed via (9). Since $R_o \gg R_{mp}^{(o)}$, the optimal duty cycle $D \approx 0.72$ is relatively high. Hence, greater matching errors occur when D tends to zero rather than to unity. But $D \rightarrow 0$ precisely when R_l is subestimated, i.e., $\Delta R_l < 0$. For the same reason,



(a) Plot of efficiency in terms of load mismatch.



(b) Plots of output power.

Fig. 9 Results for heating load mismatch simulation, which consist of a plot of η in terms of ΔR_l and b time plot of $p(t)$ for each constant- η interval

the optimal η margin is asymmetrical and narrower at its $\Delta R_l < 0$ side.

Most importantly, the wide ΔR_l margin for which optimal efficiency was obtained demonstrates that PWHS-MPPT is robust with regard to estimation error. In this sense, it is concluded that, in practice, changes in R_l which may happen over time are not likely to impact PWHS-MPPT performance.

Conclusion

A novel and high-efficiency MPPT algorithm for PWHSs has been proposed. Its innovation consists in using measurements from irradiance and temperature sensors, coupled with estimation of inverter input impedance, to perform analytical tracking. It fills a relevant research gap in the MPPT literature, since existing methods for PWHSs are either inefficient or exceedingly sensitive to sample time selection. The proposed method was validated via computer simulations, whose results have shown it is: (a) more efficient than previous approaches; (b) insensitive to sample time; and (c) robust to estimation error. It is thus concluded that the objective set out in this work, namely proposing an efficient and simple to implement PWHS-specific MPPT method, has been achieved. It is important to note that the main limitation of this study is that its practical application is restricted to PWHSs. However, in theory, it is valid for any PV system with variable DC bus voltage and an impedance load.

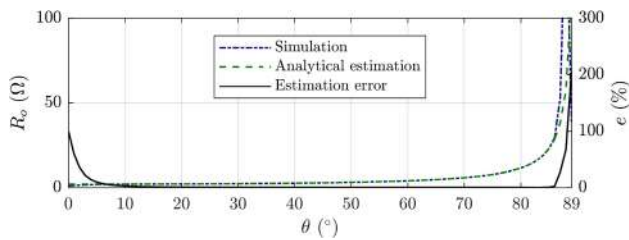


Fig. 10 Plot of input impedance estimation error against θ_l

In future work, we intend to investigate generalizations of PWS-MPPT to three-phase PWSs and how to improve the input impedance estimation by using fewer assumptions in its derivation.

Appendix A estimation accuracy

To assess the accuracy of (9), a simulation experiment is carried out in Scilab 6.1.0 as follows. An inverter with load Z_l is directly fed by a constant voltage $V_o = 100$ V and the input DC current I_o is recorded, thus enabling the computation of R_o . For this simulation, $m_a = 1$, $m_f = 25$, $f_c = 60$ Hz and $|Z_l| = 1$ Ω are considered. The simulation is iterated for $\theta_l = 0^\circ, 1^\circ, \dots, 89^\circ$ and the obtained DC input impedance values R_o^{sim} are compared to those computed from (14), denoted as R_o^{est} , by means of the relative error:

$$e(\theta_l) = \frac{|R_o^{sim}(\theta_l) - R_o^{est}(\theta_l)|}{R_o^{sim}(\theta_l)} \quad (\text{A.1})$$

The results are plotted in Fig. 10 and corroborate the analysis carried out in ‘‘Comparison to other methods’’ section with respect to the validity of (9). The estimation error is relatively low for ranges other than the neighborhood of $|\theta_l| = 90^\circ$, in which it rapidly diverges due to violation of the instantaneous power conservation assumption. It is also noteworthy that error increases for very small power angles, which is explained by violation of the current harmonic filtering assumption used when deriving Theorem 1. This is not a major drawback, since the inverter output filter (and, in practice, system inductances) ensure that, despite having a small value, θ_l does not tightly approach zero.

Declarations

Statements and Declarations The authors have no known competing interests to declare. No funding was received to assist with the preparation of this manuscript. The datasets generated and/or analyzed during the current study are available from the corresponding author on reasonable request.

References

- Clift, D.H., Suehrcke, H.: Control optimization of pv powered electric storage and heat pump water heaters. *Sol. Energy* **226**, 489–500 (2021). <https://doi.org/10.1016/j.solener.2021.08.059>
- Matuska, T., Sourek, B.: Performance analysis of photovoltaic water heating system. *Int. J. Photoenergy* **2017**, 7540250 (2017). <https://doi.org/10.1155/2017/7540250>
- Alajmi, A., Rodríguez, S., Sailor, D.: Transforming a passive house into a net-zero energy house: a case study in the pacific northwest of the U.S. *Energy Convers. Manag.* **172**, 39–49 (2018). <https://doi.org/10.1016/j.enconman.2018.06.107>
- Joshi, S.S., Dhoble, A.S.: Photovoltaic -thermal systems (pvt): technology review and future trends. *Renew. Sustain. Energy Rev.* **92**, 848–882 (2018). <https://doi.org/10.1016/j.rser.2018.04.067>
- Venkatramanan, D., John, V.: Dynamic modeling and analysis of buck converter based solar pv charge controller for improved mppt performance. *IEEE Trans. Ind. Appl.* **55**(6), 6234–6246 (2019). <https://doi.org/10.1109/TIA.2019.2937856>
- Kim, K.A., Seo, G.-S., Cho, B.-H., Krein, P.T.: Photovoltaic hot-spot detection for solar panel substrings using ac parameter characterization. *IEEE Trans. Power Electron.* **31**(2), 1121–1130 (2016). <https://doi.org/10.1109/TPEL.2015.2417548>
- Kim, J.-S., Kwon, J.-M., Kwon, B.-H.: High-efficiency two-stage three-level grid-connected photovoltaic inverter. *IEEE Trans. Industr. Electron.* **65**(3), 2368–2377 (2018). <https://doi.org/10.1109/TIE.2017.2740835>
- Wu, T.-F., Chang, C.-H., Lin, L.-C., Kuo, C.-L.: Power loss comparison of single- and two-stage grid-connected photovoltaic systems. *IEEE Trans. Energy Convers.* **26**(2), 707–715 (2011). <https://doi.org/10.1109/TEC.2011.2123897>
- Li, S., Attou, A., Yang, Y., Geng, D.: A maximum power point tracking control strategy with variable weather parameters for photovoltaic systems with dc bus. *Renew. Energy* **74**, 478–488 (2015). <https://doi.org/10.1016/j.renene.2014.08.056>
- Cheng, G.S.-X., Mulkey, S.L., Chow, A.J.: Smart microgrids and dual-output off-grid power inverters with DC source flexibility. US Patent 9871379B2, January 2018
- Butler, B.L.: Photovoltaic DC heater systems. US Patent 9518759B2 (2016)
- Fanney, A.H., Dougherty, B.P.: Photovoltaic solar water heating system. US Patent 5293447A (1994)
- Newman, M., Newman, G.: Solar Photovoltaic water heating system. US Patent 0153913A1 (2014)
- Bollipo, R.B., Mikkili, S., Bonthagorla, P.K.: Hybrid, optimal, intelligent and classical pv mppt techniques: a review. *CSEE J. Power Energy Syst.* **7**(1), 9–33 (2021). <https://doi.org/10.17775/CSEEJPES.2019.02720>
- Yap, K.Y., Sarimuthu, C.R., Lim, J.M.-Y.: Artificial intelligence based mppt techniques for solar power system: a review. *J. Modern Power Syst. Clean Energy* **8**(6), 1043–1059 (2020). <https://doi.org/10.35833/MPCE.2020.000159>
- Subudhi, B., Pradhan, R.: A comparative study on maximum power point tracking techniques for photovoltaic power systems.



- IEEE Trans. Sustain. Energy **4**(1), 89–98 (2013). <https://doi.org/10.1109/TSTE.2012.2202294>
17. Jatelly, V., Azzopardi, B., Joshi, J., Venkateswaran, V.B., Sharma, A., Arora, S.: Experimental analysis of hill-climbing mppt algorithms under low irradiance levels. *Renew. Sustain. Energy Rev.* **150**, 111467 (2021). <https://doi.org/10.1016/j.rser.2021.111467>
 18. CyboEnergy: Off-Grid CI-Mini-1200H for Electrical Water Heaters. Rancho Cordova, CA, USA (2019). CyboEnergy. http://www.cyboenergy.com/products/cimini1200h_spec.html
 19. Elgendy, M.A., Zahawi, B., Atkinson, D.J.: Assessment of perturb and observe mppt algorithm implementation techniques for pv pumping applications. *IEEE Trans. Sustain. Energy* **3**(1), 21–33 (2012). <https://doi.org/10.1109/TSTE.2011.2168245>
 20. De Soto, W., Klein, S.A., Beckman, W.A.: Improvement and validation of a model for photovoltaic array performance. *Sol. Energy* **80**(1), 78–88 (2006). <https://doi.org/10.1016/j.solener.2005.06.010>
 21. Siddique, H.A.B., Xu, P., De Doncker, R.W.: Parameter extraction algorithm for one-diode model of pv panels based on datasheet values. In: 2013 International Conference on Clean Electrical Power (ICCEP), pp. 7–13 (2013). <https://doi.org/10.1109/ICCEP.2013.6586957>
 22. Blair, N., DiOrio, N., Freeman, J., Gilman, P., Janzou, S., Neises, T., Wagner, M.: System advisor model (sam) general description (version 2017.9.5). NREL/ TP-6A20-70414 (2018)
 23. Teodorescu, R., Liserre, M., Rodriguez, P.: *Grid Converters for Photovoltaic and Wind Power Systems*. Wiley, Hoboken (2011)
 24. Glasner, I., Appelbaum, J.: Advantage of boost vs. buck topology for maximum power point tracker in photovoltaic systems. In: Proceedings of 19th Convention of Electrical and Electronics Engineers in Israel, pp. 355–358 (1996). <https://doi.org/10.1109/EEIS.1996.566988>
 25. Erickson, R.W., Maksimović, D.: *Fundamentals of Power Electronics*. Springer, London (2020)
 26. Hauke, B.: Basic calculation of a boost converter's power stage. Application Report SLVA372C, 1–49 (2014). <https://doi.org/10.1109/IEEESTD.2018.8495141>
 27. Rashid, M.H.: *Power Electronics: Devices, Circuits, and Applications*. Pearson, London (2014)
 28. Mohan, N., Undeland, T.M., Robbins, W.P.: *Power Electronics: Converters, Applications, and Design*. Wiley, Bridgewater (2003)
 29. Femia, N., Petrone, G., Spagnuolo, G., Vitelli, M.: Optimization of perturb and observe maximum power point tracking method. *IEEE Trans. Power Electron.* **20**(4), 963–973 (2005). <https://doi.org/10.1109/TPEL.2005.850975>
 30. Ishaque, K., Salam, Z., Lauss, G.: The performance of perturb and observe and incremental conductance maximum power point tracking method under dynamic weather conditions. *Appl. Energy* **119**, 228–236 (2014). <https://doi.org/10.1016/j.apenergy.2013.12.054>
 31. Akagi, H., Watanabe, E.H., Aredes, M.: *Instantaneous Power Theory and Applications to Power Conditioning*. IEEE Press Series on Power and Energy Systems. Wiley, Bridgewater (2017)
 32. Masoum, M.A.S., Dehbonei, H., Fuchs, E.F.: Theoretical and experimental analyses of photovoltaic systems with voltage and current-based maximum power-point tracking. *IEEE Trans. Energy Convers.* **17**(4), 514–522 (2002). <https://doi.org/10.1109/TEC.2002.805205>

Publisher's Note Springer Nature remains neutral with regard to jurisdictional claims in published maps and institutional affiliations.

Springer Nature or its licensor holds exclusive rights to this article under a publishing agreement with the author(s) or other rightsholder(s); author self-archiving of the accepted manuscript version of this article is solely governed by the terms of such publishing agreement and applicable law.





Response surface methodology of nickel and cobalt recovery from battery using acid as leaching agent

Nur Vita Permatasari^{1,2} · H. Hadiyanto^{2,3,4} · Adji Kawigraha¹ · Budi Warsito^{5,6} · Marcelinus Christwardana^{4,7} 

Received: 5 June 2022 / Accepted: 29 August 2022 / Published online: 13 September 2022
© The Author(s), under exclusive licence to Islamic Azad University 2022

Abstract

The need for batteries will increase change from conventional vehicles to electric vehicles. Electric vehicles are used as an effort to reduce CO₂ emissions that can cause global warming. The acceleration for the development of the electric vehicle industry is also supported by Indonesia's ability to produce nickel which is a commodity in electric batteries. Battery waste that is not managed properly can cause environmental problems and result in human health due to hazardous and toxic materials waste. Battery waste also has economic value for its supporting metals. This recycling is also one of the measures to break down the excessive exploitation (mining) of nature which causes environmental damage and can reduce the cost of producing raw materials by around 50–70%. This study purpose to recycle battery waste in order to obtain quantitative data on the recovery of Ni and Co with hydrometallurgical techniques, where battery waste will be leached using sulfuric acid solution with the help of peroxide acid at a certain time, temperature and stirring speed. Optimization is done using the Behnken–Box where the variables reviewed are solid–liquid ratio variables (2–10% (S/L), acid concentration (0.5–2.5 M) and temperature (40–80 °C). The recovery optimization process of Ni and Co obtained optimal conditions at solid–liquid ratio of 2.5%, sulfuric acid concentration of 1 M, and temperature 80 °C which resulted Ni and Co recovery of 99.9 and 97.8%, respectively, from experiment.

Keywords Lithium-ion batteries · Cobalt · Nickel · Recycling · Response surface methodology

Introduction

Currently, batteries are a viable alternative as energy drivers [1]. Future battery consumption will grow as demand for electric cars increases [2]. This is closely tied to the government's attempts to produce electric cars, which are still being refined. Electric cars are more energy efficient than

conventional automobiles [3]. By 2030, it is expected that 245 million electric vehicles will have been produced [4]. Nickel is the primary raw element in lithium-ion batteries, which contributes to the development of the electric vehicle industry [5]. Abundant nickel ore deposits in Indonesia also contribute to the market's expansion [6]. As roughly a quarter of CO₂ is generated by the transportation sector,

✉ H. Hadiyanto
hadiyanto@live.undip.ac.id

✉ Marcelinus Christwardana
marcelinus@lecturer.undip.ac.id

¹ Mining Technology Research Center, National Research and Innovation Agency, Kawasan PUSPIPTEK Serpong, South Tangerang 15314, Indonesia

² Master Program of Environmental Sciences, School of Postgraduate Studies, Diponegoro University, Jl. Imam Bardjo SH., Pleburan, Semarang 50241, Indonesia

³ Department of Chemical Engineering, Diponegoro University, Jl. Prof. Sudarto SH., Tembalang, Semarang 50275, Indonesia

⁴ Master Program of Energy, School of Postgraduate Studies, Diponegoro University, Jl. Imam Bardjo SH., Pleburan, Semarang 50241, Indonesia

⁵ Department of Statistic, Diponegoro University, Jl. Prof. Sudarto SH., Tembalang, Semarang 50275, Indonesia

⁶ Doctoral Program of Environmental Sciences, School of Postgraduate Studies, Diponegoro University, Jl. Imam Bardjo SH., Pleburan, Semarang 50241, Indonesia

⁷ Department of Chemistry, Diponegoro University, Jl. Prof. Sudarto SH., Tembalang, Semarang 50275, Indonesia



electrification is a technological method to minimize air pollution in crowded places with the goal of lowering greenhouse emissions. This is done to minimize environmental pollutants and encourage healthy via the use of pollution-free gasoline, which reduces emissions and has a low carbon footprint, as well as to combat climate change [7].

Lithium-ion batteries (LIBs) are used in electric cars due to their high capacity, high operating voltage, high energy density, low weight, and compact [8]. Increasing the performance of electric vehicles also necessitates a higher density power supply. Increased battery use will inevitably lead to an increase in the number of spent batteries released into the environment. Obviously, this will lead to an increase in heavy metal pollution and a decline in environmental quality. Because the electrolyte includes ethylene carbonate, propylene carbonate, lithium hexafluorophosphate, etc., and the binder comprises polyvinylidene fluoride, battery waste is classed as hazardous and toxic materials [9].

The disposal of LIBs waste might cause health hazards by entering the food chain. Around 20% cobalt, 5–10% t nickel, 5–7% lithium, 15% organic compounds, and 7% polymers make up LIBs, the exact proportions of which vary somewhat from different manufacturers [10]. According to Ordoez et al., [11], from the 4000 tons of LIBs trash gathered in 2005, 1100 tons of heavy metals and over 200 tons of hazardous electrolytes were produced. Used LIBs that are discarded in the environment without treatment will pollute soil, ground water, rivers, and lakes, which may contaminate drinking, bathing, and washing water [12]. Cobalt overexposure to the nervous system may induce metallosis [13]. In addition to hazardous materials, LIBs waste also includes toxic compounds that pose grave hazards to ecosystems and human health [14]. Considering its application in electric cars, this battery's vast size necessitates special waste disposal procedures.

According to Tang et al., [15], the global production of LIBs reached 2.05 billion in 2005 and 5.86 billion in 2012, and will progressively expand in the years to come. Future increases in the manufacture of electric cars will undoubtedly increase LIBs waste. In light of the aforementioned, it is vital to recycle spent batteries in an attempt to decrease environmental contamination and boost their economic worth. This recycling operation is also a kind of assistance for the decrease of environmentally damaging ore mining as raw material. Hydrometallurgical recycling of spent batteries is one of solution to recover nickel and cobalt metals.

The hydrometallurgical process was selected owing to its cheap cost, simple procedure, low energy needs, environmental friendliness as a result of the reduction of air and waste water emissions, and low toxic gas emissions, in addition to its high metal recovery purity [16, 17]. The Co recovery achieved by recycling LIBs for ranges from 80 to 95% [10, 18], while the Ni recovery is 99% [16, 19].

According to Bankole et al., [20], battery recycling makes it possible to reduce energy consumption and CO₂ emissions, conserve natural resources, avoid mining and import of raw materials, minimize environmental toxicity, generate economic benefits, reduce waste, and address safety concerns. For this reason, recycling of LIBs needs to be done to reduce environmental problems as well as to obtain precious metals nickel and cobalt.

In the near future, electric vehicles will replace conventional vehicles. Electric vehicles powered by lithium-ion batteries are deemed capable of contributing positively to the environment. The usage of lithium-ion batteries is also the replacement of fossil fuels with renewable energy. In the long run. In line with Government Regulation No. 55 of 2019 on the Program for the Acceleration of Battery-Based Electric Vehicles for Road Transportation, Indonesia will also use battery-powered electric vehicles [21]. Lithium batteries are used in electric vehicles owing to their superior performance in terms of energy density, safety, and service life. The present demand for lithium batteries in Indonesia is fairly high, especially for annual power usage [22]. Indonesia anticipates that its domestic lithium-ion battery production for electric vehicles would increase by 2030, sufficient for millions electric automobile and motorbikes [23]. This lithium-ion battery forecast is further bolstered by the development of a lithium plant in Indonesia by a business that will specialize in lithium batteries and manufacture lithium raw materials yearly with a nickel demand and a cobalt requirement [24]. Future lithium battery production forecasts must, of course, account for the resulting trash. In addition to building the lithium-ion battery energy sector, the Indonesian government is also exploring the processing of battery waste. Since 2015, these company has provided transportation, collecting, storage, usage, processing, and disposal services for battery trash, which will be disposed of via a recycling process by several state-owned enterprises (SOEs) [25].

In the report by Jung et al., [26], stated that leaching on Lithium Cobalt Dioxide (LiCoO₂) which is a cathode material using sulfuric acid (H₂SO₄) as a leaching agent. Meanwhile, for used lithium-ion battery cathode leaching using H₂SO₄ as a leaching agent the reaction is very slow, this is because LiCoO₂ have bonds entities between the chemical properties of oxygen and cobalt (O–Co–O) comparable and so strong that breaking these bonds requires more energy [27]. Study by Sun & Qiu, [28] was found that 2 M H₂SO₄ was able to produce a leaching efficiency of 76%, while using 3 M H₂SO₄ at 70 °C achieved an efficiency of 99%. Increasing the acid concentration higher is not recommended because able to increase the consumption of reagents in the total recovery process and it is possible to damage the environment. To increase the efficiency of leaching can use a lower acid. Roshanfar et al., [29] reported that adding H₂O₂

as a reducing agent during the leaching process reduces Co^{3+} to Co^{2+} .

The most important variables for metal recovery from LIBs waste are temperature, acid concentration, and solids-to-liquids ratio [30]. Response Surface Methodology (RSM) can be used to discover optimum LIBs metal recovery conditions. RSM is a statistical technique for designing factorial experiments that lowers the number of trials while assessing the effect of several factors on a desired result [31]. In addition, RSM permits the examination of several factors' effects on one or more response variables.

Tanong et al. investigated the parameters affecting the solubilization of metals from a mixture of waste batteries using the response surface approach [16]. Li et al. used response surface methods to optimize the synergistic leaching of precious metals from used lithium-ion batteries by the sulfuric acid-malonic acid system [32]. Using a hydrothermal technique, Zhan et al. attempted to extract manganese from waste Zn–Mn dry batteries [33]. The optimization of operating parameters for the recovery of Ni and Co from lithium-ion batteries employing a leaching agent in the form of a strong acid using the RSM method has never been conducted, and this work is thought essential for resolving environmental concerns in addition to the recovery of nickel and cobalt as high-value metals.

The purpose of this investigation is to optimize the operating conditions for Ni and Co recovery from LIBs utilizing H_2SO_4 as the leaching medium. By optimizing these operating parameters, it is possible to reduce the amount of energy and leaching medium utilized in the recovery process. RSM was used to investigate and optimize the impacts of temperature, acid concentration, and solid-to-liquid ratio on leaching Ni and Co recovery. Since no previous researchers has ever attempted something like that, we may claim this concept as our academic novelty and originality.

Materials and method

Materials and Sample preparation

The materials used are Lithium-ion Battery Waste which obtained from garbage dump in Semarang area, H_2SO_4 , as leaching media was purchased from Sigma-Aldrich (St. Louis, Missouri, USA), H_2O_2 , HNO_3 , and HCl were acquired from Merck (Kenilworth, New Jersey, USA). Preparation of LIBs waste involves removing the LIBs casing and draining its content (then called 'black mass') which consisted of electrolyte, metal oxide, and carbon, by immersion in 5% NaCl for 24 h. Then, the material is crushed into smaller pieces utilizing crushing and burning at $700\text{ }^\circ\text{C}$ for one hour in a Tunnel Kiln in order to remove polymers and impurities [34]. Afterward, separate the cathode powder by scraping the portion that is

connected to the aluminum sheet or by washing the powder for one hour to separate it from the unneeded material. The de-ionized washing method is used to prevent the accumulation of dust. The sample was then separated using a Shieve Shaker Retsch AS 400 (Haan, Germany) as the last step in preparation in order to get black mass with the size of 80 mesh. The material was then dried in an oven at $100 \pm 5\text{ }^\circ\text{C}$ for three hours. The black mass material is ready for use in the process of characterization, in which each analysis is conducted twice.

Characterization of black mass

The purpose of characterizing black mass was to determine its mineral composition, shape, and predominant constituents. Characterization of Black Mass utilizing XRF, XRD, and SEM equipment. The preparation for XRD and XRF testing should be in liquid form. The necessary preparation is dissolving the black mass with aqua regia which consists of concentrated HCl and concentrated HNO_3 with volume ratio of 3:1. XRF Rigaku Nex-CG (Tokyo, Japan) was used to measure black mass composition, while XRD Rigaku MiniFlex (Tokyo, Japan) was used to measure crystal elements from black mass, and SEM Phenom Pro X (Massachusetts, USA) was used to analyze the black mass morphology.

Leaching process

The leaching process is a step taken to extract solid–liquid cobalt and nickel metals that are present in solid shape in the shape of a cathode using an acid solution. Leaching has been done by immersing black mass into H_2SO_4 and 5% H_2O_2 at a speed of 300 rpm for 90 min (Fig. 1). After completing the leaching process, the mixture was filtered to separate the filtrate (liquid phase) and residue/sediment. The calculation of the recovery value is shown in the following formula [13, 35, 36]

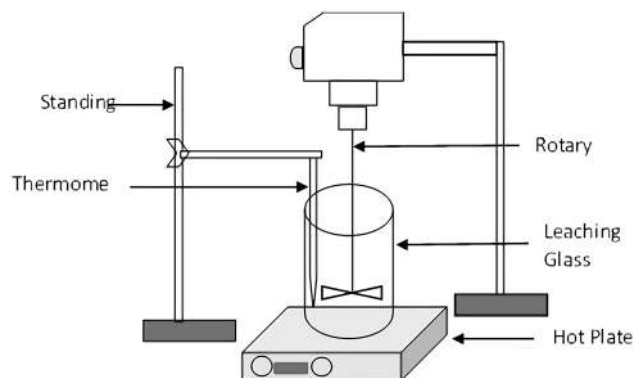
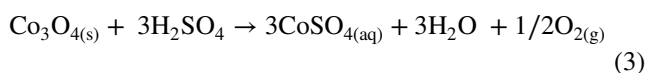
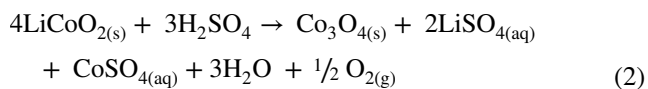


Fig. 1 Schematic diagram of experimental setup used for leaching tests

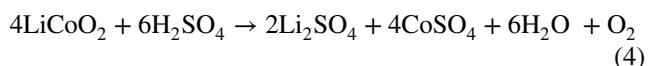


$$\% \text{Recovery} = \frac{\text{Total metal content leached in acid}}{\text{Total metal content dissolved in aqua regia}} \times 100\% \quad (1)$$

The leaching LiCoO_2 with H_2SO_4 involves reduction Co^{3+} in the solid phase to Co^{2+} in the liquid phase [23]. CoO_2 first time forming Co_3O_4 solids when excess H_2SO_4 will be changed to CoSO_4 which dissolves as shown in the reaction below [37]:



Total:



Optimization of Leaching by RSM and statistical analysis

Response surface method or responsive surface method is a collection of statistical and mathematical methods. Used to model the response that is influenced by more than one factor (independent variable), the goal is to optimize the desired response. The responsive surface method is the interaction between factors. The main principle of this method is to determine the influence between independent variables on the response or yield so that a model of the relationship between the independent variables and the response is obtained and the optimum conditions are obtained to obtain the best response. If there is a linear relationship between the independent variable and the response, then the order model can be used with Eq. (5) below [38]:

$$Y = \beta_0 + \sum_{i=1}^k \beta_i X_i + \sum_{i=1}^k \beta_{ii} X_i^2 + \sum_{i=1}^k \sum_{i<j}^k \beta_{ij} X_i X_j + \varepsilon \quad (5)$$

where Y is the response, X_i and X_j are independent variables, β_0 is the intercept and β_i is the linear coefficient and ε is the error. The next step is to take the response surface function, then look for a combination of factors that produce a response to find the partial derivative of each factor [39]. The response design was carried out using Design Expert 11 software with Box–Behnken. Some of the variables used in this study are fixed variables and independent variables. The fixed variable is the black mass particle size of 80 mesh;

time for 4 h and a speed of 300 rpm. As for the independent variables can be seen Table 1 below.

This independent variable was chosen based on the consideration that the optimum temperature in the previous research test was 60 °C. Therefore, the midpoint is at a temperature of 60 °C by designing the optimum temperature in the lower and upper limit ranges of 40–80 °C. For the same reason, the author also determines the lower and upper limits for solid liquids in the range of 2–10% in order to get a mean value of 5%, and the concentration of H_2SO_4 in the range of 0.5–2.5 M so that the median value is 1.5 M. While for the optimized response variable, namely recovery Ni (Y_1) and recovery Co (Y_2). Then, RSM will provide condition data that must be run in the laboratory to see the suitability of the model. There are 15 running that must be done based on Table 2 below.

Result and discussion

Discharging lithium-ion battery

In order to prepare for the lithium-ion battery waste recovery procedure, the remaining power or battery charge must be drained. The remaining battery power poses a possible threat to human safety since a short circuit between the batteries might produce a fire or explosion. By immersing the battery in a solution of pure salt (NaCl), which is readily accessible and very inexpensive, the battery may be discharged or its residual power eliminated. Twenty-four hours were spent immersed in a 5% NaCl solution. Below (Fig. 2) is the result of a 24-h immersion in 5% NaCl.

According to the results, 5% NaCl is able to drop the voltage of the lithium-ion battery by 98%, from 3.4533 to 0.0664 V. During the process of immersing a lithium battery in a salt solution, gas bubbles will emerge slowly from the battery, but the longer the immersion duration, the higher the number of gas bubbles that will emerge from the exposed portion of the battery. The release of gas bubbles from the battery indicates the discharge process, which is an electrolytic reaction of NaCl salt solution. The discharge of the battery is shown in the response that follows [40] and the complete reaction can be shown in Eq. (6)–(12) below:

Table 1 Independent variables

Variable	Unit	Level		
		Low (− 1)	Medium (0)	High (+ 1)
Solid liquid	%	2	6	10
H_2SO_4 Concentration	M	0.5	1.5	2.5
Temperature	°C	40	60	80



Table 2 Research results based on recovery Ni and Co (Experimental vs. Predicted)

Run	X1: solid–liquid ratio (%)	X2: H ₂ SO ₄ (M)	X3: temp (C)	Ni recovery			Co recovery		
				Experiment	Predicted	Error	Experiment	Predicted	Error
1	10	0.5	60	75.7	80.8	– 5.06	70.3	75.0	– 4.68
2	6	2.5	40	99.9	101.5	– 1.63	93.9	94.3	– 0.40
3	2	0.5	60	99.9	99.2	0.69	99.9	101.4	– 1.47
4	6	2.5	80	94.9	97.7	– 2.75	97.1	96.6	0.55
5	6	0.5	80	99.9	98.3	1.62	89.9	87.5	2.40
6	6	1.5	60	96.8	97.5	– 0.73	93.5	91.8	1.70
7	10	1.5	80	99.9	96.5	3.44	82.4	82.7	– 0.32
8	2	1.5	80	99.9	102.2	– 2.31	97.8	101.3	– 3.52
9	6	1.5	60	99.9	97.5	2.37	99.4	91.8	7.60
10	10	2.5	60	94.9	95.6	– 0.69	93.9	96.7	– 2.82
11	2	2.5	60	97.7	92.6	5.06	94.5	94.1	0.38
12	6	1.5	60	95.9	97.5	– 1.63	92.9	91.8	1.10
13	6	0.5	40	95.4	92.7	2.75	90.3	88.9	1.45
14	2	1.5	40	99.9	103.3	– 3.44	91.6	94.2	– 2.58
15	10	1.5	40	95.9	93.6	2.31	89.6	89.0	0.63

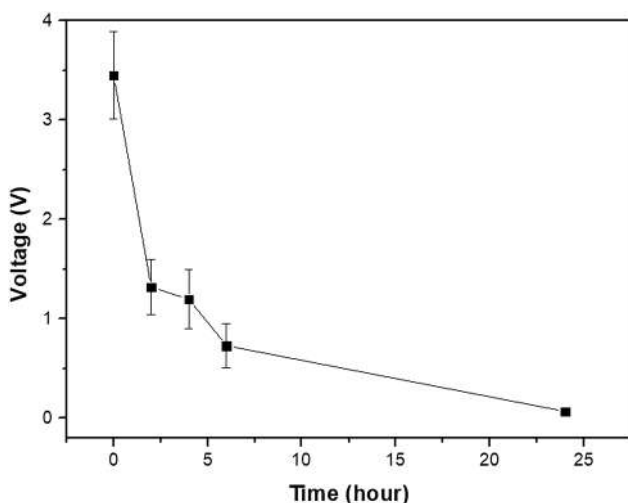
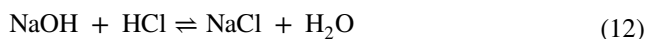
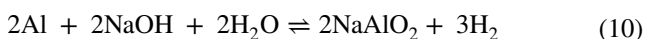


Fig. 2 Battery voltage analysis during discharging process



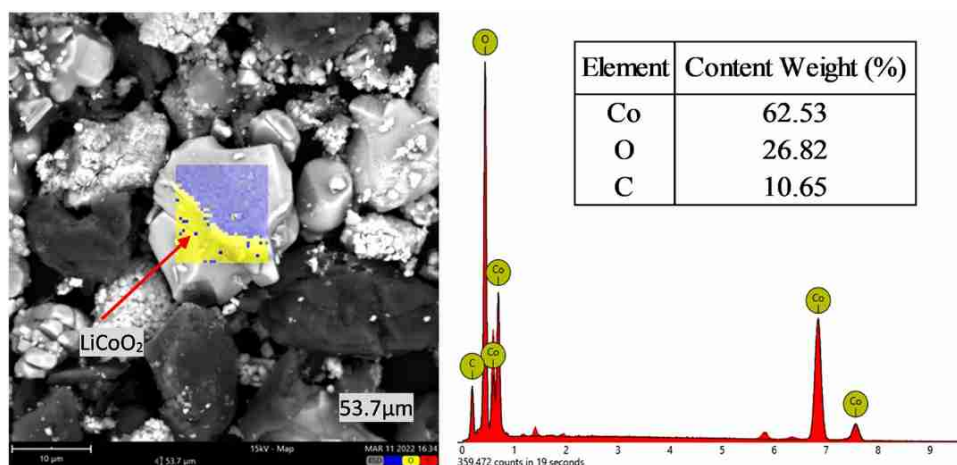
In Eq. (6), electrolysis of NaCl salt is followed by the formation of sodium hydroxide in Eq. (7); moreover, electrolysis of water (Eq. (8)) is followed by the synthesis of Al(OH)₃ in Eq. (11). When utilizing a conductor such as Cu for short-circuit current between the positive and negative electrodes, the method of draining the battery differs from electrolysis of a NaCl salt solution. Based on this reaction, bubbles of gases such as Cl₂, H₂, and O₂ are produced. The white foam produced by soaking is aluminum hydroxide, which is created throughout the process.

Characterization of black mass

SEM analysis

Tests using SEM–EDS were carried out to analyze or characterize the chemical elements present in the sample by using X-ray excitation. SEM–EDS analysis produced a peak of the electromagnetic emission spectrum of the atomic structure of each typical element. Tests using SEM–EDS were carried out three times at different extraction locations to ensure that the metal content in the black mass powder was evenly distributed in other parts. SEM was carried out to obtain the initial morphology of the black mass before and after leaching [41]. Figure 3 (left) shows the black mass with 5000× magnification. It can be observed that the black mass is made up of metals, metal oxides, and carbon, with carbon being dark in color and metal or metal oxides being lighter in color due to light reflection. LiCoO₂ is thought

Fig. 3 SEM images of black mass and its EDS spectra with element mapping. Arrow shows the distribution of elements in LiCoO_2



to be the light-colored particles. The size of these particles ranges from 6 to 18 μm , with an average of $10.7 \pm 4.4 \mu\text{m}$. The boundary between Co and O, or cobalt oxide, may also be seen via element mapping on the surface of LiCoO_2 particles. Meanwhile, according to the EDS findings in Fig. 3 (right), the proportions of Co, O, and C were 62.53%, 26.82%, and 10.65%, respectively, with Co dominating the element composition. This is not too much different from the research conducted by Nshizirungu et al., [13] is Co of 62.86, O is 31.60 and C is 5.54%. SEM/EDS analysis confirmed residual carbon along with LiCoO_2 cathode material as a result of organic combustion. The carbon source can be acetylene black which is used for cathode conductivity in electronics [42].

XRD analysis

X-ray diffraction (XRD) is also used to determine the phase purity and crystallinity of the black mass sample (Fig. 4). The black mass is characterized as LiCoO_2 , $\text{Li}_{0.06}\text{Mg}_{0.03}\text{Mn}_{0.44}\text{Ni}_{0.03}\text{O}$, and graphite, which is supported by research conducted by Nshizirungu et al., [13] and Esmaeili et al., [43] wherein LiCoO_2 is produced in the black mass. The existence of LiCoO_2 in the black mass shows that valuable metals may still be recovered, in addition to the fact that graphite is a by-product of heating at 700 $^\circ\text{C}$ for one hour. Because carbon is inert throughout the leaching process, graphite will rise after the leaching process, and vice versa, LiCoO_2 will decrease after the leaching process [44].

During the drying process, HCoO_2 may decompose, resulting in the presence of CoO in the peeled powder. Due to the release of HF at high temperatures, it is possible to identify Co_3O_4 as the PVDF binder in cathode materials, which results from the transition of LiCoO_2 [45–47]. When compared to Co_3O_4 , leaching CoO in acid solution requires no additional reductant. The average grain size of black matter was 25.12 nm, higher than the average size in

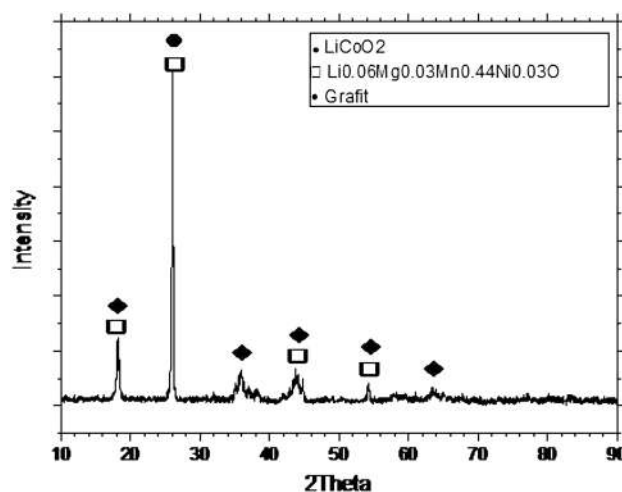


Fig. 4 Characterization of Cathode Black Mass

the SEM image. During XRD analysis, agglomeration of certain particles may have happened.

XRF analysis

The XRF analysis results are shown in Table 3 below. Based on the test, the XRF equipment analyzes the metals Mg, Al, Ca, Cr, Mn, Fe, Co, Ni, Cu, and Zn. It is known that the concentrations of Ni in solution are 21.7% and Co in solution is 30.4%, which are the concentrations of Ni and Co before to leaching and will serve as a reference for the recovery of Ni and Co after leaching. Each acquired result will be compared in order to determine the optimal circumstances for each step. This comparison is based on the nickel and cobalt metal content recovery percentages.

Optimization of leaching using response surface methodology (RSM)

To ensure that the projected model accurately estimates the experimental data, it must be tested against a set of experimental data. The coefficient of determination (R^2) must be strong in an experimental model. According to the ANOVA in Table 4, the R^2 value for nickel recovery is 0.778, while R^2 for Co recovery is 0.842.

At every phase in the design, Predicted Residual Sum of Square (PRESS) is used to anticipate the model. It has a good model since the press values for Ni recovery and Co recovery are 1730.82 and 390.7, respectively. To get a decent result, the p -value may also be shown. The P value

is used to demonstrate that the created model's prediction parameters are statistically significant. A valid p -value is less than 0.05. In Table 4 for Ni recovery, the model has a p value more than 0.05, but in Table 5 for Co recovery, those with model yields greater than 0.05 are β_3 C, β_{13} AC and β_{23} BC. The P value is used to prove that the prediction parameters of the developed model are significant. A lack of fit test was also run to determine the disparity between the second order models. The p -value is the parameter that influences the lack of fit. A good model is one in which there is no lack of fit (does not accept H_0).

Based on the Ni recovery hypothesis presented in Table 4, a decent model does not accept H_0 or p -values less than 5%. In the meanwhile, based on Table 5, the p -value for recovery

Table 3 Results of black mass composition using XRF

	Element (%)									
	Mg	Al	Ca	Cr	Mn	Fe	Co	Ni	Cu	Zn
Black mass	1.244	0.987	0.084	0.040	26.0	4.4	30.4	21.7	15.0	0.372

Table 4 Estimated regression coefficients for the quadratic polynomial model of Ni recovery

Parameter	Predicted coefficient	Standard error	DF	p value
β_0 Intercept	97.53	2.78	1	0.2391
β_1 A–Solid–Liquid Ratio	– 3.88	1.7	1	0.0717
β_2 B–[H ₂ SO ₄]	2.06	1.7	1	0.2795
β_3 C–Temperature	0.4375	1.7	1	0.8073
β_{12} AB	5.35	2.41	1	0.0767
β_{13} AC	1	2.41	1	0.6949
β_{23} BC	– 2.37	2.41	1	0.3689
β_{11} A ²	– 2.05	2.5	1	0.4493
β_{22} B ²	– 3.43	2.5	1	0.2291
β_{33} C ²	3.42	2.5	1	0.2301
Lack of fit			3	0.1119 ($p > 0.05$)
Pure error				
R^2	0.7782		Adj R^2	0.3792
Press	1730.82		RMSE	23.15

Table 5 Estimated regression coefficients for the quadratic polynomial model of Co recovery

Parameter	Predicted coefficient	Standard error	DF	p Value
β_0 Intercept	91.8	1.01	1	0.0072
β_1 A–Solid–Liquid Ratio	– 5.95	1.38	1	0.0026
β_2 B–[H ₂ SO ₄]	3.62	1.38	1	0.0303
β_3 C–Temperature	0.225	1.38	1	0.8745
β_{12} AB	7.25	1.95	1	0.0059
β_{13} AC	– 3.35	1.95	1	0.1244
β_{23} BC	0.9	1.95	1	0.657
Lack of fit			6	0.5102 ($p > 0.05$)
Pure error			2	
R^2	0.8415		Adj R^2	0.7226
Press	390.7		RMSE	15.24

Co is larger than 0.05, hence H_0 is approved or there is no lack of fit. Based on results of the conducted experiments, Tables 4 and 5 serve as a response surface model for solid liquid, acid concentration, and temperature. The resultant model is a re-arrangeable mathematical equation: Yield Recovery Ni or Co equals Y , Solid–Liquid equals X_1 , acid concentration equals X_2 , and temperature equals X_3 , so:

$$\begin{aligned} \text{Ni Recovery} = & 97.5333 - 3.875 X_1 + 2.0625 X_2 \\ & + 0.4375 X_3 + 5.35 X_1 X_2 + 1 X_1 X_3 \\ & - 2.375 X_2 X_3 - 2.05417 X_1^2 - 3.42917 X_2^2 \\ & + 3.42083 X_3^2 \end{aligned} \quad (12)$$

$$\begin{aligned} \text{Co Recovery} = & 91.8 - 5.95 X_1 + 3.625 X_2 + 0.225 X_3 \\ & + 7.25 X_1 X_2 - 3.35 X_1 X_3 + 0.9 X_2 X_3 \end{aligned} \quad (13)$$

The generated model will be deemed precise enough to accurately forecast the real process conditions. In addition to the three statistical tests listed above, it is necessary to conduct a test based on the magnitude of the divergence between the actual value of the experiment and the value predicted by the model.

Interaction between variables

Interaction between concentration of H_2SO_4 and solid–liquid ratio

It is evident from Fig. 5a and b that the concentration of sulfuric acid and the solid-to-liquid ratio are related. The red color of the contour implies that the more the recovery, the greater the red color. In fact, the ratio of solid liquid to changeable acid content has a good effect on the recovery of Ni and Co

in the contour region of 2–4%. According to studies by Jha et al. [48], the proportion of Li and Co leaching reduced as pulp density increased. At low pulp density, the surface area per unit volume of solution is greater, resulting in a higher leaching percentage, while raising the density decreases the available surface area per unit volume of solution, resulting in a lower leaching percentage. The rate of reaction in diffusion-controlled leaching processes is proportional to the differential between the lixiviant concentration at the mineral reaction surface and the concentration in the bulk solution [49]. Increasing acid concentration raises the concentration gradient, which accelerates the diffusion of the dissolved acid reactant to the reaction surface, hence accelerating leaching. With an increase in temperature, the rate-limiting step shifted from chemical reaction limited to diffusion restricted.

Interaction between temperature and solid–liquid ratio

Figure 6a and b depicts the relationship between temperature and solid–liquid ratio during the recovery of nickel and cobalt. A rise in temperature will accelerate the pace of the reaction [19]. But an increase in the percent solid–liquid ratio has the opposite effect. At a percentage solid–liquid ratio of 6–8%, the value of recovery declined, particularly for Co. For Co and Ni, trends in the influence of temperature on leaching were identified. The greatest temperature increases the amount and velocity of leaching. At higher temperatures, responding species contain more energy, leading to a rise in the proportion of species with adequate energy to react, which, according to the Arrhenius equation, raises the rate of reaction [50–53]. Kinetics of leaching as a function of Solid–liquid ratios. Sulfuric acid solution interacted with the powdered $LiCoO_2$ sample in a liquid–solid non-catalytic reaction.

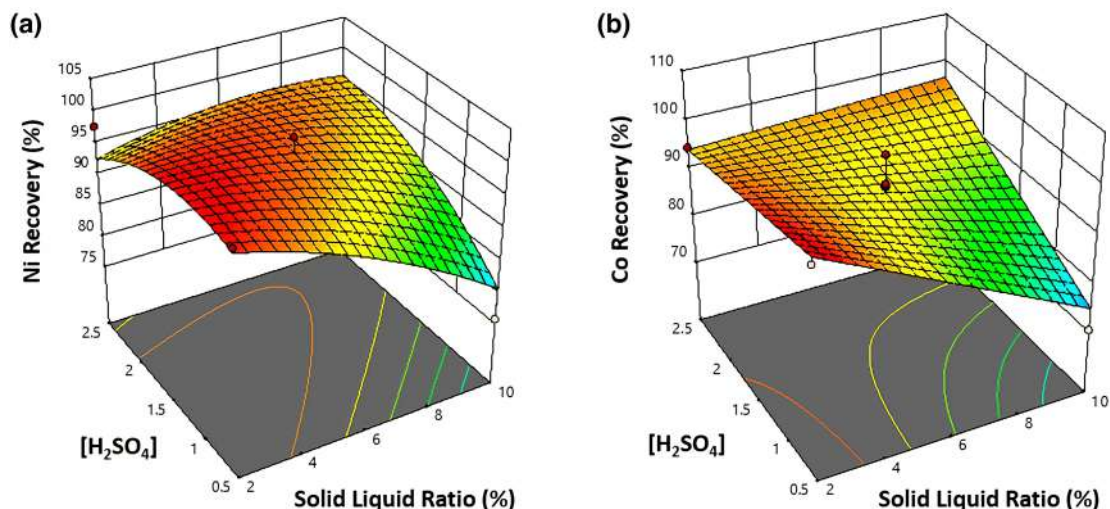


Fig. 5 Interaction 3D Surface of H_2SO_4 and Solid–Liquid Ratio on Recovery of a Ni and b Co

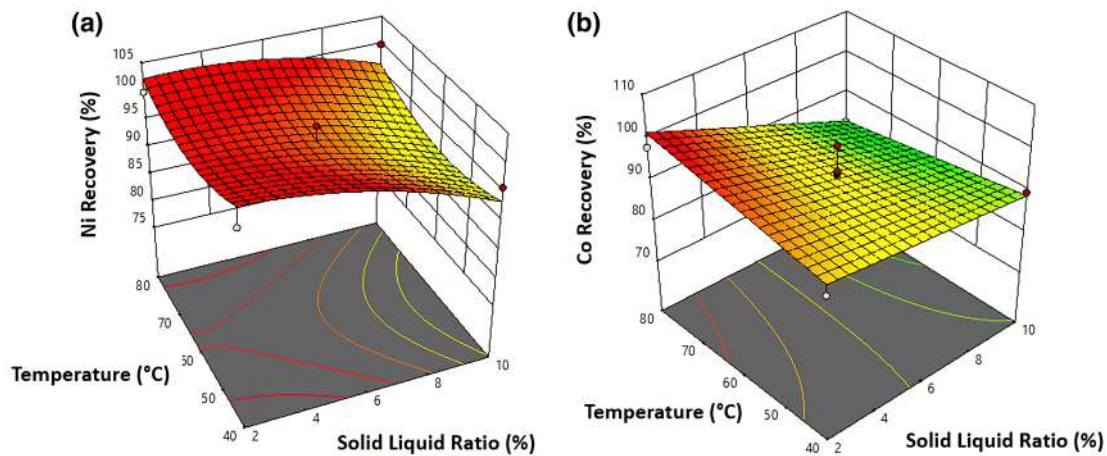


Fig. 6 Interaction 3D Surface of Temperature and Solid–Liquid Ratio on Recovery of **a** Ni and **b** Co

It is possible to determine the kind of response using a shrinking-core model. The shrinking-core model is based on the premise that the reaction will start at the particle's outer surface [54]. Precipitated product gets into fluid during intense rotation, resulting in a decreasing core of unreacted solid during intermediate conversions. The next section will establish which step has the most impact on LiCoO_2 leaching.

Interaction between temperature and H_2SO_4

Figure 7a and b demonstrates that high temperature and H_2SO_4 result in greater Ni and Co recovery. According to research Takacova et al., [44], a leaching temperature of 80 °C enables the complete recovery of Co. A further rise in temperature to a level near to the boiling point will

accelerate the process. According to the Arrhenius equation, the rate of leaching will rise exponentially for chemical reaction-controlled systems. There are no complete data on the influence of temperature on the solubility of these metal organic acid complexes, although leaching evidence shows that the solubility of the metal sulfate complexes rises with temperature. After the equilibrium of leaching has been attained, the metal recovery in solution decreases in all temperature. As the pH of the leaching solution rose over time, metals precipitated as hydroxides. Li et al. [55] also observed a decline in metal concentrations, which they ascribed to hydroxide precipitation. The second potential cause is the adsorption of metal ions onto the carbon electrode, which decreases the metal concentration in solution over time. The concentration of sulfuric acid has little influence on the rate of metal leaching. There was sufficient

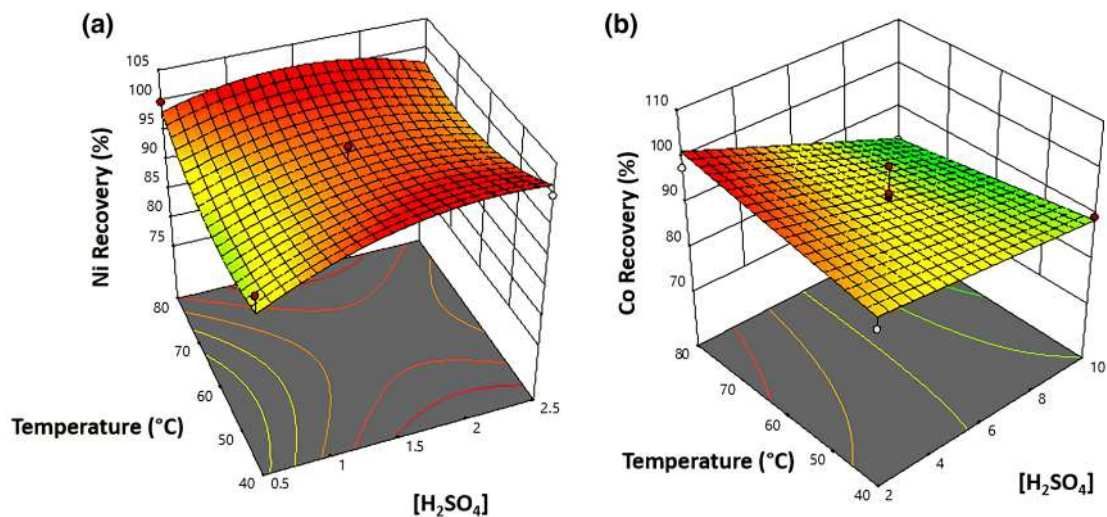


Fig. 7 Interaction 3D Surface of Temperature and H_2SO_4 on Recovery of **a** Ni and **b** Co



surplus acid in solution to describe the leaching reaction rate as a pseudo-zero-order function of acid concentration.

Optimization of model

Following a series of analytical procedures, the software design expert will offer Table 6 with optimization ideas based on the supplied design. Table 6 provides recommendations for the recovery of Ni and Co when leaching used lithium batteries: 2.0% (S/L); 1.5 M H₂SO₄ at a temperature of 80 °C will generate the highest result for Ni and Co recovery. Verification of the model done research again in the laboratory to look at the suitability of the experimental results with the model obtained. Experimental verification was carried out on 2% solid–liquid ratio; 1.5 M Acid concentration and at 80 °C resulted in Ni and Co recovery of 99.9 and 97.8%, while the predicted values for optimization of Ni recovery and Co recovery were 101.761% and 101.087%, or in other words Ni and Co are fully recovered. From these results, the tolerance value for predictions and experiments can be calculated, for Ni recovery of 1.83% and Co recovery of 3.25%.

Challenge and future prospect

Increasing electric vehicle potential will undoubtedly increase the amount of lithium-ion battery trash that must be controlled. Even though they do not need fossil fuels, which are difficult to replenish, electric vehicles have a service life of around 10 years. After that point, you must replace it with a new one, particularly the old electric battery. Future obstacles will include the handling of battery waste. Due to the presence of dangerous and hazardous substances that might harm the environment, the battery waste management system must be adequate. Still included in battery trash are important metals such as lithium, nickel, cobalt, aluminum, and manganese. Utilizing the recycling process, from which useful components may be extracted and reused, is undoubtedly the best method for managing battery waste. Recycling offers several options, including bioleaching, pyrometallurgical, and hydrometallurgical processes. Utilizing bacteria/microbes capable of oxidizing metals at 37 °C, bioleaching or bio-mining is conducted. In the bioleaching process, there is no carbon footprint and reduced pollutants [56]. In the meanwhile, the pyrometallurgical method of recycling used batteries will

be expensive due to the specialized equipment required to combat the toxic pollutants produced by the smelting process. In this investigation, a hydrometallurgical method using a waste-metal-extracting solution was selected. Hydrometallurgical technology is the use of a solution to extract a mineral or metal. The benefits of the hydrometallurgical process are cheap cost, a simple process, low energy needs, environmental friendliness as a result of the reduction of air and waste water emissions, and low hazardous gas emissions [16]. The use of sulfuric acid in the hydrometallurgical process presents a barrier since sulfuric acid is corrosive and requires specific treatment. However, this sulfuric acid is recyclable and reusable accordance with reference paper [57]. Utilizing a nanofiltration membrane, it is possible to recycle sulfuric acid. This approach is ecologically beneficial for the recovery of diverse acid solutions from industrial acid effluent, since the membrane-based nanofiltration process generates superior selective acid permeation and acid stability. Other study by Wang et al., used diffusion dialysis to recover sulfuric acid from coal acid leaching [58]. With the addition of pure acid, sulfuric acid may be reused in the leaching process, as demonstrated by the excellent separation of sulfuric acid recovery. Opportunities and hopes for the use of battery waste recycling include reducing the impact on the environment; furthermore, in the future, the management of battery waste through the recycling process will become a circular economy and foster the growth of a new economy, as battery waste still contains reusable components [59]. A further advantage of battery waste management is that it is capable of conserving natural resources with minimal mineral content, so that in its implementation it is also capable of conserving energy from the mining process to metal extraction and reducing import reliance on battery raw materials. Recycling used batteries may potentially cut the price of rather costly electric vehicles.

Conclusion

This research examines the recycling or recycling of lithium-ion batteries in order to get the valuable metals nickel and cobalt utilizing hydrometallurgical procedures and tools such as SEM, XRD, and XRF. Using the Response Surface Method based on the Box–Behnken equation, the percentage of solid liquid, acid concentration, and

Table 6 Optimization by RSM

Variables	Optimum condition	Value of response			
		Predicted	Experiment	Error (%)	
Solid–Liquid Ratio (%)	2	Recovery Ni (%)	101.761	99.9	1.83
Acid Concentration (M)	1.5	Recovery Co (%)	101.087	97.8	3.25
Temperature (°C)	80				

temperature that influence nickel and cobalt recovery were observed. Solid liquid is measured between 2 and 10% to get a mean value of 5%; H_2SO_4 concentration is measured between 0.5 and 2.5 M to obtain a mean value of 1.5 M; and temperature is measured between 40 and 80 °C to obtain a mean value of 60 °C. The RSM-based optimization approach generates an optimum condition that illustrates the correlations between the relevant variables. The best conditions for the recovery of Ni and Co were found to be 2.0% (S/L), 1.5 M H_2SO_4 concentration, and temperature of 80 °C, which resulted Ni and Co recovery of 99.9 and 97.8%, respectively, from simulation, as well as 101.761% and 101.087% from verification experiment.

Acknowledgements This research did not receive any specific grant from funding agencies in the public, commercial, or not-for-profit sectors.

Declarations

Conflict of interest All authors declare that they have no conflicts of interest.

References

- Li, M., Lu, J., Chen, Z., Amine, K.: 30 years of lithium-ion batteries. *Adv. Mater.* **30**(33), 1800561 (2018)
- Martins, L.S., Guimarães, L.F., Junior, A.B.B., Tenório, J.A.S., Espinosa, D.C.R.: Electric car battery: an overview on global demand, recycling and future approaches towards sustainability. *J. Environ. Manag.* **295**, 113091 (2021)
- Holmberg, K., Erdemir, A.: The impact of tribology on energy use and CO₂ emission globally and in combustion engine and electric cars. *Tribol. Int.* **135**, 389–396 (2019)
- Aretxabaleta, I., De Alegría, I.M., Andreu, J., Kortabarria, I., Robles, E.: High-voltage stations for electric vehicle fast-charging: trends, standards, charging modes and comparison of unity power-factor rectifiers. *IEEE Access* **9**, 102177–102194 (2021)
- Li, J., Manthiram, A.: A comprehensive analysis of the interphasial and structural evolution over long-term cycling of ultrahigh-nickel cathodes in lithium-ion batteries. *Adv. Energ. Mater.* **9**(45), 1902731 (2019)
- Lim, B., Kim, H.S., Park, J.: Implicit interpretation of Indonesian export bans on LME nickel prices: evidence from the announcement effect. *Risks* **9**(5), 93 (2021)
- Adu-Gyamfi, M.N., Raj, A., Golding, P., Perez, L., Golding, D., Contreras, L.R., Narayan, M.: Moving towards renewable energy to mitigate carbon emissions from fossil fuel. *Am. J. Environ. Sci. Eng.* **6**(2), 91–100 (2022)
- Goodenough, J.B., Kim, Y.: Challenges for rechargeable Li batteries. *Chem. Mater.* **22**, 587–603 (2010)
- Sambamurthy, S., Raghuvanshi, S., Sangwan, K.S.: Environmental impact of recycling spent lithium-ion batteries. *Procedia CIRP* **98**, 631–636 (2021)
- Myung, S., Hyung, N., Soo, J.: Development of a metal recovery process from Li-ion battery wastes. *Hydrometallurgy* **79**, 172–181 (2005)
- Ordoñez, J., Gago, E.J., Girard, A.: Processes and technologies for the recycling and recovery of spent lithium-ion batteries. *Renew. Sust. Energ. Rev.* **60**, 195–205 (2016)
- Sommerville, R., Shaw-Stewart, J., Goodship, V., Rowson, N., Kendrick, E.: A review of physical processes used in the safe recycling of lithium ion batteries. *Sustain. Mater. Technol.* **25**, e00197 (2020)
- Nshizirungu, T., Rana, M., Jo, Y., Park, J.: Rapid leaching and recovery of valuable metals from spent Lithium Ion batteries (LIBs) via environmentally benign subcritical nickel-containing water over chlorinated polyvinyl chloride. *J. Hazard. Mater.* **396**, 122667 (2020)
- Kang, D.H.P., Chen, M., Ogunseitun, O.A.: Potential environmental and human health impacts of rechargeable lithium batteries in electronic waste. *Environ. Sci. Technol.* **47**(10), 5495–5503 (2013)
- Tang, X., Tang, W., Duan, J., Yang, W., Wang, R., Tang, M., Li, J.: Recovery of valuable metals and modification of cathode materials from spent lithium-ion batteries. *J. Alloys Compd.* **874**, 159853 (2021)
- Tanong, K., Coudert, L., Mercier, G., Blais, J.F.: Recovery of metals from a mixture of various spent batteries by a hydrometallurgical process. *J. Environ. Manag.* **181**, 95–107 (2016)
- Li, L., Ge, J., Chen, R., Wu, F., Chen, S., Zhang, X.: Environmental friendly leaching reagent for cobalt and lithium recovery from spent lithium-ion batteries. *Waste Manage.* **30**(12), 2615–2621 (2010)
- Chen, L., Tang, X., Zhang, Y., Li, L., Zeng, Z., Zhang, Y.: Process for the recovery of cobalt oxalate from spent lithium-ion batteries. *Hydrometallurgy* **108**(1–2), 80–86 (2011)
- Meshram, P., Pandey, B.D., Mankhand, T.R.: Recovery of valuable metals from cathodic active material of spent lithium ion batteries: Leaching and kinetic aspects. *Waste Manage.* **45**, 306–313 (2015)
- Bankole, O.E., Gong, C., Lei, L.: Battery recycling technologies: recycling waste lithium ion batteries with the impact on the environment in-view. *J. Environ. Ecol.* **4**(1), 14 (2013)
- Government Regulation No 55 Year 2019 about Acceleration of the Battery Electric Vehicle Program for Road Transportation.: (2019) <https://peraturan.bpk.go.id/Home/Details/116973/perpres-no-55-tahun-2019#:~:text=PERPRES%20No.%2055%20Tahun%202019,Transportasi%20Jalan%20%5BJDIH%20BPK%20R1%5D>
- Sutopo, W., Zakaria, R., Wardayanti, A., Fahma, F.: Mapping of inbound flows in supply chain of lithium-ion industry in Indonesia. *Int. J. Sustain. Transp. Technol.* **1**(1), 15–20 (2018)
- Prianjani, D., Sutopo, W., Hisjam, M., Pujiyanto, E.: Sustainable supply chain planning for swap battery system: case study electric motorcycle applications in Indonesia. *IOP Conf. Ser. Mater. Sci. Eng.* **495**(1), 01208 (2019)
- Pandyaswargo, A.H., Wibowo, A.D., Maghfiroh, M.F.N., Rezqita, A., Onoda, H.: The emerging electric vehicle and battery industry in Indonesia: actions around the nickel ore export ban and a SWOT analysis. *Batteries* **7**(4), 80 (2021)
- Zakiyya, H., Distya, Y.D., Ellen, R.: A review of spent lead-acid battery recycling technology in Indonesia: comparison and recommendation of environment-friendly process. *IOP Conf. Ser. Mater. Sci. Eng.* **288**(1), 012074 (2018)
- Jung, J.C., Sui, P., Zhang, J.: A review of recycling spent lithium-ion battery cathode materials using hydrometallurgical treatments. *J. Energy Storage* **35**, 102217 (2021)
- Vu, C., Han, K.N., Lawson, F.: Leaching behaviour of cobaltous and cobalto-cobaltic oxides in ammonia and in acid solutions. *Hydrometallurgy* **6**(1–2), 75–87 (1980)



28. Sun, L., Qiu, K.: Vacuum pyrolysis and hydrometallurgical process for the recovery of valuable metals from spent lithium-ion batteries. *J. Hazard. Mater.* **194**, 378–384 (2011)
29. Roshanfar, M., Golmohammadzadeh, R., Rashchi, F.: An environmentally friendly method for recovery of lithium and cobalt from spent lithium-ion batteries using gluconic and lactic acids. *J. Environ. Chem. Eng.* **7**(1), 102794 (2019)
30. He, L.P., Sun, S.Y., Song, X.F., Yu, J.G.: Leaching process for recovering valuable metals from the LiNi_{1/3}Co_{1/3}Mn_{1/3}O₂ cathode of lithium-ion batteries. *Waste Manage.* **64**, 171–181 (2017)
31. Hadiyanto, H., Widayat, W., Pratiwi, M.E., Christwardana, M., Muylaert, K.: Effect of pH, cationic inducer, and clam shells as bio-flocculant in the optimization of the flocculation process for enhanced microalgae harvesting using response surface methodology. *Environ. Pollut. Bioavailab.* **34**(1), 338–351 (2022)
32. Li, P., Luo, S.H., Su, F., Zhang, L., Yan, S., Lei, X., Hou, P.: Optimization of synergistic leaching of valuable metals from spent lithium-ion batteries by the sulfuric acid-malonic acid system using response surface methodology. *ACS Appl. Mater. Interfaces* **14**(9), 11359–11374 (2022)
33. Zhan, L., Ren, X., Xu, Z.: Hydrothermal leaching behavior of manganese from waste Zn–Mn dry batteries. *ACS Sustain. Chem. Eng.* **9**(8), 3137–3144 (2021)
34. Jiang, X.T., Wang, P., Li, L.H., Yu, J., Yin, Y.X., Hou, F.: Recycling process for spent cathode materials of LiFePO₄ batteries. *Mater. Sci. Forum* **943**, 141–148 (2019)
35. Lie, J., Lin, Y.C., Liu, J.C.: Process intensification for valuable metals leaching from spent NiMH batteries. *Chem. Eng. Process.* **167**, 108507 (2021)
36. Fu, Y., He, Y., Yang, Y., Qu, L., Li, J., Zhou, R.: Microwave reduction enhanced leaching of valuable metals from spent lithium-ion batteries. *J. Alloys Compd.* **832**, 154920 (2020)
37. Ferreira, D.A., Prados, L.M.Z., Majuste, D., Mansur, M.B.: Hydrometallurgical separation of aluminium, cobalt, copper and lithium from spent Li-ion batteries. *J. Power Sources* **187**(1), 238–246 (2009)
38. Myers, R.H., Khuri, A.I., Carter, W.H.: Response surface methodology: 1966–1988. *Technometrics* **31**(2), 137–157 (1989)
39. Hadiyanto, H., Christwardana, M., Widayat, W., Jati, A.K., Laes, S.I.: Optimization of flocculation efficiency and settling time using chitosan and eggshell as bio-flocculant in *Chlorella pyrenoidosa* harvesting process. *Environ. Technol. Innov.* **24**, 101959 (2021)
40. Lu, M., Zhang, H., Wang, B., Zheng, X., Dai, C.: The re-synthesis of LiCoO₂ from spent lithium ion batteries separated by vacuum-assisted heat-treating method. *Int. J. Electrochem. Sci.* **8**(6), 8201–8209 (2013)
41. Chen, X., Cao, L., Kang, D., Li, J., Zhou, T., Ma, H.: Recovery of valuable metals from mixed types of spent lithium ion batteries. Part II: selective extraction of lithium. *Waste Manage.* **80**, 198–210 (2018)
42. Nayaka, G.P., Pai, K.V., Santhosh, G., Manjanna, J.: Recovery of cobalt as cobalt oxalate from spent lithium ion batteries by using glycine as leaching agent. *Biochem. Pharmacol.* **4**(2), 2378–2383 (2016)
43. Esmaeili, M., Rastegar, S.O., Beigzadeh, R., Gu, T.: Ultrasound-assisted leaching of spent lithium ion batteries by natural organic acids and H₂O₂. *Chemosphere* **254**, 126670 (2020)
44. Takacova, Z., Havlik, T., Kukurugya, F., Orac, D.: Cobalt and lithium recovery from active mass of spent Li-ion batteries: theoretical and experimental approach. *Hydrometallurgy* **163**, 9–17 (2016)
45. Freitas, M.B.J.G., Garcia, E.M.: Electrochemical recycling of cobalt from cathodes of spent lithium-ion batteries. *J. Power Sources* **171**(2), 953–959 (2007)
46. Fouad, O.A., Farghaly, F.I., Bahgat, M.: A novel approach for synthesis of nanocrystalline γ -LiAlO₂ from spent lithium-ion batteries. *J. Anal. Appl. Pyrolysis* **78**(1), 65–69 (2007)
47. Liu, Y.J., Hu, Q.Y., Li, X.H., Wang, Z.X., Guo, H.J.: Recycle and synthesis of LiCoO₂ from incisors bound of Li-ion batteries. *Trans. Nonferrous Met. Soc. China* **16**(4), 956–959 (2006)
48. Jha, M.K., Kumari, A., Jha, A.K., Kumar, V., Hait, J., Pandey, B.D.: Recovery of lithium and cobalt from waste lithium ion batteries of mobile phone. *Waste Manage.* **33**(9), 1890–1897 (2013)
49. Musariri, B., Akdogan, G., Dorfling, C., Bradshaw, S.: Evaluating organic acids as alternative leaching reagents for metal recovery from lithium ion batteries. *Miner. Eng.* **137**, 108–117 (2019)
50. Gaines, L.: The future of automotive lithium-ion battery recycling: charting a sustainable course. *Sustain. Mater. Technol.* **1**, 2–7 (2014)
51. He, L.P., Sun, S.Y., Mu, Y.Y., Song, X.F., Yu, J.G.: Recovery of lithium, nickel, cobalt, and manganese from spent lithium-ion batteries using L-tartaric acid as a leachant. *ACS Sustain. Chem. Eng.* **5**(1), 714–721 (2017)
52. Lee, C.K., Rhee, K.I.: Preparation of LiCoO₂ from spent lithium-ion batteries. *J. Power Sources* **109**(1), 17–21 (2002)
53. Li, L., Zhai, L., Zhang, X., Lu, J., Chen, R., Wu, F., Amine, K.: Recovery of valuable metals from spent lithium-ion batteries by ultrasonic-assisted leaching process. *J. Power Sources* **262**, 380–385 (2014)
54. Ferrier, R.J., Cai, L., Lin, Q., Gorman, G.J., Neethling, S.J.: Models for apparent reaction kinetics in heap leaching: a new semi-empirical approach and its comparison to shrinking core and other particle-scale models. *Hydrometallurgy* **166**, 22–33 (2016)
55. Li, L., Fan, E., Guan, Y., Zhang, X., Xue, Q., Wei, L., Chen, R.: Sustainable recovery of cathode materials from spent lithium-ion batteries using lactic acid leaching system. *ACS Sustain. Chem. Eng.* **5**(6), 5224–5233 (2017)
56. Baniasadi, M., Graves, J.E., Ray, D.A., De Silva, A.L., Renshaw, D., Farnaud, S.: Closed-loop recycling of copper from waste printed circuit boards using bioleaching and electrowinning processes. *Waste Biomass Valorization* **12**(6), 3125–3136 (2021)
57. Yun, T., Woo, J., Kwak, S.: Recovery of sulfuric acid aqueous solution from copper-refining sulfuric acid wastewater using nanofiltration membrane process. *J. Environ. Manage.* **223**(May), 652–657 (2018)
58. Wang, K., Zhang, Y., Huang, J., Liu, T., Wang, J.: Hydrometallurgy Recovery of sulfuric acid from a stone coal acid leaching solution by diffusion dialysis. *Hydrometallurgy* **173**(March), 9–14 (2017)
59. Rarotra, S., Sahu, S., Kumar, P., Kim, K.H., Tsang, Y.F., Kumar, V., Lisak, G.: Progress and challenges on battery waste management: a critical review. *ChemistrySelect* **5**(20), 6182–6193 (2020)

Publisher's Note Springer Nature remains neutral with regard to jurisdictional claims in published maps and institutional affiliations.

Springer Nature or its licensor holds exclusive rights to this article under a publishing agreement with the author(s) or other rightsholder(s); author self-archiving of the accepted manuscript version of this article is solely governed by the terms of such publishing agreement and applicable law.



Parameters identification for photovoltaic system via improved electromagnetism-like approach and quadrature technique

Ola Ragb¹ · Hanan Bakr¹ · O. Civalek²

Received: 22 April 2022 / Accepted: 21 August 2022 / Published online: 13 September 2022
© The Author(s), under exclusive licence to Islamic Azad University 2022

Abstract

Mathematical modelling of photovoltaic modules is substantial for performance analysis of PV cell. So, improved electromagnetism-like algorithm and differential quadrature approach are implemented to evaluate the parameters of photovoltaic single-, double- and three-diode model. Three tested cases are investigated on various PV systems like Kyocera polycrystalline (KC200GT), polycrystalline (Solarex MSX-60) and monocrystalline (R.T.C France). A MATLAB code is designed to solve this problem. The validity of the presented algorithms is explained by comparison of the computed results with other studied methods and calculating various statistical errors. Also, the results are verified by 10 different experimental I–V sets under various meteorological conditions for every panel. It's found that the solutions of the presented approaches show high convergence speed and accuracy compared with different results where the standard deviation of the root mean square error reached $4.31\text{E}-4$ A between calculated results and experimental measured data and achieved less CPU execution time 1.269 s for R.T.C France. Furthermore, various changed conditions including cell temperature and irradiance conditions are used to validate each method. Also, we compute the maximum power point to get the efficiency of each solar cell where PDQM achieves the best value of efficiency as 16.564 and fill factor = 74.5103 with CPU time = 0.520 s for KC200GT solar panel. Calculation solutions display that the presented techniques can obtain higher parameters identification precision.

Keywords Photovoltaic · Single diode · Double diode · Triple diode · Electromagnetism-like algorithm · Differential quadrature approach

Introduction

Recently, renewable energy sources (RES) have been used in generating electricity in various parts of the world. Solar photovoltaic (PV) is represented as a form of RES, where at the end of 2020 the capacity of PV reached 713 GW [1]. Technologies of PV are being developed using different types of semiconductors. These types are monocrystalline, polycrystalline or amorphous which are used to convert solar energy to useful electrical energy [2].

Improving these systems efficiency requires an accurate modelling for performance estimation. Therefore, a precise

evaluation modules parameters are highly significant in increasing the PV module quality through fabrication and module modelling. Also, the calculation of these parameters by mathematical modelling can play a major role in the simulation, optimization, performance evaluation, control and supervision of solar cells. But the major drawback in precise modelling is the information absence about the accurate values of these parameters. At maximum power point (MPP), PV cell can supply maximum power, but this MPP will change when the solar irradiance and the temperature of PV module vary. Therefore, it's substantial to evaluate MPP for different irradiances and temperatures. It can be done by precise modelling of PV module. The electrical modelling of PV module should demonstrate whole of losses within PV modules and the current–voltage (I–V) characteristics of PV systems [3].

The perfect modelling of PV module is implemented as a photogenerated current (I_{ph}), where it is proportional to the solar irradiance (G) falling on it. Although actual I_{ph} varies because of the electrical and optical losses into the

✉ Hanan Bakr
htaha@eng.zu.edu.eg

¹ Department of Engineering Mathematics and Physics,
Faculty of Engineering, Zagazig University, P.O. 44519,
Zagazig, Egypt

² Department of Medical Research, China Medical University
Hospital, China Medical University, Taichung, Taiwan



positive–negative (p–n) junction of the PV model, which guide to the single-diode model (SDM) of the PV system, for getting high accurate modelling of the PV model losses, the double-diode model (DDM) is used in appearing recombination in the space charge region (SCR) in addendum to SDM losses. Recently, the three-diode model (TDM) was displayed to explain previous losses and recombination in defect regions and grain border. The number of SDM parameters are five parameters which are, I_{ph} , series resistance (R_s) that is wiring and contact losses, parallel resistance (R_{sh}) that is leakage current losses within the p–n junction, and diode parameters are reverse saturation current (I_o) and ideality factor (A). Also, DDM is introduced as seven parameters (five parameters of SDM plus 2 parameters of the second diode). TDM is represented as nine parameters (seven parameters of DDM plus 2 parameters of the third diode) [4].

The modelling operation can be split into preparation of the mathematical model of the PV system and the algorithms of parameters estimation. The main challenge in PV cell is famed via the nonlinearity, instability and complexity of (I–V) and power–voltage (P–V) characteristics equation. The link between photovoltaic (I–V) is both nonlinear and implicit and it is based on various factors like irradiance (G), module temperature (T) and its distribution, wire losses, spectrum, dust accumulation, shading and soiling. So, it's necessary to product a high precise mathematical model that can best find the ideal behaviour and represent the relationship between (I–V). Many mathematical techniques have been advanced to describe the electric and thermal manner of PV cell with a various plane of complexity [5].

These parameters influence directly on the efficiency of the full PV- module. So, it must determine these parameters. To estimate the optimal values of these parameters, much research offered various methods which may be analytical, numerical and meta-heuristic techniques. Analytical technique is characterized by speed of computation and accurate solutions [3]. Khatib et al. [4] introduced a group of correlation to evaluate the PV parameters under meteorological variables. Lim et al. [5] presented the analytical approach to derive the parameters of (SDM) depending on comprehensive calculation and I–V curve. Numerical methods depend on some algorithms which deal with each point on the PV property curve [6]. Villalva et al. [7] proposed a numerical technique for solving PV model. A major drawback of numerical methods is wanting the many of calculation and time to obtain the accurate solutions. Also, these methods are gives slow convergence when the number of parameters to be evaluated increasing [8]. Stochastic optimization is introduced to cope the drawback of exact and numerical

approaches by beginning the optimization with indiscriminate parameters in the consideration area [9]. Between stochastic optimization methods, meta-heuristic techniques are the ultimate common, where meta-heuristic algorithms are used as stochastic optimization methods to obtain the convergence and efficiency of determination the value of PV parameters. Also, genetic algorithm, wind-driven optimization, Harris Hawks optimization and coyote optimization algorithm are the most common example for evolutionary and swarm intelligence algorithms. Recently, artificial intelligence assisted meta-heuristic algorithms to study the most complicated, multi-variable problems [10].

Many algorithms developed to evaluate the optimal parameters of PV system. Among them, Ismail et al. [11] and Moldovan et al. [12] applied a genetic algorithm to get the parameters of PV system using different temperatures and irradiances. Benkercha et al. [13] combined flower pollination algorithm (FPA) with the feature of independency on initial conditions to evaluate the parameters of PV system. Hasanien [14] applied shuffled frog leaping algorithm (SFLA) to define the values of parameters of SDM. Jacob et al. [15] investigated artificial immune system (AIS) for solving parameter evaluation of (DDM). Soon and Low [16] proposed particle swarm optimization (PSO) together with opposite barrier constraint to obtain the values of PV cell parameters. Ebrahimi et al. [17] introduced flexible particle swarm optimization (FPSO) to solve PV cell model. Other algorithms such as simulated annealing algorithm (SA) [18], wind-driven optimization (WDO) [19], pattern search (PS) [20, 21], crow search algorithm (CSA) [22], coyote optimization algorithm (COA) [23], imperialist competitive algorithm (ICA) [24], whale optimization algorithm (WOA) [25–29], sunflower optimization algorithm (SFO) [30], Harris Hawks optimization (HHO) [31], grasshopper optimization algorithm (GOA) [32], total error minimization (TEM) [33], marine predators algorithm (MPA) [34], tree growth-based optimization algorithm (TGA) [35], artificial bee colony algorithm (ABC) [36, 37], guaranteed convergence particle swarm optimization (GCPSO) [38] and performance-guided JAYA algorithm (PGJAYA) [39]. Haider et al. [40] introduced electromagnetism-like algorithm to optimally evaluate associated parameters of DDM. Tan et al. [41] developed electromagnetism-like mechanism algorithm for the optimization of a PV system. Ridha et al. [42] offered improved electromagnetism-like algorithm (IEM) to get the parameters of a SD PV system.

Differential quadrature (DQ) is a numerical approach for studying differential equations. The DQ technique defines as the derivative of a function at each position through a linear summation of every functional value over a mesh line. The



estimation of solution depends on determining the weighting coefficients and grid points. PDQ approach produces highly accurate results and stability with the initial and boundary value problems at less CPU time [43–45]. This method reduced PV equation to a collection of nonlinear algebraic equations.

In this work, improved electromagnetism-like algorithm and differential quadrature approach are employed to estimate of the five, seven and nine parameters of the PV system. The development of this technique is adopted by developed nonlinear equation of the domestic search move. Moreover, the process computation of the gross force is simplified to minimize the complication of the calculated IEM algorithm. Three cases of PV generating are examined like Kyocera polycrystalline (KC200GT), polycrystalline (Solarex MSX-60) and monocrystalline (R.T.C France). A MATLAB code is designed to solve this problem. A real 10 measured I–V data are applied to validate the presented methods and compared the results with other solutions. Also, the solutions are verified with other approaches depending on different statistical criteria. Then, the computed results display the superiority of the presented schemes as it attains less error, less CPU time and a smaller number of evaluations of the objective function. Further, various changed conditions including different temperatures and radiation intensities are used to validate this method. Further, a maximum power point and fill factor are calculated to get efficiency of each solar model.

Mathematical modelling

The PV system can be expressed as a mathematical model which is formed by three models, SDM [46, 47], DDM [47] and triple-diode model [31].

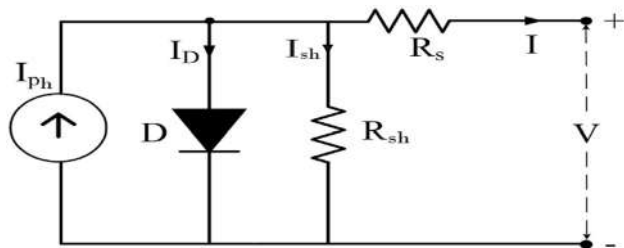


Fig. 1 SDM of PV system

Single-diode model (SDM) of the PV system

The electrical equivalent circuit of SDM of the PV system is offered in Fig. 1. By applying Kirchoff’s Current Law, the output current (I) of the solar model can be expressed as [46, 47]:

$$I = I_{ph} - I_D - I_{sh} = I_{ph} - I_o \left(e^{\frac{V+IR_s}{AV_t}} - 1 \right) - \frac{V + IR_s}{R_{sh}} \tag{1}$$

where V is the output voltage, I_{ph} is the photocurrent, I_D is the current through the diode, I_o and A are the saturation current and ideality factor of the diode, R_s and R_{sh} are series and parallel resistance. V_t is the thermal voltage for PV cell which equal [46, 47]:

$$V_t = \frac{KT}{q} \tag{2}$$

where K , q and T are Boltzmann constant, electron charge and cell temperature.

Double-diode model (DDM) of the PV system

From Fig. 2, it can be observed that there are two diodes to get more accurate voltage–current properties.

The current–voltage (I–V) equation for DDM can be formulated as [47]:

$$I = I_{ph} - I_{D1} - I_{D2} - I_{sh} = I_{ph} - I_{o1} \left(e^{\frac{V+IR_s}{A_1V_t}} - 1 \right) - I_{o2} \left(e^{\frac{V+IR_s}{A_2V_t}} - 1 \right) - \frac{V + IR_s}{R_{sh}} \tag{3}$$

where I_{o1} and I_{o2} are saturation currents of first and second diodes D_1, D_2 . A_1 and A_2 are the ideality factors of the two diodes D_1 and D_2 .

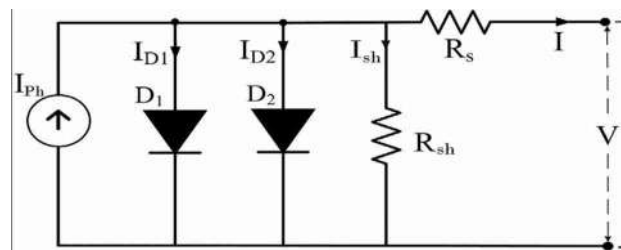


Fig. 2 Equivalent circuit of DDM

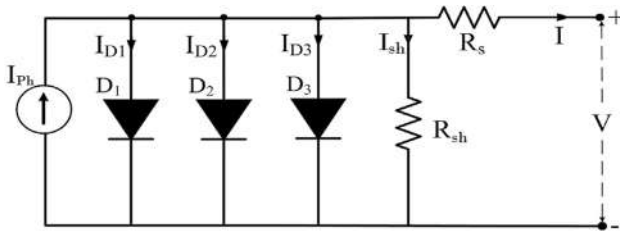


Fig. 3 Three-diode PV model

$$R_{sh} = \frac{G_{stc}}{G} R_{sh, stc} \tag{8}$$

$$V_t = \frac{T}{T_{stc}} V_{t, stc} \tag{9}$$

where G_{stc} and T_{stc} are irradiance and cell temperature at short circuit, G and T are irradiance and cell temperature at known operating condition.

Triple-diode model (TDM) of the PV system

Figure 3 exhibits the electrical circuit for triple-diode model where three diodes used to increase the performance of the PV system.

Depending on the Kirchhoff current rule, the equation of output current is written as follows [31]:

$$I = I_{ph} - I_{D1} - I_{D2} - I_{D3} - I_{sh} = I_{ph} - I_{o1} \left(e^{\frac{V+IR_s}{A_1 V_t}} - 1 \right) - I_{o2} \left(e^{\frac{V+IR_s}{A_2 V_t}} - 1 \right) - I_{o3} \left(e^{\frac{V+IR_s}{A_3 V_t}} - 1 \right) - \frac{V + IR_s}{R_{sh}} \tag{4}$$

where I_{o1} , I_{o2} and I_{o3} are the saturation currents of 1st, 2nd and 3rd diodes D_1 , D_2 and D_3 . A_1 , A_2 and A_3 are the ideality factors of the three diodes D_1 , D_2 and D_3 .

It's found that I_{ph} , I_o , R_{sh} , R_s and V_t are dependent on both radiation and temperature as follows [48]:

$$I_{ph} = \frac{G}{G_{stc}} I_{ph, stc} (1 + k_i (T - T_{stc})) \tag{5}$$

$$I_o = I_{o, stc} \left(\frac{T}{T_{stc}} \right)^3 \exp \left(\left(\frac{q E_g}{k} \right) \left(\frac{1}{T_{stc}} - \frac{1}{T} \right) \right) \tag{6}$$

$$R_s = R_{s, stc} \tag{7}$$

Objective function formulation

To evaluate the parameters of PV systems, the minimization error between experimental and computed currents is needed. Thus, we want objective function to solve the optimization problem. So, root mean square error (RMSE) between the experimental current (I_e) and the computed current (I) is the best choice as objective function. Here, it is necessary to utilize a dataset of N samples of experimental current for each PV module. So, the objective function can be described as [25–27]:

$$F(\lambda) = RMSE(\lambda) = \sqrt{\frac{1}{N} \sum_{i=1}^N f(V_{e_i}, I_{e_i}, \lambda)^2} \tag{10}$$

where λ represents five, seven and nine parameters for PV systems, and N is the number of experimental data.

For SDM

$$\lambda = [I_{ph}, I_o, A, R_s, R_{sh}]$$

$$F(\lambda) = \sqrt{\frac{1}{N} \sum_{i=1}^N \left(I_{e_i} - I_{ph} + I_o \left(e^{\frac{V_{e_i} + I_{e_i} R_s}{A V_t}} - 1 \right) + \frac{V_{e_i} + I_{e_i} R_s}{R_{sh}} \right)^2} \tag{11}$$

For DDM

$$\lambda = [I_{ph}, I_{o1}, I_{o2}, A_1, A_2, R_s, R_{sh}]$$

$$F(\lambda) = \sqrt{\frac{1}{N} \sum_{i=1}^N \left(I_{e_i} - I_{ph} + I_{o1} \left(e^{\frac{V_{e_i} + I_{e_i} R_s}{A_1 V_t}} - 1 \right) + I_{o2} \left(e^{\frac{V_{e_i} + I_{e_i} R_s}{A_2 V_t}} - 1 \right) + \frac{V_{e_i} + I_{e_i} R_s}{R_{sh}} \right)^2} \tag{12}$$

For TDM

$$\lambda = [I_{ph}, I_{o1}, I_{o2}, I_{o3}, A_1, A_2, A_3, R_s, R_{sh}]$$

$$F(\lambda) = \sqrt{\frac{1}{N} \sum_{i=1}^N \left(I_{e_i} - I_{ph} + I_{o1} \left(e^{\frac{V_{e_i} + I_{e_i} R_s}{A_1 V_i}} - 1 \right) + I_{o2} \left(e^{\frac{V_{e_i} + I_{e_i} R_s}{A_2 V_i}} - 1 \right) + I_{o3} \left(e^{\frac{V_{e_i} + I_{e_i} R_s}{A_3 V_i}} - 1 \right) + \frac{V_{e_i} + I_{e_i} R_s}{R_{sh}} \right)^2} \tag{13}$$

where RMSE is a comparison with the calculated current and I_{e_i} experimental PV current, V_{e_i} is experimental PV voltage, N is points of I–V curve. Finally, mathematical modelling section displays the electrical equivalent circuit and the output current equation of SDM, DDM and TDM in Eqs. (1), (3) and (4), respectively. Furthermore, the computed output current is utilized for extracting the objective function through the Root Mean Square Error (RMSE) between the experimental current (I_e) and the computed current (I).

Solution of the problem

Two different schemes, improved electromagnetism-Like algorithm and differential quadrature method are used to evaluate the estimated 5, 7 and 9 Solar cell parameters and determine maximum power point to get the efficiency and fill factor of each solar cell, as follows:

Improved electromagnetism-like mechanism algorithm

Owing to the easy and efficiency of EM approaches in solving many mathematical engineering and programming problems, so it is using in evaluating the parameters of PV system.

In general, the search technique of EM can be separated into its exploration and exploitation parts. The EM algorithm initiates with a population of randomly generated points from the feasible region. The exploration part of EM proceeds a much global search by shifting the particles in accordance with the superposition theorem. EM simulates the attraction–repulsion mechanism of charges to obtain a global optimal solution by using bounded variables. Particles with better objective values will apply attracting forces while particles with worse objective values will apply repulsion forces onto other particles. The particles are then shifted based on superposition theorem and they are utilized to find a direction for every point to move on subsequent iterations. The regions that have maximum attraction will indicate other points to move towards them. As well, a repulsion is also introduced to search a new region for better

solutions. We describe this algorithm as simple following steps as [40–42]:

Initialization

This algorithm begins with a population of randomly created points from the feasible area between the corresponding upper and lower limits of each parameter as in Table 2. This population consists of individual vectors (i) while each vector includes (K) particles (parameters) that need to be optimized. The (K) dimensional individual vectors are initialized to be distributed uniformly as:

$$X_k^i = L_k + \theta (U_k - L_k) \tag{14}$$

where θ is a random number within [0, 1] interval. U_k, L_k are the upper and lower bound.

Local search

Local search is used to collect local information within neighbourhood for point X^i . LSITER and δ are two control parameters used as the local search. LSITER is the number of the iteration that the local search repeats and δ is a multiplier factor as a random number within [0, 1] interval for the neighbourhood search. To enhance the performance, convergence and accuracy of this algorithm, a small search step L is represented as:

$$L = \frac{2}{1 + \exp\left(\frac{10 * LSITER}{MAXITER}\right)} \tag{15}$$

MAXITER is the extreme number of generations.

After that, the individual vector X_k^i is replaced by Y_k^i if the objective function value of Y_k^i is less than vector X_k^i within

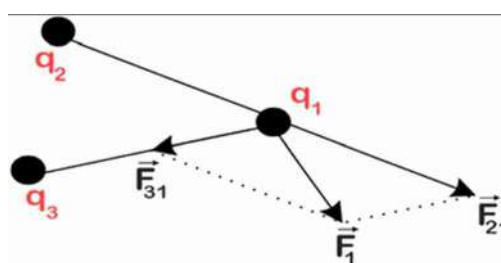


Fig. 4 Total force and q^i

the iteration of local search. Finally, the neighbourhood search for the individual vector ends and the new best individual and its objective function value are updated. If the new solution offers no improvement, the local search will re-iterate until a pre-determined maximum iteration number (MAXITER) is reached.

Charge calculation

The total force exerted onto an individual vector by another individual vector that is calculated based on the charges of these vectors. The charge of each point is evaluated by its current objective value compared to the best particle in the iteration. The charge of every particle q^i , setting the force of attraction or repulsion to another particles, the charge of (i) individual vector X_k^i is calculated by:

$$q^i = \exp \left(-\mu \frac{F(X^i) - F(X^{best})}{\sum_{K=1}^{\epsilon} F(X^K) - F(X^{best})} \right) \tag{16}$$

where μ is overall range of the parameters. ϵ is the size of population. $F(X^{best})$ is the fitness value of each particle.

Total exerted force calculation

The charges are computed for all points and the total forces created by one particle onto another particle can be calculated. According to electromagnetism theory, the total force onto one particle is directly proportional to the product of the charges and inversely proportional to the distance among the particles. Therefore, individual vectors with higher objective function values attract other individual vectors, while the individual vectors with lower objective function values repel the others. From Eq. (17), the overall force exerted on each point is computed after all the forces of attraction and repulsion are defined as shown in Fig. 4:

$$F^i = \sum_{j \neq i}^{\epsilon} \left\{ \begin{array}{l} (X^j - X^i) \frac{q^i q^j}{\|X^j - X^i\|^2}, \text{ if } F(X^j) < F(X^i) \text{ attraction} \\ (X^i - X^j) \frac{q^i q^j}{\|X^j - X^i\|^2}, \text{ if } F(X^j) \geq F(X^i) \text{ repulsion} \end{array} \right\} \tag{17}$$

Particle movement

To get optimal particles, all particles are replaced with the best particle located onto a new particle location in the space. This particle movement is vital to ensure better global search of possible optimal solutions. The particle movement between lower and upper limits is determined as:

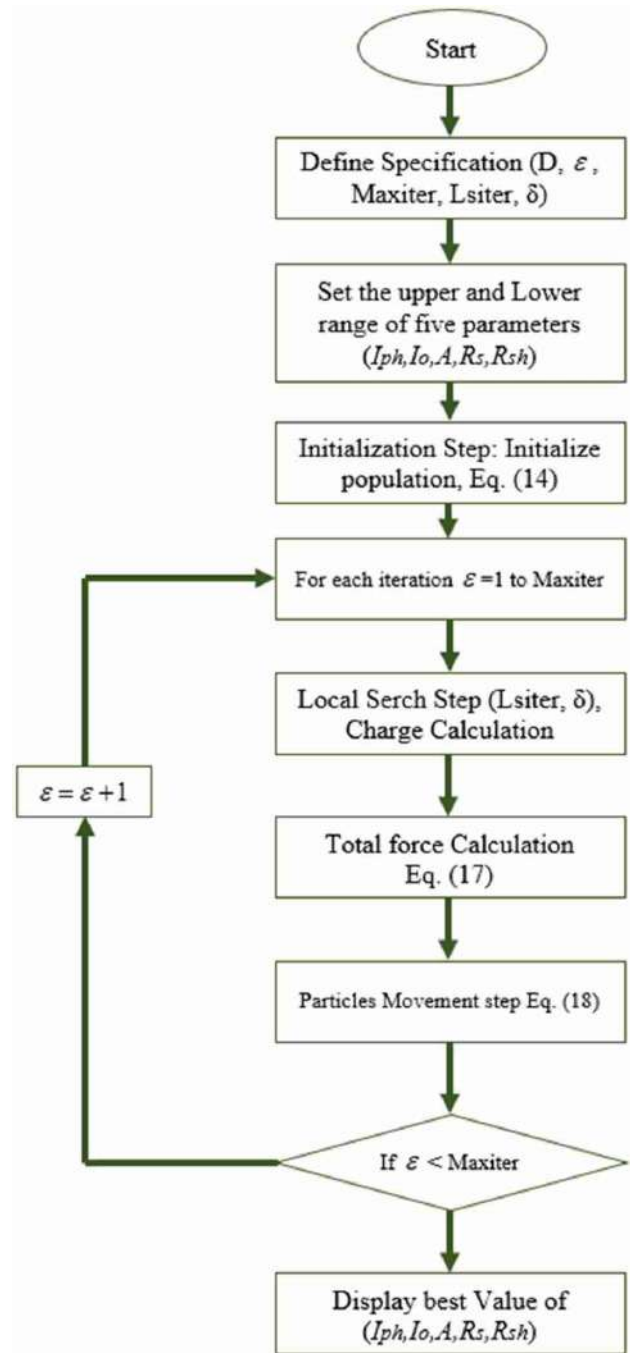


Fig. 5 Flow chart of extracting PV parameters based on IEM approach

$$X_K^i = \left\{ \begin{array}{l} X_K^i + \theta \frac{F_K^i}{\|F_K^i\|} (U_K - X_K^i), \text{ if } F_K^i > 0 \\ X_K^i + \theta \frac{F_K^i}{\|F_K^i\|} (X_K^i - L_K), \text{ if } F_K^i \leq 0 \end{array} \right\} \tag{18}$$

The last four stages of IEM algorithm are repeated until the pre-determined maximum iteration number (MAX-ITER) is reached and then, the best values of particles

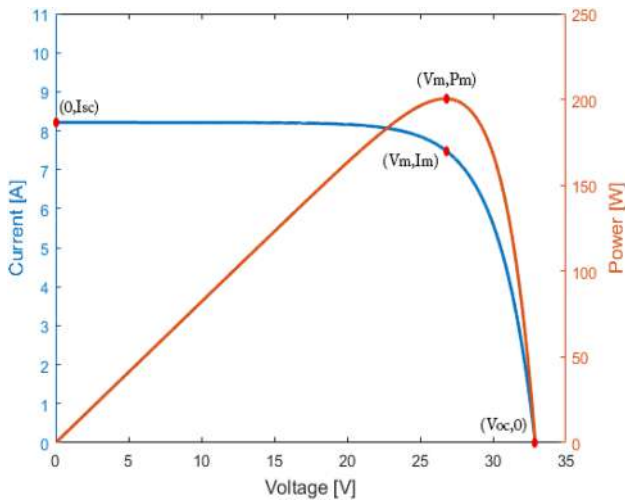


Fig. 6 Typical I–V and P–V curves of KC200GT model

(parameters) will be displayed. Figure 5 exhibits the flow chart of IEM approach for evaluating the parameters of PV systems by five procedures.

Polynomial-based differential quadrature technique

The presented objective function is derived from the P–V curve of the PV module which has unique maximum power point (MPP) as displayed in Fig. 6. This MPP will vary as the temperature and the solar irradiance of PV module varies. Different operating conditions of both temperature and solar irradiance are studied for the three kinds of PV modules stated in paper. The maximum power point of the obtained curve from polynomial differential quadrature (PDQ) technique should be matched with the datasheet curve. Referring to Fig. 6, the following equations can be determined as:

$$P(V) = I \cdot V = I_{sc} \left(1 - c_1 \left(e^{\frac{V}{c_2 V_{oc}}} - 1 \right) \right) \cdot V \quad (19)$$

where I_{sc} and V_{oc} are the short circuit current and open circuit voltage.

$$c_1 = \left(1 - \frac{I_m}{I_{sc}} \right) e^{\frac{-V_m}{c_2 V_{oc}}}, \quad c_2 = \frac{\frac{V_m}{V_{oc}} - 1}{\ln \left(1 - \frac{I_m}{I_{sc}} \right)}$$

where I_m, V_m are maximum power current and voltage.

To get MPP, differentiate Eq. (19) with respect to voltage such as:

$$\left. \frac{dP}{dV} \right|_{V=V_m, I=I_m} = 0 \quad (20)$$

$$\begin{aligned} \frac{dP}{dV} &= \left(-I_{sc} \frac{c_1}{c_2 V_{oc}} e^{\frac{V}{c_2 V_{oc}}} \right) + I_{sc} - \left(c_1 I_{sc} e^{\frac{V}{c_2 V_{oc}}} \right) + (c_1 I_{sc}) \\ &= s - (w V) - \left(t e^{\frac{V}{r}} \right) = 0 \end{aligned} \quad (21)$$

where $w = I_{sc} \frac{c_1}{c_2 V_{oc}} e^{\frac{V}{c_2 V_{oc}}}$, $s = c_1 I_{sc} + I_{sc}$, $t = c_1 I_{sc}$, $r = c_2 V_{oc}$.

The shape function is used in PDQ technique is Lagrange interpolation polynomial. The unknown ψ and its m th derivatives can be defined as a weighted linear sum of nodal points, ψ_i , ($i = 1 : M$), as [43–45]:

$$\psi(X_i) = \sum_{j=1}^M \frac{\prod_{k=1, k \neq j}^M (X_i - X_k)}{(X_i - X_j) \prod_{j=1, j \neq k}^M (X_j - X_k)} \psi(X_j), \quad (i = 1 : M) \quad (22)$$

$$\left. \frac{\partial^m \psi}{\partial X^m} \right|_{X=X_i} = \sum_{j=1}^M H_{ij}^{(m)} \psi(X_j), \quad (i = 1, M) \quad (23)$$

ψ represents the field quantities I, V . M is the number of grid points. The weighting coefficients of 1st derivative $H_{ij}^{(1)}$ can be determined as:

$$H_{ij}^{(1)} = \begin{cases} \frac{1}{(X_i - X_j)} \prod_{k=1, k \neq i, j}^M \frac{(X_j - X_k)}{(X_i - X_k)} & i \neq j \\ - \sum_{j=1, j \neq i}^M H_{ij}^{(1)} & i = j \end{cases} \quad (24)$$

By replacing Eq. (24) into Eq. (21), the MPP equation can be expressed as:

$$\sum_{j=1}^M H_{ij}^{(1)} P_j = s - (w_i V_i) - \left(t e^{\frac{V_i}{r}} \right), \quad (i = 1, M). \quad (25)$$

Statistical analysis

Several statistical tests are utilized to evaluate the convergence of the presented algorithm and know the goodness of the curve fit among computed values and measured data. Also, the solutions by IEM are compared with

Table 1 Electrical specifications of KC200GT, MSX-60 and R.T.C France at the STC

Type parameter	KC200GT [49]	MSX-60 [50]	R.T.C France [51]
P_{max} (W)	200	60	0.3
V_{mp} (V)	26.3	17.1	0.45
I_{mp} (A)	7.61	3.5	0.691
V_{oc} (V)	32.9	21.1	0.573
I_{sc} (A)	8.21	3.8	0.76
K_i (A/°C)	0.00318	0.00247	0.000266
K_v (V/°C)	-0.123	-0.08	-0.0023

different algorithms. There are seven criteria are determined as follows:

$$1. \text{Root mean square error (RMSE)} = \sqrt{\frac{1}{N} \sum_{i=1}^N (I - I_{ei})^2} \tag{26}$$

$$2. \text{Mean bias error (MBE)} = \frac{1}{N} \sum_{i=1}^N (I - I_{ei}) \tag{27}$$

Table 2 Lower and upper bounds of nine PV parameters

Parameter	A_1	A_2	A_3	R_s (Ω)	R_{sh} (Ω)	I_{ph} (A)	I_{o1} (μA)	I_{o2} (μA)	I_{o3} (μA)
Lower value	1	1	1	0.01	100	0.01	1	1	1
Upper value	2	2	2	0.4	1000	10	10^{-6}	10^{-6}	10^{-6}

Table 3 SDM, DDM and TDM PV parameters for KC200GT solar cell, obtained by proposed IEM and various optimization methods at ($G = 1000 \text{ W/m}^2, T = 25 \text{ °C}$)

Model type		Single-diode PV model							
Parameter	Algorithm	Proposed IEM	GA [11, 12]	SA [6, 18, 19]	PS [20, 21]	WDO [19]	ICA [24]	FPSO [17]	PGJAYA [39]
I_{ph} (A)		8.2183	8.2112	8.2109	8.2104	8.1812	8.21	8.2186	8.21666157
I_o (μA)		9.6575	0.9220	3.3484	7.1836	0.4423	0.10946	0.001436	0.00228368
A		1.738	1.4819	1.6118	1.7	1.4172	1.3079	1.05528	1.07729991
R_s (Ω)		0.0169	0.1067	0.0796	0.0339	0.1132	0.0039	0.24939	0.34351050
R_{sh} (Ω)		765.034	728.58	713.11	624.382	747.41	188.2103	130.28134	773.811733
Model type		Double-diode PV model							
Parameter	Algorithm	Proposed IEM	GA [19]	SA [6, 18, 19]	PS [20, 21]	WDO [19]	ICA [24]	CSA [22]	
I_{ph} (A)		8.2103	8.2103	8.2102	8.2107	8.1914	8.21	8.21	
I_{o1} (μA)		8.909	1.29E-4	5.24E-3	5.22E-4	40.746	0.1429	0.0173	
I_{o2} (μA)		5.23E-4	0.053	0.00212	3.12E-4	1.632	2.643E-3	5.75 E-4	
A_1		1.728	1.17	1.12	1.01	1.9667	1.3274	1.3009	
A_2		1.7302	1.4324	1.5631	1.9	1.537	1.0851	1.2906	
R_s (Ω)		0.0196	0.0691	0.01783	0.031	0.99	0.0038	0.02	
R_{sh} (Ω)		732.696	763.3564	862.97	793.215	784.4062	108.7844	342.146	
Model type		Triple-diode PV model							
Parameter	Algorithm	Proposed IEM	GA [28]	SA [28]	WOA [25–29]	SFO [30]	MPA [34]	COA [23]	GOA [32]
I_{ph} (A)		8.2184	8.14	8.25	8.231	8.212	8.19	8.1256	8.229174
I_{o1} (μA)		6.14669	0.015	0.019	0.027	0.043	0.02804	0.023354	0.0288
I_{o2} (μA)		0.5476	4.59 E-4	3.77 E-4	4.68 E-4	2.22 E-4	4.814 E-4	1.865 E-4	2.8 E-4
I_{o3} (μA)		1.205E-2	1.02 E-4	4.6 E-4	4.93 E-4	1.35	4.687 E-4	4.912 E-4	2.797 E-4
A_1		1.6916	1.19	1.2	1.32	1.25	1.3054	1.3938	1.219762
A_2		1.725	1.496	1.2	1.24	1.99	1.214	1.0486	1.091667
A_3		1.4808	1.38	1.48	1.022	1.84	1.5412	1.0167	1.499932
R_s (Ω)		0.0272	0.362	0.378	0.342	0.238	0.3741	0.2735	0.224810
R_{sh} (Ω)		727.451	311.80	327.6	341.39	606.12	330.9143	286.2602	310.8623

Table 4 SDM, DDM and TDM PV parameters for MSX-60 solar cell, computed by proposed IEM and different optimization techniques at ($G = 1000 \text{ W/m}^2, T = 25 \text{ }^\circ\text{C}$)

Model type		Single-diode PV model						
Parameter	Algorithm	Proposed IEM	GA [52]	PSO [52]	SA [53]	TEM [33]	LSE [54]	NLS [54]
I_{ph} (A)		3.808	3.8039	3.8203	3.8721	3.8	3.8598	3.81
I_o (μA)		0.4747	0.0499	0.0593	2.971	0.091	1.265E-3	9.99E-4
A		1.438	1.2759	1.2716	1.387	1.3	1.0365	1.3
R_s (Ω)		0.105	0.222	0.2221	0.2234	0.12	0.32	0.33
R_{sh} (Ω)		356.304	365.831	376.671	406.346	164.54	117.99	99.05
Model type		Double-diode PV model						
Parameter	Algorithm	Proposed IEM	COA [55]	TEM [33]	Analytical Method [56]	Numerical Method [56]	Iteration Method [57]	Newton Method [58]
I_{ph} (A)		3.8	3.8418	3.8	3.8752	3.8046	3.8	3.8084
I_{o1} (μA)		2.27E-2	0.04958	4.7E-4	3.612E-4	3.99E-4	4.704E-4	4.87E-4
I_{o2} (μA)		5.3E-4	0.009549	4.7E-4	9.3773	4.033	4.704E-4	6.15E-4
A_1		1.208	1.2569	1	1	0.9985	1	1
A_2		1.95	1.9345	1.2	2	2	1.2	1.99
R_s (Ω)		0.2017	0.2495	0.27	0.3084	0.3397	0.35	0.3692
R_{sh} (Ω)		280.043	267.57	116.53	280.6449	280.217	176.4	169.047
Model type		Triple-diode PV model						
Parameter	Algorithm	Proposed IEM	GA [30]	SA [30]	WOA [29, 30]	SFO [30]	MPA [34]	GOA [32]
I_{ph} (A)		3.8079	3.801	3.792	3.756	3.80111	3.6741	3.698
I_{o1} (μA)		0.07647	0.0164	1.98E-2	2.1E-2	4.98E-2	2.81E-2	0.02187
I_{o2} (μA)		9.77E-4	4.82E-4	4.76E-4	3.68E-4	7.24E-4	3.52E-4	2.294E-4
I_{o3} (μA)		5.93E-4	1.29E-4	2.62E-4	3.97E-4	0.0142	4.16E-4	2.118E-4
A_1		1.2912	1.21	1.29	1.30	1.282	1.4012	1.375876
A_2		1.2793	1.25	1.22	1.23	1.8043	1.0789	1.074414
A_3		1.3096	1.30	1.28	1.03	1.4364	1.4011	1.094849
R_s (Ω)		0.1518	0.181	0.211	0.195	0.20598	0.18745	0.110955
R_{sh} (Ω)		282.071	280.22	298.59	277.37	578.3468	280.1452	349.8458

3. Absolute error (AE) = $|I - I_{ei}|$ (28)

4. Mean absolute error (MAE) = $\frac{1}{N} \sum_{i=1}^N |I - I_{ei}|$ (29)

5. Summation of absolute error (SAE) = $\sum_{i=1}^N |I - I_{ei}|$ (30)

6. Coefficient of determination (R^2)

$$= 1 - \frac{\sum_{i=1}^N (I - I_{ei})^2}{\sum_{i=1}^N (I - \bar{I}_{ei})^2}, \quad \bar{I}_{ei} = \frac{1}{N} \sum_{i=1}^N I_{ei}$$
 (31)

7. Test statistic (TS) = $\sqrt{\frac{(N - 1) \text{MBE}^2}{\text{RMSE}^2 - \text{MBE}^2}}$. (32)

I is computed current. i is a grade of solar radiation ($i = 1, N$).

Finally, solution of the problem section explains the steps of the improved electromagnetism-like algorithm (IEM) to optimize solar cell parameters and polynomial differential quadrature method (PDQM) to compute the maximum power point to get the efficiency and fill factor of each PV module. Furthermore, this section displays the statistical analysis that evaluates the convergence and accuracy of the IEM algorithm.

Results and discussion

In this section, the performance of proposed IEM algorithm is evaluated for parameter extraction of SDM, DDM and TDM of various PV modules. Presented algorithms are used

Table 5 SDM, DDM and TDM PV parameters for R.T.C France, computed by Proposed IEM and different optimization approaches at ($G = 1000 \text{ W/m}^2, T = 25 \text{ }^\circ\text{C}$)

Model type		Single-diode PV model									
Parameter	Algorithm	Proposed IEM	GA [59, 60]	SA [20, 60]	PS [60]	WDO [19]	ICA [24]	TGA [35]	PSO [60, 61]	GCPSO [38]	PGJAYA [39]
I_{ph} (A)		0.76086	0.762	0.762	0.7617	0.7608	0.7603	0.76038	0.76077	0.760787	0.7608
I_o (μA)		0.32301	0.809	0.4798	0.998	0.3223	0.1465	0.23082	0.32454	0.310685	0.3230
A		1.492	1.5751	1.5172	1.6	1.4808	1.4421	1.44792	1.48165	1.477268	1.4812
R_s (Ω)		0.03638	0.0299	0.0345	0.0313	0.0367	0.0389	0.03799	0.03636	0.036546	0.0364
R_{sh} (Ω)		53.7188	42.373	43.1034	64.1026	57.746	41.1577	53.6778	53.855	52.88987	53.7185
Model type		Double-diode PV model									
Parameter	Algorithm	Proposed IEM	GA [62, 63]	SA [18]	PS [20]	WDO [19]	WOA [64, 65]	ABC [36]	GCPSO [38]	PGJAYA [39]	
I_{ph} (A)		0.7606	0.7608	0.7623	0.7602	0.7606	0.7646	0.7608	0.7608295	0.7608	
I_{o1} (μA)		0.0192	1E-4	0.4767	0.9889	0.2531	1.7641	0.0407	0.1341156	0.21031	
I_{o2} (μA)		0.88087	1E-4	0.01	0.0001	0.0482	2.0948	0.2874	8.0417831	0.88534	
A_1		1.285	1.3355	1.5172	1.6	1.511	1.6839	1.4495	1.4030570	1.4450	
A_2		1.844	1.481	2	1.192	1.3843	2.1583	1.4885	2.4999999	2.0000	
R_s (Ω)		0.0346	0.0364	0.0345	0.032	0.03743	0.0277	0.0364	0.0379689	0.0368	
R_{sh} (Ω)		53.667	53.7185	43.1034	81.3	52.6608	64.2652	53.78	60.999517	55.8135	
Model type		Triple-diode PV model									
Parameter	Algorithm	Proposed IEM	ABC [36, 37]	TGA [35]	COA [23]	EPFO [66]	OBWOA [23, 67]	STBLO [23, 68, 69]			
I_{ph} (A)		0.7602	0.7607	0.7611	0.76088	0.76079	0.76077	0.7608			
I_{o1} (μA)		0.1136	0.2	0.30477	0.20945	0.13538	0.2353	0.2349			
I_{o2} (μA)		0.7999	0.5	0.25571	0.19142	0.15877	0.2213	0.2297			
I_{o3} (μA)		0.1007	0.21	0.32399	0.23742	0.6435	0.4573	0.2297			
A_1		1.444	1.4414	1.9999	1.75399	1.4114	1.4543	1.4541			
A_2		1.784	1.9	1.4623	1.4396	1.9035	2	2			
A_3		1.855	2	2	1.9	1.8329	2	2			
R_s (Ω)		0.030313	0.03687	0.0363	0.03692	0.03728	0.03668	0.0367			
R_{sh} (Ω)		56.9849	55.8344	51.14	53	56.533	55.4448	55.2641			

Table 6 RMSE, MBE, AE, MAE, SAE, R^2 and TS of the proposed IEM for SDM, DDM and TDM of different solar models at ($G = 1000 \text{ W/m}^2, T = 25 \text{ }^\circ\text{C}$)

Model Type	SDM			DDM			TDM		
	Solar Cell	MSX-60	R.T.C France	MSX-60	R.T.C France	MSX-60	R.T.C France	MSX-60	R.T.C France
RMSE by IEM		4.85E-3	4.31E-4	4.47E-3	6.02E-3	5.18E-3	5.325E-4	4.944E-3	7.178E-4
WDO [19]		-	8.4E-4	-	-	-	1.06E-3	-	-
FPSO [17]		2.821E-2	-	-	-	-	-	-	-
PGJAYA [39]		1.54545E-3	9.86E-04	-	-	-	9.82E-04	-	-
GA [28]		-	1.88E-2	-	-	0.2171	2.9E-3	-	-
SA [28]		-	1.875E-3	-	-	0.2122	3.0E-3	-	-
WOA [28]		-	-	-	-	0.1174	-	-	-
TGA [35]		-	9.75E-4	-	-	-	8.488E-4	-	8.251E-4
GCPSO [40]		-	7.730E-4	-	-	-	7.182E-4	-	-
SFO [30]		-	-	-	-	0.031746	-	-	-
COA [55]		-	-	-	1.94E-2	-	-	-	-
MBE by IEM		5.29E-4	3.59E-4	0.00265	2.16E-3	1.095E-3	1.359E-4	9.95E-4	6.841E-4
AE by IEM		5.89E-6	2.26E-4	7.975E-5	2.73E-3	3.81E-4	1.908E-4	1.82E-4	5.0512E-4
MAE by IEM		4.14E-3	4.083E-3	3.79E-3	5.67E-3	4.52E-3	4.392E-4	4.199E-3	6.841E-4
MAE by ICA [24]		-	5.66E-4	5.26E-4	-	-	-	-	-
SAE by IEM		0.12849	4.67E-3	0.0569	0.04542	0.1402	0.0013	0.05878	0.0021
R^2 by IEM		0.99994	0.95948	0.99999	0.99997	0.9826	1.5476	0.983	0.9995
TS by IEM		0.60034	5.218	2.7568	1.0181	1.1841	0.3734	0.741	4.4468
CPU Time (sec)		1.2892	1.296	1.412	1.401	1.625	1.427	1.651	1.614

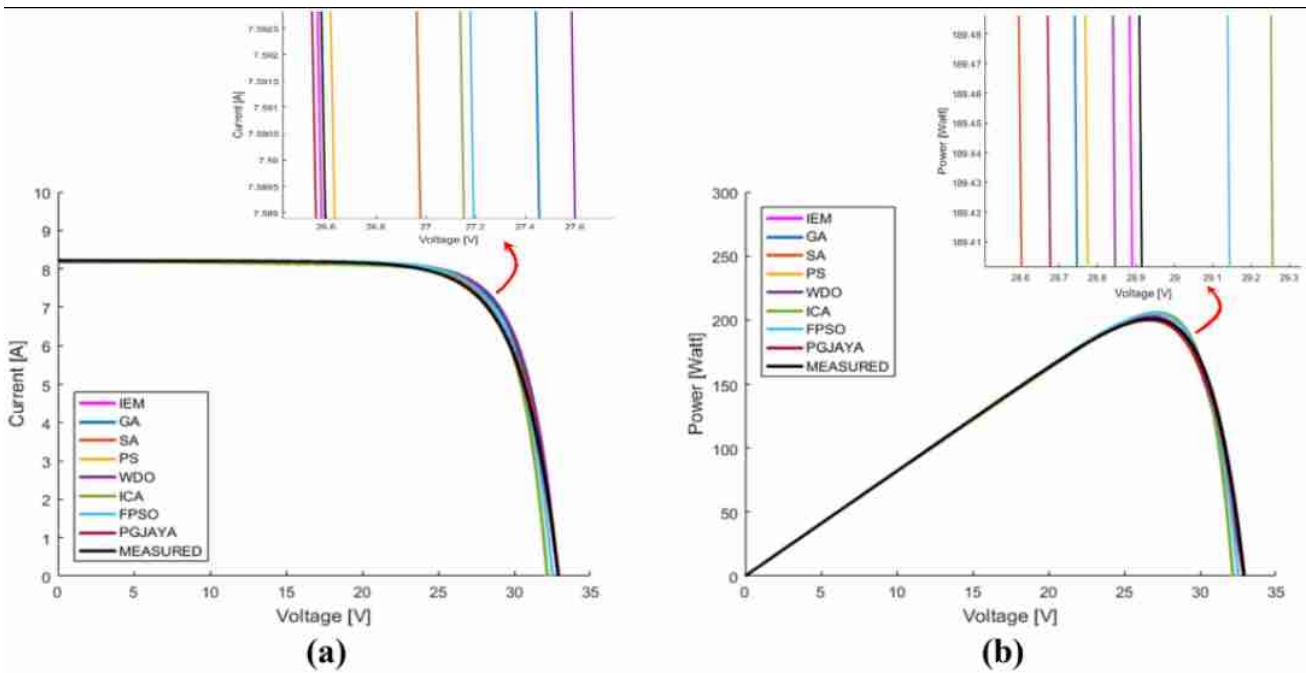


Fig. 7 a I–V curves and b P–V curves of KC200GT computed via presented IEM and other algorithms for the SD model

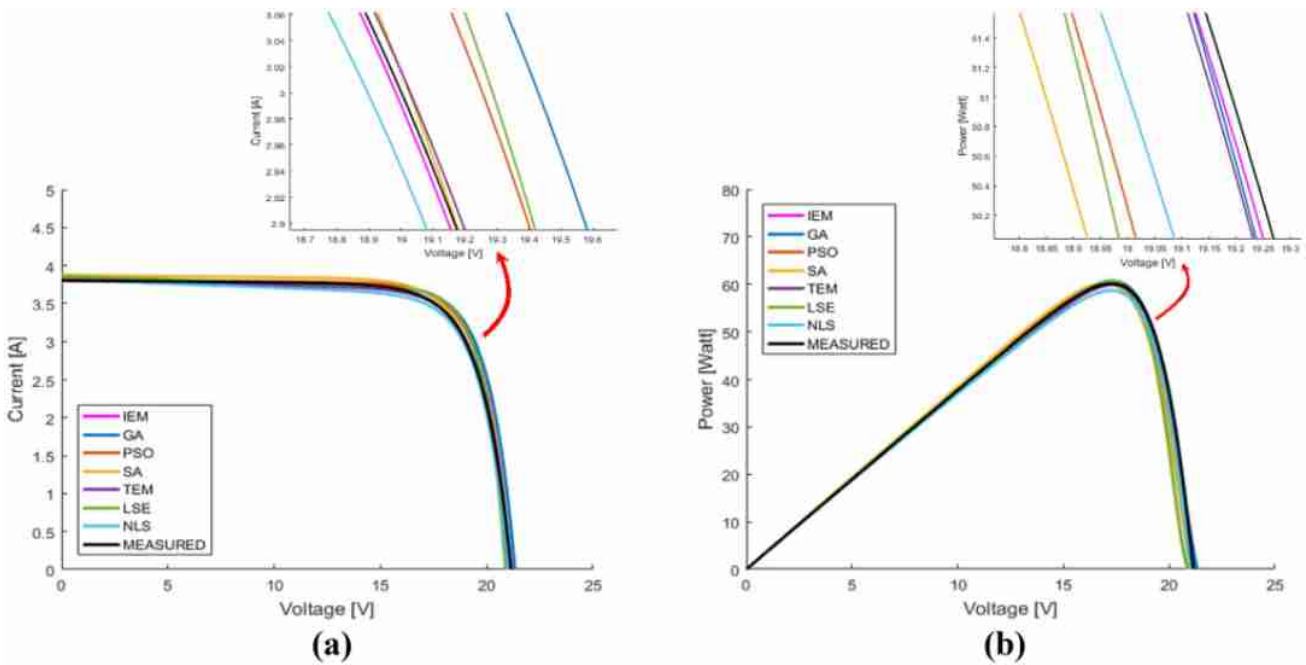


Fig. 8 a I–V curves and b P–V curves of MSX-60 computed via presented IEM and other algorithms for the SD model

for two kinds of PV system polycrystalline and monocrystalline. Kyocera module (KC200GT) and Solarex MSX-60 are given in [49, 50] are polycrystalline. R.T.C France [51] is applied as monocrystalline. Table 1 illustrates the electrical specifications of these kinds. Table 2 shows the values of

lower and higher bounds of the nine PV parameters which agreed with those used in other papers. In the meanwhile, the population size N and MAXITER are selected to be 10D and 500, respectively. Two control parameters δ and LSITER are

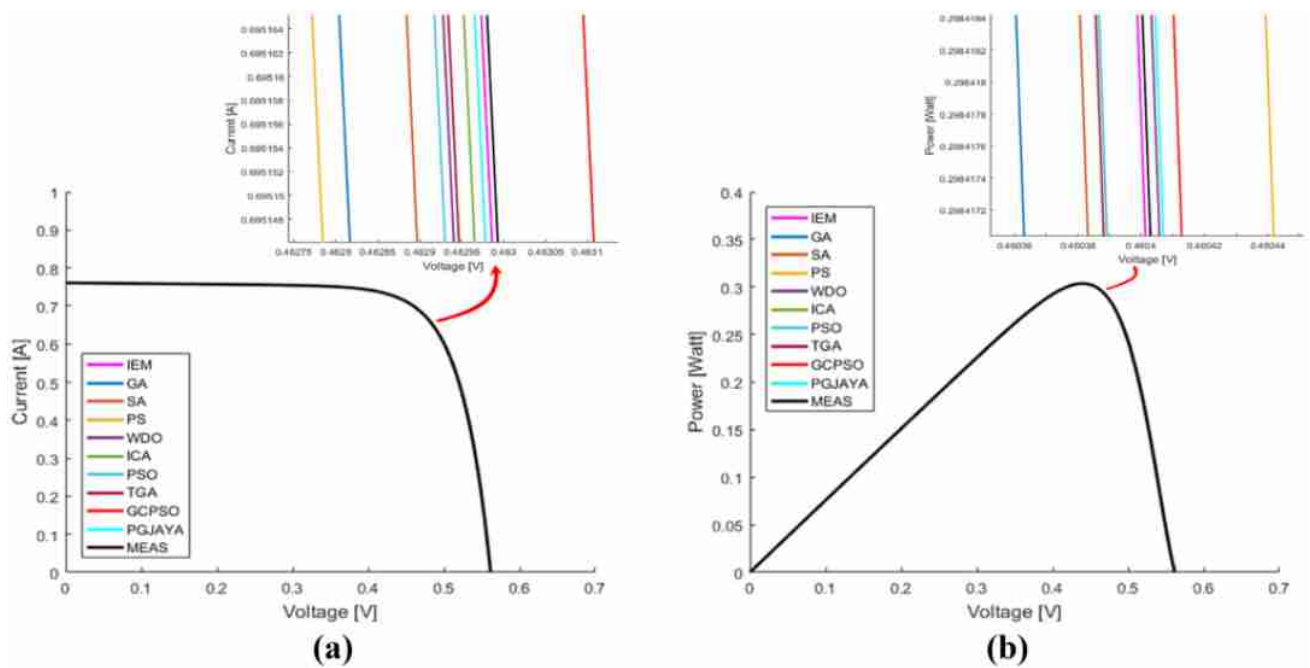


Fig. 9 a I–V curves and b P–V curves of R.T.C France computed via presented IEM and various algorithms for the SD model

Table 7 Evaluated model parameters for SDM of KC200GT, Msx-60, R.T.C France solar cells, obtained by proposed IEM at different environmental conditions

Environmental condition		$G = 1000 \text{ W/m}^2 - T = 50 \text{ }^\circ\text{C}$		
Parameter	Solar cell	KC200GT	MSX-60	R.T.C France
I_{ph} (A)		8.2828	3.86	0.76676
I_o (μA)		8.2825	0.9932	0.6551
A		1.56	1.3647	1.5461
R_s (Ω)		0.079	0.13164	0.0302
R_{sh} (Ω)		742.885	397.285	53.8982
Environmental condition		$G = 600 \text{ W/m}^2 - T = 25 \text{ }^\circ\text{C}$		
Parameter	Solar cell	KC200GT	MSX-60	R.T.C France
I_{ph} (A)		4.9294	2.28	0.4568
I_o (μA)		5.0784	0.397	0.4812
A		1.6879	1.439	1.598
R_s (Ω)		0.0348	0.107	0.0383
R_{sh} (Ω)		712.737	399.097	59.723

assumed 0.01 and 30, respectively, to obtain better results according to many attempts of running the algorithm.

Tables 3, 4 and 5 show that the five, seven and nine optimal parameters for three kinds of PV module are obtained via the proposed IEM and compared with GA, SA, PS, WDO, ICA, FPSO, CSA, SFO, MPA, COA, GOA, PSO, TEM, LSE, NLS, exact method, numerical technique, iteration approach, Newton method, ABC, TGA, EPSO, OBWOA, STBLO and PGJAYA algorithms.

It can be noticed that the parameters values obtained by the proposed IEM are approximately close to those presented by other works. Table 6 shows statistical errors criteria (RMSE, MBE, AE, MAE, SAE, R^2 and TS) of the proposed IEM and other algorithms for SDM, DDM and TDM of different solar models at STC ($G = 1000 \text{ W/m}^2$, $T = 25 \text{ }^\circ\text{C}$). Definitely, the similarity of the results between IEM and other algorithms is remarkable and the differences are slight. It clearly shows that the IEM achieved

Table 8 Evaluated model parameters for DDM of KC200GT, Msx-60, R.T.C France solar cells, obtained by proposed IEM and ICA method at different environmental conditions

Environmental Condition		$G = 1000 \text{ W/m}^2 - T = 50 \text{ }^\circ\text{C}$				
Solar Cell		KC200GT		MSX-60	R.T.C France	
Parameter	Method	IEM	ICA [24]	IEM	IEM	ICA [24]
I_{ph} (A)		8.288	8.2895	3.8613	0.7667	0.7612
I_{o1} (μA)		9.9129	0.80422	$8.30\text{E}-2$	0.08951	2.0677
I_{o2} (μA)		$9.45\text{E}-4$	22.52	$3.59\text{E}-4$	0.9216	0,004,248
A_1		1.5809	1.2455	1.175	1.3847	1.4578
A_2		1.753	1.0469	1.951	1.725	0.7814
R_s (Ω)		0.0753	0.0196	0.20075	0.0301	0.0386
R_{sh} (Ω)		733.337	402.138	281.633	53.9829	38.6933
Parameter		$G = 600 \text{ W/m}^2 - T = 25 \text{ }^\circ\text{C}$				
Solar cell		KC200GT		MSX-60	R.T.C France	
Parameter	Method	IEM	ICA [24]	IEM	IEM	ICA [24]
I_{ph} (A)		4.9278	4.926	2.28	0.4561	0.4562
I_{o1} (μA)		3.971	0.023441	$4.87\text{E}-2$	$1.906\text{E}-2$	0.52604
I_{o2} (μA)		$3.39\text{E}-4$	0.51296	$5.32\text{E}-4$	0.7804	1.5151
A_1		1.658	1.20547	1.269	1.351	1.572
A_2		1.972	1.00938	1.949	1.737	1.113
R_s (Ω)		0.0413	0.111148	0.224	0.0395	0.0375
R_{sh} (Ω)		753.711	167.984	294.823	58.71	72.097

Table 9 Evaluated model parameters for TDM of KC200GT, Msx-60, R.T.C France solar cells, obtained by proposed IEM at different environmental conditions

Environmental condition		$G = 1000 \text{ W/m}^2 - T = 50 \text{ }^\circ\text{C}$		
Parameter	Solar cell	KC200GT	MSX-60	R.T.C France
I_{ph} (A)		8.2895	3.8615	0.7667
I_{o1} (μA)		9.664	0.391	0.1535
I_{o2} (μA)		$9.72\text{E}-4$	$1.415\text{E}-4$	0.1409
I_{o3} (μA)		$7.05\text{E}-4$	$5.157\text{E}-4$	0.8277
A_1		1.577	1.285	1.4473
A_2		1.418	1.316	1.537
A_3		1.745	1.376	1.809
R_s (Ω)		0.07549	0.155	0.0302
R_{sh} (Ω)		712.705	272.864	58.688
Parameter		$G = 600 \text{ W/m}^2 - T = 25 \text{ }^\circ\text{C}$		
Parameter	Solar cell	KC200GT	MSX-60	R.T.C France
I_{ph} (A)		4.9264	2.28	0.4566
I_{o1} (μA)		3.878	$6.808\text{E}-2$	0.0437
I_{o2} (μA)		$7.52\text{E}-4$	$8.35\text{E}-4$	0.3496
I_{o3} (μA)		$5.02\text{E}-4$	$5.96\text{E}-4$	0.7163
A_1		1.656	1.294	1.393
A_2		1.559	1.292	1.794
A_3		1.746	1.41	1.944
R_s (Ω)		0.0546	0.211	0.0492
R_{sh} (Ω)		738.15	297.095	56.771

Table 10 RMSE, MBE, AE, MAE, SAE, R^2 and TS of the proposed IEM for SDM, DDM and TDM of different solar models at ($G = 1000 \text{ W/m}^2, T = 50 \text{ }^\circ\text{C}$)

Model type	SDM			DDM			TDM		
	Solar cell	MSX-60	R.T.C France	MSX-60	R.T.C France	MSX-60	R.T.C France	MSX-60	R.T.C France
RMSE by IEM	KC200GT	0.0145	1.03E-3	0.01064	0.0104	0.0098	1.09E-3	0.0109	1.23E-3
MBE by IEM	KC200GT	0.01166	6.59E-4	0.007365	0.00552	0.006492	4.81E-4	0.00706	5.67E-4
AE by IEM	KC200GT	0.005199	4.3E-4	0.002354	0.003153	0.000881	4.28E-4	0.002394	3.95E-4
MAE by IEM	KC200GT	0.0138	9.83E-4	0.00966	0.009398	0.008744	1.023E-3	0.009918	1.113E-3
MAE by ICA [24]		-	-	0.02	-	-	1.7E-3	-	-
SAE by IEM	KC200GT	0.1521	0.10735	0.1063	0.05639	0.104933	6.14E-3	0.05951	6.676E-3
R^2 by IEM	KC200GT	0.8397	0.99986	0.91532	0.99964	0.99997	0.99997	0.944961	0.9598
TS by IEM	KC200GT	4.2219	1.85835	3.0316	1.39998	2.9151	1.09011	1.90267	1.15978
CPU Time (sec)	KC200GT	1.2902	1.298	1.409	1.493	1.615	1.451	1.641	1.604

Table 11 RMSE, MBE, AE, MAE, SAE, R^2 and TS of the proposed IEM for SDM, DDM and TDM of different solar models at ($G = 600 \text{ W/m}^2, T = 25 \text{ }^\circ\text{C}$)

Model type	SDM			DDM			TDM		
	Solar cell	MSX-60	R.T.C France	MSX-60	R.T.C France	MSX-60	R.T.C France	MSX-60	R.T.C France
RMSE by IEM	KC200GT	0.01194	0.00133	0.011868	0.010711	0.01208	1.241E-3	0.00904	1.03E-3
MBE by IEM	KC200GT	0.009278	4.81E-4	0.00553	0.004161	0.008976	2.39E-4	0.00296	3.59E-4
AE by IEM	KC200GT	0.00143	4.2E-6	0.0013	0.000042	0.000035	2.07E-4	0.00132	2.04E-4
MAE by IEM	KC200GT	0.00982	0.00921	0.0104	0.008797	0.01001	1.103E-3	0.00712	8.56E-4
MAE by ICA [24]		-	-	0.011	-	-	1.3E-3	-	-
SAE by IEM	KC200GT	0.1571	0.1013	0.1674	0.070377	0.1622	8.826E-3	0.05696	0.008557
R^2 by IEM	KC200GT	0.9998	0.9997	0.99988	0.99975	0.9998	0.99821	0.99982	0.99986
TS by IEM	KC200GT	4.77228	1.3445	2.0414	1.1153	4.2994	0.519917	0.91689	1.117
CPU Time (sec)	KC200GT	1.29	1.288	1.497	1.483	1.623	1.491	1.6203	1.6152

very less RMSE values compared to other algorithms. For KC200GT module, the results show that the RMSE obtained by IEM is $4.85\text{E}-4$ A in SDM, $4.47\text{E}-3$ A in DDM and $5.18\text{E}-3$ A in TDM. For MSX-60 module, the RMSE obtained by IEM is $4.81\text{E}-3$ A in SDM, $6.02\text{E}-3$

A in DDM and $4.944\text{E}-3$ A in TDM. For R.T.C France module, the RMSE obtained by IEM is $4.31\text{E}-4$ A in SDM, $5.325\text{E}-3$ A in DDM and $7.178\text{E}-3$ A in TDM. The IEM algorithm achieved very less execution time where the least CPU time for the IEM algorithm is achieved at

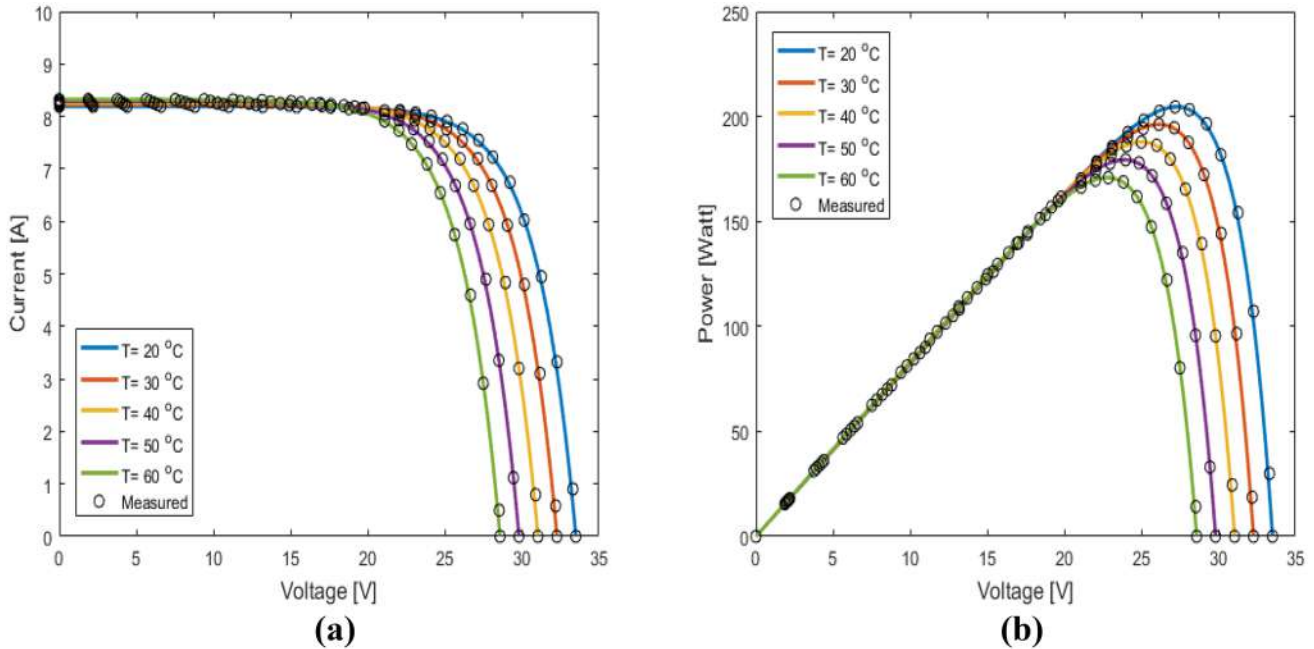


Fig. 10 a I–V curves and b P–V curves of the KC200GT by IEM under various temperatures ($G = 1000 \text{ W/m}^2$)

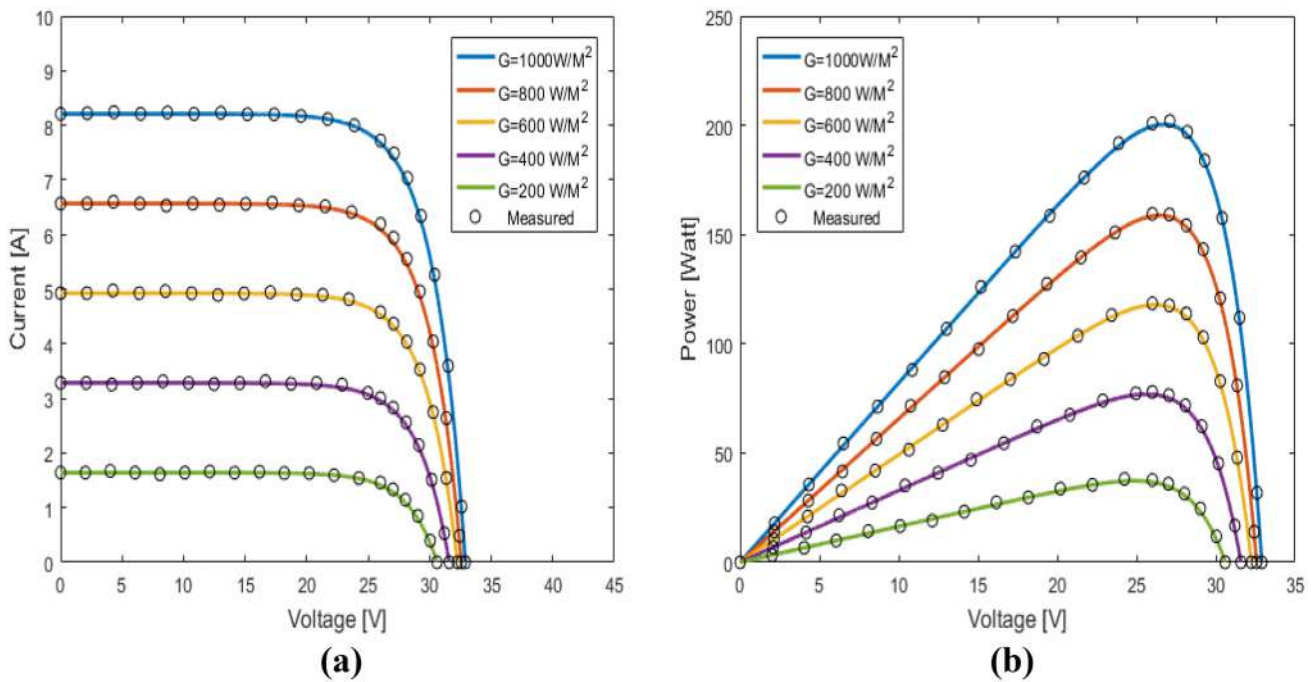


Fig. 11 a I–V curves and b P–V curves of the KC200GT by IEM for various irradiances ($T = 25^\circ\text{C}$)

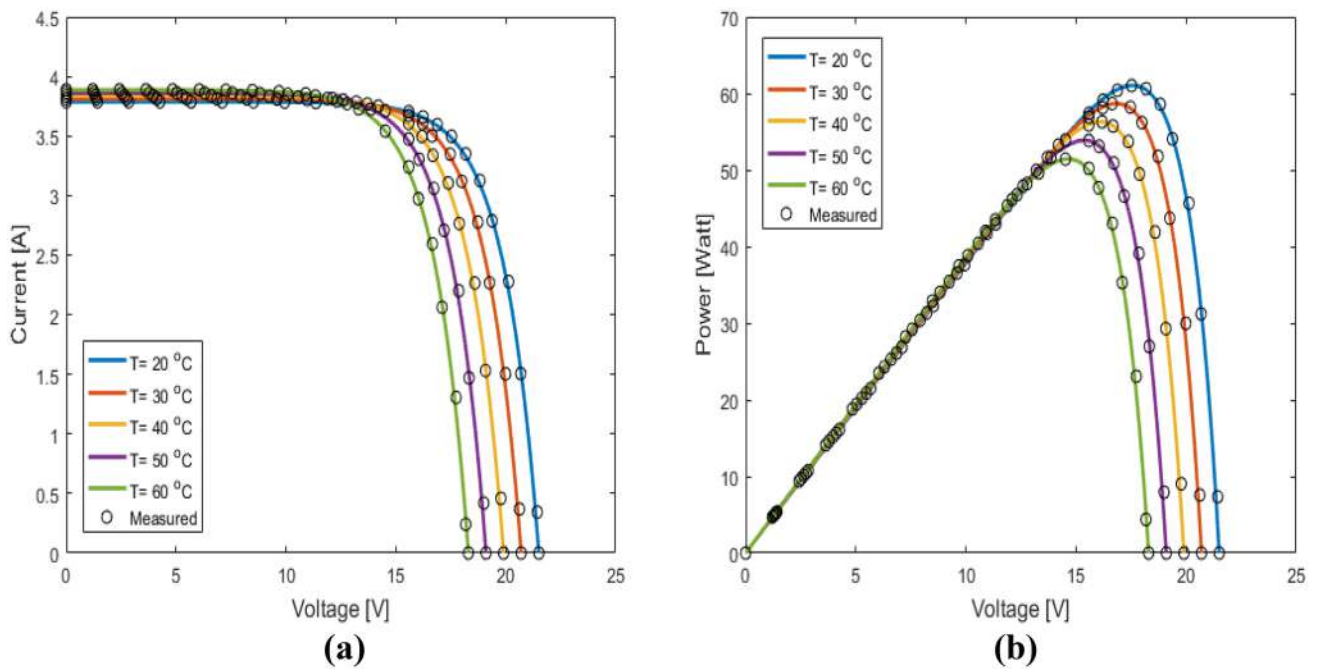


Fig. 12 a I–V curves and b P–V curves of the MSX-60 by IEM for various temperatures ($G = 1000 \text{ W/m}^2$)

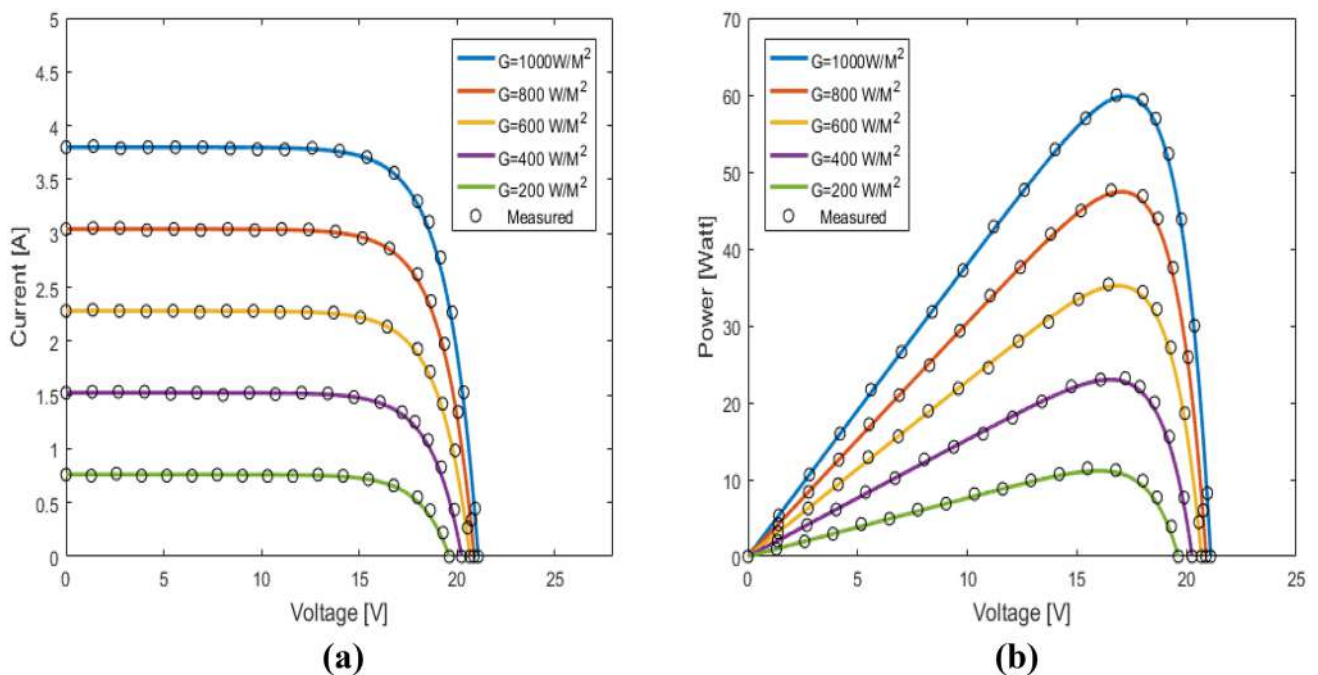


Fig. 13 a I–V curves and b P–V curves of the MSX-60 by IEM for various irradiances ($T = 25 \text{ }^\circ\text{C}$)

1.269 s for SDM R.T.C France, 1.401 s for DDM MSX-60 and 1.614 s for TDM R.T.C France. Therefore, the results clearly confirmed that the presented IEM algorithm is high accurate and more stable than different algorithms.

More results for the proposed algorithm are demonstrated in Figs. 7, 8 and 9 which describe the properties of I–V and P–V curves of the SDM for KC200GT, MSX-60 and R.T.C France. Also, it shows that both I–V and P–V curve properties from the IEM algorithm are high accurate and

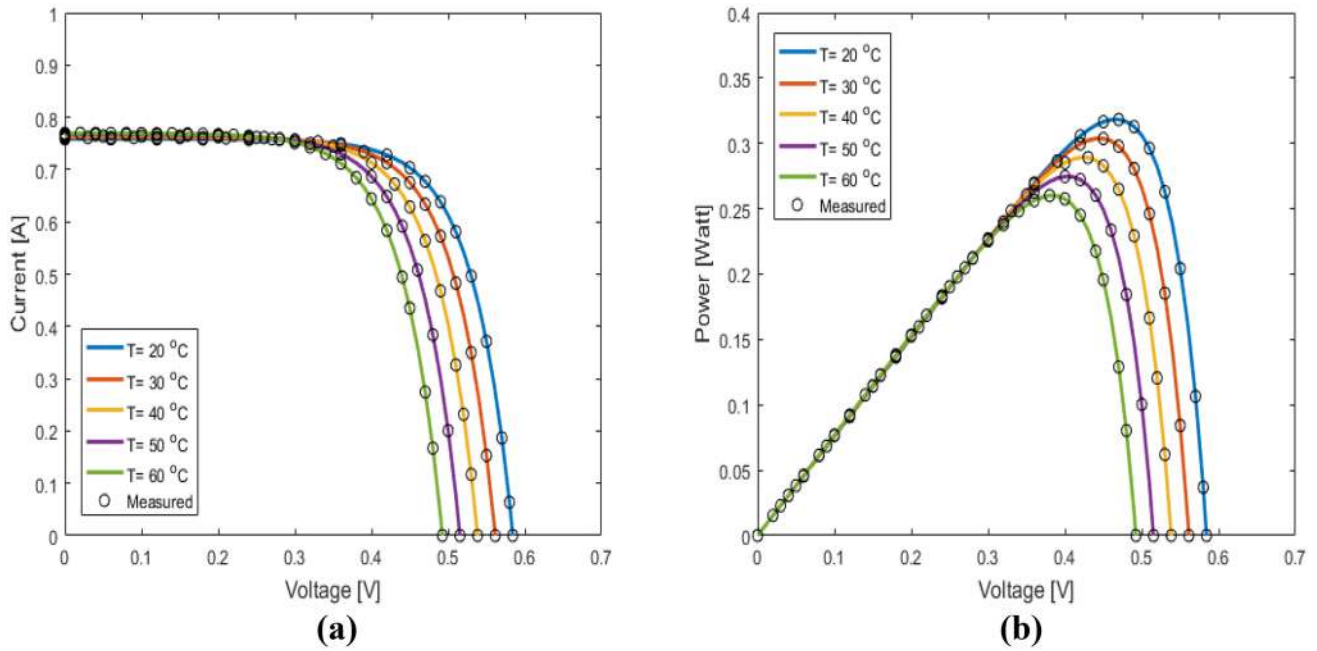


Fig. 14 **a** I–V curves and **b** P–V curves of the R.T.C France by IEM for various temperatures ($G = 1000 \text{ W/m}^2$)

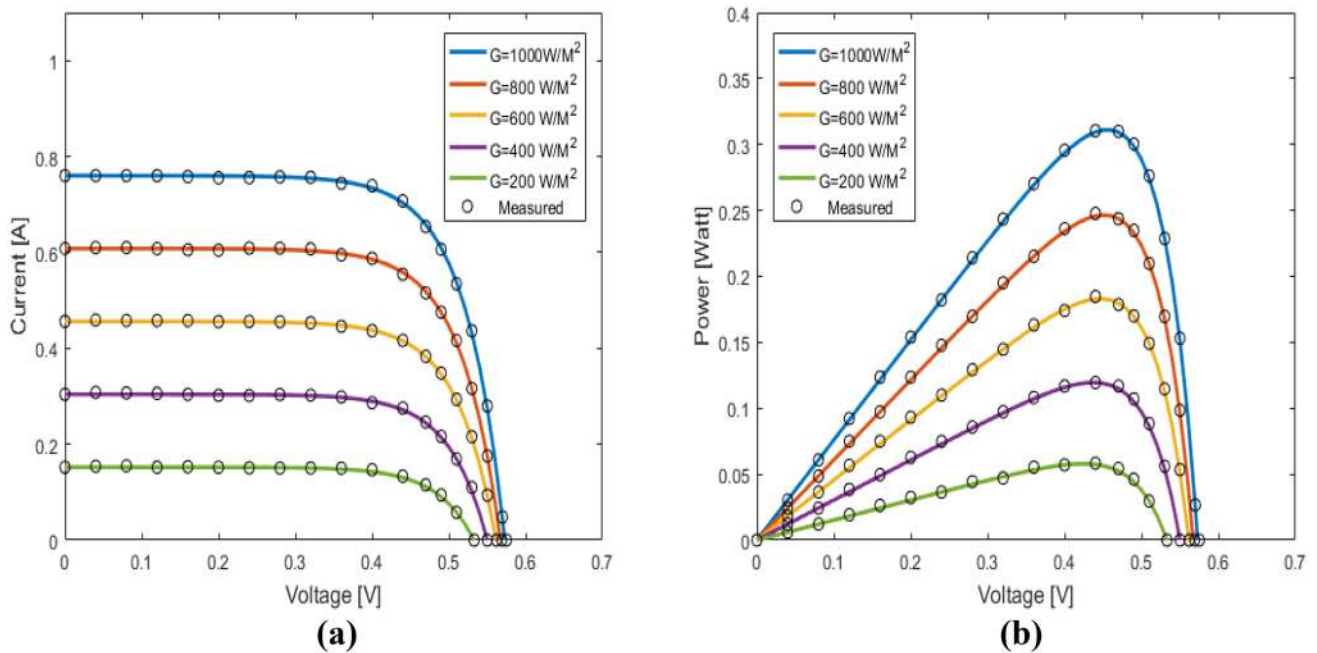


Fig. 15 **a** I–V curves and **b** P–V curves of the R.T.C France by IEM for various irradiances ($T = 25 \text{ }^\circ\text{C}$)

very close for the measured data than other algorithms. To confirm the best performance among the algorithms and the superiority of obtained results by the proposed IEM, the SDM parameters obtained for KC200GT, MSX-60 and R.T.C France which are tabulated in Tables 3, 4 and 5 are

used in simulating the corresponding I–V and P–V curves that are shown in Figs. 7, 8 and 9 in comparison with the measured data curve. The zoomed curve in these figures to clarify the extent of compatibility between the different algorithms. Referring to Figs. 7, 8 and 9, the I–V and P–V

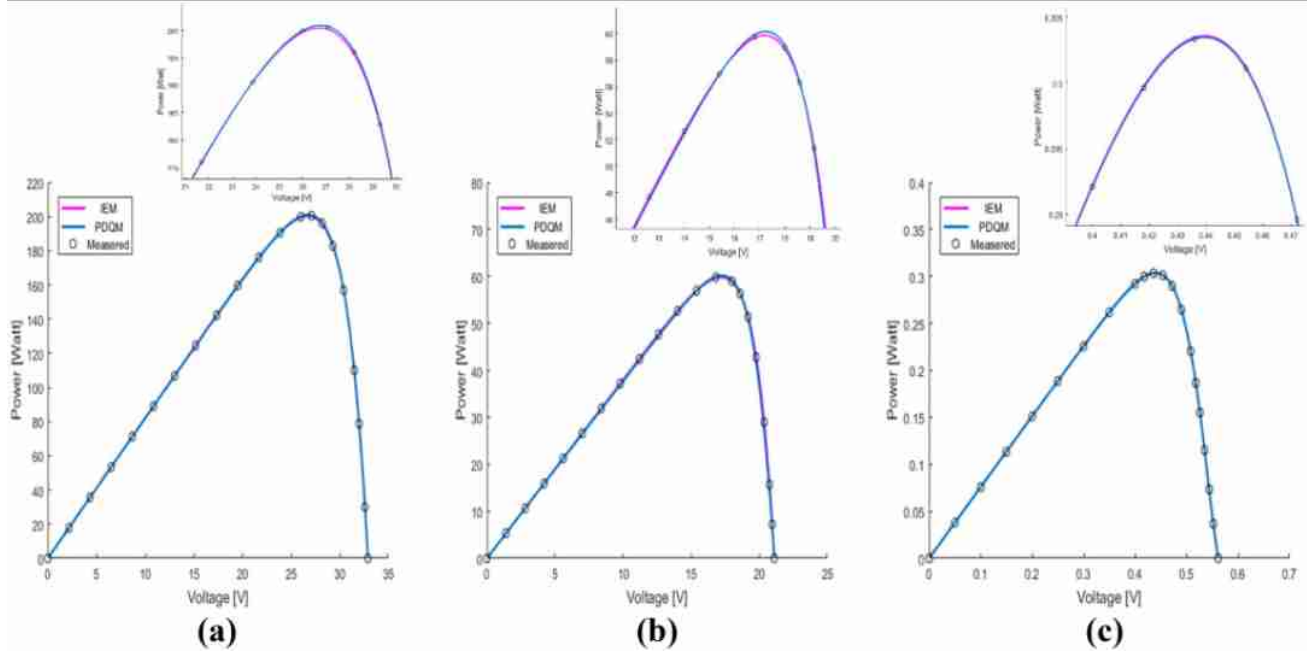


Fig. 16 The P–V characteristic curves of **a** KC200GT, **b** MSX-60 and **c** R.T.C France PV module computed via IEM and PDQM at $G = 1000 \text{ W/m}^2$, $T = 25 \text{ }^\circ\text{C}$

curves obtained via the proposed IEM are closely matching with the curve of measured data which verifies the RMSE of IEM in Table 6.

Tables 7, 8 and 9 offer the optimal values of PV model parameters at different environmental conditions. From these tables, it's obvious that the value of parameters of PV solar cell increased when irradiance G increased, while it's decreased if temperature T increased. Table 10 shows statistical errors criteria of the proposed IEM and other algorithms for SDM, DDM and TDM of different solar models at ($G = 1000 \text{ W/m}^2$, $T = 50 \text{ }^\circ\text{C}$) and Table 11 shows statistical errors criteria at ($G = 600 \text{ W/m}^2$, $T = 25 \text{ }^\circ\text{C}$). It clearly shows that the IEM achieved very less RMSE values compared to other algorithms where IEM scored the least RMSE in R.T.C France module which is $1.03\text{E-}3 \text{ A}$ in SDM. Tables 10 and 11 insist on the proposed IEM is accurate and efficient algorithm for different solar cells with different irradiances and temperatures. Also, Table 10 exhibits that least execution time for the proposed algorithm is 1.208 Sec for SDM R.T.C France, 1.409 s for DDM KC200GT solar cell and 1.604 s for TDM R.T.C France at $G = 1000 \text{ W/m}^2$, $T = 50 \text{ }^\circ\text{C}$, while Table 11 displays the least execution time for this algorithm as 1.198 Sec for SDM R.T.C France, 1.483 s for DDM MSX-60 solar cell and 1.6152 s for TDM R.T.C France at $G = 600 \text{ W/m}^2$, $T = 25 \text{ }^\circ\text{C}$. Moreover, from Tables 6, 10 and 11, the value of statistical parameters of the IEM responses show that the statistical parameters are the best when irradiance increased and the worst when temperature increased. Also, it's noticed that different statistical analyses computed

by the presented IEM for R.T.C France are the better PV module compared with KC200GT and MSX-60.

To verify the reliability of the proposed IEM, the IEM corresponding I–V and P–V characteristics have been plotted and compared with experimentally measured data under different environmental conditions. Figures 10, 11, 12, 13, 14 and 15 display the effect of temperature variations and various irradiation conditions on I–V and P–V curves via utilizing IEM algorithm. For KC200GT module, Fig. 10 displays the I–V and P–V characteristics of the proposed IEM and compared with the measured data under constant irradiance 1000 W/m^2 and various temperature conditions (20, 30, 40, 50 and $60 \text{ }^\circ\text{C}$). also, Fig. 11 displays the I–V and P–V characteristics of the proposed IEM and compared with the measured data under constant temperature $25 \text{ }^\circ\text{C}$ and different irradiance intensities (200, 400, 600, 800 and 1000 W/m^2) likewise, Figs. 12 and 13 display the I–V and P–V characteristics under different environmental conditions for MSX-60 and Figs. 14 and 15 for R.T.C France. It's obvious that the calculated I–V and P–V curves by the IEM algorithm and those of measured data are very close. Also, these figures demonstrate that the high reliability in the presented PV cell regardless of change in temperature and irradiation conditions. Moreover, these figures demonstrate the current, voltage and power are increased when increasing the irradiance. But these values decreased when the temperature increased.

Figure 16 offers that the PDQ technique is very matching with measured data than IEM for KC200GT and MSX-60

Table 12 Comparison between proposed IEM and PDQM for KC200GT solar cell under variations of temperature and irradiance conditions

T °C	G W/m ²	IEM		PDQM	
		Fill factor	Efficiency	Fill factor	Efficiency
20	1000	74.426	16.549	74.5103	16.564
	800	74.48	16.466	74.859	16.479
	600	75.33	16.417	75.36	16.423
	400	75.18	16.049	75.23	16.226
	200	74.42	15.39	74.49	15.902
30	1000	73.754	15.859	73.846	15.879
	800	74.126	15.779	74.209	15.797
	600	74.657	15.732	74.722	15.746
	400	74.506	15.324	74.585	15.556
	200	73.754	15.38	73.846	15.243
40	1000	73.025	15.162	73.135	15.185
	800	73.394	15.086	73.499	15.108
	600	73.919	15.041	74.013	15.06
	400	73.77	14.704	73.875	14.879
	200	73.025	14.101	73.135	14.578
50	1000	72.234	14.459	72.358	14.506
	800	72.599	14.387	72.72	14.411
	600	73.119	14.344	73.234	14.366
	400	72.971	14.023	73.096	14.193
	200	72.234	13.447	72.358	13.905
60	1000	71.372	13.75	71.5101	13.777
	800	71.733	13.682	71.869	13.707
	600	72.246	13.64	72.379	13.665
	400	72.101	13.335	72.242	13.5
	200	71.372	12.788	71.51	13.226
Execution time (sec)		1.291 at $G=1000$, $T=20$		0.520 at $G=1000$, $T=20$, $M=23$	

solar cells. But, for R.T.C France the IEM is the best. The zoomed curve in Fig. 16 to clarify the slight difference between PDQM and IEM with measured data at STC.

From this study, it's remarkable that the performance of the solar model is linked by determining the efficiency. Thus, Tables 12, 13 and 14 show that the effect of efficiency on the type of KC200GT, MSX-60 and R.T.C France solar cell. Also, these tables display the influence of temperature and irradiation conditions on the efficiency of solar cell. Further, we calculated the fill factor (FF) in these tables where it is one of the key values in setting the efficiency of solar PV module.

Fill factor (FF) is offered by the relation concerned [70]:

$$FF = \frac{V_m I_m}{V_{oc} I_{sc}} \quad (33)$$

So, the efficiency of solar cell can be expressed as [70]:

$$\eta = \frac{P_{max}}{P_{in}} = \frac{V_m I_m}{I A} = \frac{FF V_{oc} I_{sc}}{I A} \quad (34)$$

where I , A are the solar intensity and the area on which solar radiation falls.

These tables compared also between two methods IEM and PDQM. The best value of efficiency is 16.564 and $FF=74.5103$ at $G=1000$ W/m², $T=20$ °C, Grid points $M=23$ and CPU time=0.520 s for KC200GT solar cell by using PDQM. However, the values of efficiency and FF for KC200GT solar cell at $G=1000$ W/m², $T=20$ °C by proposed IEM are 16.549, $FF=74.426$ and CPU time = 1.291 s. For MSX-60 solar cell the value of efficiency is 12.33 and $FF=74.953$ with CPU time = 0.522 by using PDQM. But, for R.T.C France the value of efficiency is 12.522 and $FF=71.477$ with CPU time = 1.295 by using IEM algorithm. While, by using PDQM the value of efficiency is 12.476 and CPU time = 0.521. So, PDQM is the best method for determining the efficiency and fill factor. Furthermore, the values of efficiency and fill factor increased with increased irradiation conditions and decreased when increased temperature.



Table 13 Comparison between proposed IEM and PDQM MSX-60 solar cell under variations of temperature and irradiance conditions

T °C	G W/m ²	IEM		PDQM	
		Fill factor	Efficiency	Fill factor	Efficiency
20	1000	74.948	12.329	74.953	12.33
	800	75.327	12.267	75.327	12.268
	600	75.866	12.23	75.851	12.228
	400	75.758	11.957	75.711	12.081
	200	74.948	11.466	74.953	11.837
30	1000	74.327	11.849	74.336	11.85
	800	74.703	11.79	74.712	11.791
	600	75.237	11.754	75.24	11.754
	400	75.086	11.491	75.099	11.613
	200	74.327	11.019	74.336	11.376
40	1000	73.652	11.361	73.659	11.362
	800	74.024	11.304	74.035	11.305
	600	74.554	11.27	74.567	11.272
	400	74.404	11.017	74.424	11.135
	200	73.652	10.565	73.659	10.907
50	1000	72.916	10.864	72.917	10.864
	800	73.284	10.81	73.292	10.811
	600	73.808	10.777	73.824	10.78
	400	72.916	10.536	73.681	10.649
	200	72.916	10.104	72.917	10.43
60	1000	72.11	10.36	72.102	10.359
	800	72.474	10.308	72.475	10.308
	600	72.993	10.277	73	10.279
	400	72.846	10.047	72.862	10.154
	200	72.11	9.635	72.102	9.944
Execution time (sec)		1.283 at $G = 1000$, $T = 20$		0.522 at $G = 1000$, $T = 20$, $M = 23$	

Conclusion, limitations and future research

This section summarizes the aims of the study, describes what this study contributes to the field, summarizes the findings and the conclusion. Moreover, this section offers the limitations of the utilized techniques in this study and provides suggestions for future research.

Conclusion

The purpose of modelling solar modules is clearly to identify their manner in every operating conditions that presents a great role in the studies of photovoltaic electricity generating systems. This literature focused on the modelling of photovoltaic equivalent circuit based on different diode models; single-, double- and three-diode models. Two approaches of decision have been offered in order to extract accurately various specific parameters of the I–V and P–V characteristics.

These methods are An improved electromagnetism-like algorithm and differential quadrature approach are used for obtaining high accurate, speed of convergence and rapid identification of the (five, seven and nine) unknown parameters and the maximum power point of the proposed equivalent electrical circuit of solar cells. Polycrystalline (KC200GT, Solarex MSX-60) and Monocrystalline (R.T.C France) are two different kinds of PV systems have been applied for the implementing of the proposed IEM. Different operating meteorological conditions are studied in the literature, and the IEM and PDQM extracted the optimal PV parameters, fill factor and the efficiency in each case. The optimal parameters computed by the presented IEM are compared with the other solutions by various algorithms based on numerous statistical analysis (seven parameter). The computed I–V and P–V curves by the presented IEM and PDQM are compared with the experimental curves and other different algorithms. The solutions computed by the presented methodologies insist of the accuracy, efficiency



Table 14 Comparison between proposed IEM and PDQM for R.T.C France under variations of temperature and irradiance conditions

T °C	G W/m ²	IEM		PDQM	
		Fill factor	Efficiency	Fill factor	Efficiency
20	1000	71.477	12.522	71.212	12.476
	800	71.838	12.46	71.56	12.412
	600	72.352	12.422	72.141	12.386
	400	72.206	12.144	72.237	12.238
	200	71.477	11.646	71.49	11.974
30	1000	71.212	12.333	71.008	12.298
	800	71.572	12.272	71.297	12.224
	600	72.084	12.235	71.84	12.193
	400	71.939	11.961	71.936	12.047
	200	71.212	11.47	71.248	11.796
40	1000	70.938	12.142	70.789	12.117
	800	71.297	12.081	71.079	12.045
	600	71.807	12.045	71.529	11.998
	400	71.662	11.775	71.625	11.855
	200	70.938	11.292	71.029	11.623
50	1000	70.655	11.949	70.562	11.934
	800	71.012	11.89	70.852	11.863
	600	71.52	11.854	71.26	11.811
	400	71.376	11.588	71.328	11.665
	200	70.655	11.113	70.802	11.447
60	1000	70.361	11.755	70.326	11.749
	800	70.717	11.696	70.616	11.679
	600	71.223	11.661	71.025	11.628
	400	71.079	11.4	71.092	11.485
	200	70.361	10.932	70.566	11.27
Execution time (sec)		1.295 at $G = 1000$, $T = 20$		0.521 at $G = 1000$, $T = 20$, $M = 23$	

and stability of the IEM and PDQM in evaluating the PV cell optimal parameters. IEM results are compared with other parameter extraction optimization approaches like GA, SA, PS, WDO, WOA, ICA, FPSO, CSA, COA, GOA, PGJAYA and the proposed IEM achieves better RMSE values and execution time than the other techniques, where RMSE value reached $4.31E-4$ and execution time 1.269 s for SDM of R.T.C France solar system. So, the two presented schemes are the best with shortest execution time which also they are very close with measured data. Further, PDQM achieves the best value of efficiency is 16.564 and $FF = 74.5103$ at $G = 1000$ W/m², $T = 20$ °C, Grid points $M = 23$ and CPU time = 0.520 s for KC200GT solar panel.

Limitations

There are two possible limitations in this study. First, IEM algorithm is a stochastic algorithm not analytical method which is characterized by speed of computation and accurate solutions due to solving mathematical expressions for

equivalent circuit parameters based on some input data (manufacturer data) but that only for SDM, in DDM and TDM, IEM is better than analytical method because the unknown parameters are more than mathematical expressions which extracted from equivalent circuits. Second, IEM algorithm like the other stochastic algorithms in PV parameters extraction methods needs accurate measurement data to depend on the root mean square error (RMSE) between the experimental current and the computed current that was chosen as objective function; on the contrary, the analytical method.

Future research

In future research, IEM algorithm can be applied to optimize solar cell parameters on more specialized PV modules as organic, the perovskite and multi-junction. Moreover, PDQM can be employed to tracking the maximum power point in partial shading and non-uniform solar irradiance conditions in PV array and locate the local (LMPP) points and the global (GMPP) point.



Acknowledgements This work is not funded by any organization.

Data and code availability The raw and/or processed data, as well as the MATLAB code, required to reproduce the findings from this research can be obtained from the corresponding author [D.S.] upon reasonable request.

Declarations

Conflict of interest The authors declare that they have no known competing financial interests or personal relationships that could have appeared to influence the work reported in this paper.

References

- IRENA: Renewable capacity statistics 2021. <https://www.irena.org/Statistics/Statistical-Notes-and-Methodology>. (2021)
- Dambhare, M.V., Butey, B., Moharil, S.V.: Solar photovoltaic technology: a review of different types of solar cells and its future trends. *J. Phys. Conf. Ser.* **1913**, 012053 (2021). <https://doi.org/10.1088/1742-6596/1913/1/012053>
- Tamrakar, R., Gupta, A.: A Review extraction of solar cell modelling parameters. *Int. J. Innov. Res. Electr. Electron. Instrum. Control Eng.* **3**, 55–60 (2015). <https://doi.org/10.17148/ijreice.2015.3111>
- Khatib, T., Sopian, K., Kazem, H.A.: Actual performance and characteristic of a grid connected photovoltaic power system in the tropics: a short term evaluation. *Energy Convers. Manag.* **71**, 115–119 (2013). <https://doi.org/10.1016/j.enconman.2013.03.030>
- Lim, L.H.I., Ye, Z., Ye, J., Yang, D., Du, H.: A linear identification of diode models from single I-V characteristics of PV panels. *IEEE Trans. Ind. Electron.* **62**, 4181–4193 (2015). <https://doi.org/10.1109/TIE.2015.2390193>
- Yetayew, T.T., Jyothsna, T.R.: Parameter extraction of photovoltaic modules using Newton Raphson and simulated annealing techniques. In: 2015 IEEE Power, Communication and Information Technology Conference PCITC 2015—Proc., pp. 229–234 (2016). <https://doi.org/10.1109/PCITC.2015.7438166>
- Villalva, M.G., Gazoli, J.R., Filho, E.R.: Comprehensive approach to modeling and simulation of photovoltaic arrays. *IEEE Trans. Power Electron.* **24**, 1198–1208 (2009). <https://doi.org/10.1109/TPEL.2009.2013862>
- Appelbaum, J., Peled, A.: Parameters extraction of solar cells: a comparative examination of three methods. *Sol. Energy Mater. Sol. Cells* **122**, 164–173 (2014). <https://doi.org/10.1016/j.solmat.2013.11.011>
- Spall, J.C.: An overview of the simultaneous perturbation method. *Johns Hopkins Apl Tech. Dig.* **19**, 482–492 (1998)
- Yao, X., Liu, Y., Lin, G.: Evolutionary programming made faster. *IEEE Trans. Evol. Comput.* **3**, 82–102 (1999). <https://doi.org/10.1109/4235.771163>
- Ismail, M.S., Moghavvemi, M., Mahlia, T.M.I.: Characterization of PV panel and global optimization of its model parameters using genetic algorithm. *Energy Convers. Manag.* **73**, 10–25 (2013). <https://doi.org/10.1016/j.enconman.2013.03.033>
- Moldovan, N., Picos, R., Garcia-Moreno, E.: Parameter extraction of a solar cell compact model using genetic algorithms. In: Proceedings of 2009 Spanish Conference on Electron Devices, CDE'09. 00, pp. 379–382 (2009). <https://doi.org/10.1109/SCED.2009.4800512>
- Benkercha, R., Moulahoum, S., Colak, I., Taghezouit, B.: PV module parameters extraction with maximum power point estimation based on flower pollination algorithm. In: Proceedings of 2016 IEEE International Power Electronics and Motion Control Conference PEMC 2016, pp. 442–449 (2016). <https://doi.org/10.1109/EPEPEMC.2016.7752038>
- Hasanien, H.M.: Shuffled Frog leaping algorithm for photovoltaic model identification. *IEEE Trans. Sustain. Energy* **6**, 509–515 (2015). <https://doi.org/10.1109/TSTE.2015.2389858>
- Jacob, B., Balasubramanian, K., Babu, T.S., Rajasekar, N.: Parameter extraction of solar PV double diode model using artificial immune system. In: 2015 IEEE International Conference on Signal Processing, Informatics, Communication and Energy Systems SPICES 2015. (2015). <https://doi.org/10.1109/SPICES.2015.7091390>
- Low, K.S., Soon, J.J.: Photovoltaic model identification using particle swarm optimization with inverse barrier constraint. *IEEE Trans. Power Electron.* **27**, 3975–3983 (2012)
- Ebrahimi, S.M., Salahshour, E., Malekzadeh, M., Gordillo, F.: Parameters identification of PV solar cells and modules using flexible particle swarm optimization algorithm. *Energy* **179**, 358–372 (2019). <https://doi.org/10.1016/j.energy.2019.04.218>
- El-Naggar, K.M., AlRashidi, M.R., AlHajri, M.F., Al-Othman, A.K.: Simulated annealing algorithm for photovoltaic parameters identification. *Sol. Energy* **86**, 266–274 (2012). <https://doi.org/10.1016/j.solener.2011.09.032>
- Derick, M., Rani, C., Rajesh, M., Farrag, M.E., Wang, Y., Busawon, K.: An improved optimization technique for estimation of solar photovoltaic parameters. *Sol. Energy* **157**, 116–124 (2017). <https://doi.org/10.1016/j.solener.2017.08.006>
- AlHajri, M.F., El-Naggar, K.M., AlRashidi, M.R., Al-Othman, A.K.: Optimal extraction of solar cell parameters using pattern search. *Renew. Energy* **44**, 238–245 (2012). <https://doi.org/10.1016/j.renene.2012.01.082>
- Alrashidi, M.R., El-Naggar, K.M., Alhajri, M.F.: Parameters estimation of double diode solar cell model. *Eng. Technol.* **7**, 93–96 (2013)
- Omar, A., Hasanien, H.M., Elgendy, M.A., Badr, M.A.L.: Identification of the photovoltaic model parameters using the crow search algorithm. *J. Eng.* **2017**, 1570–1575 (2017). <https://doi.org/10.1049/joe.2017.0595>
- Qais, M.H., Hasanien, H.M., Alghuwainem, S., Nouh, A.S.: Coyote optimization algorithm for parameters extraction of three-diode photovoltaic models of photovoltaic modules. *Energy* **187**, 116001 (2019). <https://doi.org/10.1016/j.energy.2019.116001>
- Fathy, A., Rezk, H.: Parameter estimation of photovoltaic system using imperialist competitive algorithm. *Renew. Energy* **111**, 307–320 (2017). <https://doi.org/10.1016/j.renene.2017.04.014>
- Abd Elaziz, M., Oliva, D.: Parameter estimation of solar cells diode models by an improved opposition-based whale optimization algorithm. *Energy Convers. Manag.* **171**, 1843–1859 (2018). <https://doi.org/10.1016/j.enconman.2018.05.062>
- Oliva, D., Abd El Aziz, M., Ella Hassanien, A.: Parameter estimation of photovoltaic cells using an improved chaotic whale optimization algorithm. *Appl. Energy* **200**, 141–154 (2017). <https://doi.org/10.1016/j.apenergy.2017.05.029>
- Xiong, G., Zhang, J., Shi, D., He, Y.: Parameter extraction of solar photovoltaic models using an improved whale optimization algorithm. *Energy Convers. Manag.* **174**, 388–405 (2018). <https://doi.org/10.1016/j.enconman.2018.08.053>
- Elazab, O.S., Hasanien, H.M., Elgendy, M.A., Abdeen, A.M.: Parameters estimation of single- and multiple-diode photovoltaic model using whale optimisation algorithm. *IET Renew. Power Gener.* **12**, 1755–1761 (2018). <https://doi.org/10.1049/iet-rpg.2018.5317>
- Xiong, G., Zhang, J., Yuan, X., Shi, D., He, Y., Yao, G.: Parameter extraction of solar photovoltaic models by means of a hybrid differential evolution with whale optimization algorithm. *Sol. Energy*



- 176, 742–761 (2018). <https://doi.org/10.1016/j.solener.2018.10.050>
30. Qais, M.H., Hasanien, H.M., Alghuwainem, S.: Identification of electrical parameters for three-diode photovoltaic model using analytical and sunflower optimization algorithm. *Appl. Energy* **250**, 109–117 (2019). <https://doi.org/10.1016/j.apenergy.2019.05.013>
 31. Qais, M.H., Hasanien, H.M., Alghuwainem, S.: Parameters extraction of three-diode photovoltaic model using computation and Harris Hawks optimization. *Energy* **195**, 117040 (2020). <https://doi.org/10.1016/j.energy.2020.117040>
 32. Elazab, O.S., Hasanien, H.M., Alsaidan, I., Abdelaziz, A.Y., Muyeen, S.M.: Parameter estimation of three diode photovoltaic model using grasshopper optimization algorithm. *Energies* **13**, 497 (2020). <https://doi.org/10.3390/en13020497>
 33. Abdullah, M.N., Hussin, M.Z., Jumaat, S.A., Radzi, N.H., Awalin, L.J.: Estimation of photovoltaic module parameters based on total error minimization of I-V characteristic. *Bull. Electr. Eng. Inform.* **7**, 425–432 (2018). <https://doi.org/10.11591/eei.v7i3.1274>
 34. Soliman, M.A., Hasanien, H.M., Alkuhayli, A.: Marine predators algorithm for parameters identification of triple-diode photovoltaic models. *IEEE Access* **8**, 155832–155842 (2020). <https://doi.org/10.1109/ACCESS.2020.3019244>
 35. Diab, A.A.Z., Sultan, H.M., Aljendy, R., Al-Sumaiti, A.S., Shoyama, M., Ali, Z.M.: Tree growth based optimization algorithm for parameter extraction of different models of photovoltaic cells and modules. *IEEE Access* **8**, 119668–119687 (2020). <https://doi.org/10.1109/ACCESS.2020.3005236>
 36. Oliva, D., Cuevas, E., Pajares, G.: Parameter identification of solar cells using artificial bee colony optimization. *Energy* **72**, 93–102 (2014). <https://doi.org/10.1016/j.energy.2014.05.011>
 37. Chen, X., Xu, B., Mei, C., Ding, Y., Li, K.: Teaching–learning–based artificial bee colony for solar photovoltaic parameter estimation. *Appl. Energy* **212**, 1578–1588 (2018). <https://doi.org/10.1016/j.apenergy.2017.12.115>
 38. Nunes, H.G.G., Pombo, J.A.N., Mariano, S.J.P.S., Calado, M.R.A., Felipe de Souza, J.A.M.: A new high performance method for determining the parameters of PV cells and modules based on guaranteed convergence particle swarm optimization. *Appl. Energy* **211**, 774–791 (2018). <https://doi.org/10.1016/j.apenergy.2017.11.078>
 39. Yu, K., Qu, B., Yue, C., Ge, S., Chen, X., Liang, J.: A performance-guided JAYA algorithm for parameters identification of photovoltaic cell and module. *Appl. Energy* **237**, 241–257 (2019). <https://doi.org/10.1016/j.apenergy.2019.01.008>
 40. Haider, H.T., Muhsen, D.H., Mahdi, H.F.: Electromagnetism-like algorithm-based parameters estimation of double-diode PV-module model. *IOP Conf. Ser. Mater. Sci. Eng.* **1076**, 012002 (2021). <https://doi.org/10.1088/1757-899x/1076/1/012002>
 41. Tan, J.D., Koh, S.P., Tiong, S.K., Ali, K., Koay, Y.Y.: An electromagnetism-like mechanism algorithm approach for photovoltaic system optimization. *Indones. J. Electr. Eng. Comput. Sci.* **12**, 333–340 (2018). <https://doi.org/10.11591/ijeecs.v12.i1.pp333-340>
 42. Ridha, H.M., Gomes, C., Hizam, H.: Estimation of photovoltaic module model's parameters using an improved electromagnetic-like algorithm. *Neural Comput. Appl.* **32**, 12627–12642 (2020). <https://doi.org/10.1007/s00521-020-04714-z>
 43. Shu, C.: *Differential Quadrature and its Application in Engineering*. Springer, London (2000)
 44. Du, H., Lim, M.K., Lin, R.M.: Application of generalized differential quadrature method to structural problems. *Int. J. Numer. Methods Eng.* **37**, 1881–1896 (1994). <https://doi.org/10.1002/nme.1620371107>
 45. Wu, T.Y., Liu, G.R.: Differential quadrature as a numerical method to solve differential equations. *Comput. Mech.* **24**, 197–205 (1999). <https://doi.org/10.1007/s004660050452>
 46. Shongwe, S., Hanif, M.: Comparative analysis of different single-diode PV modeling methods. *IEEE J. Photovolt.* **5**, 938–946 (2015). <https://doi.org/10.1109/JPHOTOV.2015.2395137>
 47. Et-torabi, K., Nassar-eddine, I., Obbadi, A., Errami, Y., Rmaily, R., Sahnoun, S., El Fajri, A., Agunaou, M.: Parameters estimation of the single and double diode photovoltaic models using a Gauss-Seidel algorithm and analytical method: a comparative study. *Energy Convers. Manag.* **148**, 1041–1054 (2017). <https://doi.org/10.1016/j.enconman.2017.06.064>
 48. Ma, T., Gu, W., Shen, L., Li, M.: An improved and comprehensive mathematical model for solar photovoltaic modules under real operating conditions. *Sol. Energy* **184**, 292–304 (2019). <https://doi.org/10.1016/j.solener.2019.03.089>
 49. Kyocera: Kyocera KC200GT high efficiency multicrystal photovoltaic module. <https://www.datasheets.com/en/part-details/kc200gt-kyocera-62747508>. (2011)
 50. Solarex: Solarex MSX-60 photovoltaic module. <https://www.digchip.com/datasheets/parts/datasheet/922/MSX60.php>. (1997)
 51. Easwarakhanthan, T., Bottin, J., Bouhouch, I., Boutrif, C.: Nonlinear minimization algorithm for determining the solar cell parameters with microcomputers. *Int. J. Sol. Energy* **4**, 1–12 (1986). <https://doi.org/10.1080/01425918608909835>
 52. Benouareth, I., Khelil, K., Abadlia, I.: Photovoltaic panels extraction under evolutionally algorithms: a comparative study. In: *International conference on automatic control, telecommunications and signals (ICATS15)*, pp. 1–7 (2015)
 53. Hussein, A.M.: Extraction of unknown parameters of PV modules. In: *2017 9th IEEE-GCC Conference and Exhibition*, pp. 1–9 (2018). <https://doi.org/10.1109/ieegcc.2017.8448245>
 54. Ayang, A., Wamkeue, R., Ouhrouche, M., Salomé, N.E., Djongyang, N.: Parameters estimation of single-diode photovoltaic module/array using least square estimator: a comparative study. In: *5th International conference on control & signal processing (CSP-2017), Proceeding of engineering and technology–PET*, vol. 26. pp. 122–123 (2017)
 55. Čalasan, M., Jovanović, D., Rubežić, V., Mujović, S., Dukanović, S.: Estimation of single-diode and two-diode solar cell parameters by using a chaotic optimization approach. *Energies* **12**, 4209 (2019). <https://doi.org/10.3390/en12214209>
 56. Kumar, M., Kumar, A.: An efficient parameters extraction technique of photovoltaic models for performance assessment. *Sol. Energy* **158**, 192–206 (2017). <https://doi.org/10.1016/j.solener.2017.09.046>
 57. Ishaque, K., Salam, Z., Taheri, H.: Accurate MATLAB simulink PV system simulator based on a two-diode model. *J. Power Electron.* **11**, 179–187 (2011). <https://doi.org/10.6113/JPE.2011.11.2.179>
 58. Elbasat, A.A., Ali, H., Abd-El Sattar, M.: Novel seven-parameter model for photovoltaic modules. *Sol. Energy Mater. Sol. Cells* **130**, 442–455 (2014). <https://doi.org/10.1016/j.solmat.2014.07.016>
 59. Jervase, J.A., Bourdoucen, H., Al-Lawati, A.: Solar cell parameter extraction using genetic algorithms. *Meas. Sci. Technol.* **12**, 1922–1925 (2001). <https://doi.org/10.1088/0957-0233/12/11/322>
 60. Chin, V.J., Salam, Z.: A new three-point-based approach for the parameter extraction of photovoltaic cells. *Appl. Energy* **237**, 519–533 (2019). <https://doi.org/10.1016/j.apenergy.2019.01.009>
 61. Hamid, N.F.A., Rahim, N.A., Selvaraj, J.: Solar cell parameters identification using hybrid Nelder-Mead and modified particle swarm optimization. *J. Renew. Sustain. Energy* **8**, 015502 (2016). <https://doi.org/10.1063/1.4941791>
 62. Gnetchejo, P.J., Essiane, S.N., Ele, P., Wamkeue, R., Wapet, D.M., Ngoffe, S.P.: Enhanced vibrating particles system algorithm for



- parameters estimation of photovoltaic system. *J. Power Energy Eng.* **07**, 1–26 (2019). <https://doi.org/10.4236/jpee.2019.78001>
63. AlRashidi, M.R., AlHajri, M.F., El-Naggar, K.M., Al-Othman, A.K.: A new estimation approach for determining the I-V characteristics of solar cells. *Sol. Energy* **85**, 1543–1550 (2011). <https://doi.org/10.1016/j.solener.2011.04.013>
64. Chen, S., Gholami Farkoush, S., Leto, S.: Photovoltaic cells parameters extraction using variables reduction and improved shark optimization technique. *Int. J. Hydrogen Energy* **45**, 10059–10069 (2020). <https://doi.org/10.1016/j.ijhydene.2020.01.236>
65. Elazab, O.S., Hasanien, H.M., Elgendy, M.A., Abdeen, A.M.: Whale optimisation algorithm for photovoltaic model identification. *J. Eng.* **2017**, 1906–1911 (2017). <https://doi.org/10.1049/joe.2017.0662>
66. Diab, A.A.Z., Sultan, H.M., Do, T.D., Kamel, O.M., Mossa, M.A.: Coyote optimization algorithm for parameters estimation of various models of solar cells and PV modules. *IEEE Access* **8**, 111102–111140 (2020). <https://doi.org/10.1109/ACCESS.2020.3000770>
67. Yousri, D., Babu, S., Allam, D., Ramachandaramurthy, V.K., Eteiba, M.B.: Fractional chaotic ensemble particle swarm optimizer for identifying the single, double, and three diode photovoltaic models' parameters. *Energy* **195**, 116979 (2020). <https://doi.org/10.1016/j.energy.2020.116979>
68. Batzelis, E.I., Papathanassiou, S.A.: A method for the analytical extraction of the single-diode PV model parameters. *IEEE Trans. Sustain. Energy* **7**, 504–512 (2016). <https://doi.org/10.1109/TSTE.2015.2503435>
69. Niu, Q., Zhang, H., Li, K.: An improved TLBO with elite strategy for parameters identification of PEM fuel cell and solar cell models. *Int. J. Hydrogen Energy* **39**, 3837–3854 (2014). <https://doi.org/10.1016/j.ijhydene.2013.12.110>
70. Chander, S., Purohit, A., Sharma, A., Nehra, S.P., Dhaka, M.S.: A study on photovoltaic parameters of mono-crystalline silicon solar cell with cell temperature. *Energy Rep.* **1**, 104–109 (2015). <https://doi.org/10.1016/j.egy.2015.03.004>

Publisher's Note Springer Nature remains neutral with regard to jurisdictional claims in published maps and institutional affiliations.

Springer Nature or its licensor holds exclusive rights to this article under a publishing agreement with the author(s) or other rightsholder(s); author self-archiving of the accepted manuscript version of this article is solely governed by the terms of such publishing agreement and applicable law.





Rapid optimization of 3D printed sediment microbial fuel cells

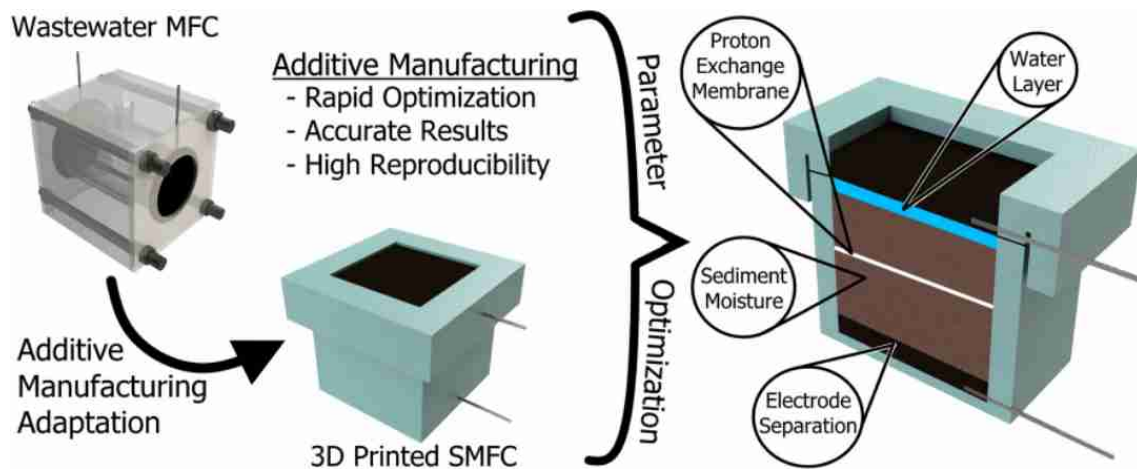
Andrew Kim¹ · Amanda Simson¹

Received: 24 June 2022 / Accepted: 20 August 2022 / Published online: 6 September 2022
© The Author(s), under exclusive licence to Islamic Azad University 2022

Abstract

Sediment microbial fuel cells (SMFCs) are promising sustainable technologies for their ability to remediate sediment while converting waste into usable energy. While SMFCs are low-cost and easily constructed, they have not been widely adopted because unoptimized SMFCs exhibit low power densities. This work used additive manufacturing (AM), commonly called 3D printing, to facilitate the optimization of SMFCs for maximum bioelectricity generation. Various SMFC parameters, including sediment moisture, the presence of a water layer, the use of a proton exchange membrane (PEM), and electrode separation, are investigated using SMFCs designed for reliable and rapid testing. Daily rehydration was critical for stable bioelectric output, with higher moisture content increasing power density by as much as 150%. SMFCs with no water layer between the sediment and cathode exhibited significantly lower internal resistances that increased power density by 72–134%. The PEM increased power density by approximately 3% but made the SMFC more susceptible to dehydration. Shortening the electrode separation distance from 53 to 33 mm decreased internal resistance and the proton diffusion distance, resulting in the highest areal and volumetric power densities. The champion SMFC exhibited an average open-circuit voltage of 661 mV and a maximum areal and volumetric power density of 3.26 mW m^{-2} and 98.9 mW m^{-3} .

Graphical abstract



Keywords Sediment microbial fuel cell · Additive manufacturing · 3D printing · Power optimization · Freshwater Sediment

✉ Amanda Simson
amanda.simson@cooper.edu

¹ Department of Chemical Engineering, The Cooper Union for the Advancement of Science and Art, New York, NY 10003, USA

Introduction

Besides well-known renewable energy sources, including solar, wind, and hydro, there has been growing interest in biologically derived energy [1]. Microbial fuel cells (MFCs) are bioreactors that typically use anaerobic bacteria



to oxidize organic substrates usually found in waste. The metabolism of electrogenic bacteria commonly found in wastewater and sediment, such as *Rhodospirillum rubrum* and the *Geobacter* specie, releases electrons outside of the cell that can be harvested as electricity [2]. Sediment MFCs (SMFCs) are MFCs that have their anodes buried under a layer of sediment, often from lakes [3], oceans [4], municipal waste [5], or compost [6]. SMFCs are promising sustainable technologies because they can remediate sediment while generating electricity [7]. SMFCs are also affordable, low maintenance, and operate under ambient conditions [8]. Thus, SMFCs have been used to power sensors in remote environments [9], charge portable electronics [10], electrochemically detect toxic substances [11], purify municipal sewage [2], and degrade landfill leachate [12].

The power densities of solid-phase SMFCs (3–1100 mW m^{-2} [13]) are often lower than liquid-phase wastewater MFCs (100–3000 mW m^{-2} [14]) because SMFCs often have higher internal resistance and slower proton diffusion, among other factors [15]. However, SMFCs may be optimized to produce more energy than some wastewater MFCs by controlling SMFC parameters, such as the electrode material [16], surface area [17], and sediment feed [18]. The electrode separation distance is important to optimize, as decreasing separation reduces internal resistance but risks oxygen diffusion to the anode [19]. For example, Sajana et al. found that decreasing the distance between the anode and cathode from 100 to 50 cm increased the power density by 10% (3.96 mW m^{-2}) [20]. Similarly, many electrode separation studies examine only SMFCs with a column of water above the sediment instead of SMFCs with only sediment [21–25]. SMFCs without a water column, such as soil MFCs [26] and compost MFCs [27], are seldom compared to SMFCs with a liquid layer in the same work. Wolinska et al. determined that having a column of water above the sediment resulted in a 21-times-lower power output (1.5 mW m^{-2}) than the sediment-only SMFC (32 mW m^{-2}) [28]. Because sediments in streams, farms, and rivers undergo periodic flooding, more work should be done to compare SMFCs with submerged and non-submerged sediment. Also, most SMFC studies often forego the PEM by assuming that the costs are prohibitive and do not compare the performance of their SMFCs with and without a PEM [29–31]. The few studies that compare the performance of PEM SMFCs and membrane-less SMFCs examine SMFCs with sediment submerged under water, such as the recent work by Liu et al. that found that a PEM improved power density by around 20% [32]. Lastly, most SMFC studies investigate lake [3], marine [4], municipal waste [5], or polluted river sediment [33], but few study urban stream sediment [34]. The power-generating performance of SMFCs using sediment in metropolitan areas should be investigated and improved to implement this renewable technology in energy-hungry

cities. This work addresses the aforementioned shortcomings of current SMFC research by comparing the power output of an SMFC using urban stream sediment in submerged vs. non-submerged conditions and with vs. without a PEM with non-submerged sediment.

Additive manufacturing (AM), colloquially called 3D printing, has gained much interest in engineering research for enabling design freedom and rapid prototyping [35]. AM has been utilized to fabricate unique electrodes for MFCs with customizable surface area, shape, and roughness to maximize biofilm growth and substrate diffusion [36]. For example, Jannelli et al. 3D printed conductive PLA electrodes in a two-chamber wastewater MFCs, yielding a maximum power density of 18.6 mW m^{-2} [37]. Also, AM allows the fabrication of unique and complex reactor designs that minimize assembly complexity, increasing the economic viability of MFCs. Papaharalabos et al. 3D printed a uniquely shaped wastewater MFC reactor aptly called the “Twist n’ Play” that did not require glues nor screws to assemble [38]. More recently, a 3D-printed SMFC reactor was designed by Nguyen et al. in a wedge shape to be easily pushed into muddy soil for immediate use, exhibiting a maximum power density of 485.2 mW m^{-2} [30]. The aforementioned MFC studies used AM to replace specific SMFC components or create novel SMFC reactors that improved the economic value of SMFCs. In contrast, this study uses AM to design an SMFC reactor that can rapidly test key parameters with low cost, high reproducibility, and accessible data collection.

In this work, SMFC reactors were 3D printed to test the effects of sediment moisture, a water layer above the sediment, PEM use, and electrode separation. The goals of the reactor design were to minimize production cost, construction/assembly time, and complexity in gathering electrical performance data. The testing-focused SMFC reactors were used to optimize the potential power output of stream sediment in batch operation without artificial feeding. Despite the unique composition of each sediment sample, clear trends emerged from testing each of the four variables, highlighting how each parameter should be controlled for the highest possible energy production.

Materials and methods

Sample collection

Sediment samples were collected from the Bulgwangcheon Stream (37°35'40.9 “N 126°54'54.1 “E) in northwest Seoul, South Korea. The 9 km freshwater stream flows from the foot of the Bukhan mountain and is a tributary of the Hangang River. The water depth was approximately 30 cm above the sediment. The top 5 cm of the stream sediment

was discarded, and the lower layer sediment was collected. The sediment was distributed equally in three different reactors. Each of the four studied variables was tested using two different sediment samples collected at the same location, reported herein as SED 1 and SED 2. It is important to note that the SED 1 and SED 2 used to test each variable are unique (see Table S.2 in the Supplementary Information provided). For example, SED 1 used in optimizing moisture content is different from SED 1 used in optimizing electrode separation. Because samples were freshly collected before each trial in February–April, the weather conditions on the collection day differed between sediment samples, with ambient temperatures ranging between 6 and 17 °C.

SMFC construction and operation

An Anet A8 3D printer was used to print the SMFC reactors using biocompatible PLA plastic (see Table S.1 in the Supplementary Information for print settings). 5 mm-thick graphite felt and 89 µm-thick Nafion PFSA N-1135 membrane were acquired from SinoPro (Korea). The graphite felt and Nafion PEM were cut into 3.5 cm squares, and the graphite felt was connected to stainless steel current collectors. The rectangular prism-shaped SMFC reactors have dimensions of $3.5 \times 3.5 \times 4.5 \text{ cm}^3$ ($1 \times w \times h$), with the height variable during the electrode separation optimization. SMFCs were rehydrated with 2 mL of tap water every day unless otherwise stated. A detailed description of SMFC construction, optimization, and operation is available in Supplementary 2.

Sediment and energy analysis

Sediment moisture was measured using a 4-in-1 soil survey instrument that measured moisture in 5 discrete ranges: less than 5%, 5–10%, 10–20%, 20–30%, and more than 30%. Sediment moisture was measured by placing the probe at the center of the SMFC reactor volume before rehydration. Key measures that define an MFC's energy performance include its open-circuit voltage (V_{OC}), closed-circuit voltage (V_{CC}), and power density [39]. All voltage measurements were done using an AstroAi AM330 digital multimeter. The circuit setup may be found in the supplementary information provided. The areal and volumetric power densities were calculated by dividing the power of the SMFC by the surface area of the cathode and the internal volume of the reactor, respectively.

$$P = V_{CC}^2 * \frac{R_{ext}}{(R_{int} + R_{ext})^2} \quad (1)$$

Equation 1 shows the power output of a standard voltage divider circuit derived using Watt's law and Ohm's law, with

the closed-circuit voltage (V_{CC}), external resistance (R_{ext}), and internal resistance (R_{int}). Based on Eq. 1, maximum power is achieved when R_{int} equals R_{ext} . By treating the SMFC as a non-ideal voltage source in a voltage divider circuit, the internal resistance of the SMFC was approximated as equivalent to the external resistance that yielded maximum power output [40].

Results and discussion

Additive manufacturing

A commonly used horizontal, membrane-less wastewater MFC design was converted to a vertical SMFC using 3D printing as shown in Fig. 1a. One factor that was studied was the time required to print and assemble the horizontal and vertical SMFC reactors. The 3D printed horizontal SMFC required over 2 h to 3D print and 30 min to assemble. In contrast, the final vertical SMFC required 25% less time to 3D print than the horizontal reactor and took under 10 min to assemble. The vertical design also made it easy to sample the sediment, obtain electronic performance data, and investigate the effects of various SMFC parameters (Fig. 1b). In addition to being much faster to produce and convenient to sample from, the vertical reactor did not suffer from water leakage. Because the printed plastic was flexible, the horizontal SMFC flexed and could not seal well under high pressure (even with silicone gaskets), resulting in water leakage. As shown in Fig. 1c, the horizontal SMFC exhibited a sharp V_{OC} decline in under 20 h, whereas the vertical SMFC reactor had a steady rise in V_{OC} over 100 h (Fig. 1c), likely due to the horizontal SMFC rapidly dehydrating due to water leakage.

SMFC optimization

Sediment moisture

SMFCs running in batch operation with an air-exposed cathode can experience dehydration. The effects of sediment moisture were tested on two sediment samples using two identical SMFC reactors, with only one reactor receiving daily rehydration. Figure 2a, b presents the V_{OC} of the dehydrated and rehydrated SMFCs. For the first sediment sample, both SMFCs exhibited nearly identical V_{OC} s in the first 45 h. However, the V_{OC} of the dehydrated SMFC became unstable between 45 and 75 h and decreased sharply afterward, whereas the rehydrated SMFC exhibited a steadily increasing V_{OC} even after 140 h. Similarly, for the second sediment sample, the initial V_{OC} s of the dehydrated and rehydrated reactors were almost identical for the first 20 h. Afterward, the V_{OC} of the rehydrated SMFC continued to grow for 20

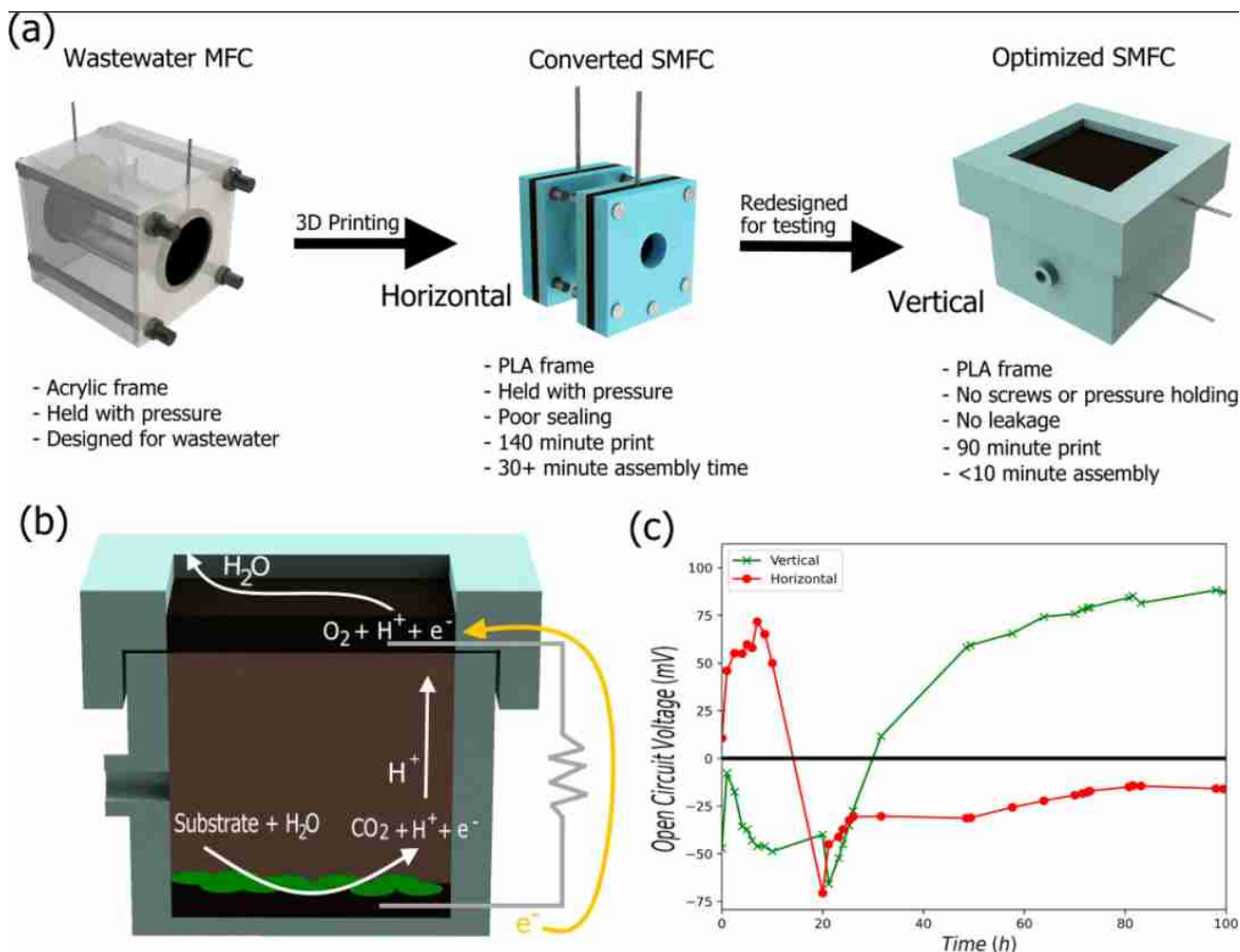


Fig. 1 **a** The development of the final vertical SMFC design using AM, starting with a common wastewater MFC reactor [41]. **b** Schematic illustration of SMFC operation and how different variables may

be easily tested. **c** V_{OC} vs. Time for the horizontal, converted SMFC and the vertical, optimized SMF

more hours, while the V_{OC} of the dehydrated SMFC stabilized, resulting in a 22% higher V_{OC} for the rehydrated SMFC (Fig. 2b). Dehydration was more significant in the first sediment sample than in the second, as indicated by the sharp V_{OC} decrease in Fig. 2a that is not present in Fig. 2b. These results are interesting because it suggests that the rate of dehydration was significantly different between the two sediment samples, possibly due to differences in sediment composition, ambient temperature, relative humidity, or other variables between the two trials. For example, silty sediment with high clay content would retain moisture better than gravel-like sediment with large grains. Nevertheless, the lower V_{OC} for dehydrated SMFCs is likely due to decreased bacteria growth and metabolism, as the metabolic pathway for bacterial extracellular electron transport requires water [42]. Moreover, the viability of stream sediment bacteria depends on high moisture content because such bacteria

adapted for survival in water-saturated sediment, resulting in less biofilm growth on the dehydrated SMFC in this work.

Low sediment moisture makes the sediment less effective for power generation by decreasing sediment conductivity and proton diffusion [43]. Both the dehydrated and rehydrated SMFCs had sediment moisture contents above 30% even after 5 days, which was sufficient to result in similar internal resistances around 1.5 k Ω in the second sediment sample (Fig. 2c). Li et al. similarly found small differences in internal resistance for sediments with moisture contents above 30%, whereas decreasing to 16.7% moisture increased internal resistance by fivefold [43]. Because sufficient sediment moisture is required to maintain high sediment conductivity, rehydration would be vital for outdoor SMFCs under direct sunlight. Despite having similar internal resistances, the power output of the rehydrated SMFC was more than two times greater for both sediment samples (Fig. 3d) at

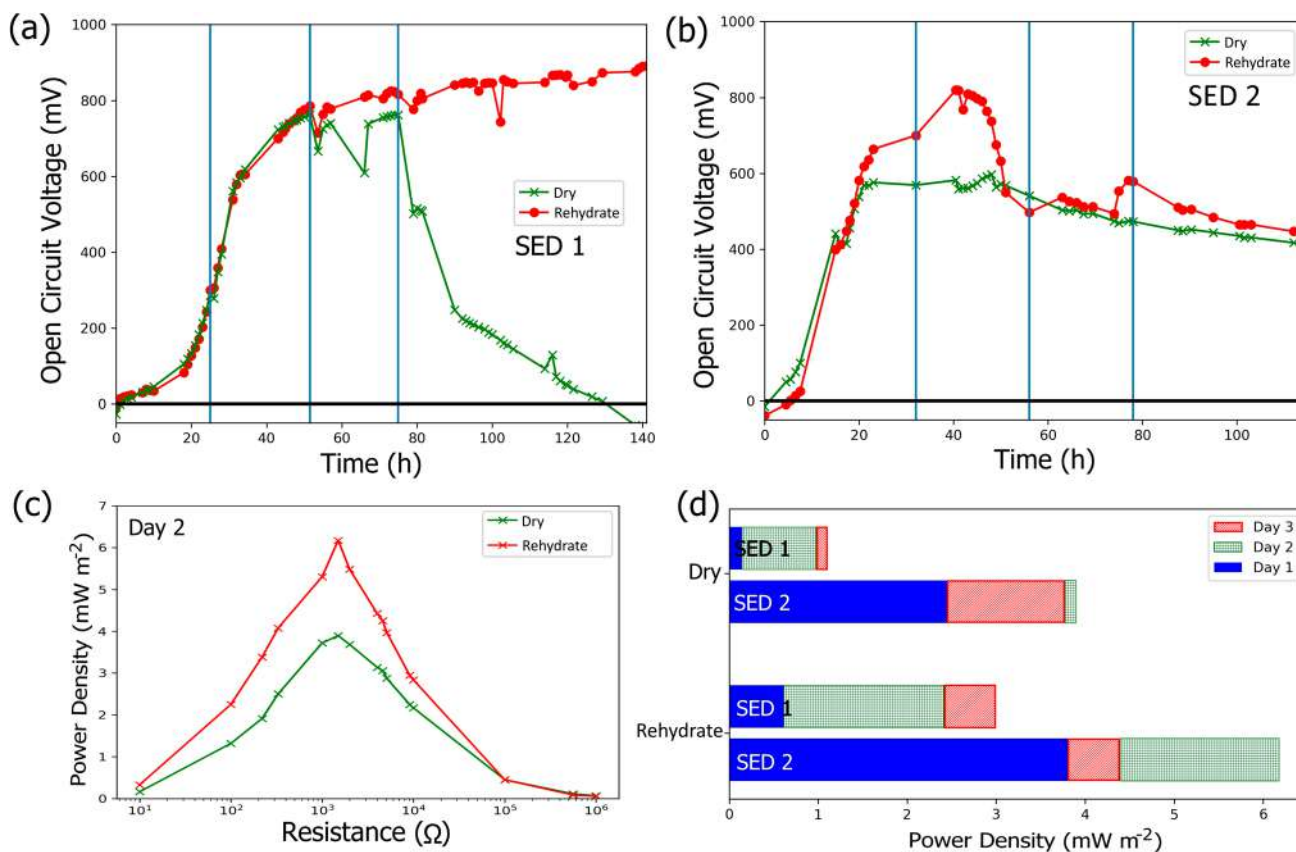


Fig. 2 The V_{OC} vs. Time of the dehydrated and rehydrated SMFCs for **a** SED 1 and **b** SED 2. The vertical blue lines when the rehydrated SMFC was rehydrated. **c** Power vs. Resistance curve for SED 2 after

d Maximum areal power density for SMFC reactors with different initially added water content for SED 1 and 2

3.90 (SED 1) and 6.17 mW m^{-2} (SED 2), likely due in part to increased proton diffusion from the anode to the cathode with greater sediment moisture content. Similarly, other studies of batch SMFCs hydrated their reactors to preserve moisture contents of around 70% for maximum power output [42, 44]. The decrease in power output with dehydration is consistent even with PEM implementation (Sect. 3.2.3) and different electrode separations (Sect. 3.2.4). Thus, rehydration is essential for generating maximum power output by increasing bacterial activity, decreasing proton diffusion, and maintaining high sediment conductivity.

Water layer

The effect of a water layer between the sediment and air cathode on SMFC performance was examined by adding different amounts of freshwater between the sediment and cathode. SMFCs with 15 mL (W-15) or 30 mL (W-30) of water-modeled benthic SMFCs, which are commonly used in lakes and marine environments [3]. In contrast, SMFCs with no water layer (W-0), such as compost SMFCs [45], are non-benthic but may be flooded to become temporarily

benthic. As shown in Fig. 3a,b, the benthic SMFC with the tallest freshwater column exhibited the lowest average V_{OC} and V_{OC} growth rate in both sediment samples. For the benthic SMFCs, decreasing the water layer from 30 to 15 mL resulted in a 40% (SED 1) and 86% (SED 2) higher average V_{OC} . This poor performance for the SMFC with the most water (W-30) compared to the SMFC with a smaller water layer (W-15) was likely due to the thin 5-mm sediment layer on the anode for W-30, which may not have had the initial bacterial population nor substrate to develop a thick biofilm. The non-benthic SMFC (W-0) had slightly higher V_{OC} s than W-15 for both trials (772 compared to 730 mV for SED 1 and 694 compared to 693 mV for SED 2). The similarly high V_{OC} s for the SMFCs with thicker sediment layers further suggested that sufficient sediment was necessary for high V_{OC} output. The V_{OC} growth rate was sensitive to differences in sediment, suggested by W-15 having a similar growth rate to the benthic W-30 SMFC for the first sediment sample but non-benthic SMFC in the other sediment sample. However, the non-benthic SMFCs consistently had the highest V_{OC} and V_{OC} growth rates, suggesting that sufficient sediment is favorable for initial biofilm growth on the anode.

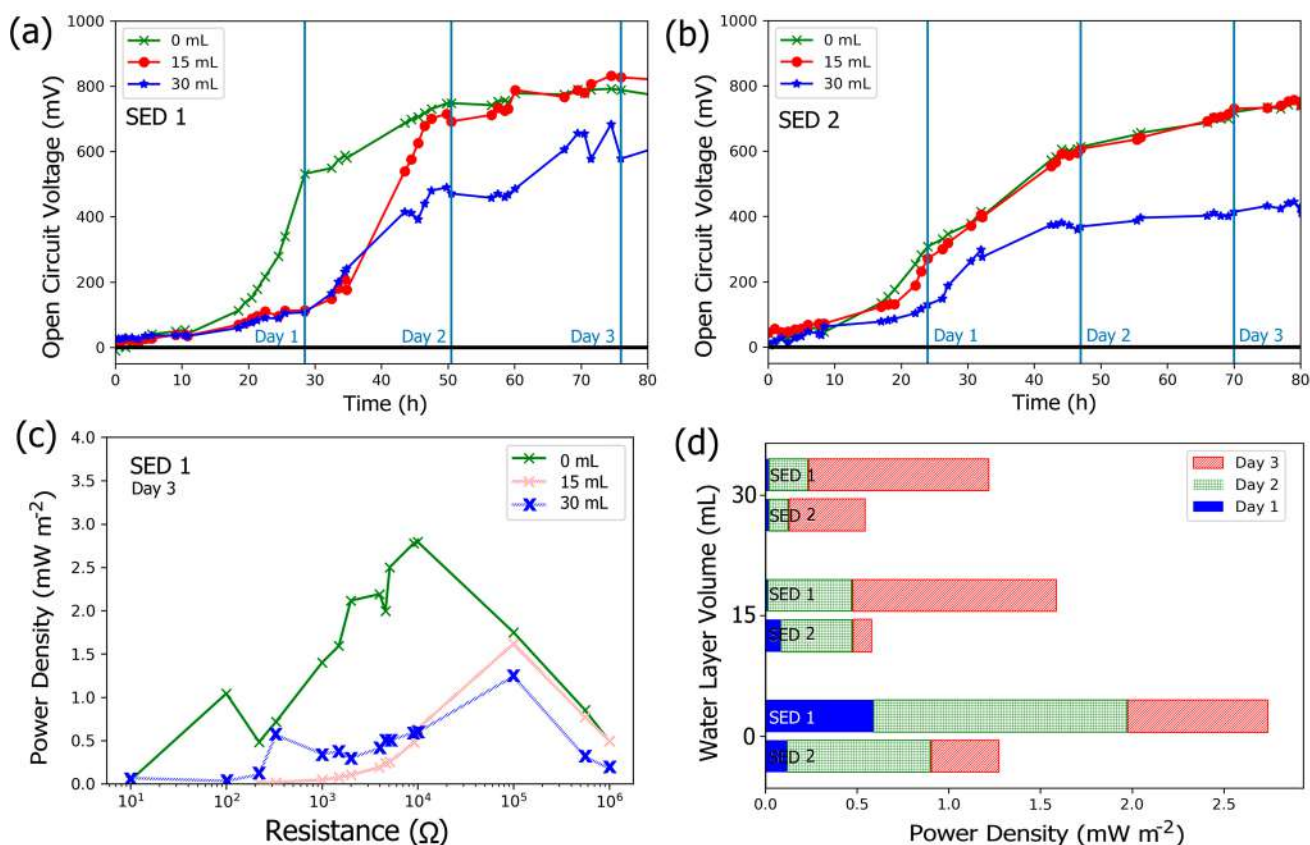


Fig. 3 The V_{OC} over 80 h for W-0, W-15, and W-30 for **b** SED 1 and **a** SED 2. The vertical blue lines indicate when the V_{CC} were measured. **c** Power vs. resistance curve for SED 1 measured after 2 days.

d Maximum areal power density for SED 1 and 2. The power density on Day 1 may not be clearly visible for W-15 and W-30 due to the small power generation

In addition to producing higher V_{OC} , the non-benthic SMFCs produced higher power output than benthic SMFCs (with a freshwater layer). The maximum power density of the non-benthic SMFC was 2.79 (SED 1) and 1.30 mW m⁻² (SED 2), about 50% higher than W-15 and more than 100% higher than W-30 for both sediment samples (Fig. 3d). Figure 3b shows how the internal resistance of the non-benthic SMFC was 10 kΩ compared to 100 kΩ for both benthic SMFCs, likely because the freshwater was less conductive than the moist sediment. Freshwater sources exhibit low conductivities between 1 and 10 μS cm⁻¹ because of low ion content [46], whereas sediment has many soluble salts that increase sediment conductivity to between 10 μS cm⁻¹ and 1000 mS cm⁻¹ [47]. Li et al. found that sediment with a low 2.86% salt content and 37.5% moisture content exhibited a high conductivity of 12 000 μS cm⁻¹, more than 1000 times more conductive than freshwater [43].

Another reason why the benthic SMFC performed worse than the non-benthic SMFC is that the benthic SMFCs may have had less oxygen diffusion at the air cathode. The floating air cathodes of the benthic SMFCs were observed to be partially underwater, especially after rehydration, reducing

the number of active sites for reduction with atmospheric oxygen. In contrast, the graphite felt cathode in the non-benthic SMFC did not sink into the dense sediment, maximizing the active sites for a higher reduction reaction rate, which is critical for higher power output [39]. Similarly, Muaz et al. claimed that their SMFC experienced reduced power output due to reduced oxygen diffusion when the graphite felt cathode in their SMFC was partially covered by sludge [48]. Overall, the results in this section suggest that power-generation-focused SMFCs using sediment from freshwater sources may be more efficient in non-benthic configurations.

Proton exchange membrane

The necessity of a PEM for SMFC operation was investigated by comparing three identical SMFCs, two with a Nafion PEM and one without a PEM. The effects of a PEM were investigated because SMFCs often forego the separation membrane due to high cost and limited improvement to SMFC performance [49]. Moreover, membranes are prone to biofouling [50], which contradicts how SMFCs are designed

to maximize bacterial growth. As expected, the two reactors with the PEMs (Mem A & Mem B) had nearly identical V_{OC} curves for both sediment samples (Fig. 4a, b). The membrane-less SMFCs had similarly high average V_{OC} s of above 740 mV (about 6% lower than the membrane SMFCs) with about 20% lower V_{OC} growth rates, suggesting excellent biofilm growth, albeit slightly less than the membrane-containing SMFCs.

The power output of the SMFCs with a PEM was not substantially higher than the membrane-less SMFCs. The 30% higher power output for membrane SMFCs in the first sediment sample was likely due to improved electronic isolation with the PEM. However, the improvement was limited because the PEM did not lower the high internal resistance of the SMFCs (Fig. 4c). Interestingly, in the second sediment sample, one of the membrane SMFCs produced only a 3% higher power density than the membrane-less SMFC, whereas the other membrane SMFC had 67% higher power. This inconsistency may have been due to small differences in the sediment composition and water content between the membrane reactors. Regardless, the minor and uncertain

benefits to power output when using a PEM make it difficult to justify implementation in low-cost SMFCs.

While implementing a PEM improved the power output of the SMFCs, the PEM-containing reactor was more sensitive to dehydration. This was done by comparing the performance of two dehydrated reactors, one with a PEM and one without, and one rehydrated SMFC with a PEM. As shown in Fig. 4d, the dehydrated membrane-less SMFC retained nearly 100% of their maximum V_{OC} even after 60 h for SED 1, whereas the dehydrated membrane SMFC exhibited an erratic V_{OC} and a low V_{OC} retention of about 60%. The rehydrated membrane also maintained its V_{OC} , as expected (see Sect. 3.2.1 on the effects of rehydration). Similarly, for the other sediment samples, the rehydrated membrane SMFC retained nearly 100% of its V_{OC} for 50 h, whereas the dehydrated membrane SMFC had about 0% retention after only 33 h, underscoring the necessity of high sediment moisture content. Unlike the first sediment sample, the dehydrated membrane-less SMFC suffered from dehydration in the second sediment sample, reemphasizing how sediment properties affect

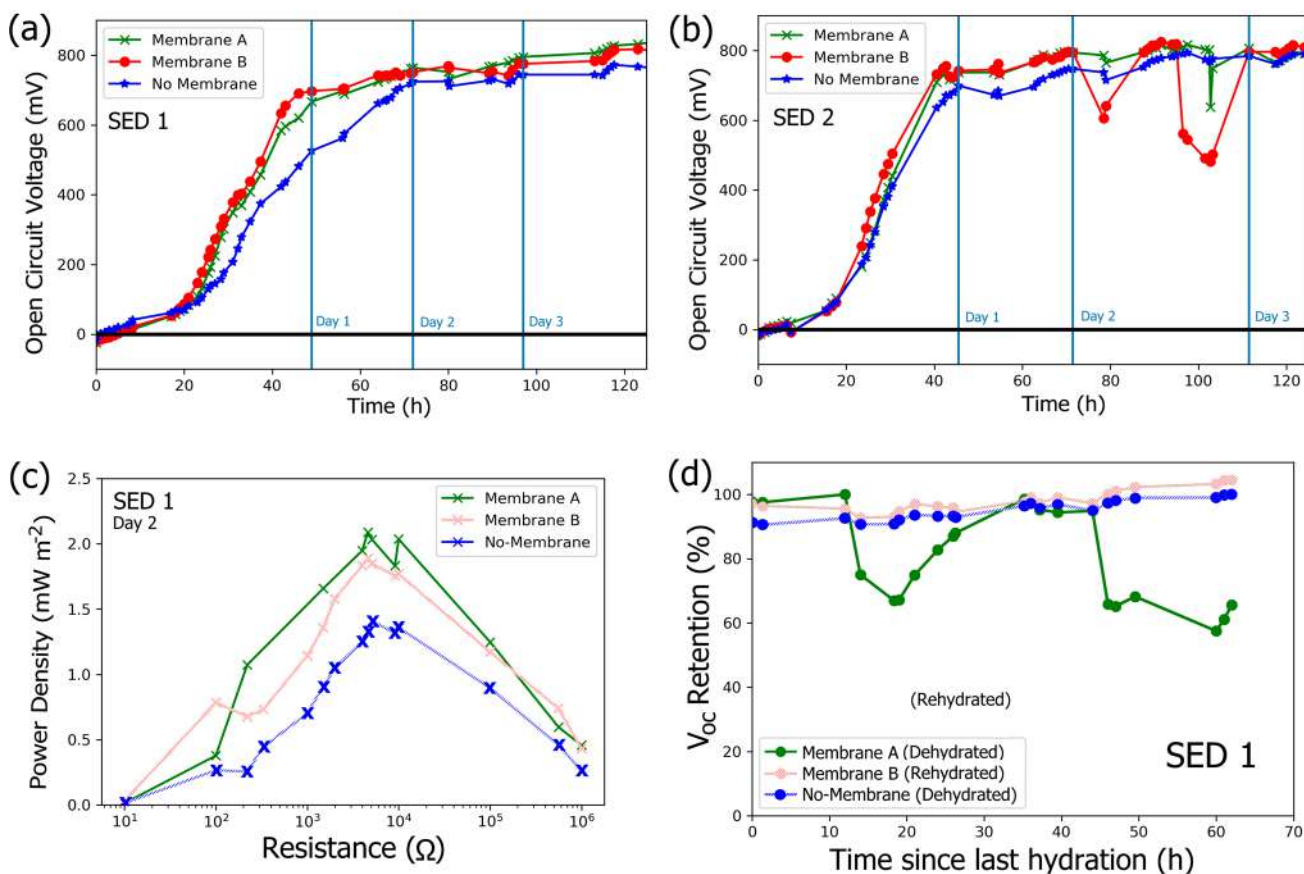


Fig. 4 a V_{OC} over 100 h for SED 1 and b SED 2 for SMFCs with or without a PEM. The vertical blue lines indicate when the V_{CC} were measured. c Power vs. resistance curve for SED 1 measured

after 2 days. d The percent retention of V_{OC} for SED 1 after stopping hydration for one of the membrane SMFCs and the membrane-less SMFC

the dehydration rate. For SED 2, the dehydrated membrane-less SMFC retained its V_{OC} significantly longer, with 10% V_{OC} retention after 60 h (twice as long as the dehydrated membrane SMFC). The sensitivity to dehydration was caused by the Nafion PEMs exhibiting significantly reduced proton conductivity when dehydrated [51]. Thus, SMFCs operating using dryer sediment, which may not be regularly rehydrated, could perform worse with a PEM than without the membrane. Even though high sediment moisture is required for good proton conduction, SMFCs with high freshwater content suffer from higher internal resistances, as discussed in Sect. 3.2.2. Future work should be done to see whether internal resistance or proton conduction is more significant to optimize. Overall, the PEM increased V_{OC} and power output, though not substantially, but the membrane may lead to more dehydration-sensitive SMFCs. Given the additional cost and potential for fouling, these results suggest that an SMFC may forgo the membrane with minimal loss of performance.

Electrode separation

The effect of electrode separation distance on SMFC performance was examined by using AM to fabricate reactors with heights of 33, 43, and 53 mm. As shown in Fig. 5a, b, all three reactors (33-SMFC, 43-SMFC, and 53-SMFC, respectively) exhibited similarly high average V_{OC} s above 760 mV for SED 1 and 620 mV for SED 2. The high V_{OC} s for all reactors suggest good biofilm formation and oxygen isolation at the anode. There was no clear relationship between electrode separation distances and V_{OC} at the tested distances.

While there was no correlation between electrode separation distance and V_{OC} , SMFCs with shorter electrode separation distances had the highest power densities. The shortest SMFC had the highest areal and volumetric power densities for both sediment samples, which decreased with increasing electrode separation distance (Fig. 5c). The high power density of the shortest SMFC is partly due to its small internal resistance of 4.6 k Ω compared to those for the 43-SMFC (5.1 k Ω) and 53-SMFC (100 k Ω) measured for SED 1. Moreover, larger distances

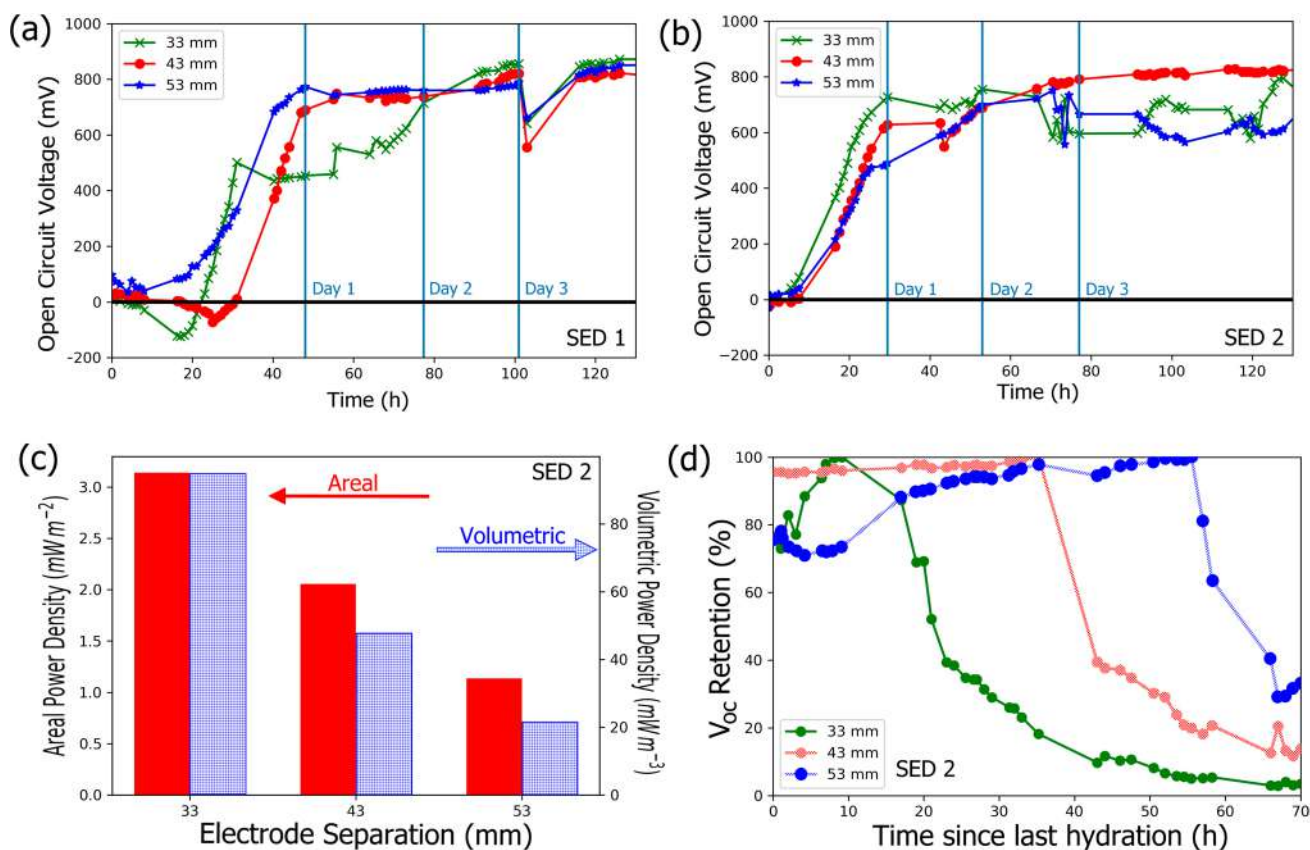


Fig. 5 V_{OC} over 130 h for SMFC reactors with varying electrode separation distances of 33, 43, and 53 mm for **a** SEM 1 and **b** SEM 2. The vertical blue lines indicate when the V_{CC} were measured. **c** The

maximum areal and volumetric power densities of SMFCs with varying heights measured after 3 days for SED 2. **d** The V_{OC} retention after stopping daily rehydration for SMFCs with different heights



between the anodes have been shown to yield lower power output due to the longer proton transport distance between the anode and cathode [52]. Because changing the reactor height also changed the SMFC volume, the volumetric power density more clearly demonstrated that the SMFC power output did not scale with increased sediment volume, with the shortest reactor having more than 4 times the power density of the tallest reactor for SED 2 at 95.1 mW m^{-3} . Thus, multiple smaller SMFCs connected in series or parallel may be more efficient for bioelectricity generation than a larger SMFC reactor with the same total volume. For example, Prasad et al. showed that connecting five SMFCs in series into seven parallel rows (a total of 35 reactors) consolidated the energy output enough to charge a 12 V battery for 6.5 min [53]. The SMFCs used by Prasad et al., however, were large 1L plastic containers with excess sediment below the anode because the anode to air cathode distance was minimized to 3 cm [53]. The results of the small SMFCs used in this work suggest that as long as there is sufficient sediment for biofilm growth, many smaller volume SMFCs with short electrode distances can potentially be used to yield a greater power output at the same total volume because the smallest SMFCs exhibited the highest power densities.

The effect of electrode separation distance on an SMFC's sensitivity to dehydration was investigated by subjecting the different height reactors to dehydration. The taller SMFCs exhibited better resistance against dehydration, as shown in Fig. 5d, while the shortest reactor had a V_{OC} retention decrease to 40% after 20 h of dehydration. Increasing the reactor height to 43 and 53 mm doubled and tripled the time to reach 40% V_{OC} retention, respectively. Results from the other sediment samples showed similar trends, with 33-SMFC having a 0 mV after only 25 h of dehydration, whereas the 53 mm reactor exhibited almost 100% V_{OC} retention. Because of the air-exposed cathode, water naturally evaporated from the sediment below the cathode and slowly progressed toward the anode. The results suggest that dehydration near the cathode is not as significant as dehydration near the anode, likely because the biofilm on the anode requires water to live and metabolize. Therefore, a larger electrode separation distance increases the time before the anode is affected by dehydration. As discussed in Sect. 3.2.3, high proton conduction through a PEM requires high sediment moisture near the membrane. Since taller SMFCs take longer to dehydrate, PEMs may be more effectively implemented in taller SMFCs. Despite having smaller power densities, taller SMFCs may be more resilient against dehydration, which may be important for batch applications like compost-based SMFCs.

Optimization of all parameters

AM was used to reliably investigate the effects of sediment moisture, a water layer, PEM use, and electrode separation in SMFC power output. The performance of SMFCs investigated in this work is summarized in Fig. 6. AM enabled the rapid optimization of an SMFC that outperformed some SMFCs in the literature, summarized in Table 1. Overall, the various SMFC parameters investigated in this work had V_{OC} s (374–824 mV) and power densities ($0.55\text{--}6.17 \text{ mW m}^{-2}$) well within the expected ranges of 300–1160 mV and $1\text{--}78 \text{ mW m}^{-2}$ (Table 1). While the specific performance improvements after optimizing each variable were expected to differ based on the sediment sample tested, clear trends emerged that suggest that the power output of SMFCs can be significantly improved in general by controlling various operation parameters.

The SMFCs in this study fall toward the lower end of the expected power density range due to the simple SMFC operation and stream sediment properties. For one, the study was conducted in batch mode without artificial feeding and aeration, unlike many of the high-energy producing SMFCs [28, 29, 33]. Moreover, the high-power SMFCs in Table 1 used sediment from polluted areas with high concentrations of substrates that facilitate electrogenic bacterial metabolism [48, 54], whereas this investigation used sediment from a clean freshwater stream. Despite such limitations, optimizing various parameters in these simple SMFCs led to power densities comparable to those produced by more complex SMFCs [20, 55, 56]. Thus, optimizing SMFC parameters is an essential step in improving SMFC performance, and AM enables the rapid optimization of such critical SMFC parameters tailored for the specific sediment used.

For future research, the design of the SMFC should be modified to allow sediment sampling and rehydration without requiring the cathode lid to be removed. The effects of feeding the SMFC with different waste organic materials, like banana peels or coffee grounds, should also be investigated as fed SMFCs have reported higher power output [28, 29, 33]. Moreover, the capacity of SMFCs to recycle and safely decompose organic waste should be studied. One of the largest limitations of this study was the lack of biological analytical equipment, which restricted the depth of analysis. Future work should be done using tools that can identify bacteria species, population size, sediment composition, and chemical oxygen demand (COD) removal, which may provide insights into the few unexplained results in this work. An SMFC should be redesigned to allow as much continuous and non-intrusive biological data collection as possible. Lastly, a long-term study should be conducted to see the effects of the different parameters at month-long or year-long time scales.



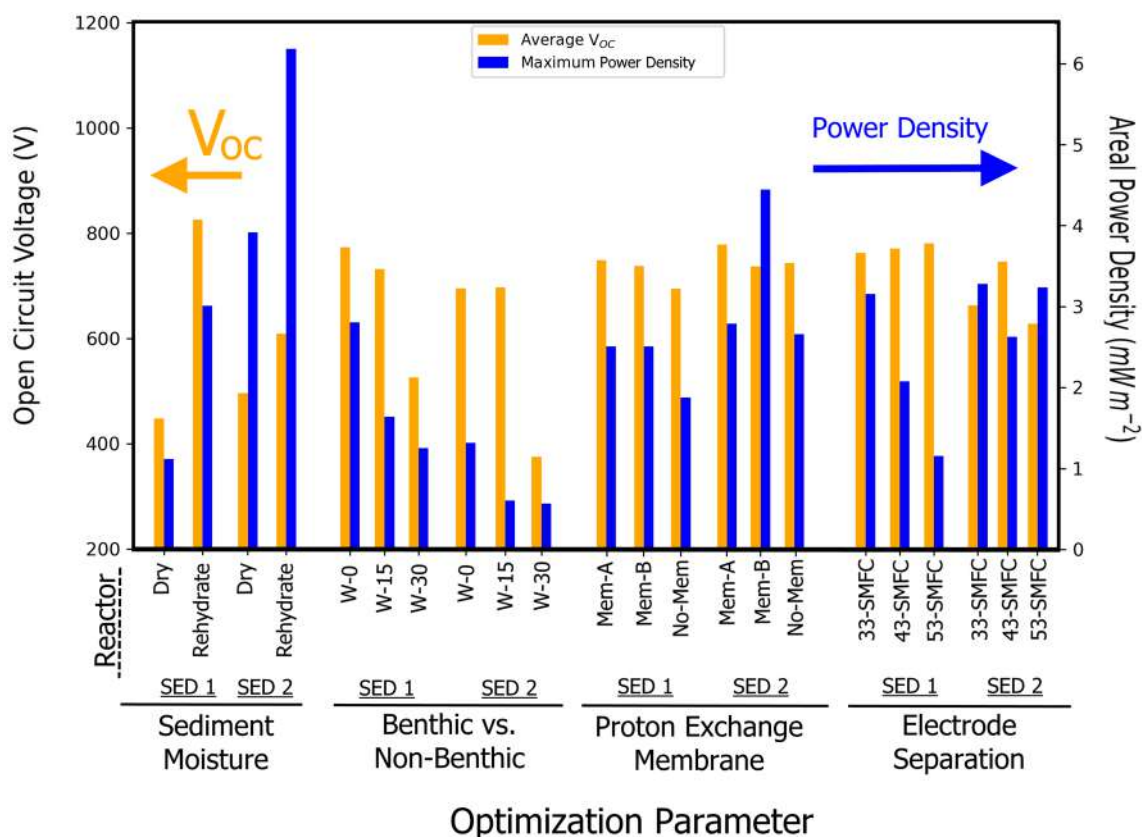


Fig. 6 The steady-state V_{OC} , maximum V_{OC} , and maximum areal power density of various SMFC reactors based on various optimization parameters: water/sediment ratio, PEM, and reactor height

Conclusion

Additive manufacturing was used to design an SMFC for investigating the effects of sediment moisture, water overlayer, PEM usage, and electrode separation on SMFC power output. This work uniquely used 3D printing as a tool for scientific investigation, with iterative modifications to standard wastewater MFC reactors resulting in a final design that emphasized fast assembly, low cost, and reliable rapid testing. Also, unlike most SMFC research, this study investigated the power-generating potential of SMFCs using urban stream sediment in one of the largest cities in the world. The results of this investigation found that SMFCs require sufficient moisture content to increase biofilm growth and proton conduction, while moisture content above 30% did not significantly affect internal resistance. Daily rehydration was required for stable SMFC V_{OC} output. SMFCs with a freshwater layer between the air cathode and sediment

performed up to 125% worse than sediment-only SMFCs, likely due to the water increasing internal resistance and decreasing oxygen reduction. SMFCs with PEMs exhibited slightly improved bioelectrical performance by as little as 3% compared to membrane-less SMFCs. However, SMFCs with PEMs exhibited shorter lifespans in batch operation due to higher sensitivity to dehydration. Shorter electrode separation distances increased power by shortening the proton diffusion distance and decreasing internal resistance, indicated by the almost 2-times-higher power density with a 33 mm separation than a 53 mm separation. The optimized SMFC exhibited a power density of $3.26 mW m^{-2}$ ($98.9 mW m^{-3}$) and an average V_{OC} of 661 mV. However, because the power output of the SMFCs was dependent on the sediment sample, a membrane-less, non-benthic, 43-mm-separated (mostly optimized) SMFC exhibited the highest power output of $6.17 mW m^{-2}$ ($143.6 mW m^{-3}$). Hence, rapid preliminary SMFC optimization via AM-facilitated testing should be performed for the specific sediment under investigation.

Table 1 The performance and key features of SMFCs ordered by increasing power densities

Sediment	Feed	Electrode	Water Column	Average V_{OC} (mV)	Internal Resistance (Ω)	Power Density (mW m^{-2})	Highlight	Ref
Lake	Acetate	Carbon paper	Yes	387	14.6 k	1	SMFC was tested without optimization	[3]
Flower soil	–	Zn/Cu (Cat/An)	Yes	1160	–	2	Differing anode/cathode material	[55]
Aquaculture pond	Aquaculture water	Graphite plates	Yes	740	415	4	Three stacked anodes with large 90 cm electrode separation	[20]
Activated sludge	Nutrition solution	Graphite felt	Yes	750	25 k	6	Pt catalyst coated anode	[57]
Rice paddy	–	graphite felt	Yes	701	156	6	Operated directly in a rice paddy field	[57]
Aquaculture pond	Cellulose	Carbon felt	Yes	580	1950	7	Sediment artificially enriched with cellulose	[56]
River	Polluted river water	Carbon felt	Yes	546	320	25	Continuous Flow operation with plants	[33]
River	Waste water	Carbon fiber brush	Yes	560	215	26	Floating macrophyte with aerated pump	[54]
Peaty Soil	Glucose	Graphite plates	No	372 ^{*a}	–	32	3 anodes and 5 cathodes	[28]
Sludge	–	Graphite felt	No	927 ^{*b}	–	41	Moisture, pH, electrode distance, and temperature optimized	[48]
Industrial Waste Area	Glucose	Graphite felt	Yes	300 ^{*c}	1000	78	Two chamber SMFC with aerated cathode side	[29]
Urban Stream	–	Graphite felt	No	607	1500	6	3D printed SMFC	This work optimization

* V_{CC} measured instead of V_{OC} with external resistances of ^a1 Ω , ^b220 Ω , ^c1000 Ω

Supplementary Information The online version contains supplementary material available at <https://doi.org/10.1007/s40095-022-00524-2>.

Acknowledgements This research did not receive any specific grant from funding agencies in the public, commercial, or not-for-profit sectors.

Author contributions Andrew Kim was involved in conceptualization, methodology, investigation, formal analysis, visualization, writing — original draft, writing — review and editing. Amanda Simson contributed to conceptualization, visualization, writing — review and editing, funding acquisition, supervision.

Data availability Most of the data generated or analyzed during this study are included in this published article and its supplementary information files. All datasets generated during and/or analyzed during the current study are available from the corresponding author on reasonable request.

Declarations

Conflict of interest The authors declare no conflicts of interest.

References

1. Quan, X.-C., Quan, Y.-P., Tao, K., Jiang, X.-M.: Comparative investigation on microbial community and electricity generation in aerobic and anaerobic enriched MFCs. *Bioresour. Technol.* **128**, 259–265 (2013). <https://doi.org/10.1016/j.biortech.2012.10.001>
2. Zhang, G., Zhao, Q., Jiao, Y., Wang, K., Lee, D.-J., Ren, N.: Efficient electricity generation from sewage sludge using biocathode microbial fuel cell. *Water Res.* **46**, 43–52 (2012). <https://doi.org/10.1016/j.watres.2011.10.036>
3. Martins, G., Peixoto, L., Ribeiro, D.C., Parpot, P., Brito, A.G., Nogueira, R.: Towards implementation of a benthic microbial fuel cell in lake Furnas (Azores): Phylogenetic affiliation and electrochemical activity of sediment bacteria. *Bioelectrochemistry* **78**, 67–71 (2010). <https://doi.org/10.1016/j.bioelechem.2009.07.003>
4. González-Gamboa, N., Tapia-Tussell, R., Kamaraj, S.K., Valdés-Lozano, D., Domínguez-Maldonado, J., Alzate-Gaviria, L.: Scale Up of a marine sediment microbial fuel cells stack with a floating aerated cathode using a circuit storage energy from ultra-low power. *Waste Biomass Valoriz.* (2020). <https://doi.org/10.1007/s12649-020-01289-7>
5. Mian, M.M., Liu, G., Fu, B.: Conversion of sewage sludge into environmental catalyst and microbial fuel cell electrode material: a review. *Sci. Total Environ.* **666**, 525–539 (2019). <https://doi.org/10.1016/j.scitotenv.2019.02.200>
6. Moqsud, M.A., Omine, K., Yasufuku, N., Hyodo, M., Nakata, Y.: Microbial fuel cell (MFC) for bioelectricity generation from organic wastes. *Waste Manag.* **33**, 2465–2469 (2013). <https://doi.org/10.1016/j.wasman.2013.07.026>
7. An, J., Kim, B., Nam, J., Ng, H.Y., Chang, I.S.: Comparison in performance of sediment microbial fuel cells according to depth of embedded anode. *Bioresour. Technol.* **127**, 138–142 (2013). <https://doi.org/10.1016/j.biortech.2012.09.095>
8. Sacco, N.J., Figuerola, E.L.M., Pataccini, G., Bonetto, M.C., Erijman, L., Cortón, E.: Performance of planar and cylindrical carbon electrodes at sedimentary microbial fuel cells. *Bioresour. Technol.* **126**, 328–335 (2012). <https://doi.org/10.1016/j.biortech.2012.09.060>
9. DeLong, E.F., Chandler, P.: Power from the deep. *Nat. Biotechnol.* **20**, 788–789 (2002). <https://doi.org/10.1038/nbt0802-788>
10. Prasad, J., Tripathi, R.K.: Scale-up and control the voltage of sediment microbial fuel cell for charging a cell phone. *Biosens. Bioelectron.* **172**, 112767 (2021). <https://doi.org/10.1016/j.bios.2020.112767>
11. Zhao, S., Liu, P., Niu, Y., Chen, Z., Khan, A., Zhang, P., Li, X.: A novel early warning system based on a sediment microbial fuel cell for in situ and real time hexavalent chromium detection in industrial wastewater. *Sensors* **18**, 642 (2018). <https://doi.org/10.3390/S18020642>
12. Greenman, J., Gálvez, A., Giusti, L., Ieropoulos, I.: Electricity from landfill leachate using microbial fuel cells: comparison with a biological aerated filter. *Enzyme Microb. Technol.* **44**, 112–119 (2009). <https://doi.org/10.1016/j.enzmictec.2008.09.012>
13. De Schampelaire, L., Rabaey, K., Boeckx, P., Boon, N., Verstraete, W.: Outlook for benefits of sediment microbial fuel cells with two bio-electrodes. *Microb. Biotechnol.* **1**, 446–462 (2008). <https://doi.org/10.1111/J.1751-7915.2008.00042.X>
14. Chaturvedi, A., Kundu, P.P.: Recent advances and perspectives in platinum-free cathode catalysts in microbial fuel cells. *J. Environ. Chem. Eng.* **9**, 105662 (2021). <https://doi.org/10.1016/j.jece.2021.105662>
15. Guo, Y., Wang, J., Shinde, S., Wang, X., Li, Y., Dai, Y., Ren, J., Zhang, P., Liu, X.: Simultaneous wastewater treatment and energy harvesting in microbial fuel cells: an update on the biocatalysts. *RSC Adv.* **10**, 25874–25887 (2020). <https://doi.org/10.1039/D0RA05234E>
16. Song, T.-S., Peng-Xiao Wu, X.-Y., Zhou, C.C.: Electrophoretic deposition of multi-walled carbon nanotube on a stainless steel electrode for use in sediment microbial fuel cells. *Appl. Biochem. Biotechnol.* **170**, 1241–1250 (2013). <https://doi.org/10.1007/s12010-013-0274-3>
17. Yang, Y., Yan, L., Song, J., Xu, M.: Optimizing the electrode surface area of sediment microbial fuel cells. *RSC Adv.* **8**, 25319–25324 (2018). <https://doi.org/10.1039/C8RA05069D>
18. Xin, X., Hong, J.: Insights into microbial community profiles associated with electric energy production in microbial fuel cells fed with food waste hydrolysate. *Sci. Total Environ.* **670**, 50–58 (2019). <https://doi.org/10.1016/j.scitotenv.2019.03.213>
19. Kondaveeti, S., Lee, S.H., Park, H.D., Min, B.: Specific enrichment of different *Geobacter* sp. in anode biofilm by varying inter-spatial distance of electrodes in air-cathode microbial fuel cell (MFC). *Electrochim. Acta.* **331**, 135388 (2020). <https://doi.org/10.1016/j.electacta.2019.135388>
20. Sajana, T.K., Ghangrekar, M.M., Mitra, A.: Effect of operating parameters on the performance of sediment microbial fuel cell treating aquaculture water. *Aquac. Eng.* **61**, 17–26 (2014). <https://doi.org/10.1016/j.aquaeng.2014.05.004>
21. Alipanahi, R., Rahimnejad, M.: Effect of different ecosystems on generated power in sediment microbial fuel cell. *Int. J. Energy Res.* **42**, 4891–4897 (2018). <https://doi.org/10.1002/er.4199>
22. Prasad, J., Tripathi, R.K.: Energy harvesting from sediment microbial fuel cell to supply uninterruptible regulated power for small devices. *Int. J. Energy Res.* **43**, 2821–2831 (2019). <https://doi.org/10.1002/er.4370>
23. Im, S.-W., Lee, H.-J., Chung, J.-W., Ahn, Y.-T.: The Effect of electrode spacing and size on the performance of soil microbial fuel cells (SMFC). *J. Korean Soc. Environ. Eng.* **36**, 758–763 (2014). <https://doi.org/10.4491/KSEE.2014.36.11.758>
24. Sajana, T.K., Ghangrekar, M.M., Mitra, A.: Effect of pH and distance between electrodes on the performance of a sediment microbial fuel cell. *Water Sci. Technol.* **68**, 537–543 (2013). <https://doi.org/10.2166/WST.2013.271>
25. Zhang, F., Tian, L., He, Z.: Powering a wireless temperature sensor using sediment microbial fuel cells with vertical arrangement of electrodes. *J. Power Sources.* **196**, 9568–9573 (2011). <https://doi.org/10.1016/J.JPOWSOUR.2011.07.037>
26. Bose, D., Santra, M., Sanka, R.V.S.P., Krishnakumar, B.: Bioremediation analysis of sediment-microbial fuel cells for energy recovery from microbial activity in soil. *Int. J. Energy Res.* **45**, 6436–6445 (2021). <https://doi.org/10.1002/er.6163>
27. Ganjar, S., Syafrudin, S., Irawan, W.W., Cagayana, C., Meishinta, A., Erika, L.: Effect of moisture content on power generation in dual graphene anode compost solid phase microbial fuel cells (DGACSMFCs). *E3S Web Conf* **73**, 05004 (2018). <https://doi.org/10.1051/e3sconf/20187305004>
28. Wolińska, A., Stepniewska, Z., Bielecka, A., Ciepelski, J.: Bioelectricity production from soil using microbial fuel cells. *Appl. Biochem. Biotechnol.* **173**, 2287–2296 (2014). <https://doi.org/10.1007/s12010-014-1034-8>
29. Abbas, S.Z., Rafatullah, M., Khan, M.A., Siddiqui, M.R.: Bioremediation and electricity generation by using open and closed sediment microbial fuel cells. *Front. Microbiol.* **10**, 1–12 (2019). <https://doi.org/10.3389/fmicb.2018.03348>
30. Nguyen, H.U.D., Nguyen, D.T., Taguchi, K.: A compact, membrane-less, easy-to-use soil microbial fuel cell: Generating electricity from household rice washing wastewater. *Biochem. Eng. J.* **179**, 108338 (2022). <https://doi.org/10.1016/J.BEJ.2022.108338>
31. Ma, F., Yin, Y., Li, M.: Start-up process modelling of sediment microbial fuel cells based on data driven. *Math. Probl. Eng.* (2019). <https://doi.org/10.1155/2019/7403732>



32. Liu, S.H., Su, Y.H., Chen, C.C., Lin, C.W., Huang, W.J.: Simultaneous enhancement of copper removal and power production using a sediment microbial fuel cell with oxygen separation membranes. *Environ. Technol. Innov.* **26**, 102369 (2022). <https://doi.org/10.1016/J.ETI.2022.102369>
33. Calignano, F., Tommasi, T., Manfredi, D., Chiolerio, A.: Additive manufacturing of a microbial fuel cell—a detailed study. *Sci. Rep.* (2015). <https://doi.org/10.1038/srep17373>
34. Strack, G.: Additive manufacturing approaches for biological power generation. *Curr. Opin. Electrochem.* **17**, 167–173 (2019). <https://doi.org/10.1016/j.coelec.2019.06.002>
35. Jannelli, E., Di Trolio, P., Flagiello, F., Minutillo, M.: Development and performance analysis of biowaste based microbial fuel cells fabricated employing additive manufacturing technologies. *Energy Procedia.* **148**, 1135–1142 (2018). <https://doi.org/10.1016/j.egypro.2018.08.029>
36. Papaharalabos, G., Greenman, J., Melhuish, C., Ieropoulos, I.: A novel small scale Microbial Fuel Cell design for increased electricity generation and waste water treatment. *Int. J. Hydrogen Energy.* **40**, 4263–4268 (2015). <https://doi.org/10.1016/j.ijhydene.2015.01.117>
37. Abazarian, E., Gheshlaghi, R., Mahdavi, M.A.: Impact of light/dark cycle on electrical and electrochemical characteristics of algal cathode sediment microbial fuel cells. *J. Power Sources.* **475**, 228686 (2020). <https://doi.org/10.1016/j.jpowsour.2020.228686>
38. Kamau, J.M., Mbui, D.N., Mwaniki, J.M., Mwaura, F.B., Kamau, G.N.: Microbial fuel cells: influence of external resistors on power, current and power density. *J. Thermodyn. Catal.* (2017). <https://doi.org/10.4172/2157-7544.1000182>
39. Logan, B.E., Hamelers, B., Rozendal, R., Schröder, U., Keller, J., Freguia, S., Aelterman, P., Verstraete, W., Rabaey, K.: Microbial fuel cells: methodology and technology†. *Environ. Sci. Technol.* **40**, 5181–5192 (2006). <https://doi.org/10.1021/es0605016>
40. Wang, C.-T., Lee, Y.-C., Liao, F.-Y.: Effect of composting parameters on the power performance of solid microbial fuel cells. *Sustainability* **7**, 12634–12643 (2015). <https://doi.org/10.3390/su70912634>
41. Li, X., Wang, X., Zhao, Q., Zhang, Y., Zhou, Q.: In situ representation of soil/sediment conductivity using electrochemical impedance spectroscopy. *Sensors* **16**, 625 (2016). <https://doi.org/10.3390/S16050625>
42. Taşkan, B., Bakır, M., Taşkan, E.: Enhanced power generation from algal biomass using multi-anode membrane-less sediment microbial fuel cell. *Int. J. Energy Res.* **45**, 2011–2022 (2021). <https://doi.org/10.1002/er.5894>
43. Liang, C., Das, K.C., McClendon, R.W.: The influence of temperature and moisture contents regimes on the aerobic microbial activity of a biosolids composting blend. *Bioresour. Technol.* **86**, 131–137 (2003). [https://doi.org/10.1016/S0960-8524\(02\)00153-0](https://doi.org/10.1016/S0960-8524(02)00153-0)
44. Rusydi, A.F.: Correlation between conductivity and total dissolved solid in various type of water: a review. *IOP Conf. Ser. Earth Environ. Sci.* **118**, 012019 (2018). <https://doi.org/10.1088/1755-1315/118/1/012019>
45. Katsube, T.J., Klassen, R.A., Das, Y., Ernst, R., Calvert, T., Cross, G., Hunter, J., Best, M., DiLabio, R., Connell, S.: Prediction and validation of soil electromagnetic characteristics for application in landmine detection. In: *Detection Remediation Technologies Mines Minelike Targets VIII*. **5089**, 1219 (2003). <https://doi.org/10.1117/12.486983>
46. Muaz, M.Z.M., Abdul, R., Vadivelu, V.M.: Recovery of energy and simultaneous treatment of dewatered sludge using membrane-less microbial fuel cell. *Environ. Prog. Sustain. Energy.* **38**, 208–219 (2019). <https://doi.org/10.1002/ep.12919>
47. Mohd Zaini Makhtar, M., Tajarudin, H.A.: Electricity generation using membrane-less microbial fuel cell powered by sludge supplemented with lignocellulosic waste. *Int. J. Energy Res.* **44**, 3260–3265 (2020). <https://doi.org/10.1002/er.5151>
48. Kim, A., Hak Kim, J., Patel, R.: Modification strategies of membranes with enhanced anti-biofouling properties for wastewater treatment: a review. *Bioresour. Technol.* **345**, 126501 (2021). <https://doi.org/10.1016/j.biortech.2021.126501>
49. Kunimatsu, K., Bae, B., Miyatake, K., Uchida, H., Watanabe, M.: ATR-FTIR study of water in nafion membrane combined with proton conductivity measurements during hydration/dehydration cycle. *J. Phys. Chem. B.* **115**, 4315–4321 (2011). <https://doi.org/10.1021/jp112300c>
50. Moon, J.M., Kondaveeti, S., Lee, T.H., Song, Y.C., Min, B.: Minimum interspatial electrode spacing to optimize air-cathode microbial fuel cell operation with a membrane electrode assembly. *Bioelectrochemistry* **106**, 263–267 (2015). <https://doi.org/10.1016/j.bioelechem.2015.07.011>
51. Prasad, J., Tripathi, R.K.: Voltage control of sediment microbial fuel cell to power the AC load. *J. Power Sources.* **450**, 227721 (2020). <https://doi.org/10.1016/j.jpowsour.2020.227721>
52. Xu, J.Y., Xu, H., Yang, X.L., Singh, R.P., Li, T., Wu, Y., Song, H.L.: Simultaneous bioelectricity generation and pollutants removal of sediment microbial fuel cell combined with submerged macrophyte. *Int. J. Hydrogen Energy.* **46**, 11378–11388 (2021). <https://doi.org/10.1016/j.ijhydene.2020.06.007>
53. Kabutey, F.T., Ding, J., Zhao, Q., Antwi, P., Quashie, F.K., Tankapa, V., Zhang, W.: Pollutant removal and bioelectricity generation from urban river sediment using a macrophyte cathode sediment microbial fuel cell (mSMFC). *Bioelectrochemistry* **128**, 241–251 (2019). <https://doi.org/10.1016/j.bioelechem.2019.01.007>
54. Prasad, J., Tripathi, R.K.: Maximum electricity generation from low cost sediment microbial fuel cell using copper and zinc electrodes. In: *IEEE International Conference on Information, Communication, Instrumentation and Control (ICICIC)*. (2017). 2018-Jan, 1–4 (2018). <https://doi.org/10.1109/ICOMICON.2017.8279078>
55. Bhande, R., Noori, M.T., Ghangrekar, M.M.: Performance improvement of sediment microbial fuel cell by enriching the sediment with cellulose: Kinetics of cellulose degradation. *Environ. Technol. Innov.* **13**, 189–196 (2019). <https://doi.org/10.1016/j.eti.2018.11.003>
56. Liu, B., Ji, M., Zhai, H.: Anodic potentials, electricity generation and bacterial community as affected by plant roots in sediment microbial fuel cell: Effects of anode locations. *Chemosphere* **209**, 739–747 (2018). <https://doi.org/10.1016/j.chemosphere.2018.06.122>
57. Kaku, N., Yonezawa, N., Kodama, Y., Watanabe, K.: Plant/microbe cooperation for electricity generation in a rice paddy field. *Appl. Microbiol. Biotechnol.* **79**, 43–49 (2008). <https://doi.org/10.1007/s00253-008-1410-9>

Publisher's Note Springer Nature remains neutral with regard to jurisdictional claims in published maps and institutional affiliations.

Springer Nature or its licensor holds exclusive rights to this article under a publishing agreement with the author(s) or other rightsholder(s); author self-archiving of the accepted manuscript version of this article is solely governed by the terms of such publishing agreement and applicable law.





Influence of nearby urban buildings on the wind field around a wind turbine: a case study in Dundalk Institute of Technology

Yu-Chin Chien¹ · Yan-Ting Lin² · Huei Chu Weng¹ · Raymond Byrne³ · Pao-Hsiung Chiu⁴

Received: 30 March 2022 / Accepted: 10 September 2022 / Published online: 22 September 2022
© The Author(s), under exclusive licence to Islamic Azad University 2022

Abstract

In this paper, an urban environmental wind field distribution around the wind turbine is numerically investigated by using ANSYS Fluent with the $k-\omega$ SST turbulence model. A computational domain designed with an octagonal prism shape is used to simulate wind from eight different directions. As a case study, the wind field and wind power output at the location of the 850 kW wind turbine in the Dundalk Institute of Technology campus are analyzed. The simulated inlet wind speeds adopted are 6 m/s, 12 m/s, 14 m/s, and 22 m/s. The simulation results show that, at both high and low wind speeds, specific wind directions would generate wakes behind tall narrow buildings and affect the wind speed at the location of the wind turbine. The local acceleration of the wind speed could only occur next to buildings. Moreover, in a low-speed southwesterly wind, the wind speed at the location of the wind turbine will be significantly reduced due to the presence of low-wide buildings. When the wind of 14 m/s comes from the south–east direction and the wind of 6 m/s comes from the north–east direction, the maximum percentage changes in wind speed and power output are -2.41% and -5.59% , respectively.

Keywords Computational fluid dynamics · Wind flow model · Wind field simulation · Urban environment · Building aerodynamics

Introduction

The use of conventional fossil fuels such as coal, oil, and natural gas, is facing the environmental disaster of global warming and climate change. World energy consumption of the earth's natural resources has rapidly increased during the twenty-first century. To meet the rising demand for energy due to global economic and technological growth, the exploration of renewable energy and clean energy has become an important issue. Wind energy is one of the most

important sources of renewable energy and has the advantages of being environmentally friendly and sustainable from manufacturing to power generation [1–3]. Through the blades, gearboxes, and generators, the wind energy contained in the atmospheric flow can be simply extracted and further converted into daily electricity.

A wind farm is a cluster of multiple wind turbines in the same location used to generate electricity which can be built both onshore and offshore. Since the potential of offshore wind energy is higher than onshore, several offshore wind farms have been rapidly developed in recent years [4]. In the development of a wind farm, the selection of a suitable site can generate more power from wind energy. Traditionally, the wind energy potential of an area was assessed by the measurements recorded on the meteorological tower in that area [5, 6]. However, a limited number of measurement stations could not represent the distribution of wind energy over the whole region. For a relatively flat area, geostatistical techniques (such as inverse distance weighted interpolation and semi-empirical radiometric terrain correction approach) are sometimes used to estimate the wind resource map in the vicinity of the relative reference measurement stations [7, 8]. With the development of measurement equipment, remote

✉ Huei Chu Weng
hcweng@cycu.edu.tw

¹ Department of Mechanical Engineering, Chung Yuan Christian University, Taoyuan 320314, Taiwan
² Mechanical and System Engineering Program, Institute of Nuclear Energy Research, Atomic Energy Council, Taoyuan 325207, Taiwan
³ Centre for Renewables and Energy, Dundalk Institute of Technology, Dundalk, Co. Louth A91 K584, Ireland
⁴ Institute of High Performance Computing, Agency for Science, Technology and Research (A*STAR), Singapore 138632, Singapore



wind measurement devices (such as SODAR and LIDAR) have been widely used as an alternative to traditional meteorological towers in recent decades [9–12]. An intercomparison of mast-mounted cup anemometer and remote sensing instrument in the wind measurements was described by Lang and McKeogh [13]. The results showed that both LIDAR and SODAR remote sensing techniques recorded lower wind speeds than the cup anemometers. However, the installation and maintenance of the mast-mounted equipment would consume giant economic and human resources for the measurement sites in complex areas. Another technical and economic feasibility method is to reconstruct the real terrain in a wind tunnel through a scale model for specific terrain [14–16].

Recently, due to the increase in computer computing speed, computational fluid dynamics (CFD) methods are widely used to simulate wind fields in large-scale and complex terrain [17–19]. Blocken et al. [20] presented a CFD study of wind flow over a natural complex terrain in Galicia, Spain. The results showed that the topography could lead to an increase in wind speed for a range of specific wind directions. Huang and Zhang [21] simulated wind field over complex terrain around Siu Ho Wan station in Hon Kong and showed that the numerical results were in good agreement with the wind tunnel data in Tse et al. [22]. Niyomtham et al. [23] evaluate the wind energy potential over the Andaman Coast of Thailand, using a couple of mesoscale atmospheric model, microscale wind flow model, and CFD modeling. On the other hand, CFD is frequently used to analyze urban microclimate [24]. Ramponi et al. [25] used numerical simulation to investigate the influences of urban density and street width on urban ventilation performance. For a single building, the ambient wind field has the characteristics of a vortex, wake, through-flow, and angular flow, while for a group of buildings, the ambient wind field has the characteristics of a shading, pyramid, venture, and channel. When the natural wind blows a building, the airflow may change direction or increase/decrease speed due to the geometry of the building and the relative position of its neighboring buildings, which means that the structure of a building or the layout of the buildings is not only changing the distribution of wind speed but also suggest potential wind energy resource development and utilization [26]. Therefore, CFD can identify potential wind energy areas in densely built-up urbanized areas and further determine the location of wind turbine installations [27, 28]. Kalmikov et al. [29] used CFD simulations to evaluate the wind energy potential of the Massachusetts Institute of Technology campus and to further analyze the physical mechanisms of wind energy differences between the west side to the east side.

According to Global Wind Atlas, Ireland is one of the windiest countries in the European Union, which has a prevailing westerly wind from the Atlantic Ocean [30]. The extensive

coastal territory of Ireland illustrates it has an excellent location for the commercial and academic development of onshore wind turbines. In August 2005, the Dundalk Institute of Technology (DkIT), located on the east coast of Ireland, became the first college in the world to install a commercial wind turbine on its campus [31]. The rotor diameter and tower height of the Vestas V52 horizontal axis wind turbine (850 kW) are 52 m and 60 m, respectively. Cooney et al. [31] presented a comprehensive study on the performance of the Vestas V52 wind turbine located in an urban environment. The measured power curve of the DkIT wind turbine exhibited a good correlation with the manufacturer-stated power curve. The annual energy output of the DkIT wind turbine was significantly reduced by the seasonal effects at the wind turbine location with relatively low mean wind speed. Byrne et al. [32, 33] further used SCADA data, Irish wind atlas, and LIDAR measurements to investigate the influence of various obstacle features (such as the local buildings and regional topography) on the energy performance of the DkIT wind turbine. The results indicated that the low broad buildings with heights of 20% of the turbine hub height have a significantly negative impact on energy performance compared to the taller narrow buildings. Moreover, the mesoscale effects caused by the hills 8–15 km away from the wind turbine site also have an energy performance reducing impact.

The aforementioned literature review shows the influences of mesoscale and microscale on the wind turbine energy performance at a peri-urban coastal location. However, in complex terrain, the use of traditional wind speed measurement methods for wind resource assessment has its limitations. On the contrary, the CFD method not only can clearly observe the changes in wind field caused by the environment and topography but also can further assume the wind energy output of the wind turbine in this area. In the present study, the CFD method was adopted to simulate the wind field in a peri-urban coastal topology. Although Byrne et al. [32, 33] analyzed the influence of neighboring obstacle features on the energy performance of the DkIT wind turbine by using long-term measurements. In fact, the extent of the influence of the local buildings on the wind turbine ambient wind field could be further examined by the CFD method under different wind directions and wind speeds. Therefore, the main objective of this study is to investigate the effect of the nearby urban buildings of the DkIT campus on the environmental wind field of the Vestas V52 wind turbine under different wind directions and wind speeds.

Methods

This section introduces the numerical simulation method for the ambient wind field of the DkIT campus. Firstly, the architectural geometry data of the simulation area were

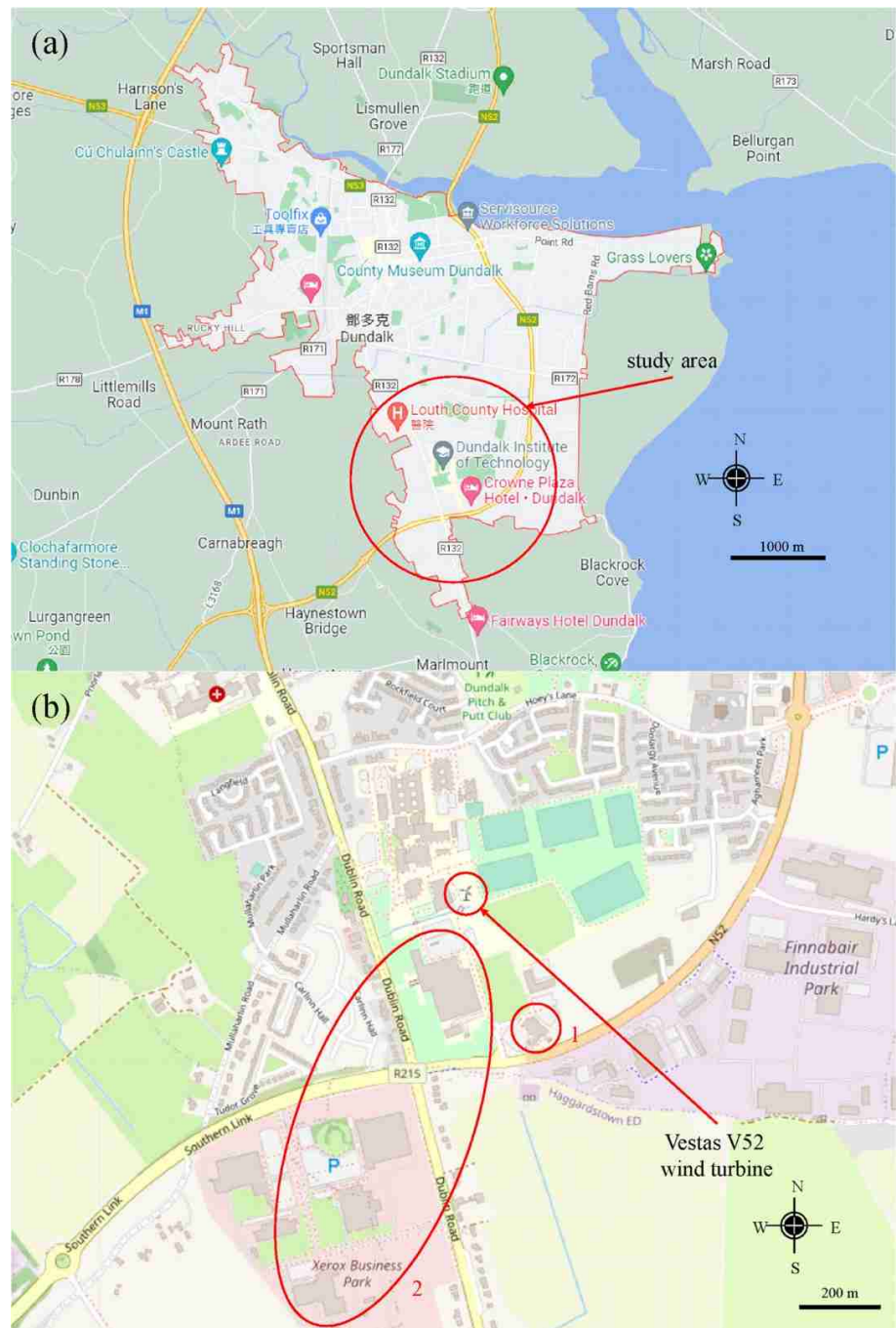


obtained through Open-Street-Map. Then, the Solid Works software was used to edit the 3D CAD geometry model. Next, the geometry model was imported into ANSYS Fluent to construct the computational domain and set the boundary conditions. Finally, the numerical simulation results were used to observe the wind field distribution and capture the wind speed value flowing through the location of the wind turbine. The wind power output of the wind turbine was further estimated from the wind speed value.

Architectural geometry data

In this study, the wind field was simulated in the east part of Ireland-Dundalk Institute of Technology as shown in Fig. 1a. The simulation area was set to cover a radius of 1.1 km, centered on the wind turbine on the DkIT campus. Figure 1b shows the location of the Vestas V52 wind turbine within the DkIT campus. On the southeast side, there is a 47-m-high hotel at a distance of 335 m, which is the tallest building in the area (marked by 1); while on the southwest side, there

Fig. 1 Schematic diagram of the study area **a** the geographical location of Dundalk, Ireland (Source: Google Maps); **b** architectural geometry information around the DkIT campus (Source: Open-Street-Map)



are several low wide buildings of 7–12 m in height at a distance of 150–1100 m (marked by 2). In order to apply the actual building topography in CFD wind field simulation, this study first obtained the architectural geometry data in the simulation area through Open-Street-Map and then used Solid Works software to build and edit the 3D CAD geometric model. The entire 3D architectural geometry model created in this study is shown in Fig. 2a. In order to analyze the influence of eight different wind directions on the ambient wind field, an octagonal prism flow field area was established as shown in Fig. 2b, where the distance between the top and bottom of the octagonal prism is 1 km and the distance between the lateral symmetrical surfaces is 5 km. Figure 2c shows a zoomed-in view around the Vestas V52 wind turbine. Finally, the building geometry model and the flow field area were imported into ANSYS Fluent, and then the mesh was delineated.

Meshing grid

Because of the complexity of the flow field model, the whole area was set up with the tetrahedron cells and triangular prisms as shown in Fig. 3. The defeaturing size was set at 50 m in the mesh properties. Both curvature and proximity size functions were used to capture and refine the mesh of architectural geometry. Figure 4 reports the unstructured fine mesh is created to accurately simulate the flow field near the buildings. In addition, face meshing and inflection were used on the octagonal faces except for the bottom face. The maximum layer and growth rate were set to 20 and 1.2 in inflation. The overall number of elements used is close to 7 million.

Boundary conditions and equation model

Figure 5 shows the boundary condition setting for the octagonal column flow field. The inlet and outlet boundary conditions were set to velocity inlet and pressure outlet, respectively, the ground and building surface were set to the no-slip boundary, and symmetric boundary conditions were used on the sides and top of the octagonal column. In general, when simulating an outdoor environment wind field, the wind speed and turbulence characteristics of the atmospheric boundary layer are often used as the inlet wind speed profile. In order to simplify the simulation analysis, the inlet and outlet of the flow field were set up with a uniform wind speed and a normal atmospheric pressure for different directions of wind conditions. In ANSYS Fluent software, the pressure-based algorithm was used to simulate the steady flow field for the solver; the $k-\omega$ SST turbulent flow model was chosen for the flow field solution, and the Quick scheme discrete method was used for the momentum equation.

Wind field analysis

In order to analyze the influence of the buildings in the vicinity of the DkIT campus on the environmental wind field of the Vestas V52 wind turbine, as shown in Fig. 6, a spherical surface was drawn above the wind turbine position with the radius of the blade at the height of the hub. The average wind speed $u_{V52,avg}$ at the position of the Vestas V52 wind turbine was obtained by calculating the wind speed through the surface of the sphere. Moreover, the power output of the wind turbine at the current average wind speed can be further obtained from the power curve of Vestas V52. Figure 7 shows the power curve of the Vestas V52 wind turbine at different wind speeds. From the curve, it can be seen that the power output will be constant when the wind speed exceeds 16 m/s. Therefore, for the effect of neighboring buildings on the power output of the wind turbine, only inlet wind speeds of 6 m/s, 12 m/s, and 14 m/s were considered in this study. The average wind speed relative change $U(\%)$ was used to indicate the magnitude of the increase or decrease in the average wind speed relative to the inlet wind speed u_{in} under the influence of the building as is defined as:

$$U(\%) = \frac{u_{V52,avg} - u_{in}}{u_{in}} \times 100\% \quad (1)$$

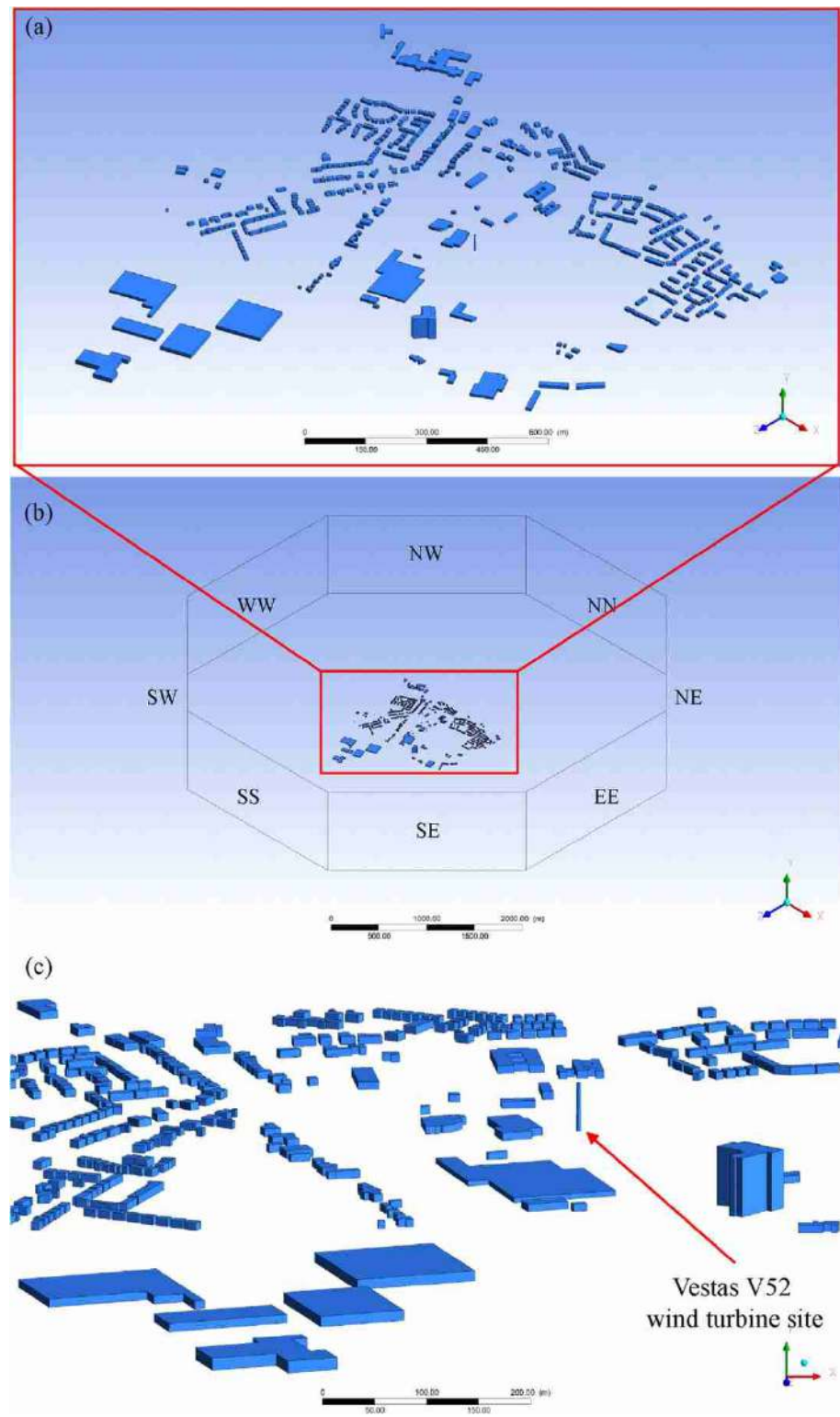
The average power output relative change $P(\%)$ could be further calculated by converting the above wind speed values to power curves. It should be noted that the above equation assumes that the azimuth angle of the wind turbine is not taken into account, and the average wind speed $u_{V52,avg}$ through the sphere monitor is captured by the wind turbine.

Results and discussion

In order to investigate the effect of the local buildings of the DkIT campus on the Vestas V52 wind turbine ambient wind field under different wind directions and wind speeds. The CFD method was adopted to simulate the wind field in this area. Figure 8 shows the influence of wind speed from low speed to high speed on the position of the Vestas V52 wind turbine by comparing eight different inlet wind directions. In general, the average wind speed at the location of the wind turbine decreases in most wind directions from low speed to high speed due to the influence of nearby urban buildings as indicated in the previous study [32]. Except for the west (WW) wind directions (6 m/s, 12 m/s, 14 m/s and 22 m/s) and the northwest (NW) wind directions (6 m/s and 22 m/s) show the results of average wind speed enhancement. The results indicate that most of the wind directions



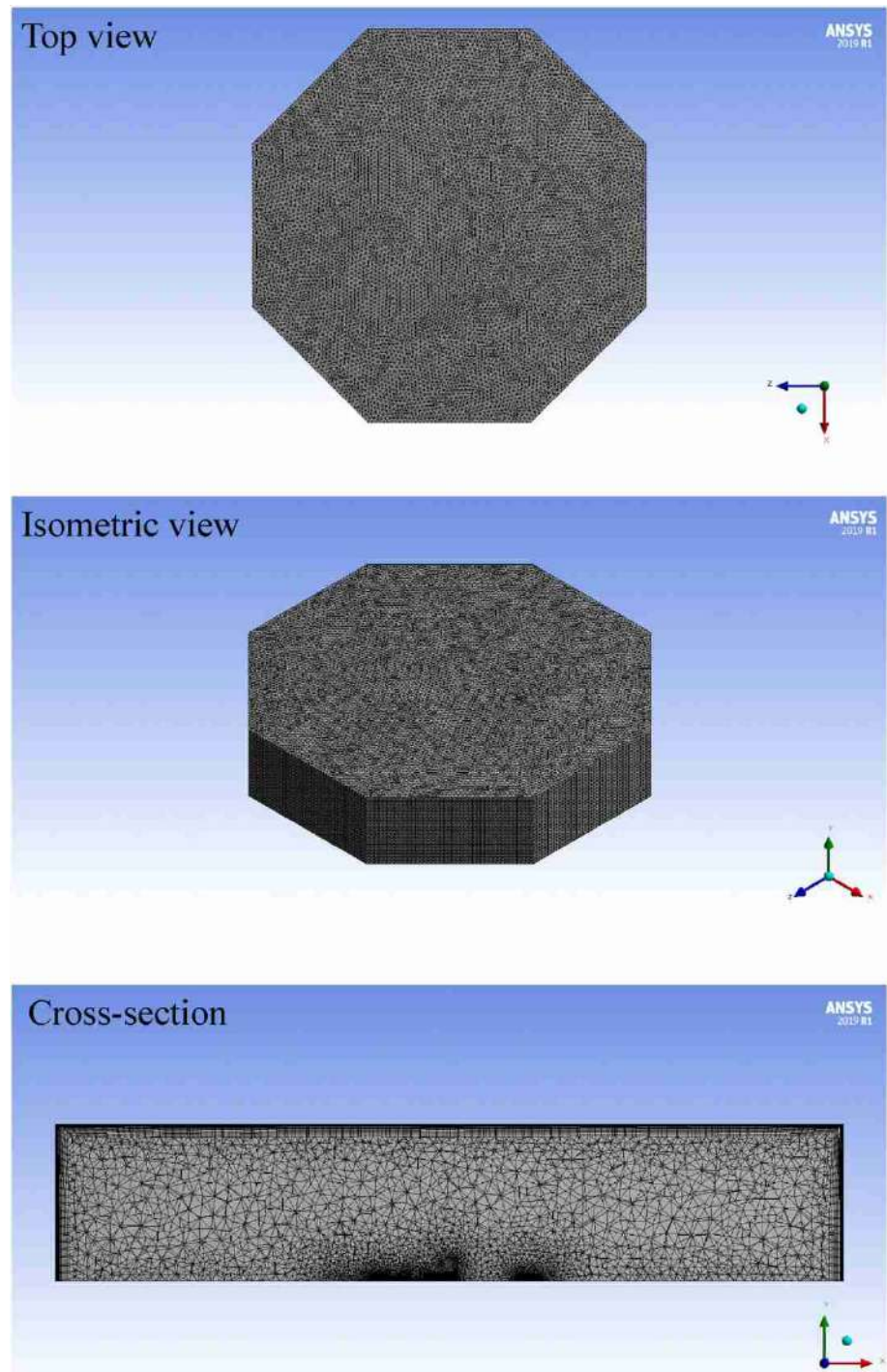
Fig. 2 Architectural geometry of the study area: **a** overall view of the entire architectural layout **b** computational domain of octagonal column **c** part view from the south side



are weakened after passing the obstacle features. The maximum average wind speed decrease (-2.41%) occurred when the 14 m/s wind was in the south–east (SE) direction; the maximum mean wind speed increase (0.74%) occurred when the 22 m/s wind was in the west (WW) direction. Figures 9,

10 and 11 show the distribution of wind fields in the vicinity of the Vestas V52 wind turbine at different wind speeds in the southeast, south, and southwest, respectively. It can be observed that both low-speed and high-speed winds show local acceleration on both sides of the tall narrow building



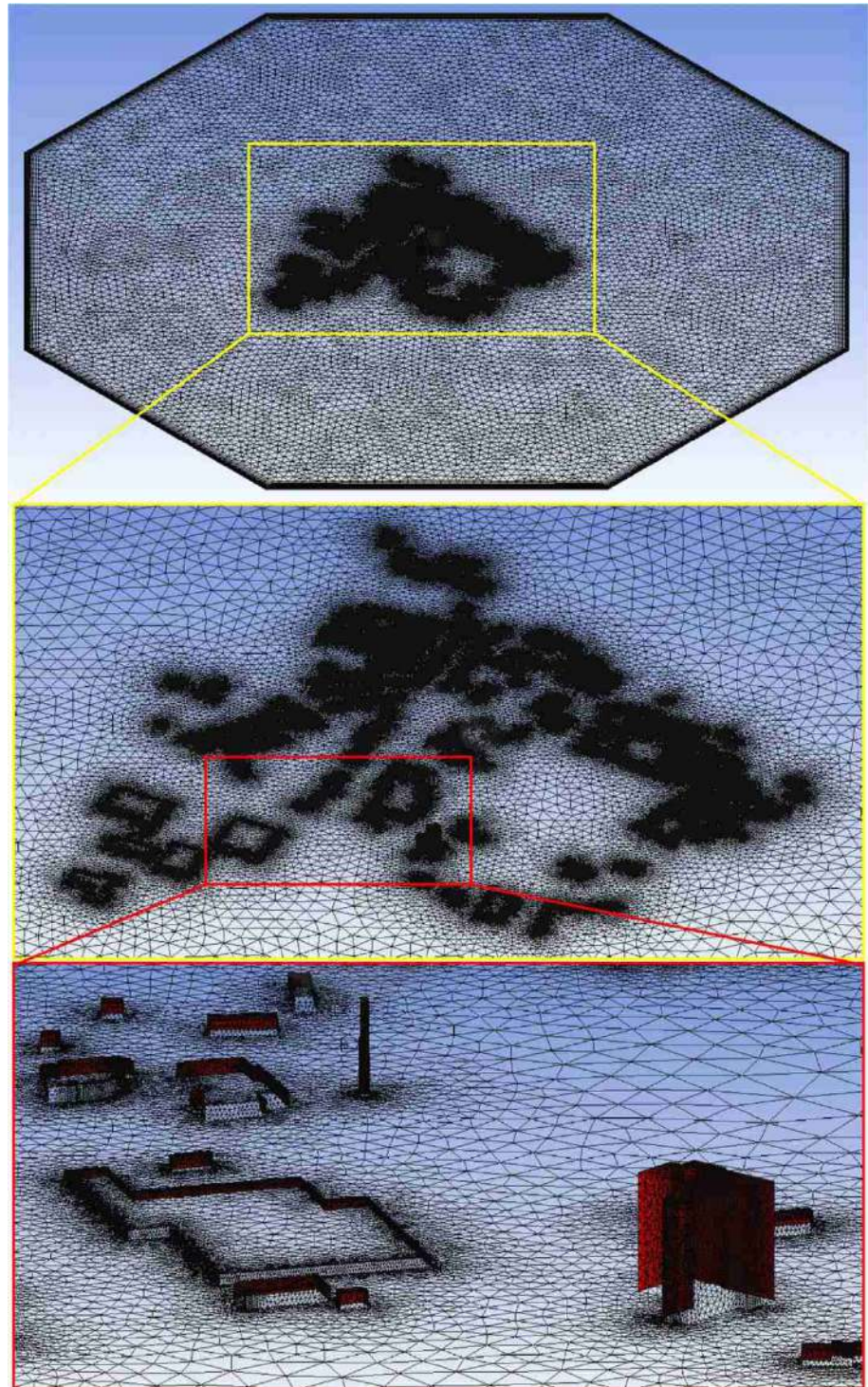
Fig. 3 Meshing grid

and generate wake at the rear. In the southeast wind direction, the wake behind the tall narrow building will directly affect the wind field at the location of the wind turbine, thus causing a decrease in the average wind speed. On the other hand, the wake of the low wide buildings is also generated

downstream above it. This means that in the use of urban wind energy, it is necessary to consider not only the wake effect of the tall narrow building but also the downstream wake effect caused by the low wide buildings. As the wind speed increases to 14 m/s, there is a local acceleration above



Fig. 4 Close-up of the mesh for the study area

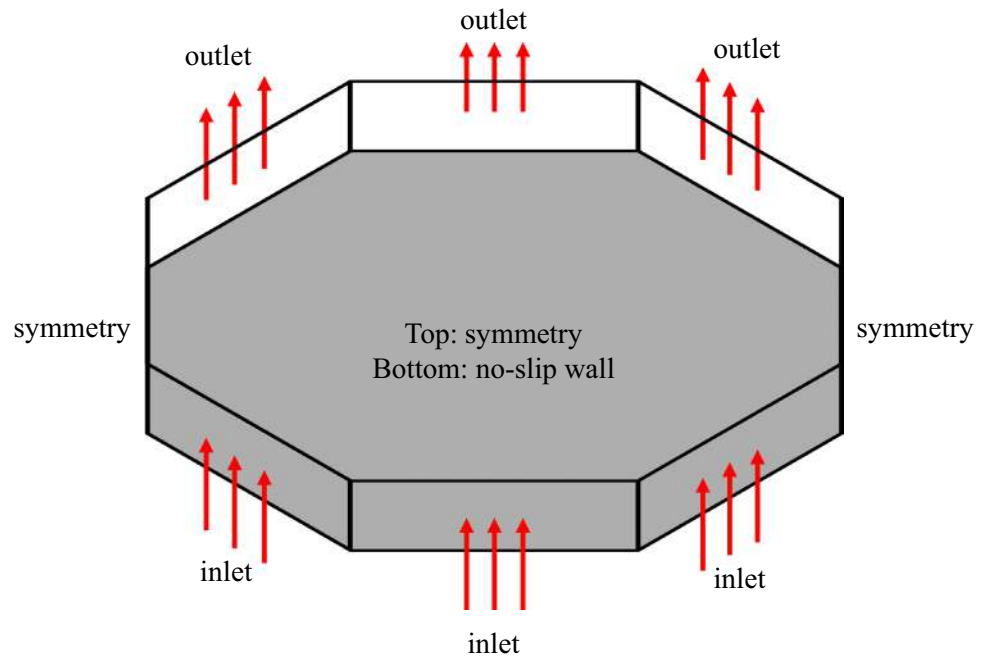


the low buildings, and this area of local acceleration expands as the wind speed increases. In the south direction, the wind flows over the low wide buildings in the southwest, creating

a narrow wake; the area of local acceleration above the low wide buildings also expands as the wind speed increases.

After obtaining the average wind speed, the average power output of the wind turbine can be deduced from the

Fig. 5 Boundary conditions



power curve of the Vestas V52 wind turbine. The effect of the local buildings of the DkIT campus on the Vestas V52 wind turbine average power output under different wind directions and wind speeds can be further investigated. Figure 12 shows the effect of wind from low speed to high speed on the average power output of the Vestas V52 wind turbine by comparing different wind directions. From the results, it can be seen that the power output has the most obvious variation in the low wind speed environment, that is, the nearby urban buildings have the most drastic effect on the wind turbine power output in the low wind speed environment. The wind turbine power output is less affected by vicinity buildings in high wind speed environments. This means that in high wind speed environments, the local buildings do not have a significant effect on the wind turbine power output. The maximum output power decrease (-5.59%) occurs when the 6 m/s wind is in the northeast (NE) direction; the maximum output power increase (1.76%) occurs when the 6 m/s wind is in the west (WW) direction. In summary, in the low wind speed environment, both the tall narrow building and the low wide buildings have an impact on the wind speed and power output in the southeast and southwest wind directions. The results are consistent with the previous study [32], the local buildings in the west southwest and south southeast directions can influence the energy performance of the wind turbine site.

Conclusions

By the CFD method, the degree of influence of the local buildings on the wind turbine ambient wind field under different wind directions and wind speeds can be obtained. This study has investigated the influence of nearby urban buildings on the environmental wind field of the DkIT Vestas V52 wind turbine. The combined results showed that the wind generates wakes in a specific direction behind tall narrow buildings and affects the wind speed and power output at the location of the wind turbine, while low wide building clusters could also generate wakes downstream above them. As the wind speed increases, the area of local acceleration at the tall narrow building sides and above the lower wide building would gradually increase. In a low wind speed environment, the wind speed and power output of the wind turbine location would be affected by the southeast and southwest wind directions of tall narrow buildings and low wide buildings, respectively. With the gradual increase in ambient wind speed, the nearby urban buildings have a lower impact on the changes in wind turbine power output. This study may benefit the control strategy and site selection of the wind turbine in the urban region. Future research can combine the big data obtained from experimental measurements and CFD simulations with artificial intelligence to further predict the wind power output of a single or a cluster of multiple wind turbines.



Fig. 6 Overall and isometric view of the architectural geometry around the Vestas V52 wind turbine

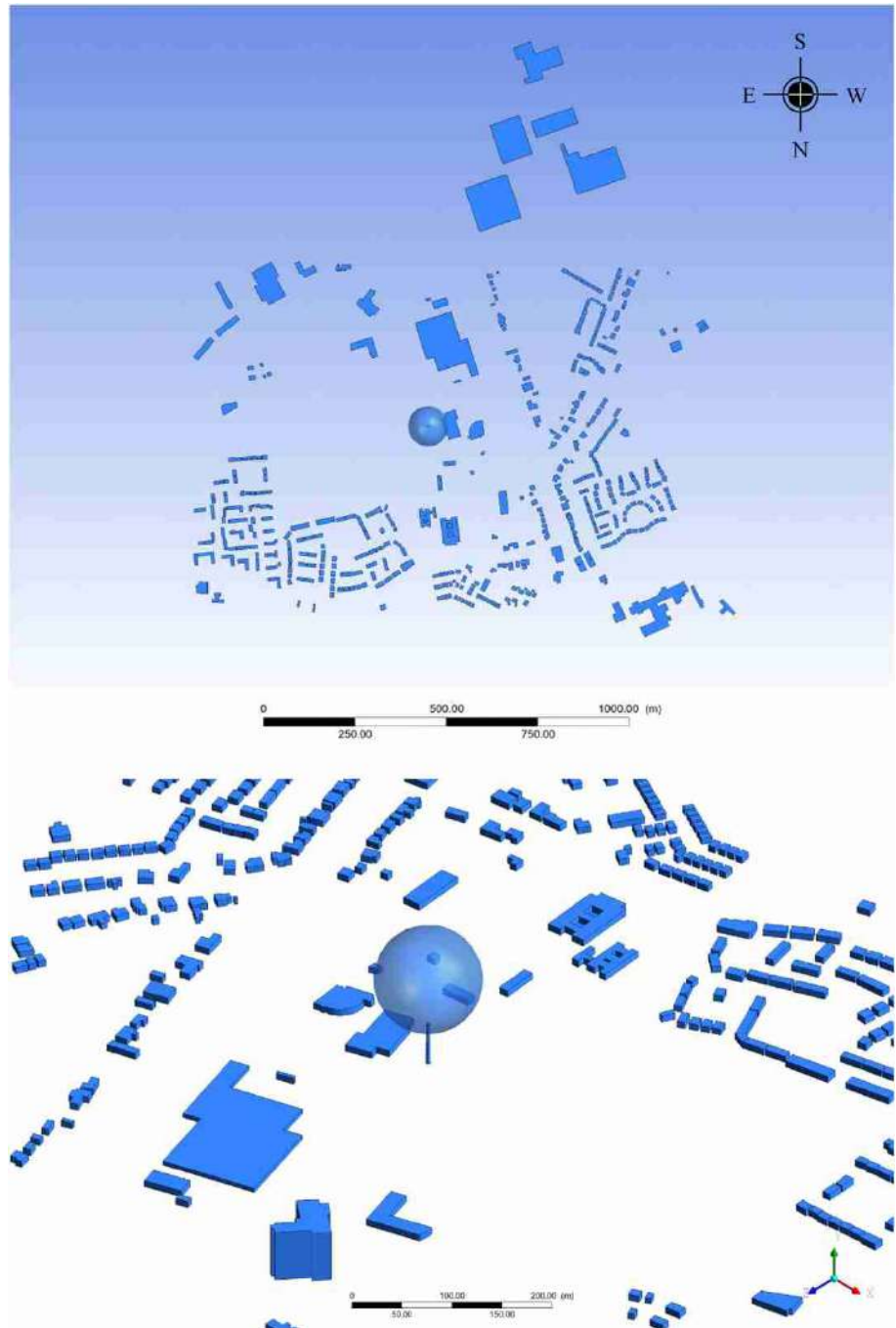


Fig. 7 Manufacturer-stated power curve of the Vestas V52 wind turbine [34]

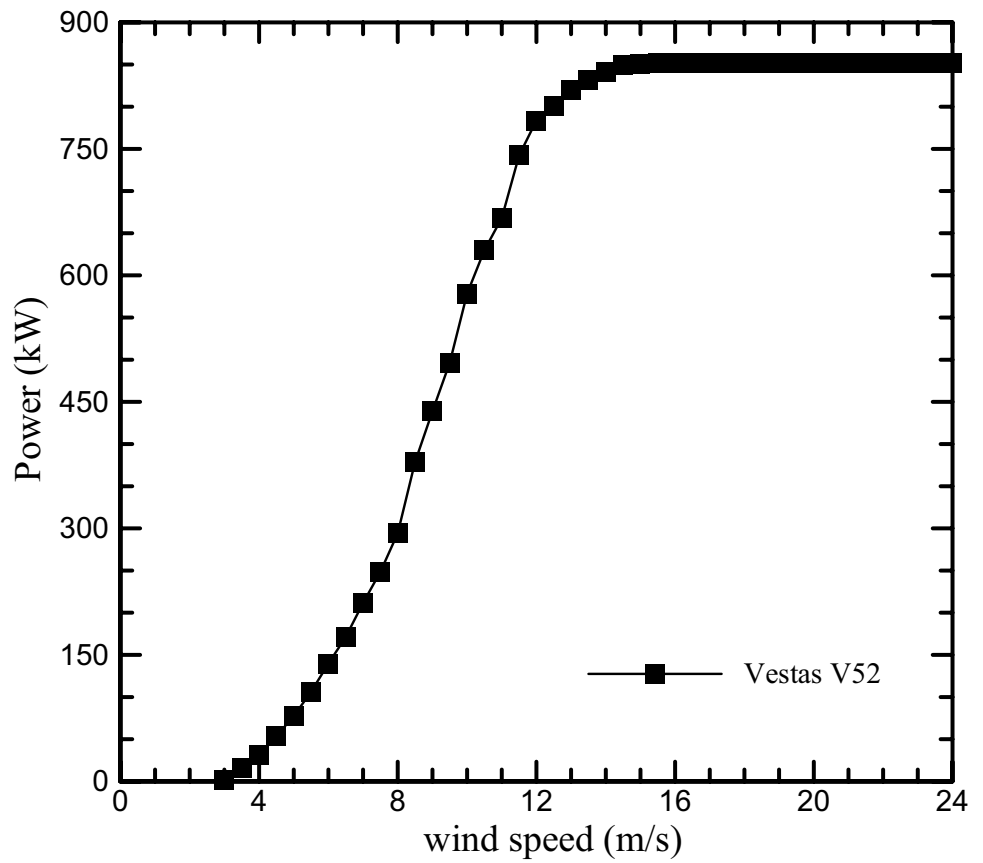
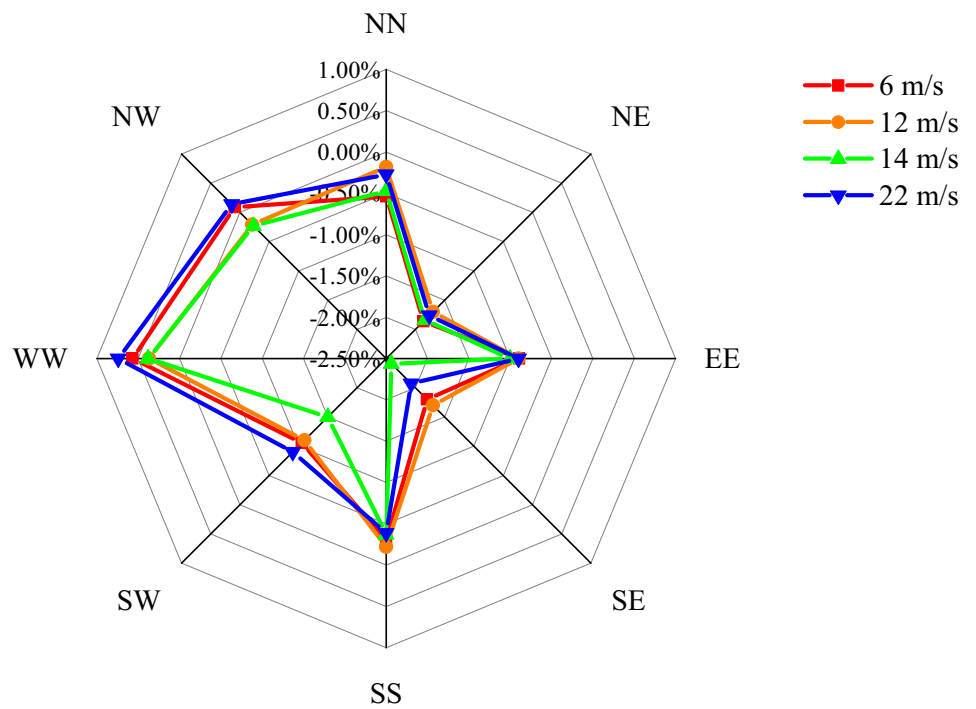


Fig. 8 Wind rose chart for average wind speed relative change



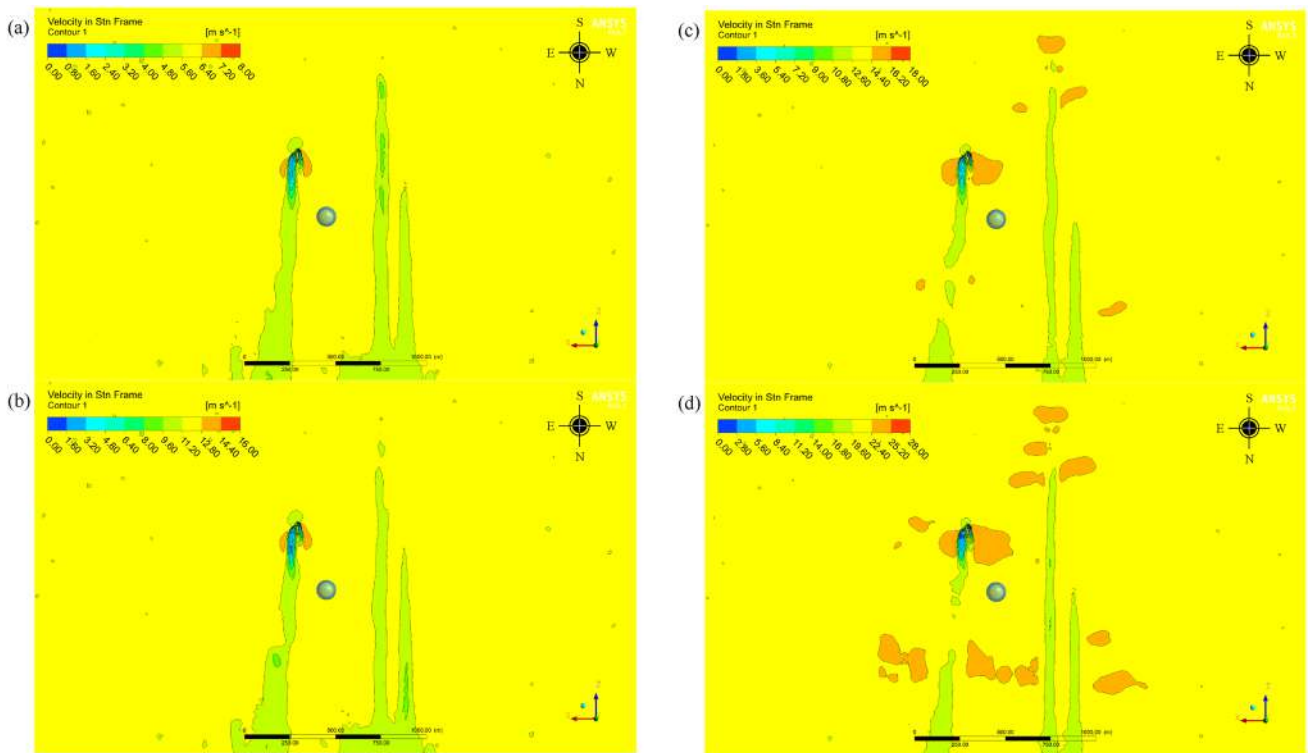


Fig. 9 Simulation velocity magnitude contours of SS case: **a** $u_{in} = 6$ m/s; **b** $u_{in} = 12$ m/s; **c** $u_{in} = 14$ m/s; **d** $u_{in} = 22$ m/s

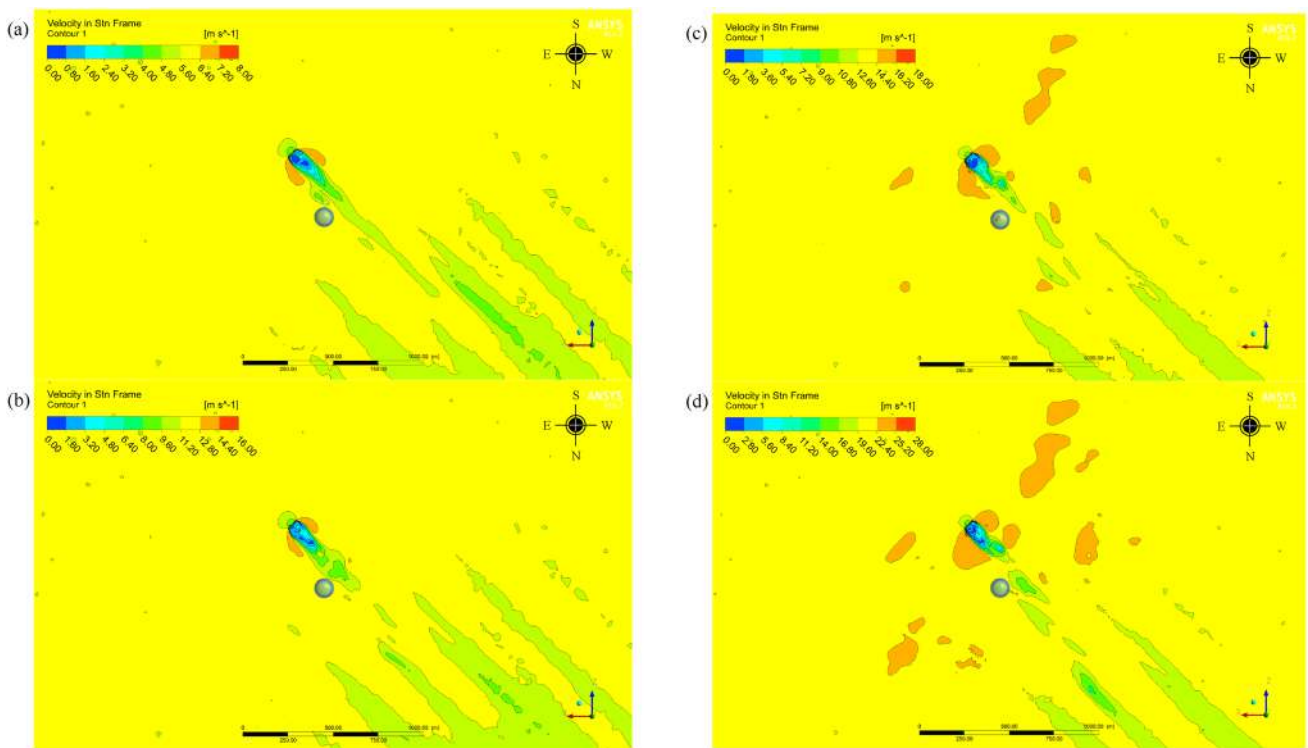


Fig. 10 Simulation velocity magnitude contours of SE case: **a** $u_{in} = 6$ m/s; **b** $u_{in} = 12$ m/s; **c** $u_{in} = 14$ m/s; **d** $u_{in} = 22$ m/s

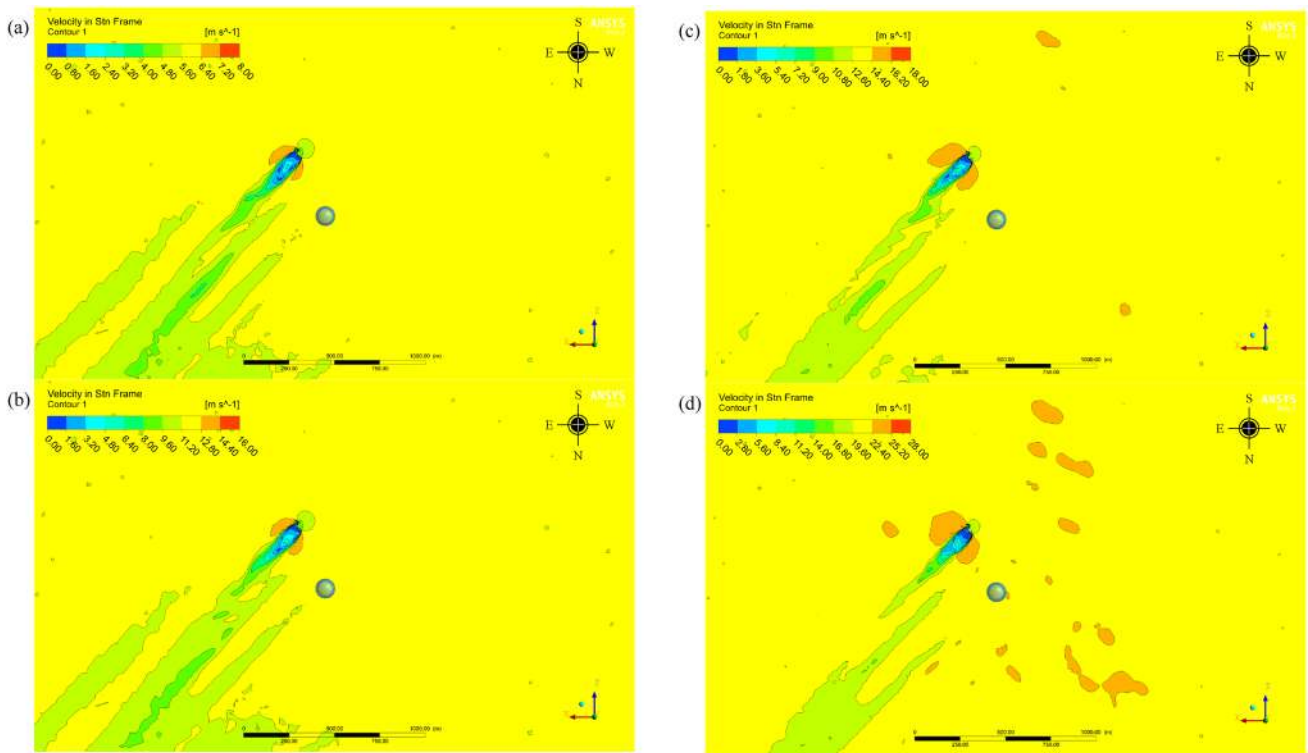
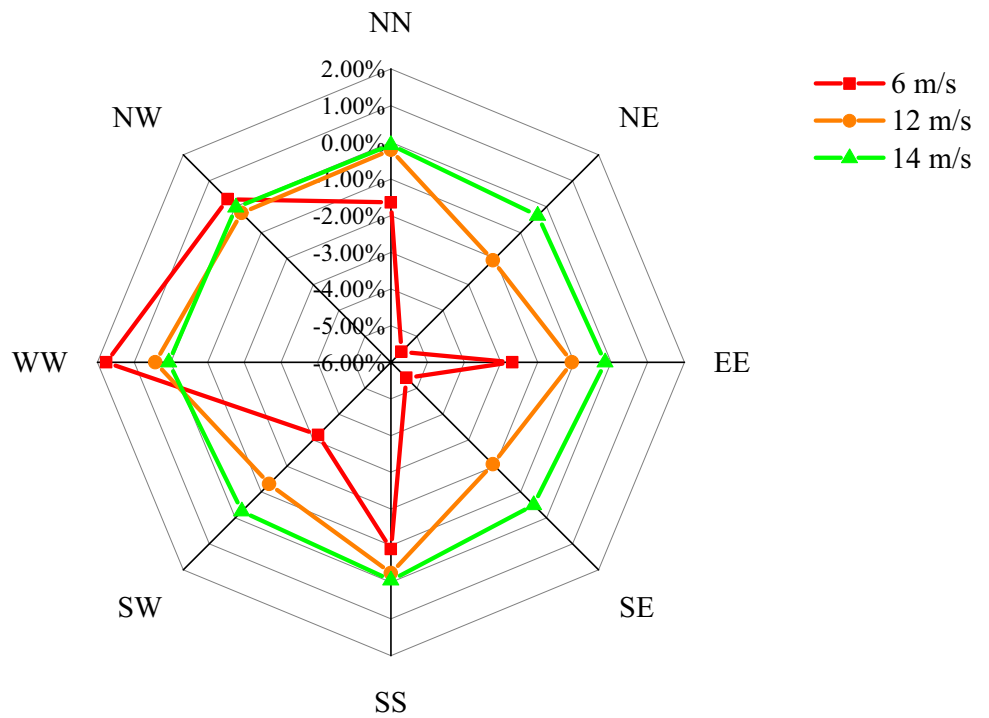


Fig. 11 Simulation velocity magnitude contours of SW case: **a** $u_{in} = 6 \text{ m/s}$; **b** $u_{in} = 12 \text{ m/s}$; **c** $u_{in} = 14 \text{ m/s}$; **d** $u_{in} = 22 \text{ m/s}$

Fig. 12 Power rose chart for average power output relative change at different wind speeds



Acknowledgements The authors also wish to acknowledge the support of the INTERREG VA SPIRE2 project. This research was supported by the European Union's INTERREG VA Programme (Grant No. INT-VA/049), managed by the Special EU Programmes Body (SEUPB). The views and opinions expressed in this document do not necessarily reflect those of the European Commission or the Special EU Programmes Body (SEUPB). The authors also acknowledge the Research Office at Dundalk Institute of Technology. The authors also acknowledge IEA Wind Task 41, Enabling wind to contribute to a distributed energy future.

Authors' contribution Y-TL and RB conceptualized the study. Y-CC, Y-TL, and HCW conducted laboratory works, provided the statistics, processed the data and fulfilled the analysis, wrote the draft. HCW provided software and performed the analysis supervision, draft writing supervision. RB and P-HC performed the analysis supervision, final manuscript writing and editing. All authors read and approved the final manuscript.

Funding This work was supported by the Ministry of Science and Technology, Taiwan (Grant Number 108-3116-F-042A-006-).

Data availability The data used to support the findings of this study are available from the corresponding author upon request.

Declarations

Conflict of interest The authors declare they have no competing interests.

References

- Porte-Agel, F., Bastankhah, M., Shamsoddin, S.: Wind-turbine and wind-farm flows: a review. *Bound. Layer Meteorol.* **174**, 1–59 (2020). <https://doi.org/10.1007/s10546-019-00473-0>
- Olabi, A.G., Wilberforce, T., Elsaid, K., Salameh, T., Sayed, E.T., Husain, K.S., Abdelkareem, M.A.: Selection guidelines for wind energy technologies. *Energies* **14**, 3244 (2021). <https://doi.org/10.3390/en14113244>
- Chaudhuri, A., Datta, R., Kumar, M.P., Davim, J.P., Pramanik, S.: Energy conversion strategies for wind energy system: electrical, mechanical and material aspects. *Materials* **15**, 1232 (2022). <https://doi.org/10.3390/ma15031232>
- Díaz, H., Guedes Soares, C.: Review of the current status, technology and future trends of offshore wind farms. *Ocean Eng.* **209**, 107381 (2020). <https://doi.org/10.1016/j.oceaneng.2020.107381>
- Farrugia, R.N., Sant, T.: Modelling wind speeds for cup anemometers mounted on opposite sides of a lattice tower: a case study. *J. Wind Eng. Ind. Aerodyn.* **115**, 173–183 (2013). <https://doi.org/10.1016/j.jweia.2012.11.006>
- Baseer, M.A., Meyer, J.P., Rehman, S., Mahbub Alam, Md., Al-Hadhrani, L.M., Lashin, A.: Performance evaluation of cup-anemometers and wind speed characteristics analysis. *Renew. Energy* **86**, 733–744 (2016). <https://doi.org/10.1016/j.renene.2015.08.062>
- Hanslian, D., Hosek, J.: Combining the VAS 3D interpolation method and wind atlas methodology to produce a high-resolution wind resource map for the Czech Republic. *Renew. Energy* **77**, 291–299 (2015). <https://doi.org/10.1016/j.renene.2014.12.013>
- Ozelkan, E., Chen, G., Ustundag, B.B.: Spatial estimation of wind speed: a new integrative model using inverse distance weighting and power law. *Int. J. Digit. Earth* **9**, 733–747 (2016). <https://doi.org/10.1080/17538947.2015.1127437>
- Cheyne, E., Jakobsen, J.B., Snæbjörnsson, J., Reuder, J., Kumer, V., Svardal, B.: Assessing the potential of a commercial pulsed lidar for wind characterisation at a bridge site. *J. Wind Eng. Ind. Aerodyn.* **161**, 17–26 (2017). <https://doi.org/10.1016/j.jweia.2016.12.002>
- Rehman, S., Mohandes, M.A., Alhems, L.M.: Wind speed and power characteristics using LiDAR anemometer based measurements. *Sustain. Energy Technol. Assess.* **27**, 46–62 (2018). <https://doi.org/10.1016/j.seta.2018.03.009>
- Dai, L.D., Xin, J.Y., Zuo, H.C., Ma, Y.X., Zhang, L., Wu, X.R., Ma, Y.J., Jia, D.J., Wu, F.K.: Multilevel validation of doppler wind lidar by the 325 m meteorological tower in the planetary boundary layer of Beijing. *Atmosphere* **11**, 1051 (2020). <https://doi.org/10.3390/atmos11101051>
- Kogaki, T., Sakurai, K., Shimada, S., Kawabata, H., Otake, Y., Kondo, K., Fujita, E.: Field measurements of wind characteristics using lidar on a wind farm with downwind turbines installed in a complex terrain region. *Energies* **13**, 5135 (2020). <https://doi.org/10.3390/en13195135>
- Lang, S., McKeogh, E.: LIDAR and SODAR measurements of wind speed and direction in upland terrain for wind energy purposes. *Remote Sens.* **3**, 1871–1901 (2011). <https://doi.org/10.3390/rs3091871>
- El Kasmi, A., Masson, C.: Turbulence modeling of atmospheric boundary layer flow over complex terrain: a comparison of models at wind tunnel and full scale. *Wind Energy* **13**, 689–704 (2010). <https://doi.org/10.1002/we.390>
- Mattuella, J.M.L., Loredou-Souza, A.M., Oliveira, M.G.K., Petry, A.P.: Wind tunnel experimental analysis of a complex terrain micro-siting. *Renew. Sust. Energy Rev.* **54**, 110–119 (2016). <https://doi.org/10.1016/j.rser.2015.09.088>
- Wang, Z., Zou, Y.F., Yue, P., He, X.H., Liu, L.L., Luo, X.Y.: Effect of topography truncation on experimental simulation of flow over complex terrain. *Appl. Sci.* **12**, 2477 (2022). <https://doi.org/10.3390/app12052477>
- Dhunni, A.Z., Lollchund, M.R., Rughooputh, S.D.D.V.: A high-resolution mapping of wind energy potentials for Mauritius using computational fluid dynamics (CFD). *Wind Struct. Int. J.* **20**, 565–578 (2015). <https://doi.org/10.12989/was.2015.20.4.565>
- Yan, B.W., Li, Q.S.: Coupled on-site measurement/CFD based approach for high-resolution wind resource assessment over complex terrains. *Energy Convers. Manag.* **117**, 351–366 (2016). <https://doi.org/10.1016/j.enconman.2016.02.076>
- Sessarego, M., Shen, W.Z., van der Laan, M.P., Hansen, K.S., Zhu, W.J.: CFD simulations of flows in a wind farm in complex terrain and comparisons to measurements. *Appl. Sci.* **8**, 788 (2018). <https://doi.org/10.3390/app8050788>
- Blocken, B., van der Hout, A., Dekker, J., Weiler, O.: CFD simulation of wind flow over natural complex terrain: case study with validation by field measurements for Ria de Ferrol, Galicia Spain. *J. Wind Eng. Ind. Aerodyn.* **147**, 43–57 (2015). <https://doi.org/10.1016/j.jweia.2015.09.007>
- Huang, W.F., Zhang, X.B.: Wind field simulation over complex terrain under different inflow wind directions. *Wind Struct. Int. J.* **28**, 239–253 (2019). <https://doi.org/10.12989/was.2019.28.4.239>
- Tse, K.T., Li, S.W., Fung, J.C.H.: A comparative study of typhoon wind profiles derived from field measurements, meso-scale numerical simulations, and wind tunnel physical modeling. *J. Wind Eng. Ind. Aerodyn.* **131**, 46–58 (2014). <https://doi.org/10.1016/j.jweia.2014.05.001>
- Niyomtham, L., Lertsathittanakorn, C., Waewsak, J., Gagnon, Y.: Mesoscale/microscale and CFD modeling for wind resource assessment: application to the Andaman Coast of Southern Thailand. *Energies* **15**, 3025 (2022). <https://doi.org/10.3390/en15093025>



24. Toparlar, Y., Blocken, B., Maiheu, B., van Heijst, G.J.F.: A review on the CFD analysis of urban microclimate. *Renew. Sustain. Energy Rev.* **80**, 1613–1640 (2017). <https://doi.org/10.1016/j.rser.2017.05.248>
25. Ramponi, R., Blocken, B., de Coo, L.B., Janssen, W.D.: CFD simulation of outdoor ventilation of generic urban configurations with different urban densities and equal and unequal street widths. *Build. Environ.* **92**, 152–166 (2015). <https://doi.org/10.1016/j.buildenv.2015.04.018>
26. Toja-Silva, F., Kono, T., Peralta, C., Lopez-Garcia, O., Chen, J.: A review of computational fluid dynamics (CFD) simulations of the wind flow around buildings for urban wind energy exploitation. *J. Wind Eng. Ind. Aerodyn.* **180**, 66–87 (2018). <https://doi.org/10.1016/j.jweia.2018.07.010>
27. Yang, A.-S., Su, Y.-M., Wen, C.-Y., Juan, Y.-H., Wang, W.-S., Cheng, C.-H.: Estimation of wind power generation in dense urban area. *Appl. Energy* **171**, 213–230 (2016). <https://doi.org/10.1016/j.apenergy.2016.03.007>
28. Ku, C.-A., Tsai, H.-K.: Evaluating the influence of urban morphology on urban wind environment based on computational fluid dynamics simulation. *ISPRS Int. J. Geo-Inf.* **9**, 399 (2020). <https://doi.org/10.3390/ijgi9060399>
29. Kalmikov, A., Dupont, G., Dykes, K., Chan, C.: Wind power resource assessment in complex urban environments: MIT campus case-study using CFD analysis. In: Proceedings of the AWEA 2010 WINDPOWER Conference, Dallas, TX, USA, 23–26 May 2010
30. Jamdade, P.G., Jamdade, S.G.: Evaluation of wind energy potential for four sites in Ireland using the Weibull distribution model. *J. Power Technol.* **95**, 48–53 (2015)
31. Cooney, C., Byrne, R., Lyons, W.: Performance characterisation of a commercial-scale wind turbine operating in an urban environment, using real data. *Energy Sustain.* **36**, 44–54 (2017). <https://doi.org/10.1016/j.esd.2016.11.001>
32. Byrne, R., Hewitt, N.J., Grif, P., Macartain, P.: Observed site obstacle impacts on the energy performance of a large scale urban wind turbine using an electrical energy rose. *Energy Sustain. Dev.* **43**, 23–37 (2018). <https://doi.org/10.1016/j.esd.2017.12.002>
33. Byrne, R., Hewitt, N.J., Griffiths, P., MacArtain, P.: An assessment of the mesoscale to microscale influences on wind turbine energy performance at a peri-urban coastal location from the Irish wind atlas and onsite LiDAR measurements. *Sustain. Energy Technol. Assess.* **36**, 100537 (2019). <https://doi.org/10.1016/j.seta.2019.100537>
34. Vestas Wind Systems: V52-850 kW the turbine that goes anywhere. https://users.wpi.edu/~cfurlong/me3320/DProject/V52_850kW_US.pdf (2005)

Publisher's Note Springer Nature remains neutral with regard to jurisdictional claims in published maps and institutional affiliations.

Springer Nature or its licensor holds exclusive rights to this article under a publishing agreement with the author(s) or other rightsholder(s); author self-archiving of the accepted manuscript version of this article is solely governed by the terms of such publishing agreement and applicable law.





Predicting photovoltaic power generation using double-layer bidirectional long short-term memory-convolutional network

Mohammed Sabri¹ · Mohammed El Hassouni²

Received: 28 May 2022 / Accepted: 7 September 2022 / Published online: 28 September 2022
© The Author(s), under exclusive licence to Islamic Azad University 2022

Abstract

Accurate photovoltaic (PV) power prediction is critical for PV power plant safety and stability. The main restrictions influencing the accuracy of the PV power forecast are the variability and intermittency of solar energy. Therefore, this study proposes a hybrid deep learning model for PV power forecast that is successfully developed using the combination of the bidirectional long short-term memory (BLSTM) and convolutional neural network (CNN) and is applied to the actual dataset collected in the DKASC PV system in Alice Springs, Australia. The proposed architecture is a structure of two major branches. BLSTM is used first to extract the bidirectional temporal characteristics of PV power. Next, CNN was used to capture the spatial characteristics. The prediction results of the hybrid model are compared with those of the single model LSTM, BLSTM, CNN, gated recurrent unit, recurrent neural network (RNN), and the hybrid network (LSTM–CNN, CNN–LSTM) in order to demonstrate the higher performance of the proposed hybrid prediction model. By comparing statistical performance indicators such as root mean square error (RMSE), mean absolute error (MAE), mean square error (MSE), and coefficient of determination (R^2) values with other existing deep learning models, the performance of the proposed BLSTM–CNN model has been demonstrated. The results indicate that the BLSTM–CNN model has the highest precision with the lowest MSE of 0.0089, MAE of 0.0531, RMSE of 0.0944, and highest R^2 of 0.9993. BLSTM–CNN can enhance forecasting accuracy while also accurately capturing the various temporal–spatial characteristics of PV power.

Keywords Photovoltaic power forecasting · Deep learning · Bidirectional long short-term memory · Convolutional neural network

Abbreviations

AI	Artificial intelligence	GRU	Gated recurrent unit
ARMA	Autoregressive and moving average	LSTM	Long short-term memory
BLSTM	Bidirectional long short-term memory	MAE	Mean absolute error
BPNN	Back propagation neural network	MSE	Mean square error
CNN	Convolutional neural network	NWP	Numerical weather prediction
DKASC	Desert Knowledge Australia Solar Centre	PV	Photovoltaic
ELM	Extreme learning machine	RMSE	Root mean square error
GA	Genetic algorithm	RCC	Radiation classification coordinate
		RNN	Recurrent neural network
		SVM	Support vector machine
		SDA	Customized similar day analysis
		WPD	Wavelet packet decomposition

Mohammed Sabri and Mohammed El Hassouni have contributed equally to this work.

✉ Mohammed Sabri
mohammed_sabri3@um5.ac.ma
Mohammed El Hassouni
mohamed.elhassouni@flsh.um5.ac.ma

¹ LRIT, Mohammed V University in Rabat, 1014 Rabat, Morocco
² FLSH, Mohammed V University in Rabat, 1014 Rabat, Morocco

List of symbols

b_j^1	Bias for the j th feature map
f_t	Output of the forget gate at time t
m	Index value of the filter
n	Number of units per window
i_t	Output of the input gate at time t
o_t	Output of an LSTM block at time t
R	Pooling size



R^2	Coefficient of determination
x	Input vector for power production
y_{ij}^1	Output of the first convolutional layer
W	Weight parameters of layers

Introduction

Energy is one of the most important factors in the process of industrialization and modernization, and it plays a critical role in technological and economic progress. Furthermore, massive population growth has exacerbated the global energy crisis. Electricity demand continues to rise, which has a negative influence on the environment [52]. As a result, several governments and regions are enacting laws to encourage the development of renewable energy [30]. Solar energy has become a crucial means of solving environmental and energy concerns due to its clean and plentiful properties [43]. The randomness and intermittent nature of PV power generation, on the other hand, makes integrating it into current energy networks extremely difficult [48]. Accurate PV power prediction is critical for ensuring the power grid's security and storing alternative energy sources for a reasonable amount of time [2].

Different prediction approaches have been presented in recent years to forecast PV power output, which can be split into four groups: Physical method [36], statistical method [8], machine learning method [47], and hybrid method [32] are four types of PV power predicting techniques that have been established based on various forecasting principles.

The physical model forecasts PV power based on geological variables and meteorological data (i.e., air pressure, humidity, solar radiation, cloud volume, etc.) provided by the meteorological stations. After that, it creates a physical model based on the PV panel parameters, and then directly the PV generation power is calculated. The physical model is less reliant on previous data, but it is more complex to model because there are several unknown parameters [11].

Based on statistical data, time series models predict PV power. The impact of meteorological conditions is not considered throughout the forecasting phase; just the time factor is taken into account. To forecast PV output, a range of statistical approaches have been used, for example, the Markov Chain method [33, 42], gray theory [55], autoregressive and moving average (ARMA) models [6, 25]. A prior understanding of the PV system's complicated photoelectric conversion link is not required for statistical modeling, but only a partial comprehension and realization using numerous data analysis approaches. However, the statistical approach uses a huge quantity of data to calculate and requires more time. With the rapid growth of artificial intelligence (AI) in recent years, Machine learning

models with strong learning capacity and nonlinear mapping capability have been widely employed in PV power forecasting [18]. Furthermore, machine learning models can forecast PV generation power from easily available data, eliminating the need for complicated computations and other costly expenditures. For example, support vector machine (SVM) [31], back propagation neural network (BPNN) [19], extreme learning machine (ELM) [3] and Elman neural network [51]. These approaches forecast the generation capacity of PV power plants only based on historical data, without requiring any knowledge of PV power plants such as the number of panels, panel capacity [34]. Traditional single algorithms frequently neglect the fact that output power changes with a wide range of meteorological variables, which might lead to inaccurate forecasting [12]. Hybrid methods, which combine a variety of effective techniques, are more effective and efficient when compared to other ways for PV generation forecast [7]. Some examples of hybrid models used in PV power prediction are: support vector machine (SVM) and ant colony optimization (ACO) [37], convolution neural network (CNN) and gated recurrent unit (GRU) [40], bidirectional LSTM model with a genetic algorithm (GA) [58]. (SDA–GA–ELM) based on customized similar day analysis (SDA), genetic algorithm, and extreme learning machine [59].

The deep learning theory, introduced by Hinton et al. [15] has recently gained a lot of traction. With the advancement at a rapid pace of artificial intelligence techniques, deep learning models have a wider and more robust nonlinear network structure than classic machine learning models [28]. Some have already produced excellent results in predicting PV power generation, LSTM proposed by Hochreiter and Schmidhuber [16] has been extensively used to forecast PV power. The LSTM is a recursive neural network that can increase the network's storage space and retain historical data for later use, it has the advantage of detecting long-term time series relationships. Gao et al. [13] proposed an LSTM model based on meteorological data to forecast the daily power production of PV power plants using weather categorization. Chen et al. [4] proposed a new method for very-short-term PV power prediction that combines similar time period collection using RCC (radiation classification coordinate) with LSTM. Lee et al. [27] proposed two models LSTM and GRU to predict PV power generation in a peak zone. The CNN is perfect for processing and analyzing high-dimensional data. For time series forecasting, some researchers employ CNN. For wind and solar energy forecasting, Díaz-Vico et al. [9] employed a CNN with input data from a numerical weather prediction system (NWP), the CNN's excellent feature extraction capacity is demonstrated by the prediction results. Sabri



et al. [41] proposed a new hybrid deep learning model (CNN–GRU) to predict the PV power output, the convolutional layer extracts the characteristics of the input data, while the GRU maintains the crucial details to improve prediction performance.

A new form of LSTM, known as the bidirectional LSTM (BLSTM), has recently been used for classification and regression problems. By structurally incorporating two forward and backward LSTM layers, the BLSTM can consider data from both the past and the future at the same time [24]. The BLSTM network has recently been utilized in electricity price forecasting [5], urban solid waste forecasting [21], and air pollution forecasting [35]. Aside from developing a time series forecasting model with BSLTM, other researchers have attempted to enhance BLSTM's efficiency by combining the advantages of BLSTM and CNN to improve the prediction effect. Lawal et al. [26] proposed short-term wind forecasting at various elevations above ground level using a hybrid of 1D CNN and the BLSTM network. Unal et al. [46] proposed a spatiotemporal deep learning architecture to forecast energy consumption using the hybrid model CNN–BLSTM. Joseph et al. [22] proposed a novel hybrid deep learning model based on BLSTM and CNN for predicting traffic congestion in a smart city.

Weather forecast data has a restricted forecasting range, and historical PV power time series are non-periodic and non-stationary making classical AI algorithms ineffective. Specifically, to overcome current obstacles and attain the objectives of accurate PV power predicting. The following considerations contribute to the hypothesis of the proposed method in this paper: According to the current study, BLSTM has a high ability to extract bidirectional temporal characteristics, CNN can extract spatial characteristics. It is found that considering the combination of BLSTM and CNN model to predict PV power can achieve more accurate results.

Therefore, a new hybrid model of PV power forecasting, the BLSTM–CNN model, is suggested in this study based on the mechanistic characteristics of time series data. The main research contents of this paper are as follows:

1. To get acceptable prediction results, the input dataset is placed through a preprocessing step where redundant, outlier, or missing values are eliminated.
2. A hybrid PV power prediction network is proposed that takes into account the temporal–spatial characteristics extraction order.
3. The bidirectional temporal characteristics of the data are extracted first using the BLSTM model and then the spatial characteristics of the data are extracted using the CNN model while considering the PV data features.

Methods and materials

Convolutional neural network

A major component of a convolutional neural network is the convolution layer [23]. Convolution layer C and numerous filters are coupled to the input matrix, with each filter holding an $i \times i$ weight matrix. Find the convolution matrix using a filtered scan of the input matrix. The CNN layer can extract local features from high-layer inputs and send them down to lower layers for more sophisticated features [54]. Equation (1) is the result of the vector y_{ij}^1 output from the first convolutional layer, where x is the input vector for power production, and n is the number of units per window. The output vector x of the previous layer is used to calculate y . w is the weight of the kernel, σ is the activation function, b_j^1 represents the bias for the j th feature map, and m is the index value of the filter. The result of Eq. (2) is the vector y_{ij}^l output from the l_{th} convolutional layer.

$$y_{ij}^1 = \sigma \left(b_j^1 + \sum_{m=1}^M w_{m,j}^1 x_{i+m-1,j}^0 \right) \quad (1)$$

$$y_{ij}^l = \sigma \left(b_j^l + \sum_{m=1}^M w_{m,j}^l x_{i+m-1,j}^0 \right). \quad (2)$$

The pooling layer is a crucial component of CNN, and it is utilized to minimize the convolution matrix's dimension. Eq. (3) represents the max-pooling layer operation. T is the step that specifies how far the input data area will be relocated, and R is the pooling size that is smaller than y .

$$p_{ij}^l = \max_{r \in R} y_{i \times T + r, j}^{l-1} \quad (3)$$

Bidirectional long short-term memory neural network

In 1982, Hopfield proposed the recurrent neural network (abbreviated as RNN) [17]. Because of its unique network structure, which differs from traditional neural networks, each component of the RNN maintains the hidden layer parameters, allowing the current component to retain the memory of the information produced by the pre-order components. Figure 1 illustrates a comprehensive overview of RNN. Nevertheless, there is a clear disadvantage to RNN when the data series is too long, or the time interval is too large. The continuous multiplication impact in gradient reverse multiplication causes the vanishing

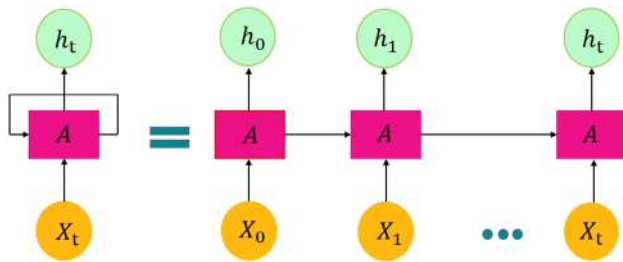


Fig. 1 General overview of recurrent neural networks [20]

gradient issue, rendering RNNs unable to train effectively. This problem was well handled by Schmidhuber's LSTM network, which he introduced in 1997 [16]. The forget gate, output gate, and input gate are used to build a memory unit in LSTM [56], which replaces the memory unit in RNN.

The process of the three gates specific to the LSTM is described in the following details:

Forget gate Unwanted data can be discarded if desired. By reading the current moment's input x_t and the previous moment's output h_{t-1} , and assigning a weight between 0 and 1 to each data in the cell state C_{t-1} at the previous moment, 0 denotes "all discarded" whereas 1 denotes "all retained." The LSTM network can adjust this weight to improve the model through continual feedback learning. The following is the output f_t :

$$f_t = \sigma(W_f \cdot [h_{t-1}, x_t] + b_f). \quad (4)$$

Input gate It is used to figure out what data should be saved in the cell state. The sigmoid layer defines what value needs to be updated, and the output of the input gate is designated as i_t . The tanh layer generates new \tilde{C}_t , that is, ready-to-add information to the cell state:

$$i_t = \sigma(W_i \cdot [h_{t-1}, x_t] + b_i) \quad (5)$$

$$\tilde{C}_t = \tanh(W_c \cdot [h_{t-1}, x_t] + b_c). \quad (6)$$

Then, multiply the cell state at the previous moment by the forget gate output function f_t , and update the cell state at the previous moment. Add the newly generated candidate information and calculate the current unit state as follows:

$$C_t = f_t * c_{t-1} + i_t * \tilde{C}_t. \quad (7)$$

Output gate Filter to ensure that just what is required in the cell state is output. It is also split into two layers: The tanh layer updates the cell state requirement to a value between -1 and 1 . The output is designated as o_t , and the sigmoid layer defines which part of the cell state is output, and finally outputs h_t :

$$o_t = \sigma(W_o \cdot [h_{t-1}, x_t] + b_o) \quad (8)$$

$$h_t = o_t * \tanh(C_t) \quad (9)$$

where o_t, i_t, f_t are the output gate, input gate, and the output value of the forget gate, respectively. The $b_{f,i,o}$ and $W_{f,i,o}$ are the bias vectors and weight matrices. σ is a sigmoid function.

BLSTM stands for bidirectional LSTM and is commonly employed for natural language processing. In terms of time series forecasting, BLSTM may outperform LSTM. BLSTM is made up of two fundamental LSTMs [14]: a forward LSTM that utilizes past information and a backward LSTM that utilizes future information, allowing information from time $t-1$ and time $t+1$ to be utilized at time t . Usually, BLSTM is more efficient than LSTM and RNN in general since both past and future information may be used.

The calculating equation of the y_t :

$$y_t = g(W_y[h_t; h'_t] + b_y) \quad (10)$$

$$h_t = f(W_t[c_{t-1}; x] + b_t) \quad (11)$$

$$h'_t = f(W'_t[c'_{t-1}; x] + b'_t) \quad (12)$$

where h'_t and h_t is the hidden output of the backward LSTM cell and of the forward LSTM cell at time t , respectively, W'_t is the weight matrix of the backward LSTM cell, W_t is the weight matrix of the forward LSTM cell at the time t , b'_t is the bias vectors of the backward LSTM cell at the time t , b_t is the bias vectors of the forward LSTM cell at the time t .

BLSTM–CNN hybrid neural networks

Hybrid models, on average, outperform single models. Maintaining the utility of BLSTM and CNN in consideration. We leveraged the complementary capabilities of both models to construct a new operational temporal and spatial extracting features model to predict PV power generation more precisely. In this paper, a hybrid approach called BLSTM–CNN is suggested to forecast PV power generation using a series connection of BLSTM and CNN, as illustrated in Fig. 2. The suggested approach excels at pulling complex characteristics and patterns from weather factors obtained for PV power generation forecasting. The historical time series PV power data is initially fed into the BLSTM model as an input, and the temporal characteristics of the data are extracted utilizing the BLSTM model's capability of processing time series data. The resulting temporal characteristics are then transmitted to the CNN model input layer to extract the data's spatial characteristics. A CNN often contains numerous levels of convolutional-pooling layers, with many convolution operations conducted at each level

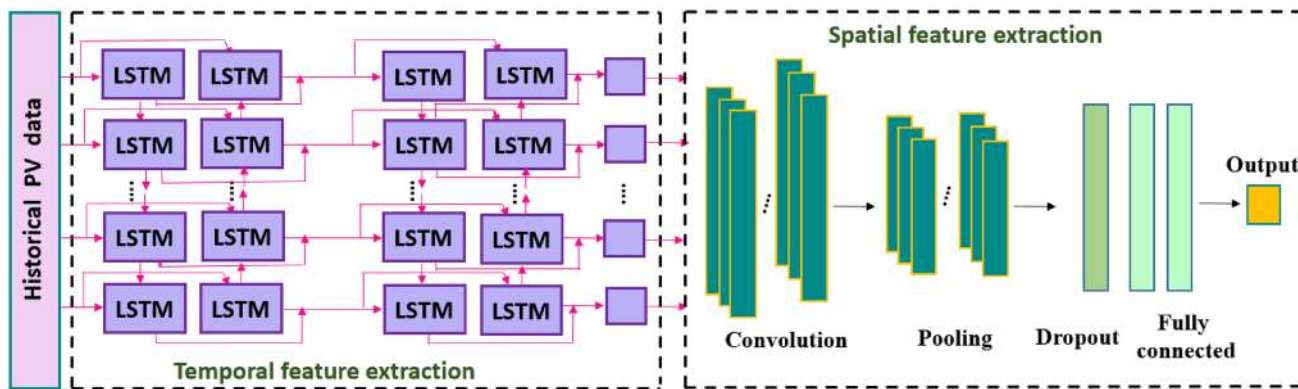


Fig. 2 The structure of hybrid model BLSTM–CNN [57]

to capture significant data. CNN applies weights to weather factors depending on their effect on PV power. Finally, a fully connected layer is employed to gather the data and forecast the PV power generation using extracted characteristics. The dropout layer is also introduced to the model to minimize model overfitting.

Dataset description

In this study, the PV data from 1B DKASC, Alice Springs PV system was chosen as a case study [10]. For this experiment, data from October 1, 2020, to January 27, 2021, with a resolution of 5 min were chosen. The input parameters are global horizontal radiation ($W/m^2 \times sr$), weather temperature Celsius ($^{\circ}C$), diffuse horizontal radiation ($W/m^2 \times sr$), current phase average (A), weather relative humidity (%) and wind direction (\hat{A}°), while the output is set to active power data (kW). To increase the effectiveness and precision of the model forecast, the data must be preprocessed and filtered before being fed into it. Preprocessing involves eliminating abnormal data, completing missing values, and normalizing the data. The data is separated into two parts: 80% for training and 20% for testing. The BLSTM–CNN hybrid model has two primary parts. The first one is the bidirectional long-term dependencies are learned using the temporal modeling tool BLSTM after data preprocessing. The second one is 1D CNN, which is applied to extract the data’s spatial characteristics. In order to evaluate the effectiveness of the proposed BLSTM–CNN. Five single deep learning models CNN, GRU, LSTM, RNN, BLSTM, and two hybrid models LSTM–CNN and CNN–LSTM are also used as comparison models for predicting the output of PV power. The metrics used to measure model prediction efficiency and accuracy are RMSE, MSE, MAE, R^2 . The experimental results were completed in Python 3.7 and a personal computer with a 64-bit operating system, Intel (R)

Core (TM) i7-4600 CPU@2.10GHZ 2.70GHZ and 8.00 GB of RAM. The framework of PV power output forecasting is shown in Fig. 3.

Model evaluation indexes

To compare the performance of various predictive models, we utilize the mean absolute error (MAE), root mean square error (RMSE), mean square error (MSE), and coefficient of determination (R^2) [39]. Definitions of these evaluation indexes are as follows.

$$MAE = \frac{1}{N} \sum_{i=1}^N |y_i - \tilde{y}_i| \tag{13}$$

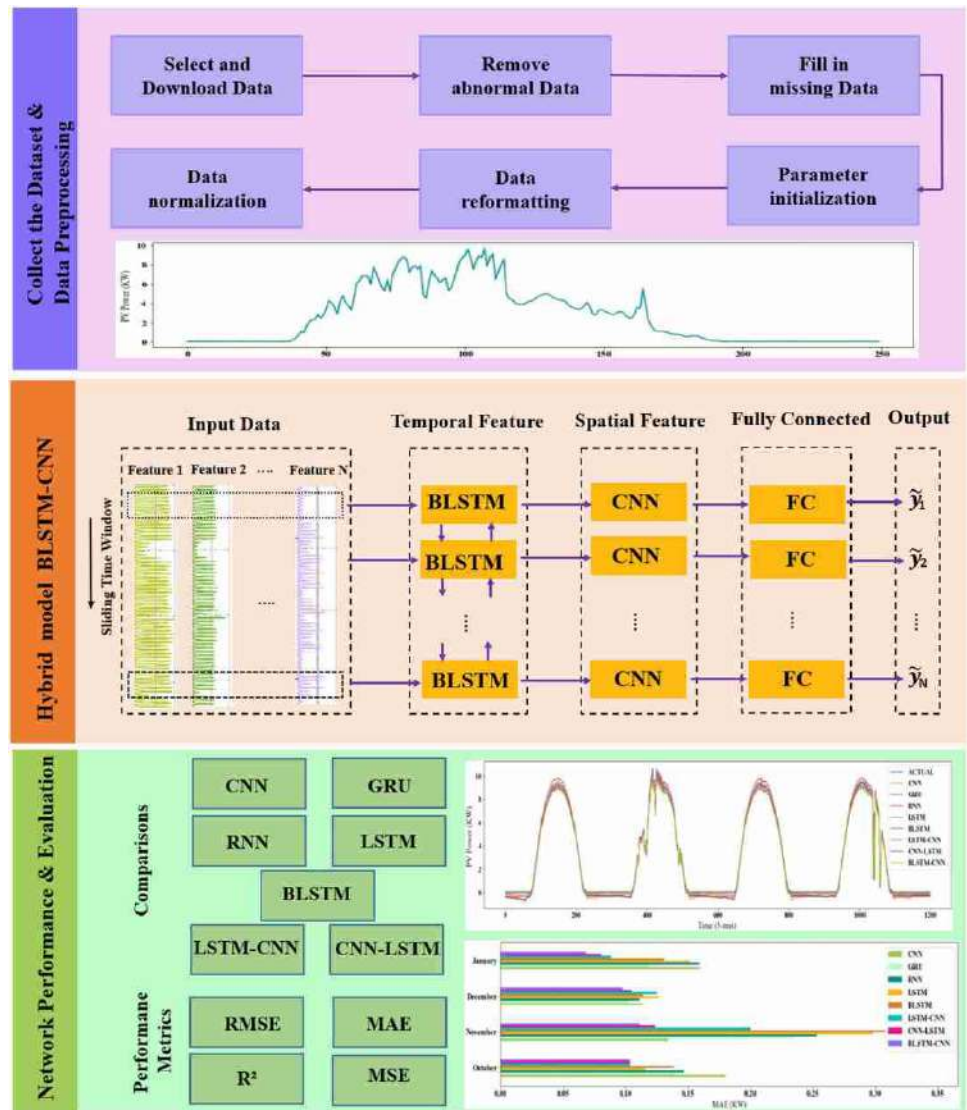
$$MSE = \frac{1}{N} \sum_{i=1}^N (y_i - \tilde{y}_i)^2 \tag{14}$$

$$RMSE = \sqrt{\frac{1}{N} \sum_{i=1}^n (y_i - \tilde{y}_i)^2} \tag{15}$$

$$R^2 = 1 - \frac{\sum_{i=1}^N (y_i - \tilde{y}_i)^2}{\sum_{i=1}^N (y_i - \bar{y}_i)^2} \tag{16}$$

where y_i is the real PV power generation value, \tilde{y}_i predicted value and N is the number of y_i . \bar{y}_i is the average of the real PV power generation in the test set.

Fig. 3 Framework of proposed model



Modeling results

Results and comparisons

This research proposes a hybrid model (BLSTM–CNN) for PV power prediction. The BLSTM model was used to extract bidirectional temporal features. Set up two hidden layers using the filtered index data in the BLSTM model, where Units = 128; Units = 256. The obtained temporal characteristics are then sent to the CNN model input layer, which uses the convolutional layer and pooling layer to extract spatial features of the dataset. In the CNN model, 2 layers of convolutional layers and 2 layers of pooling layers are used, there are 128 and 256 convolution kernels, respectively. In the convolutional layer, the kernel size is 3*3. The

Table 1 Parameters setting of the proposed method

Type	Filter	Kernel size	Stride
BLSTM (128)	–	–	–
BLSTM (256)	–	–	–
Convolution	128	3	1
Activation (Relu)	–	–	–
Max-pooling	–	2	2
Convolution	256	3	1
Activation (Relu)	–	–	–
Max-pooling	–	2	2
Dropout (0.2)	–	–	–
Dense (512)	–	–	–
Dense (256)	–	–	–

dropout layer [44] was also included in the model to avoid overfitting issues during training, which could reduce prediction accuracy. The batch size of the proposed model is 500. Finally, two layers of the fully connected layer with 512 and 256 neurons, respectively, output of the PV power generation forecasting result. The parameters settings of the suggested model in this work are shown in Table 1. Five single deep learning models CNN, GRU, LSTM, RNN, BLSTM, and two hybrid models LSTM–CNN and CNN–LSTM were

used as comparison models for PV power output forecasting to verify the effectiveness of the suggested BLSTM–CNN model in this work. The RMSE, MSE, MAE, and R^2 metrics are used to evaluate model forecasting accuracy and effectiveness.

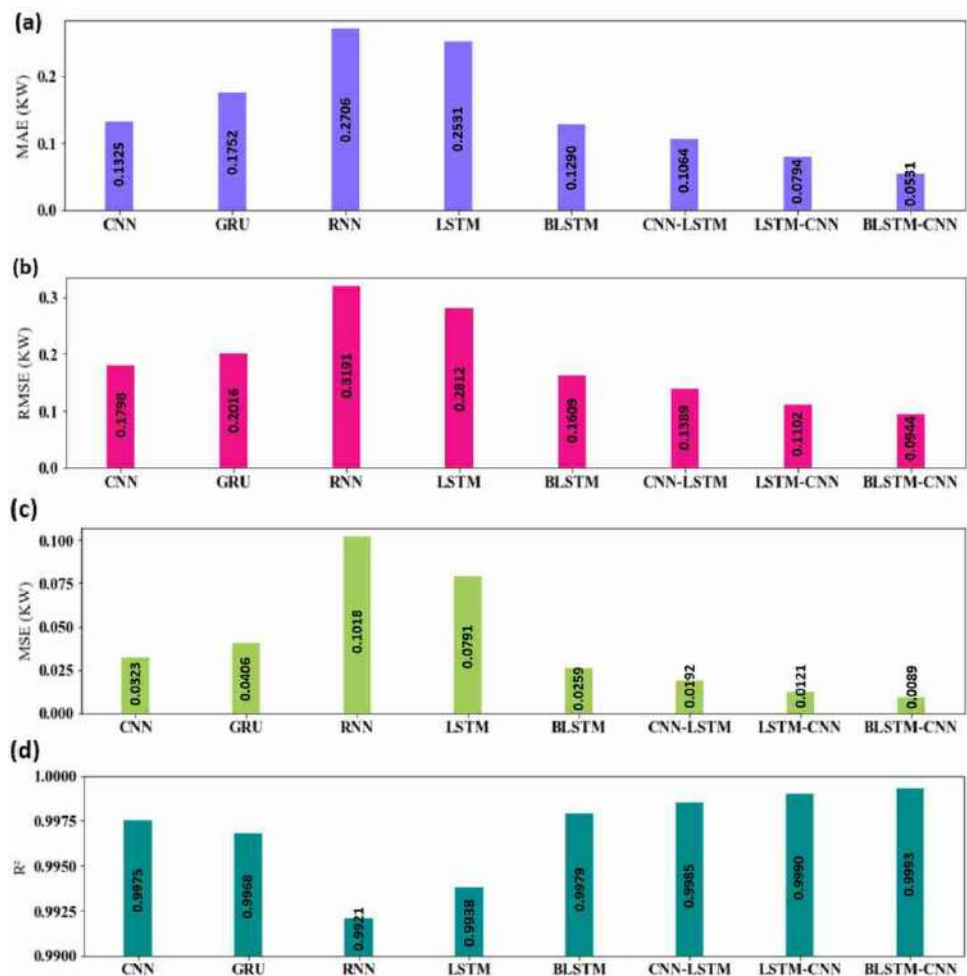
Table 2 shows the forecasting results of the eight models. Table 2 shows that the proposed BLSTM–CNN has lower values of RMSE, MSE, MAE values, and the highest value of R^2 than the other seven models. To make the data in Table 2 more visible. Figure 4 illustrates the results of the various models evaluation criteria. PV power generation data for one day in 2021 were chosen randomly as validation data to test the efficiency of the BLSTM–CNN model. Figure 5a shows a comparison of forecasted and actual values. For all times in the range, the forecasting curves show high consistency with the actual data. As shown in Fig. 5b, the error between the forecasted and actual values is illustrated by the rose curve.

Subsequently, the suggested forecasting model’s performance and stability are tested in four months to ensure the BLSTM–CNN forecasting reliability and efficacy. The collected data is separated into four months: October,

Table 2 The results of the forecasting model

Model	RMSE	MAE	MSE	R^2
CNN [49]	0.1798	0.1325	0.0323	0.9975
GRU [53]	0.2016	0.1752	0.0406	0.9968
RNN [27]	0.3191	0.2706	0.1018	0.9921
LSTM [13]	0.2812	0.2531	0.0791	0.9938
BLSTM [38]	0.1609	0.1290	0.0259	0.9979
CNN–LSTM [45]	0.1389	0.1064	0.0192	0.9985
LSTM–CNN [50]	0.1102	0.0794	0.0121	0.9990
BLSTM–CNN	0.0944	0.0531	0.0089	0.9993

Fig. 4 The MAE, RMSE, MSE, and R^2 criterion in different models



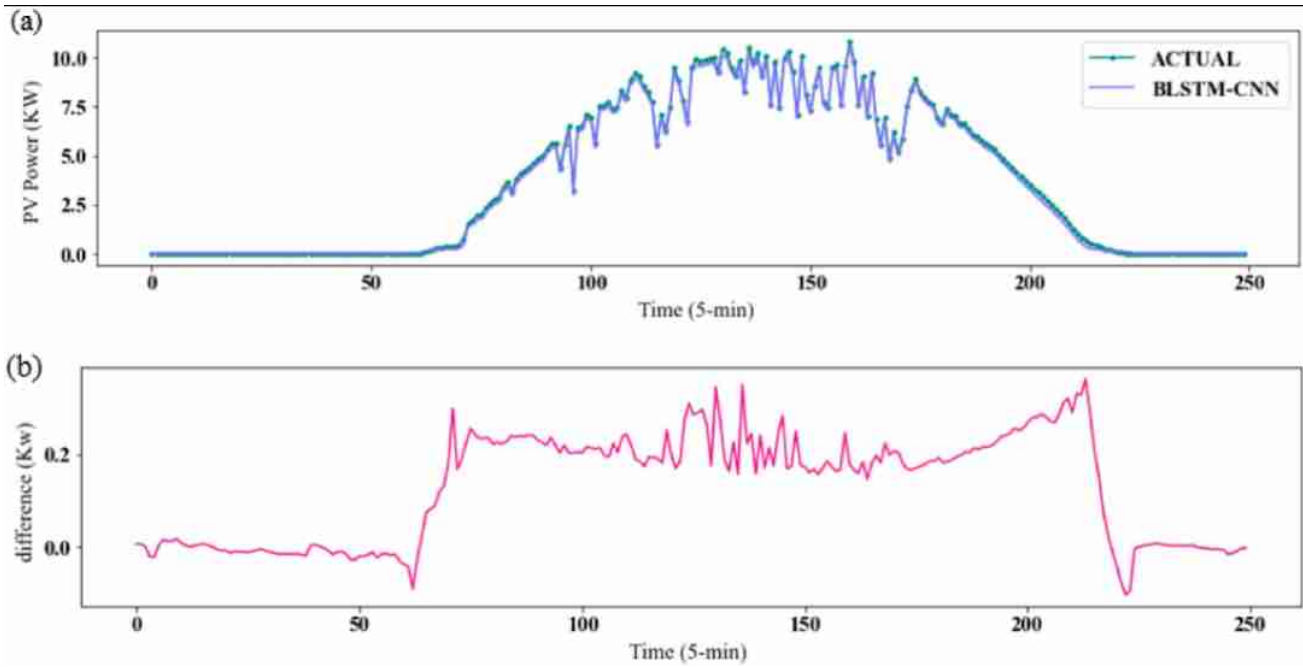


Fig. 5 Comparison between model predictions and actual values (a). Error between the forecasted and actual values (b)

Table 3 Statistical values of the experimental PV power (KW) data

Dataset	Samples	Numbers	Mean	Std.	Minimum	Maximum
October	All samples	8928	2.7547	3.5559	-0.0215	10.5396
	Training set	7142	2.6843	3.5070	-0.0203	10.5396
	Testing set	1786	3.0359	3.7330	-0.0215	10.0366
November	All samples	8639	2.8974	3.5440	-0.0199	11.0413
	Training set	6911	2.8447	3.5168	-0.0199	11.0413
	Testing set	1728	3.1084	3.6440	-0.0184	10.4283
December	All samples	8908	2.3949	3.2452	-0.0188	11.6942
	Training set	7126	2.2086	3.0685	-0.0187	10.8382
	Testing set	1782	3.1400	3.7824	-0.0188	11.6942
January	All samples	7658	2.9545	3.6139	-0.0222	11.4737
	Training set	6126	3.0698	3.6956	-0.0222	11.4737
	Testing set	1532	2.4936	3.2268	-0.0158	10.5551

November, December, and January. Each month’s data is divided into two parts: 80% for training and 20% for testing. Table 3 shows the partition of training and testing sets in four months.

Table 4 shows the results of various models CNN, GRU, RNN, LSTM, BLSTM, CNN–LSTM, LSTM–CNN, and BLSTM–CNN for the PV power forecasting in different months October, November, December, and January. The hybrid models outperform the single models in terms of prediction accuracy. In addition, the prediction effect of the BLSTM–CNN hybrid model is better than that of the two hybrid models (LSTM–CNN and CNN–LSTM). The result indicates that BLSTM–CNN outperforms other models in

terms of prediction accuracy in four months, although various models can be used to forecast PV power generation, no single model consistently always outperforms the others, which confirms the proposed model’s ability to extract temporal–spatial features, which allows it to create a complicated relationship between input data and target PV power generation. For better visualization, the evaluation criteria result in different months of the various models is also illustrated in Fig. 6.

A four-day from each month was chosen at random for further examination. Figure 7 illustrates the prediction results for these sixteen days using the proposed model and seven comparable models. It is evident that all the

Table 4 Error evaluation results of BLSTM–CNN and other deep learning models in four datasets

Dataset	Model	RMSE	MAE	MSE	R^2
October	CNN	0.2139	0.1514	0.0457	0.9967
	GRU	0.1205	0.0803	0.0145	0.9989
	RNN	0.1928	0.1335	0.0371	0.9973
	LSTM	0.1517	0.1188	0.0230	0.9983
	BLSTM	0.1240	0.1085	0.0153	0.9988
	CNN–LSTM	0.1083	0.0843	0.0117	0.9991
	LSTM–CNN	0.0795	0.0516	0.0063	0.9995
	BLSTM–CNN	0.0471	0.0350	0.0022	0.9998
November	CNN	0.3123	0.2626	0.0975	0.9926
	GRU	0.4720	0.3851	0.2228	0.9832
	RNN	0.5490	0.4462	0.3014	0.9772
	LSTM	0.3941	0.3425	0.1553	0.9882
	BLSTM	0.3443	0.3265	0.1185	0.9910
	CNN–LSTM	0.1986	0.1844	0.0394	0.9970
	LSTM–CNN	0.1524	0.1265	0.0232	0.9982
	BLSTM–CNN	0.1333	0.1114	0.0177	0.9986
December	CNN	0.1430	0.1268	0.0225	0.9984
	GRU	0.2656	0.2069	0.0705	0.9950
	RNN	0.1696	0.1220	0.0287	0.9979
	LSTM	0.3569	0.2846	0.1273	0.9910
	BLSTM	0.1896	0.1411	0.0359	0.9974
	CNN–LSTM	0.1300	0.1051	0.0169	0.9988
	LSTM–CNN	0.1158	0.0797	0.0134	0.9990
	BLSTM–CNN	0.0728	0.0591	0.0053	0.9996
January	CNN	0.1153	0.0909	0.0133	0.9987
	GRU	0.4503	0.3246	0.2027	0.9805
	RNN	0.4104	0.3155	0.1684	0.9838
	LSTM	0.1512	0.1164	0.0228	0.9978
	BLSTM	0.1541	0.1042	0.0237	0.9977
	CNN–LSTM	0.1020	0.0664	0.0104	0.9989
	LSTM–CNN	0.0914	0.0642	0.0083	0.9991
	BLSTM–CNN	0.0939	0.0608	0.0088	0.9991

models perform well in terms of predictions. The suggested hybrid deep learning model outperforms five single models and two hybrid models in terms of prediction accuracy. The BLSTM–CNN curve and the actual value curve are very close and show better prediction performance, especially at night and during peak power.

Comparison of the proposed hybrid BLSTM–CNN model with state-of-the-art methods

The historical data in this paper comes from the DKASC in Australia. Different state-of-the-art methodologies were conducted and examined with solar producing plants from the DKASC in previous studies. The comparison results are shown in Fig. 8.

Chen et al. [4] proposed a simple and efficient RCC–LSTM model for PV power prediction. The RCC (radiation classification coordinate) method as a tool is used for gathering identical time periods, then LSTM is used to extract characteristics from time series PV power data. The data was gathered from the Yulara in Alice Springs for two years (2017–2018) with a resolution of the historical dataset as 5 min. The average MAE value obtained is 0.587.

Zhou et al. [29] proposed a hybrid deep learning model (WPD–LSTM) for short-term PV power forecasting. The data was gathered from DKASC, Alice Springs from June 1, 2014, to June 12, 2016. The average MAE value obtained is 0.2357. Zhou et al. [59] proposed a hybrid model (SDA–GA–ELM) based on extreme learning machine (ELM), genetic algorithm (GA), and customized similar day analysis (SDA) to forecast hourly PV power generation. The dataset was collected from Jan 14, 2017, to Oct 15, 2018, with a resolution of 1 h from DKASC. The average MAE value obtained is 0.2367.

Wang et al. [50] proposed a hybrid model (LSTM–CNN) for PV power forecasting. The data was collected from 1B DKASC, Alice Springs PV for half-year data with a resolution of the historical dataset as 5 min. The average MAE value obtained is 0.2210. Zhen et al. [58] proposed a hybrid model (GA–BLSTM) for ultra-short-term PV power prediction. The data was collected from 8 PV plants ranging from 2017 to 2019 with resolution of the historical dataset as 5 min. The average MAE value obtained is 0.242. Abdel-Basset et al. [1] proposed a novel deep learning architecture namely (PV-Net), to enable efficient extraction of positional and temporal features in PV power sequences, the gates of the GRU are modified utilizing convolutional layers (named Conv-GRU) for forecasting short-term PV energy production. The data was collected from 1B DKASC, Alice Springs PV throughout five years (2015–2019) with a resolution of the historical dataset as 5 min. The average MAE value obtained is 0.398.

When the above research's results are compared, the suggested BLSTM–CNN has the minimum MAE value. It is obvious that the suggested model outperforms prior researches and provides higher PV generation predicting performance.

However, the suggested model has a few flaws that must be investigated further. For example, in this research, the structure and training hyper-parameters of the model were found by experimentation, which is time-consuming. As a result, automated settings estimation approaches, like heuristic optimization algorithms, will be utilized in our future research to pick and improve the parameters of the neural network more effectively.



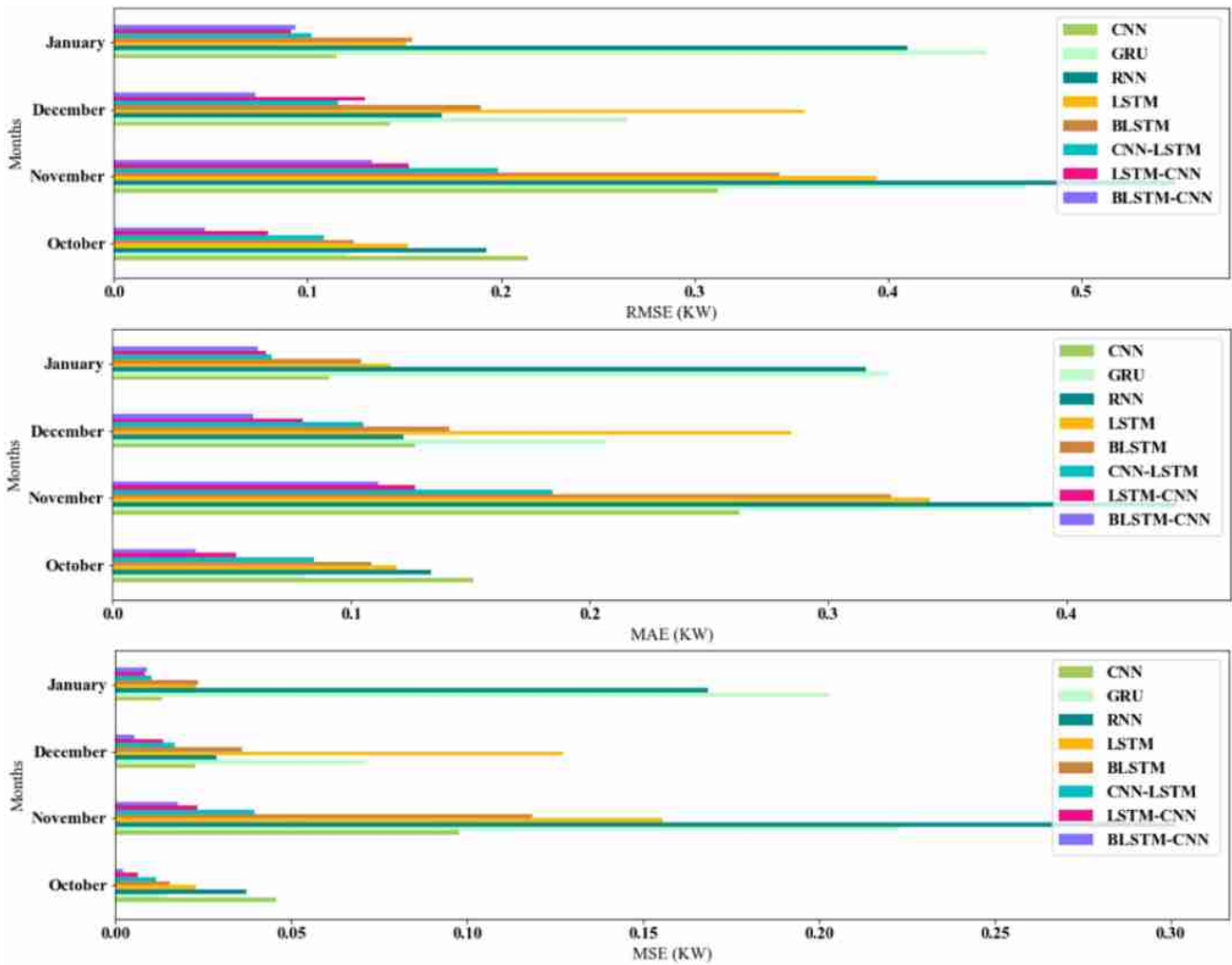


Fig. 6 Evaluation criteria results of BLSTM–CNN and other popular models in four datasets

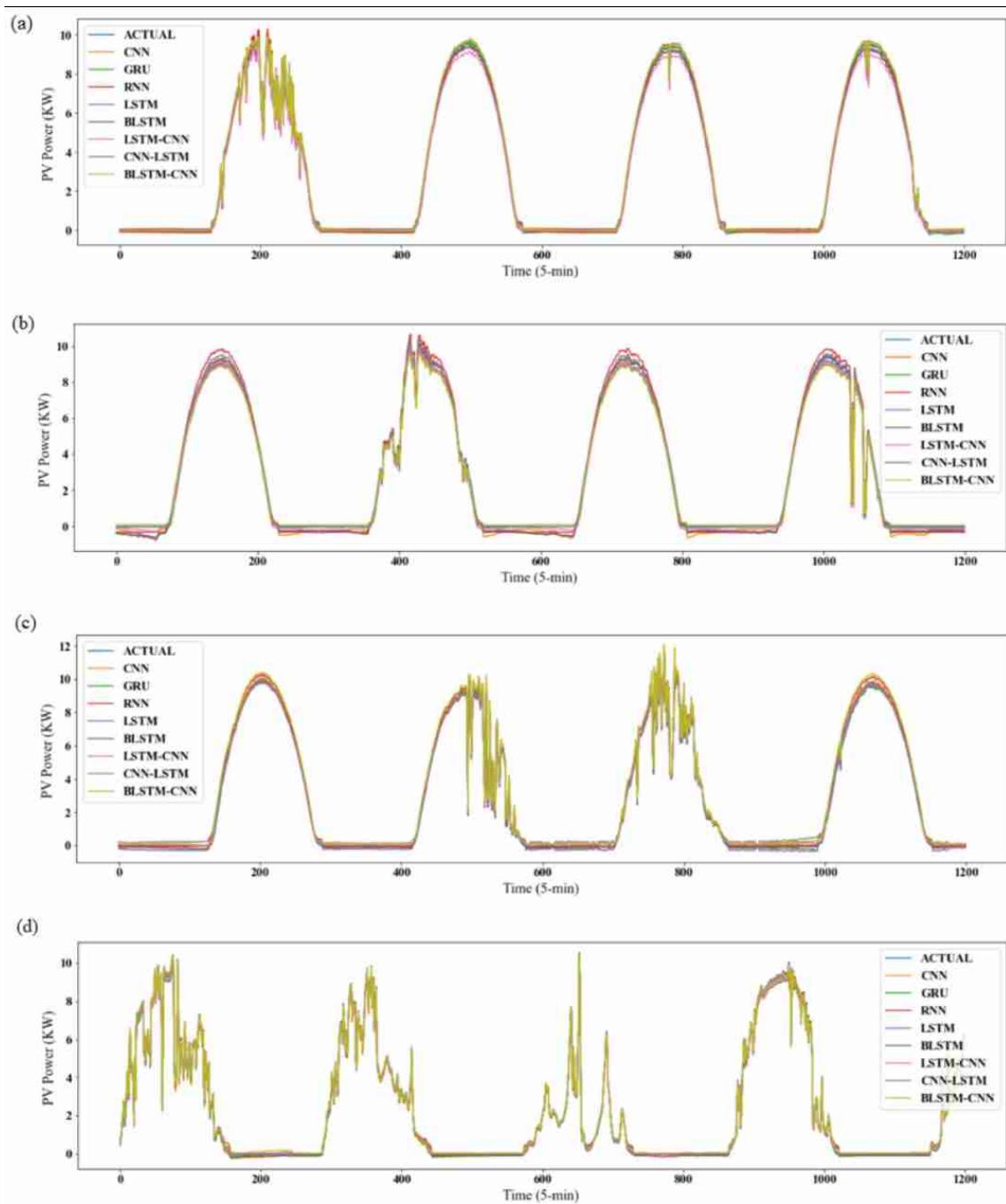


Fig. 7 The forecasting results of the different model and actual PV power in October (a), November (b), December (c), January (d)

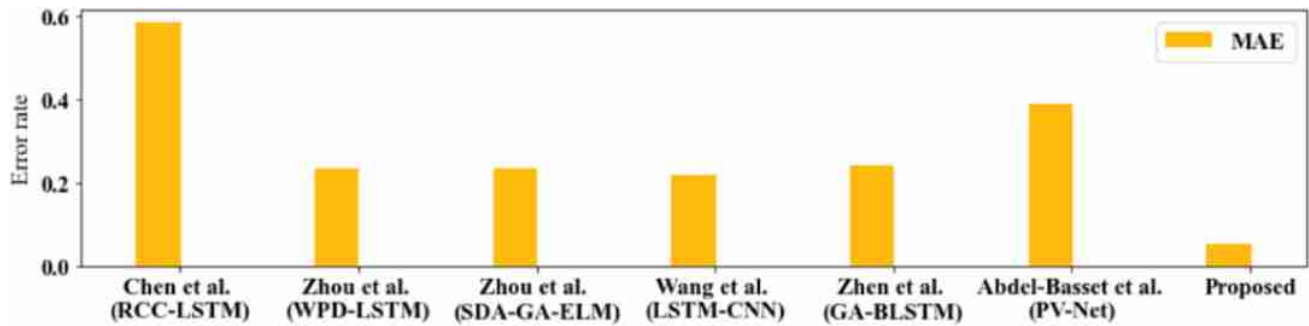


Fig. 8 Comparison of the proposed hybrid BLSTM–CNN model with previous studies

Conclusion

Accurate PV power forecasting plays an important role in the maintenance, control, management, and operation of PV power generation systems. In this research, a novel hybrid PV power generation forecasting model based on a deep learning algorithm namely BLSTM–CNN was suggested to increase the accuracy and reliability of PV power generation forecasting. More specifically, BLSTM automatically extracts bidirectional temporal correlation characteristics of PV data and CNN extracts spatial correlation characteristics of PV data to produce the final PV power forecasting results. Four evaluation measures and five single deep learning (CNN, GRU, RNN, LSTM, BLSTM) and two hybrid models (LSTM–CNN, CNN–LSTM) were employed for the experimental study to validate the proposed model’s predicting performance. The BLSTM–CNN model is proposed and used in a novel way in the field of PV power forecasting with the highest R^2 value of 0.9993, the lowest RMSE value of 0.0944, MAE value of 0.0531, MSE value of 0.0089. In terms of forecasting accuracy, the results indicate that the proposed model outperforms other traditional classical models. In the next study, the hybrid model will be combined with more sophisticated deep learning models to extract temporal and spatial features separately, resulting in more precise PV power forecast results. Moreover, the proposed model can also be enhanced and used in other domains, such as wind speed forecasting and residential load forecasting.

Author Contributions MS: writing—original draft preparation, methodology, visualization, software, validation, formal analysis. MEH: review and editing.

Declarations

Conflict of interest The authors declare that they have no known competing financial interests or personal relationships that could have appeared to influence the work reported in this paper.

References

1. Abdel-Basset, M., Hawash, H., Chakraborty, R.K., et al.: Pvnnet: an innovative deep learning approach for efficient forecasting of short-term photovoltaic energy production. *J. Clean. Prod.* **303**(127), 037 (2021)
2. Agoua, X.G., Girard, R., Kariniotakis, G.: Short-term spatio-temporal forecasting of photovoltaic power production. *IEEE Trans. Sustain. Energy* **9**(2), 538–546 (2017)
3. Behera, M.K., Majumder, I., Nayak, N.: Solar photovoltaic power forecasting using optimized modified extreme learning machine technique. *Eng. Sci. Technol. Int. J.* **21**(3), 428–438 (2018)
4. Chen, B., Lin, P., Lai, Y., et al.: Very-short-term power prediction for PV power plants using a simple and effective RCC-LSTM model based on short term multivariate historical datasets. *Electronics* **9**(2), 289 (2020)
5. Cheng, H., Ding, X., Zhou, W., et al.: A hybrid electricity price forecasting model with Bayesian optimization for German energy exchange. *Int. J. Electr. Power Energy Syst.* **110**, 653–666 (2019)
6. Chu, Y., Urquhart, B., Gohari, S.M., et al.: Short-term reforecasting of power output from a 48 MWe solar PV plant. *Sol. Energy* **112**, 68–77 (2015)
7. Das, U.K., Tey, K.S., Seyedmehmoudian, M., et al.: Forecasting of photovoltaic power generation and model optimization: a review. *Renew. Sustain. Energy Rev.* **81**, 912–928 (2018)
8. De Giorgi, M.G., Congedo, P.M., Malvoni, M.: Photovoltaic power forecasting using statistical methods: impact of weather data. *IET Sci. Meas. Technol.* **8**(3), 90–97 (2014)
9. Díaz-Vico, D., Torres-Barrán, A., Omari, A., et al.: Deep neural networks for wind and solar energy prediction. *Neural Process. Lett.* **46**(3), 829–844 (2017)
10. DKASC Alice Springs (2021) 1B: Trina. <http://dkasolarcentre.com.au/locations/alice-springs?source=1B>
11. Dolara, A., Leva, S., Manzolini, G.: Comparison of different physical models for PV power output prediction. *Sol. Energy* **119**, 83–99 (2015)
12. Du, P., Wang, J., Yang, W., et al.: Multi-step ahead forecasting in electrical power system using a hybrid forecasting system. *Renew. Energy* **122**, 533–550 (2018)
13. Gao, M., Li, J., Hong, F., et al.: Day-ahead power forecasting in a large-scale photovoltaic plant based on weather classification using LSTM. *Energy* **187**(115), 838 (2019)
14. He, Y.L., Chen, L., Gao, Y., et al.: Novel double-layer bidirectional LSTM network with improved attention mechanism for predicting energy consumption. *ISA Trans.* **127**, 350–360 (2022). <https://doi.org/10.1016/j.isatra.2021.08.030>



15. Hinton, G.E., Salakhutdinov, R.R.: Reducing the dimensionality of data with neural networks. *Science* **313**(5786), 504–507 (2006)
16. Hochreiter, S., Schmidhuber, J.: Long short-term memory. *Neural Comput.* **9**(8), 1735–1780 (1997)
17. Hopfield, J.J.: Neural networks and physical systems with emergent collective computational abilities. *Proc. Natl. Acad. Sci.* **79**(8), 2554–2558 (1982)
18. Hossain, M., Mekhilef, S., Danesh, M., et al.: Application of extreme learning machine for short term output power forecasting of three grid-connected PV systems. *J. Clean. Prod.* **167**, 395–405 (2017)
19. Hu, Y., Lian, W., Han, Y., et al.: A seasonal model using optimized multi-layer neural networks to forecast power output of PV plants. *Energies* **11**(2), 326 (2018)
20. Jaihuni, M., Basak, J.K., Khan, F., et al.: A novel recurrent neural network approach in forecasting short term solar irradiance. *ISA Trans.* **121**, 63–74 (2022)
21. Jammeli, H., Ksantini, R., Abdelaziz, F.B., et al.: Sequential artificial intelligence models to forecast urban solid waste in the city of Sousse, Tunisia. *IEEE Trans. Eng. Manag.* (2021). <https://doi.org/10.1109/TEM.2021.3081609>
22. Joseph, L.L., Goel, P., Jain, A., et al.: A novel hybrid deep learning algorithm for smart city traffic congestion predictions. In: 2021 6th International Conference on Signal Processing, pp. 561–565. Computing and Control (ISPPC), IEEE (2021)
23. Kim, T.Y., Cho, S.B.: Predicting residential energy consumption using CNN-LSTM neural networks. *Energy* **182**, 72–81 (2019)
24. Kulshrestha, A., Krishnaswamy, V., Sharma, M.: Bayesian BILSTM approach for tourism demand forecasting. *Ann. Tour. Res.* **83**(102), 925 (2020)
25. Lan, H., Zm, Liao, Zhao, Y.: ARMA model of the solar power station based on output prediction. *Electr. Meas. Instrum.* **48**(2), 31–35 (2011)
26. Lawal, A., Rehman, S., Alhems, L.M., et al.: Wind speed prediction using hybrid 1d CNN and BLSTM network. *IEEE Access* **9**, 156–679 (2021)
27. Lee, D., Kim, K.: PV power prediction in a peak zone using recurrent neural networks in the absence of future meteorological information. *Renew. Energy* **173**, 1098–1110 (2021)
28. Li, C., Tang, G., Xue, X., et al.: The short-term interval prediction of wind power using the deep learning model with gradient descend optimization. *Renew. Energy* **155**, 197–211 (2020)
29. Li, P., Zhou, K., Lu, X., et al.: A hybrid deep learning model for short-term PV power forecasting. *Appl. Energy* **259**(114), 216 (2020)
30. Liu, J.: China's renewable energy law and policy: a critical review. *Renew. Sustain. Energy Rev.* **99**, 212–219 (2019)
31. Malvoni, M., De Giorgi, M.G., Congedo, P.M.: Data on support vector machines (SVM) model to forecast photovoltaic power. *Data Brief* **9**, 13–16 (2016)
32. Mellit, A., Massi Pavan, A., Ogliaeri, E., et al.: Advanced methods for photovoltaic output power forecasting: a review. *Appl. Sci.* **10**(2), 487 (2020)
33. Miao, S., Ning, G., Gu, Y., et al.: Markov chain model for solar farm generation and its application to generation performance evaluation. *J. Clean. Prod.* **186**, 905–917 (2018)
34. Nguyen, N.Q., Bui, L.D., Van Doan, B., et al.: A new method for forecasting energy output of a large-scale solar power plant based on long short-term memory networks a case study in Vietnam. *Electr. Power Syst. Res.* **199**(107), 427 (2021)
35. Nguyen Dinh, T., Phan Hoang, N.: Air pollution forecasting using regression models and lstm deep learning models for Vietnam. In: International Conference on Future Data and Security Engineering, Springer, 264–275 (2021)
36. Ogliaeri, E., Dolara, A., Manzoloni, G., et al.: Physical and hybrid methods comparison for the day ahead PV output power forecast. *Renew. Energy* **113**, 11–21 (2017)
37. Pan, M., Li, C., Gao, R., et al.: Photovoltaic power forecasting based on a support vector machine with improved ant colony optimization. *J. Clean. Prod.* **277**(123), 948 (2020)
38. Peng, T., Zhang, C., Zhou, J., et al.: An integrated framework of Bi-directional long-short term memory (BiLSTM) based on sine cosine algorithm for hourly solar radiation forecasting. *Energy* **221**(119), 887 (2021)
39. Sabri, M., El Hassouni, M.: A comparative study of LSTM and RNN for photovoltaic power forecasting. In: Int. Conf. Adv. Technol. Humanity, pp. 265–274. Springer, Cham (2022)
40. Sabri, M., El Hassouni, M.: A novel deep learning approach for short term photovoltaic power forecasting based on GRU-CNN model. In: E3S Web of Conferences, EDP Sciences, 00064 (2022)
41. Sabri, N.M., El Hassouni, M.: Accurate photovoltaic power prediction models based on deep convolutional neural networks and gated recurrent units. *Energy Sourc. Part A Recovery Util. Environ. Eff.* **44**(3), 6303–6320 (2022)
42. Sanjari, M.J., Gooi, H.: Probabilistic forecast of PV power generation based on higher order Markov chain. *IEEE Trans. Power Syst.* **32**(4), 2942–2952 (2016)
43. Shi, Y., He, W., Zhao, J., et al.: Expected output calculation based on inverse distance weighting and its application in anomaly detection of distributed photovoltaic power stations. *J. Clean. Prod.* **253**, 119965 (2020)
44. Srivastava, N., Hinton, G., Krizhevsky, A., et al.: Dropout: a simple way to prevent neural networks from overfitting. *J. Mach. Learn. Res.* **15**(1), 1929–1958 (2014)
45. Tovar, M., Robles, M., Rashid, F.: PV power prediction, using CNN-LSTM hybrid neural network model Case of study: Temixco-Morelos, Mexico. *Energies* **13**(24), 6512 (2020)
46. Ünal, F., Almalaq, A., Ekici, S.: A novel load forecasting approach based on smart meter data using advance preprocessing and hybrid deep learning. *Appl. Sci.* **11**(6), 2742 (2021)
47. Voyant, C., Notton, G., Kalogirou, S., et al.: Machine learning methods for solar radiation forecasting: a review. *Renew. Energy* **105**, 569–582 (2017)
48. Wang, H., Yi, H., Peng, J., et al.: Deterministic and probabilistic forecasting of photovoltaic power based on deep convolutional neural network. *Energy Convers. Manag.* **153**, 409–422 (2017)
49. Wang, K., Qi, X., Liu, H.: A comparison of day-ahead photovoltaic power forecasting models based on deep learning neural network. *Appl. Energy* **251**(113), 315 (2019)
50. Wang, K., Qi, X., Liu, H.: Photovoltaic power forecasting based LSTM-convolutional network. *Energy* **189**(116), 225 (2019)
51. Wang, S., Wang, Y., Cheng, Y., et al.: An improved model for power prediction of PV system based on Elman neural networks. In: 2020 Asia Energy and Electrical Engineering Symposium (AEEES), IEEE, 902–907 (2020)
52. Wang, Y.: The analysis of the impacts of energy consumption on environment and public health in China. *Energy* **35**(11), 4473–4479 (2010)
53. Wojtkiewicz, J., Hosseini, M., Gottumukkala, R., et al.: Hour-ahead solar irradiance forecasting using multivariate gated recurrent units. *Energies* **12**(21), 4055 (2019)
54. Wu, Q., Guan, F., Lv, C., et al.: Ultra-short-term multi-step wind power forecasting based on CNN-LSTM. *IET Renew. Power Gener.* **15**(5), 1019–1029 (2021)
55. Yamada, F., Wazawa, Y., Kobayashi, K., et al.: Prediction of next day solar power generation by gray theory and neural networks. *Trans. Inst. Electr. Eng. Jpn B* **134**(6), 494–500 (2014)
56. Yan, Y., Hy, Xing: A sea clutter detection method based on LSTM error frequency domain conversion. *Alex. Eng. J.* **61**(1), 883–891 (2022)



57. Zhen, H., Niu, D., Yu, M., et al.: A hybrid deep learning model and comparison for wind power forecasting considering temporal-spatial feature extraction. *Sustainability* **12**(22), 9490 (2020)
58. Zhen, H., Niu, D., Wang, K., et al.: Photovoltaic power forecasting based on GA improved Bi-LSTM in microgrid without meteorological information. *Energy* **231**, 120908 (2021)
59. Zhou, Y., Zhou, N., Gong, L., et al.: Prediction of photovoltaic power output based on similar day analysis, genetic algorithm and extreme learning machine. *Energy* **204**, 117894 (2020)

Publisher's Note Springer Nature remains neutral with regard to jurisdictional claims in published maps and institutional affiliations.

Springer Nature or its licensor holds exclusive rights to this article under a publishing agreement with the author(s) or other rightsholder(s); author self-archiving of the accepted manuscript version of this article is solely governed by the terms of such publishing agreement and applicable law.





Modeling and design of a new system cascade solar still test for thermal performance

Wafae El Hafid¹ · Souad Abderafi¹ · Kamal Amghar^{2,3} · Hafsa Bouhrim⁴

Received: 28 May 2022 / Accepted: 9 September 2022 / Published online: 20 September 2022
© The Author(s), under exclusive licence to Islamic Azad University 2022

Abstract

The objective of this paper is to study the performance of a cascade solar still as a function of the variation in solar intensity and the thickness of the glass cover. In this context, the present work examined different cities of Morocco; however, Tetouan (north of Morocco), Oujda (west of Morocco), Casablanca (east of Morocco) and Ouarzazate (south of Morocco) were targeted. In addition, the effect values of 3, 5 and 7 mm glass cover thicknesses were studied. The effect of these parameters on the water productivity of the inclined cascade solar still was performed by simulation using ANSYS-FLUENT software. The simulation model was successfully validated using the experimental data available in the literature. The results show that the absorber plate temperature and the hourly productivity of the inclined cascade solar still with a glass cover thickness of 3, 5 and 7 mm, under the climatic conditions of Ouarzazate region, reach maximum values of 78; 75 and 71 °C and 1.78; 1.58 and 1.26 kg/m² per hour at 2 pm, compared to other regions. The results of this work show that the new design of the inclined cascade solar still with a minimum thickness of the glass cover in a region with a higher solar intensity increase the temperature of the absorber plate, causing an increase in the thermal energy inside the solar still, resulting in a rapid increase in water evaporation, which has the role of increasing the production of distilled water compared to other types of solar still. On the other hand, the economic analysis of the studied system shows that the cost of distilled water does not exceed 0.0093\$/L.

Keywords Cascade solar still · Numerical simulation · Glass cover · Solar intensity · Productivity · Cost of distilled water

Abbreviations

CFD	Computational fluid dynamics
MSF	Multi-stage flash
MED	Multi-effect distillation
TVC	Thermal vapor compression
MD	Membrane distillation
RO	Reverse osmosis

ED	Electrodialysis
CPL	Cost per liter

List of symbols

f	Fluid
P	Pressure
Amb	Ambient
atm	Atmospheric
e	Thickness, m
T	Temperature, K
dT	Incremental rise, °C
L	Length, m
H	Height, m
x,y	Cartesian coordinate, m

✉ Wafae El Hafid
wafae.elhafid@gmail.com;
wafae.elhafid@research.emi.ac.ma

¹ MOSEM2PI, Mohammadia Engineering School (EMI), Mohammed V University in Rabat, Rabat, Morocco

² LME, Faculty of Sciences, First Mohammed University, 60000 Oujda, Morocco

³ LSIA, National School of Applied Sciences (ENSAH), Abdelmalek Essaâdi University, Al Hoceima, Morocco

⁴ LMMT Laboratory, Electromechanical Department, Higher National School of Mines of Rabat (ENSMR), Avenue Hadj Ahmed Cherkaoui, Agdal, Rabat, Morocco

Introduction

Water is an essential element for all living beings on earth since the creation of the universe. It covers about 75% of the earth's surface. However, 28% of this water is fresh, only 0.36% is usable by humans and 96.54% is salty [1].



Population growth, industrial development, improved living standards, inefficient water use and climate change have resulted in an unprecedented need for freshwater in the world [2]. According to Jayaswal et al. [3], every year, one million people die because of polluted water, two billion have no sanitation facilities and more than one billion people do not have access to drinking water. Several solutions are proposed to face this problem, for the benefit of countries located in Africa that have a potential in sea water or brackish water. Indeed, there are many desalination technologies, whether at the R&D level [4, 5] or at the industrial level [6, 7], to produce fresh water from these two sources of water. Desalination by solar energy of sea or brackish water is one of the best technologies to the problem of water scarcity [8]. Solar distillation is a very old technique that has been used for several centuries for the desalination of seawater. In 1551, Arab alchemists realized the first solar still. Later, other scientists, including Della Porta in 1589, Lavoisier in 1862 and Maucho in 1869 made and developed solar stills [9]. The use of solar energy as a primary source of desalination is considered one of the most promising applications for producing drinking water [10]. There are many solar desalination techniques that have classified into two types, direct and indirect solar desalination. The difference between the two types of desalination is that in indirect desalination, solar energy is used indirectly, that is, by combining conventional desalination techniques, such as membrane distillation (RO and ED) and thermal distillation (MSF, VC, TVC, MED, MD), with solar thermal or photovoltaic collectors for heat production, whereas direct desalination uses a technique based on the evaporation and condensation of water thanks to solar energy which can be used directly in the solar still [11].

In this work, we are interested in direct solar distillation processes for several reasons. First, their design is simple and easy to manufacture. Second, they are clean, have no negative effect on the environment, are cheaper and require less maintenance than other processes [12]. Despite the many advantages of the solar distiller, its productivity in fresh water is low, so researchers aim to improve them [13]. There are different types of solar stills which use the same operating principle, but they can be different in terms of design, such as single-slope, double-slope, hemispherical, pyramidal, tubular and cascade solar stills [14]. Dumka et al. [15] experimentally and theoretically studied the techno-economic performance of a conventional single-slope solar still (CSS) and a modified solar still (MSS) with an ultrasonic fogger and a cotton cloth envelope. Their results show that the MSS was 53.12% more efficient than the CSS. Sharshir et al. [13] improved heat transfer by integrating linen wicks (LWs) and carbon black nanoparticles (CBNs) into the double slope cascade solar still (SDSSS). Comparing it to the traditional solar still (TSS), the authors showed that the addition of LWs and CBNs increases

the freshwater productivity and energy efficiency by 80.57 and 110%, respectively. El Hadi Attia et al. [16] were interested in improving the performance of conventional hemispherical solar stills. They tested the addition of a fin with two different configurations, in order to increase the absorption surface and transmit heat to the salt water. It was found that the use of fins with a length of 2 cm and a spacing of 7 cm improved the productivity of the distiller up to 56.73%. Kabeel et al. [17] experimentally studied the performance of a triangular pyramidal solar still with an absorber plate coated with TiO_2 nanoparticles doped in black paint. By testing the effect of different water depths, they found that this type of absorbent plate with minimal water depth improved the efficiency of the system by 12% compared to the absorber without nanoparticle. El-Said et al. [18] increased the productivity of the tubular solar still by 34% compared to conventional solar still, using a vibrated porous media. The latter allowed the increase in the absorption and heat transfer performance. Shyora et al. [19] presented a comparative analysis between two types of the single slope and cascade solar still of the same size, in the same climatic condition Gandhinagar, Gujarat during the months of December 2018 and February 2019. They concluded that the cascade solar still has a high productivity of 23.88% compared to conventional solar still. Saadi et al. [20] developed a new design of the cascade solar still with an integration of a multi-plate evaporator that has been tested in Algerian weather conditions. They concluded that the proposed new design of the cascade solar still is more efficient than the conventional solar still. Rashidi et al. [21] used a nanofluid to increase the performance of a cascade solar still. They found that the daily production of this device is improved by 22% with a 5% nanoparticle concentration. Montazeri et al. [22] studied the performance of two cascade solar stills, the first with a conventional absorbent plate and the second with a modified absorbent plate. They concluded that the modification of the absorbent plate makes it possible to absorb the maximum amount of solar radiation, which leads to a 49.2% improvement in the efficiency of the solar cascade distiller compared to the conventional cascade solar still. Panchal et al. [23] studied the performance of the cascade solar still with different concentrations of the MgO and TiO_2 nano-fluids varied from 0.1 to 0.2%. They concluded that the MgO nanofluid improves the performance of the cascade solar still more than the TiO_2 nanofluid due to their lower specific heat capacity and higher thermal conductivity. Kabeel et al. [24] experimentally studied two solar stills, one conventional and the other with a cascade modified by adding baffles to the vertical walls of the still, and also tested the effect of the width and depth of the plateaus on their performance. They concluded that the productivity of cascade solar still with 5 mm depth and 120 mm tray width is 57.3% higher than that of conventional solar still. Omara et al. [25] made a comparative study between two single slope and cascade solar stills modified by adding internal reflectors,



which were tested under the same weather conditions. They concluded that the cascade solar still with and without internal reflectors always has a high efficiency compared to the conventional solar still. Omara et al. [26] studied the daily efficiency of a cascade solar still. They concluded that the yield of the cascade solar still can reach about 5.84 L/m^2 per day with the cost of a liter of distillate can reach 0.03 \$. Abujazar et al. [27] evaluated numerically and experimentally the performance of an inclined cascade solar still that was made of copper. The results show that the maximum hourly productivity in the inclined cascade solar still for the experimental and theoretical models was approximately 605 and $474 \text{ mL/m}^2 \text{ h}$. Bouziad et al. [28] experimentally studied the thermal performance and productivity of a cascade solar distiller characterized by the same components as a conventional solar still, but the absorber plate consists of horizontal and inclined surfaces with baffles on the inside. This solar still has achieved significant productivity compared to the different types of solar stills described above. The stepped solar still gives a maximum productivity of $7 \text{ kg/m}^2 \text{ d}$, obtained for the Rabat city of Morocco, having a low solar intensity. Bibliographic analysis shows that the solar still is an important technique, but one of its major problems is the weakness of freshwater production due to the horizontal position of the plate which intercepts less solar radiation than an inclined surface. In addition, among the main criteria that affect the performance of a solar still, the design and meteorological criteria must be studied for a better performance of the solar still [13, 29]. This analysis shows us that it is still possible to improve the performance of the stepped solar still, by acting on these two criteria.

The main aim of the present work is to improve the performance of the inclined cascade solar still in terms of the productivity and cost of distilled water, based on the effects of the solar intensity and the thickness of the glass cover, which have not been dealt with in the literature. For this purpose, associated specific objectives will be pursued. In first time, reliability of the CFD model will be tested, before its use in numerical experiences. After that, parametric sensitivity study will be followed numerically, to obtain the optimal design of solar still, based on different thicknesses of its glass cover. The effect of solar intensity will also be tested for Moroccan sites, where the solar still unit can be installed. In the end, performance of the solar still will be evaluated based on water productivity and water production cost.

Experimental

The performance of the solar still was studied numerically by simulation in ANSYS CFD software. This software was chosen for being an efficient CFD tool, especially when dealing with complex phenomena as fluid flow and heat transfer. However, the CFD model of the evaporation and

condensation processes allows to study the flow and heat transfer phenomena present in the studied process. Figure 1 represents the flow diagram of the numerical algorithm. As shown in this figure, the first step consists of designing the inclined cascade solar still, then making the mesh and introducing the chosen operating conditions in ANSYS Fluent. After these three steps, the resolution of the governing equation is carried out and the simulation results relating to the temperature of the absorber plate are finally obtained and analyzed. The convergence criterion is considered acceptable once the sum of the residuals is less than 10^{-6} [30]. The procedure followed for each step is shown in the figure that is described below.

Solar still design

The first step carried out, for the realization of the various numerical experiments using the inclined cascade solar still consists in realizing its geometry in 3D. The SolidWorks software interface was used to design this system that is

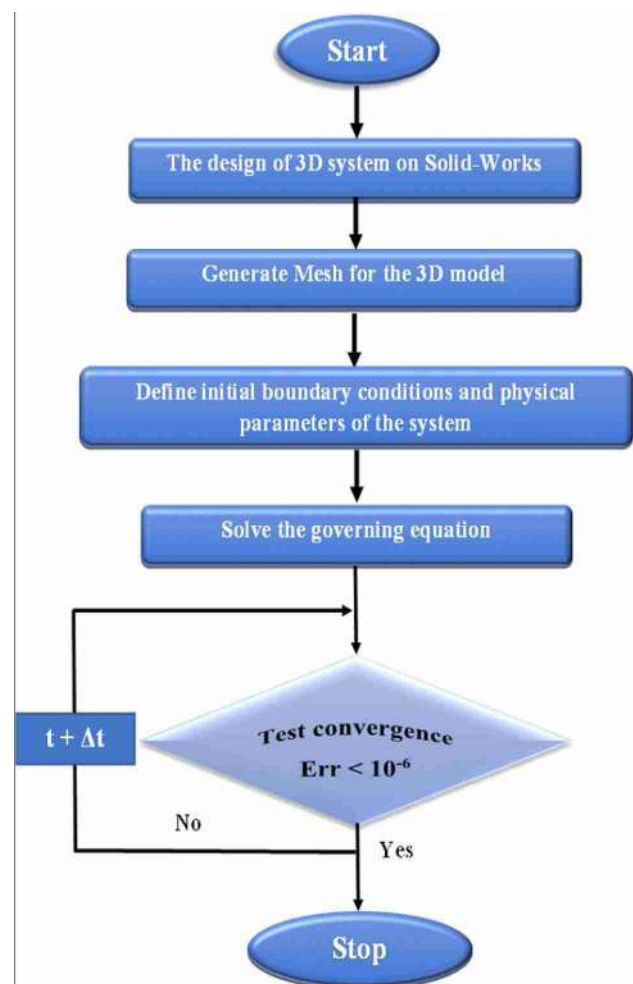


Fig. 1 Flow diagram of the numerical algorithm



represented in Fig. 2. The studied solar still consists of the same components as a conventional solar still, except that the aluminum absorber plate is characterized by horizontal and inclined surfaces with reflectors. The absorber plate is therefore divided into several small basins that allow for a minimum depth of water and painted black to absorb the maximum of solar radiation. This causes a quick heating of the water, which is ensured by a better orientation of the system, the use of baffles allows to slow down the speed of flow of the salt water inside the solar still [28]. The ordinary glass cover is used for its good transmission of visible radiation, its simplicity, and its low cost. The basin of the solar still is made of aluminum, and it is used for its better resistance to corrosion, its low weight, and its ease of use. The insulation is done by a coating inside the basin to reduce heat loss to the outside. A synthetic rubber mat is used to prevent leaks at the bottom of the basin. The model parameters and their corresponding physical properties exploited in the calculation are given in Table 1.

Solar still operates by the use of solar radiation which passes through the transparent inclined cover. Then, it is absorbed by the coating of the basin which heats up and emits thermal heat to the cover which in turn reflects a large part to the basin and a small part and transmitted outside. As a result of the multiples reflections between the cover and the basin, the water heats up and a part evaporates and condenses on the inside of the cover because of its low temperature compared to that of the vapor. The water droplets are formed, and under the effect of gravity, they slide until they reach the collector placed at the bottom of the cover [35].

Creating mesh

The obtained geometry of the inclined cascade solar still (Fig. 2) was imported from SolidWorks, in order to generate the mesh in Ansys. In mesh generation, the problem domain is divided into many small cells. This step represents the

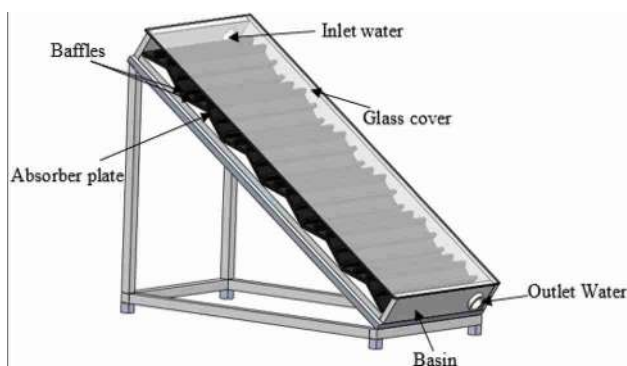


Fig. 2 Schematic of the inclined cascade solar still, obtained by SolidWorks

preliminary phase for any numerical resolution. The model equations are solved using ANSYS software, for each cell to simulate the physical phenomena. In this study, a tetrahedral-type mesh was selected to include tetrahedral elements. This type of mesh was chosen because the shape of the inclined cascade solar still geometry is constituted by different surfaces (rectangular, circular...). The tetrahedral mesh type is the most suitable and can provide accurate results with moderate computation time. Figure 3 shows the obtained mesh of the computational domain in 3D view. After the meshing step, gravity is activated as the only responsible for the water movement inside the inclined cascade solar still.

Initial condition and boundary condition

Before performing the analysis, the initial conditions of the model (for $t=0$ s) were first defined to involve the volumetric fractions of each phase. The multiphase model was activated with three phases; air, water, and vapor. ANSYS fluent automatically assumes that the air is defined as a primary phase and present in each cell. To create the water phase in the domain, it is necessary to connect the lower region to provide a constant filling level equal to the chosen

Table 1 Physical parameters used in this work

	Specific heat [J. Kg ⁻¹ K ⁻¹]	Thermal conductivity [[W.m ⁻¹ K ⁻¹]	Ref.	Density [Kg.m ⁻³]	Refs.
Glass cover	800	1.02	[28]	2530	[31]
Brackish water	4190	0.67		1022	[32]
Absorbent plate	896	230		2700	[33]
Insulation	670	0.059		200	[34]

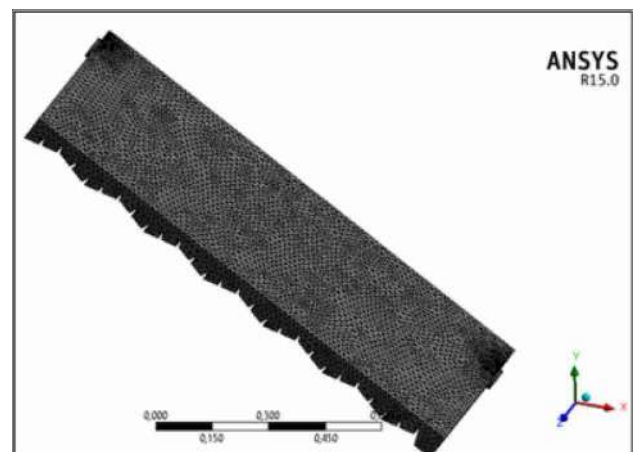


Fig. 3 Mesh Geometry of the inclined cascade solar still, obtained by ANSYS



depth. For this a water level inside the absorber plate in the inclined cascade, solar still was assumed to be 4 cm, which means that the water volume fraction is initialized to 1 in this region and is 0, outside this region. At the end of the simulation, regardless of the drop in the water level in the absorber plate, the same amount of water is introduced into the absorber plate for balancing. It was specified that there is no vapor at first.

To solve the formulated system of equations (Energy balance equations), the finite volume method is adopted in ANSYS fluent. The assumptions taken into consideration for the current problem resolution are

- The thermo-physical properties of working fluid and components of cascade solar still are supposed to be temperature independent;
- The temperature of all surfaces was equal to the ambient temperature;
- No heat loss occurs between the cascade solar still and the ambient air;

The boundary conditions adopted for this model are mainly to consider the side walls as adiabatic walls due to the insulation in the experimental study [28]. However, the boundary and initial conditions required to solve the energy balance equations are given by Eqs. (1–6):

- At the inlet of collector:

$$T_{\text{int}} = T_f(x = 0) = T_a \quad (1)$$

$$P = P_{\text{atm}} \quad (2)$$

$$\left(\frac{\partial T}{\partial y}\right)_{x=0} = 0 \quad (3)$$

- At the outlet of collector:

$$P = P_{\text{atm}} \quad (4)$$

$$\left(\frac{\partial T}{\partial y}\right)_{x=L} = 0 \quad (5)$$

- At the boundary of absorber plate:

$$\left(\frac{\partial T}{\partial y}\right)_{y=H} = 0 \text{ and } \left(\frac{\partial T}{\partial x}\right)_{y=0} = 0 \quad (6)$$

Moroccan sites tested

The typical inputs needed in numerical experiences are the geographic coordinates of the cities where the solar still can

be installed, which in our case studied are those of Morocco. This country has an important potential for solar radiation which can be estimated at a value of 5 kWh/m²/years [36]. In order to exploit the potential of groundwater in future climatic conditions and meet the needs of freshwater in different regions of Morocco, the effect of solar intensity on freshwater production has been tested. However, several sunny sites may be chosen to develop the technology of solar stills, but another criterion must be considered in addition to that of solar irradiation, which is related to the presence of brackish water. To target all regions of Morocco, meeting these criteria, five cities can then be chosen: Tetouan (North of Morocco), Oujda (East of Morocco), Rabat and Casablanca (West of Morocco) and Ouarzazate (South of Morocco). These different sites are illustrated in Fig. 4. The geographic coordinates for these cities studied are taken from the Meteoblue website [37] and are given in Table 2.

Results and discussion

Simulation model reliability

According to the experimental data available in the literature [28], the latitude and longitude, of Rabat city for the days of March 27, 28 and 29, 2017, are exploited for the validation of the CFD model of the inclined cascade solar still. This CFD model reliability is analyzed by comparing the calculated values of the absorber plate temperature (T_{Cal}) to experimental one (T_{Exp}) obtained from the literature [28]. This comparison is given in Table 3 and presented in Fig. 5. The latter shows that the different values almost followed the diagonal and the correlation coefficient (R^2) is around 99%, for the three days studied. Regarding the Mean Absolute Error (MAE) and Maximum Error (ME), the model allows us to carry out a simulation of the plate temperature with satisfactory error that does not exceed 5%. On the one hand, the difference between the calculated and experimental values can be attributed to the experimental errors. On the other hand, the CFD model is considered ideal for calculating the thermal performance along the cascade solar still, and the characteristics are chosen from the same properties of the absorber plate used in the experiment. Additionally, in the simulation, the ideal boundary conditions of the insulated side walls are considered the same with those present in the literature [28]. Despite these different hypotheses, the simulation model remains reliable and allows to estimate the plate temperatures with a very satisfactory error.

Sensitivity analysis

The effect of glass cover thickness and the solar intensity in different regions of Morocco were tested. The



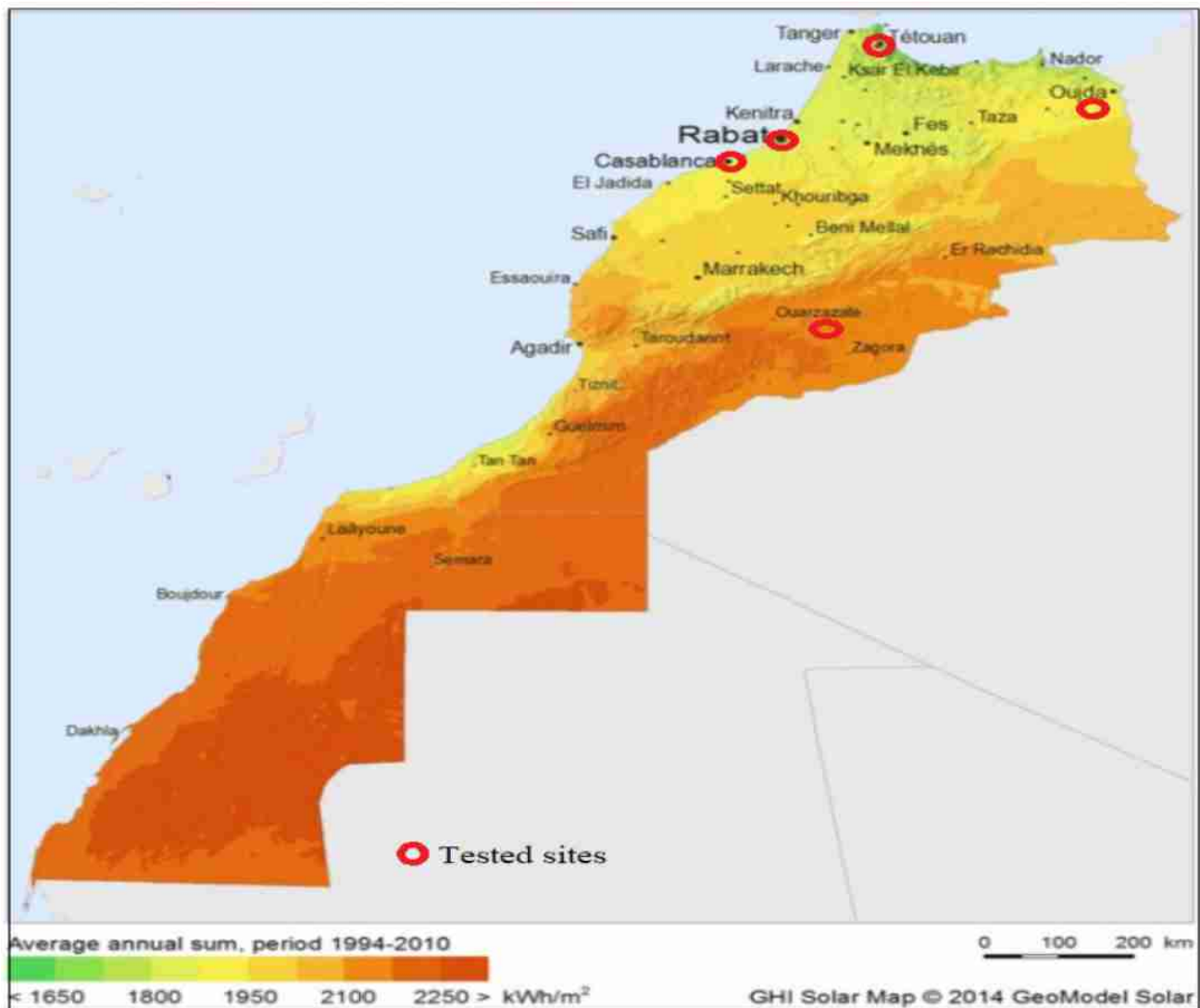


Fig. 4 Sites selected in this study [38]

Table 2 Geographic coordinates of the cities under study [37]

City	Latitude (N)	Longitude (w)
Rabat	34.013	-6.833
Tetouan	35.578	-5.368
Oujda	34.681	-1.909
Casablanca	33.583	-7.679
Ouarzazate	30.919	-6.908

Table 3 Errors and correlation coefficients for model validation

Date	MAE (%)	ME (%)	R^2 (%)
27/04/2017	2.62	5.26	99.94
28/04/2017	2.80	4.69	99.86
29/04/2017	2.34	4.55	99.75

previously validated CFD model of the inclined cascade solar still was exploited for the parametric sensitivity analysis. Based on commercially available experimental devices, three values of thickness were considered: 3, 5 and 7 mm, to test the performance of the inclined cascade solar still. However, the effect of these three thickness values on the productivity of the system studied was achieved by simulation, using the Ansys Fluent software. The latitude and longitude of Tetouan, Oujda, Casablanca and Ouarzazate are taken into consideration, for the day June 25, 2019, which has a higher solar intensity compared to other days of the year. The hourly variation in solar intensity for this day is given in Fig. 6 for the four cities of Morocco. It is obtained by exploiting existing intensity data [37]. According to this figure, the city of Ouarzazate



Fig. 5 Comparison of the temperature values calculated by simulation with those obtained experimentally for the day **a** 27/04/2017, **b** 28/04/2017 and **c** 29/04/2017

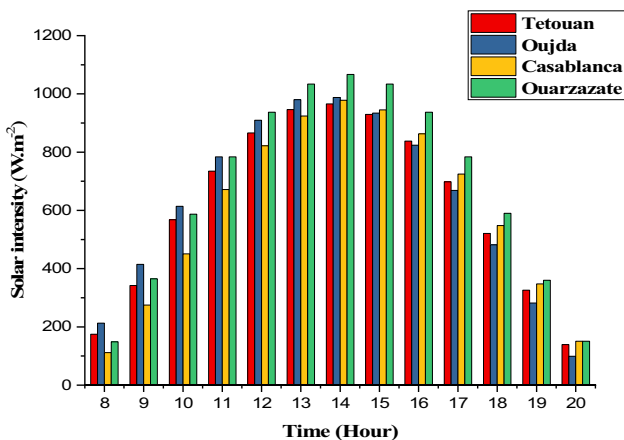
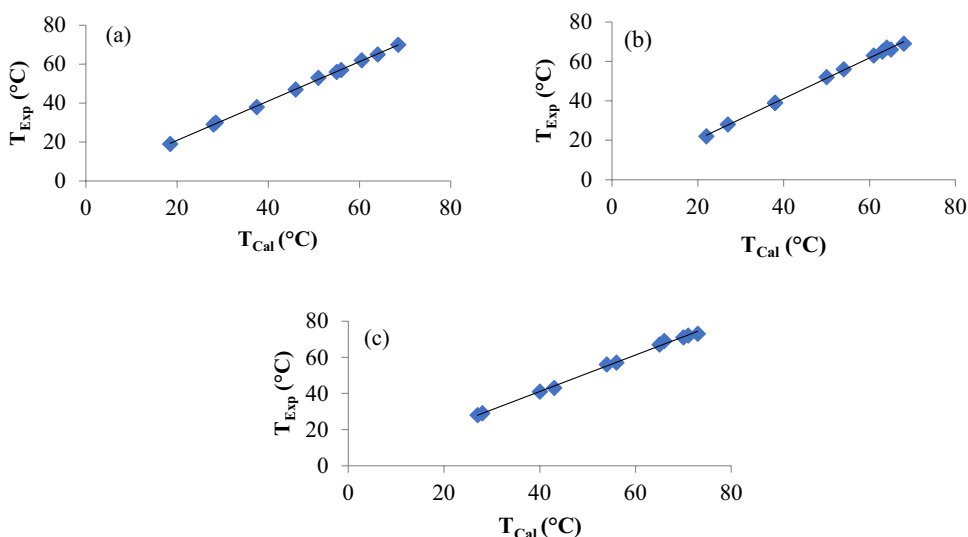


Fig. 6 Hourly variation in solar intensity in different regions of Morocco

has a higher solar intensity compared to other cities. The effects of the studied parameters are presented below.

Solar intensity effect

The effect of solar intensity is studied using the geographic coordinates of the Tetouan, Oujda, Casablanca and Ouarzazate (Table 2). Figure 7 shows the hourly variation in the absorber plate temperature, compared to the variation in the solar intensity for different regions of Morocco, along the day of June 25, 2019. The results show that the variation in the absorber plate temperature follows the same variation in the solar intensity during the day studied. In fact, the solar intensity increases from 8-AM to 2-PM, in all studied cities, where it reaches a maximum value for a maximum solar radiation intensity reached in the middle of the day. The temperature profile of the absorber plate increases progressively

from morning to midday, during intense sunshine. Consequently, the insolation increases, and the temperature of the absorber reaches a maximum of ~ 67 °C for a solar irradiance of ~966 W/m² for Tetouan (North of Morocco) ~69 °C for a solar irradiance of ~ 988 W/m² for Oujda (East of Morocco), ~66 °C for a solar irradiance of ~978 W/m² for Casablanca (West of Morocco) and ~75 °C for a solar irradiance of ~1067 W/m² for Ouarzazate (South of Morocco). Then, the temperature of the absorber plate decreases due to the decrease in solar intensity after reaching a maximum value for the four regions of Morocco from 2 PM to 7 Pm. Moreover, the figure shows that the region of Ouarzazate in south of Morocco, which has a higher solar intensity than other regions (Tetouan, Oujda and Casablanca), allows the temperature of the absorber plate to increase to a maximum value of ~75 °C, this shows that the solar intensity has a direct and important effect on the performance of the solar still. Therefore, the higher the solar irradiation, the higher the temperature of the absorber plate, which will lead to a rapid increase in evaporation and condensation of water on the inner side of the solar still cover, and therefore, a greater production of distilled water [39].

Thicknesses effect

The effect of three glass cover thicknesses equal to 3, 5 and 7 mm is tested, respectively. Figure 8 shows the hourly variation in the absorber plate temperature for this different glass cover thicknesses, compared to the same variation in the solar intensity for the four studied regions of Morocco, for the day of 25 June 2019. This figure shows that the temperature variation in the absorber plate for the three glass cover thicknesses follows the same solar intensity variation along the day. Indeed, the temperature increases from around 8 AM to 2 PM, where the maximum

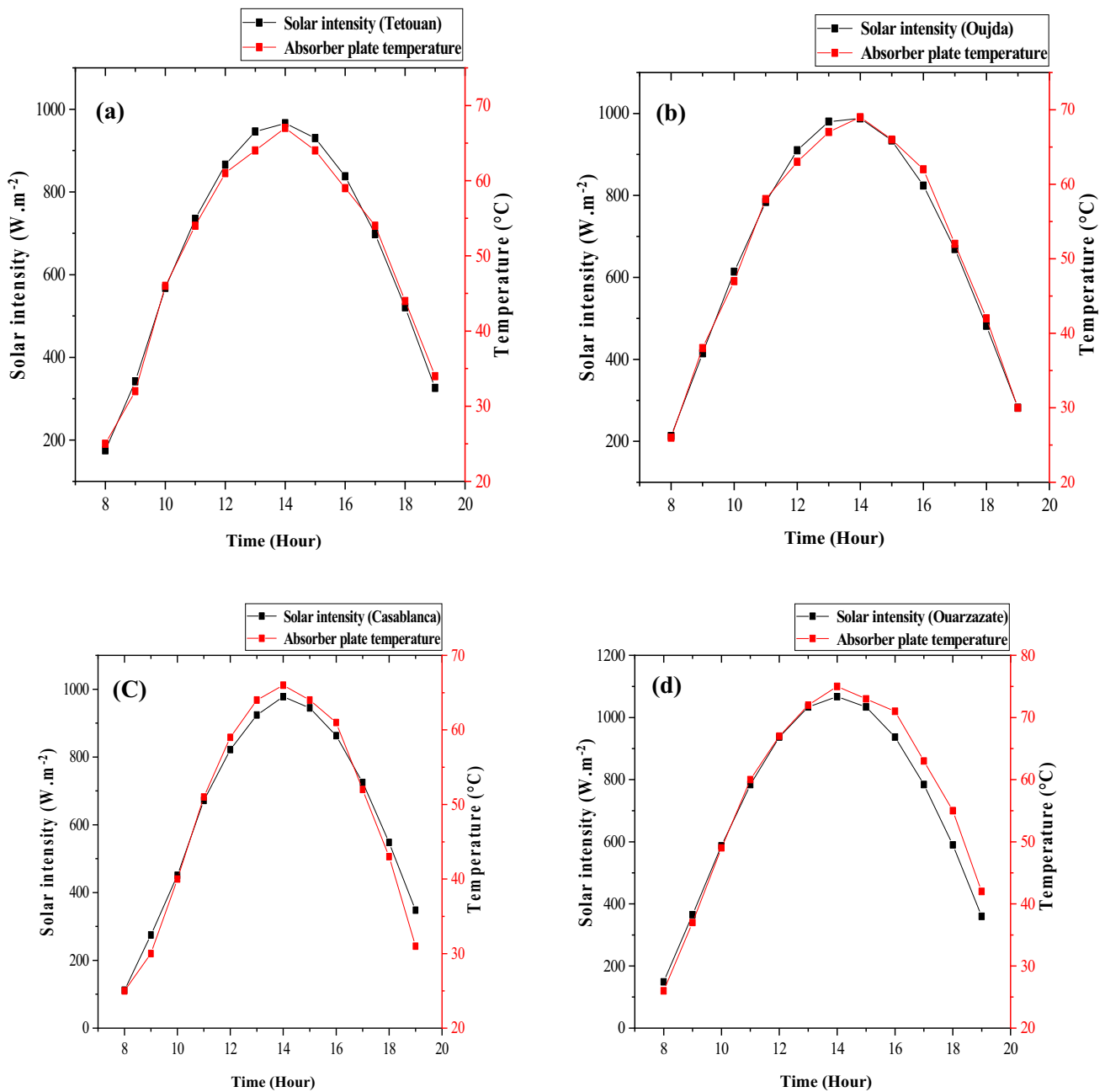


Fig. 7 Hourly variation in the absorber plate temperature versus the variation in solar intensity for the cities: **a** Tetouan, **b** Oujda, **c** Casablanca and **d** Ouarzazate

temperature of the absorber plate for cover thicknesses of 3, 5 and 7 mm is reached, respectively, more than ~68, ~67 and ~65 °C for a solar intensity of ~966 W/m² for Tetouan, ~72, ~69 and ~68 °C for a solar intensity of ~988 W/m² for Oujda, ~69, ~66 and ~62 °C for a solar intensity of ~978 W/m² for Casablanca and ~78, ~75 and ~71 °C for a solar intensity of ~1067 W/m² for Ouarzazate. Then, the temperature of the absorber plate decreases from 14 to 19 °C due to the decrease in the solar intensity. The temperature of the absorber plate is a very important factor to

increase the distilled water. In fact, the higher temperature of the absorber plate leads to more water heating and more evaporation inside the cascade solar still [39]. Thus, it can be seen from the figure that the thickness of the cover has a significant effect on the temperature of the absorber plate. According to the results, we note that the 3 mm of thickness glass cover increases the temperature of the absorber plate to a maximum value of ~68, ~72, ~69 and ~78 °C, respectively: Tetouan, Oujda, Casablanca and Ouarzazate compared to the other values of thickness 5 and 7 mm. This

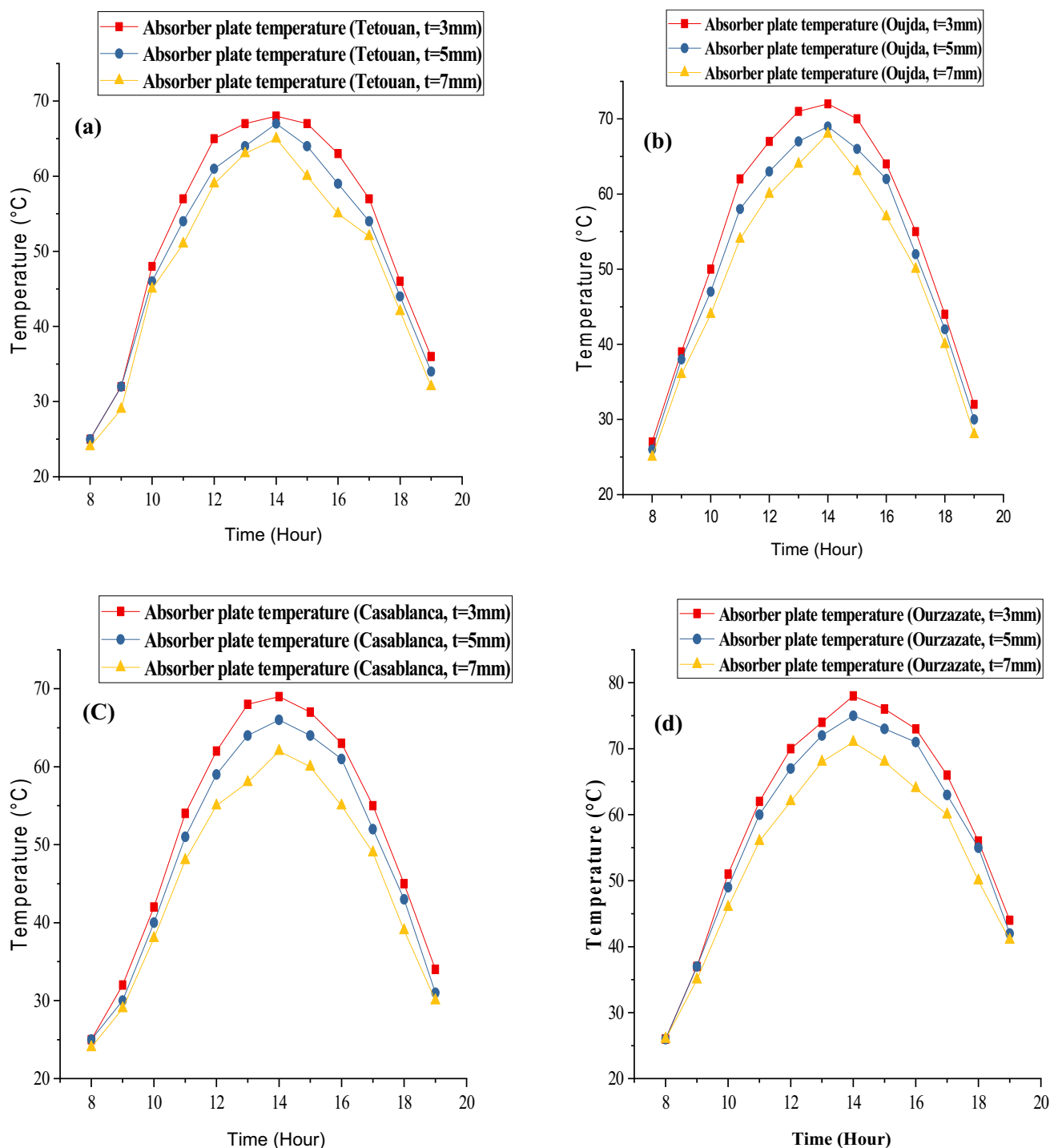


Fig. 8 Hourly variation in the absorber plate temperature for the different thicknesses of the glass cover of the inclined cascade solar still for the cities: **a** Tetouan, **b** Oujda, **c** Casablanca and **d** Ouarzazate

is mainly due to the properties of the glass. When the glass has a large thickness, then the solar intensity takes time to pass through the glass, which increases the heat losses [40]. On the other hand, the thinner the glass, the more the amount of solar radiation enters the cascade solar still, which causes

an increase in the temperature of the absorber plate and then an increase in the thermal energy inside the studied system. Moreover, the figure shows that the city of Ouarzazate has a high absorber plate temperature compared to other regions with the same thickness of the 3 mm glass cover

of solar still. Figure 9 shows, as well, the contour of this maximum temperature of the absorber plate that reaches a value of ~ 78 °C, because the Ouarzazate region has a high solar intensity that allows to increase the temperature of the absorber plate. On the other hand, a high temperature gradient is present between the water and the glass, which promotes condensation and evaporation of water.

Solar still performance

The performance of the inclined cascade solar still was studied based on the calculation of water productivity and its production cost. The results obtained are presented and analyzed in this section.

Water productivity

Water productivity of the inclined cascade solar still was obtained based on the CFD model and was calculated using the equation defined by Kaviti [41]. Figure 10 illustrates the hourly variation in the productivity obtained by the inclined cascade solar still, compared to the variation in the solar intensity for different regions of Morocco and for the three thicknesses of the glass cover of 3, 5 and 7 mm, along the day of June 25, 2019. This figure shows that the hourly productivity of the studied system with three thicknesses of glass cover follows the same variation in the solar intensity along the day for the different regions of Morocco. For that, the hourly productivity increases from 8 A.M. to 2 P.M., where it reaches a maximum value of ~ 1.12 , ~ 1.07 and ~ 0.98 kg/m².Hr of solar intensity ~ 966 W/m², for Tetouan. On the other hand, the productivity of Oujda around ~ 1.32 , ~ 1.16 and ~ 1.12 kg/m².Hr of solar intensity 988 W/m², similarly, Casablanca is of ~ 1.16 , ~ 1.03 and ~ 0.87 kg/m².Hr of solar intensity 978 W/m². Ouarzazate is as well of ~ 1.78 , ~ 1.58 and ~ 1.26 kg /m².Hr of solar intensity 1067 W/m², which correspond, respectively, to 3, 5 and 7 mm of glass cover

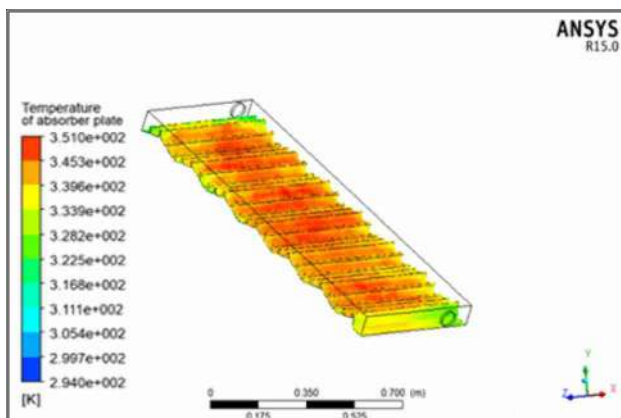


Fig. 9 Temperature profile of the absorber plate

thickness. These results show that the higher the solar intensity, the greater the amount of water distilled from the system studied, mainly due to the increase in the temperature of the absorber plate, which reaches its maximum value at ~ 67 , ~ 69 , ~ 66 and ~ 75 °C, respectively, for the cities: Tetouan, Oujda and Casablanca Ouarzazate (Fig. 7), which causes a rapid increase in evaporation and condensation of water. Thereafter, productivity decreases with the decrease in solar intensity from 2:00 pm to 7:00 pm. This figure also shows that the region of Ouarzazate has a higher productivity compared to other regions, due to the higher solar intensity in this city. It can be seen that regions with higher solar intensity allow for an increase in distillate. This is mainly due to the increase in the temperature of the absorber plate, which causes an increase in the thermal energy inside the solar still and consequently a rapid increase in the evaporation and condensation of water on the inner side of the cover. The inclined cascade solar still equipped with a 3-mm-thick glass cover has a good absorptivity and transmissivity of solar intensity compared to those of 5 and 7 mm, which causes an increase in freshwater productivity throughout the day for the four Moroccan regions studied. This is mainly due to the physical properties of the glass [39], the thinner the glass, the more amount of solar intensity enters the cascade solar still.

Economic analysis

An economic analysis was carried out to calculate the cost of distilled water from the inclined cascade solar still. Increasing the productivity of a solar still with a high cost can also increase the cost of distilled water. In solar stills, the operating cost is zero because they are powered by solar energy, which is free, abundant, and available everywhere. Therefore, the cost of producing distilled water mainly depends on the cost of manufacturing and installing the solar stills system. For this, when designing a solar stills system, the manufacturing costs must be considered. The economic study of an inclined cascade solar still is carried out using method based on different factors affecting the cost of distilled water produced by the solar still. It is assumed that the desalination system operates 340 days in the year [20], as Morocco has a solar intensity throughout the year. By flowing the equation presented by Kabeel [42], the calculation of the water production cost, using inclined cascade solar still, was obtained for the different thicknesses and cities considered. Figure 11 presents the results obtained, for the day of June 25, 2019. According to this figure, the parameters of solar intensity and thickness of the glass cover of 7; 5 and 3 mm of the studied system have an important effect on the cost of distilled water. The results show that the thickness of the 3 mm glass cover has a lower cost of distilled water compared to the thicknesses of 5 and 7 mm. The cost of



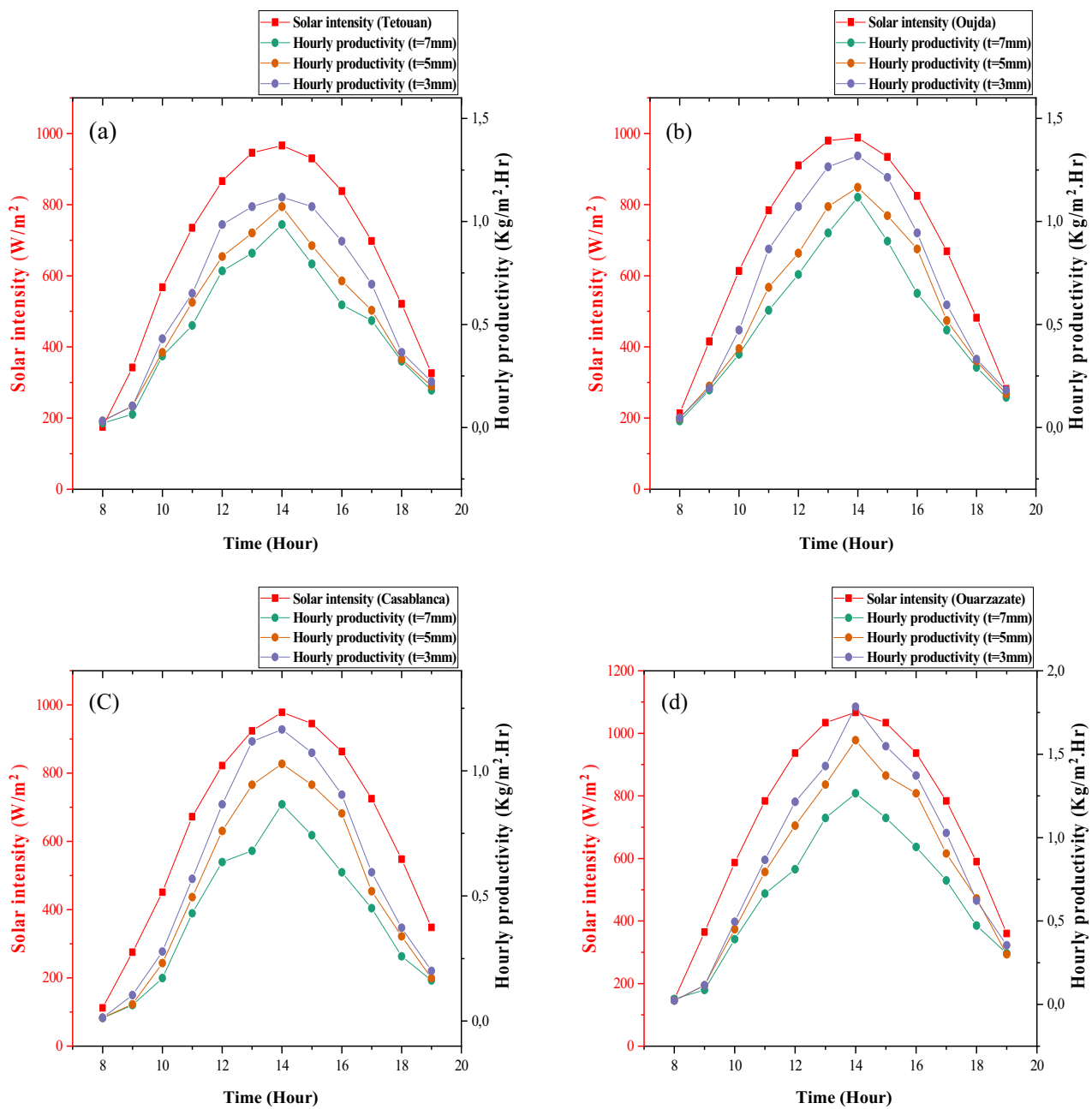


Fig. 10 Hourly productivity of the inclined cascade solar distiller with different thickness of glass cover, under the variation in solar intensity for the cities: **a** Tetouan, **b** Oujda, **c** Casablanca and **d** Ouarzazate

distilled water for the three thicknesses of the glass cover of the system studied in the climatic conditions of the Ouarzazate region is lower than other regions (Tetouan, Oujda and Casablanca), due to high productivity in this region that presents a high solar intensity, which can reach about 0.0068\$/L for a thickness of 3 mm.

The performance assessment of the inclined cascade solar still in terms of productivity and distilled costs obtained in this work is very interesting in comparison with other works treated in the literature [20, 24, 27]. In these works of the

literature, each of these authors tried to improve the performance of the solar still by modifying one of its parameters. Table 4 shows the comparison between the results existing in the literature for the various studies of improvement of the solar stills in cascade with that of the present work. These works are conducted in different regions of the world characterized by different climates, but the same solar intensity was taken into account in order to compare its performances. As can be seen from this table, the design considered in the present work of the cascade solar still is more productive

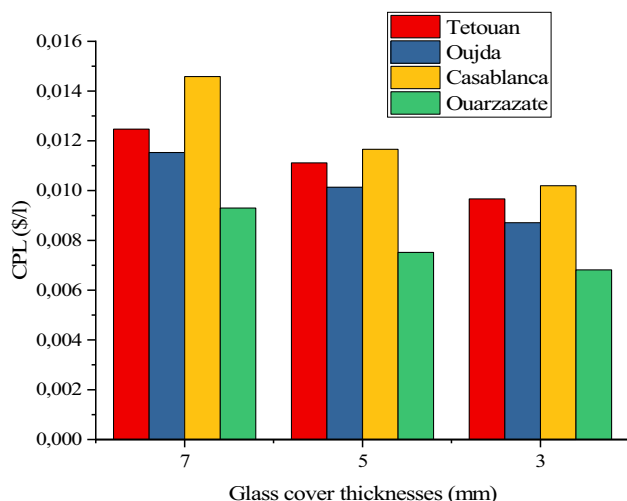


Fig. 11 The cost of distilled water obtained by our system for three thicknesses values of glass cover

with a low cost of distilled water than the others studied in the literature. The productivity and cost of distilled water obtained by the cascade solar still reach a value of $5.82 \text{ L/m}^2 \cdot \text{d}$ and $0.01 \text{ \$/L}$ by the integration of an internal Multi-Tray vertical evaporator [20], $4.38 \text{ L/m}^2 \cdot \text{d}$ and $0.047 \text{ \$/L}$ [27] by using copper, and $6.38 \text{ L/m}^2 \cdot \text{d}$ and $0.039 \text{ \$/L}$ by adding deflectors to the vertical walls of the solar still [24]. However, a productivity and a cost obtained in our case are $8 \text{ L/m}^2 \cdot \text{d}$ and $0.0093 \text{ \$/L}$, respectively. By comparing this value to the lowest among the different cases considered, it can see that Saadi et al. [20] also was obtained a low cost, but corresponding to a low productivity. This comparison makes it possible to deduce an increase in productivity of 27% and a decrease in cost of 7% in the present work. The low-cost difference is explained by the manufacturing price of the studied prototype which is estimated at 130.83 and 85.47 \$ in our case and that of Saadi et al. [20], respectively. Indeed, the manufacturing cost has a direct effect on the cost of distilled water [42], which in our case is higher due to the complex geometry of the prototype. But the higher productivity is mainly due to the new design of the absorber plate which

has a very important advantage. The distribution of brackish water in several waterfall-shaped basins with horizontal and sloping trays containing baffles provides a minimum depth of salt water. The low thickness of the cover also allows a large amount of solar radiation to be transferred to the solar distiller, resulting in an increase in thermal energy inside the solar still. Therefore, a rapid increase in the evaporation of water causes an increase in the productivity of distilled water. It is found that the productivity of solar still has a significant effect on the cost of distilled water, the higher the productivity, the lower the cost of the distilled water by the solar still.

Conclusion

The main aim of the current paper was to improve the performance of a newly designed cascade solar still in terms of productivity and cost of distilled water through two parameters which are solar intensity and glass cover thickness. The methodology followed was based on the CFD model. Firstly, a 3D geometry of the inclined cascade solar still was created and the multi-phase model was developed in ANSYS software, initial and boundary conditions were defined. Secondly, the model was validated by comparing the values of predicted and experimental absorber plate temperature. This comparison shows that the value of MAE and ME is equal to 3% and 5%, respectively, allowing to conclude to the model reliability. Then, it was used to conduct sensitivity analysis to evaluate the effect of solar intensity in different regions of Morocco, as well as the effect of the thickness of the glass cover. The results show the best performance in terms of water productivity and its cost production for the different studied parameters. However, the maximum productivity of the inclined cascade solar still with a thickness of 3 mm of the glass cover and under the climatic conditions of the Ouarzazate region (south of Morocco) can reach more than 1.78 kg/m^2 per hour with a cost of distilled water of $0.0068 \text{ \$/L}$. It is found that the new design of the absorber plate with a minimum thickness of the glass cover in a region which has a higher solar intensity makes

Table 4 Comparison of existing stepped solar still to that of the present work

Type of modification	Climatic condition	Maximum solar radiation (W/m^2)	Month	Productivity ($\text{L/m}^2 \cdot \text{d}$)	CPL ($\text{\$/L}$)	Réfs.
Integration of an internal Multi-Tray vertical evaporator	Algeria	1049	18 July	5.82	0.010	[20]
Inclined copper-stepped solar	Malaysia	1000	19 October	4.38	0.047	[27]
With wicks on vertical side	Egypt	1000	08 August	6.38	0.039	[24]
Horizontal and inclined surfaces with baffles Glass cover thickness	Maroc	1067	25 June	8	0.0093	Present work



it possible to increase the productivity of the cascade solar still. The limitation that may occur in ANSYS FLUENT is related to the CPU time; in fact, it takes a lot of time to get to the final results. However, this could be handled by using a performant computer.

In perspective, other parameters will be taken into account in order to further improve the productivity of the solar still and to develop a solar distillation installation at the national level.

Funding This research did not receive any specific Grant from funding agencies in the public, commercial, or not-for-profit sectors.

Declarations

Conflict of interest There are no conflict to declare.

References

- Xiao, G., Wang, X., Ni, M., Wang, F., Zhu, W., Luo, Z., Cen, K.: A review on solar stills for brine desalination. *Appl. Energy* **103**, 642–652 (2013). <https://doi.org/10.1016/j.apenergy.2012.10.029>
- Gude, V.G.: Desalination and water reuse to address global water scarcity. *Rev. Environ. Sci. Bio/Technol.* **16**(4), 591–609 (2017). <https://doi.org/10.1007/s1157-017-9449-7>
- Jayaswal, K., Sahu, V., Gurjar, B.R.: Water pollution, human health and remediation. In: Bhattacharya, S., Gupta, A.B., Gupta, A., Pandey, A. (eds.) *Water Remediation*, pp. 11–27. Springer Singapore, Singapore (2018). https://doi.org/10.1007/978-981-10-7551-3_2
- Eddouibi, J., Abderafi, S., Vaudreuil, S., Bounahmidi, T.: Water desalination by forward osmosis: dynamic performance assessment and experimental validation using MgCl₂ and NaCl as draw solutes. *Comput. Chem. Eng.* **149**, 107313 (2021). <https://doi.org/10.1016/j.compchemeng.2021.107313>
- Chaoui, I., Ndiaye, I., Eddouibi, J., Abderafi, S., Vaudreuil, S., Bounahmidi, T.: Experimental and theoretical parametric study of forward osmosis system using NH₄HCO₃ and NaCl draw solutes. *Chem. Eng. Res. Des.* **180**, 402–413 (2022). <https://doi.org/10.1016/j.cherd.2022.01.006>
- Liponi, A., Wieland, C., Baccioli, A.: Multi-effect distillation plants for small-scale seawater desalination: thermodynamic and economic improvement. *Energy Convers. Manag.* **205**, 112337 (2020). <https://doi.org/10.1016/j.enconman.2019.112337>
- Qasim, M., Badrelzaman, M., Darwish, N.N., Darwish, N.A., Hilal, N.: Reverse osmosis desalination: a state-of-the-art review. *Desalination* **459**, 59–104 (2019). <https://doi.org/10.1016/j.desal.2019.02.008>
- Fang, S., Tu, W., Mu, L., Sun, Z., Hu, Q., Yang, Y.: Saline alkali water desalination project in Southern Xinjiang of China: a review of desalination planning, desalination schemes and economic analysis. *Renew. Sustain. Energy Rev.* **113**, 109268 (2019). <https://doi.org/10.1016/j.rser.2019.109268>
- Tiwari, G.N., Sahota, L.: History of passive solar-distillation systems. In: Tiwari, G.N., Sahota, L. (eds.) *Advanced Solar-Distillation Systems*, pp. 121–155. Springer Singapore, Singapore (2017). https://doi.org/10.1007/978-981-10-4672-8_3
- Sampathkumar, K., Arjunan, T.V., Senthilkumar, P.: Water desalination by solar energy. In: Sharma, S.K., Sanghi, R. (eds.) *Wastewater Reuse and Management*, pp. 323–351. Springer Netherlands, Dordrecht (2013). https://doi.org/10.1007/978-94-007-4942-9_11
- Bait, O.: Direct and indirect solar-powered desalination processes loaded with nanoparticles: a review. *Sustain. Energy Technol. Assess.* **37**, 100597 (2020). <https://doi.org/10.1016/j.seta.2019.100597>
- Chandrashekhara, M., Yadav, A.: Water desalination system using solar heat: a review. *Renew. Sustain. Energy Rev.* **67**, 1308–1330 (2017). <https://doi.org/10.1016/j.rser.2016.08.058>
- Sharshir, S.W., Eltawil, M.A., Algazzar, A.M., Sathyamurthy, R., Kandeal, A.W.: Performance enhancement of stepped double slope solar still by using nanoparticles and linen wicks: energy, exergy and economic analysis. *Appl. Therm. Eng.* **174**, 115278 (2020). <https://doi.org/10.1016/j.applthermaleng.2020.115278>
- Gnanadason, M.K., Kumar, P.S., Wilson, V.H., Kumaravel, A.: Productivity enhancement of a single basin solar still. *Desalin. Water Treat.* **55**(8), 1998–2008 (2015). <https://doi.org/10.1080/19443994.2014.930701>
- Dumka, P., Jain, A., Mishra, D.R.: Energy, exergy, and economic analysis of single slope conventional solar still augmented with an ultrasonic fogger and a cotton cloth. *J. Energy Storage* **30**, 101541 (2020). <https://doi.org/10.1016/j.est.2020.101541>
- Attia, M.E.H., Kabeel, A.E., Abdelgaied, M., El-Maghlany, W.M., Bellila, A.: Comparative study of hemispherical solar distillers iron-fins. *J. Clean. Prod.* **292**, 126071 (2021). <https://doi.org/10.1016/j.jclepro.2021.126071>
- Kabeel, A.E., Sathyamurthy, R., Sharshir, S.W., Muthumanokar, A., Hitesh Panchal, N., Prakash, C., Prasad, S., Nandakumar, S., Kady, M.S.E.: Effect of water depth on a novel absorber plate of pyramid solar still coated with TiO₂ nano black paint. *J. Clean. Prod.* **213**, 185–191 (2019). <https://doi.org/10.1016/j.jclepro.2018.12.185>
- El-Said, E.M., Elshamy, S.M., Kabeel, A.E.: Performance enhancement of a tubular solar still by utilizing wire mesh packing under harmonic motion. *Desalination* **474**, 114165 (2020). <https://doi.org/10.1016/j.desal.2019.114165>
- Shyora, A., Patel, K., Panchal, H.: Comparative analysis of stepped and single basin solar still in climate conditions of Gandhinagar Gujarat during winter. *Int. J. Ambient Energy* **42**(14), 1649–1659 (2021). <https://doi.org/10.1080/01430750.2019.1612781>
- Saadi, Z., Rahmani, A., Lachtar, S., Soualmi, H.: Performance evaluation of a new stepped solar still under the desert climatic conditions. *Energy Conv. Manag.* **171**, 1749–1760 (2018). <https://doi.org/10.1016/j.enconman.2018.06.114>
- Rashidi, S., Bovand, M., Rabbar, N., Esfahani, J.A.: Steps optimization and productivity enhancement in a nanofluid cascade solar still. *Renew. Energy* **118**, 536–545 (2018). <https://doi.org/10.1016/j.renene.2017.11.048>
- Montazeri, M., Banakar, A., Ghobadian, B.: Enhancement of cascade solar still productivity with sloping absorber plate. *Maejo Int. J. Sci. Technol.* **11**(1), 35 (2017)
- Panchal, H., Ravishankar Sathyamurthy, A.E., Kabeel, S.A., et al.: Annual performance analysis of adding different nanofluids in stepped solar still. *J. Therm. Anal. Calorim.* **138**(5), 3175–3182 (2019). <https://doi.org/10.1007/s10973-019-08346-x>
- Kabeel, A.E., Khalil, A., Omara, Z.M., Younes, M.M.: Theoretical and experimental parametric study of modified stepped solar still. *Desalination* **289**, 12–20 (2012). <https://doi.org/10.1016/j.desal.2011.12.023>
- Omara, Z.M., Kabeel, A.E., Younes, M.M.: Enhancing the stepped solar still performance using internal reflectors. *Desalination* **314**, 67–72 (2013). <https://doi.org/10.1016/j.desal.2013.01.007>
- Omara, Z.M., Kabeel, A.E., Younes, M.M.: Enhancing the stepped solar still performance using internal and external reflectors.



- Energy Convers. Manag. **78**, 876–881 (2014). <https://doi.org/10.1016/j.enconman.2013.07.092>
27. Abujazar, M.S.S., Fatihah, S., Lotfy, E.R., Kabeel, A.E., Sharil, S.: Performance evaluation of inclined copper-stepped solar still in a wet tropical climate. *Desalination* **425**, 94–103 (2018). <https://doi.org/10.1016/j.desal.2017.10.022>
 28. Bouzaid, M., Ansari, O., Taha-Janani, M., Oubrek, M.: Experimental and theoretical analysis of a novel cascade solar desalination still. *Tech. Sci. Press FDMP* **14**(3), 177–200 (2018)
 29. Abujazar, M.S.S., Fatihah, S., Rakmi, A.R., Shahrom, M.Z.: The effects of design parameters on productivity performance of a solar still for seawater desalination: a review. *Desalination* **385**, 178–193 (2016). <https://doi.org/10.1016/j.desal.2016.02.025>
 30. Rashidi, S., Akar, S., Bovand, M., Ellahi, R.: Volume of fluid model to simulate the nanofluid flow and entropy generation in a single slope solar still. *Renew. Energy* **115**, 400–410 (2018). <https://doi.org/10.1016/j.renene.2017.08.059>
 31. Kharchenko, V., Vasant, P. (eds.): *Handbook of Research on Energy-Saving Technologies for Environmentally-Friendly Agricultural Development*. IGI Global (2019)
 32. HOLZBECHER, E.O.: *Modeling density-driven flow in porous media: principles, numerics, software*. Springer Science & Business Media (1998)
 33. Hoomans, B.P.B., Kuipers, J.A.M., Briels, W.J., van Swaaij, W.P.M.: Discrete particle simulation of bubble and slug formation in a two-dimensional gas-fluidised bed: a hard-sphere approach. *Chem. Eng. Sci.* **51**(1), 99–118 (1996). [https://doi.org/10.1016/0009-2509\(95\)00271-5](https://doi.org/10.1016/0009-2509(95)00271-5)
 34. Gimenez, I., Farooq, M.K., El Mahi, A., Kondratas, A., Assarar, M.: Experimental analysis of mechanical behaviour and damage development mechanisms of PVC foams in static tests. *Mater. Sci.* **10**(1), 34–39 (2004)
 35. Panchal, H.N., Patel, S.: An extensive review on different design and climatic parameters to increase distillate output of solar still. *Renew. Sustain. Energy Rev.* **69**, 750–758 (2017). <https://doi.org/10.1016/j.rser.2016.09.001>
 36. Ouammi, A., Zejli, D., Dagdougui, H., Benchrifa, R.: Artificial neural network analysis of Moroccan solar potential. *Renew. Sustain. Energy Rev.* **16**(7), 4876–4889 (2012). <https://doi.org/10.1016/j.rser.2012.03.071>
 37. Meteoblue. <https://www.meteoblue.com/>
 38. MASEN. <http://www.masen.ma/>
 39. Thakar, N.S., Panchal, H.N., Thakkar, V.N.: Performance analysis of various parameters on glass cover of solar distiller—Experimental study. *Int. J. Adv. Eng. Res. Dev.* **1**(3), 231–242 (2014)
 40. Panchal, H.: Performance investigation on variations of glass cover thickness on solar still: experimental and theoretical analysis. *Technol. Econom. Smart Grids Sustain. Energy* **1**(1), 1–11 (2016). <https://doi.org/10.1007/s40866-016-0007-0>
 41. Kaviti, A.K., Yadav, A., Shukla, A.: Inclined solar still designs: a review. *Renew. Sustain. Energy Rev.* **54**, 429–451 (2016). <https://doi.org/10.1016/j.rser.2015.10.027>
 42. Kabeel, A.E., Hamed, A.M., El-Agouz, S.A.: Cost analysis of different solar still configurations. *Energy* **35**(7), 2901–2908 (2010). <https://doi.org/10.1016/j.energy.2010.03.021>

Publisher's Note Springer Nature remains neutral with regard to jurisdictional claims in published maps and institutional affiliations.

Springer Nature or its licensor holds exclusive rights to this article under a publishing agreement with the author(s) or other rightsholder(s); author self-archiving of the accepted manuscript version of this article is solely governed by the terms of such publishing agreement and applicable law.





Comparison of dense optical flow and PIV techniques for mapping surface current flow in tidal stream energy sites

J. McIlvenny¹ · B. J. Williamson¹ · I. A. Fairley² · M. Lewis³ · S. Neill³ · I. Masters² · D. E. Reeve²

Received: 14 April 2022 / Accepted: 13 August 2022 / Published online: 2 September 2022
© The Author(s) 2022

Abstract

Marine renewable energy site and resource characterisation, in particular tidal stream energy, require detailed flow measurements which often rely on high-cost in situ instrumentation which is limited in spatial extent. We hypothesise uncrewed aerial vehicles (UAV) offer a low-cost and low-risk data collection method for tidal stream environments, as recently techniques have been developed to derive flow from optical videography. This may benefit tidal and floating renewable energy developments, providing additional insight into flow conditions and complement traditional instrumentation. Benefits to existing data collection methods include capturing flow over a large spatial extent synchronously, which could be used to analyse flow around structures or for site characterisation; however, uncertainty and method application to tidal energy sites is unclear. Here, two algorithms are tested: large-scale particle image velocimetry using PIVlab and dense optical flow. The methods are applied on video data collected at two tidal stream energy sites (Pentland Firth, Scotland, and Ramsey Sound, Wales) for a range of flow and environmental conditions. Although average validation measures were similar (~20–30% error), we recommend PIVlab processed velocity data at tidal energy sites because we find bias (underprediction) in optical flow for higher velocities (> 1 m/s).

Keywords Tidal stream · Remote sensing · Energy · Drones · UAV · Optical flow

Introduction

Marine renewable energy offers electricity generation from highly predictable sources [1–3]. Both offshore wind and tidal energy are being developed globally to move towards a net-zero carbon future. Flow data in such developments are routinely collected for a variety of reasons, such as initial site characterisation [4], device micro-siting [5] and flow around structures and turbines [6, 7].

Data collection for marine renewable energy site selection, resource characterisation and turbine placement often involves fixed seabed instrumentation or boat-based measurements such as Acoustic Doppler Current Profilers

(ADCP). Bottom-mounted ADCPs provide a point-based measurement in a single location, whilst boat-based ADCP measurements are non-synchronous and typically of a low spatial resolution. ADCP measurements, whilst still essential, do carry high risk and cost. X-band radar is an effective method of deriving surface currents over a large area and has been used in tidal flows [8], however comes with high instrument and operating costs, particularly in remote environments. Small UAV technology is increasingly accessible with consumer off the shelf UAVs providing flexible platforms with high-quality video and effective battery life at a relatively low cost. These systems have been increasingly used in marine science [9]. UAV surveys incur less financial risk, and less physical risk, as the UAVs are typically lightweight and highly manoeuvrable [10].

For the marine renewable industry, video-derived flow will provide a valuable addition to existing data capture methods, measuring surface flow in a low cost and low-risk way. Capturing flow over a large spatial area is extremely useful throughout the lifecycle of a floating or seabed development enabling initial site sift and selection,

✉ J. McIlvenny
jason.mcilvenny@uhi.ac.uk

¹ Environmental Research Institute, North Highland College, University of the Highlands and Islands, Ormlie Road, Thurso KW14 7EE, Scotland

² Swansea University, Swansea, Wales

³ Bangor University, Bangor, Wales



characterisation, device micro-siting and flow-structure analysis over different periods.

Flow derived from optical videography began as a laboratory technique originally derived from laser-based particle measurements [11]. Flow derived from downward-looking video offers a way of measuring surface flow over a large spatial area capturing fine spatio-temporal detail of flow characteristics. UAV-derived video can also provide an additional tool to rapidly define surface flow characteristics such as high-velocity jets and other turbulent features in tidal streams; therefore, UAVs could offer an essential tool for the tidal energy industry. Various methods are available for deriving flow from video, each with advantages and disadvantages; however, their applicability to tidal energy site characterisation is unknown. Here, we compare two methods: large-scale particle image velocimetry (LSPIV) and Gunnar-Farneback dense optical flow.

Particle tracking techniques have been increasingly used for flow measurement in rivers [12–16]. LSPIV relies on the flow being seeded with artificial or natural particles and is highly accurate in a wide variety of natural flow conditions [17]. However, LSPIV does have drawbacks, as the technique relies on natural particles such as foam or debris on the surface; insufficient particles require artificial seeding which is labour intensive and not appropriate for tidal environments on a large scale. The technique also has a reduced ability to derive flow from a low-intensity image gradient [18]. However, it has been shown to provide good results when ephemeral turbulent structures advected by the mean flow are tracked, sometimes termed surface structure image velocimetry [19], and it would be this approach that could be used at tidal sites.

PIVlab is a GUI-based particle image velocimetry (PIV) software written in the MATLAB environment [20–22]. PIVlab uses a cross-correlation algorithm to derive the most probable particle displacement in small image subsections [20]. PIVlab has been applied to natural environments in the past for extracting river velocity and is accurate when compared with in situ measurement [23–27] and has also been used to estimate river discharge [25, 27–29]. Use of PIVlab for measurement of tidal flows, including at tidal stream sites, has been demonstrated [30, 31]; however, good results were dependent on site and environmental conditions. Therefore, investigation of alternative surface velocimetry approaches is warranted to seek wider ranging applicability of UAVs for tidal resource assessment.

Various optical flow algorithms are available for surface water movement detection, some of which have been applied to the marine environment [32]. Here, the Gunnar-Farneback dense optical flow is used as a method of deriving flow from consecutive optical images by using pixel intensity and calculating the movements of each pixel between consecutive frames [33]. This has the benefits of being less

computationally expensive and does not require seeded particles to calculate flow. Disadvantages are the technique assumes spatial smoothness whereby surrounding pixels are assumed to have the same general movement of the target pixel. The technique also requires consistency in pixel intensity between frames. The Gunnar-Farneback method of optical flow has been cited to be potentially useful for natural flow conditions [33–35]. The Gunnar-Farneback method is a two-frame motion estimation based on polynomial expansion [33]. The technique uses a neighbourhood around each pixel to identify its most likely movement between two frames and utilises a pyramid decomposition which enables the algorithm to handle large pixel motions, where pixel displacements are greater than the neighbourhood size.

Although both these techniques have been well established in the fluvial environment and applied to surf-zone currents [36, 37], optical flow approaches have yet to be tested in oceanic waters with different surface characteristics. This study tests whether the optical flow algorithm offers a more reliable way to inform on surface water flow in a tidal channel with relevance to the tidal energy industry.

This study compares field measurements of flow speeds in tidally energetic channels between LSPIV utilising PIVlab and dense optical flow techniques using the Gunnar-Farneback algorithm. The objectives of this study are to compare two velocimetry techniques, LSPIV and optical flow, against underway ADCP data and drifter data using short downward-looking videos of a section of tidal flow. Further, the study will test the techniques in two well understood tidal energy sites to test the effects of differing environmental conditions on the techniques and to understand the transferability of the technique to different sites.

Methods

Experimental and study sites

Data were collected from two energetic tidal channels targeted for renewable energy developments, the Inner Sound of the Pentland Firth in the North of Scotland, and Ramsey Sound in Wales. The sites were chosen as representative test cases for this study for the purpose of being able to transfer the techniques used here to other less understood sites. The Inner Sound is a tidal channel that separates the Orkney Islands from Mainland Scotland (Fig. 1). The Inner Sound is being developed as a tidal energy site and currently has active turbines deployed in the channel at the time of writing. The channel is a constriction between the Atlantic Ocean and North Sea producing fast tidal currents over 3 m/s in places [4]. The mean water depth is 19 m with a maximum of approximately 36 m in the channel. Due to the flow speed, high levels of turbulence are present in the



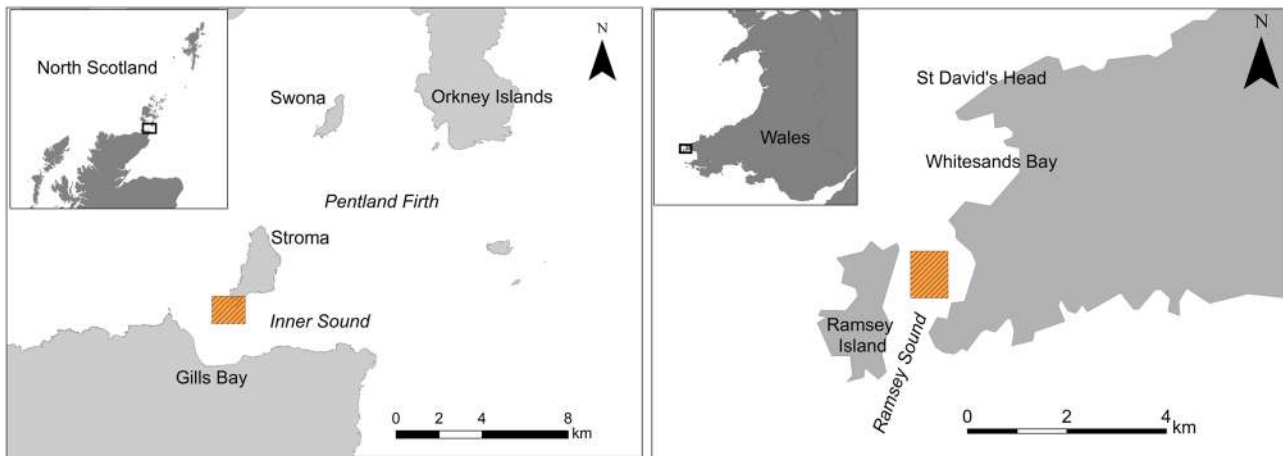


Fig. 1 Inner Sound, Pentland Firth, Scotland (left) and Ramsey Sound, Wales (right). Measurement areas in orange shaded box

Inner Sound. One common turbulent feature is the presence of kolk boils [10]. Kolk boils are rotating vertical plumes of water associated with obstacle interaction and high shear near the seabed where vortices are formed which emigrate towards the surface. They present on the surface often as smooth circular or semi-circular areas of water due to the eruption of vertical flow and water displacement.

Ramsey Sound lies between the island of Ramsey and the Welsh mainland (Fig. 1). It has long been a focus for tidal stream energy extraction: the Tidal Energy Ltd. DeltaStream device was deployed in 2015. Tidal renewable energy in Wales is an emerging market with several companies receiving funding to develop the sector and deploy devices connected to the national grid. Cambrian Offshore is redeveloping the Ramsey Sound site with aim of deploying a tidal turbine in the channel.

The current regime in Ramsey Sound is forced by a progressive tidal wave, meaning that peak flows are around high and low water; current speeds in Ramsey Sound are up to 3 m/s [38, 39]. The bathymetry in the area is highly variable leading to both spatial and temporal (flood versus ebb) differences in turbulence metrics [5] and hence the surface features required for surface velocimetry. The mean depth is 20 m, whilst maximum depth is approximately 70 m.

UAV surveys

At both sites, short stationary hovers recording video were carried out for several minutes at a time. In addition, boat-based ADCP and GPS drifters were used to provide validation measurements for UAV-derived surface flow measurements. UAV and validation techniques were different between the two sites due to site conditions, but the experimental methodology was designed to be comparable.

Inner Sound

Fieldwork at the Inner Sound was conducted on the 2nd of May 2021. GPS drifter recovery challenges in fast flows and a highly exposed site meant only boat-based ADCP measurements were conducted at the Pentland Firth site. A downward-looking Teledyne Workhorse Sentinel 600 kHz ADCP was used with a blanking distance of 0.88 m at a depth of 1.78 m which provided clearance of the boat hull. The ADCP was set to ping as fast as possible with an approximate ping rate of 2 Hz with data averaged over 1-s intervals. Bin depths were set to 2 m. The first depth bin was used to compare with the video-derived flow (depth bin of 2.66 – 4.66 m). Boat speed was kept to a minimum (2 knots) during the ADCP transects, with position recorded by D-GPS and bottom-tracking enabled. ADCP transects were carried out immediately after the UAV flight.

A DJI Phantom 4 Pro 2.0 UAV was used at the Inner Sound with standard GPS. The wind speed during the survey was < 10 knots with overcast consistent lighting conditions. The UAV was orientated with the long axis (width) of the video recording in parallel to the current flow direction at altitudes of 120 m above sea level and downward-facing nadir video. As flights are over the open water, no ground control points are possible for georectification. Instead, GPS coordinates from the flight log data of the centre of each image frame were used. The mean of the GPS coordinate was used for all GPS points acquired in the flight log over the length of the stationary hover video (1 min). For the Inner Sound data, the drift around the central hover point was < 1 m with a mean GPS horizontal dilution of precision (HDOP) of 0.54 over the duration of the video clip. The video recording mode was 30 frames per second with an image size of 4096*2160 pixels. The ground resolution was calculated using the image width of 4096 pixels, sensor

width of 13.2 mm, sensor height 8 mm, and a focal length of 8.8 mm. Combined with the camera specifications and average flight altitude during the video calculated from flight logs yielded a ground (sea surface) sampling pixel size of 5.05 cm per pixel. When flying at approximately 120 m in altitude, this results in a video frame with a horizontal field of view of 206.84 m and a vertical field of view of 109.08 m. The video excerpt for this study was 60 s in length, comprising 1800 frames.

For dense optical flow, the mean GPS position from the flight log throughout the video was used to rectify the images with the calculated image height and width. Yaw from the flight log was used for image rotation from geographic north. No lens correction was carried out as the lens distortion on these consumer UAVs has been reported as being very low [40] and would be the same for each type of processing method. However, methods do exist to correct for these distortions such as the checkerboard method [41]. Images were calibrated using the length of each image whereby a length is calculated from camera specifications for PIVlab.

Ramsey Sound

Fieldwork at Ramsey Sound was conducted on the 14th of May 2021; five flights were conducted from peak current down to slack water. Nadir videos of 60-s duration were made of the flow at altitudes of 120 m, again with the long axis parallel to the flow direction; eleven videos were selected for analysis where there was good overlap with validation data. Weather conditions were variable with wind speeds up to 6.3 mph and a cloudless sky. All videos had bright, constant illumination with sun glinting off turbulent surface features; also observable in the imagery were small wind-driven ripples in the same direction as the flow and small standing waves opposing the flow. Validation data were collected with both boat-based ADCP surveys and GPS drifter runs. Four GPS drifters, the design of which is described in Fairley et al. [30], were deployed and recovered from a RIB such that they transited through the field of view of the UAV. It has been shown that the presence of a small number of drifters in the field of view does not impact on results compared to the case with no drifter [30]. At the same time, ADCP transects preceded the UAV video collection. These transects were collected with a similar set-up to the Inner Sound transects. WinRiver II software was used to acquire data from a pole-mounted 600 kHz Teledyne Sentinel ADCP. GPS and wind data were incorporated from an AIRMAR 200WX meteorological station. The first bin started at 0.82 m below surface, and bin height was 0.5 m. The ADCP was set to ping at 2 Hz; alternating between water profile and bottom track pings to allow for relative vessel motion correction.

Image pre-processing

Prior to processing in PIVlab, individual frames were first extracted from the video to image stills. The image stills had pre-processing steps applied before analysis to improve the measurement quality. For optical flow, video frames were processed on the fly. For comparison of techniques, the same image pre-processing steps were applied to both the optical flow frames and PIV frames. Image pre-processing improved performance in both optical flow and PIV techniques (Fig. 2). The image pre-processing steps applied were in order as follows:

- Image was converted to greyscale.
- Contrast Limited Adaptive Histogram Equalisation (CLAHE) is a variant of adaptive histogram equalisation, where the image or tiles histogram is altered to better distribute intensity values, CLAHE also limits over amplification of contrast. The algorithm was performed on image tiles and tiles combined using bilinear interpolation to remove any boundaries [42].
- The MATLAB (2021a, MathWorks) `imadjust` function (adjust image intensity values) maps the intensity values in grayscale image to new values. This saturates the bottom 1% and the top 1% of all pixel values. This operation increased the contrast of the output image.

Processing

PIVlab

Various post-processing is available in PIVlab such as smoothing and high-pass filtering. These were not applied to the results for comparison with the optical flow results. All processing was carried out using an Intel Core i7-2600 k CPU 3.40 GHz with 4 cores. No graphics card processing was used. Three passes of the interrogation window were used within PIVlab with a first pass of 128×128 pixels second pass of 64×64 pixels and a third pass of 32×32 pixels. After the PIVlab processing was complete, the mean vectors were computed from all the consecutive frame vectors, giving temporal mean flow vectors for the entire video clip.

Dense optical flow

MATLAB offers built-in methods for dense optical flow of which there are three algorithms available. Equations for the Gunnar-Farneback dense optical flow algorithm are explained elsewhere [33, 34, 43]. A MATLAB script was written which reads in the video, performs image pre-processing and dense optical flow. Temporal mean optical flow vectors for each pixel



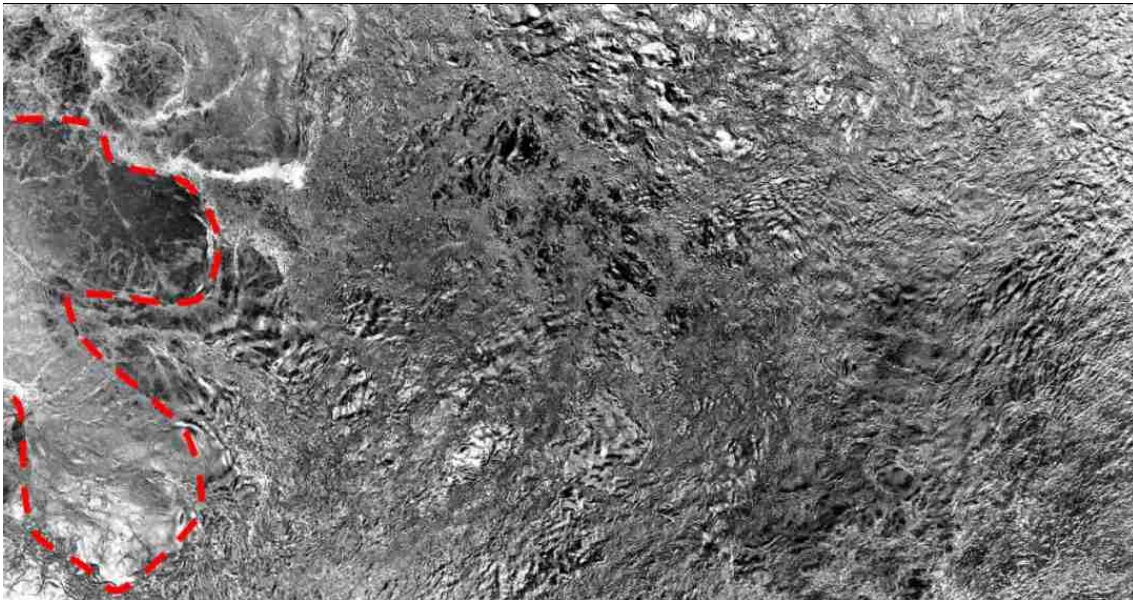


Fig. 2 Example of a processed downward-looking video frame of sea surface. Dotted line outlines surface expression of a kolk boil exhibiting a smooth surface due to vertical water movement

for the whole video were calculated from the sum of all vectors divided by the number of frames in the video.

Image complexity metric

A simple edge-detection algorithm was used to show the difference in image complexity and structures between the Inner Sound and Ramsey Sound. Image segmentation using the Sobel method was carried out on processed greyscale video frames. Sobel edge detection undertakes a spatial gradient measurement on an image where regions of high spatial frequency correspond to edges within the images. Structures on the surface of the water primarily caused by turbulence and foam patches which are beneficial to both optical flow and LSPIV were attempted to be captured by the Sobel edge detection as a metric for the suitability of the video for the flow analysis.

Wind ripples present in the Ramsey Sound data were visually measured by tracking individual wind ripple crests between frames. This was done manually by marking the position of individual crests then measuring the distance travelled in pixels.

Results

Inner Sound

A 60-s-long video recorded at 30 frames per second was analysed using PIVlab and Gunnar-Farneback dense optical

flow. The video was analysed using every other frame resulting in a total of 900 frames. It could be visually seen that the UAV was at the edge of a fast-flowing jet with slower-moving water also visible to the right. In addition, the video contained a region of active kolk boils in the far left of the video frame, consisting of smooth circular regions which slowly traversed the video frame (Fig. 3).

Visual results (Fig. 3) showed good similarity between the two techniques with general flow patterns being consistent. Both the PIVlab and optical flow averaged results were then geo-rectified for comparison with ADCP data. The ADCP data compared were from a transect immediately after the flight. Point data were extracted from both PIVlab and optical flow rectified TIFF files matching locations of point data from the ADCP data. Linear regression was used to compare the datasets. There was a short difference in time between the UAV survey and the ADCP transect. The UAV flight video began at 13:36:10 and ended at 13:37:40; ADCP measurements were taken from 13:39:55 until 13:43:03.

A linear fit between ADCP magnitude and PIVlab generated magnitudes derived an r-squared value of 0.47, with 0.74 RMSE for $y = x$ and a p-value of < 0.001 for a sample group of 72 measurements. A linear fit between ADCP magnitude data and optical flow derived magnitude derived an r-squared value of 0.47 with 0.61 m/s RMSE for $y = x$, and p-value of 0.001. When the magnitude values derived from PIVlab and optical flow were compared with each other, this yields a linear fit derived r-squared value of 0.98 with 0.24 m/s RMSE for $y = x$, and p-value of < 0.001 (Fig. 4, Table 1).



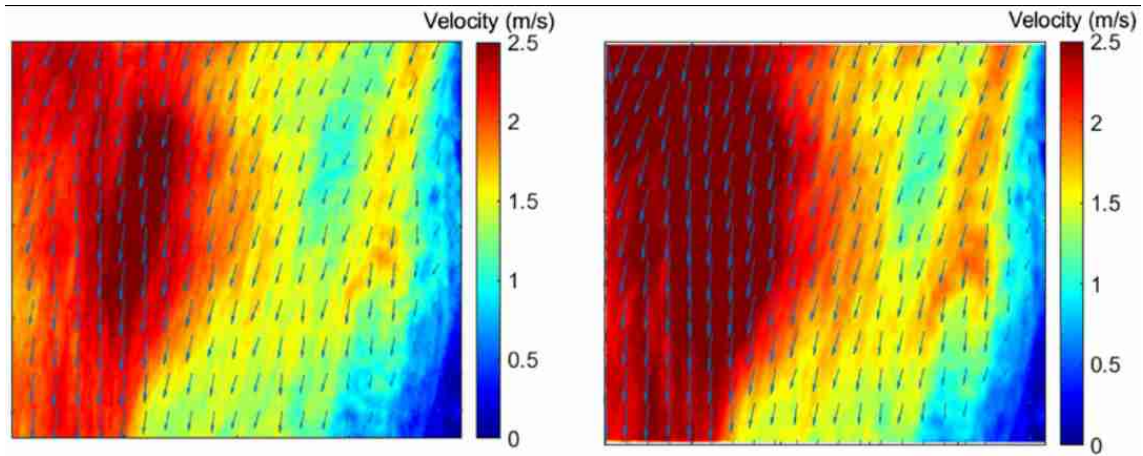


Fig. 3 Visual results of averaged flow and direction derived from optical flow from the 1-min video at 120-m altitude in the Inner Sound (left) and averaged flow derived from PIVlab of the same video (right)

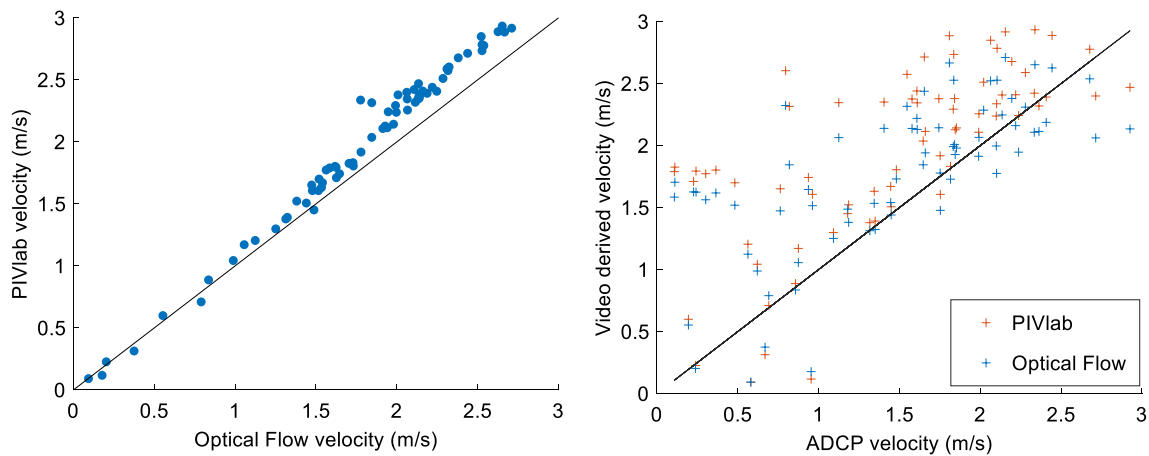


Fig. 4 A comparison of PIVlab magnitudes versus optical flow magnitudes (left) and optical flow and PIVlab magnitudes against ADCP magnitudes (right). 1:1 Line plotted in both graphs

Table 1 Validation metrics for the Inner Sound site

Method	Validation set	RMSE (m/s)	r^2	Mean percentage absolute error (%)
PIVlab	ADCP	0.74	0.47	60.6
Optical Flow	ADCP	0.61	0.47	73.8

For directional comparison, when comparing ADCP directions with PIVlab directions 37% were within 10 degrees and 79% within 30 degrees. Directions derived from optical flow compared to ADCP measurements were more favourable, with 49% within 10 degrees and 84% within 30 degrees. Comparing PIVlab against optical flow, 37% were below 10 degrees of difference and 96% were below 30 degrees.

Figure 5 plots ADCP velocity with ADCP error velocity coded in colour plotted against the longitude. The ADCP error velocity is the difference between two estimates of vertical velocity and offers a built-in means to estimate ADCP data quality. Also plotted are the derived velocity estimates for each ADCP data point from optical flow and PIVlab results from a mean flow of all frames from the 60-s video clip. The optical flow and PIVlab results were georectified to extract each flow point at each ADCP data point position. A mismatch between the PIVlab/optical Flow and ADCP results can be seen between approximately -3.14° and -3.1406° longitude (Fig. 5), where a jet-like feature was present on the mean optical flow and PIVlab results.

Fig. 5 All ADCP data from transects within 1 h of flight. ADCP values are colour coded with ADCP error velocity (m/s). Values extracted from PIVlab and optical flow are averaged results from 60-s video over ADCP transect position. Optical Flow and PIVlab data extracted for each ADCP data point from georectified mean flow image

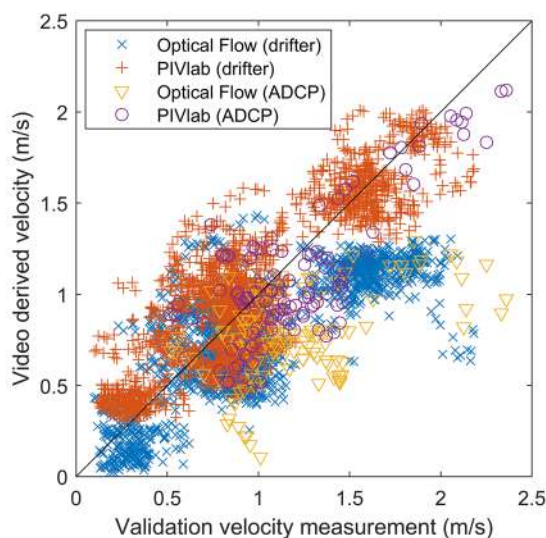
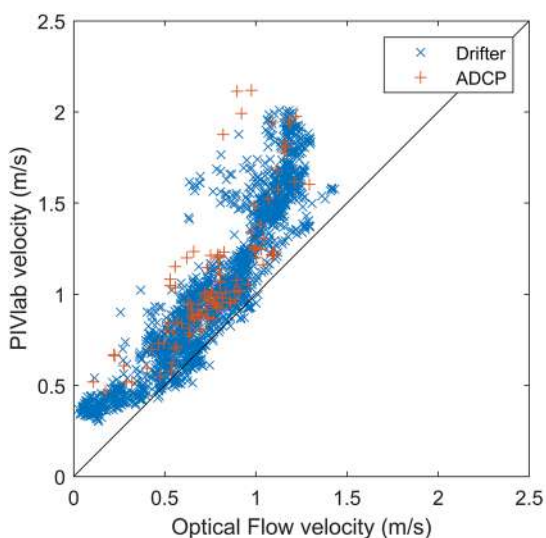
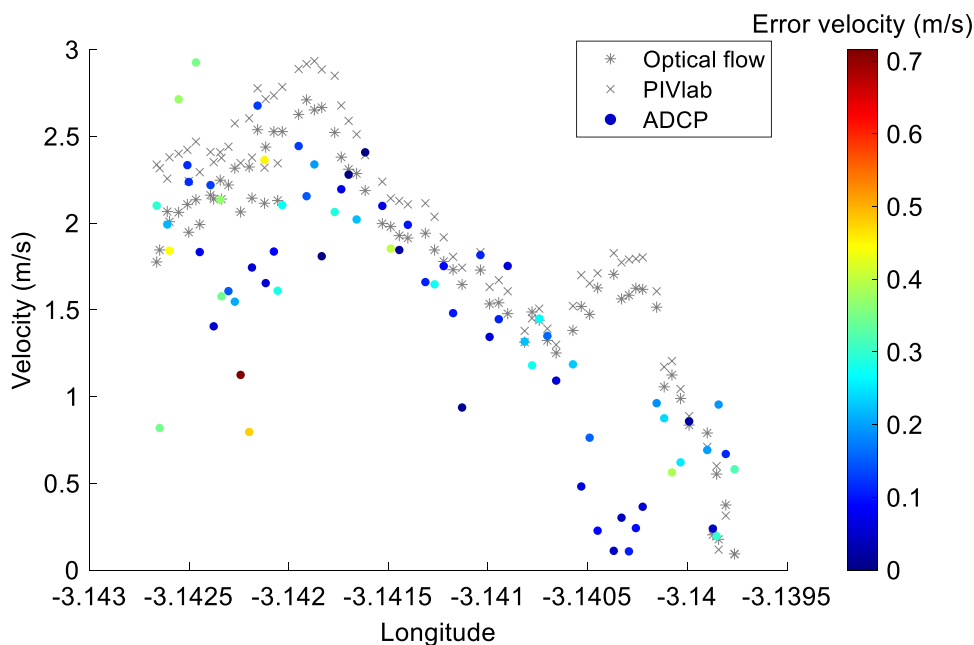


Fig. 6 Comparison between optical flow derived speeds and PIVlab derived speeds at validation data points for the Ramsey Sound dataset (left); comparison between validation velocity measurements

and video derived velocities for optical flow and PIVlab against both drifter and ADCP measurements (right). The black line in both plots is the 1:1 line

Ramsey Sound

Results from Ramsey Sound show similar patterns between video-derived current methods against both validation measures, for both ADCP and surface drifters (see Fig. 6 and Table 2). Both methods performed similarly at lower velocities (Fig. 6, left), but optical flow did not perform as well as PIVlab in flows exceeding 1 m/s. For higher measured velocities, optical flow underpredicted the velocity, whereas PIVlab matched the measurements better. This is

Table 2 Validation metrics for the Ramsey Sound site

Method	Validation set	RMSE (m/s)	r ²	Mean percentage absolute error (%)
PIVlab	Drifter	0.24	0.74	30
PIVlab	ADCP	0.28	0.60	22
Optical flow	Drifter	0.37	0.58	33
Optical flow	ADCP	0.55	0.21	35

problematic for optical flow because it is higher velocity regions that tidal stream developers are most interested in. A similar comparison for all equivalent points in the images for both PIVlab and optical flow shows the same pattern (Fig. 6, right). Table 2 gives error and correlation statistics for the two methods and sets of validation data. Root mean squared errors are better for the PIVlab results, but the differences in mean percentage error are lower; this is because for optical flow the errors are greater at higher velocities.

Image complexity

The differing effectiveness of each technique may be explained by image complexity or ‘clutter’, as these features are required for tracking to obtain video-derived current. By using the Sobel edge-detection algorithm, a comparison of information present in the images for flow analysis can be made to investigate the differing effectiveness of each technique. For each video, 30 individual frames were processed with Sobel edge detection. All pixels which were defined as an edge were summed as a percentage of total pixels in each image.

For the Ramsey Sound video clip during low-speed current conditions, close to tidal slack water (Ramsey Sound, slow, Fig. 7), the 30 individual frames treated with Sobel edge detection resulted in 10.00% mean, 10.24% maximum and 9.70% minimum percentage of edge pixels with an IQR of 0.19. Fast current conditions close to peak flow (Ramsey Sound, fast, Fig. 7) had 4.58% mean, 4.65% maximum and 4.50% minimum percentage of edge pixels with an IQR of 0.03. The Inner Sound frames had 14.20% mean, 16.20% maximum and minimum of 13.50% with an IQR of 0.312. The two sites yielded differing imagery due to the scales of turbulent features and wind conditions (Fig. 7).

Figure 7 shows the result from the first individual frame of each video showing a low percentage of detected edge pixels for both Ramsey Sound slow and fast current conditions, whilst a greater number of detected edge pixel in the Inner Sound site.

Visually the presence of wind ripples in the Ramsey Sound data are the dominant surface feature. By tracking ripple crests in MATLAB and measuring distance travelled, wind ripples were estimated to be progressing at 0.98 m/s during measurement in low current conditions and 0.75 m/s during measurement in the fast current conditions. The wind ripples moved across the surveyed area at an approximately 25-degree angle to the current flow direction during data collected at fast flow conditions and in the same direction as current propagation during low flow conditions with wind ripple wave speed velocities between 0.75 m/s and 1 m/s. Ripple wave speed was estimated by measuring wavelength of several wind ripples in pixels. Wave frequency was estimated by threshold

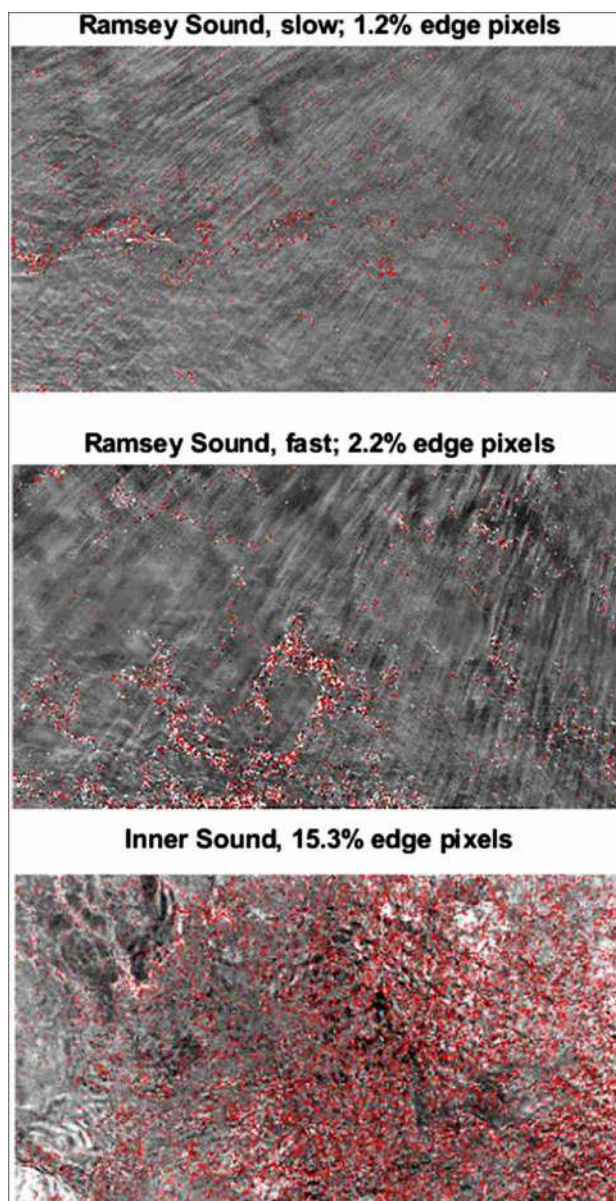


Fig. 7 Sobel edge detection on an individual greyscale video frames with total percentage of edge detected pixels (red)

segmenting an individual frame, taking a pixel intensity profile and running fast Fourier transform (FFT) analysis on the signal. Similar wind ripple wave speeds were found when directly measuring the progress in pixels of individual ripple crests between frames (approximate 1 m/s).

By running optical flow on two individual frames rather than an average of all frames, wind ripples are the dominant feature in terms of the estimated flow with the vast majority of flow vectors in line with wind ripple direction and speed (Fig. 8).



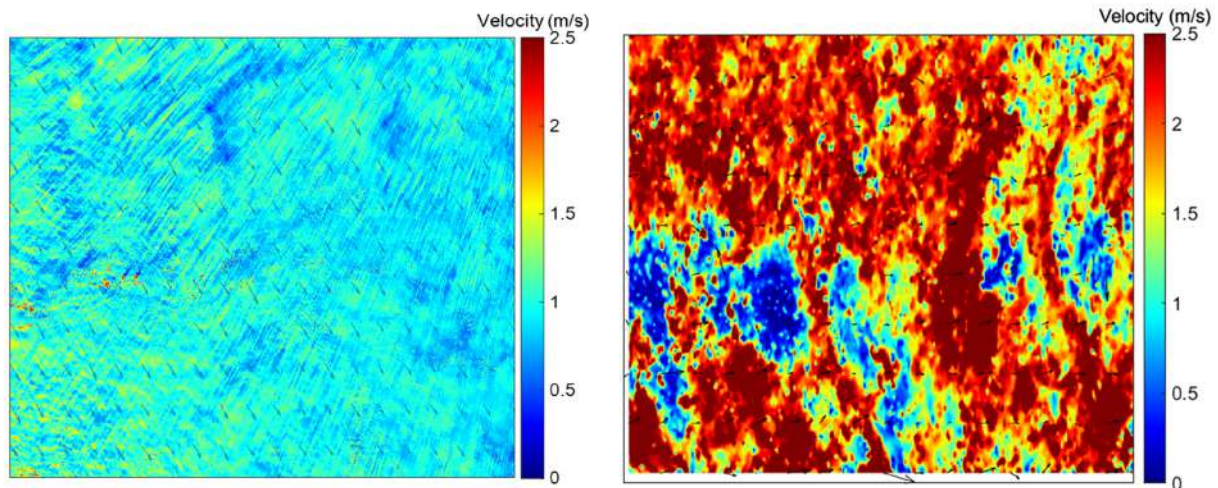


Fig. 8 Left optical flow results between two individual frames in Ramsey Sound in fast tidal flow conditions (> 2 m/s). Right same frames analysed with PIVlab. Wind ripples are progressing north-west to south-east

Discussion

UAV surveys were undertaken in two tidal stream sites both of which are being developed for tidal stream energy, with turbines already operational in the Inner Sound, Pentland Firth, and previous turbines planned for deployment in Ramsey Sound. The aim of this paper was to compare two methods of deriving flow from downward-looking optical video footage, comparing PIVlab (LSPIV) and the Gunnar-Farneback (dense optical flow). Both LSPIV and dense optical flow techniques are shown to be suitable for the derivation of flow from optical videos in these environments; however, results here indicate the LSPIV method may be more effective in tidal stream sites.

The flight altitude of 120 m was chosen as the maximum in the UK at which a UAV can operate without special permission and offers an acceptable spatial coverage for tidal channel data capture of the order of 110×210 m per frame. Reasonable agreement between ADCP data in the Inner Sound using the dense optical flow and PIVlab may indicate that this flying altitude and resolution are suitable for the measurement of flow at these locations. The effect of flying altitude on LSPIV and optical flow has been investigated in other environments; higher flying altitude resulted in lower resolution and poorer results from LSPIV with a comparable UAV [17], albeit in a riverine environment. The altitude, resolution and coverage, together with spatial and temporal averaging, eventually becomes an application-specific trade off, for example spatial coverage of a tidal stream site for initial site selection and sift.

From a processing perspective, optical flow simplifies processing, as analysis can be performed directly from the video using a single script. PIVlab requires frames to be

extracted as greyscale images, then pre-processed prior to LSPIV analysis. The block correlation method of LSPIV is more computationally expensive than the optical flow algorithm, although it can be run under parallel processing in the MATLAB environment and is available under the Python language with GPU support via the OpenPIV software library. The Gunnar-Farneback dense optical flow algorithm is also implemented in the Python-based OpenCV library which supports GPU processing to greatly increase processing speeds.

Inner Sound

Similarity in flow magnitude and direction to the ADCP data was sufficient to show the validity of both PIVlab and optical flow techniques for the Inner Sound data. However, in some parts of the flow, there were large differences between the calculated flow speed by optical flow and PIVlab and the ADCP results. The differences observed may be partially explained by non-concurrent ADCP and UAV flights, with ADCP measurements beginning 2 min and 15 s after the UAV flight in these highly spatio-temporally variable environments. Furthermore, ADCP measurements were averaged over 1 s whilst flow derived from the video was averaged over the video duration of 60 s. PIVlab derived higher velocities in the area of higher flow indicated by the ADCP results between -3.141° and -3.143° longitude (Fig. 5, the left of the video frame), which resulted in a higher RMSE value between PIVlab and the ADCP values. The higher flow speed resulting from PIVlab may be more realistic to surface velocity. It is expected that surface velocity is greater than ADCP-derived velocity, as the ADCP data are from the first depth bin (2.66 – 4.66 m) and not the surface velocity.

Assuming a logarithmic velocity profile with depth, surface velocity is expected to be greater; however, further measurements of actual surface velocity using an alternative validation measure would be required to confirm this.

There was a mean difference in flow velocity between the PIVlab and optical flow results of 7.3%. A mismatch in flow speeds was evident in both PIVlab and optical flow between approximately -3.14° and -3.1406° longitude (Fig. 5). This area was associated with a jet of high flow which was fluctuating in time and space during the measurement period. To examine this, an animation was made (Supplementary Material) by processing 20-s slices of the video using optical flow. The mean flow for each 20 s slice was used to construct an animation which showed the jet frequently moving and showing changes in velocity. Therefore, it was possible that this jet was not present during the ADCP transect whilst it was evident in the optical flow and PIVlab results.

The surface expressions of kolk boils were present in the video on the left of the frame. Kolk boils are a turbulent feature associated with bottom obstacles and high shear which are common within the Inner Sound [10]. The surface expression of kolk boils is often a very smooth surface associated with the vertical movement of water. ADCP results indicate that within the area of the kolk boil activity near-surface velocity was in excess of 1.8 m/s and up to 2.7 m/s. PIVlab derived flow for this area was between 2.1 m/s and 2.5 m/s whilst optical flow derived velocities were between 1.8 m/s and 1.2 m/s. Unlike optical flow, the presence of the kolk boils did not appear to affect PIVlab results where it was thought that the smooth surface may result in a lack of natural tracer particles required for the analysis. However, the kolk boils in the Inner Sound often appear as large-scale features with very smooth surfaces, and where larger kolk boils are present, there may be a large enough area with no trackable features as to affect PIVlab results.

The results show that for this downward-looking video in the Inner Sound tidal channel, PIVlab processing was more accurate when compared to ADCP data than optical flow. However, both results show divergence from ADCP data in one area of flow which can be explained by the difference in sampling time between the ADCP measurements, PIVlab averaging and the fact the ADCP results are below surface. Both PIVlab and optical flow techniques showed reasonable agreement with one another which supports the view that discrepancies between the optical flow and ADCP data may be due to the differences in sampling time and sampled volume between the methods.

Ramsey Sound

Weather conditions differed during data collection in the Ramsey Sound with low wind speeds (6.3 mph). Despite the low wind speeds, the wind present was enough to generate

surface wind ripples which are evident in the still images visually. The presence of this signal in the data provided an additional test for the two techniques.

At Ramsey Sound, PIVlab performed better than optical flow (PIVlab, RMSE = 0.24 m/s and 0.28 m/s versus optical flow, RMSE = 0.37 m/s and 0.55 m/s). However, the optical flow results were similar in accuracy to the Inner Sound results. Comparison of both the drifter and ADCP data showed that optical flow had good results in low flow conditions, but poorer results when flow speed increased over 1 m/s. This divergence in flow above 1 m/s was investigated by comparing surface detail between the two sites and doing further processing on individual frames.

PIVlab results showed consistent agreement with both the ADCP data and the drifter speeds. In addition, the accuracy of the PIVlab results increased at higher flow speeds, which are more of an interest to tidal developers given power is proportional to speed squared, and typical turbine cut-in speeds of > 1 m/s.

Optical flow assumes spatial smoothness (that neighbouring pixels have similar movement) and brightness consistency where pixel intensity does not change significantly between frames [44]. Illumination was highly consistent between frames, so this latter point is unlikely to be a factor.

Image complexity

Wind conditions, lighting conditions, surface waves and turbulence were observed to affect optical flow results, as observed elsewhere [45]. Analysis of image complexity showed that the Inner Sound video frames contained a greater degree of surface texture, which was evident from both visual comparison and results using edge detection; however, it is noted that the lower amount of surface detail present in the Ramsey Sound data was not so low as to affect either technique where there was still an abundance of trackable features present. The performance of the PIVlab results against ADCP and drifter data provided further evidence that this was not a factor.

Further examination focused on secondary wind ripples which are visually the dominant feature in the Ramsey Sound frames, evident as stripe features seen in the on the greyscale image (Fig. 7). By processing individual frames, it can be seen that these smaller-scale wind ripples, which are migrating over the background tidal flow, violate the first assumption of optical flow (requires spatial smoothness), as these surface structures become more pronounced at higher velocities, and hence the difference between neighbouring pixels. Wind ripples were traveling at approximately 1 m/s, explaining the divergence in results between the ADCP data and the optical flow results where flow speeds exceeded 1 m/s. At higher flow speeds, optical flow results are being dominated by the signature of the surface wind ripples



averaging out the underlying tidal flow signal. Optical flow analysis accounts for the movement of all pixels rather than LSPIV using natural particles present on the water surface, and so by considering all pixels, the wind ripple signal has a large effect on the net flow computed by optical flow.

Conclusion

Remote measurement of surface-flow conditions from a small UAV provides a method to rapidly investigate detailed flow conditions in tidal streams over a large spatial scale. Consumer UAVs are now widely available, providing a low-risk and low-cost method of data collection. Many different algorithms exist for deriving flow from nadir videography; here, two common techniques used widely in the fluvial environment were tested as a potential technique for use by tidal energy developers.

At the Inner Sound site, results between both methods were similar, with reasonable comparison with the ADCP data, except for one area of the video where flow speeds derived from videography were very different from ADCP data. This identified a potential limitation in the methodology of this study whereby the non-concurrent nature of the measurements and ADCP measuring beneath the surface may limit using such datasets for validation given the high spatio-temporal variability in these sites. Potentially future studies may utilise methods of surface-flow validation for videography-derived flow which are similar such as X-band radar with concurrent measurement.

Results from Ramsey Sound highlighted an important consideration when choosing between processing techniques. Ramsey Sound videos were collected in higher wind speeds in the presence of wind ripples which acted as a primary dominant signal for optical flow. PIVlab processed velocity showed good performance in the presence of wind ripples. The optical flow results showed a clear deviation from the validation data in velocities in excess of 1 m/s where optical flow underpredicted flows for higher velocities. As wind ripples are a common feature in many tidal channels, often occurring at different angles to the mean tidal flow, PIVlab processing may be the preferred technique to use in tidal-channel environments.

The results from this study indicate that videography techniques could provide a fast, low-cost and low-risk method of deriving an estimate of flow conditions over a large surface area in the marine environment. However, there are differences between processing techniques and more research is required to investigate the effect of environmental variables and different methods to validate the data. After such investigation, it is recommended that these tools be considered by renewable energy developers as a useful spatiotemporal method of collecting surface-flow data

in complement with other techniques. In addition, it may be possible for data collection to be scaled up to satellites to investigate global tidal potential in high detail; optical flow has already been applied to satellite data on a larger scale to measure ocean currents [43]. This might be particularly useful for characterising potential in difficult to reach areas or in developing countries.

Supplementary Information The online version contains supplementary material available at <https://doi.org/10.1007/s40095-022-00519-z>.

Acknowledgements The authors would like to acknowledge the financial support of the EPSRC Supergen ORE Hub (EP/S000747/1)-funded V-SCORES project. The financial support of the Selkie Project is also acknowledged. The Selkie Project is funded by the European Regional Development Fund through the Ireland Wales Cooperation programme. We also acknowledge the support of SEEC (Smart Efficient Energy Centre) at Bangor University, part-funded by the European Regional Development Fund (ERDF), administered by the Welsh Government. M Lewis also wishes to acknowledge the EPSRC fellowship METRIC: EP/R034664/1. We gratefully acknowledge the constructive comments from the reviewers of this manuscript.

Funding Engineering and Physical Sciences Research Council, EP/S000747/1, Benjamin J. Williamson

Declarations

Conflict of interest The authors declare that they have no conflict of interest. The datasets generated during and/or analysed during the current study are available from the corresponding author on reasonable request.

Open Access This article is licensed under a Creative Commons Attribution 4.0 International License, which permits use, sharing, adaptation, distribution and reproduction in any medium or format, as long as you give appropriate credit to the original author(s) and the source, provide a link to the Creative Commons licence, and indicate if changes were made. The images or other third party material in this article are included in the article's Creative Commons licence, unless indicated otherwise in a credit line to the material. If material is not included in the article's Creative Commons licence and your intended use is not permitted by statutory regulation or exceeds the permitted use, you will need to obtain permission directly from the copyright holder. To view a copy of this licence, visit <http://creativecommons.org/licenses/by/4.0/>.

References

- Garrett, C., Cummins, P.: The power potential of tidal currents in channels. *Proc. R. Soc.* **461**, 2563–2575 (1998). <https://doi.org/10.1098/rspa.2005.1494>
- Bryden, I.G., Couch, S.J.: ME1-marine energy extraction: tidal resource analysis. *Renew. Energy* **31**, 133–139 (2006). <https://doi.org/10.1016/j.renene.2005.08.012>
- Coles, D., Angeloudis, A., Greaves, D., Hastie, G., Lewis, M., Mackie, L., McNaughton, J., Miles, J., Neill, S.P., Piggott, M.D., Risch, D., Scott, B., Spalding, C., Stallard, T., Thies, P., Walker, S., White, D., Willden, R., Williamson, B.J.: A review of the UK and British Channel Islands practical tidal stream resource. *Proc.*



- R. Soc. A. **477**, 20210469–20210469 (2021A). <https://doi.org/10.1098/rspa.2021.0469>
4. Goddijn-Murphy, L., Woolf, D.K., Easton, M.C.: Current patterns in the Inner Sound, Pentland Firth from underway ADCP Data. *J. Atmos. Oceanic Tech.* **30**(1), 96–111 (2013). <https://doi.org/10.1175/JTECH-D-11-00223.1>
 5. Togneri, M., Masters, I.: Micrositing variability and mean flow scaling for marine turbulence in Ramsey Sound. *J. Ocean Eng. Mar. Energy* **2**, 35–46 (2016). <https://doi.org/10.1007/s40722-015-0036-0>
 6. Coles, D., Greenwood, C., Vogler, A., Walsh, T., Taaffe, D.: Assessment of the turbulent flow upstream of the MeyGen Phase 1A tidal stream turbines. Presented at the 4th Asian Wave and Tidal Energy Conference, Taipei (2018)
 7. Guerra, M., Hay, A.E., Karsten, R., Trowse, G., Cheel, R.A.: Turbulent flow mapping in a high-flow tidal channel using mobile acoustic Doppler current profilers. *Renewable Energy* **177**, 759–772 (2021). <https://doi.org/10.1016/j.renene.2021.05.133>
 8. McCann D.L., Bell P.S.: Marine Radar Derived Current Vector Mapping at a Planned Commercial Tidal Stream Turbine Array in the Pentland Firth, U.K. MTS/IEEE Oceans 2014 Conference, St Johns, Newfoundland, Canada, 14–19 September (2014), <https://doi.org/10.1109/OCEANS.2014.7003186>
 9. Johnston, D.W.: Unoccupied aircraft systems in marine science and conservation. *Ann. Rev. Mar. Sci.* **11**, 1439–463 (2019). <https://doi.org/10.1146/annurev-marine-010318-095323>
 10. Slingsby, J., Scott, B.E., Kregting, L., McIlvenny, J., Wilson, J., Couto, A., Roos, D., Yanez, M., Williamson, B.J.: Surface characterisation of Kolk-boils within tidal stream environments Using UAV imagery. *J. Mar. Sci. Eng.* **9**, 484 (2021). <https://doi.org/10.3390/jmse9050484>
 11. Lindken, R., Rossi, M., Große, S., Westerweel, J.: Micro-particle image velocimetry (PIV): Recent developments, applications, and guidelines. *Lab Chip* **9**, 2551–2567 (2009). <https://doi.org/10.1039/B906558J>
 12. Mendes, L.P.N., Ricardo, A.M.C., Bernardino, A.J.M., Ferreira, R.L.M.: Comparison of PIV and optical flow for river flow applications. In: Uijtewaal, W., Mário J., Valero, F.D., Chavarrias, V., Arbós, C.R., Schielen, R., Crosato (Eds.). *A River Flow 2020*, Proceedings of the 10th Conference on Fluvial Hydraulics, Delft, Netherlands, 7–10 July (2020)
 13. Sun, X., Shiono, K., Chandler, J.H., Rameshwaran, P., Sellin, R.H.J., Fujita, I.: Discharge estimation in small irregular river using LSPIV. *Proc. Inst. Civil Eng. Water Manag.* **163**(5), 247–254 (2010). <https://doi.org/10.1680/wama.2010.163.5.247>
 14. Lewis, Q.W., Rhoads, B.L.: LSPIV measurements of two-dimensional flow structure in streams using small unmanned aerial systems: 2. Hydrodynamic mapping at river confluences. *Water Resour. Res.* **54**, 7981–7999 (2018). <https://doi.org/10.1029/2018WR022551>
 15. Muste, M., Fujita, I., Hauet, A.: Large-scale particle image velocimetry for measurements in riverine environments. *Water Resour. Res.* (2008). <https://doi.org/10.1029/2008WR006950>
 16. Fujita, I., Muste, M., Kruger, A.: Large-scale particle image velocimetry for flow analysis in hydraulic engineering applications. *J. Hydraul. Res.* **36**(3), 397–414 (1998). <https://doi.org/10.1080/00221689809498626>
 17. Liu, W.C., Lu, C.H., Huang, W.C.: Large-scale particle image velocimetry to measure streamflow from videos recorded from unmanned aerial vehicle and fixed imaging system. *Remote Sens.* **13**, 2661 (2021). <https://doi.org/10.3390/rs13142661>
 18. Khalid, M., Pénard, L., Mémin, E.: Optical flow for image-based river velocity estimation. *Flow Meas. Instrum.* **65**, 110–121 (2019). <https://doi.org/10.1016/j.flowmeasinst.2018.11.009>
 19. Leitão, J.P., Salvador, H.P., Lüthi, B., Scheidegger, A., Mathew, M.V.: Urban overland runoff velocity measurement with consumer-grade surveillance cameras and surface structure image velocimetry. *J. Hydrol.* **565**, 791–804 (2018). <https://doi.org/10.1016/j.jhydrol.2018.09.001>
 20. Thielicke, W., Sonntag, R.: Particle Image Velocimetry for MATLAB: Accuracy and enhanced algorithms in PIVlab. *J. Open Res. Softw.* **9**, 12 (2021). <https://doi.org/10.5334/jors.334>
 21. Thielicke, W.: The Flapping Flight of Birds - Analysis and Application. PhD thesis, Rijksuniversiteit Groningen (2017) <http://irs.ub.rug.nl/ppn/382783069> Accessed 21 October 2021 <https://doi.org/10.13140/RG.2.2.18656.94728>
 22. Thielicke, W., Stamhuis, E.J.: PIVlab – towards user-friendly, affordable and accurate digital particle image velocimetry in MATLAB. *J. Open Res. Softw.* **2**(1), e30–e30 (2014). <https://doi.org/10.5334/jors.bl>
 23. Tauro, F., Piscopia, R., Grimaldi, S.: Streamflow observations from cameras: large-scale particle image velocimetry or particle tracking velocimetry? *Water Resour. Res.* **53**(12), 374–394 (2017). <https://doi.org/10.1002/2017WR020848>
 24. Detert, M., Johnson, E.D., Weitbrecht, V.: Proof-of-concept for low-cost and non-contact synoptic airborne river flow measurements. *Int. J. Remote Sens.* **38**(8–10), 2780–2807 (2021). <https://doi.org/10.1080/01431161.2017.1294782>
 25. Lewis, Q.W., Rhoads, B.L.: LSPIV measurements of two-dimensional flow structure in streams using small unmanned aerial systems: 1. Accuracy assessment based on comparison with stationary camera platforms and in-stream velocity measurements. *Water Resour. Res.* **54**, 8000–8018 (2018). <https://doi.org/10.1029/2018WR022550>
 26. Koutalakis, P., Tzoraki, O., Zaimes, G.: UAVs for hydrologic scopes: application of a low-cost UAV to estimate surface water velocity by using three different image-based methods. *Drones* **3**, 14 (2019). <https://doi.org/10.3390/drones3010014>
 27. Pearce, S., Ljubičić, R., Peña-Haro, S., Perks, M., Tauro, F., Pizarro, A., Dal Sasso, S.F., Strelnikova, D., Grimaldi, S., Maddock, I., Paulus, G., Plavšić, J., Prodanović, D., Manfreda, S.: An Evaluation of image velocimetry techniques under low flow conditions and high seeding densities using unmanned aerial systems. *Remote Sens.* **12**, 232 (2020). <https://doi.org/10.3390/rs12020232>
 28. Legleiter, C.J., Kinzel, P.J., Nelson, J.M.: Remote measurement of river discharge using thermal particle image velocimetry (PIV) and various sources of bathymetric information. *J. Hydrol.* **554**, 490–506 (2017). <https://doi.org/10.1016/j.jhydrol.2017.09.004>
 29. Kinzel, P.J., Legleiter, C.J.: sUAS-based remote sensing of river discharge using thermal particle image velocimetry and bathymetric lidar. *Remote Sens.* **11**, 2317 (2019). <https://doi.org/10.3390/rs11192317>
 30. Fairley, I., Williamson, B.J., McIlvenny, J., King, N., Masters, I., Lewis, M., Neill, S., Glasby, D., Powell, B., Naylor, K., Robinson, M., Reeve, D.E.: Drone-based large-scale particle image velocimetry applied to tidal stream energy resource assessment. *Renew. Energy* (2022). <https://doi.org/10.1016/j.renene.2022.07.030>
 31. Fairley, I., Williamson, B., McIlvenny, J., Lewis, M., Neill, S., Masters, I., Williams, A.J., Reeve, D.E.: A preliminary assessment of the use of drones to quantify current velocities at tidal stream sites. In: *European Wave and Tidal Energy Conference 2021*. Plymouth (2021)
 32. Jung, D., Lee, J.S., Baek, J.Y., Nam, J., Jo, Y.H., Song, K.M., Cheong, Y.I.: High temporal and spatial resolutions of sea surface current from low-altitude remote sensing. *J. Coast. Res.* **90**, 282–288 (2019). <https://doi.org/10.2112/SI90-035.1>
 33. Farneback, G.: Two-Frame Motion Estimation Based on Polynomial Expansion. *J. Lect. Notes Comput. Sci.* 363–370 (2003) https://doi.org/10.1007/3-540-45103-X_50
 34. Farneback, G.: Fast and accurate motion estimation using orientation. In: *Proceedings of the 15th IAPR International Conference*



- on Pattern Recognition, Barcelona, Spain, 3–8 September. 32 (2000) <https://doi.org/10.1109/ICPR.2000.905291>
35. Farneback, G.: Very high accuracy velocity estimation using orientation tensors, parametric motion, and simultaneous segmentation of the motion field. In Proceedings of the IEEE International Conference on Computer Vision, Cambridge, MA, USA, 6 August (2002) <https://doi.org/10.1109/ICCV.2001.937514>
 36. Dérian, P., Almar, R. 2007 Wavelet-Based Optical Flow Estimation of Instant Surface Currents From Shore-Based and UAV Videos. *IEEE Transactions on Geoscience and Remote Sensing*, <https://doi.org/10.1109/TGRS.2017.2714202>
 37. Brouwer, R.L., de Schipper, M.A., Rynne, P.F., Graham, F.J., Reniers, A.J.H.M., MacMahan, J.H.: Surfzone monitoring using rotary wing unmanned aerial vehicles. *J. Atmos. Oceanic Tech.* **32**(4), 855–863 (2015). <https://doi.org/10.1175/JTECH-D-14-00122.1>
 38. Fairley, I., Evans, P., Wooldridge, C., Willis, M., Masters, I.: Evaluation of tidal stream resource in a potential array area via direct measurements. *Renew. Energy* **57**, 70–78 (2015). <https://doi.org/10.1016/j.renene.2013.01.024>
 39. Evans, P., Mason-Jones, A., Wilson, C., Wooldridge, C., O'Doherty, T., O'Doherty, D.: Constraints on extractable power from energetic tidal straits. *Renewable Energy* **81**, 707–722 (2015). <https://doi.org/10.1016/j.renene.2015.03.085>
 40. Streßer, M., Carrasco, R., Horstmann, J.: Video-based estimation of surface currents using a low-cost quadcopter. *IEEE Geosci. Remote Sens. Lett.* **14**(11), 2027–2031 (2017). <https://doi.org/10.1109/LGRS.2017.2749120>
 41. Lee, S.H., Lee, J.Y., Choi, J.S.: Lens distortion correction using a checkerboard pattern. in: Proceedings of the 7th ACM SIGGRAPH International Conference on Virtual-Reality Continuum and Its Applications in Industry, Singapore, 44. (2008) <https://doi.org/10.1145/1477862.1477917>
 42. Zuiderveld, K.: Contrast Limited Adaptive Histogram Equalization. *Graphic Gems IV*. San Diego: Academic Press Professional. 474–485 (1994) <https://doi.org/10.1016/B978-0-12-336156-1.50061-6>
 43. Wu, H., Zhao, R., Gan, X., Ma, X.: Measuring surface velocity of water flow by dense optical flow method. *Water* **11**, 2320 (2019). <https://doi.org/10.3390/w11112320>
 44. Nemade, N. & Gohokar, V. V. 2019. Comparative Performance Analysis of Optical Flow Algorithms for Anomaly Detection (May 18, 2019). Proceedings of International Conference on Communication and Information Processing ICCIP (2019) <http://dx.doi.org/https://doi.org/10.2139/ssrn.3419775>
 45. Liao, B., Hu, J., Gilmore, R.O.: Optical flow estimation combining with illumination adjustment and edge refinement in live-stock UAV videos. *Comput. Electron. Agric.* **180**, 105910 (2021). <https://doi.org/10.1016/j.compag.2020.105910>

Publisher's Note Springer Nature remains neutral with regard to jurisdictional claims in published maps and institutional affiliations.





Modelling the regional effect of transmittance loss on photovoltaic systems due to dust

Abdulrahman Almufarrej¹ · Tohid Erfani¹

Received: 8 February 2022 / Accepted: 21 May 2022 / Published online: 16 July 2022
© The Author(s) 2022

Abstract

The regional differences and environmental challenges are key factors in measuring the efficiency of renewable systems. The loss of transmittance due to weather events, such as dust, clouds/rain, extreme heat, and humidity, is one of the main factors causing reduction in energy generation from photovoltaic (PV) systems' ideal energy production potentials. Existing literature analysed the impact of transmittance loss due to dust on PV systems' performances, recommending frequent system cleaning to maintain the highest energy production level. In this paper we build a mathematical model to quantify the effect of dust accumulation on the transmittance losses. The model predicts the transmittance losses of PVs at tilts between 0° and 90°, exposed to Kuwait's climate with and without cleaning. We use the model to analyse the performance of recommended tilts for optimum energy production (overall and seasonal) based on Kuwait's geographical location. The results demonstrate that the recommended regional optimum tilt (30°) for maximum energy generation is applicable only if the system is cleaned at least once a week. Tilts of 50° and higher can perform better when the frequency of cleaning is once every two weeks or less. This is an important observation that can guide the design, installation, and maintenance (frequency of cleaning) of the PV systems.

Keywords Renewable energy systems · Photovoltaic system · Dust · Transmittance loss · PV tilt

Introduction and background

Arid regions are typically characterised with a dry and hot weather and frequent winds, carrying particles in various size and chemical composition [1]. In such regions, the climate influences the way energy is consumed to control the indoor thermal conditions and buildings design [2]. In addition, it has impact on energy production systems that rely in renewable resource; different researchers in different regions analysed PVs' productivity to explain the impact of regional climatic characteristics on the systems' performance [3]. The key elements with direct impact on dust accumulation levels on PV systems designs are the tilt of the PVs [4], the cover material of the PV [5] and the duration of exposure to the

natural environment without cleaning the panels [6]. The dust impact on PV systems' efficiency is a direct result of the loss in transmittance from its surface. This loss in transmittance is caused by solid particles obstructing the solar radiation from penetrating the panel's surface of the PV collector. In this paper, we include the dust effect as a factor in the selection criteria of alternative PV positions, which in most cases was only governed by the solar incidence angle particular to the region and location of installation.

In Kuwait, according to the 2020 statistical yearbook issued by the ministry of electricity and water, the government is targeting to increase the capacity and production of electricity from renewable resources up to 15% by 2030 [7]. The report includes details of one power plant (Al-Shygaya Power Plant) that operates using renewable resources to produce electricity, recording only 0.02% of the total electricity generated in Kuwait (mostly relying on hydrocarbon fuels). Furthermore, the report mentions five new future projects, all of which consider solar energy as a renewable resource to generate electricity. With such major investments in Kuwait and considering solar power as a renewable resource, the recommended approach in

✉ Abdulrahman Almufarrej
abdulrahman.almufarre.17@ucl.ac.uk

Tohid Erfani
t.erfani@ucl.ac.uk

¹ Civil, Environmental and Geomatic Engineering
Department, University College London (UCL), London,
UK



literature for sustaining optimum energy production rates against dust is to increase the frequency of cleaning. There is still a gap in literature in support of alternative adaptive methods rather than recommending intensive cleaning and maintenance requirements. The objective of this paper is to investigate an alternative adaptive approach by quantifying the effect of dust, while taking the frequency of cleaning as a decision factor. By modelling the relationship between PV tilts and the duration of their exposure without cleaning, we trade-off between alternative tilts (to the theoretical optimum tilts) and the frequency of cleaning while achieving optimum energy production rates.

The effect of dust on systems relying on solar power, as a renewable source, to generate energy has been the focus of many studies [7–11]. Dust accumulation can differ based on the technology used; the performance of focused lenses [12], mirrors [13] and flat PVs [4] has been investigated with the purpose of identifying the effect of dust and the frequency of maintenance and cleaning required. Furthermore, the effect of dust accumulation also differs based on the location of the study [6]. Manufacturer's specifications of similar technologies can also impact the rate of dust accumulation [14], based on the material of surfaces (PV covers) exposed to the environment [15] and their positioning (tilt and orientation) [16].

In regions where dust events are more frequent, analyses detailing the effect of dust on the transparent covers of flat plate solar energy collectors was reported [17]. The study took place in India and the duration of exposure was a month. The surfaces were set at different tilts (from 0° to 90° at 10° increments). Within that duration, the corresponding loss in transmittance was at its highest on a horizontal plate (69%) and at its lowest on the vertical plate (12%), being exposed to the natural conditions without cleaning. One key observation is that the loss in transmittance becomes significantly higher when the tilts of plates are less than 40°. All plates tilted at 40° and beyond had a loss in transmittance of less than 23%.

One of the earlier studies, specific to PVs performance in Kuwait's region, evaluated the performance of solar systems and their power generation potentials [18]. The reported loss in efficiency due to dust was significant; 17% drop in efficiency was recorded after only 6 days of exposure to the natural conditions. Also in Kuwait, the performance of flat-surface solar devices was analysed [19]. The panels were exposed to the natural conditions for 38 days at tilts between 0° and 60°; The corresponding transmittance losses were between 64 and 17%, respectively. It is also noted that the horizontally placed panel (0° tilt) registered a 30% loss in transmittance after only 3 days. Both [18, 19] indicate that significant losses in efficiency/transmittance are expected within a period that is less than a week, especially for panels placed at tilts closer to (or are) horizontal.

In a comparison between the results reported based on the weather conditions in India and Kuwait [17, 19], an experiment was designed to evaluate the regional effect of dust on the transmittance in Egypt; In a study specific to panels with a glass cover, the experiment analysed the effect of dust on the transmittance of surfaces tilted between 0° and 90° [24]. The panels were exposed to the natural conditions close to agricultural fields for a year. They reported losses in transmittance (averaged for each 30 days of exposure) between 27% for PVs at 0° tilt and 3.5% for PVs at 90° tilt.

The comparison showed that Egypt and India data are closer in transmittance loss values when the tilts of surfaces are more than 50°. Kuwait's data did not investigate tilts larger than 60°. Furthermore, based on the three different set of data, it was suggested that panels with tilts less than 60° will require a minimum cleaning frequency of once a week in order to maintain the loss in transmittance at low levels.

Further, the effect of dust on transparent covers of solar collectors with respect to different orientations and tilts was investigated [16]. The experiment took place in Egypt using 100 glass samples positioned at eight orientations (at increments of 45° starting from the true North orientation) and 7 tilts between 0° and 90°. The transmittance of the glass samples was measured periodically and after every rain event for a period of 7 months. Some of the glass samples were cleaned every month, after measuring the effect of dust on the transmittance. Other glass samples were kept uncleaned during the whole testing period (7 months). Also, the dust disposition did not vary in significant amounts between the different orientations at each tilt. The average of transmittance losses after 30 days of exposure range from 28% for a horizontally positioned surface, and 6% for the vertically positioned surfaces. While the total transmittance losses after the 7 months of exposure without cleaning range from 53% for a horizontally positioned surface, and 14% for the vertically positioned surfaces.

Also in Egypt, data were collected from two sets of polycrystalline silicon PV modules tilted at 15°, 20°, 30° and 45° [9]. One set was cleaned weekly and the second set was kept uncleaned for 10 months. The study did not focus on measuring the loss in transmittance, it was specific in measuring the impact of dust on the output power of the tested PV module. The maximum difference recorded in output power between the uncleaned set of panels and the weekly cleaned set, tilted at 15°, is 40%; while, the maximum difference in output power between the uncleaned set of panels and the weekly cleaned set, tilted at 45°, is 25%. For the weekly cleaned set during summer and autumn seasons, the panels at 15° tilt yielded more energy than the other tilts; while during winter seasons, the panels at 30° tilt yielded more energy than the other tilts. As for the uncleaned set, the optimum tilt for energy production throughout the year is 30°. It is unfortunate that the experiment was limited to PVs tilted



only between 15° and 45°. Furthermore, the analysis does not quantify the losses due to dust within the week prior to the scheduled cleaning, measured in the earlier literature to be of significance.

Controlled conditions laboratory-based experiments have also been reported in literature to analyse the effect of dust on the transmittance of surfaces [1, 10, 20, 21]. In these studies, the transparent surfaces are subject to wind and dust for a period of time, using fans to distribute the dust particles and lights to simulate the sun radiation. In those cases, the results are useful to understand a specific parameter's influence in the relationship between the dust and the loss in transmittance, eliminating all other environmental factors. However, in order to model a prediction of transmittance loss, the effect of all the environmental/regional influences that can control or limit the effect of dust are to be considered.

Most of the studies, specific to arid regions, recommend the earliest removal of dust particles from the collector's surfaces to bring back the energy production to the optimum rates [22]. An experimental setup was used to evaluate and compare monocrystalline PV modules outputs at different tilts in Kuwait [23]. The results argued that panels installed at 50° tilt can yield to a yearly power output close to the panels installed at the optimum tilt of 30°. However, their analysis comes short to discuss if the relationship between the dust and tilts of surfaces was the reason that PVs with higher tilts generated energy close to rates produced by PVs tilted at optimum position. Furthermore, there was no mention of the frequency of cleaning that took place, before or after recording the system's output. In this paper, we re-evaluate the optimum tilt positioning of PVs in consideration of the regional (Kuwait's) dust factor. By creating a prediction model for the transmittance losses at different tilts, the daily PV energy generation data are recalculated with the inclusion of a dust reduction factor. The total yearly energy generation rates are then evaluated at different tilts and for different cleaning scenarios (cleaning frequency) to explore alternative tilts that achieve better performance. The novelty in our approach is that our model recommends an adaptive method to the regional impact of dust, recognising the cleaning scenarios as a key factor while deciding on the tilt of PVs.

Methodology

To model the transmittance losses due to dust, parameters such as the climate/location, positioning of PVs (tilt/orientation), the material of PV covers, the duration of exposure and the cleaning schedules must be identified. To predict the amount of loss in transmittance from PV covers, the climate characteristics where the system is installed must

be specified. The prediction model is built using data of PV panels installed at tilts between 0° and 90°, with measurements of dust accumulation on their uncleaned surfaces span from one day to 210 days of exposure in Kuwait. The positioning of PVs' tilt and orientation are key installation elements for maximum energy generation. However, by comparing the results of dust accumulation rates at different orientations, in most cases the difference is less than 2% [16, 24]. Hence, our prediction of the transmittance losses within the days of exposure at tilts between 0° and 90° is assumed to be at the same rate at every orientation.

The data used in the prediction model are from losses reported for PVs with glass covers, being the most commonly used/productive cover material in the region. First, we group the data available from studies conducted based on experiments specific to Kuwait's environment [8, 18, 19, 25]. We collect the data associated with transmittance losses of surfaces that were not cleaned during the period of the experiment or consider the reported losses before cleaning, and when it took place. Second, we take into account the data available from regions with similar climate and environmental conditions (in Egypt and India) [5, 16, 17, 25] to increase the reliability and the accuracy of the model. Based on the data, the model predicts the transmittance loss percentage within 40 days of exposure, at any tilt between 0° and 90°.

For the prediction model we use Kriging method due to the nature of our regional geographical specific data [26]. Kriging is specifically useful as predicting model for data at different spatial location while capturing the regional variabilities of each data set [27]. We use different data sets from multiple studies with similar regional/environmental characteristics to strengthen the model's reliability. Kriging method uses covariate information to accurately capture the relationship between multi-variables data sets and is made of two components: the regression model $f(\cdot)$ and the correlation model $\mathcal{R}(\cdot)$. In our case, the Kriging predictor looks like,

$$TL(t, d) = f(t, d) + \varepsilon(t, d) \quad (1)$$

as a function of two variables, the tilt (t) and the days of exposure (d). ε have zero mean and covariance related to the correlation function $\mathcal{R}(\cdot)$ as

$$\mathcal{R}(\theta, x) = \prod_{j=1}^n \mathcal{R}_j(\theta, x_j) \quad (2)$$

where θ is the correlation parameter and x are the data value at set j . As a rule of thumb, the Gaussian, or the spline functions are fit better when the function is continuously differentiable, likely showing a parabolic behaviour near the origin. A linear, or exponential perform better if the prediction displays a linear behaviour near the origin. θ



is optimally found using the variance of data set and the determinant of \mathcal{R} [26].

In our model we use linear regression for $f(t, d)$ and Gaussian correlation function $\exp(-\theta x^2)$ at tilts between 0° and 90° and within days of exposure up to 40 days. In the regression models the shape and the structure of the model is pre-defined within the polynomial class of functions, which is not always an accurate shape for a given data set. However, the Kriging interpolation adapts itself nonlinearly to the data set given the extra component in Eq. (1) using the covariance of data in a Gaussian process [28].

In the module we assume that the prediction of dust accumulation follows the same trajectory and reset once the PVs are cleaned. In reality, dust events cannot be accurately predicted nor follow the same occurrence frequency every month. However, the data used in building the prediction model are from different seasons/years, representing the yearly impact of dust on the performance of PVs.

We assess the accuracy of our prediction by calculating the coefficient of determination (R^2), the mean absolute error (MAE) and the mean squared error (MSE), indicating the strength (goodness of fit) of the model. R^2 is function of the regression sum of squares (SSR) and the total sum of squares (SST):

$$R^2 = \text{SSR}/\text{SST} \quad (3)$$

where SST can also be calculated by the summation of SSR and the sum of squares of errors (SSE). Accordingly, the value of R^2 is between one and zero. The closer the value of R^2 to 1, the stronger the prediction is (as the value of SSE will be closer to zero).

The MAE is calculated by averaging the summation of the absolute values of the model's errors:

$$\text{MAE} = \frac{1}{n} \sum_{i=1}^n |e_i|, \quad (4)$$

while the MSE is calculated by averaging the summation of the model's error squared values:

$$\text{MSE} = \frac{1}{n} \sum_{i=1}^n e_i^2. \quad (5)$$

The MAE and the MSE values range between one and zero as well. The closer their values to zero, the better competency in prediction the model has.

Results and discussion

The multivariable prediction model estimates the transmittance losses, at any given tilt between 0° and 90° and within 40 days of exposure (Fig. 1). Transmittance losses are at

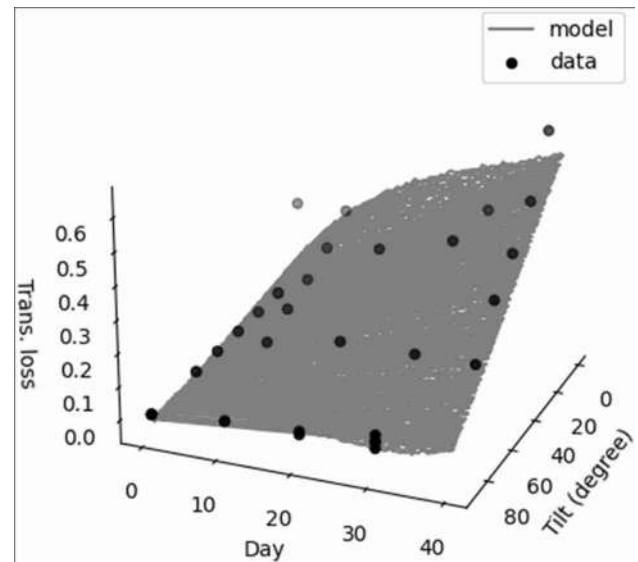


Fig. 1 Prediction model of transmittance loss at different tilt

their lowest when the tilts are closer to 90° . At each tilt, the transmittance losses increase with time. However, as the tilts increase, the rate of loss in transmittance gets lower. The two-dimensional views highlight the transmittance loss data versus prediction against the days of exposure (Fig. 2a) and against the different tilts (Fig. 2b). One key observation is the difference between the transmittance loss at tilt 0° and tilt 90° by day 30, reaching almost 50%. Figures 1 and 2 indicate that the prediction model converges with most of the data point, and the strength of the prediction is determined by calculating the R^2 , the MAE and the MSE (Table 1).

The value of R^2 is 0.928 (very close to 1), indicating a strong fit between the data points and the prediction model. As for the MAE and the MSE, their values are 0.026 and 0.002, respectively. Both MAE and MSE are close to zero, indicating that the errors between the data points and the predictions are very minor.

To show the impact of dust and tilt selection, we need to apply the dust reduction/prediction model to the solar energy generation potentials in Kuwait. Using GIS solar modelling technology,¹ Kuwait's optimum tilt, providing the highest yearly energy generation potential is 29° . GIS models rely on satellite solar radiation measurements which are considered an alternative to ground/on-site measurements. The GIS model we have used has been the subject of analysis and validation, and was reportedly providing the best statistics for all of irradiance components identified in six different models [29]. The energy production varies at different seasons (within a year), and greater energy generation potentials

¹ GIS model provided by www.solargis.com.



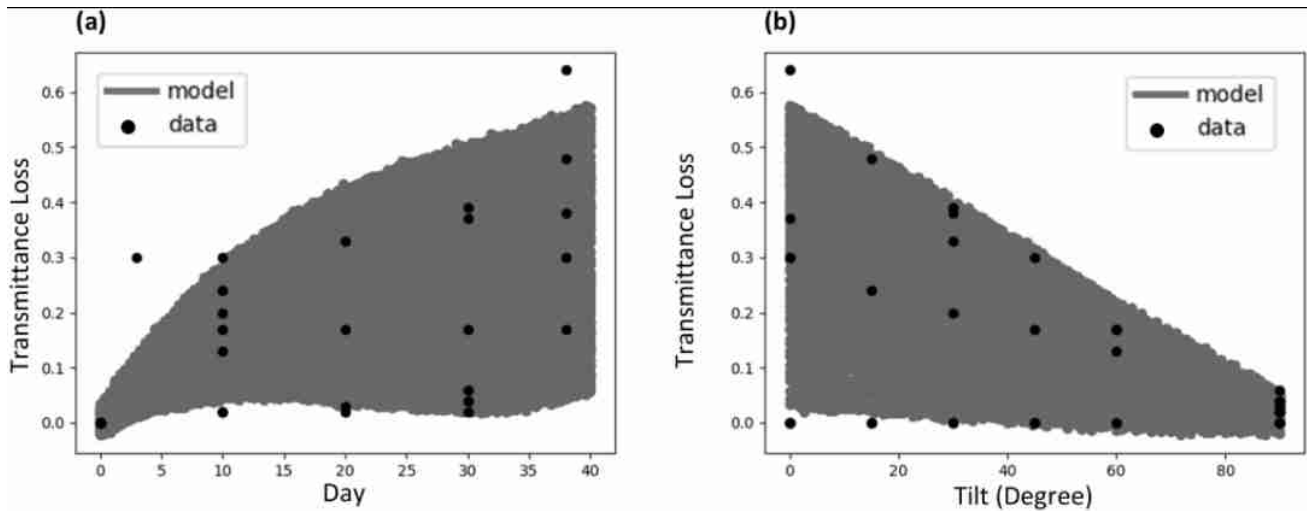


Fig. 2 Two dimensional views of the transmittance loss data versus prediction. **a** Transmittance loss versus days of exposure, **b** transmittance loss versus tilt

Table 1 Prediction model accuracy indicators

	Accuracy indicator	Value
1	R^2	0.928
2	MAE	0.026
3	MSE	0.002

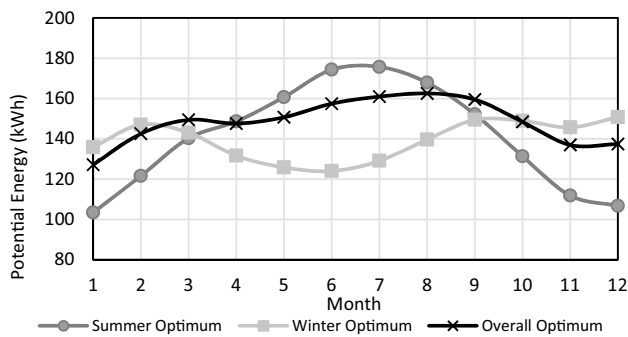


Fig. 3 Monthly energy generation rates at Kuwait's optimum PV tilts

can be achieved at different tilts in some months more than others. The optimum summer energy production tilt is 6° and the optimum winter energy production tilt is 52°.

Using a solar energy simulation model,² we calculate the daily potential solar energy output of a 1 MWh system based on the regional conditions on Kuwait. Within a year, Fig. 3 breaks down the monthly values of energy that can be generated from a 1 KWh PV system. It is important

² Renewables calculation model provided by www.renewables.ninja.

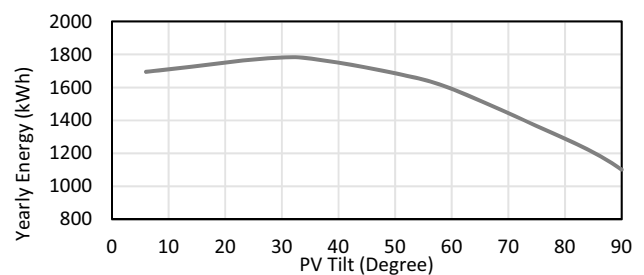


Fig. 4 Simulated yearly potential solar energy at different tilts

to mention that the solar energy simulation platform uses hourly recorded satellite measurements at any selected location within a full year. Accordingly, the energy values consider the fluctuation in energy generation due to any detected environmental factors that can affect the amount of solar radiation measured, that being clouds or dust.

By comparing the yearly energy production rates between the different tilts, the summer optimum tilt generated 5% less energy than the overall optimum tilt, while the winter optimum tilt generated 6% less energy than the overall optimum tilt. To identify the pattern of yearly energy generation potential corresponding to different PV tilts, we increase the data points by simulating the yearly solar energy generation potential from four more tilts. The pattern of yearly energy generation potential at different PV tilts is presented in Fig. 4.

Since all of these measurements assume clean surfaces of the solar system at all time, our dust prediction model is needed to account for the accumulation of dust due to the surfaces' exposure to the environment (in Kuwait) until a cleaning event takes place. However, before applying the

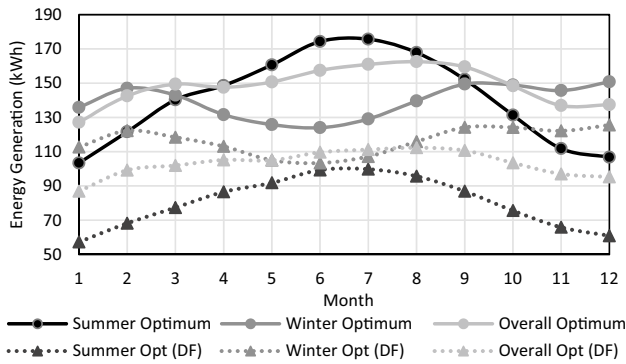


Fig. 5 Monthly energy comparison for optimum tilts (1st scenario)

transmittance loss factor, the relationship between transmittance losses in a PV system and the corresponding energy losses must be quantified. The loss in transmittance can impact the energy output differently, based on the specifications of the solar/PV systems used. In this particular example, recorded data estimating the factor at which the transmittance losses influences the energy performance of a solar desalination plant is used [30].

We use three cleaning scenarios as explain below. In the first one, we assume that the PV panels are being cleaned once by the end of each month. This means that our daily predictions for transmittance loss are factored in the daily energy generation values, in consideration of the relationship between energy losses and transmittance losses for each month. Then, reset the daily predictions for transmittance losses at beginning of the next month.

The monthly energy generation is summed up at each tilt and the monthly patterns are shown in Fig. 5. Given the trend of the reduction in the transmittance loss prediction model, the patterns of yearly energy corresponding to optimum tilts have changed. With higher tilts, there will be lower impact due to dust on the optimum energy generation values.

The percentage of yearly energy losses from the optimum values, due to dust, is 43%, 30% and 17% corresponding to 6°, 29° and 52°, respectively. With higher tilts (winter optimum), the solar system is estimated to outperform the summer optimum and the overall optimum. The difference in the total yearly energy production between the winter optimum and the summer and overall optimums is 31% and 11%, respectively.

The second scenario assumes that the surfaces are being cleaned twice in a month, once at the middle of the month and a second time at the end on the month. Being applied in the model, the daily energy generated is factored by the prediction of transmittance/energy daily loss up to day 15. Then, the transmittance/energy daily loss prediction model is reset to start again on day 16 up to the end of the month. The percentage of yearly energy losses from the optimum

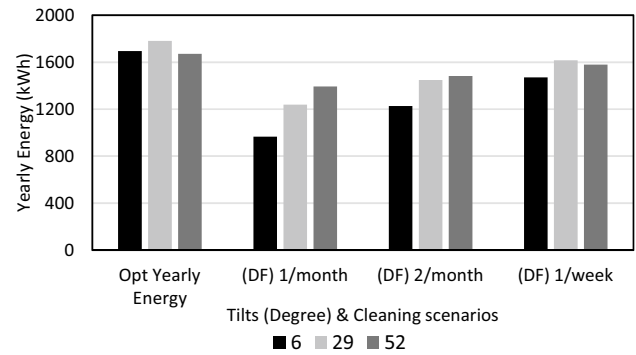


Fig. 6 Yearly energy generated (kWh) at different cleaning scenarios

values is 28%, 19% and 11% corresponding to 6°, 29° and 52°, respectively. The difference in the total yearly energy production between the winter optimum (which remained being the highest producing tilt as in the first scenario) and the summer and overall optimums are 17% and 2%, respectively.

The Third scenario considers that the cleaning is being done by the end of every week. With this scenario a change happens to the order of which tilt can generate more energy from the previous scenarios. The percentage of yearly energy losses from the optimum values is 13%, 9% and 5% corresponding to 6°, 29° and 52°, respectively. The overall optimum tilt (29°) in this scenario has the most yearly energy generation value. The difference in the total yearly energy production between the overall optimum and the summer and winter optimums are 9% and 2%, respectively.

Figure 6 summaries the yearly energy generated for PVs at tilt 6°, 29° and 52°. The first set of columns on the left represents the yearly energy generated without the consideration of dust (or daily cleaning). The next set from the left considers system cleaning by the end of every month. The set follows, represents system cleaning at day 15 and the last day of every month. The last set on the right considers cleaning by the end of every week.

To understand the effect of the cleaning frequency on the energy losses, Fig. 7 shows the patterns of yearly energy generated, corresponding to different tilts, for every scenario simulated and compared with the optimum values.

From Fig. 6, the amount of energy that can be generated by PVs positioned at the optimum summer tilt (6°) and cleaned once a week will produce energy almost equal to the energy produced by PVs tilted at the winter optimum tilt (52°) but clean twice a month. Furthermore, the winter optimum tilt (52°), cleaned once a week preforms better than the PVs positioned at the optimum tilt being cleaned once or twice a month. Figure 7 shows the effect of the frequency of PV cleaning, and how the dust effect on the transmittance becomes less as the tilt increases.

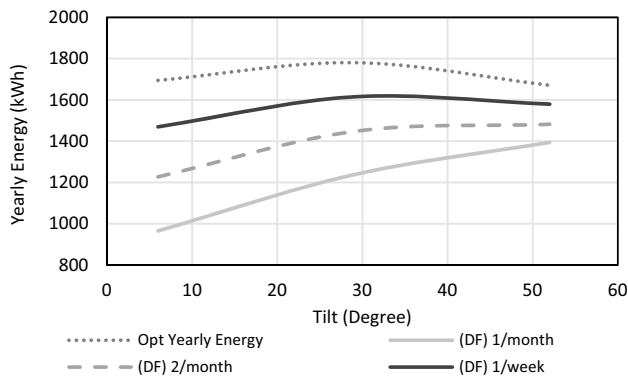


Fig. 7 Comparison of energy generation patterns at different cleaning scenarios

Those results indicated that the dust accumulation and the frequency of cleaning can influence the tilt position of PVs and the objective of maximising their energy production. The module is useful in suggesting alternative tilts that are not only based on the regional-optimum angle of solar radiance. Due to dust and its varying accumulation rate at different tilts, the optimum tilt for producing energy becomes a function of the days of exposure and the frequency of cleaning that can be decided by the user. The model can be the basis for cost–benefit analysis, taking into account the amounts of resources required (water and manpower) to clean the PV’s and their associated costs, as well as the potential damage from the accumulating dust particles on the PV surfaces, in deciding the optimum tilt for energy production.

Future research

While our model can be limited to the relationship between the transmittance loss, PV tilt and the duration of exposure in Kuwait and regions with similar climate/dust-fall rates, the same approach can be adapted to study the performance of PV’s in other regions. Our methodology can be applied to analyse the performance of PVs against snow fall and its accumulation rate in regions where snow is common with a long winter season. Furthermore, more on-site experiments to test the output of PV systems within a full year, using different set of panels, at different tilts and cleaned at different durations are needed. While such experiments might be lengthy and time consuming, the output will provide detailed data of the seasonal impact of dust, as well as the possible transmittance recovery/deterioration from the rare rainfall events.

Conclusion

The impact of dust accumulation on PV systems’ efficiency has been addressed in several studies. Regional data and laboratory experiments were used to quantify the amount of dust on the systems’ surfaces, evaluate the losses in efficiency and determine the frequency of cleaning required. The optimum PV tilt is theoretically calculated based on the regional angle of solar radiance, to give the highest amount of yearly energy generation potential. As the amount of dust accumulating on a surface is highly associated with its tilt, we have built a prediction model to assess the performance of PVs at different tilts. Instead of recommending the frequency of cleaning needed to sustain the performance of that optimum position, we use the prediction model to assess the most efficient tilt for energy production, while considering different scenarios for the frequency of cleaning.

We model the relationship between the loss in transmittance from a PV cover and its tilt, being exposed to the environmental conditions in Kuwait. Given the regional nature of dust events, the prediction model is built using the Kriging method, based on data specific to Kuwait and regions with similar climate characteristics. The results from the prediction model indicate that the transmittance loss can reach more than 50% within a month of exposure in Kuwait due to dust. The closer the surfaces tilt to being horizontal, the rate of loss in transmittance becomes higher.

The optimum tilt for yearly energy generation based on solar radiation calculations for Kuwait is 29°, and based on our prediction model, will only produce the highest amount of energy if cleaned at least once a week. The optimum tilt for energy generation changes based on the frequency of cleaning, and higher tilts become more efficient when the duration of exposure without cleaning increases. With weekly cleaning, the losses in energy production (compared to energy production rates without factoring in the dust prediction model) are 9% and 5% corresponding 29° and 52°, respectively. The difference in yearly energy between PVs at 29° and 52° tilts becomes only 2%. Every other scenario, with cleaning frequency of less than once a week, disputes the recommended tilt of 29°, as it no longer remains the optimum yearly energy generation tilt.

Acknowledgements We acknowledge the support of Kuwait Petroleum Corporation (KPC) and its subsidiary Kuwait Oil Company (KOC).

Declarations

Conflict of interest On behalf of all authors, the corresponding author states that there is no conflict of interest.

Open Access This article is licensed under a Creative Commons Attribution 4.0 International License, which permits use, sharing, adaptation, distribution and reproduction in any medium or format, as long as you give appropriate credit to the original author(s) and the source, provide a link to the Creative Commons licence, and indicate if changes were made. The images or other third party material in this article are included in the article's Creative Commons licence, unless indicated otherwise in a credit line to the material. If material is not included in the article's Creative Commons licence and your intended use is not permitted by statutory regulation or exceeds the permitted use, you will need to obtain permission directly from the copyright holder. To view a copy of this licence, visit <http://creativecommons.org/licenses/by/4.0/>.

References

- Hassan, A.H., Rahoma, U.A., Elminir, H.K.: Effect of airborne dust concentration on the performance of PV modules. *J. Astron. Soc. Egypt* **13**, 24–38 (2005)
- Almufarrej, A.M., Erfani, T.: Climate, buildings' envelope design and energy patterns: improving energy performance of new buildings in Kuwait. *Eng. Constr. Archit. Manag.* (2021). <https://doi.org/10.1108/ecam-04-2021-0360>
- Al-Otaibi, A., Al-Qattan, A., Fairouz, F., Al-Mulla, A.: Performance evaluation of photovoltaic systems on Kuwaiti schools' rooftop. *Energy Convers. Manag.* **95**, 110–119 (2015). <https://doi.org/10.1016/j.enconman.2015.02.039>
- Asl-Soleimani, E., Farhangi, S., Zabihi, M.S.: The effect of tilt angle, air pollution on performance of photovoltaic systems in Tehran. *Renew. Energy* **24**, 459–468 (2001). [https://doi.org/10.1016/S0960-1481\(01\)00029-5](https://doi.org/10.1016/S0960-1481(01)00029-5)
- Nahar, N.M., Gupta, J.P.: Effect of dust on transmittance of glazing materials for solar collectors under arid zone conditions of India. *Sol. Wind Technol.* **7**, 237–243 (1990). [https://doi.org/10.1016/0741-983X\(90\)90092-G](https://doi.org/10.1016/0741-983X(90)90092-G)
- Kazem, H.A., Chaichan, M.T.: The effect of dust accumulation and cleaning methods on PV panels' outcomes based on an experimental study of six locations in Northern Oman. *Sol. Energy* **187**, 30–38 (2019). <https://doi.org/10.1016/j.solener.2019.05.036>
- Sarver, T., Al-Qaraghuli, A., Kazmerski, L.L.: A comprehensive review of the impact of dust on the use of solar energy: history, investigations, results, literature, and mitigation approaches. *Renew. Sustain. Energy Rev.* **22**, 698–733 (2013). <https://doi.org/10.1016/j.rser.2012.12.065>
- AlBusairi, H.A., Möller, H.J.: Performance evaluation of CdTe PV modules under natural outdoor conditions in KUWAIT. In: 5th World Conf. Photovolt. Energy Convers., 25th European Photovoltaic Solar Energy Conference and Exhibition, Valencia, Spain, pp. 29–36 (2010)
- Abdeen, E., Orabi, M., Hasaneen, E.S.: Optimum tilt angle for photovoltaic system in desert environment. *Sol. Energy* **155**, 267–280 (2017). <https://doi.org/10.1016/j.solener.2017.06.031>
- Jiang, H., Lu, L., Sun, K.: Experimental investigation of the impact of airborne dust deposition on the performance of solar photovoltaic (PV) modules. *Atmos. Environ.* **45**, 4299–4304 (2011). <https://doi.org/10.1016/j.atmosenv.2011.04.084>
- Goossens, D., Van Kerschaver, E.: Aeolian dust deposition on photovoltaic solar cells: the effects of wind velocity and airborne dust concentration on cell performance. *Sol. Energy* **66**, 277–289 (1999). [https://doi.org/10.1016/S0038-092X\(99\)00028-6](https://doi.org/10.1016/S0038-092X(99)00028-6)
- Miller, D.C., Kurtz, S.R.: Durability of Fresnel lenses: a review specific to the concentrating photovoltaic application. *Sol. Energy Mater. Sol. Cells* **95**, 2037–2068 (2011). <https://doi.org/10.1016/j.solmat.2011.01.031>
- Roth, R.B., Pettit, E.P.: Effect of soiling on solar mirrors and techniques used to maintain high reflectivity. *Sol. Mater. Sci.* (1980). <https://doi.org/10.2172/5249717>
- Alamoud, A.R.M.: Performance evaluation of various flat plate photovoltaic modules in hot and arid environment. *J. King Saud Univ. Eng. Sci.* **12**, 235–242 (2000). [https://doi.org/10.1016/S1018-3639\(18\)30716-5](https://doi.org/10.1016/S1018-3639(18)30716-5)
- Ali, H.M., Zafar, M.A., Bashir, M.A., Nasir, M.A., Ali, M., Siddiqui, A.M.: Effect of dust deposition on the performance of photovoltaic modules in city of taxila, Pakistan. *Therm. Sci.* **21**, 915–923 (2017). <https://doi.org/10.2298/TSCI140515046A>
- Elminir, H.K., Ghitas, A.E., Hamid, R.H., El-Hussainy, F., Beheary, M.M., Abdel-Moneim, K.M.: Effect of dust on the transparent cover of solar collectors. *Energy Convers. Manag.* **47**, 3192–3203 (2006). <https://doi.org/10.1016/j.enconman.2006.02.014>
- Garg, H.P.: Effect of dirt on transparent covers in flat-plate solar energy collectors. *Sol. Energy* **15**, 299–302 (1974)
- Wakim, F.: Introduction of PV Power Generation to Kuwait. Kuwait Institute for Scientific Research (1981)
- Sayigh, A.A.M., Al-Jandal, S., Ahmed, H.: Dust effect on solar flat surfaces devices in Kuwait (1985)
- Al-Hasan, A.Y.: A new correlation for direct beam solar radiation received by photovoltaic panel with sand dust accumulated on its surface. *Sol. Energy* **63**, 323–333 (1998). [https://doi.org/10.1016/S0038-092X\(98\)00060-7](https://doi.org/10.1016/S0038-092X(98)00060-7)
- Sulaiman, S.A., Hussain, H.H., Siti, N., Leh, H.N., Razali, M.S.I.: Effects of dust on the performance of PV panels. *World Acad. Sci. Eng. Technol.* **5**, 2028–2033 (2011)
- Alshebani, M.: A critical review of solar energy and dust in Gulf Countries. *Int. J. Eng. Res. Appl.* **11**, 43–73 (2021). <https://doi.org/10.9790/9622-1101044373>
- Bunyan, H., Ali, W.: Investigating of proper photovoltaic panel tilt angle to be used as shading device in Kuwait. *J. Eng. Res. Appl.* **5**, 1–8 (2015)
- Kimber, A., Mitchell, L., Nogradi, S., Wenger, H.: The effect of soiling on large grid-connected photovoltaic systems in California and the Southwest Region of the United States. In: *Conf. Rec. 2006 IEEE 4th World Conf. Photovolt. Energy Conversion, WCPEC-4*, vol 2, pp. 2391–2395 (2006). <https://doi.org/10.1109/WCPEC.2006.279690>
- Hegazy, A.A.: Effect of dust accumulation on solar transmittance through glass covers of plate-type collectors. *Renew. Energy* **22**, 525–540 (2001). [https://doi.org/10.1016/S0960-1481\(00\)00093-8](https://doi.org/10.1016/S0960-1481(00)00093-8)
- Sacks, J., Welch, W.J., Mitchell, T.J., Wynn, H.P.: Design and analysis of computer experiments. *Stat. Sci.* **4**, 15–51 (1989). <https://doi.org/10.1214/ss/1177012413>
- Cressie, N.: Spatial prediction and ordinary kriging. *Math. Geol.* **20**, 405–421 (1988). <https://doi.org/10.1007/BF00892986>
- Lophaven, S.N., Søndergaard, J., Nielsen, H.B.: *Kriging Toolbox Dace* (2002)
- Ineichen, P.: Long term satellite hourly, daily and monthly global, beam and diffuse irradiance validation. In: *Interannual Variability Analysis. (Adapted to CM-SAF product from the IEA 2013 report), C. SAF Clim. Monit. 4th User Work. Adapted to CM-SAF product from the IEA 2013 report.* http://www.cuepe.ch/archives/annexes-iae/ineichen-2014_long-term-saf-validation.pdf (2014)
- El-nashar, A.M.: Seasonal effect of dust deposition on a field of evacuated tube collectors on the performance of a solar desalination plant. *Desalination* **239**, 66–81 (2009). <https://doi.org/10.1016/j.desal.2008.03.007>

Publisher's Note Springer Nature remains neutral with regard to jurisdictional claims in published maps and institutional affiliations.



contain 19 articles

springer

تابستان ۱۴۰۲

September 2023